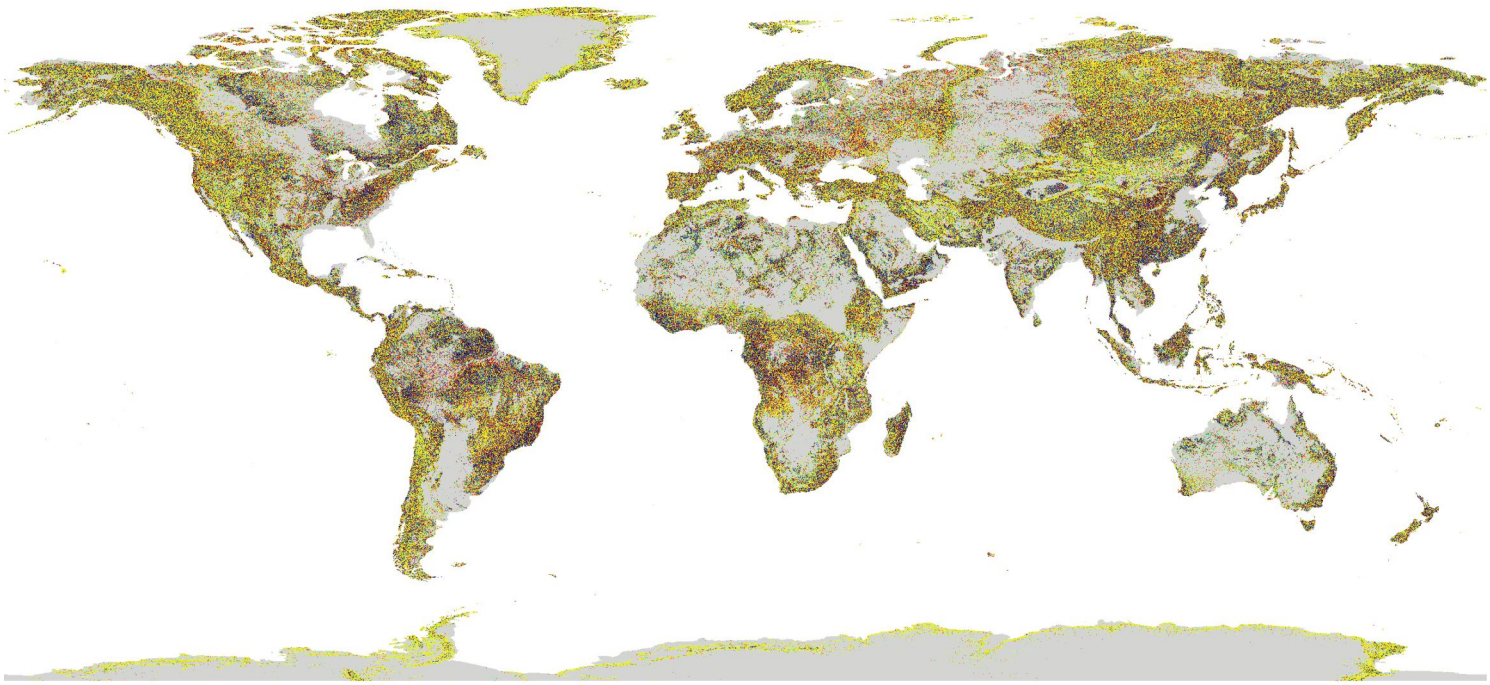
Geomorphometry for Geosciences



Editors:
Jarosław Jasiewicz, Zbigniew Zwoliński, Helena Mitasova, Tomislav Hengl

geomorphometry.org

Geomorphometry for Geosciences

This volume is a contribution
to the 4th International Conference on Geomorphometry
Geomorphometry 2015: Conference and Workshops
Geomorphometry for natural hazards geomodelling
Poznań (Poland), June 22-26, 2015

Adam Mickiewicz University in Poznań - Institute of Geoecology and Geoinformation
International Society for Geomorphometry
Association of Polish Geomorphologists
International Association of Geomorphologists' Working Group on Landform Assessment for Geodiversity

Geomorphometry for Geosciences

Editors:
Jarosław Jasiewicz, Zbigniew Zwoliński, Helena Mitasova, Tomislav Hengl

Poznań 2015

© 2015 by Authors & Institute of Geoecology and Geoinformation, Adam Mickiewicz University in Poznań

Editors:
Jarosław Jasiewicz, Institute of Geoecology and Geoinformation, Adam Mickiewicz University in Poznań, Poland
Zbigniew Zwoliński, Institute of Geoecology and Geoinformation, Adam Mickiewicz University in Poznań, Poland
Helena Mitasova, Department of Marine Earth and Atmospheric Sciences, North Carolina State University, NC, USA
Tomislav Hengl, International Soil Reference and Information Centre, Wageningen University and Research, the Netherlands

ISBN ISBN 978-83-7986-059-3

This publication is supported by: Ministry of Science and Higher Education of Poland, Adam Mickiewicz University in Poznań, Esri Polska

Book folding: Jarosław Jasiewicz, Jakub Nowosad

Cover image: 90m resolution geomorphometry map of the World (geomorphons mode) by Mitasova, H., Jasiewicz, J., Stepinski, T., Neteler., M., Gebbert, S., (2014) Analysis of Giga-size Earth Observation Data in Open Source GRASS GIS 7 - from Desktop to On-line Solutions, AGU Fall Meeting, SF, California, 2014

Citation: Jasiewicz J., Zwoliński Zb., Mitasova H., Hengl T. (eds), 2015. Geomorphometry for Geosciences. Adam Mickiewicz University in Poznań - Institute of Geoecology and Geoinformation, International Society for Geomorphometry, Poznań, pp. 278.

Publisher: Bogucki Wydawnictwo Naukowe, Poznań 2015

Printed in Poland from camera-ready materials provided by the Authors

Table of Contents

Manfred Zink, Alberto Moreira
TanDEM-X: A Challenging Radar Mission for Generating a New Earth's Topography 1

Christopher Wecklich, Carolina Gonzalez, Benjamin Bräutigam
Height Accuracy for the First Part of the Global TanDEM-X DEM Data 5

Carlos Grohmann
'Radiography of the Amazon' DSM/DTM data: comparative analysis with SRTM, ASTER GDEM 9

Piotr Woźniak
High resolution elevation data in Poland 13

Shangmin Zhao, Li Wang and Wenjiao Wu
Vertical error distribution of ASTER GDEM V2 data based on ICESat/GLA14 data:taking Shanxi Plateau of China as an example 15

Zbigniew Zwoliński and Joanna Gudowicz
Geomorphometric analysis of morphoclimatic zones on the Earth 19

Vincent Lecours, Vanessa Lucieer, Margaret Dolan and Aaron Micallef
An Ocean of Possibilities: Applications and Challenges of Marine Geomorphometry 23

Jozef Minar, Jozef Minar and Ian S. Evans
Towards exactness in geomorphometry 27

Karin Ebert, Jerker Jarsjö and Karin Ekstedt
Effects of future sea level rise – the example of the island of Gotland, Sweden 31

Liyang Xiong and Guoan Tang
Pre-Quaternary paleotopography reconstruction in the Ordos platform and its integration in the loess landform evolution modeling 35

Peter Guth
Geomorphometry of Normal Faults: Abyssal Hills and Continental Rifts 39

Marco Bacenetti, Luca Ghiraldi, Marco Giardino and Luigi Perotti
Analysis of morphometric index to evaluate the tectonic activity: case study from Germanasca valley (NW Italy) 43

Peter Bandura, Jozef Minár, Tatiana Harciníková and Lucian Drăguţ
Towards delineation of the morphostructural division of the Western Carpathians using object-based image analysis 47

Yuichi S. Hayakawa, Hidetsugu Yoshida, Lucian Dragut and Takashi Oguchi
Comparative analysis of manual and automatic extractions of hummock landforms in Mt. Gassan, northwestern Japan 51

Domenico Guida, Antonello Cestari, Alba Cuomo, Francesco Dramis, Vincenzo Palmieri and Vincenzo Siervo
The Salerno University Geomorphological Informative Mapping System: the Licosa polygenetic case study (Cilento European geopark, southern Italy) 53

Piotr Wężyk
Making the invisible visible – the DTM modelling in complex environments 57

Waldemar Kociuba
Geometrical parameters of TLS-based DEM acquisition for a small Arctic catchment (Svalbard SW) 61

Marjan Temovski and Ivica Milevski
DEM based geomorphometric analyses of karst surface in the Republic of Macedonia 65

Michal Gallay, Ján Kaňuk, Jaroslav Hofierka, Zdenko Hochmuth and John Meneely
Mapping and geomorphometric analysis of 3-D cave surfaces: a case study of the Domica Cave, Slovakia 69

Marek Kasprzak, Artur Sobczyk, Szymon Kostka and Anna Haczek
Surface geophysical surveys and LiDAR DTM analysis combined with underground cave mapping – an efficient tool for karst system exploration: Jaskinia Niedźwiedzia case study (Sudetes, SW Poland) 75

Ian Evans and Nicholas J. Cox
Size and shape of glacial cirques 79

Andrea Mandarino, Francesca Ferraris and Marco Firpo
Understanding landscape evolution by using DEM analysis, low order channels gradient and Asymmetry Factor: the case study of the upper Scrivia river basin (Northern Apennines, Italy) 83

Fayuan Li and Mingwei Zhao
Slope landscape change in a simulated watershed 87

Ivica Milevski and Anita Milevska
Improvement of slope angle models derived from medium to fine-scale DEM's Key study: Skopje area 91

Markus Metz
Searching for water: hydrological modelling concepts in GRASS GIS 95

Tomasz Niedzielski, Bartlomiej Mizinski, Dapeng Yu
Hydrological forecasting in real time: an experimental integrated approach 97

Jarosław Jasiewicz, Jolanta Czerniawska
Conditional hydrological simulations as a tool for analysis of denudational transformation of post-glacial plains 103

Laura Coco, Viviana Cestrone and Marcello Buccolini
Geomorphometry for studying the evolution of small basins: an example in the Italian Adriatic foredeep 107

Libor Burian, Andrey Mitusov and Jean Poesen
Relationships of attributes of gullies with morphometric variables 111

Adam Łajczak, Barbara Czajka and Ryszard Kaczka
Reinterpretation of morphometry of headwater areas using LiDAR data in homoclinal flysch mountain ridge modelled by landslides. Case study of the Babia Góra Mt., the Western Carpathians 115

Ovidiu Csillik, Ian S. Evans and Lucian Drăguț
Automated transformation of slope and surface curvatures to avoid long tails in frequency distributions 119

Xiaoli Huang, Kai Liu and Liyang Xiong
The Influence of DEM Resolution on the Extraction of Terrain Texture 123

Bartłomiej Szypuła
Relief Index (RI) as a simple tool for geomorphometry 127

Shuanglin Liu, Fayuan Li, Ruqiao Jiang, Ruixue Chang and Wei Liu
A Method of Automatic Topographic Recognition Based on Slope Spectrum 129

Vincent Lecours, Alvin Simms, Rodolphe Devillers, Vanessa Lucieer and Evan Edinger
Finding the Best Combinations of Terrain Attributes and GIS software for Meaningful Terrain Analysis 133

Scott Peckham
Longitudinal Elevation Profiles of Rivers: Curve Fitting with Functions Predicted by Theory 137

Tomasz F. Stepinski, Jaroslaw Jasiewicz, Pawel Netzel and Jacek Niesterowicz
Doing Geomorphometry with Pattern Analysis 141

Przemysław Stpiczyński, Dominik Szałkowski, Leszek Gawrysiak and Łukasz Chabudziński
Hybrid implementation of evaluation of primary topographic parameters using GPU-accelerated clusters 145

Sergio Camiz and Maurizio Poscolieri
Geomorpho: a program for the classification of terrain units 149

Jarosław Jasiewicz, Alfred Stach, Jakub Nowosad
Terrain misclassification problem – analysis using pattern simulation approach 153

Anita Bernatek
Visualizing morphometric changes in a piping system using DEM and GIS analysis: the Bieszczady Mts., Poland 157

Charles Jackson
Caution: dust storms may do exist (and so do mountains): Modeling dust source suitability within an object-oriented geoecology 161

Viktor Kaufmann and Andreas Kellerer-Pirklbauer
Regional quantification of rock glacier movement in Central Austria using authoritative data sources 165

Rafal Wawer and Artur Lopatka
Thermal satellite scenes in single event modelling of wind erosion 169

Vaclav Petras, Helena Mitasova and Anna Petrasova
Mapping gradient fields of landform migration 173

Marco Giardino, Luigi Perotti, Walter Alberto, Sara Ratto
Multidimensional approach to natural instabilities in mountain areas: how geomorphometry can improve both hazard modelling and risk perception 177

Janusz Wasowski, Fabio Bovenga, Raffaele Nutricato, Davide Oscar Nitti and Maria Teresa Chiaradia
High resolution satellite SAR multi temporal interferometry for regional scale detection of landslide and subsidence hazards 181

François Clapuyt, Veerle Vanacker, Kristof Van Oost and Fritz Schlunegger
Very-high resolution monitoring of movement of surface material within a landslide 185

Xavier Bodin, Dario Trombotto and Alvaro Soruco
Evaluation of a terrestrial photogrammetry method for the study of high mountain dynamics. Quebrada del Medio rock glacier, Mendoza, Argentina 189

Mario Kummert and Reynald Delaloye
Quantifying sediment transfer between the front of an active alpine rock glacier and a torrential gully 193

Rafał Kroczak and Tomasz Bryndal
An attempt to assess the influence of road network on flash flood wave parameters. The case study of the Carpathian Foothills 197

Mihai Niculita
Automatic extraction of landslide flow direction using geometric processing and DEMs 201

Daniele Strigaro, Massimiliano Moretti, Matteo Mattavelli, Mattia De Amicis, Valter Maggi and Antonello Provenzale
Development of GIS methods to assess glaciers response to climatic fluctuations: a Minimal Model approach 205

Cheng-Zhi Qin, Xue-Wei Wu, Yanjun Lu, Jing-Chao Jiang and A-Xing Zhu
Case-based formalization of knowledge on digital terrain analysis 209

Magdy Torab and Nora Dalal
Natural hazards mapping of mega waves on the NW coast of Egypt 213

Piotr Kłapyta and Natalia Kolecka
Combining laser scanning with field mapping and Schmidt-hammer relative age dating - examples from the Babia Góra range (Westen Carpathians, Poland) 217

Aleksander Adamczyk, Marcin Sobiech, Agata Urbańska and Wojciech Wysota
Geomorphometric analysis of glacial curvilineations (GCL) in Dobrzyń Lakeland, Central Poland 221

Lucas Ruiz and Xavier Bodin
Analysis and improvement of surface representativeness of high resolution Pléiades DEMs: Examples from glaciers and rock glaciers in two areas of the Andes 223

Ruqiao Jiang and Guoan Tang
A Method of Depression Filling with Consideration of Local Micro-relief Features 227

Marcin Brach and Jarosław Chormański
Comparison of digital elevation models of riparian wetland generated from airborne laser scanning of different accuracy 231

Edina Józsa
Extracting possible terrace surfaces from digital elevation models – methodological issues and case study from Hungary 235

Ângelo Moura Araújo, Paulo Pereira, Renato Henriques and Diamantino Pereira
Water resources assessment using GIS procedures: application in Ceará State (Brazil) 237

Adriana Sărășan and Lucian Drăguț
Assessing contextual information from SRTM data as abasis for classifying landform types. Case study: dune fields 241

Maciej Hajdukiewicz
The potential accuracy of the survey of landform changes using archival orthophotos: case study of the Białka River valley 243

Milena Różycka, Aleksandra Michniewicz, Piotr Migoń and Marek Kasprzak
Identification and morphometric properties of landslides in the Bystrzyckie Mountains (Sudetes, SW Poland) based on data derived from airborne LiDAR 247

Małgorzata Mazurek
Geomorphometric attributes of channel heads initiated by seepage erosion in a postglacial zone (NW Poland) 251

Virginia Ruiz-Villanueva, Markus Stoffel and Hanna Hajdukiewicz
Understanding large wood deposition during floods: a modelling approach 255

Cezary Kaźmierowski, Jakub Ceglarek, Jerzy Cierniewski, Jarosław Jasiewicz, Sławomir Królewicz and Michał Wyczałek
Soil surface roughness quantification using DEM obtained from UAV photogrammetry 259

Claudia Scopesi, Ivano Rellini, Marco Firpo, Michael Maerker, Elmar Schmaltz and Silvia Olivari
Assessment of an extreme flood event using rainfall-runoff simulation based on terrain analysis in a small Mediterranean catchment(Vernazza, Cinque Terre National Park) 263

Zbigniew Zwoliński and Ewa Sznigir
Spatial distribution of hypsometric curves within the Parsęta River drainage basin (Poland) as a geoindicator of geomorphological hazards 267

Zbigniew Zwoliński and Estera Stefańska
Relevance of moving window size in landform classification by TPI 273

Preface

Geomorphometry is the science of quantitative land surface analysis also known under names Digital Terrain Modelling, Digital Terrain Analysis and/or relief analysis. It has deep roots in geomorphology and finally oriented towards supervised and unsupervised landform classification. This volume is a contribution to the 4th bi-annual global meeting of the International Society for Geomorphometry (ISG). Every two years world-wide top specialists on geocomputation of digital elevation data meet to discuss existing and emerging trends of DEM acquisition, processing and application. Themes in this volume revolve around three main threads. Data acquisition concentrates on different methods of high resolution of new elevation data acquisition: from local through regional to world-wide scale. Geoprocessing thread focuses on novel method of computation of big elevation data as well as improvement of existing ones. Finally application path presents among others how different data and methods gives a new prompt to the various aspects of monitoring natural processes and natural hazards geomodelling. However the interdisciplinary nature of geomorphometry makes it a key science for natural hazards: from land observations which can serve as ground truth to mathematical models. Therefore the key theme of the Conference and workshops Geomorphometry 2015 is *Geomorphometry for natural hazards geomodelling*. Changes in appearance of land surface are either incremental or more abrupt if caused by catastrophic processes such as floods, earthquakes, landslides, tornadoes, storms, etc. The possibility of prediction of resultant hazards is one of the most important challenges for many disciplines of environmental sciences, geomorphological modelling had focused on incremental processes with catastrophic processes or natural hazards receiving less attention. Development of new technologies of data acquisition and new software as well as monitoring of Earth surface both on global and local scales provides a growing amount of worldwide-extend high resolution DEMs which require a new kind of geomorphometric tools capable of handling, analyzing, and visualizing large quantities of data in real time.

We are grateful to all members of the ISG Scientific Committee and selected regular members of the ISG for their reviewing of submitted contributions.

Jarosław Jasiewicz, Zbigniew Zwoliński, Helena Mitasova, Tomislav Hengl

Geomorphometry.org/2015

TanDEM-X: A Challenging Radar Mission for Generating a New Earth's Topography

Manfred Zink and Alberto Moreira
German Aerospace Center (DLR)
Microwaves and Radar Institute (HR)
82230 Weßling/Oberpfaffenhofen, Germany
Manfred.Zink@dlr.de

Abstract — **TanDEM-X is a challenging radar mission. It consists of a synthetic aperture radar interferometer with two almost identical satellites flying in a closely controlled formation. With a typical separation between the satellites of 120 to 500 m a global Digital Elevation Model (DEM) with 2 m relative height accuracy at 12 m posting is being generated. While the main mission phase for DEM data acquisition has been finished by mid-2014, the processing of the global TanDEM-X DEM will be concluded by mid-2016. Final DEMs for Australia, large parts of North America, South America, Africa and Siberia are already available for scientific and commercial applications. The results achieved so far are well within the expected performance for the global DEM. A 15-month science phase of the TanDEM-X mission started in October 2014 which offers the opportunity to generate DEMs with even higher accuracy for selected areas, and to explore and demonstrate the new scientific applications of this unique mission.**

Index Terms—**Synthetic Aperture Radar (SAR), Spaceborne SAR, Interferometry, Digital Elevation Model (DEM).**

I. INTRODUCTION

TanDEM-X is the first radar interferometer in space that employs two satellites operating in a closely controlled formation flight. TerraSAR-X, the first satellite of the formation, was launched in June 2007 and is providing high-resolution X-band radar images for commercial and scientific applications [1], [2], [2]. TanDEM-X, an almost identical satellite to TerraSAR-X, was launched in June 2010 [4] and is equipped with an additional 36 kg cold gas tank to allow precise maneuvers for keeping the formation flight. In addition, TanDEM-X has a larger solid-state mass memory with 768 Gbit (twice the size of TerraSAR-X) to support the on-board data buffering and downlink of the large data amount during interferometric acquisitions. While both radar satellites are operated during the interferometric acquisition mode, either the TerraSAR-X or the TanDEM-X satellite is used for acquiring high-resolution 2-D radar images.

The primary objective of the TanDEM-X mission is the generation of a global Digital Elevation Model (DEM) of the Earth's surface with unprecedented accuracy as the basis for a wide range of commercial applications as well as for scientific research. It is expected that this data set will become a new reference in geosciences and remote sensing applications since its 3-D information content is ca. 30 times more accurate than the presently available global scale DEM data set. The first DEM data sets are available since January 2014 and the complete DEM will be available by mid-2016.

TanDEM-X has an ambitious time schedule to reach its main mission goal. After the commissioning phase, the first four years were dedicated to the global DEM acquisitions. To facilitate dual-baseline phase unwrapping all land masses were covered at least twice in the same looking direction but with different baselines. Difficult mountainous terrain required additional acquisitions viewing from the opposite direction to allow filling gaps due to shadow and layover. The main mission phase dedicated to DEM acquisition has been finished by mid-2014. By the end of 2014 final DEMs for approx. 35% of the landmasses will be available. The data quality assessment shows that all specifications for the DEM accuracy are being met.

The baseline geometry in these first 4 years was optimized for DEM performance (see Fig. 1). A limited number of scientific acquisitions was included during this first mission phase depending on the available satellite resources and the suitability of the baseline values for fulfilling the scientific requirements. With the start of the science phase in October

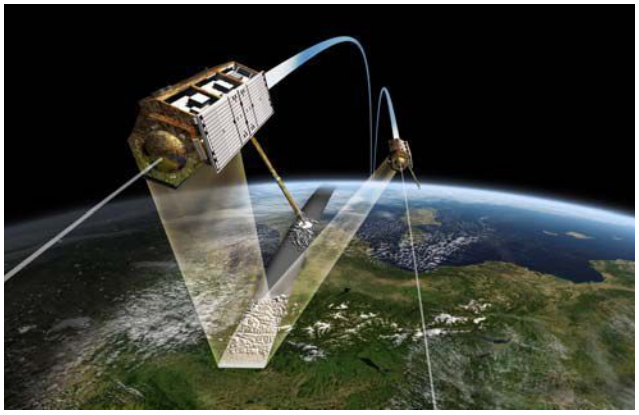


Fig. 1. – TanDEM-X artistic view. With across-track baseline values ranging from 120 to 500 m interferometric radar data for generating a high-resolution global Digital Elevation Model (DEM) has been acquired between December 2010 and mid-2014.

In: Geomorphometry for Geosciences, Jasiewicz J., Zwoliński Zb., Mitasova H., Hengl T. (eds), 2015. Adam Mickiewicz University in Poznań - Institute of Geoecology and Geoinformation, International Society for Geomorphometry, Poznań

2015 the data acquisition and the baseline settings are now dedicated to the secondary objectives of TanDEM-X. Beyond the generation of a global DEM, local DEMs of even higher accuracy level (posting of 6 m and relative vertical accuracy of 0.8 m) and applications based on Along-Track Interferometry (ATI) like measurements of ocean currents are important secondary mission objectives. Along-track interferometry also allows for innovative applications to be explored and can be performed by the so-called dual-receive antenna mode on each of the two satellites and/or by adjusting the along-track distance between TSX and TDX to the desired value. Furthermore, TanDEM-X supports the demonstration and application of new SAR techniques, with focus on multistatic SAR, polarimetric SAR interferometry, digital beam forming and super resolution.

II. The Ground Segment

The missions TerraSAR-X and TanDEM-X jointly share the same space segment consisting of the TSX and TDX satellites orbiting in close formation and are operated using a common ground segment, that was originally developed for TerraSAR-X and that has been extended for the TanDEM-X mission [5]-[8]. Specific new developments are described in the following.

The spatial baseline between the TSX and TDX is derived at millimeter accuracies from on-board GPS measurements taken by the two-frequency IGOR GPS receivers.

A key issue in operating both missions jointly is the different acquisition scenarios: whereas TerraSAR-X requests are typically single scenes for individual scientific and commercial customers, the global DEM requires a global mapping strategy. This strategy has also to account for the current formation flying geometry which, in turn, depends on the orbit parameters selected and for any given orbit configuration permits generating a digital elevation model only within a certain latitude range.

The two satellites downlink their data to a global network of ground stations: Kiruna in Sweden, Inuvik in Canada, and O'Higgins in the Antarctic. The global acquisitions for the digital elevation model alone absorbed a data volume of more than 350 Terabytes. After a brief quality check, the data have been recorded on tape and shipped to DLR in Oberpfaffenhofen for processing and archiving.

The entire processing chain is a new TanDEM-X specific development. Major design drivers result from the acquisition strategy which requires the combination of several (global) coverages and application of multi-baseline processing techniques based on supporting intermediate products. Absolute height calibration relies on a selected set of reference points of the globally distributed elevation data provided by the laser altimeter from NASA's ICESat mission.

III. Close Formation Flight

An orbit configuration based on a helix geometry has been selected for safe formation flying. The helix like relative movement of the satellites along the orbit is achieved by combination of an out-of-plane (horizontal) orbital displacement imposed by different ascending nodes with a radial (vertical) separation imposed by the combination of different eccentricities and arguments of perigee. Since the satellite orbits never cross, the satellites can be arbitrarily shifted along their orbits. This enables a safe spacecraft operation without the necessity for autonomous control. Cross- and along-track baselines ranging from 120 m to 10 km and from 0 to several 100 km, respectively, can be accurately adjusted depending on the measurement requirement [7].



Fig. 2. – Predicted height accuracy of the TanDEM-X DEM derived from the interferometric coherence after the first and second global acquisition which were performed from December 2010 until March 2013. Subsequent data acquisitions until mid-2014 are not included in this prediction.

IV. Mission Status and Outlook

After the launch in June 2010 the monostatic commissioning phase was dedicated to calibration and performance verification and revealed calibration accuracies and overall performance of the TDX SAR system and its products as good as for TSX. Following comprehensive testing of the various safety measures close formation was achieved mid October 2010 and the operations at typical distances between 120 and 500 m is running remarkably smooth and stable since then.

The subsequent bistatic commissioning phase of the TanDEM-X mission concentrated on checking out the complete bistatic chains from acquisition planning to bistatic and interferometric processing and generation of so-called Raw DEMs. Global DEM acquisitions started in December 2010. Parallel to the first month of operational data acquisition the team concentrated its efforts on the calibration of the bistatic interferometer. Correction of differential delays between TSX and TDX was necessary to facilitate the utilization of radargrammetry for resolving the 2π-ambiguity band. A comprehensive monitoring system has been established to evaluate the performance of each individual data take and provide feedback to the TanDEM-X acquisition planning for additional acquisitions. Phase, delay and baseline calibration have reached such an accuracy level [10], that more than 90% of all Raw DEMs are within ±10 m of DEM derived from SRTM/ICESat data already before the final calibration step using ICESat data as reference heights.

The first and second global coverage (except Antarctica) were completed in January 2012 and March 2013 respectively. After some gap-filling, Antarctica was mapped for the first time under local winter conditions. In early August 2013 the helix formation was changed to allow imaging of mountainous areas from the opposite viewing geometry. To enable the highly successful dual-baseline phase unwrapping also for these areas a third and fourth coverage was acquired. Afterwards the satellite were maneuvered back to the original formation and Antarctica was covered again at larger baselines. The primary data acquisition program was concluded by mid-2014. Since then gap-filling is being performed in parallel to the science phase.

Until the end of the science phase in December 2015 even more accurate DEMs on local scales will be generated. Applications based on Along-Track Interferometry (ATI) and new SAR techniques, with focus on multistatic SAR, polarimetric SAR interferometry, digital beam forming and super resolution will be demonstrated.

V. Conclusions

Accurate calibration of radar system delay, phase synchronization between the TSX and TDX radar systems as well of the interferometric baselines have been successfully carried out showing excellent system performance (cf. Fig. 2). While the main DEM acquisition phase has been finished in mid-2014, the generation of the global TanDEM-X DEM has commenced and about 35% of the land surface is already available (see examples in Fig. 3 and 4). The results achieved so far are well within the expected performance for a global DEM with 2 m height accuracy.

During the science phase of TanDEM-X, DEMs of even higher accuracy will be produced for selected areas. In addition, this dedicated mission phase featuring interferometric acquisitions with flexible and even larger baselines in experimental modes is focused in the demonstration of the scientific capabilities of this unique mission.

TanDEM-X has demonstrated the feasibility of an interferometric radar mission with close formation flight and delivers an important contribution for the concept and design of future SAR missions. One example is Tandem-L, a mission proposal for monitoring dynamic processes on the Earth surface with unprecedented accuracy [11], [12].



Fig. 3. – Digital Elevation Model (DEM) generated by TanDEM-X over the Finke Gorge National Park, close to Alice springs, Australia.

REFERENCES

[1] Moreira, A., Krieger, G., Hajnsek, I., Hounam, D., Werner, M., Riegger, S., Settelmeyer, E.: TanDEM-X: a TerraSAR-X Add-on Satellite for Single-Pass SAR Interferometry, Proceedings of the International Geoscience and Remote Sensing Symposium - IGARSS, Ancorage, Alaska, 2004.

[2] Krieger, G., Moreira, A., Fiedler, H., Hajnsek, I., Werner, M., Younis, M., Zink, M.: Tan-DEM-X: A Satellite Formation for High Resolution SAR Interferometry. IEEE Transactions on Geoscience and Remote Sensing, vol. 45, no. 11, pp. 3317-3341, Nov. 2007.

[3] Zink, Manfred; Bachmann, Markus, Bräutigam, Benjamin, Fritz, Thomas, Hajnsek, Irena, Moreira, Alberto, Wessel, Birgit, and Krieger, Gerhard: TanDEM-X: The New Global DEM Takes Shape. IEEE Geoscience and Remote Sensing Magazine, vol. 2, No. 2, pp. 8-23, June 2014.

[4] Pitz, W., Miller, D.: The TerraSAR-X Satellite. IEEE Transactions on Geoscience and Remote Sensing, vol. 48, no. 2, pp. 615–622, Feb. 2010.

[5] Buckreuss, S., Schättler, B., The TerraSAR-X Ground Segment, IEEE Transactions on Geoscience and Remote Sensing, vol. 48, no. 2, pp. 623-632, 2010.

[6] Schättler, B., Kahle, R., Metzig, R., Steinbrecher, U., The Joint TerraSAR-X/TanDEM-X Ground Segment, Proc. IGARSS 2011, pp. 2298 – 2301, IEEE, 24.-29. Jul 2011, Vancouver, Canada.

[7] Kahle, R., Schlepp, B.: Extending the TerraSAR-X Flight Dynamics System for TanDEM-X. 4th International Conference on Astrodynamics Tools and Techniques. 3-6 May 2010, Madrid.

[8] Breit, H., Younis, M., Balss, U., Niedermeier, A., Grigorov, C., Hueso Gonzalez, J., Krieger, G., Eineder, M., Fritz, T.: Bistatic Synchronisation and Processing of TanDEM-X Data, Proceedings of IGARSS, Vancouver, 2011.

[9] Krieger, G., M. Zink, Bachmann, M., Bräutigam, B., Breit, H., Fiedler, H., Fritz, T., Hajnsek, I., Hueso Gonzalez, J., Kahle, R., König, R., Schättler, B., Schulze, D., Ulrich, D., Wermuth, M., Wessel, B., Moreira, A.: TanDEM-X. In: Distributed Space Missions for Earth System Monitoring, Chapter 13, Springer, 2012, pp. 387 – 435.

[10] Bachmann, M., Hueso Gonzalez, J., Krieger, G., Schwerdt, M., Walter Antony, J., De Zan, F.: Calibration of the Bistatic TanDEM-X Interferometer. European Conference on Synthetic Aperture Radar (EUSAR), Nuremberg, Germany, 2012.

[11] Krieger, G., Hajnsek, I., Papathanassiou, K., Younis, M., Moreira, A.: Interferometric Synthetic Aperture Radar (SAR) Missions Employing Formation Flying. Proceedings of the IEEE, vol. 98, no. 5, 2010.

[12] Moreira, A., G. Krieger, I. Hajnsek, K. Papathanassiou, M. Pardini, M. Eineder, M. Shimada, T. Motohka, M. Watanabe, M. Ohki, A. Uematsu and S. Ozawa; Tandem-L: Monitoring Earth's Dynamics with PolInSAR. Proceedings of the PolInSAR Workshop, Frascati, Italy, 2015.

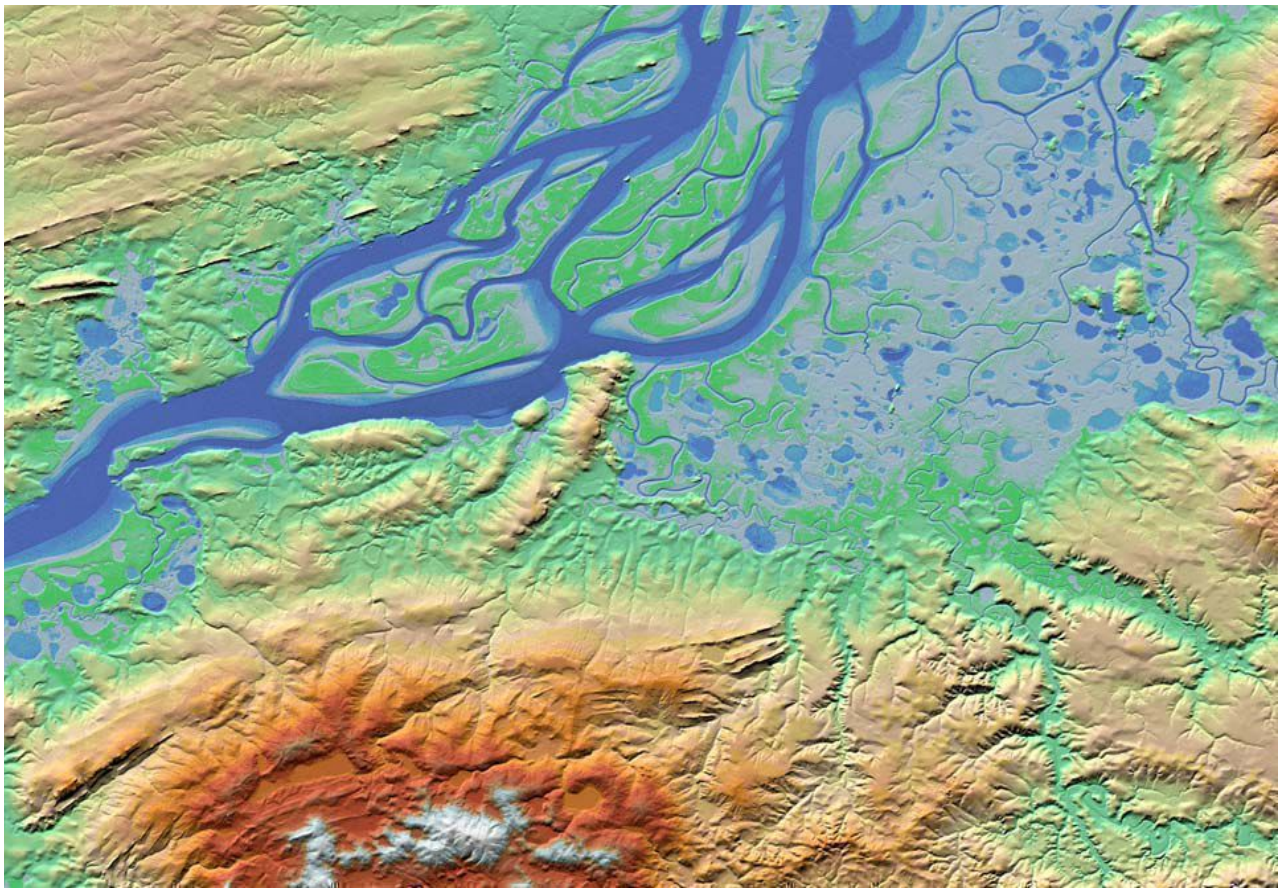


Fig. 4. – Digital Elevation Model (DEM) generated by TanDEM-X over Kara Sea, Pyasina river, Russia

Height Accuracy for the First Part of the Global TanDEM-X DEM Data

Christopher Wecklich, Carolina Gonzalez, Benjamin Bräutigam
Microwaves and Radar Institute, German Aerospace Center (DLR)
Oberpfaffenhofen, Germany

Abstract— **The TanDEM-X system is an innovative radar mission, which is comprised of two formation flying satellites, with the primary goal of generating a global Digital Elevation Model (DEM) of unprecedented accuracy. TanDEM-X, being a large single-pass radar interferometer, achieves this accuracy through a flexible baseline selection enabling the acquisition of highly accurate cross-track interferograms that are not impacted by temporal decorrelation or atmospheric disturbances. At least two global coverages (four in the case of difficult terrain) are combining into a homogenous global DEM mosaic consisting of 1° by 1° geocells. This paper provides a quality summary of the currently available part of the TanDEM-X global DEM with respect to the DEM absolute and relative height accuracy as well as to void density per geocell.**

***Index Terms*—Synthetic Aperture Radar (SAR), Interferometry, bistatic SAR, Digital Elevation Model (DEM), Spaceborne SAR, absolute/relative height accuracy, voids.**

I. INTRODUCTION

Digital Elevation Models (DEMs) are raster-based digital datasets representing the partial or complete topography of a planetary body and are of fundamental importance for a wide range of scientific and commercial applications. In the realm of global DEMs, spaceborne remote sensing is the most efficient way to acquire a global DEM and, within the ±60º latitude band, data from the Shuttle Radar Topography Mission (SRTM) has been the primary source of elevation information [1]. Above 60º latitude and for Antarctica only lower resolution data are available on a large scale. Since 2010 the German Aerospace Center (DLR) has been operating Germany's first two formation flying Synthetic Aperture Radar (SAR) satellites, TerraSAR-X and TanDEM-X, with the objective to generate an updated global DEM which exceeds the presently available global data sets in terms of resolution, coverage, and quality by orders of magnitude. The

The TanDEM-X project is partly funded by the German Federal Ministry for Economic Affairs and Energy (Förderkennzeichen 50 EE 1035).

baseline between the two SAR sensors can be flexibly adjusted for single-pass SAR interferometry which provides the opportunity for accurate cross-track and along-track interferograms overcoming the limitations of atmospheric disturbance and temporal decorrelation in multi-pass data [2].

The primary mission of TanDEM-X is the generation of a world-wide, consistent, current, and high-precision DEM, with a spatial resolution of 0.4 arcseconds (12 m at the equator) and according to the height accuracy specifications listed in Table 1. This paper presents a general introduction into how the TanDEM-X global DEMs are generated as well as the latest quality status (Section II). This is followed by a section each dedicated to the evaluation of absolute and relative height accuracy of the first part of global DEM products (Sections III and IV, respectively). Finally a summary comparison between SRTM and TanDEM-X data in regard to void density is presented.

II. TANDEM-X GLOBAL DEM

A. DEM Generation

SAR interferometry is based on the evaluation of the phase difference between two coherent radar signals acquired from slightly different spatial and/or temporal positions. Using this principle, TanDEM-X is able to measure the range difference between the two satellites and a given scatterer on the ground with millimeter accuracy. The height of the scatterer is then inferred from this range difference by geometric triangulation. As the TanDEM-X radar operates in the X-band, the resulting height represents the reflecting surface of the radar backscatter.

The mapping strategy is to cover all land masses at least twice [3]. The first coverage is acquired at small baselines which facilitates the unwrapping process of the interferometric phase into absolute height values and minimizes decorrelation effects between the two interferometric channels. The second coverage is acquired with large baselines providing an improved relative height accuracy. Difficult terrain is covered

In: Geomorphometry for Geosciences, Jasiewicz J., Zwoliński Zb., Mitasova H., Hengl T. (eds), 2015. Adam Mickiewicz University in Poznań - Institute of Geoecology and Geoinformation, International Society for Geomorphometry, Poznań

TABLE 1: Global DEM Height Accuracy Performance Parameters

Parameter	Specification	Requirement
Absolute Height Accuracy	90% linear error - globally	≤ 10 meters
Relative Height Accuracy	90% linear point-to-point error in 1° x 1 ° geocell	≤ 2 meters (slope ≤ 20%)
		≤ 4 meters (slope > 20%)

at least four times. Examples of difficult terrain are mountains, which require an opposite viewing geometry to compensate radar shadowing and layover effects; forests, which require small baselines to minimize volume scattering decorrelation; and deserts, which require a steep viewing angle for an improved backscatter return [4].

When all the input data of a larger region (i.e. several thousands of square kilometers) are available, the tilts and offsets are calibrated out against ICESat data (a small subset of selected ICESat points) and difference between overlapping TanDEM-X acquisitions. The ICESat dataset was selected because of its global coverage, consistency, and precision [5]. Finally, the mosaicking processor combines all elevation data and produces the output DEM geocells of 1° by 1° size (ca. 110 km by 110 km at equator) [6].

B. DEM Status

The TanDEM-X global DEM acquisition started in December 2010 and the first global coverage (except Antarctica) was completed in January 2012. By the end of July 2014, the Earth's entire land masses had been mapped at least twice (four times in the case of difficult terrain) with varying baselines. Of the nearly 20,000 final DEM geocells to be produced, approximately 50 percent are available as of April 2015. Delivery of DEM products commenced in 2014 and the complete global DEM is expected to be available in late 2016.

III. Absolute Height Accuracy

Table 1 shows that the final DEM product generated by the TanDEM-X system is specified with an absolute height accuracy of at most 10 meter with a 90% linear error. The absolute height accuracy of the TanDEM-X data will be globally validated using the majority of ICESat points that have not already been utilized in the calibration process. When evaluating the absolute height accuracy, only the first 1,000 points with the lowest height variation between DEM pixels within an ICESat footprint are considered. This approach was taken so that geocells with fewer validation points (e.g. coastal regions) are evaluated with similar weight as geocells with more copious comparison points. As the ICESat data is laser-based, there can be an offset to the radar-based TanDEM-X measured height, especially over vegetation or ice where the signal penetration of the two systems can differ [7].

The most current height statistics, as of April 2015, of the available DEMs is shown in Table 2. Of all the ICESat data points that overlap with the available TanDEM-X data (on the order of 35 million), over 8.7 million are within the top 1,000 points of thus generated DEMs. The mean of the height deviation between these validation points and the DEM data is quite small, only 15 centimeters. The linear accuracy level of the validation points for 10 meters is very high at 99.77%. The system specification of an absolute global height accuracy of at most 10 meters with a 90% linear error is met and far exceeded with an accuracy of 1.07 meters.

In addition to the global specification, the absolute height accuracy is also monitored on a geocell basis for all validation points in the geocell. Only twelve out of 9,691 geocells have an absolute height accuracy greater than 10 m, however all of these geocells suffer from volume decorrelation (forest), floating ice sheets, or too few ICESat validation points. The top plot in Figure 1 shows a per geocell overview of the absolute height error for the continent of Africa and the Middle East which was finalized at the start of April 2015. The vast majority of these geocells (over 3,000) have an absolute height accuracy of less than 2 m, 247 geocells are between 2 and 5 m and only 22 are between 5 and 8 m. It is expected that the quality of DEMs over more mountainous terrain will impact the global statistics.

IV. Relative Height Accuracy

The DEM relative height accuracy is important for derivative products that make use of the local differences between adjacent elevation values, such as slope, aspect calculations, and drainage networks. As the system is very well calibrated and tilts and trends are negligible, the relative height accuracy is well described solely by the random errors

TABLE 2: Absolute height accuracy statistics of the TanDEM-X DEM data available as of April 2015

Number of DEM Geocells	9,691
Accumulated Number of Validation Points	8,741,165
Mean Height Deviation of Validation Points (m)	0.15
Accumulated Absolute Height Accuracy of 10 m (linear error)	99.77%
Accumulated Absolute Height Accuracy with 90% Linear Error (m)	1.07

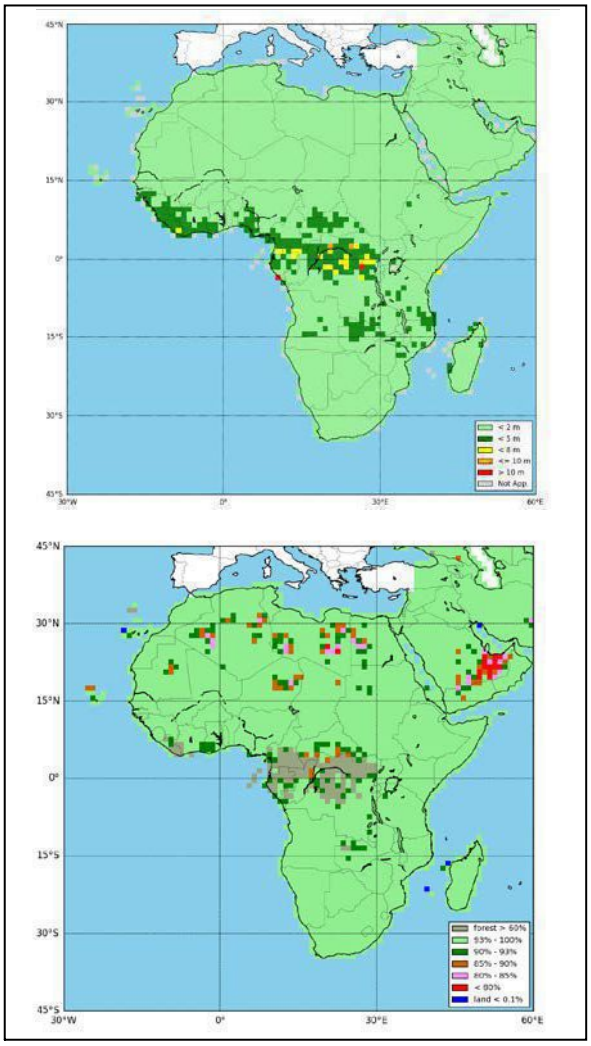


Figure 1: Available TanDEM-X Final DEMs absolute (top) and relative (bottom) height accuracy over Africa and the Middle East per geocell.

in the system, and can be calculated after suppressing the systematic errors and anomalies.

The relative height accuracy per pixel can be estimated from the coherence (and number of looks) between the two SAR channels of the interferogram [2]. As the coherence is a measure for the amount of noise in the interferogram, the respective relative height accuracy is given as the standard deviation (σ) of the corresponding error. The single point height accuracy per pixel is saved into a height error map inside the TanDEM-X product.

The relative height accuracy specification describes the point-to-point error within a 1° x 1° geocell and it states that the confidence level in each geocell shall be above 90% with a height accuracy of 2 m for flat terrain and 4 m for steep terrain. The error distributions of the pixels are assumed to have a Gaussian form. By this, the transformation from single-point accuracy to point-to-point accuracy can be performed by a multiplication of the standard deviation (σ) by $\sqrt{2}$ [2]. The confidence level for the height accuracy Δh over a geocell can be computed by first summing the Gaussian error distribution functions of all m pixels, separated by flat and steep terrain as follows:

$$sP(\Delta h) = \sum_{i=1}^{m} \frac{1}{\sigma_i \cdot 2 \cdot \sqrt{\pi}} e^{-\frac{\Delta h^2}{4 \cdot \sigma_i^2}}$$

The combined confidence level is calculated based on the sum of the areas under the sum probability densities, $sP(\Delta h)$ [8].

9,099 out of 9,691 geocells have a relative height accuracy of more than 90% for the specified 2 m (4 m) of flat (steep) terrain or are not evaluated due to too few data points (e.g. small islands) or sea ice coverage. Furthermore, 514 geocells with lower relative height accuracy are dominated by highly forested areas. Due to volume decorrelation, the coherence estimation is artificially deteriorated and consequently the height accuracy is also artificially deteriorated [2]. Hence, up to now only 143 geocells, or 1.5% of the produced geocells, do not meet the relative height accuracy specification. As an example, the bottom plot in Figure 1 shows the relative height accuracy confidence level for the final TanDEM-X DEMs in Africa and the Middle East.

V. DEM VOIDS SUMMARY

Voids, i.e. invalid pixels, in DEM data arise when a pixel's height cannot be determined during processing and can occur for various reasons, including phase unwrapping anomalies, low return signal power, or shadow/layover effects.

The most up-to-date TanDEM-X statistics show that out of the 9,691 geocells produced thus far, only 175 or 1.8 %, of the geocells contain more than 1 percent of invalid pixels over land. In comparison, over 20% of the geocells in the SRTM version 1.0 data have over 1 percent pixels that are invalid.

Figure 2 shows a comparison of the void percentage per geocell for both the SRTM and TanDEM-X data in Africa and the Middle East. The difference in percent of voids per geocell demonstrates the highly improved quality of the TanDEM-X data. This is especially true in the desert areas of the Sahara and Saudi Arabia, where, a mentioned above, TanDEM-X

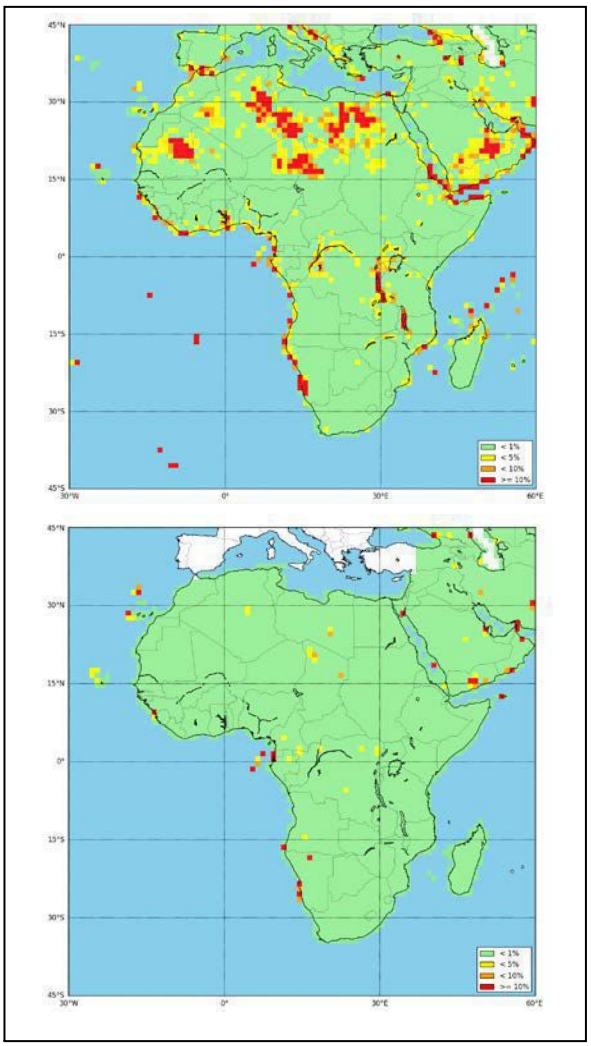


Figure 2: Void Percentage per geocell for SRTM (top) and available TanDEM-X (bottom) data.

performed at least two additional coverages with a steep viewing angle for an improved backscatter return [4].

VI. CONCLUSION

The TanDEM-X mission is an innovative system for spaceborne radar remote sensing, enabling the systematic acquisition of a global, highly accurate digital elevation model (DEM) with unprecedented resolution and accuracy. First parts of the global TanDEM-X DEM became available in 2014 and as of April 2015, 9,691 geocells are available covering 58% of the Earth's land mass.

The final DEM product shall demonstrate an absolute height accuracy of no more than 10 meter with a 90% linear error when evaluated against ICESat data. It has been shown in this paper that the first available part DEMs has reached a level of absolute height accuracy on the order of one meter using almost 8.7 million validation points.

The relative height accuracy of full-resolution DEMs from Tandem-X are specified to meet a linear point-to-point accuracy of 2 m (4 m) with a 90% confidence level for flat (steep) terrain within a geocell. 9,548 out of 9,691 geocells fulfill the relative height accuracy specification.

The percentage of void/invalid pixels over land per geocell in the TanDEM-X DEM data is extremely low with less than 2% of the thus far produced geocells containing over 1% of invalid pixels.

In conclusion, the results presented in this paper for the absolute and relative height accuracy as well as void count of the TanDEM-X DEM data demonstrates the exceptional quality of this global Digital Elevation Model.

REFERENCES

[1] T.G. Farr, P. Rosen, E. Caro, R. Crippen, R. Duren,S. Hensley, M. Kobrick, M. Paller, E. Rodriguez, L. Roth, D. Seal, S. Shaffer, J. Shimada, J. Umland, M. Werner, M. Oskin, D. Burbank, D. Alsdorf, "The Shuttle Radar Topography Mission," Reviews of Geophysics, Vol. 45, 2007.

[2] G. Krieger, A. Moreira, H. Fiedler, I. Hajnsek, M. Werner, M. Younis, M. Zink, "TanDEM-X: A Satellite Formation for High Resolution SAR Interferometry," IEEE Transactions on Geoscience and Remote Sensing, vol. 45, no. 11, pp. 3317-3341, 2007.

[3] D. B. Tridon, M. Bachmann, D. Schulze, C. Ortega-Mìguez, M. D. Polimeni, M. Martone, J. Böer, and M. Zink, "TanDEM-X: DEM acquisition in the third year era," Int. J. of Space Science and Engineering, vol. 1, no. 4, pp. 367–381, 2014.

[4] M. Martone, P. Rizzoli, B. Bräutigam, and G. Krieger, "First two years of TanDEM-X mission: interferometric performance overview," Radio Science, vol. 48, pp. 617–627, October 2013.

[5] J. Hueso Gonzalez, M. Bachmann, R. Scheiber, G. Krieger, "Definition of ICESat Selection Criteria for their use as Height References for TanDEM-X," IEEE Transactions on Geoscience and Remote Sensing, vol. 48, no. 6, pp. 2750-2757, 2006.

[6] B. Wessel, A. Gruber, A. Wendleder, M. Huber, M. Breunig, U. Marschalk, D. Kosmann, A. Roth, "Production Chain towards First Calibrated and Mosaicked TanDEM-X DEMs," IEEE International Geoscience And Remote Sensing Symposium (IGARSS), Vancouver, Canada, 2011

[7] M. Huber, B. Wessel, D. Kosmann, A. Felbier, V. Schwieger, M. Habermeyer, A. Wendleder, A. Roth: "Ensuring Globally the TanDEM-X Height Accuracy: Analysis of the Reference data sets ICESat, SRTM and KGPS-Tracks" IEEE International Geoscience and Remote Sensing Symposium (IGARSS), Cape Town, South Africa, 2009

[8] C. Gonzalez, B. Bräutigam, M. Martone, P. Rizzoli, "Relative Height Error Estimation Method for TanDEM-X DEM Products", European Conference on Synthetic Aperture Radar, Berlin, Germany, 2014

‘Radiography of the Amazon’ DSM/DTM data: comparative analysis with SRTM, ASTER GDEM

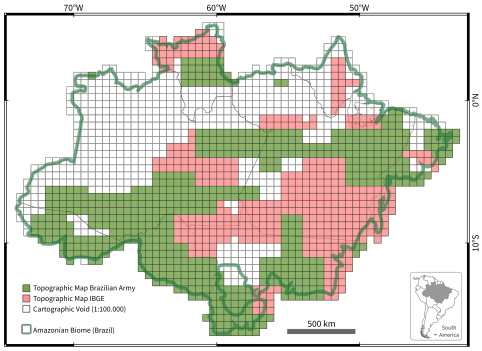
Carlos Henrique Grohmann
Institute of Energy and Environment
University of São Paulo (IEE-USP)
São Paulo, Brazil
guano@usp.br

Abstract—**This paper presents a preliminary comparison of Digital Elevation Models SRTM, Topodata and ASTER GDEM with data from the 'Radiography of the Amazon' project (RAM), for a small study area north of Barcelos city, Amazonas State, Northern Brazil. The RAM project is run by the Division of Geographical Service of the Brazilian Army, and intents to map ca. 1.8 million sq.km. of the Amazon region using InSAR in the P and X bands.The analysis showed that ASTER GDEM presents a high level of noise and artefacts from the automatic image processing chain, with low correlation to the morphology depicted in the other DEMs. RAM Digital Surface Models (i.e., canopy height) have a good correlation with SRTM and Topodata DEMs, although with higher elevation due the use of X-band Radar, which does not penetrates the forest canopy. RAM Digital Terrain Models exhibits the topography under the forest allowing the identification of morphological features that could be hidden under the vegetation. Future studies should be carried out to determine, for instance, the level of detail of DTM-derived drainage networks as well as to evaluate the noise of 5m-resolutions DTMs and possible filtering or smoothing procedures.**

I. INTRODUCTION

The Brazilian Legal Amazon Region encompasses 5.2 million square kilometres. Around 1.8 million square kilometres do not have cartographical information in scales larger than 1:250,000, being known as a ‘cartographic void’ [1] (Fig.1). In order to address this issue, the Brazilian Government created the Amazon Cartography project, with three sub-projects: Land Cartography (also known as Radiography of the Amazon), Geological Cartography and Nautical Cartography [2].

The Land Cartography subproject, under the responsibility of the Division of Geographical Service (DSG) of the Brazilian Army, intents to map the cartographic void of the Amazon region using airborne InSAR in the P (75 cm), L (23 cm) and X (3,1 cm) bands. Mapping will be carried out at 1:100,000 and 1:50,000 scales, covering 1,142,000 km^2 in areas of dense tropical forest and 658,000 km^2 in non-forest areas (natural open fields and anthropized areas) [1].



1. Current status of cartographic mapping in the Legal Amazon Region (adapted from [2])

InSAR Mapping with P, L and X bands allows generation of Digital Terrain Models (DTMs - elevation at ground level), Digital Surface Models (DSMs - elevation of forest canopy) and derived products such as vegetation height and geomorphological classifications [3][4].

In this work we present a preliminar comparison between data from the 'Radiography of the Amazon’ project (RAM) with SRTM, Topodata and ASTER GDEM, for a study area north of Barcelos city, Amazonas State, northern Brazil (area location in Fig. 2).

II. MATERIALS AND METHODS

The Brazilian Army allowed research-level access to RAM data after a formal request was submitted to the Division of Geographical Service. RAM products are distributed according to 1:50,000 scale topo sheets, in 32-bit GeoTIFF files, with spatial resolution of *ca*. 5 meters. In this work we used DTMs and DSMs downloaded from the Brazilian Army Geographic Data Base (BDGEx) [5].

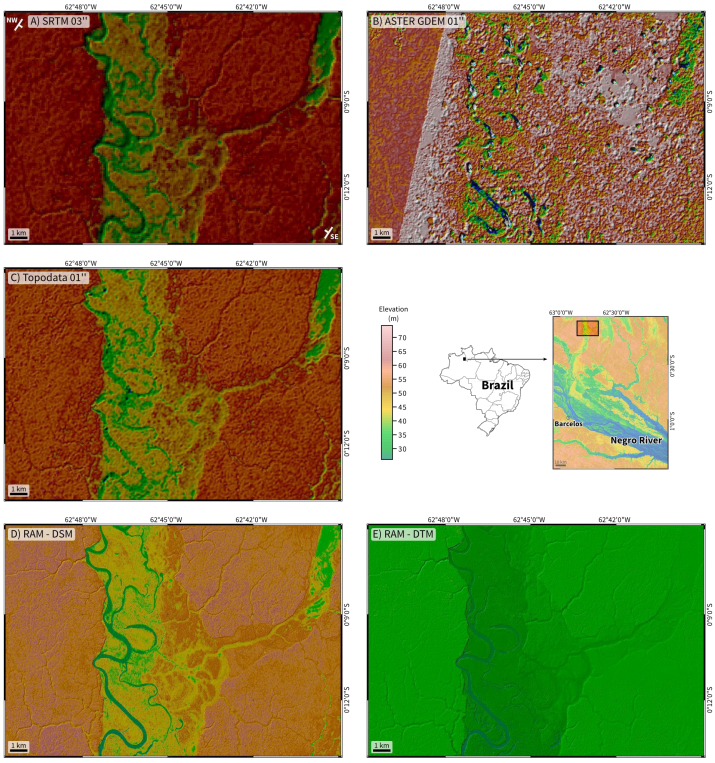
In: Geomorphometry for Geosciences, Jasiewicz J., Zwoliński Zb., Mitasova H., Hengl T. (eds), 2015. Adam Mickiewicz University in Poznań - Institute of Geoecology and Geoinformation, International Society for Geomorphometry, Poznań

SRTM V3.0 data was downloaded from the LPDAAC Data Pool [6] with spatial resolution of 3 arcsec (*ca*. 90m). Topodata is a refinement of original 3-arcsec SRTM to 1-arcsec (*ca*. 30m) with kriging [7][8]; data is distributed by the Brazilian National Institute of Space Research (INPE) [9]. ASTER GDEM version 2 [10] was downloaded from ERSDAC [11], with nominal spatial resolution of 30m. All data was analysed in GRASS-GIS [12], through Python scripts using the Pygrass library [13] to access GRASS' datasets.

III. RESULTS

Fig. 2 shows the elevation of the analysed data, descriptive statistics are presented in Table I, histograms of elevation in Fig. 3, and NW-SE topographic profiles in Fig. 4 (location of profiles in Fig. 2A).

SRTM (Fig. 2A) and Topodata (Fig. 2C) provide a good representation of the landforms in the study area, while ASTER GDEM (Fig. 2B) shows artefacts inherent to the automatic processing of optical imagery and do not depict the local landscape correctly.



2. Shaded relief images of analysed data (illuminant at 315º, inclination 25º). The colorscale is the same for all images.

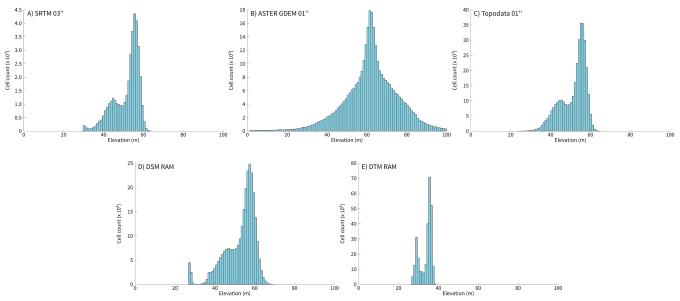
I. DESCRIPTIVE STATISTICS OF ANALYSED ELEVATION DATA

Data	Min	Max	Mean	Median	Std.Dev.	Assim.	Kurt.
SRTM	28.24	64.38	51.72	54.16	6.62	-1.02	0.35
GDEM	-62.00	160.0	61.68	62.00	15.37	-0.62	4.67
Topodata	13.15	66.07	51.81	54.12	6.52	-0.92	0.09
DSM RAM	26.22	74.12	52.83	55.35	7.85	-1.20	1.34
DTM RAM	25.19	39.39	33.80	35.26	3.26	-0.77	-0.91

Distribution of elevation values (Fig. 3) is, generally, asymmetric with two modes representing the forest canopy and the alluvial plain in the central portion of the study area. The exception to this behaviour is ASTER GDEM, with unimodal distribution and high standard deviation (Fig. 3B).

RAM Digital Surface Model (Fig. 2D) shows a histogram of elevation values similar to SRTM and Topodata, without artefacts (Fig. 3D). The higher spatial resolution allow for a greater detail in the fluvial landforms and it is possible to observe sutil variations of elevation of the forest canopy.

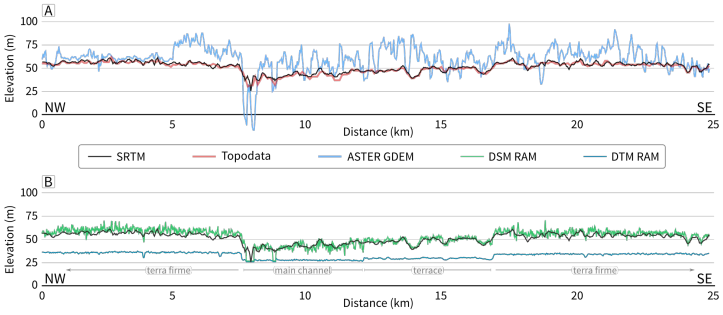
RAM Digital Terrain Model (Fig. 2E) has the smaller standard deviation and range of the analysed data. The distribution of elevation highlights the differences between flood-prone and dry areas (*terra firme*).



3. Histograms of elevation values.

The topographic profiles are useful to visually compare the relations among the analysed data. In Fig. 4A, it is possible to see the similarity between SRTM (black line) and Topodata (red line), although in some places the interpolated data shows an inverse behaviour or underestimate the original data (note the fluvial valley at about 8 km from the origin of the profile, for instance). ASTER GDEM (blue line) is only locally similar to SRTM and do not provide a real representation of the landscape.

Profiles for RAM data are presented in Fig. 4B. DSM data (green line) shows a good visual correlation with SRTM (black line). As one could expect, SRTM values are, in general, lower than RAM DSM, since SRTM was acquired with C band (5.6 cm), which allows for some penetration of the Radar signal in the canopy. RAM DTM (blue line)shows not only the main morphological division between flood-prone and dry areas, but also a subdivision of the lower sector, with a main channel and a fluvial terrace.



4. Topographic profiles (NW-SE) of analysed data. Location of profiles is shown in Fig. 2A.

IV. Discussions and Conclusions

This paper presented a preliminary comparison of Digital Elevation Models SRTM, Topodata and ASTER GDEM with data from the Brazilian Army's 'Radiography of the Amazon' project (RAM).

The analysis showed that ASTER GDEM presents a high level of noise and artefacts from the automatic image processing chain, with low correlation to the morphology depicted in the other DEMs.

RAM Digital Surface Models (i.e., canopy height) have a good correlation with SRTM and Topodata DEMs, although with higher elevation due the use of X-band Radar, which does not penetrates the forest canopy.

RAM Digital Terrain Models exhibits the topography under the forest allowing the identification of morphological features that could be hidden under the vegetation.

Future studies should be carried out to determine, for instance, the level of detail of DTM-derived drainage networks as well as to evaluate the noise present in 5m-resolutions DTMs and possible filtering and/or smoothing procedures.

Acknowledgment

This work was supported by a collaborative Dimensions of Biodiversity-BIOTA grant supported by FAPESP (2012/50260-6), National Science Foundation (NSF), and National Aeronautics and Space Administration (NASA); and by CNPq grant 306294/2012-5. The authors are thankful to the Brazilian Army for data use authorisation. ASTER GDEM data provided by METI/Japan Space Systems.

References

1. Correia, A.H., 2011. “Metodologias e Resultados Preliminares do Projeto Radiografia da Amazônia”. In XV Simpósio Brasileiro de Sensoriamento Remoto - SBSR.

2. CENSIPAM - Centro Gestor e Operacional do Sistema de Protecão da Amazônia, 2008. “Projeto Cartografia da Amazônia: Documento de referência”. Presidência da República, Casa Civil, Brasil, 63p.

3. Correia, A.H., Almeida, F., Oliveira, G.P., Silva, D.L.A., Manfrin, S., 2010. “Projeto Radiografia da Amazônia: Metodologia de Producão Cartográfica com Imagens SAR (Bandas X e P)”. In XXIV Congresso Brasileiro de Cartografia.

4. Oliveira, G.P., Saldanha, M.F.S., Correia, A.H., 2013. “Projeto Radiografia da Amazônia: colorizacão e estratificacão vegetal de dados SAR”. In XVI Simpósio Brasileiro de Sensoriamento Remoto - SBSR.

5. Brazilian Army Geographic Data Base (BDGEx). http://www.geoportal.eb.mil.br

6. Land Processes Distributed Active Archive Center (LPDAAC): https://lpdaac.usgs.gov/data_access/data_pool/

7. Valeriano, M.M., Kuplich, T.M., Storino, M., Amaral, B.D., Mendes, J.N., Lima, D.J., 2006. “Modeling small watersheds in Brazilian Amazonia with shuttle radar topographic mission-90m data” Computers & Geosciences, 1169-1181.

8. Valeriano, M.M. and Rossetti, D.F., 2011. “Topodata: Brazilian full coverage refinement of SRTM data” Applied Geography (Sevenoaks), 300-309.

9. Topodata - Geomorphometric Data Base for Brazil: http://www.dsr.inpe.br/topodata/index.php

10. Tachikawa, T., Hato, M., Kaku, M., Iwasaki, A., 2011. “ Characteristics of ASTER GDEM version 2” Geoscience and Remote Sensing Symposium (IGARSS), 3657-3660.

11. Earth Remote Sensing Data Analysis Center (ERSDAC): http://gdem.ersdac.jspacesystems.or.jp

12. Neteler, M., Bowman, M.H., Landa, M., Metz, M., 2012. “GRASS GIS: A multi-purpose open source GIS” Environmental Modelling & Software, 124-130.

13. Zambelli, P., Gebbert, S., Ciolli, M., 2013. “Pygrass: An Object Oriented Python Application Programming Interface (API) for Geographic Resources Analysis Support System (GRASS)” Geographic Information System (GIS) ISPRS International Journal of Geo-Information, 201-219.

High resolution elevation data in Poland

Piotr Woźniak
Department of Geodesy and Cartography and GIS systems
Head Office of Geodesy and Cartography
Warsaw, Poland
piotr.wozniak@gugik.gov.pl

Abstract—**Governments around the world undertake many countrywide projects and initiatives .to increase public safety using geospatial data and latest achievements in ITC sector. This paper present polish effort to collect and deliver high resolution elevation data for flood risk and hazard mapping process and hints regarding elevation data utilization in other sectors of polish economy.**

I. INTRODUCTION

Directive 2007/60/EC on the assessment and management of flood risks imposes upon member states the obligation of preparing flood hazard and flood risk maps until the end of the year 2013.

To meet those requirements polish Government launched project ISOK - Informatic System for Country Protection against extraordinary hazards. ISOK is implemented by the consortium consisting of Water Management Board, Institute of Meteorology and Water management, Head Office of Geodesy and Cartography, Communication Institute and Government Center for Security. One of crucial tasks is to establish new dataset of high resolution elevation data indispensable for production of flood hazard and risk maps. Utilization of those maps in combination with other datasets will influence spatial planning in Poland strongly and in result increase safety of people and infrastructure in following years "Fig.1".

II. DATA PRODUCTION AND APPLICATIONS

From the March 2011 GUGiK signed 33 contracts with companies from Poland, USA, Portugal, Germany, Holland, Slovenia for acquisition ALS and production of DTM/DSM covering 289'000 km2 (93% of polish territory). During 4 years of production campaign more than 1,3 trillion ALS points will be measured which states more than 10'000 points per each second of campaign. ALS data are collected in two standards: I standard 4 points/m2 covering 275'000 km2 and II standard 12 points/m2 covering 14'000 km2 - (94 cities).

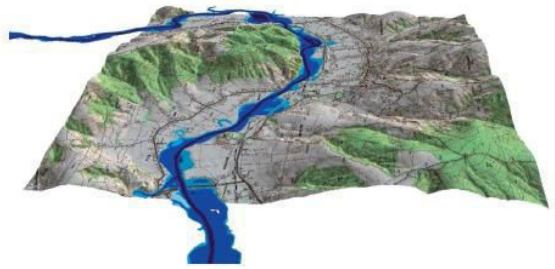


Figure 1. Example of flooding areas visualization.

ALS is collected mainly during off leaf season which means that weather plays a crucial role and only over a dozen of flight days are available for contractors during a year. Process of elevation data quality control is also outsourced so GUGiK is responsible for tendering procedure, contracts supervision, final step of quality control and data delivery to ISOK project consortium partners.

Before end of December 2014 more than 270'000km2 of ALS/DTM/DSM is already done and shared dataset is adopted not only for purposes of hydrological modelling by Institute of Meteorology and Water Management – National Research Institute but for many other applications like geological cartography (Polish Geological Institute – National Research Institute), archeology (Polish Academy of Science – "Fig. 2" presents discovery made by this organization on the basis of DTM) and many others. So far GUGiK shared almost 4 500 000 km^2 of ALS/DTM/DSM data for more than 700 institutions and companies in Poland. Applications in sectors of environment, security and crisis management states almost 70% of total data shared and the rest is utilized in sectors of big national geospatial projects, spatial development, education, science, tourism and sport.

There is a plan to finish full coverage of polish territory with high resolution ALS/DTM/DSM data before June 2016.

In: Geomorphometry for Geosciences, Jasiewicz J., Zwoliński Zb., Mitasova H., Hengl T. (eds), 2015. Adam Mickiewicz University in Poznań - Institute of Geoecology and Geoinformation, International Society for Geomorphometry, Poznań

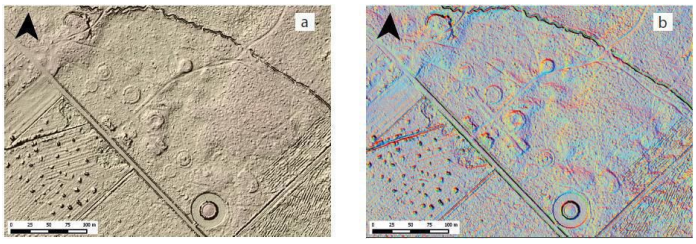


Figure 2. Antique cemetery: a) DTM shaded relief, b) PCA method visualization

TABLE I. SHARE OF HIGH RESOLUTION ELEVATION DATA IN ECONOMY SECTORS

Economy sector	***Data shared in km²***	***% of total share***
Environment	1 560 654	35,4
Security and crisis management	1 444 384	32,8
Geospatial projects	948 702	21,5
Spatial development	391 794	8,9
Science	57 928	1,3
Sport and tourism	4 157	0,1

ACKNOWLEDGMENT

Author would like to express great appreciation to ISOK project team colleagues in GUGiK, Adam Andrzejewski, Anna Marcinkowska, Marzena Kukieła, Piotr Walas, Edyta Kierys-Kukla, Anna Uziembło, Grzegorz Margasiński and Małgorzata Kaczmarczyk Koza. Successful production of high quality dataset of ALS, DTM and DSM for almost whole Poland in 4 years wouldn't be possible without their hard work and enormous engagement.

Vertical error distribution of ASTER GDEM V2 data based on ICESat/GLA14 data: taking Shanxi Plateau of China as an example

Shangmin Zhao
Department of Surveying and Mapping, College of Mining Engineering
Taiyuan University of Technology
Taiyuan, China
zhaoshangmin@tyut.edu.cn

Li Wang
Department of Surveying and Mapping, College of Mining Engineering
Taiyuan University of Technology
Taiyuan, China
wl3001@link.tyut.edu.cn

Wenjiao Wu
Department of Surveying and Mapping, College of Mining Engineering
Taiyuan University of Technology
Taiyuan, China
wwj3256@link.tyut.edu.cn

Abstract—**Taking Shanxi Plateau of China as an example, this study aims to quantitatively analyze the vertical error distribution of the ASTER GDEM V2 data using ICESat/GLA14 data as the benchmark data. The ASTER GDEM V2 and ICESat/GLA14 data were downloaded from USGS and NSIDC respectively, and the ICESat/GLA14 data was used to derive distribution of vertical errors in ASTER GDEM V2 data in the study area firstly; then, the study area was divided into geomorphic units at third class levels, the whole Shanxi Plateau, three regions and eleven subregions. In addition, vertical error distributions were analyzed in these divided geomorphic units; finally, the vertical error distributions among the topographic, landuse and NDVI classes were analyzed. The results show that the vertical error distribution presents a normal distribution in the study area, whose mean and RMSE values are -0.1m and 11.8m respectively. The study area is divided into three geomorphic regions: Central Basin, western Lvliang Mountain and eastern Taihang Mountain; the mean values of the vertical error are 1.1m, 0.0m and -0.6m respectively in the three regions. As to the RMSE values, 9.1m, 12.2m and 12.6m respectively; so the vertical error is low in the middle basin region, but high in the mountain regions of the two sides.With the values of the topographic factors (elevation, slope and relief) increasing, the value of the vertical error becomes higher accordingly. As to the aspect factor, the vertical error is symmetrical along the NE-SW axis; besides, the NE and SW directions has highest positive and negative values respectively. To the NDVI factor, the vertical error decreases with the NDVI values increasing generally; to the land use factor, the highest vertical error distributes in the forestland and grassland.**

Keywords: **vertical error distribution; ASTER GDEM V2; ICESat/GLA14; geomorphic unit; Shanxi Plateau**

I. INTRODUCTION

Digital Elevation model (DEM) data can provide significant information for many research activities [1, 2]. As one of the most used global DEM dataset, ASTER GDEM (Advanced Spaceborne Thermal Emission and Reflection Radiometer Global Digital Elevation Model) V2 data has high spatial resolution (1″) and wide coverage (83ºN–83ºS). So it is used in many applications after its release. Because the feasibility of the application using DEM data depends on its accuracy [3], it is meaningful for estimating the accuracy of the ASTER GDEM V2 data [4]. In this study, we use the ICEsat/GLA14 (the 14the product of the Geoscience Laser Altimeter System on the Ice, Cloud, and land Elevation Satellite) data to provide to an unbiased estimate of the regional accuracy of ASTER GDEM V2 data in the Shanxi Plateau of China, because the ICESat/GLA14 data has high (0.1 m (1σ) for flat bald locations and 1 m (1σ) for undulated and vegetated surface) [5].

II. STUDY AREA

The location of the study area is shown in Fig.1. From Fig.1, the study area is the Shanxi Plateau, which locates in the northern and eastern of China. With Yellow River adjoining the western and southern side, many rivers in the Shanxi Plateau flow into the Yellow River. Shanxi Plateau distributes in the eastern part of the Loess Plateau, so there is deep loess covering here.

The study area presents nearly north-south direction. With Lvliang Moutain and Taihang Mountain in its western and eastern side, there are many intermountain basins in its middle part, such as Datong Basin and Taiyuan Basin.

According to the topographic characterisitcs, the study area is divided into three geomorphic regions. These can be further divided into 12 subregions, which are shown in Fig.1.

In: Geomorphometry for Geosciences, Jasiewicz J., Zwoliński Zb., Mitasova H., Hengl T. (eds), 2015. Adam Mickiewicz University in Poznań - Institute of Geoecology and Geoinformation, International Society for Geomorphometry, Poznań

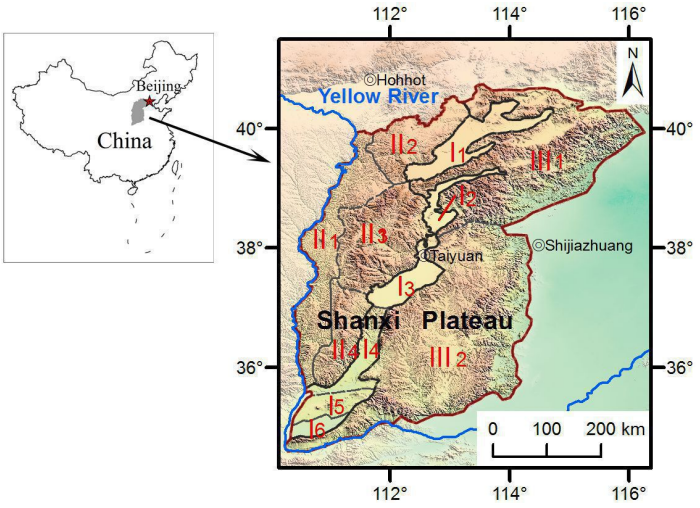


Figure 1. Location and geomorphic units in the study area

In Figure 1, I: Central Basin Region; I_1: Datong Basin Subregion; I_2: Xinding Basin Subregion; I_3: Taiyuan Basin Subregion; I_4: Linfen Basin Subregion; I_5: Emei Platform Subregion; I_6: Yuncheng Basin Subregion; II: Lvliang Mountain Region; II_1: Western Lvliang Mountain Subegion; II_2: Northern Lvliang Mountain Subegion; II_3: Central Lvliang Mountain Subegion; II_4: Southern Lvliang Mountain Subegion; III: Taihang Mountain Region; III_1: Northern Taihang Mountain Subregion; III_2: Southern Taihang Mountain Subregion.

III. METHODOLOGY AND RESULTS

A. Data Process

The data used in this research are mainly ASTER GDEM V2 data and ICESat/GLA14 data.

ASTER GDEM V2 data is the version 2 of the ASTER GDEM, which is an upgrade to version 1 and developed using an advanced algorithm and more data sources. Downloaded from USGS Global Data Explorer, the ASTER GDEM V2 data is processed through mosaic, projection and clipping, which is shown in Fig.2.

ICESat/GLA14 is collected through collected through the U.S. National Snow & Ice Data Centre (NSIDC), and extracted by NGAT tools. The extracted results have 19 phases from 2003 to 2009. The original value is reference to the Topex/Poseidon ellipsoid, so it needs to be transformed to reference the WGS84 ellipsoid using the following equation:

$$ICESat_{\_WGS84} = ICESat_{\_TOPEX} - ICESat_{\_geoid} - Offset \quad (1)$$

where $ICESat_{\_TOPEX}$ and $ICESat_{\_geoid}$ can be directly acquired from the ICESat/GLA14 data, the Offset is a constant, 0.7m[6].

Then, overlapping all the ICESat/GLA14 data 19 phases and clipped by the boundary, the result is shown in Fig.3.

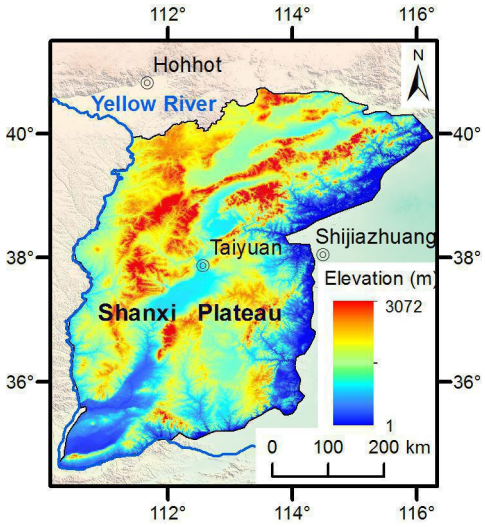


Figure 2. ASTER GDEM V2 data in the study area

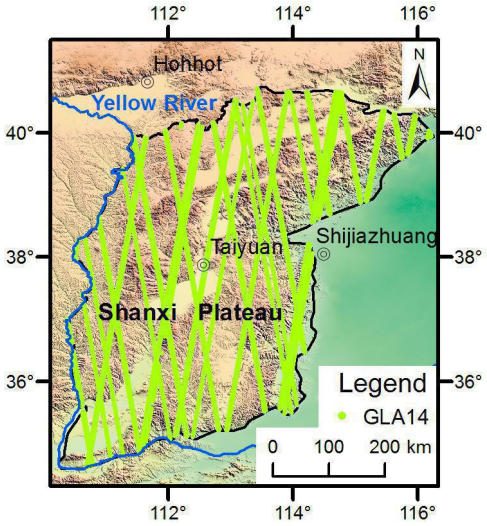


Figure 3. ICESat/GLA14 data in the study area

B. Vertical Error Distribution in the Study Area

Taking the ICESat/GLA14 data as the real value, the difference between the ICESat/GLA14 and ASTER GDEM V2 data is regareded as the vertical error. After removing the ICESat/GLA14 outliers and taking 1m as the interval, the histrogram of the vertical error in the study area is shown in Fig.4, which shows that the vertical error presents a normal distribution.

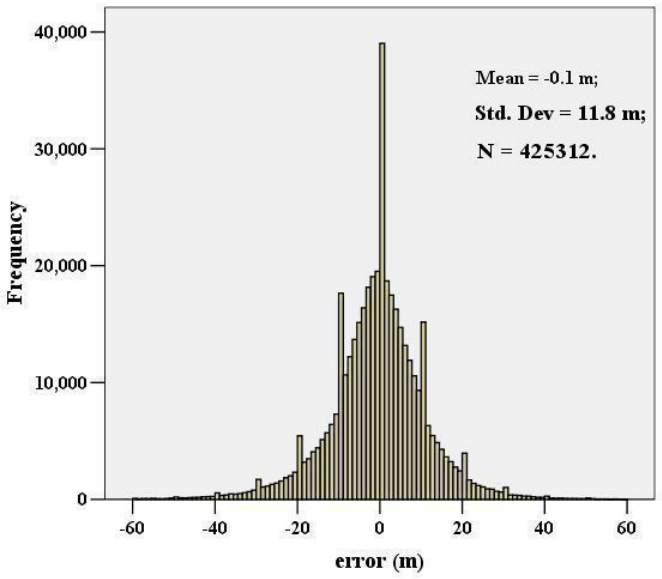


Figure 4. Vertical error distribution frequency in the study area

C. *Vertical Error Distribution in the Geomorphic Units*

The study area is divided into three geomorphic regions, the name and distribution of which are shown in Fig.1. The vertical error stattistics in the three geomorphic regions are computed in Tab.1, which shows thta the vertical error is low in th middle basin, but high in the sides mountains, and the western Lvliang Mountains has highest error values.

TABLE I. VERTICAL ERROR DISTRIBUTION IN GEOMORPHIC REGION (M)

geomorphic unit	vertical error statistics			
	samples	*mean*	*standard deviation*	*RMSE*
I	70666	1.1	9.0	9.1
II	117336	0.0	12.6	12.6
III	237310	-0.6	12.2	12.2

The Three geomorphic regions are re-divided into 12 geomorphic subregions, the vertical error stasitics of which can be shown in Tab.2, which shows: except for the northern Datong Bazsin, from north to south, the vertical error becomes high for the middle basins; this is also suitable for the western Lvliang Mountains, except for the Western Lvliang Moutain subregion; as to the eastern Taihang Mountain, the error is high in the north part but low in the south part, the reason may be because the northern part is steeper than the sourthern part.

TABLE II. VERTICAL ERROR DISTRIBUTION IN GEOMORPHIC SUBREGION (M)

unit	vertical error statistics			unit	vertical error statistics		
	mean	*Std.* [a]	*RMSE*		*mean*	*Std.* [a]	*RMSE*
I_1	-0.4	8.5	8.5	II_1	0.5	12.6	12.6
I_2	-0.7	7.3	7.3	II_2	-1.0	9.2	9.2
I_3	0.9	7.2	7.3	II_3	-0.6	12.2	12.2
I_4	0.7	8.9	9.0	II_4	1.2	15.3	15.4
I_5	4.2	11.4	12.1	III_1	-1.9	12.3	12.5
I_6	7.1	10.4	12.6	III_2	0.3	12.0	12.0

a. Standard deviation value. This is the same for the following cases.

D. *Vertical Error Distribution among the Topographic Factors*

Using the ArcGIS software, the topographic factors are computed using ASTER GDEM V2 data, which are elevation, relief, slope and aspect. Then this factors are classfied by the values. The vertical error statistics in the classes for the elevation factor are shown in Tab.3 (As the standared deviaiton value is simlar to the RMSE value, the RMSE values are ommited in the following tables to reduce space).

Tab.3 shows: with the elevation value increasing, the error changes from positive value to negative values. The absolute error and standard deviation values presents increasing tendency.

TABLE III. VERTICAL ERROR DISTRIBUTION FOR ELEVATION FACTOR (M)

class	*mean*	*Std.*	class	*mean*	*Std.*
<=500	3.2	10.5	2000-2500	-5.7	12.7
500-1000	0.1	12.7	2500-3000	-7.3	13.6
1000-1500	-1.4	13.3	>3000	-10.1	17.3
1500-2000	-2.6	12.9			

The relief factor is computed using 20*20 windows, and the vertical error distribution for the relief factor is acquired in Tab.4, which shows that the absolute error and standard deviation values increase continuously.

TABLE IV. VERTICAL ERROR DISTRIBUTION FOR RELIEF FACTOR (M)

class	*mean*	*Std.*	class	*mean*	*Std.*
<=50	1.1	7.3	200-500	-5.3	17.5
50-200	-1.2	13.0	>500	-12.0	24.1

The error distribution for the slope factor is acquired in Tab. 5, which shows: with the slope value increases, the mean value of the vertical error changes from positive value to negative value,

and decreases continuously; meanwhile, the standard deviation value increases continuously.

TABLE V. VERTICAL ERROR DISTRIBUTION FOR SLOPE FACTOR (M)

class(°)	*mean*	*Std.*	class(°)	*mean*	*Std.*
<=3	0.5	6.8	15-25	-1.9	14.3
3-8	0.1	9.3	>25	-3.9	17.8
8-15	-0.9	12.2			

The vertical error distribution for the aspect factor is acquired in Tab. 6, which shows: the standard deviation values are similar in all the direction; as to the mean value, it is symmetrical along the NE-SW axis; besides, the NE and SW directions have highest positive and negative values respectively.

TABLE VI. VERTICAL ERROR DISTRIBUTION FOR ASPECT FACTOR (M)

class(°)	*mean*	*Std.*	class(°)	*mean*	*Std.*
Flat(-1)	1.6	11.4	S(167.5-202.5)	-4.2	12.3
N(337.5-22.5) [b]	3.2	12.4	SW(202.5-247.5)	-5.9	12.7
NE(22.5-67.5)	3.7	12.8	W(247.5-292.5)	-3.9	12.0
E(67.5-112.5)	2.5	13.1	NW(292.5-337.5)	-1.3	12.1
SE(112.5-167.5)	-0.8	12.5			

b. For "N", "337.5-22.5" means "337.5-360" or "0-22.5".

E. Vertical Error Distribution among the Land Cover Factors

In order to acquire the relationship among the vertical error distribution and the land cover factors, the NDVI and land use data were acquired from remote sensing images. The NDVI data is acquire in August, 2005, the mid acquisition time for both ASTER GDEM V2 and ICESat/GLA14 data. Through classification, the vertical error distribution for the NDVI is computed in Tab. 7, which shows: the standard deviation values are similar, but the mean value changes from negative to positive with the NDVI value increasing; when the NDVI value is higher than 0.8, the mean value return to negative value.

TABLE VII. VERTICAL ERROR DISTRIBUTION FOR NDVI FACTOR (M)

class	*mean*	*Std.*	class	*mean*	*Std.*
< 0.2	-4.2	12.3	0.6-0.8	0.3	12.1
0.2-0.4	-2.0	12.6	> 0.8	-1.2	14.5
0.4-0.6	-1.1	12.4			

The vertical error distribution for the land use factor can be shown in Tab.8, which shows: the highest error values distribute in the forestland and grassland, both for the mean and standard deviation values; as to other classes, the error values are similar.

TABLE VIII. VERTICAL ERROR DISTRIBUTION FOR LAND USE FACTOR (M)

class	*mean*	*Std.*	class	*mean*	*Std.*
paddy field	-0.3	11.1	water	-0.1	11.7
dry field	0.2	10.7	building	0.2	7.8
forestland	-2.2	15.3	unused	-1.4	9.3
grassland	-2.4	13.9			

IV. DISCUSSIONS

In order to make the research results more reasonable, the accuracy of the ICESat/GLA14 data should be estimated in the study area.

V. CONCLUSIONS

By using highly precise ICESat/GLA14 data, we have been able to analyze mean vertical accuracy of the ASTER GDEM v2 product over the study area. The research results show that the vertical errors are greatest for steep slopes, high relief and altitudes, forest and grassland and high NDVI. Bias is negative for high slope gradients, relief and altitude, and for west- and south-facing slopes.

ACKNOWLEDGMENT

This research is under the auspices of the National Natural Science Foundation of China (41301469, 41171332), the Open Foundation of the LREIS and the Qualified Personnel Foundation of Taiyuan University of Technology (QPFT) (tyut-rc201221a).

REFERENCES

[1] Guha, A., Singh, V. and Parveen, R., et al. 2013. "Analysis of ASTER data for mapping bauxite rich pockets within high altitude lateritic bauxite, Jharkhand, India". International Journal of Applied Earth Observation and Geoinformation, 21, 184-194.

[2] Frey, H. and Paul, F., 2012. "On the suitability of the SRTM DEM and ASTER GDEM for the compilation of topographic parameters in glacier inventories". International Journal of Applied Earth Observation and Geoinformation, 18, 480-490.

[3] Dragut, L. and Eisank, C., 2011. "Object representations at multiple scales from digital elevation models". Geomorphology 129: 183–189.

[4] Hengl, T. and Reuter, H., 2011. How accurate and usable is GDEM? A statistical assessment of GDEM using LiDAR data. In: GEOMORPHOMETRY, 45-48, Redlands.

[5] González, J., Bachmann, M. and Scheiber, R., et al. 2010. "Definition of ICESat Selection Criteria for Their Use as Height References for TanDEM-X". IEEE Transactions on Geoscience and Remote Sensing, 48, 2750-2757.

[6] Wang, X., Cheng, X. and Huang, H., et al. 2013. "DEM production for Dome-A combining GPS and GLAS data". Journal of Remote Sensing, 17(2), 439-444.

Geomorphometric analysis of morphoclimatic zones on the Earth

Zbigniew Zwoliński
Institute of Geoecology and Geoinformation
Adam Mickiewicz University in Poznań
Poznań, Poland
zbzw@amu.edu.pl

Joanna Gudowicz
Institute of Geoecology and Geoinformation
Adam Mickiewicz University in Poznań
Poznań, Poland
gudowicz@amu.edu.pl

Abstract— **The aim of the research was the comparison of selected geomorphometric parameters for the Earth morphoclimatic zones, which are classified differently by various authors. An attempt was made to assess the classification of the zones by Büdel [3], Tricart, Cailleux [11] and Poser, Hagedorn [9]. Selected primary and secondary parameters were calculated on the basis of SRTM V4. In the next step of the study the zones were also compared to the Köppen-Geiger climate classification map [10].**

I. INTRODUCTION

Supply of various amounts of solar radiation to the terrestrial Earth's surface from the North Pole to the South Pole causes diversified reactions of geomorphological processes shaping the morphological surface of the Earth. On a diverse supply of solar radiation shall be imposed in addition to its seasonal variability throughout the year. As a result of the repeated delivery of radiation in daily, seasonal, annual, multi-year and even longer cycles and the corresponding dominant, secondary and extreme processes produce on the globe a distinctive belt system matching separate morphoclimatic zones. In view of the permanent recurrence of the same or similar geomorphological processes in similar spatial and temporal scales, is indeed a relief type well enough formed to be grasped by geomorphometric parameterization? Can individual morphoclimatic zones be classified with geomorphometric parameters? Which of the primary or secondary geomorphometric parameters best reflect diversity of the morphoclimatic zones?

The present paper is attempted reply to the above-mentioned question. Selected geomorphometric characteristics will be presented according to different authors. Morphoclimatic zone classifications by Büdel [3], Tricart, Cailleux [11] and Hagedorn, Poser [9] were evaluated. Büdel [3] claims that at each point on the earth climate determines the fundamental combination of morphogenetic processes. His classification is based primarily on morphological criteria which correlate to climate. Tricart, Cailleux' [11] proposed classification is based on two types of criteria: large climatic and biogeographic zones that provide the principal divisions, and subdivisions based on the preceding criteria combined with paleoclimatic differences. Hagedorn and Poser [9] used a combination of geomorphological processes and factors indicating the spatial order of landforms. Zonal morphological and climatic variation of the Earth, therefore, reflects the spatial distribution of the nature and intensity of the ancient and modern processes of erosion, denudation and accumulation. This also includes extreme processes causing various geomorphological hazards corresponding to each zones.

II. DATA AND METHODS

A. Data

Morphoclimatic zone maps by three authors [3], [11] and [9] are obtained from rather low accuracy, literature-published analogue sources which have digitized to get polygon vector layers with consistent coverage for the whole world. Vector data were exported to the same coordinate system.

Elevation data obtained from the Shuttle Radar Topography Mission (SRTM Version 4) were used in the study [6]. For the downloaded tiles mosaic function was used to obtain a complete digital surface model. The disadvantage of the data was the lack

In: Geomorphometry for Geosciences, Jasiewicz J., Zwoliński Zb., Mitasova H., Hengl T. (eds), 2015. Adam Mickiewicz University in Poznań - Institute of Geoecology and Geoinformation, International Society for Geomorphometry, Poznań

of coverage for areas above 56°S and above 60°N. Consequently glacial zones (polar areas) are excluded from the comparison calculation. However, this was not considered an error, because most of the Earth surface area in the glacial zone included Antarctica, Greenland and the Arctic islands, so the areas covered by more than 90-95% of the continental or local ice sheets, do not capture the real nature of the surface topography.

We also analyzed Köppen-Geiger's climatic maps [10] according to the observed data for the period 1976-2000.

B. Methodology

Selected classifications of morphoclimatic zones are based primarily on morphological criteria, however, adopted arbitrarily by the authors, without confirming the results in the quantitative analysis. Currently available digital elevation models (DEM) datasets of global extent make it possible to verify and improve the classifications presented in the literature. In order to examine previously developed maps of morphoclimatic zones multiple parameters were calculated. Primary parameters consisted of relative heights, slope [2], plan and profile curvature [13]. We used in the analysis also the secondary parameters i.e. Topographic Wetness Index [1] and Convergence Index [8]. Within the analyzed zones we also compared automatic landform classification methods based on Topographic Position Index [12], Hammond's classification [4], unsupervised nested-means algorithm and a three part geometric signature; slope gradient, local convexity, and surface texture [5].

For the primary and secondary parameters descriptive statistics such as minimum, maximum, range, mean, standard deviation within each morphoclimatic zone were calculated. Then the parameter maps have been classified on the basis of the natural distribution of Jenks method [7]. Within each morphoclimatic zone, area percentage was calculated for the derived classes of parameters, as well as the percentage of surface forms generated on the basis of automatic classification methods [4, 5, 12].

C. Hardware and software

The data prepared for calculations constitute so called typical **big data**. Apart from input data for calculations, which take up a lot of space, any step calculation data and final results require enormous computing power as well. Therefore, the data pose a big performance challenge for computer hardware and software. The best solution is to use supercomputers with very big virtual memory and big disc space. In the study, ArcGIS v. 10.1 software was used.

III. RESULTS

Because of long-lasting and demanding calculation procedures, it is estimated that all calculations will be concluded in May 2015. The results obtained so far allow looking at the end-results of undertaken analysis with optimism.

Calculations according to unsupervised nested-means algorithm [5] using these authors' data should be considered as first. Iwahashi, Pike [5] obtained terrain class values, as well as terrain series values for the entire world (see last row in Table I). The table also contains newly calculated data for terrain classes and series, for individual morphoclimatic zones according to the classifications of Büdel [3], Tricart, Cailleux [11] and Hagedorn, Poser [9]. Differences for the entire world data between the original Iwahashi, Pike [5] data and the three classifications are relatively small and fall in the range of -3.1 to 2.4%. This means that at the scale of the entire world — regardless of the morphoclimatic zone classification method — the results are similar, despite the fact that glacial zones are not allowed for in the calculations. Extremely interesting information is provided by the analysis of data for the 16-fold terrain classes, which indicate significant differences in individual morphoclimatic zones according to different classifications (Table I, Fig. 1). They show obvious differences in the morphological development of morphoclimatic zones, regardless of classification.

Maps prepared for the primary and secondary geomorphometric parameters constitute the next series of results. Not all of the parameters have proven to be fully useful for the characteristics and differentiation of morphoclimatic zones. However, in many cases the analysis of the special layout of these parameters allows to discover interesting morphogenetic observations. The unquestionable benefit of many geomorphometric parameters is the possibility to indicate the morphometric relief circumstances fostering the presence of geomorphological hazards such as flooding or landslides.

The analysis of other results, including maps resulting from automatic landform classification, is still under way. The preliminary results at the scale of individual continents indicate big interpretation possibilities.

TABLE I. TERRAIN CLASSES AND SERIES ACCORDING TO IWAHASHI AND PIKE (2007) FOR THREE MORPHOCLIMATIC CLASSIFICATIONS OF THE EARTH [%]

Author	Morphoclimatic zones	16-fold terrain classes																4-fold terrain series*			
		1	2	3	4	5	6	7	8	9	10	11	12	13	14	15	16	I	II	III	IV
		Percentage in zones																			
Büdel (1963)	Zone of pronounced valley formation	9.2	2.2	7.8	1.5	21.5	3.5	6.9	1.5	17.3	1.9	3.2	1.0	12.1	3.7	2.5	4.1	60.1	11.4	20.4	8.1
	Extratropical zone of valleys formation	16.1	1.1	8.7	1.9	17.9	2.2	7.3	2.8	12.7	2.0	3.3	1.8	8.5	4.1	2.4	7.3	55.2	9.3	21.7	13.8
	Subtropical zone of pediment and valley formation	18.1	1.0	11.4	4.2	7.7	2.0	8.6	6.2	5.8	1.7	4.8	4.2	3.7	3.4	2.9	14.4	35.3	8.1	27.6	29.0
	Tropical zone of planation surface formation	8.2	0.5	7.8	1.2	13.8	1.3	11.1	2.5	11.8	2.1	7.3	3.4	7.7	4.6	3.9	12.8	41.5	8.5	30.0	19.9
	Average	***12.9***	***1.2***	***8.9***	***2.2***	***15.2***	***2.3***	***8.5***	***3.3***	***11.9***	***1.9***	***4.7***	***2.6***	***8.0***	***4.0***	***2.9***	***9.7***	***48.0***	***9.3***	***24.9***	***17.7***
Tricart, Cailleux (1965)	Periglacial regions without permafrost	13.0	2.5	10.3	1.9	20.6	3.2	7.5	1.5	15.7	1.5	2.9	0.8	11.6	2.4	2.3	2.4	60.9	9.7	22.9	6.5
	Forest on Quaternary permafrost	7.6	3.1	5.9	1.6	25.1	3.0	8.0	1.9	21.8	0.9	3.9	0.7	12.6	0.9	2.1	0.9	67.2	7.8	19.9	5.1
	Maritime forest zone of mid-latitudes with mild winters	26.8	0.7	15.4	1.7	23.1	1.1	8.6	1.2	9.8	0.6	1.9	0.4	5.5	1.3	0.9	1.0	65.3	3.7	26.7	4.3
	Maritime forest zone of mid-latitudes with severe winters	21.4	0.2	12.1	0.5	17.2	0.3	10.4	0.9	11.3	0.4	5.0	0.8	6.1	1.4	3.6	8.4	56.1	2.3	31.1	10.5
	Mid-latitude forest zone of Mediterranean type	9.6	0.3	4.9	0.3	20.9	1.6	6.6	1.1	18.5	1.8	3.8	1.2	13.8	5.0	3.5	7.0	62.8	8.8	18.8	9.7
	Semi-desert steppes	29.2	0.9	19.2	3.9	14.6	0.9	11.2	3.6	3.7	0.5	2.6	1.8	1.0	0.8	1.1	4.9	48.5	3.1	34.2	14.1
	Semi-desert steppes with severe winters	4.6	0.7	5.3	2.5	10.0	3.2	8.4	5.7	8.5	4.3	4.9	5.6	5.1	7.6	2.6	21.1	28.2	15.8	21.2	34.8
	Deserts and degraded steppes without severe winters	3.8	0.7	4.0	2.3	6.2	2.4	8.3	5.9	9.3	3.7	8.7	7.1	7.7	6.7	5.4	17.6	27.0	13.5	26.5	33.0
	Deserts and degraded steppes with severe winters	8.6	1.9	8.6	7.8	4.8	4.5	7.8	12.0	4.4	2.6	3.8	5.6	4.7	4.4	3.0	15.7	22.5	13.4	23.1	40.9
	Savannas	5.4	0.3	5.0	0.6	21.4	1.4	12.1	1.7	13.0	2.0	7.4	2.5	4.9	4.2	3.1	15.0	44.7	7.8	27.6	19.9
	Intertropical forests	9.0	0.3	11.0	0.7	14.0	0.4	12.5	0.7	15.9	0.5	7.7	0.8	12.3	3.1	4.8	6.3	51.2	4.3	36.0	8.5
	Azonal mountain areas	39.4	2.3	18.1	5.1	7.7	1.5	6.9	4.2	2.7	0.7	2.1	1.9	1.4	0.8	1.0	4.2	51.2	5.4	28.0	15.4
	Average	***14.9***	***1.2***	***10.0***	***2.4***	***15.5***	***2.0***	***9.0***	***3.4***	***11.2***	***1.6***	***4.6***	***2.4***	***7.2***	***3.2***	***2.8***	***8.7***	***48.8***	***8.0***	***26.3***	***16.9***
Hagedorn, Poser (1974)	Most intense fluvial processes, very strong mass movements	11.0	0.4	11.3	0.8	14.0	0.3	11.5	0.6	17.2	0.4	6.9	0.5	14.3	2.3	4.6	3.9	56.5	3.4	34.3	5.7
	Fluvial processes and sheet wash	11.5	0.3	9.6	0.8	19.6	0.9	12.2	1.4	10.8	1.0	6.0	1.5	4.2	3.8	2.9	13.3	46.1	6.1	30.7	17.0
	Most intense sheet wash	5.1	0.4	6.4	1.3	13.9	1.8	12.5	3.2	9.7	2.4	8.4	4.2	4.6	4.5	3.6	18.0	33.3	9.1	30.9	26.7
	Most intense eolian processes, episodically strong sheet wash and episodic fluvial processes	3.0	0.9	4.1	3.2	5.5	3.0	7.5	7.2	7.9	4.1	7.1	7.2	6.6	7.5	4.5	20.8	22.9	15.5	23.1	38.5
	Intense slope wash and periodic strong fluvial processes	22.0	1.4	11.5	4.8	10.7	2.3	9.6	6.5	5.6	1.8	4.1	3.6	2.9	2.3	2.1	8.8	41.3	7.7	27.3	23.7
	Moderate fluvial processes, other processes especially weak	12.2	0.5	6.1	0.7	19.5	1.9	6.7	1.5	16.5	2.1	3.7	1.5	11.2	4.9	3.2	7.9	59.4	9.4	19.6	11.6
	Cryo-dynamic processes, including thermoerosion, intense slope wash and fluvial processes	25.1	1.7	13.9	2.9	18.0	1.9	7.5	2.1	10.6	0.9	2.3	0.9	7.0	1.5	1.5	2.1	60.7	6.1	25.2	8.0
	Average	***12.8***	***0.8***	***9.0***	***2.1***	***14.5***	***1.7***	***9.6***	***3.2***	***11.2***	***1.8***	***5.5***	***2.8***	***7.3***	***3.8***	***3.2***	***10.7***	***45.7***	***8.2***	***27.3***	***18.7***
Iwahashi, Pike (2007)		*13.2*	*0.9*	*9.0*	*2.1*	*14.3*	*1.8*	*9.1*	*3.3*	*10.9*	*1.9*	*5.2*	*3.0*	*7.2*	*4.0*	*3.2*	*10.9*	***45.7***	***8.7***	***26.4***	***19.3***

* Explanation of Terrain series: I - 1+5+9+13: fine texture, high convexity; II - 2+6+10+14: coarse texture, high convexity; III - 3+7+11+15: fine texture, low convexity; IV - 4+8+12+16: coarse texture, low convexity

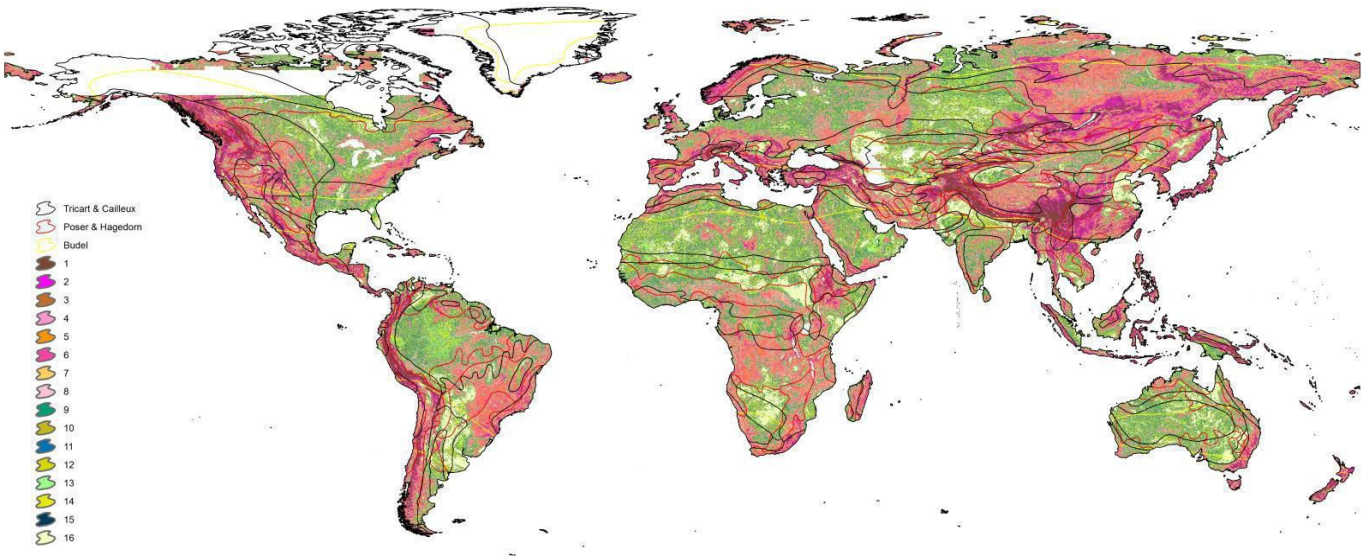


Figure 1. Spatial distribution of the terrain classes according to Iwahashi and Pike (2007) for three morphoclimatic classifications of the Earth.

IV. CONCLUSIONS

The obtained preliminary data confirm the sense of the undertaken research problem. The possibility to use big data in the calculation of geomorphometric characteristics for selected classifications of morphoclimatic zones at the scale of the entire world opens new ways of interpreting the landforms. Budel's proposal [3] should be considered the least useful of the three morphoclimatic classifications analysed. Generally, it may be assumed that the more complex the morphoclimatic classification, the better it adjusts to the spatial geomorphometric diversification of the topographic surface of the world.

Today, automatization of the digital elevation model calculation procedures constitutes one of the more important challenges of geomorphometry. The increase in the number and quality of elevation data through the creation of digital elevation models of higher and higher resolution guarantees such solutions.

REFERENCES

[1] Beven, K.J., Kirkby, M. J., Seibert, J., 1979. "A physically based, variable contributing area model of basin hydrology". Hydrolological Science Bulletin, 24:43–69.

[2] Burrough, P.A., McDonell, R.A., 1998. "Principles of Geographical Information Systems". Oxford University Press, New York, 190.

[3] Büdel, J., 1963. "Klima-genetische Geomorphologie". Geographische Rundschau, 15:269-285.

[4] Dikau, R., Brabb, E.E, Mark, R.M., 1991."Landform classification of New mexico by computer." Open File Report 91-634. U.S Geological Survey.

[5] Iwahashi, J., Pike, R., 2007. "Automated classification of topography from DEMs by an unsupervised nested-means algorithm and three-part geometric signature." Geomorphology 86, 409-440.

[6] Jarvis, A., Reuter, H.I., Nelson, A., Guevara, E., 2008. "Hole-filled seamless SRTM data V4". International Centre for Tropical Agriculture (CIAT). http://srtm.csi.cgiar.org.

[7] Jenks, G.F., 1967. "The Data Model Concept in Statistical Mapping. International Yearbook of Cartography". 7:186–190.

[8] Koethe, R., Lehmeier, F., 1996. "SARA - System zur Automatischen Relief-Analyse". User Manual, 2.

[9] Hagedorn, J., Poser, H., 1974. "Räumliche Ordnung der rezenten geomorphologischen Prozesse und Prozesskombinationen auf der Erde". Abh. Akad. Wiss. Göttingen, Math.-Physik. Kl. III/29, Göttingen: 426-439.

[10] Rubel, F., Kottek, M., 2010. "Observed and projected climate shifts 1901-2100 depicted by world maps of the Köppen-Geiger climate classification". Meteorol. Z., 19, 135-141.

[11] Tricart, J., Cailleux, A., 1965. "Introduction à la géomorphologie climatique". Traité de géomorphologie, tome I, SEDES, París, 306 p.

[12] Weiss, A., 2001. "Topographic position and landforms analysis". Poster Presentation, ESRI User Conference, San Diego, CA.

[13] Zeverbergen, L.W., C.R. Thorne. 1987. "Quantitative Analysis of Land Surface Topography". Earth Surface Processes and Landforms, 12:47–56.

An Ocean of Possibilities: Applications and Challenges of Marine Geomorphometry

Vincent Lecours
Department of Geography
Memorial University of Newfoundland
St. John's, Canada
vlecours@mun.ca

Vanessa L. Lucieer
Institute for Marine and Antarctic Studies
University of Tasmania
Hobart, Australia

Margaret F. J. Dolan
Geological Survey of Norway
Trondheim, Norway

Aaron Micallef
Department of Physics
University of Malta
Msida, Malta

Abstract— **An increase in the use of geomorphometry in the marine environment has occurred in the last decade. This has been fueled by a dramatic increase in digital bathymetric data, which have become widely available as digital terrain models (DTM) at a variety of spatial resolutions. Despite many similarities, the nature of the input DTM is slightly different than terrestrial DTM. This gives rise to different sources of uncertainties in bathymetric data from various sources that will have particular implications for geomorphometric analysis. With this contribution, we aim to raise awareness of applications and challenges of marine geomorphometry.**

I. INTRODUCTION

Exploration and characterization of the ocean floor continuously presents new possibilities and challenges. Thanks to recent and ongoing improvements in acoustic remote sensing technology, seabed relief can now be measured rapidly, extensively and at fine spatial scales [1]. Among these technologies, multibeam echosounder systems (MBES) provide some of the most detailed and accurate data currently available [2]. Most of the MBES data are collected during navigational charting efforts, with a particular focus on shallower coastal waters where the seabed relief can pose a hazard to navigation. Due to potential safety concerns, standards regarding data quality and uncertainty are high for these shallow datasets. Datasets from deeper waters, however, still lag behind in terms of quality and quantity. Owing to the technological challenges and high costs associated with bathymetric mapping of large and deeper parts of the seabed, it is estimated that only 5-10% of the oceans are mapped with a resolution comparable to that on land [3].

The adoption of terrestrial geomorphometric techniques to investigate marine environments increased in the past decade [e.g 4]. The primary digital terrain model (DTM) data source for marine geomorphometry has been bathymetry (depth) grids generated from MBES data. These DTMs are analyzed to characterize geomorphological features of the seabed, which can at times be sources of biological information (e.g. coral reefs). Bathymetric data have proven their potential to help the scientific community and government agencies advance their understanding of seabed ecosystems and geomorphological processes [5].

The terrestrial geomorphometric literature provides a rich source of potential analytical techniques for marine studies [6]. It is important, however, to acknowledge that different data collection and processing techniques used to create underwater DTM makes the nature of the input DTM different. In addition, it is more difficult to capture terrain variability underwater since changes in topography are more subdued in comparison to terrestrial landscapes. Issues encountered in terrestrial geomorphometry, such as underlying data uncertainty and the choice of the analysis algorithm and scale (resolution and neighborhood size), are also relevant underwater, but they manifest themselves differently due to the differences in the input data.

In this contribution, we review some of the most common applications and challenges encountered in marine geomorphometry and explore potential future directions.

In: Geomorphometry for Geosciences, Jasiewicz J., Zwoliński Zb., Mitasova H., Hengl T. (eds), 2015. Adam Mickiewicz University in Poznań - Institute of Geoecology and Geoinformation, International Society for Geomorphometry, Poznań

II. APPLICATIONS

A. Geohazards, Hydrodynamic and Geomorphological Mapping

In dynamic environments such as the ocean, monitoring and detecting change is often crucial. The action of hydrodynamics on the seabed can cause changes in bathymetry that can become hazards for navigation in coastal waters. Hydrographic conditions, on the other hand, are directly related to the morphology of the seabed at all scales [7]. For instance, banks are known to have far-reaching effects on currents and circulation patterns, which in turn can modify bedforms [7].

Local geomorphometric attributes have been used to develop seabed hydrodynamic models. For instance, aspect can be used as proxy for local and regional currents and gives information on the exposure of the seabed at a particular location. Curvature is thought to influence local hydrodynamics. The ruggedness of the seabed affects sedimentation and hydrological patterns near the seabed by the drag or bottom friction that influences the currents. These terrain attributes can also assist geomorphic and physiographic classifications of the seabed, as demonstrated by [8]. Regional geomorphometry can be used to study the legacy of glaciations in the geomorphology of continental shelves. The retreat of under sea ice margins leaves different geomorphic evidences than terrestrial-based ice margins, which can be found on the seabed [9] and identified using geomorphometric classifications. For instance, submarine glacial landforms, captured by multibeam bathymetric data in areas of hypothetic ice-streams, provide evidence on the style of deglaciation, the extent of ice-margins, the calving rates, and the sea level at specific periods in time [10].

Mapping subaqueous geomorphological features is also crucial in identifying potential underwater geohazards. Adaptation of terrestrial geomorphometric techniques, such as morphometric attributes and their statistical analyses, feature-based quantitative representation, and automated topographic classification, has been shown to be effective in improving current understanding of the morphology and physical processes that characterize submarine mass movements in passive glaciated margins [e.g. 11, 12].

B. Habitat Mapping

Seabed habitat mapping is probably the field that has benefitted the most from techniques of geomorphometry to date. Habitat mapping involves characterizing a habitat in terms of its physical, chemical and biological attributes [13]. Many of these attributes are known to be linked to terrain morphology, thus highlighting the potential of terrain derivatives to describe marine habitats. The abundance and distribution of marine species can be strongly influenced by many biotic and abiotic factors, but topography and geomorphology are among the most important drivers of their distribution at many scales [14]. Slope, aspect, curvatures and measures of seabed roughness have all been used in habitat mapping studies [15]. MBES data have become essential in studying marine habitats due to their remoteness and the difficulties in sampling them. Consequently, geomorphometric analysis performed on bathymetric data is also increasingly used to find surrogates (i.e. proxies) of species distribution [14, 15]. Seabed complexity and heterogeneity can allow us to numerically quantify the spatial arrangement and structure of habitats. Since the complexity of the seabed has been linked to the distribution of species at different scales, terrain attributes can be used as surrogates of species distribution [15]. The quantitative nature of terrain attributes also facilitates the analysis of relationships between environmental and biological factors and provides a mean to compare between geographic regions and also the same region over multiple time steps.

C. Human Dimension

It is estimated that more than 40% of all the Earth's ocean floor has already been altered by anthropogenic activities [16]. The physical disturbances of the seabed increase its roughness and produce changes in hydrodynamic patterns and sediment distribution that can then affect bedforms and species distribution [5]. Mapping and analyzing seabed geomorphology using geomorphometry allows monitoring changes in the shape of the seabed and identifying these variations in roughness, thus facilitating the assessment of anthropogenic impacts on some areas and potential new hazards for navigation [5].

Geomorphometric techniques can also be used in search and rescue operations. The difficulties in locating the recently vanished Malaysia Airlines aircraft (flight MH370) highlighted the lack of knowledge of seabed features in the search area [17]. The forecasting of the path of floating debris was limited by the lack of knowledge of seabed roughness and topography from which it is possible to estimate surface current directions and ocean mixing rates, both essential to these predictions [18].

III. CHALLENGES

A. Spatial Scale

As in terrestrial geomorphometry, spatial scale is an important issue to consider in marine applications. Most of the phenomena studied are likely to be observed at different scales, and the scale of analysis should always match the scale of the phenomena being observed [19]. For instance, many terrain attributes used in habitat mapping were found to be useful

surrogate for species distribution at a local scale while others were more important at broader scales [14].

The spatial resolution and extent of MBES data is dependent upon the footprint and frequency of the system. As the distance between the seabed and the sensor increases, the footprint gets bigger and the spatial resolution decreases. This makes submarine DTMs more likely to include datasets of different resolutions, meaning that geomorphometric techniques, which are sensitive to data resolution, need to be very robust in marine applications. The integration of different datasets at different scales over large areas is very challenging [13].

B. Technological Challenges

The dynamic nature of the oceans makes collection of bathymetric data dependent upon a lot of different factors that are likely to induce errors or artifacts in the final DTM. Artifacts are common in bathymetric data and can strongly affect the derivation of terrain attributes. Common errors in depth measurements include errors in the acoustic measurement itself, movements of the supporting platform, and inaccuracies in sound velocity corrections [1]. Motion-induced errors are among the most important source of errors and will vary depending on the platform used (e.g. ship or underwater vehicle). Positional accuracy is also an important challenge, especially for the use of underwater vehicles such as remotely operated vehicles (ROV) or autonomous underwater vehicles (AUV). Unlike in satellite and airborne remote sensing, underwater equipment and technologies cannot use the Global Positioning System (GPS) to accurately georeference depth measurements and location. All data are therefore positioned relatively to surface GPS using acoustic telemetry systems: the deeper the survey, the worse the positional accuracy gets [20]. When positional accuracy is lower than the spatial resolution of the DTM, artifacts can be introduced and a mismatch between the locations from different datasets can occur, which is a critical issue in change detection where dataset registration is very important. These challenges are greater in the deep sea than in coastal environments.

IV. Future of Marine Geomorphometry

A. Towards a Complete Coverage

Applications of geomorphometry in the marine environment are likely to increase as more bathymetric data become available in different types of seabed environment. MBES allow for systematic collection of data, but when the water becomes too shallow for surveying systems, it creates a gap in the continuous data. The combination of bathymetric LiDAR data with acoustic surveys will ultimately call for seamless analysis from terrestrial to marine environment. Such continuous dataset is likely to improve the study of large landforms that overlap between land and the ocean and the identification of geohazards in shallower waters, but will also increase the challenge of integrating different datasets together. On the other hand, the collection of higher resolution bathymetric data in the deep sea will become easier and more frequent with the increasing use of underwater vehicles. This will help gain additional knowledge on the structure and geomorphology of deeper environments. There is still much to learn about the complexity of the seabed at different depths and environmental settings. As stated in [5]: "It is generally assumed that seabed structure becomes less complex as one moves from the continental shelf to greater depths, but is it, or does this simply reflect our lack of knowledge?"

B. Advances in Technologies and Techniques

The ability to produce a continuous acoustic image of the surface of the seabed using multibeam acoustics has revolutionized our ability to understand marine morphodynamics and the composition and distribution of sediments, which has in turn significantly improved our knowledge of seabed processes. Technology and equipment to survey the seabed is improving in quality, accuracy and cost-efficiency, which will allow an increase in data availability and quality. Algorithms that consider the specific characteristics of underwater surveying, such as the CUBE (Combined Uncertainty and Bathymetric Estimator) [21], are being developed to improve bathymetric data processing and are likely to become more accessible through processing software. Availability of GIS tools to effectively combine multiple datasets and perform geomorphometric analyses is key in making marine geomorphometry accessible to marine scientists with a wide range of background and experience [22, 23]. Better practices to report data type, quality and scale within metadata will need to be implemented in order to allow the most informed analysis of these data [24]. New techniques are also likely to make the jump from the terrestrial literature to the marine literature. For instance, geographic object based image analysis (Geobia) has been gaining some traction in the seabed mapping community as the spatial resolution of acoustic data improves [e.g. 25, 26].

V. Conclusion

As stated in [6], "One way to promote better practice in the use of quantitative terrain analysis from bathymetric data is to ensure that studies of geomorphometry become more widespread in the marine literature, thereby making the issues surrounding quantitative terrain analysis more accessible to marine scientists from a variety of backgrounds." Marine

scientists need to be encouraged to apply geomorphometric techniques underwater to make use of the full potential of their expensive datasets.

With a few exceptions, most issues being investigated in terrestrial geomorphometry, such as uncertainty and error propagation, the choice of algorithms or the multiscale nature of DTMs are rarely considered in marine geomorphometry applications. Since the terrestrial geomorphometry community is currently trying to tackle some of these issues, it will be important for marine scientists to remain aware of developments in this field, and to build up a marine geomorphometry community to draw on experiences from terrestrial techniques.

ACKNOWLEDGMENTS

VL is funded by the Natural Sciences and Engineering Research Council of Canada. AM is funded by Marie Curie Career Integration Grant PCIG13-GA-2013 618149 within the 7th European Community Framework Programme.

REFERENCES

[1] Lurton, X., 2010. An introduction to underwater acoustics: principles and applications (second edition). *Springer/Praxis Publishing*, 704 p.

[2] Schimel, A.C.G., Healy, T.R., Johnson, D., and D. Immenga, 2010. Quantitative experimental comparison of single-beam, sidescan, and multibeam benthic habitat maps. *ICES Journal or Marine Science* 67, 1766-1779.

[3] Wright, D. and W. Heyman, 2008. Introduction to the special issue: marine and coastal GIS for geomorphology, habitat mapping, and marine reserves. *Marine Geodesy* 31, 223-230.

[4] Wilson, M.F.J., O'Connell, B., Brown, C., Guinan, J.C., and A.J. Grehan, 2007. Multiscale terrain analysis of multibeam bathymetry data for habitat mapping on the continental slope. *Marine Geodesy* 30, 3-35.

[5] Anderson, J.T., Holliday D.V., Kloser, R., Reid, D.G., and Y. Simard, 2008. Acoustic seabed classification: current practice and future directions. *ICES Journal of Marine Science* 65, 1004-1011.

[6] Dolan, M.F.J, and V.L. Lucieer, 2014. Variation and uncertainty in bathymetric slope calculations using geographic information systems. *Marine Geodesy* 37, 187-219.

[7] White, M., Mohn, C., and M.J. Orren, 2007. Physical processes and seamount productivity. In: T.J. Pitcher, T. Morato, and P.J.B. Hart, eds. *Seamounts: Ecology, Fisheries and Conservation*, Oxford: Blackwell Publishing, pp. 65-84.

[8] Harris, P., Macmillan-Lawler, M., Rupp, J., and E.K. Baker, 2014. Geomorphology of the oceans. *Marine Geology* 352, 4-24.

[9] Syvistki, J.P.M., 1991. Towards an understanding of sediment deposition on glaciated continental shelves. *Continental Shelf Research* 11, 897-937.

[10] Shaw, J., Piper, D.J.W., Fader, G.B.J., King, E.L., Todd, B.J., Bell, T., Batterson, M.J., and D.G.E. Liverman, 2006. A conceptual model of the deglaciation of Atlantic Canada. *Quaternary Science Reviews* 25, 2059-2081.

[11] Micallef, A., Berndt, C., Masson, D.G., and D.A.V. Stow, 2007. A technique for the morphological characterization of submarine landscapes as exemplified by debris flows of the Storegga Slide. *Journal of Geophysical Research* 112, F02001.

[12] Micallef, A., Berndt, C., Masson, D.G., and D.A.V. Stow, 2008. Scale invariant characteristics of the Storegga Slide and implications for large-scale submarine mass movements. *Marine Geology* 247, 46-60.

[13] Brown, C.J., Smith, S.J., Lawton, P., and J.T. Anderson, 2011. Benthic habitat mapping: A review of progress towards improved understanding of the spatial ecology of the seabed using acoustic techniques. *Estuarine, Coastal and Shelf Science* 92, 502-520.

[14] Harris, P.T., and E.K. Baker, eds., 2012. Seabed geomorphology as benthic habitats: GeoHab atlas of seabed geomorphic features and benthic habitats. Elsevier:Amsterdam, 900 p.

[15] McArthur, M.A., Brooke, B., Przeslawski, R., Ryan, D.A., Lucieer, V.L., Nichol, S., McCallum, A.W., Mellin, C., Cresswell, I.D., and L.C. Radke, 2010. On the use of abiotic surrogates to describe marine benthic biodiversity. *Estuarine, Coastal and Shelf Science* 88, 21-32.

[16] Halpern, B.S., Walbridge, S., Selkoe, K.A., Kappel, C.V., Micheli, F., D'Agrosa, C., Bruno, J.F., Casey, K.S., Ebert, C., Fox, H.E., Fujita, R., Heinemann, D., Lenihan, H.S., Madin, E.M.P., Perry, M.T., Selig, E.R., Spalding, M., Steneck, R., and R. Watson, 2008. A global map of human impact on marine ecosystems. *Science* 319, 948-952.

[17] McNutt, M., 2014. The hunt for MH370. *Science* 344, 947.

[18] Smith, W.H.F., and K.M. Marks, 2014. Seafloor in the Malaysia Airlines Flight MH370 Search Area. *EOS Transactions of the American Geophysical Union* 95, 173-180.

[19] Hobbs, N.T., 2003. Challenges and opportunities in integrating ecological knowledge across scales. *Forest Ecology and Management* 181, 223-238

[20] Rattray, A., Ierodiaconou, D., Monk, J., Laurenson, L.J.B., and P. Kennedy, 2014. Quantification of spatial and thematic uncertainty in the application of underwater video for benthic habitat mapping. *Marine Geodesy* 37, 315-336.

[21] Calder, B.R., and L.A. Mayer, 2003. Automatic processing of high-rate, high-density multibeam echosounder data. *Geochemistry, Geophysics, Geosystems* 4, 1048-1070.

[22] Lundblad, E.R., Wright, D.J., Miller, J., Larkin, E.M., Rinehart, R., Naar, D.F., Donahue, B.T., Anderson, S.M., and T. Battista, 2006. A benthic classification scheme for American Samoa. *Marine Geodesy* 29, 89-111.

[23] Erdey-Heydorn, M.D., 2008. An ArcGIS seabed characterization toolbox developed for investigating benthic habitats. *Marine Geodesy* 31, 318-358.

[24] Greene, H.G., Bizzaro, J.J., Tilden, J.E., Lopez, H., and M.D. Erdey, 2005. The benefits and pitfalls of GIS in marine benthic habitat mapping. In: D.J. Wright, and A.J. Scholz, eds. *Place matters: geospatial tools for marine science, conservation, and management in the Pacific Northwest*. Corvallis, OR: Oregon State University Press.

[25] Diesing, M., Green, S.L., Stephens, D., Lark, R.M., Stewart H.A., and D. Dove, 2014. Mapping seabed sediments: comparison of manual, geostatistical, object-based image analysis and machine learning approaches. *Continental Shelf Research* 84, 107-119.

[26] Lucieer, V.L. and G. Lamarche, 2011. Unsupervised fuzzy classification and object-based image analysis of multibeam data to map deep water substrates, Cook Strait, New Zealand. *Continental Shelf Research* 31. 1236-1247.

Towards exactness in geomorphometry

Jozef Minár[1], Jozef Minár Jr[2]
Department of Physical Geography and Geoecology[1]
Department of Mathematical Analysis and Numerical Mathematics[2]
Comenius University in Bratislava
Bratislava, Slovakia

Ian S. Evans
Department of Geography
Durham University
Durham City, England
i.s.evans@durham.ac.uk

Abstract — **Exactness of results of geomorphometric research depends not only on measurement and computational exactness but also on exact definition of measured objects and exactness of interpretation of the geomorphometric variables. The need to consider all aspects of exactness in mutual relationships is exemplified from the use of third order local point-based variables.**

I. INTRODUCTION

Geomorphometry is generally considered as one of the most exact parts of geomorphology. This may be why geomorphometry is widely used and developed also in other Earth sciences. DEM quality as well as the preciseness and accuracy of computation of geomorphometric variables are well known factors influencing the exactness of results achieved. However the quality of geomorphometric analysis depends also on exactness in the definition of objects measured, and on unambiguous interpretation of the geomorphometric variables used. Moreover all these aspects are connected and should be considered in mutual relationships (Fig 1).

These aspects are frequently considered independently from each other and interpretation exactness usually receives the least attention. A short overview of the nature and mutual dependence of these aspects is presented next, followed by an outline of the interpretation hierarchy of geomorphometric variables and an example of a comprehensive approach in the use of third order local point-based geomorphometric variables.

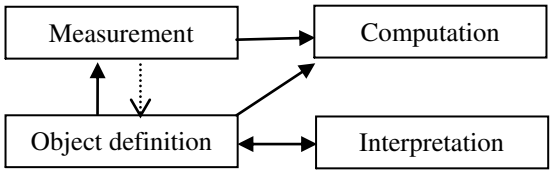


Figure 1. Mutual relationships of main aspects of exactness in geomorphometry

II. STATE OF THE ART

Although direct measurement of various geomorphometric variables is possible (see e.g. [1]) **measurement exactness** is today nearly exclusively connected with digital elevation model (DEM) creation. Altitudinal precision and grid resolution are the main attributes of quality of the most used grid-based DEMs. The quality of both is, however, created in interaction with other components of geomorphometric exactness. The primary measurements (tacheometry, photogrametry, radar or lidar) mainly give spatially irregular data; creation of a regular grid by interpolation functions represents a secondary product affected by computation error of the interpolation function. It is clear that the **exactness of object definition** is a major influence on measurement, with knock-on effects on computation and interpretation. The measured objects of geomorphometry (land surface or landforms) are often fuzzy [2]. The land surface is most frequently perceived as the boundary between lithosphere (pedosphere) on the one side and atmosphere or hydrosphere on the other side. But different ways of treating vegetation and various anthropogenic features of the surface lead to different concepts of DEM, DTM (digital terrain model) and DSM (digital surface model), with serious consequences for general geomorphometry.

The situation in specific geomorphometry is even more complex. The problem of definition of geomorphometric individuals is "evergreen" containing mainly the aspects of semantic and spatial definition (e.g. [3], [4]). The proposed hierarchic nature of landforms remains a major problem for object definition exactness. Establishing a nested hierarchy of landforms from a source DEM is one way of dealing with the problem (e.g. [5]). Another way is gradual generalization of DEM, long used in tectonic geomorphology (e.g. the concept of isobase surfaces in the sense of [6], [7]). Very accurate LiDAR measurements have made some generalization of the land surface necessary for morphodynamics (removing small temporary forms such as ploughland, molehills and vehicles). Using of wavelet transform could be a promising approach [8]. Computation of

In: Geomorphometry for Geosciences, Jasiewicz J., Zwoliński Zb., Mitasova H., Hengl T. (eds), 2015. Adam Mickiewicz University in Poznań - Institute of Geoecology and Geoinformation, International Society for Geomorphometry, Poznań

morphometric variables and derivation of specific geomorphic objects from such generalized land surfaces is important mainly from the aspect of exact morphogenetic interpretation.

Computational exactness is generally perceived to result from error in input data and in computational method (e.g. [9], [10]). However the determination of data error depends on the 'reference standard' used i.e. the definition of ideal (error-free) land surface. If landforms of higher order are studied, greater detail from more precise data may not be relevant: a generalized land surface should be used as the reference standard, but the myriad possibilities of generalization pose a problem. Moreover the correctness of delimitation of specific landforms determines the quality of computation of all indexes in specific geomorphometry.

As yet, insufficient systematic attention has been paid to **interpretation exactness**. Geomorphometric variables have not only geometrical meaning but also physical (morphodynamic and morphogenetic) meaning. While physical interpretation of simple variables can be relatively clear, interpretation of more complex variables and results (e.g. objects created by various segmentation procedures) is frequently obscure. A large part of the interpretation exactness results from relationships between basic geomorphological categories (Fig. 2) and the complexity of variables. The exactness of correspondence between geometry and its physical interpretation is fundamental. The most straightforward is the physical interpretation of dimensions and positional characteristics of geomorphic objects (Table I). Some derivatives and integrals of them bring greater interpretation risks Curvatures (see [10] for overview and terminology) can be an example. Profile curvature and normal change of slope gradient are physically clear (change of downslope gravity force component or ratio of gravity force components).

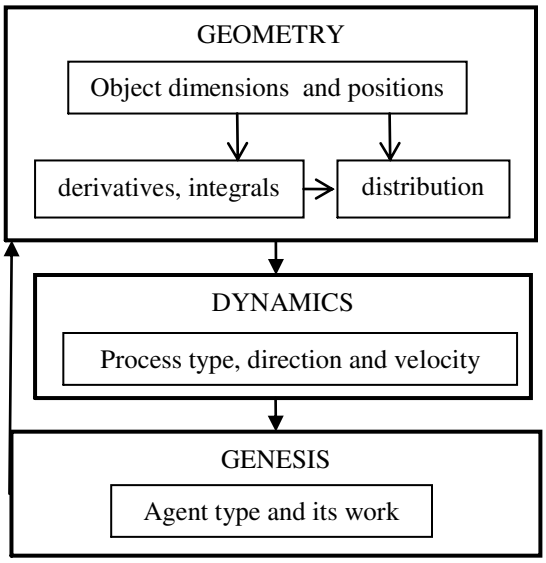


Figure 2. Relationships between basic geomorphological categories

Normal change of slope angle correlates also with acceleration of gravity flows, but precise interpretation is less clear. Similarly, all types of plan curvature reflect concentration/dispersion mechanisms, although the quantitative relations are various and complex. Combined "curvature", newly integrated in ArcGIS, has become increasingly popular despite its lack of clear physical interpretation. Roughness in terms of wavelength and amplitude [11] has a straightforward physical interpretation related to geomorphic work. Analysis of distribution patterns is more complex.

TABLE I. Fundamental dimensional and positional geometric types of geomorphometric variables

Topological dimension of:	0D	1D	2D	3D
Geometric object→ ↓Measuring	**POINT**	**LINE**	**SURFACE**	SOLID
1D (axis z) Distance	*Altitude ...*	*Mean ridgeline height ...*	*Glock's available relief ...*	*Cave height ...*
2D (axis x,y) Area, Distance in map	*Map distance of peaks ...*	*Map length of thalweg ...*	*Catchment length and area in map ...*	*Cave map area and length ...*
3D (x,y,z) Volume, Distance and Area in space	*Spatial distance of peaks ...*	*Spatial length of thalweg ...*	*Catchment length and area in space ...*	*Cave volume, surface, space length ...*

Many indexes created by combination of basic geomorphometric variables have only limited interpretation exactness unless they are based on conceptual models. Physically based indexes (e.g. topographic wetness index - [14]) have interpretation limits resulting from the generalizations used.

III. THIRD ORDER LOCAL POINT-BASED VARIABLES

The need to use all aspects of geomorphometric exactness can be exemplified for computation of third order local point-based geomorphometric varables - changes of curvatures [13], [10].

The initial target is utilization of curvature change for elementary form definition and delineation. Our concept [4] is

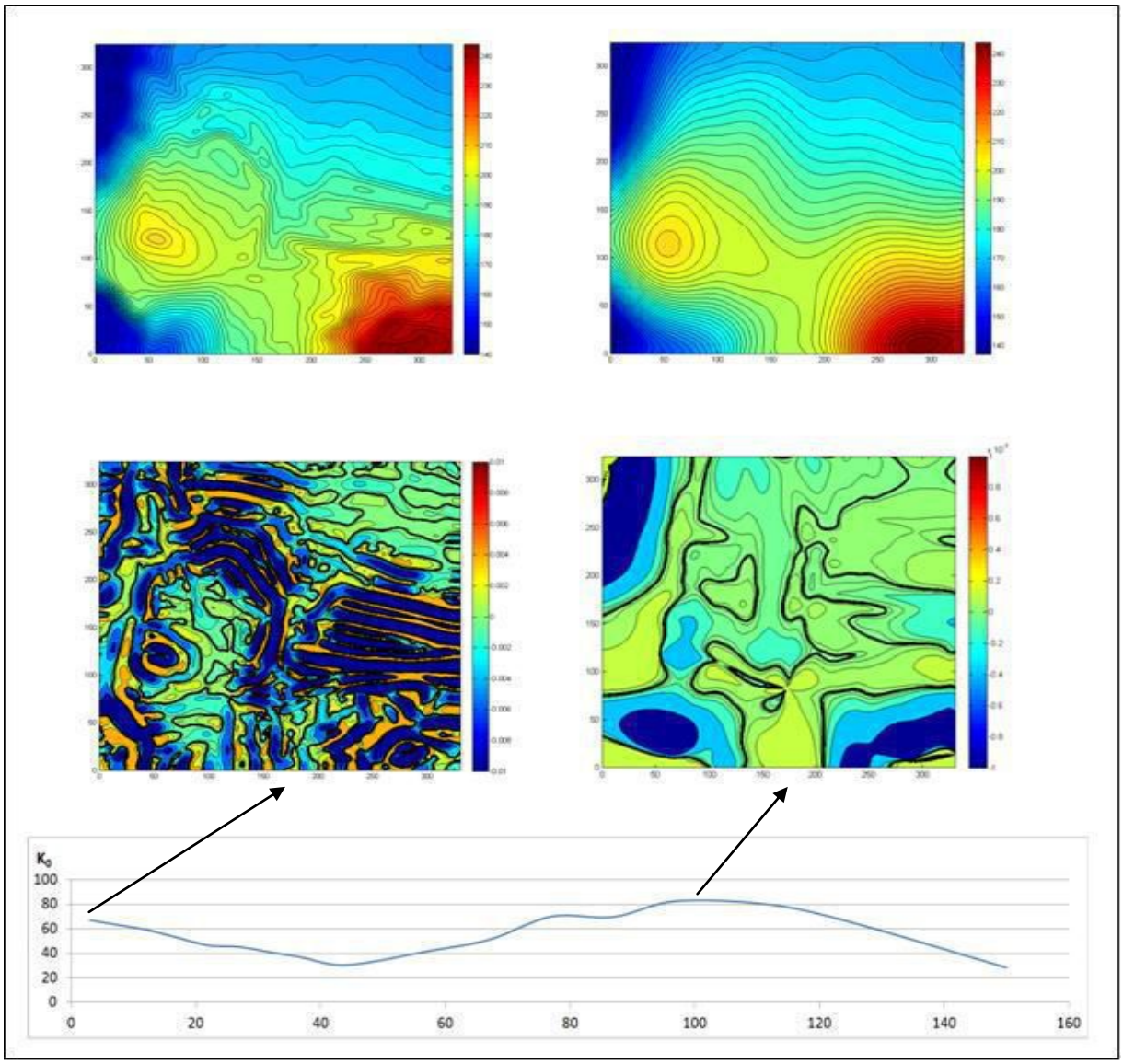


Fig 3. Contourline representation of two hierarchic levels of landforms (top) and corresponding fields of normal change of normal change of gradient - G_{nn} (centre) detected by maximization of index of concentration of G_{nn} around zero - K_0 (bottom: K_0 is a function of window size for polynomial models of 6th order.)

based on postulating the existence of dynamic equilibria of land elements in terms of constant values of altitude and some its derivatives (including 3rd. order). Because it is necessary to eliminate ephemeral landforms, the most precise DEMs have to be generalized to a level where the sought (dynamically stable) elementary forms are evident.

The basic analysis of exactness of five methods of third derivative computation [10] showed varied effectiveness. Most numerical methods that compute a derivative at a chosen grid point are linear functions of values at several nearby grid points. Method error is the difference between the exact derivative of analytical function and the derivative computed using a numerical method applied to data at grid points. Data (DEM) error is the difference between the derivative computed using the chosen numerical method applied to the 'etalon' (exact function values at grid points), and applied to function values at grid points which have some DEM error. We have documented that if for every pair of grid points DEM error is equally distributed and uncorrelated, then the expected value of the second power of data error is smallest for the Least squares method [14] out of all methods available to compute the derivative from the same set of grid points. Extending the number of computational grid points (window) reduces the data error even more but enlarges the method error. On the contrary, raising the order of polynomial reduces the method error but enlarges the data error. While enumeration of change in data error is possible for both cases, enumeration of method error is a complex mathematical problem, so determination of total error is very problematic. Therefore we developed a method generalizing the least square method suggested by [14] for 5 x 5 windows approximated by 3rd order polynomials.

Our method enables computation of derivatives for various combinations of window and polynomial order, with subsequent selection of an optimal combination of window and order of polynomial on the basis of a target function. Because of interpretation exactness, instead of profile curvature we use the gradient change and subsequently the normal change of gradient change for target function [4]. The first results suggest that, for a set of differently generalized DEMs, maximisation of a quantile-based measure of kurtosis (K_0) of change of gradient change [10] permits selection of the DEM best representing genetically well interpretable landforms of higher order in the streamline direction (Fig. 3).

Geomorphometric variables for a multi-level hierarchy of landforms usually are computed simply by changing input grid resolution [15]. Application of a theoretical assumption into the computational procedure is specific for our approach. Confirmation of the preliminary result on a larger territory could lead not only to a new tool for detection of landforms of various orders, but also demonstrate the usefulness of incorporating theory when building methodological tools in geomorphometry.

ACKNOWLEDGMENT

This work was supported by the Slovak Research and Development Agency under contract APVV-0625-11.

REFERENCES

[1] Barbosa, R.N., Wilkerson, J.B., Yoder, D.C., and H.P. Denton, 2007. "Different sensing techniques for geomorphometric measurements", Computers and Electronics in Agriculture 59, (1–2): 13–20.

[2] Deng, Y. and Wilson, J.P., 2008. "Multi-scale and multi-criteria mapping of mountain peaks as fuzzy entities. International Journal of Geographical Information Science, 22 (2): 205-218.

[3] Schmidt, J., and R. Dikau, 1999. "Extracting geomorphometric attributes and objects from digital elevation models — semantics, methods, future needs", In: Dikau, R., Saurer, H. (Eds.), GIS for Earth Surface Systems. Gebrüder Borntraeger, Berlin, pp. 153–173.

[4] Minár, J., and I.S. Evans, 2008. "Elementary forms for land surface segmentation: The theoretical basis of terrain analysis and geomorphological mapping." Geomorphology, 95: 236-259.

[5] Drăguţ, L., Eisank, C., and T. Strasser, 2011. "Local variance for multi-scale analysis in geomorphometry", Geomorphology 130: 162–172.

[6] Filosofov, V.P., 1960. "Brief Guide to Morphometric Methods in Search of Tectonic Structures", Saratov University Publishing House, Saratov [in Russian].

[7] Grohmann, C. H., Riccomini, C., and M. A. C. Chamani, 2011, "Regional scale analysis of landform configuration with base-level (isobase) maps", *Hydrology and Earth System Sciences* 15: 1493-1504.

[8] Kalbermatten, M., Van De Ville, D., Turbergd, P., Tuiaa, D., and S. Joosta, 2012. "Multiscale analysis of geomorphological and geological features in high resolution digital elevation models using the wavelet transform", Geomorphology 138: 352–363.

[9] Zhou, Q. and Liu, X., 2004. Analysis of errors of derived slope and aspect related to DEM data properties. Computers & Geosciences 30: 369–378.

[10] Minár, J, Jenčo, M., Evans, I.S., Minár, J.Jr., Kadlec, M., Krcho, J., Pacina, J., M., Burián L., and A. Benová, 2013 "Third-order geomorphometric variables (derivatives) – definition, computation and utilization of changes of curvatures." International Journal of Geographical Information Science, 27 (7): 1381-1402.

[11] Mark, D.M., 1975. "Geomorphometric parameters: A review and evaluation", Geografiska Annaler. Series A, Physical Geography, 57 (3/4): 165-177.

[12] Beven, K.J., and M.J. Kirkby, 1979. "A physically based, variable contributing area model of basin hydrology", Hydrolological Science Bulletin 24: 43–69.

[13] Evans, I.S., 2013. "Land surface derivatives: history, calculation and further development", Geomorphometry 2013 (Nanjing, China,16.-20.10. 2013). Eds. G. Tang, Q. Zhou, T. Hengl, X. Liu, F. Li, 5-8.

[14] Florinsky, I.V., 2009. "Computation of the third-order partial derivatives and derivation function from a digital elevation model, International Journal of Geographical Information Science 23 (2): 213–231.

[15] Bishop, M.P., Bonk, R., Kamp, U. Jr. and Shroder, J.F. Jr., 2001. "Terrain analysis and data modeling for alpine glacier mapping", Polar Geography 25 (3):182-201.

Effects of future sea level rise – the example of the island of Gotland, Sweden

Karin Ebert, Jerker Jarsjö, Karin Ekstedt
Department of Physical Geography and Quaternary Geology
Stockholm University

Abstract—**Sea level rise is confirmed to be an upcoming and pressing issue; on a global as well as local scale; and with it comes the necessity to adapt. Using the local case study of the island of Gotland, Sweden, we investigate the effects of future sea level rise on a multitude of features combined and thereby assess the overall impact on the environment and infrastructure of the island. Sea level is expected to rise 1 - 2 m until 2100** [1]**. We analyze what percentage of Gotland's total land surface will be submerged under the given scenario, using ArcGIS environment using LIDAR elevation data. Through successive overlay analysis of both raster and vector data, we then quantify the loss of infrastructure; including wells, roads, industrial areas and gas stations. Secondly we investigate what percentage of Gotland's natural and cultural heritage will drown.**

In this ongoing study we found that about 3% of Gotland's land area will drown. Future pressures of water extraction will yield increased risk of saltwater intrusion for a considerable part of the population. For southern Gotland, projections show that about 30% of the wells will be associated with high risk of saltwater intrusion. Furthermore, around 90% of the wells would be at medium or high risk of saltwater intrusion in that case. Even a minimum predicted sea level rise will drown the entire shore meadows and the associated breeding places for birds. We expect that current quantifications of the impact of sea level rise on multiple environmental and anthropogenic features can provide a scientifically sound basis for assessment of main consequences and costs of direct losses.

I. INTRODUCTION

Sea level rise is confirmed to be an upcoming and pressing issue; on a global as well as local scale; and with it comes the necessity to adapt. The pace at which sea level will rise is not clear, but undoubtedly, it will drown areas along the world's coasts - where we find most of our settlements and infrastructure. A natural first step towards managing this change is the investigation of the consequences of sea level rise; reversible and irreversible, on humans, nature, and connected issues such as sea water pollution by drowning contaminated areas and salt water intrusion in wells.

Several studies have considered the impact of sea level rise on a variety of environmental and anthropogenic features [2], [3] yet often they fail to take on the multi-consequential characteristic of this subject. This paper aims to fill that gap. Using the local case study of the island of Gotland, Sweden, we try to investigate the effects of future sea level rise on a multitude of features combined and thereby assess the overall impact on the environment and infrastructure of the island. Gotland is a politically stable, comparatively well-suited area, with many means to prepare for future sea level rise. Still some valuable areas like shore meadows and the connected bird life will be irreversibly lost. Still, moving towns and sanitizing of contaminated areas like gas stations will be costly and difficult, and in cases not even possible. If we see Gotland as a "miniature world", the study is extrapolated to illustrate what effects sea level rise could have globally, given rather an underestimate of the possible consequences of sea level rise.

II. SEA LEVEL RISE ON GOTLAND

Gotland is located in the Baltic Sea east of Sweden (Figure 1) and the main island has a total land area of 3 140 km², which makes it the largest island of Sweden. Administratively

In: Geomorphometry for Geosciences, Jasiewicz J., Zwoliński Zb., Mitasova H., Hengl T. (eds), 2015. Adam Mickiewicz University in Poznań - Institute of Geoecology and Geoinformation, International Society for Geomorphometry, Poznań

Gotland is both a county and a municipality of its own and it has a population of almost 60 000 people. It is an island with complete infrastructure with rich tourism, agriculture, mining and food industry [4]. The coastline of the island, which stretches 77 km, harbors unique flora and fauna and is an important economic asset as well as a valuable resource for residents and travelling visitors [5]. Sea level here, according to the fifth report of IPCC, is expected to rise 1 - 2 m until 2100; mainly as a result of the slow but ongoing and irreversible collapse of the West Antarctic Ice Sheet (WAIST) [1].

The initial analysis, which examines what percentage of Gotland's total land surface will be submerged under the given scenario, is performed in an ArcGIS environment using LIDAR elevation data. Through successive overlay analysis of both raster and vector data, we then quantify the loss of infrastructure; including for example built-up areas, wells, roads, industrial areas and gas stations. Secondly we investigate what percentage of Gotland's natural and cultural heritage will drown, including for example shore meadows, cultural grazing fields and rune stones.

Based on this information the paper then takes the overall perspective and discusses the possible environmental as well as economic implications. It considers for example saline water intrusion and the reduction in beach meadow area and in bird life; and then possible economic consequences arising from e.g. decreasing tourism, the restoration of infrastructure and of polluted areas. Discussion then finally addresses which of these losses are irreversible and which might actually be mended or prevented.

Results show that a future sea level rise between 1 and 2 meters would result in inundation of 2 to 3% of Gotland's current land area. In the relatively flat, southern part of the island, the expected inundation is twice as high. More generally, the fact that the population density is relatively high near the coast implies that a considerable part of important infrastructure will be submerged.

Application of developed models of salt water intrusion [6] furthermore shows that future pressures of water extraction, in combination with density driven intrusion of relatively heavy saltwater beyond the new future coastline will yield increased risk of saltwater intrusion for a considerable part of the population. For instance, for southern Gotland, projections show that about 30% of the wells will be associated with high risk of saltwater intrusion given a future sea level rise of 1m. Furthermore, around 90% of the wells would be at medium or high risk of saltwater intrusion in that case.

In order to quantify how conditions can change in the future, the results of the future projections are compared with current risks of salt water intrusion. Presently, the high-risk area of sea water intrusion covers 214 km^2 and contains 807 drinking water wells. Results show that 82 of these will be completely flooded given a sea level rise of 1m. Despite this loss of land, the high-risk area of the remaining part of the island would increase to 245 km^2 and contain 947 wells (in addition to the 82 in submerged ones). For a sea level rise of 2m, 165 wells would be submerged, the high risk area of remaining land would increase to 279 km^2 and contain 1081 wells.

The above quantification examples illustrate that, in addition to direct and irreversible loss of land and infrastructure such as roads, industrial land and drinking water wells, the remaining part of the island may be more vulnerable to risks such as salt water intrusion. This is due to modified hydrological and hydrogeological conditions; a larger area of the remaining island will contain low lying land, for instance. The problem could be further accentuated by pressures from increasing population and/ or population density of the coastal zone (as the island shrinks). Even the minimum predicted sea level rise will consume 99% of Gotland's shore meadows [7], a breeding place for a high variety of bird species. With the shore meadows and archeological sites disappearing, not only unique natural and cultural values, but also, as a consequence, tourism will decrease drastically.

With regard to industrial activities, the region that will be submerged by expected future sea level rise contains contaminated industrial land and infrastructure that may have adverse environmental effects such as gas stations. Sea level rise can hence imply that costs for mitigation measures addressing Gotland's current environmental problems may change due to changing environmental conditions; for completely submerged regions, costs for remediation may even become too high to be feasible, due to an increased inaccessibility of flooded or partly flooded land.

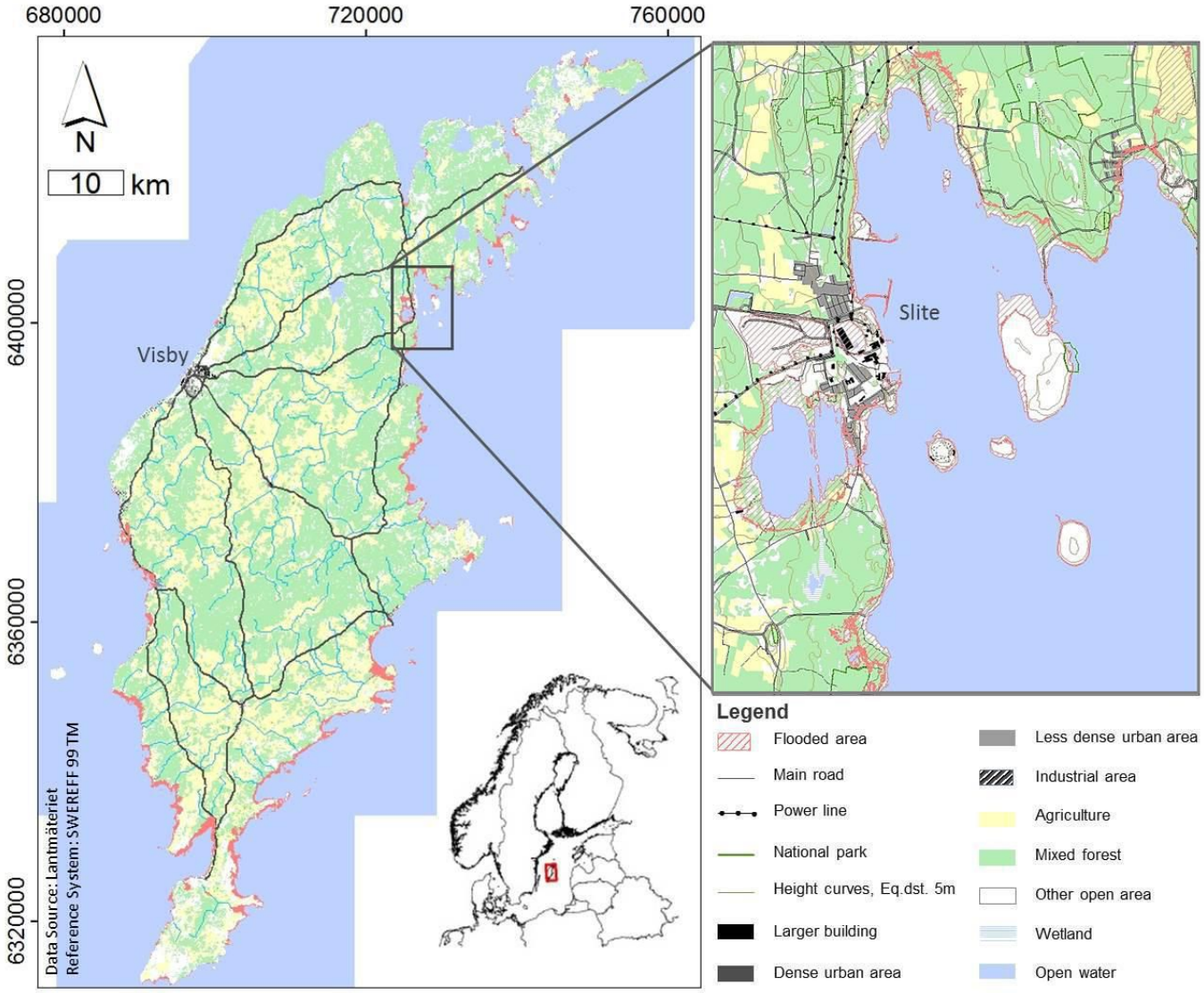


Figure 1. Gotland's land area would diminish with 3% as consequence of a 2m sea level rise. Urban areas and nature reserves would be severely affected as the majority of settlements and cultural heritage sites in Gotland are situated at the coast. In our project, we quantify the percentage of disappearing sites and discuss the long-term consequences of sea level rise. Inset map shows Gotland's location in Fennoscandia.

We expect that current quantifications of the impact of sea level rise on multiple environmental and anthropogenic features can provide a scientifically sound basis for assessment of main consequences and costs of direct losses (of land and infrastructure) and potential future costs associated with increased vulnerability, which potentially can lead to increased costs of maintaining a sufficient water security, for instance.

Notably, such knowledge can also contribute to preventing some of the expected adverse effects, by prioritized remediation of contaminated land at risk of flooding, for instance.

REFERENCES

[1] IPCC, 2014. Summary for policymakers. In: Climate Change, 2014: Impacts, Adaptation, and Vulnerability. Part A: Global and Sectoral Aspects. Contribution of Working Group II to the Fifth Assessment Report of the Intergovernmental Panel on Climate Change (Field, C.B., V.R. Barros, D.J. Dokken, K.J. Mach, M.D. Mastrandrea, T.E. Bilir, M. Chatterjee, K.L. Ebi, Y.O. Estrada, R.C. Genova, B. Girma, E.S. Kissel, A.N. Levy, S. MacCracken, P.R. Mastrandrea, and L.L. White (eds.)). Cambridge University Press, Cambridge, United Kingdom and New York, NY, USA, pp. 1 32.

[2] Kont, A., Jaagus, J., Aunap, R., 2003. Climate change scenarios and the effect of sea-level rise for Estonia. Global and Planetary Change 36, 1-15.

[3] Blankespoor, B., Dasgupta, S., Laplante, B., 2014. Sea-Level Rise and Coastal Wetlands. Ambio, DOI: 10.1007/s13280-014-0500-4

[4] Region Gotland, 2014. *Gotland i Siffror.* [PDF] Available at: http://www.gotland.se/64224 [Accessed 29 October 2014].

[5] Gotlands kommun, 2010. *ByggGotland – översiktsplan för Gotlands kommun 2010–2025*. [PDF] Available at: http://www.gotland.se/50616 [Accessed 27 June 2014].

[6] Lange, E., 2012. Saltvattenpåverkan i Gotlands dricksvattenbrunnar vid stigande havsnivåer. Undergraduate thesis in Hydrology and Hydrogeology, 15 ECTS, Department of Physical Geography and Quaternary Geology, Stockholm University.

[7] Cedergren, B., 2013. Havsnivåhöjningens påverkan på Gotlands kust och strandängar år 2100. Undergraduate thesis in Physical Geography, 15 ECTS, Department of Physical Geography and Quaternary Geology, Stockholm University.

Pre-Quaternary paleotopography reconstruction in the Ordos platform and its integration in the loess landform evolution modeling

XIONG LiYang
Key laboratory of Virtual Geographic Environment, Ministry of Education
Nanjing Normal University
Nanjing, China
xiongliyang@163.com

TANG GuoAn
Key laboratory of Virtual Geographic Environment, Ministry of Education
Nanjing Normal University
Nanjing, China
tangguoan@njnu.edu.cn

Abstract—**The information underlying the earth surface is the indicator of the environment of the past. Especially the pre-Quaternary underlying terrain of the Ordos platform in the Loess Plateau of China, a base level of soil erosion process and a start geologic node of loess deposition process during the landscape evolution process, which acted as the erosion base to control the development and evolution of the loess landform. In this study, on a basis of multi-source information including detail geologic information, several drillings, RS images and DEMs, we used GIS spatial analysis methods to virtualize and reconstruct a digital elevation model of a pre-quaternary paleotopographic surface in a severe soil erosion area of the Loess Plateau. Then, several indicators are used to quantitatively express the controlling effect of the underlying terrain to the modern terrain. Finally, we used the underlying terrain as the initial topography, employed a landscape evolution model to virtualize the process of the loess landscape formation process. The result shows, the usage of geologic information, together with the GIS spatial analysis method, could help the Geomorphometry in the virtualization of the paleotopography as well as the past environment. A relatively strong landform inheritance relationship could be found according to the significant linear positive correlation between both terrains. The Quaternary loess-deposition process exhibited an apparent accumulation in the windward direction, which supported the hypothesis of an eolian origin for loess in China. With the initial topography and landscape evolution model, we virtualize the evolution process of loess landform. Our results deepen the understandings of the paleotopography and the past environment of the Ordos platform in the Loess Plateau of China, as well as boarding the theory and method in Geomorphometry.**

I. INTRODUCTION

Dynamic phenomenon simulation has been regarded as one of the most important aspect in the environment revealing, explaining and predicting of past, now and future correspondingly towards the research of Virtual Geographic Environment (Lin et al., 2013; Li and Liu, 2006; Cao et al., 2013; Yang et al., 2013). Surface landform evolution process investigating, revealing, modelling, and further simulating have been got increasingly attention in quantitatively expressing the geomorphological process.

The Loess Plateau of China is known for its unique landforms, formed after more than two million years of loess deposition and sculpted by forces of water and wind erosion (Liu, 1985). The plateau has a complex and diverse landscape, with a specific spatial distribution pattern of the modern landforms. The loess landforms were formed and developed on the basis of inheritance of the underlying paleotopography, the morphology and distribution of which profoundly affect the combination and spatial distribution of the modern landforms (Xiong et al., 2014a, b, c). The paleotopography underlying loess refers to the original terrain prior to loess deposition of the Quaternary period. Hence, a study of the paleotopography of underlying loess and its impact on the current loess landform is critical to understanding the formation mechanisms and the evolution of the landscape of the loess landforms.

In this paper, the underlying loess paleotopography, or the loess bedrock strata, is first taken into consideration for its controlling effect on the evolution of the landscape. On the basis of geologic maps, Remote Sensing (RS) images, DEMs, and loess thickness drilling points, we construct a DEM of the paleotopographic surface through intensive sampling of outcropping paleotopographic points in an area of severe soil erosion in the Loess Plateau. A terrain analysis method is then adopted to quantify the topographic differences and to reveal the loess-deposition process during the Quaternary period. The

In: Geomorphometry for Geosciences, Jasiewicz J., Zwoliński Zb., Mitasova H., Hengl T. (eds), 2015. Adam Mickiewicz University in Poznań - Institute of Geoecology and Geoinformation, International Society for Geomorphometry, Poznań

underlying terrain and a landscape evolution model is employed to virtualize the process of the loess landscape formation process.

II. MATERIALS AND METHODS

A. Materials

DEM: SRTM (Shuttle Radar Topography Mission) with resolution 90 m was chosen as the basic DEM data source, because of its appropriate height precision and applicability to geomorphological mapping at macroscale (Zhan, 2008). Geologic map: an information source for outcropping points of bedrock in the loess area with scale 1:200,000, composed by the Institute of Geology and Geophysics of the Chinese Academy of Sciences. Remote sensing imagery was applied to positional correction within bedrock outcropping point mapping. Loess thickness distribution map (Liu, 1985): Tertiary red clay and early paleotopographic regions are designated on the geologic map. Hence, thickness distribution data of loess were used to provide further control for terrain simulation of the Tertiary surface.

B. Methods

1. Outcropping bedrock strata points detection

Coordinates and elevations for the bedrock outcrop strata points were collected based on the geologic maps, which assigned them a geologic age and rock type, such as Tertiary, Cretaceous, Jurassic (for geologic age), and basalt and limestone (for rock type). The method was implemented via the following steps. First, the bedrock outcropping points in channels or valleys with the same geologic age of Tertiary were determined based on the geologic maps. Second, an image-based positional correction of the bedrock points was done. Finally, an overall outcropping bedrock strata point dataset was constructed.

2. Underlying bedrock strata surface modelling

Based on the bedrock outcrop points, the DEM of underlying loess paleotopography in the experimental area was constructed via interpolation. Through a comparison of all the interpolation methods (Franke, 1982; Mitas and Mitasova, 1988), Spline was determined to be the most suitable method for this application because of its high accuracy, as well as its relatively low variation. Among all sampling points, 80 percent were prepared for interpolation; the rest (20 percent) were used for determining accuracy (the RMSE is 36.5 m, relative error is less than 12 percent) (Figure 1).

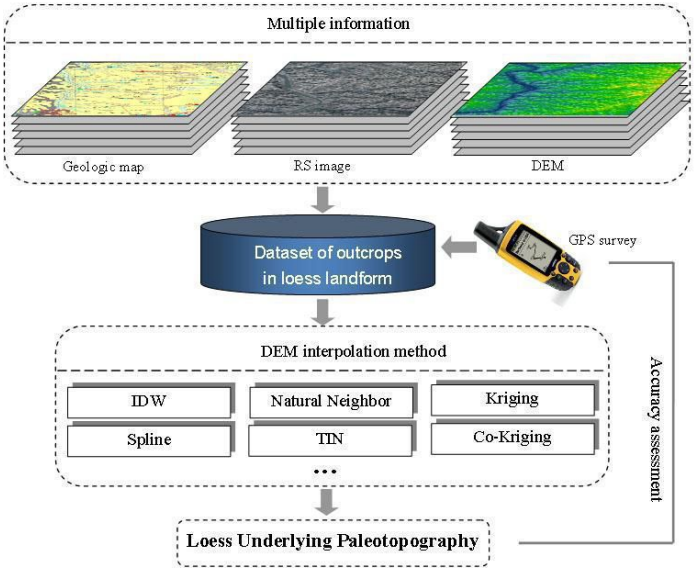


Figure 1. Virtualization and reconstruction of the underlying terrain

3. Loess landform evolution process evaluating

For both the modern terrain and the paleotopography, terrain profile characteristics and slope aspect were conducted. Terrain profile characteristics of the two surfaces was extracted from DEMs and evaluated based on of Lu et al. (2003). In the current study, the slope aspect (Burrough and McDonnell; 1998) was also calculated and a numerical statistical analysis was completed for eight different directions, N, NE, E, SE, S, SW, W and NW, which were classified to investigate the slope aspect changes.

III. RESULTS

Significant differences were subjectively found in the spatial distribution between the modern DEM surface and the underlying paleotopographic surface. At the same time, the basic trend of these two terrains had some similarities. The differences and similarities reflect the landscape evolution as it developed from the pre-Quaternary to modern landscape. Terrain analysis of profile characteristics and slope aspect were used to test the differences and similarities, reveal the evolution of the landscape and its mechanism, and evaluate the underlying paleotopography for these two terrains. And then, the study integrates the virtualized underlying terrain into the landscape evolution model to further virtualize the process of loess landscape evolution.

A. Terrain profiles

Using a group of terrain profiles extracted from DEMs of the underlying and modern terrains, the spatial relationship and distribution pattern between them can be clearly illustrated

(Figure 2). R-squared values of both equations confirm the strong inheritance of the modern terrain from the underlying paleotopography.

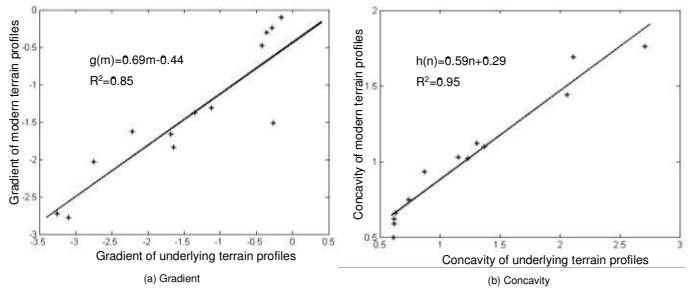


Figure 2. Linear correlations of modern terrain profiles and underlying terrain profiles

B. Slope Aspect

For this study, the slope aspect was derived for both the underlying terrain and the modern terrain, and a numerical statistical analysis was completed for eight different directions, N, NE, E, SE, S, SW, W, NW, which were classified to investigate the slope aspect changes (Figure 3). The frequency of N and NW appeared to increase significantly, while those of E and SE, by contrast, decreased significantly. In other words, a large quantity of E and SE aspects have been buried and reshaped into N and NW aspects. This result supports the hypothesis of an eolian origin for loess in China, namely, the difference of loess deposition in the windward slope (NW slope) and the leeward slope (SE slope). At the same time, other aspects also show a slight change from the underlying terrain to the modern terrain, which demonstrates the effect of water erosion mold force. The results demonstrate that the origin for loess in the study area was an interactive force that was dominated by an eolian origin, while water erosion mold force also contributed to reshaping the morphology of the loess landform during the loess-deposition process.

C. Landscape evolution process

With the virtualized underlying paleotopography and the landscape evolution model (Refice et al., 2012), the study further simulated the evolution process of loess landform. Figure 4(a, b, c, d, e, f) is the landscape evolution process under different condition. It shows that, under the controlling effect of origin terrain, the model virtualized different stages of the landform evolution process, and it appears great similarities with the true surface show in Figure 4(g, h, i), i.e. the loess hill, loess ridge and loess tableland landforms, which demonstrate the significance of the underlying origin terrain and the landscape

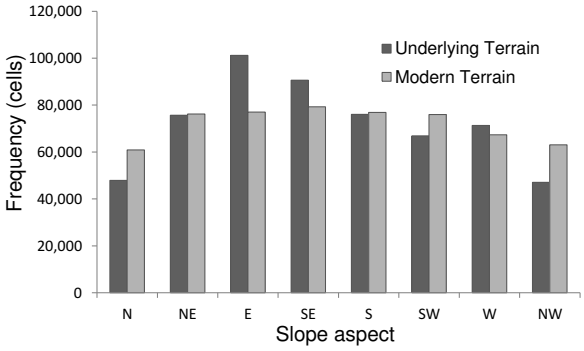


Figure 3. Comparison of modern and paleotopographic slope aspect distribution.

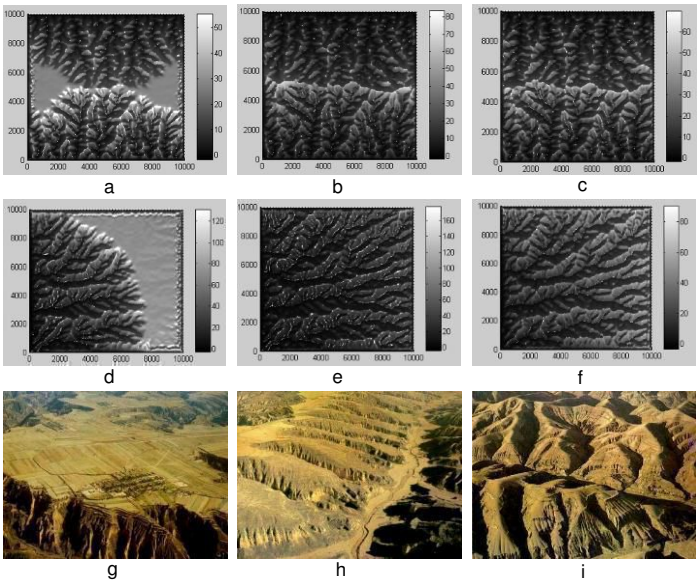


Figure 4. Evolution of a simulated surface. a, b, c, d, e and f are the landscape evolution processes under different conditions. g, h and i are loess hill, loess ridge and loess tableland landforms correspondingly.

IV. CONCLUSIONS

(1) Virtualization of the past or previous existing environment should be the content of VGEs. Multiple information reorganization and utilization could play a significant role in revealing the past, understanding now and predicting future. The virtualized and reconstructed underlying terrain profoundly controlled the formation of loess landform. The comparative analysis of paleotopography underlying loess and modern terrain was useful for revealing the geomorphological inheritance of loess landforms.

(2) The Ordos platform in China was once a smooth bedrock strata terrain in pre-Quaternary, but after more than 2 million years of loess deposition, loess accumulation, and loess transportation, the morphology of the Ordos platform has been reshaped. Moreover, the results suggest that the area for the aspects of N and NW increase significantly, while that for the aspects of E and SE decrease significantly, suggesting that the original slopes have been buried by the deposited loess dust, and after more than 2 million years of loess deposition, their original slope aspects have been reshaped into N and NW aspects to some extent. This result supports the hypothesis of an eolian origin for loess in China, namely, the difference of loess deposition in the windward slope (NW slope) and the leeward slope (SE slope).

(3) The results from the reconstruction of loess paleotopography can only be applied at a macro-level due to the limited sampling methods and density. The development of modern geophysical techniques would provide better conditions for the future study of loess landform evolution, investigating and modeling at even wider spatial scales.

ACKNOWLEDGMENT

This work was supported by the Major Scientific Research Projects of Universities in Jiangsu Province (13KJA170001), the Project Funded by the Priority Academic Program Development of Jiangsu Higher Education Institutions, the National Natural Science Foundation of China (41171320, 41271438, 41471316). The authors express their great thanks to everyone who have helped in the writing of this article.

REFERENCES

[1] Burrough, P.A., and R.A. McDonnell, 1998. “Principles of Geographical Information Systems”. Oxford University Press, New York.

[2] Cao, M., G. Tang, F. Zhang, and J. Yang, 2013. “A cellular automata model for simulating the evolution of positive–negative terrains in a small loess watershed”. International Journal of Geographical Information Science 27(7), 1349-1363.

[3] Franke, R., 1982. “Smooth Interpolation of Scattered Data by Local Thin Plate Splines”. Comp. & Maths. with Appls. 8, 237-281.

[4] Li, X., and X. Liu, 2006. “An extended cellular automation using case-based reasoning form simulating urban development in a large complex region”. International Journal of Geographical Information Science 20(10): 1109-1136.

[5] Lin, H., M. Chen, G.N. Lu, Q. Zhu, J.H. Gong, X. You, Y.N. Wen, B.L. Xu, and M.Y. Hu, 2013. “Virtual Geographic Environments (VGEs): A New Generation of Geographic Analysis Tool”. Earth-Science Reviews 126: 74-84.

[6] Liu, T., 1985. “Loess and Environment”. Science Press, Beijing.

[7] Lu, Z., J. Zhou, and H. Chen, 2003. “River bed longitudinal profile morphology of the lower Yellow River and its implication in physiography (in Chinese)”. Geogr Res, 1: 30-38

[8] Mitas, L., and H. Mitasova, 1988. “General Variational Approach to the Interpolation Problem”. Comput. Math. Applic 16, 983-992.

[9] Refice, A., E. Giachetta, and D. Capolongo, 2012. “SIGNUM: A Matlab, TIN-based landscape evolution model”. Computers & Geosciences 45, 293-303.

[10] XIONG, L., G. TANG, F. LI, B. YUAN, and Z. LU, 2014a. “Modeling the Evolution of Loess Landforms Using DEMs of Underlying Bedrock Terrain in the Loess Plateau of China”. Geomorphology 209(0): 18-26.

[11] Xiong, L., G. Tang, B. Yuan, Z. Lu, F. Li, and L. Zhang, 2014b. “Geomorphological Inheritance for Loess Landform Evolution in a severe soil erosion region of Loess Plateau of China Based on Digital Elevation Models”. Science China: Earth Sciences, Science China Earth Sciences 57(8): 1944-1952.

[12] Xiong, L., G. Tang, S. Yan, S. Zhu, and Y. Sun, 2014c. “Landform-oriented flow-routing algorithm for the dual-structure loess terrain based on digital elevation models”. Hydrological Processes 28(4): 1756-1766.

[13] Yang, J., G. Tang, M. Cao, and R. Zhu, 2013. “An intelligent method to discover transition rules for cellular automata using bee colony optimization”. International Journal of Geographical Information Science 27(10): 1849-1864.

[14] Zhan, L., 2008. “Evaluation of SRTM DEMs’ Accuracy and Investigation on Its Applicability-A case study in Shaanxi Province (in Chinese)”. Master's thesis. Nanjing: Nanjing Normal Univ.1-87

Geomorphometry of Normal Faults: Abyssal Hills and Continental Rifts

Peter L. Guth
Department of Oceanography
United States Naval Academy
Annapolis, MD 21402 USA
pguth@usna.edu

Abstract—**Normal faults in rifting environments create scarps with 10s to 100s of meters of relief, with strikes perpendicular to the spreading direction. Medium scale digital topography, with elevation spacing of 30-100 m, captures these features and allows extraction of the fault scarp orientations and relief. Digital elevation models like SRTM and ASTER GDEM cover the entire land surface at this scale, and significant underwater bathymetry exists, especially over mid-ocean ridges. Statistical techniques can identify fault scarps in these environments.**

I. INTRODUCTION

Gilbert [1] first recognized the importance of normal faulting in creating horst and graben topography in the Basin and Range province of the western United States. A century later, Macdonald and others [2] recognized abyssal hills formed by normal faulting and volcanism as the most common geomorphic feature on earth, although obscured by several km of water.

Table 1 shows the three regions discussed in this paper. The DEMs come from the recently released 1" SRTM data set and the GMRT bathymetry [3], with resolution to capture fault scarps representing multiple faulting events. Plate motions from the MORVEL model [4] show that the Afar region, a type example for continental rifting [5], lies about 200 km south of a very slow active ridge in the Red Sea. The Atlantis Massif, one of the best studied oceanic cores complexes [6], also occurs on a very slow spreading ridge segment. The area on the East Pacific Rise has one of the fastest recorded spreading rates. Figure 1 shows the three areas, with earthquake focal mechanisms [7] shown for the two slow spreading areas. The East Pacific Rise has essentially no focal mechanisms with normal faulting in the global CMT database [7], but the strike slip faults on the transforms bounding this segment have one focal plane that parallels the MORVEL model spreading direction [4]. The bathymetric data sets [3] show significant void areas due to the difficulty and cost of guaranteeing complete coverage, but are complete enough to characterize the morphology of the abyssal hills.

TABLE I. DATA SETS ANALYZED

Location	DEM	DEM Grid Size	Full Rate (mm/yr)	Plate Spreading
Afar Triangle	SRTM	1", ~30 m	18.9	54˚
Atlantis Massif	GMRT	~2",~ 53 m	22.3	102˚
East Pacific Rise	GMRT	~2", ~58 m	141.7	104˚

II. FAULT SCARP CHARACTERISTICS

A normal fault plane, and the resulting fault scarp, can be defined by the dip and strike, or by its dip and dip direction. The dip and dip direction provide the least ambiguity, and correspond directly with the slope and aspect direction computed in standard GIS operations.

The two focal mechanisms for the normal faults in the Afar region and Atlantis Massif generally have the same strike, and dip 30-60˚ in opposite directions. Typically conjugate faults will develop with both orientations, but the dip at the surface may not equal the dip of the fault plane at the earthquake focus, and erosion might reduce the dip of the fault plane [8]. Fig. 2 shows profiles across the fault scarps in the three regions.

Fig. 3 shows the distribution of aspect for selected slope categories for two of the data sets. For the SRTM data from the Afar region, the overall data set and the flatter categories show a large overabundance of aspects in the 8 principal directions, a result of the quantization resulting from the integer resolution of the elevation data. While the gridded bathymetry may be no more accurate than the SRTM data, the floating point elevations smooth the aspect distribution. Both distributions show a strong tendency for the aspects to match the plate spreading direction. The East Pacific Rise data show a number of orthogonal aspects

In: Geomorphometry for Geosciences, Jasiewicz J., Zwoliński Zb., Mitasova H., Hengl T. (eds), 2015. Adam Mickiewicz University in Poznań - Institute of Geoecology and Geoinformation, International Society for Geomorphometry, Poznań

for the slopes above 30%, which correspond with the conical volcanoes that occur in lines perpendicular to the ridge.

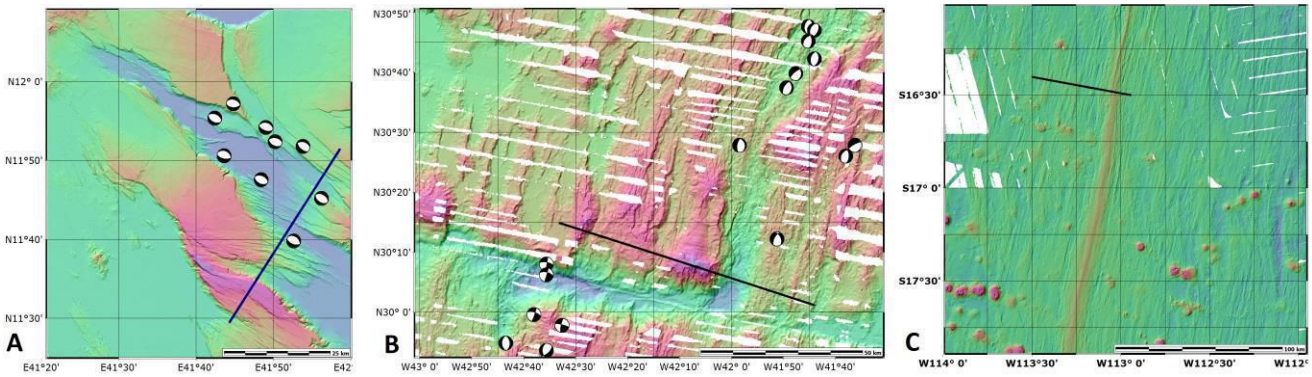


Figure 1. Normal faults from Afar Triangle (A), Atlantis Massif on the Mid Atlantic Ridge (B), East Pacific Rise south of the Garrett Fracture Zone (C).

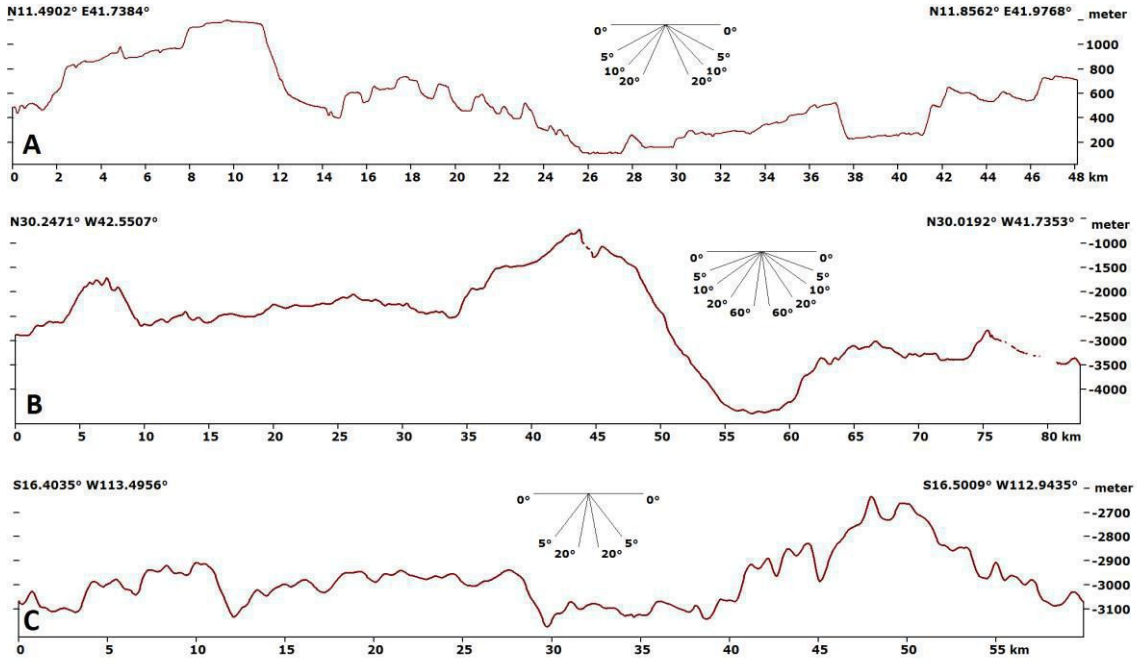


Figure 2. Topographic profiles from Afar Triangle (A, vertical exaggeration 6 times), Atlantis Massif on the Mid Atlantic Ridge (B, vertical exaggeration 4 times, with ridge axis at 57 km), and East Pacific Rise south of the Garrett Fracture Zone (C, vertical exaggeration 15 times, with ridge axis at 50 km).

Fig. 3 shows the topographic fabric [9,10], with vector overlays that show the strength of the fabric with the vector lengths, and the orientation. The rose diagrams show the fabric perpendicular to the aspect directions in Fig. 3, and parallel to the strike of the fault planes. The fabric calculates an average for a region (500 m in Afar, 750 m in the bathymetric data due to the larger grid spacing), and excludes flat regions and those with no significant trend, and the rose diagrams show a strong concentration perpendicular to the extension direction. The rose diagrams in Fig. 4 have only a small fraction of the number of points in the aspect distributions in Fig.3, and the operation of computing area averages accentuates the regional trends.

Exceptions to the regional fabric orientation occur where secondary processes alter the topography. On the Mid Atlantic Ridge (Fig. 4B), the Atlantis Fracture Zone reorients the topography to an east-west trend, which also happens on the large corrugations of the domal core complex. On the East Pacific Rise (Fig. 4C), domal volcanoes also deflect the linear pattern of abyssal hills.

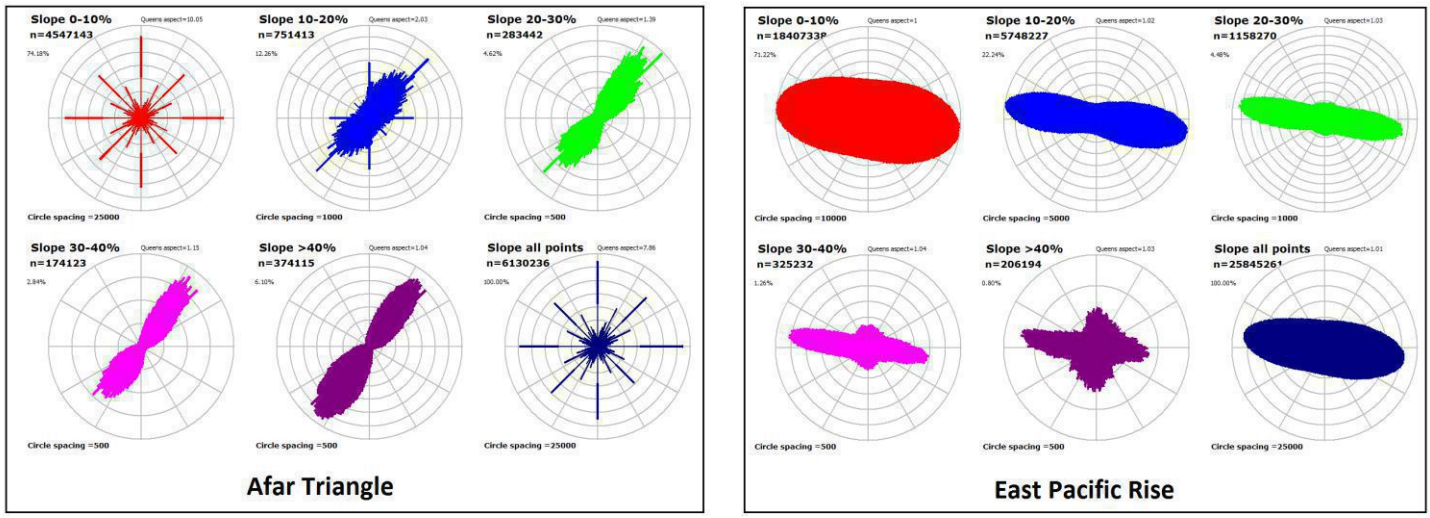


Figure 3. Aspect directions by slope category for the Afar Triangle and East Pacific Rise.

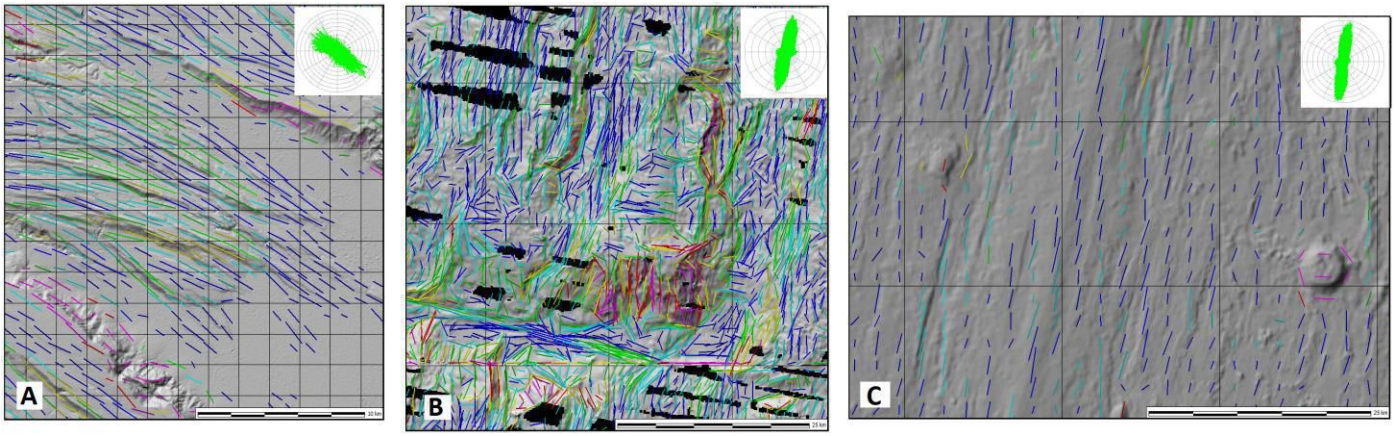


Figure 4. Topographic fabric, colored by local relief, for portions of the data sets covering the Afar Triangle (A), Atlantis Massif on the Mid Atlantic Ridge (B), and East Pacific Rise south of the Garrett Fracture Zone (C). Insets show distribution of fabric for the entire data set.

Figure 4 shows the relief in the regions used to define the topographic fabric. High values of relief distinguish the transform fault valley, core complex edifice, and submarine volcanoes from typical abyssal hills. Fig. 5 shows identification of likely fault scarps, using aspect and slope, or just the steepest slopes.

III. Conclusion and Future Work

This analysis used medium scale topography. The orientation of the terrain fabric matches the fault planes inferred from plate tectonic models, and earthquake focal mechanisms. Aspect distributions reflect the fault scarps, and the combination of slope and aspect can identify likely scarps.

With the exploding availability of lidar DEMs with typical resolution of 1 m, the techniques will be applied and compared to other work [e.g.11] in the terrestrial realm; comparable bathymetric data sets remain beyond widespread accessibility. We will also work to create fault scarp objects, and look to model the changes in scarps as they transfer motion to other faults along strike.

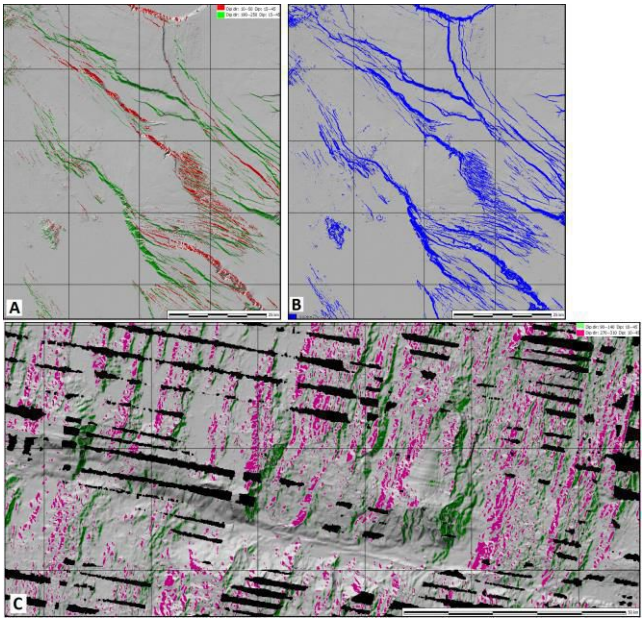


Figure 5. (A). NE-dipping (red) and SW-dipping (green) surfaces in Afar defined by slope and dip direction. (B) Steep surface in Afar. (C) E-dipping (green) and W-dipping (red) surfaces along the Atlantis Fracture Zone.

REFERENCES

[1] Gilbert, G.K., 1872, "Report of G.K. Gilbert, Geological Assistant, in Wheeler, G.M., Preliminary Report of Explorations Principally in Nevada and Arizona, U.S. Army Corps of Engineers, p.93-96.

ACKNOWLEDGMENT

Analysis done with the MICRODEM program. Recent improvements to parallelize operations greatly speed up many of these computations.

[2] Macdonald, K.C., Fox, P.J., Alexander, R.T., Pockalny, R., and Gente, P., 1996, Volcanic growth faults and the origin of Pacific abyssal hills: Nature vol. 380, p.125-129. doi:10.1038/380125a0.

[3] Ryan, W.B.F., S.M. Carbotte, J.O. Coplan, S. O'Hara, A. Melkonian, R. Arko, R.A. Weissel, V. Ferrini, A. Goodwillie, F. Nitsche, J. Bonczkowski, and R. Zemsky, 2009. "Global Multi-Resolution Topography synthesis", Geochem. Geophys. Geosyst., 10, Q03014, doi: 10.1029/2008GC002332.

[4] DeMets, C., Gordon, R. G., and Argus, D. F., 2010. "Geologically current plate motions", Geophysical Journal International, v. 181, no. 1, p. 1-80, doi: 10.1111/j.1365-246X.2009.04491.x.

[5] Morton, W. H., and R. Black, 1975. "Crustal attenuation in Afar." Afar Depression of Ethiopia, A. Pilger and A. Rosier, eds., Inter-Union Commiss. Geodyn., Sci. Rep 14.

[6] Whitney, D.L, C. Teyssier, P. Rey, and W. R. Buck, 2013, Continental and oceanic core complexes: Geological Society of America Bulletin, v. 125, no. 3-4, p. 273-298, doi:10.1130/B30754.1

[7] Ekström, G., M. Nettles, and A. M. Dziewonski, 2012. "The global CMT project 2004-2010: Centroid-moment tensors for 13,017 earthquakes", Phys. Earth Planet. Inter., 200-201, 1-9, doi:10.1016/j.pepi.2012.04.002

[8] Hilley, George E., J. R. Arrowsmith, and Lee Amoroso, 2001. "Interaction between Normal Faults and Fractures and Fault Scarp Morphology." Geophysical Research Letters 28, no. 19 , p. 3777-3780.

[9] Guth, P.L., 2003, Eigenvector analysis of digital elevation models in a GIS: Geomorphometry and quality control: in Evans, I.S., Dikau, R., Tokunaga, E., Ohmori, H., and Hirano, M., eds., Concepts and Modelling in Geomorphology: International Perspectives: Terrapub Publishers, Tokyo, p.199-220.

[10] Guth, P.L., 2001, Quantifying terrain fabric in digital elevation models, in Ehlen, J., and Harmon, R.S., eds., The environmental legacy of military operations, Geological Society of America Reviews in Engineering Geology , vol. 14, p.13-25.

[11] Hilley, G. E., S. DeLong, C. Prentice, K. Blisniuk, and JR Arrowsmith, 2010 "Morphologic Dating of Fault Scarps using Airborne Laser Swath Mapping (ALSM) Data." Geophysical Research Letters, vol. 37, no. 4, L04301, doi:10.1029/2009GL042044.

Analysis of morphometric indexes to evaluate tectonic activity and slope instabilities: a case study in the Germanasca valley (NW-Alps, Italy)

Marco Bacenetti
Department of Earth Sciences
University of Torino
Torino, Italy
marco.bacenetti@unito.it

Luca Ghiraldi
Natural Sciences Museum of Torino
Regione Piemonte
Torino, Italy
luca.ghiraldi@gmail.com

Marco Giardino
Department of Earth Sciences
University of Torino
Torino, Italy

Luigi Perotti
Department of Earth Sciences
University of Torino
Torino, Italy

Abstract— **Possible interactions between recent tectonic activity and the evolution of mountain relief have been investigated in the Germanasca Valley (Cottian Alps, NW-Italy), an area of strong heterogeneity of drainage features and slope instabilities. Analyses by remote sensing (satellite/aerial DEM and orthophoto) and field survey allowed creation of a geodatabase managed by standardized procedures into a GIS environment. Morphometric analyses have been performed for interpreting the particular geomorphological setting. Alignment and/or coincidence of significant structural and morphological features (ridges, incisions, scarps) and preferred stream orientations indicates possible structural/tectonic controls on the onset and evolution of the drainage network.**

I. INTRODUCTION

The aim of this study is the characterization of the drainage basin system of the Germanasca River (NW Italy) through the use of morphometrics and morphotectonics indexes. In order to evaluate neotectonic activity and slope instabilities of the internal sector of the Western Alps. This area is affected by a diffuse low-magnitude seismicity (ML> 3), although in the past there have been some events of greater magnitude (1980 ML=4, 8 and 1808 MS=5.5). The framework of active structures, capable of generating earthquakes of this magnitude, is not yet fully known in this Inner sector of the Cottians Alps (Western Alps).

A DEM (5x5 meters) supplied by the Piemonte Region has been imported into the GIS environment in order to evaluate the basin and river network's geomorphometry. The workflow followed can be summarized in different steps: a) drainage network extraction and hierarchization; b) evaluation of linear and areal indexes; c) analysis of azimuthal distribution of drainage pattern and lineament features. The values of these parameters have been interpolated by means of geostatistical algorithms for the creation of a serie of thematic maps.

II. GEOLOGICAL AND GEOMORPHOLOGICAL SETTING

A. *Present day geomorphology*

In the central sector of the Western Alp, the Chisone and Germanasca valleys (Figure 1) are part of the Chisone Basin, a water-drainage system (area: 590 Km^2) developed between Susa valley (to the North) and Pellice Valley (to the South).

Both Chisone and Germanasca valleys lack of a major glacial cirque at the main valley head [1; 2]. On the contrary,

In: Geomorphometry for Geosciences, Jasiewicz J., Zwoliński Zb., Mitasova H., Hengl T. (eds), 2015. Adam Mickiewicz University in Poznań - Institute of Geoecology and Geoinformation, International Society for Geomorphometry, Poznań

tributary valleys are divided by high ridges (above 3000 m a.s.l.) with evident traces of alpine glacial modelling (i.e. cirques and moraines). In contrast with previous geological literature [3; 4], studies by the Earth Sciences Department of the University of Torino demonstrate that during LGM no unique valley glacier developed along the entire Chisone and Germanasca valleys. Tributary glaciers reached the main valley bottom and sometimes joined, but never overtopped the main valley's axis.

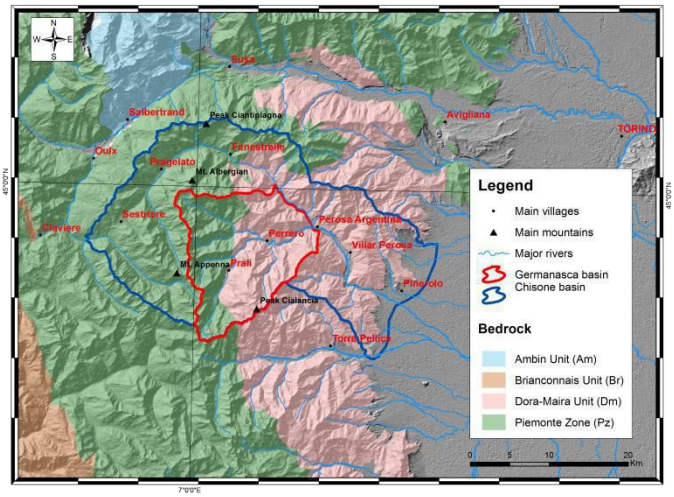


Figure 1 - View of central sector of Western Alps (Inner Cottian Alps).

Slope instabilities locally obliterated Pleistocene glacial and Holocene fluvial landforms. Many traces of large deep-seated gravitational slope deformation (DSGSD), such as counterslope scarps and trenches have been surveyed in the higher part of the valleys [5].

B. Neogene kinematics evolution

The arc of the Western Alps results from late collisional phase after convergence of the Adria plate and the European margin of the Tethys. Neogene Alpine tectonics was characterized by widespread orogen-parallel extension in the internal zones, coeval with westward propagation of the compressive front in the external zones [6]. Two main faulting stages can be distinguished within the post-metamorphic tectonic evolution of the inner Western Alps [7]: the first (late Oligocene-Early Miocene) is related to the dextral movements along the most important deformation zones; in the second (post- Early Miocene), major structures are reactivated as transtensive/normal faults. This complex kinematic evolution fits in a model of dextral transtension at the scale of the Western Alps, induced by the coexistence of two different driving forces active since the late Oligocene: the counterclockwise rotation of the Adria plate and the body forces acting inside the chain [7; 8]. This coexistence may have induced strain partitioning and, subsequently, complex spatial and chronological relations between transcurrent and extensional movements on a regional scale [7; 9].

As indicated before, the central sector of the Western Alpine Arc is an area of low-to-moderate magnitude seismic activity; however, since a few strong historical earthquakes have occurred, causing significant damage, and paleoseismic features have been recognized [10].

III. MATERIALS AND METHODS

The Germanasca basin has been classified following Strahler [11], 11 sub-basins and drainage features extracted by DEM analysis and digitized, relief proprieties and geomorphometric parameters spatially analyzed by means of the SAGA (System for Automated Geoscientific Analyses) extension of ArcGIS, and by MATLAB.

Satellite lineaments have been identified [12], then statistically classified according to their azimuthal frequencies, cumulative lengths and length (3 classes of frequencies: > 2500 m, 2500 to 5000 m, and > 5000 m.

The lineaments were identified on the satellite images according to the methodologies, proposed by [8]. The detected lineaments were, moreover, statistically analyzed according to their azimuthal frequencies, azimuthal frequencies for cumulative lengths and length classes. Frequencies were divided into three classes from the statistical distribution: less than 2500 m, 2500 to 5000 m, and more than 5000 m.

IV. RESULTS

A. Evaluation of linear and areal indexes

The Germanasca is a complex drainage network of the sixth order; 11 sub-basins have been characterized by their drainage linear and areal parameters: Hmax, Hmin, Hmean, Square, Perimeter, Hypsometric index (Hi), Strahler stream order, bifurcation ratio (Rbm), weighted bifurcation ratio (Rbw), direct bifurcation ratio (Rbd), index of bifurcation (Ir), Stream frequency, number and indexes of hierarchic anomaly (Ga, Δa, Da).

The difference between the maximum and the minimum height has been calculated in order to evaluate the energy of

relief. A moving window with search radius of 250 meters has been used, and a geothematic map has been created.

The Stream Length-gradient index (SL: slope normalized to length of river segments) provided comparisons between reaches of streams of different sizes [13], in order to investigate a possible morphogenetic role of recent tectonic activity. The results have been summarized in a second geothematic map, by using the natural neighbor interpolator (ArcGis by ESRI). The longitudinal profiles of the main rivers have been investigated in order to detect concavity and steepness indexes as well as knickpoints (Figure 2). These has been interpreted as geomorphological anomalies potentially related to surface and sub-surface deformational processes.

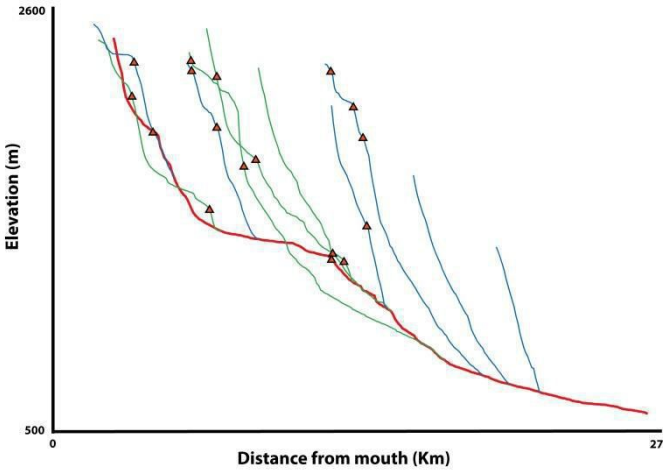


Figure 2 – Stream profile of Germanasca basin. Red: major river, blue: left tributaries, green: right tributaries. Yellow: knickpoint distribution.

B. Azimuthal distribution of lineament features and drainage patterns

Field data shows the post-metamorphic structural setting mainly consists of a tectonic network of faults and fractures formed within brittle-ductile to brittle deformation conditions.S patial and hierarchic relations derived from both field and remote sensing lineament interpretation indicates three main systems: Ln1 (N0°-N30°E), Ln2 (N55°-N70°E), Ln3 (N80°-N100°E). No differences in the lineament distribution and characteristics have been detected at the different scales and methods of analyses.

The drainage pattern of the Germanasca basin has been analyzed for assessing the azimuthal distribution of its segments. Figure 3 shows that the river change directions from N-S to W-E as the increase of the order of its stream segment.

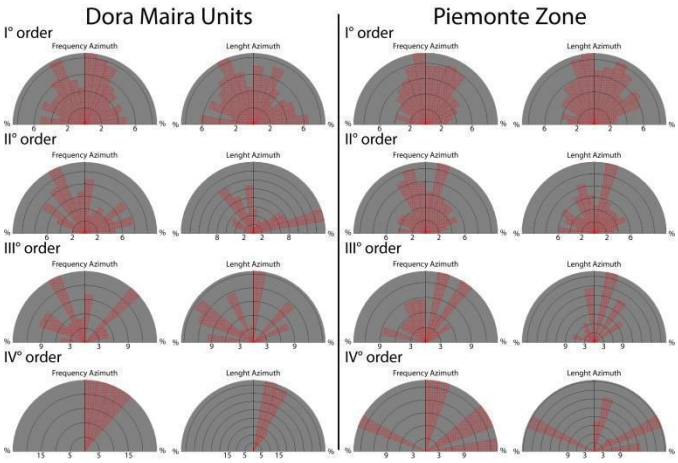


Figure 3 – Azimuthal distribution of the Germanasca drainage pattern.

V. Discussion and Conclusion

Analyses of structural and morphometric data within the Germanasca Valley allowed preliminary interpretation of geomorphological anomalies in the investigated area.

The stream network is characterized by straight deep incisions, asymmetric cross-profiles and stepped longitudinal profiles, sharp changes of channel directions and progressive river captures associated with retrogressive erosion. Higher concentrations of geomorphological anomalies are located in the upper part of drainage basin.

Alignment and/or coincidence of significant structural (faults and fractures) and morphological features (ridges, incisions, scarps) and preferred stream orientations indicates possible structural/tectonic controls on the onset and evolution of the drainage network, particularly in the middle and lower parts of Faetto Valley.

Morphometric analyses allowed identification of sectors characterized by higher frequency of nick points, SL anomalies and high values of energy relief. These coexists with increased frequencies of iso-oriented neotectonic lineaments, thus suggesting target areas of stronger morphotectonics influence on the evolution the mountain relief.

REFERENCES

1. Vai, G.B. and Cantelli, L., 2004 - Map 1 - Last Glacial Maximun (22 ± 2 ka cal BP) average air temperature of about 4.5°C lower than today. In: 32nd International Geological Congress, Florence, Italy.
2. Carraro, F., and M. Giardino, 2004 - Quaternary glaciations in the western Italian Alps: A review, in Developments in Quaternary Science, edited by J. Ehlers and P. L. Gibbard, pp. 201–208, Elsevier, Amsterdam, doi:10.1016/S1571-0866(04)80071-X.
3. Franchi S., Mattirolo E., Novarese, V. and Stella A., 1913 - Carta Geologica d'Italia. Foglio 67 "Pinerolo", Scala 1:100.000. I R. Comit. Geol. It.
4. Gabert P., 1962 - Les plaines occidentales du Po et leurs Piedmonts. Etude morphologique. Lovis Jean, Gap, 531pp.
5. Giardino, M. and Lollino, G., 2004 - Field Trip: Instrumented experimental sites for the control of landslide hazards in mountain environments: the Germanasca and Susa valleys (Northwestern Italy). In: 32nd International Geological Congress, Florence, Italy.
6. Sue C., Delacou B., Champagnac J.D., Allanic C., Tricart P. and Burkhard M., 2007 - Extensional neotectonics around the bend of the Western/Central Alps: an overview. Int. J. Earth Sci., 96, 1101-1129.
7. Perrone, G., Eva, E., Solarino, S., Cadoppi, P., Balestro, G., Fioraso, G. and Tallone, S., 2010 - Seismotectonic investigations in the inner Cottian Alps (Italian Western Alps): An integrated approach. Tectonophysics 496(1-4), 1–16.
8. Sue, C. and Tricart, P., 2003 - Neogene to ongoing normal faulting in the inner western Alps. Tectonics, 22, doi:10.1029/2002TC001426.
9. Champagnac J.D., Sue C., Delacou B., Tricart P., Allanic C. and Burkhard M., 2006 - Miocene orogen-parallel extension in the inner Western Alps revealed by dynamical fault analyses. Tectonics, 25, TC3014, doi: 10.1029/2004TC001779.
10. Collo, G., and Giardino, M, 1997 – Deformation of "Villafranchian sediments in the Chisone Valley (Western Alps, Italy). J. Geodynamics, 24 (1-4), 281-297
11. Strahler, A. N 1952 - Dynamic basis of geomorphology: Geol. Soc. America Bull., v. 63, p. 923-938
12. Morelli M and Piana F, 2006 - Comparison between remotely sensed lineaments and geological structures in intensively cultivated hills (Monferrato and Langhe domains, NW Italy). Int. J. Remote Sensing, 27, 4471-4493.
13. Seeber, L., and Gornitz V. 1983 - River profiles along the Himalayan arc as indicators of active tectonics. Tectonophysics, 92, 335-467, doi:10.1016/0040-1951(83)90201-9.

Towards delineation of the morphostructural division of the Western Carpathians using object-based image analysis

Peter Bandura, Jozef Minár, Tatiana Harciníková
Faculty of Natural Sciences
Comenius University in Bratislava
Bratislava, Slovakia
peter.bandura@uniba.sk; jozef.minar@uniba.sk

Lucian Drăguţ
Department of Geography
West University of Timişoara
Timişoara, Romania
lucian.dragut@fulbrightmail.org

Abstract— **Preliminary results of an object-based methodology for delineation of the morphostructural division of the Western Carpathians region are presented. Normalized slope gradient and vertical dissection were used as input layers. Automated object extraction was carried out using a multi-resolution segmentation algorithm implemented in the eCognition® Developer software. Visual evaluation and preliminary quantitative quality assessment of the resulting segments boundaries showed a potential of using this method for delineation of objects fairly similar to the expert-made (manually drawn) traditional geomorphologic regions. Future work on both segmentation and classification, as well as quantitative accuracy assessment of the objects is needed.**

INTRODUCTION

Description of the Western Carpathians mountain arc as an active dome-like megamorphostructure was mentioned for the first time by [1]. This mountain range can be considered as the first-order morphostructural division, which includes a mosaic of mountains and valleys (divisions of the 3rd order) [2] aggregated, at a higher level, into concentric morphostructural regions of the 2nd order. Lacika and Urbánek [3] relied on the above mentioned hierarchy to create a 2nd order morphostructural division, but only for the territory of Slovakia and without further interpretation. Minár et al. [4] proposed the most recent morphostructural subdivision of the whole Western Carpathians by integrating the traditional geomorphological regions based on both morphometric analysis and geodynamics. Use of hand-drawn traditional geomorphological regions could be considered as shortage or lack of objectivity here.

The first significant application of object-based image analysis (OBIA) in geomorphometry was introduced in the same time by [5] and [6]. Many other studies that followed showed the potential of segmentation for landform mapping.

In contemporary geomorphology and geomorphometry the demands for objective and reproducible methodological approaches are very high. Thus, we try to realize a fully automated method for delineation of morphostructural division of the Western Carpathians in a relatively objective manner. Since the active morphostructures are well-reflected in terrain morphology and therefore they should be also reflected in the traditional geomorphological regions, the regionalization using only DEM and its derivatives should be feasible. The location of the study area (boundary used here has gradational character and contains also transitional and marginal areas) and the traditional geomorphological regions can be seen in Fig. 1.

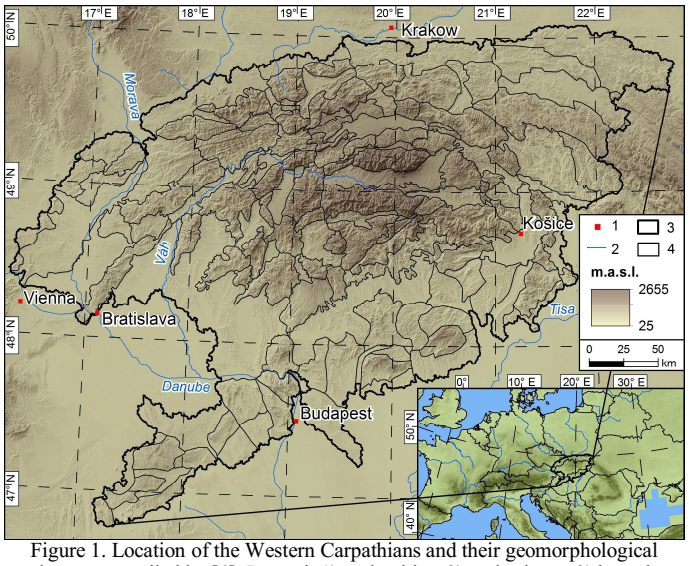


Figure 1. Location of the Western Carpathians and their geomorphological regions as compiled by [4]. Legend: 1) main cities; 2) main rivers; 3) boundary of the Western Carpathians; 4) traditional geomorphological regions

In: Geomorphometry for Geosciences, Jasiewicz J., Zwoliński Zb., Mitasova H., Hengl T. (eds), 2015. Adam Mickiewicz University in Poznań - Institute of Geoecology and Geoinformation, International Society for Geomorphometry, Poznań

METHODS

Input data and their pre-processing

SRTM V4 dataset [7] resampled to 80-meter resolution (approximated cell-size for latitude of our study area) was employed. Part of the noise was removed using r.denoise algorithm with a threshold value of 0.99 and 5 iterations [8]. The DEM was then used for the derivation of two land-surface variables - slope gradient and vertical dissection, which is often referred to by other terms, e.g. available relief or range. The latter represents the amplitude of the land surface undulation.

The slope gradient was computed with a size-changing moving window using the Characteristic scale script in LandSerf GIS [9]. This method allows to measure a surface parameter at a range of scales and find the most extreme one. The largest moving window size was set to 25 cells. The vertical dissection of terrain was computed as the standard deviation of elevation in the circle moving window with a diameter of 2 km [10].

Before performing multi-resolution segmentation, the values of the slope gradient and vertical dissection were transformed in order to bring their frequency distribution close to a normal (Gaussian) distribution. According to the results of the Normalization script developed by [11], we used logarithmic function for slope gradient and square root function for vertical dissection. The tool [11] was developed for slope gradient and curvatures, and because the vertical dissection raster had quite similar data distribution, it was successfully applied on it as well. These transformed input layers were used in the subsequent object-oriented image analysis.

Multi-resolution segmentation

The delineation of morphometric individuals was performed using multi-resolution segmentation in the eCognition® Developer software. The most fundamental parameter in multi-resolution segmentation is the scale parameter (SP), that was determined with the automated tool called Estimation of scale parameter 2 (ESP2) [12]. The tool automatically creates objects at three scale levels. The SP increments for levels were set to 1, 2 and 5 (with a starting SP of 1); values for shape and compactness parameters were set to default (0.1 and 0.5); number of loops to 200, and both hierarchical and non-hierarchical approach were applied. The segmentations were carried out for single input layers, as well as for combination of the layers. Since the SP values picked by the ESP2 are just approximations, the final values were selected by additional visual examination of the local variance graph computed in the non-hierarchical approach (as the most prominent peaks). For technical details on multi-resolution segmentation, the reader is referred to [12].

Compatibility assessment

Preliminary compatibility and significance assessment of boundaries of the delineated objects were at first done by visual comparison and then by calculation of some of the quality measures suggested by [13] against boundaries of the reference polygons – traditional geomorphological regions of the whole Western Carpathians (Fig. 1). Calculation of these quality measures is based on matching reference and delineated polygon boundaries. This was carried out by creating a series of buffers (so-called domains) with a range of widths around object boundaries (reference and delineated) and their intersection with the original boundaries (delineated and reference, respectively). As a result, two quality measures and their ratio were computed by a python script in QGIS (PyQGIS):

1. Completeness – percentage of the reference boundaries length within the delineated data domain, saying how complete the delineated network is (optimal value is 1).
2. Correctness – percentage of the delineated boundaries length within the reference data domain, saying how correct the delineated network is (optimal value is 1).

Based on their ratio (Correctness/Completeness) the most optimal segmentation was determined.

RESULTS AND DISCUSSION

To perform successful segmentation of the terrain data resulting in meaningful objects with relatively compact shape, the transformation of the data distribution is crucial. As a result of MRS, relatively homogeneous objects in terms of terrain roughness were delineated. The segmentation of individual layer allowed us to see which terrain boundaries are represented by each layer. Segmentation of both layers combined proved to be the most suitable. Based on the values from the Local Variance graph, five levels of segmentation with SP 71, 83, 115, 135 and 154, with equal weights for both layers, were carried out. Generally, the course of the object boundaries from all segmentations (not shown here) in most cases clearly divided the terrain into basic and simple block structures – mountains ranges and intermountain basins and in some cases also into their smaller parts. Since higher values of SP generally led to larger and thus less homogeneous segments, MRS with higher SP (e.g. 154) resulted in larger regions, which in some cases consist of relatively smaller mountains or plains. On the contrary, MRS with lower SP (e.g. 71 or 83) even subdivided larger structures into their smaller parts. Objects from all five segmentations were used as an input into the quantitative compatibility assessment, whose results are in the Table 1.

We included some basic statistics of both the delineated objects and the geomorphological regions.

TABLE I. COMPATIBILITY ASSESSMENT OF THE DELINEATED OBJECTS AGAINST GEOMORPHOLOGICAL REGIONS WITH THEIR BASIC STATISTICS

Level	Com	Corr	Corr/ Com	N	Mean area (km²)	Mean elevation (m a.s.l.)	SD elevation (m a.s.l.)
SP 71	0.80	0.53	0.66	536	165.66	403.97	233.93
SP 83	0.76	0.55	0.73	402	220.88	399.98	239.98
SP 115	0.67	0.61	0.91	223	398.18	408.71	238.34
SP 135	0.62	0.63	1.01	173	513.26	416.76	245.61
SP 154	0.60	0.65	1.09	142	625.31	426.91	244.71
Geomor. regions	-	-	-	144	616.6	476.2	239.89

Com – completeness; Corr – correctness; Corr/Com – ratio between them; N – number of polygons

The value of *Correctness* increases with higher SP values. On the other hand, the values of *Completeness* show the opposite trend, which is obvious because with lower SPs the delineated network and its domain are more extensive. Therefore, we combined these two measures and based on the value of their ratio the segmentation with SP 135 was selected as the most plausible (the value of the ratio is closest to 1). Resulting objects of the chosen segmentation are displayed in Fig. 2.

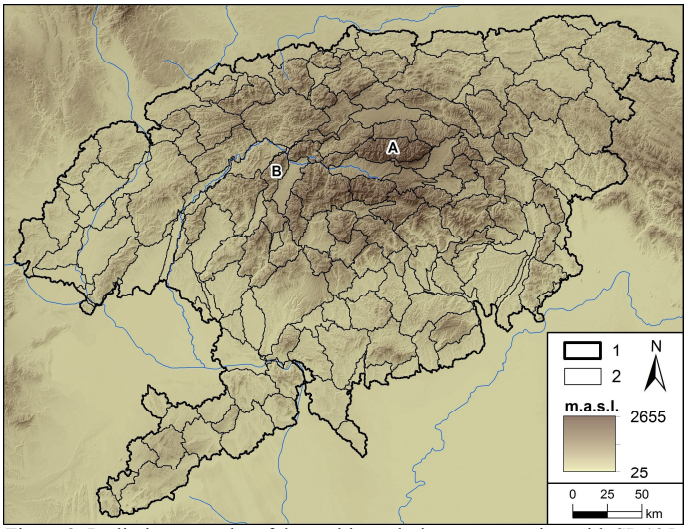


Figure 2. Preliminary results of the multi-resolution segmentation with SP 135. The High Tatras (A) and the Malá Fatra (B) mountains.
1) boundary of the Western Carpathians; 2) delineated objects.

There are several cases where the mismatch between the delineated and reference boundaries is clearly visible. There is also a small difference between the number of delineated and reference polygons as well as between their average area, which can be attributed to several reasons. Firstly, it might be caused by local differences in the level of detail in manual mapping, while the scale of segmentation holds globally. Especially in areas with large extent, highly rugged terrain and contrast topography, being the case of the Western Carpathians, the globally set SP value tends to over-segment rough areas, while under-segmenting smooth ones. This could be possibly eliminated by using refining segmentations of objects by separating mountains and basins delineated on higher (relatively rough) level, and creating lower levels with specific SPs for each domain. Secondly, traditional geomorphological regions could have been delineated also by other criteria than geomorphometric (e.g. geology, geomorphological development), and subjective decisions of the authors played some role, too. Moreover, inconsistent methodological approaches in different countries might have also contributed to different levels of detail in the reference regions. This should be eliminated by using only the Slovak part of the area for compatibility evaluation. The traditional regions here are more (and relatively consistently) detailed due to existence of subregions and parts.

Most distinctive and relatively unquestionable boundaries appear between contrasting areas - relatively flat basins bounded by high mountains with steep slopes e.g. High Tatras and Low Tatras mountains, Malá Fatra mountains and their surroundings. Thus, in these cases the boundaries are quite similar to those manually-drawn. Major differences occur in the areas where the reference polygons were apparently drawn according to other criteria than terrain morphology.

The classification shown in Fig. 3 clearly points to a gradational structure of the Western Carpathians terrain. Furthermore, the concentric clustering of objects towards the central and highest part of the area (High Tatras mountains) is clearly visible. However, this is just an example out of many possible classifications, and a feasible illustration of relatively meaningful object delineation even in this stage of research.

Future work will focus on the improvement of both object delineation (segmentation), as well as quantitative compatibility assessment of the delineated objects using both the already employed polyline-based method [13, 14], and some of the available methods designed for polygons described in e.g. [15], [16] and [17]. Even though the compatibility evaluation of segmentation is based on a comparison with the traditional geomorphological regions as the reference objects, our main goal of this part of the research is not to fully recreate these

regions, but rather to provide their alternative in more detailed way, mainly in the fuzzy and questionable areas. Furthermore, some refinement of the final objects resulting from the most plausible segmentation will be needed due to over/under-segmentation in some parts of the area.

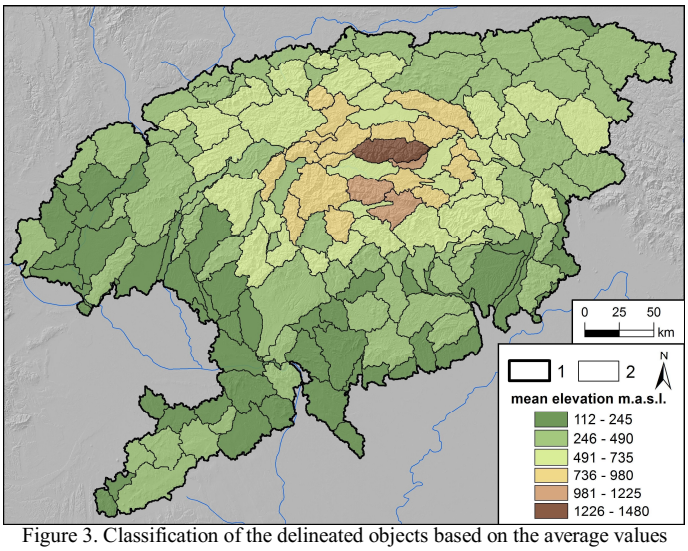


Figure 3. Classification of the delineated objects based on the average values of elevation per polygon. Classes represent multiplied values of its standard deviation. 1) boundary of the Western Carpathians; 2) delineated objects.

CONCLUSIONS

According to the results so far, object-based image analysis seems to be a suitable tool for the automated delineation of the gemorphometric divisions that represent the whole or parts of active morphostructures within the Western Carpathians. The segmentation based on layers representing meaningful morphometric characteristics such as slope gradient and vertical dissection of terrain can be used for the definition of basic morphotectonic regions. Nevertheless, further work composed of several steps mentioned in the discussion is necessary. However, using this approach, we should be able to objectivize the input objects basis for subsequent analysis resulting in morphostructural regionalization as proposed by [4].

ACKNOWLEDGEMENT

This work was supported by the Slovak Research and Development Agency under the contract No. APVV-0625-11 and by the Comenius University in Bratislava under the contract No. UK/137/2015. Peter Bandura is grateful to Ovidiu Csillik for all the help and support provided during internship in Timişoara.

REFERENCES

[1] Mazúr, E., 1965. "Major features of the Western Carpathians in Slovakia as a result of young tectonic movements". In Geomorphological Problems of Carpathians, Edited by: Mazúr, E. and O. Stehlík, SAV, Bratislava.

[2] Mazúr, E., 1979. "Morphostructures of the Western Carpathians and their development". AFRNUC. Geographica, 17: 21-34 (in Slovak)

[3] Lacika, J. and J. Urbánek, 1998. "New morphostructural division of Slovakia". Slovak Geol. Mag., 4: 17-28.

[4] Minár, J., M. Bielik, M. Kováč. D. Plašienka, M. Stankoviansky, and H. Zeyen, 2011. "New morphostructural subdivision of the Western Carpathians: An approach integrating geodynamics into targeted morphometric analysis". Tectonophysics, 502: 158-174.

[5] Drăguţ, L. and T. Blaschke, 2006. "Automated classification of landform elements using object-based image analysis". Geomorphology, 81: 330-344.

[6] Asselen, S. and A. C. Seijmonsbergen, 2006. "Expert-driven semi-automated geomorphological mapping for a mountainous area using a laser DTM". Geomorphology, 78/3-4: 309-320.

[7] Jarvis, A., H. I. Reuter, A. Nelson, and E. Guevara, 2008. "Hole-filled SRTM for the globe Version 4". Available from the CGIAR-CSI SRTM 90m Database.

[8] Stevenson, J. A., X. Sun, and N. C. Mitchell, 2010. "Despeckling SRTM and other topographic data with a denoising algorithm". Geomorphology, 114: 238-252.

[9] Wood, J., 2009. "Chapter 14 Geomorphometry in Landserf", In Geomoprhometry-Concepts, Software, Applications. Development in Soil Science, vol. 33, Edited by: Hengl, T. and H. I. Reuter.

[10] Mazúr, E. and V. Mazúrová, 1965. "The map of relative relief of the territory of Slovakia". Geografický časopis, 17: 3-18 (in Slovak).

[11] Csillik, O., I. S. Evans and L. Drăguţ. "Transformation (normalization) of slope gradient and surface curvatures, automated for statistical analyses from DEMs". Geomorphology (submitted).

[12] Drăguţ, L., O. Csillik, C. Eisank, and D. Tiede, 2014. "Automated parameterisation for multi-scale image segmentation on multiple layers. ISPRS Journal of Photogrammetry and Remote Sensing, 88: 119-127.

[13] Heipke, C., H. Mayer and C. Wiedemann, 1997. "Evaluation of automatic road extraction". Int. Arch. Photogramm. Remote Sens, 23: 47-56.

[14] Thommeret, N., J. S. Bailly, and C. Puech, 2010. "Extraction of thalwegs networks from DTMs: application to badlands. Hydrology and Earth System Sciences, 14: 1527-1536.

[15] Clinton, N., A. Holt, J. Scarborough, L. Yan, and P. Gong, 2010. "Accuracy assesment measures for object-based image segmentation goodness". Photogrammetric Engineering & Remote Sens., 76/3: 289-299

[16] Zhan, Q., M. Molenaar, K. Tempfli, and W. Shi, 2005. "Quality assessment for geo-spatial objects derived from remotely sensed data". International Journal of Remote Sensing, 26: 2953-2974.

[17] Eisank, C., M. Smith, and J. Hillier, 2014. "Assessment of multiresolution segmentation for delimiting drumlins in digital elevation models". Geomorphology, 214:452-464.

Comparative analysis of manual and automatic extractions of hummock landforms in Mt. Gassan, northwestern Japan

Yuichi S. Hayakawa
Center for Spatial Information Science
The University of Tokyo
Kashiwa, Japan

Yoshida Hidetsugu
Faculty of Letters
Meiji University
Tokyo, Japan

Lucian Dragut
Department of Geography
West University of Timişoara
Timişoara, Romania

Takashi Oguchi
Center for Spatial Information Science
The University of Tokyo
Kashiwa, Japan

Abstract—We perform comparative analysis for quantitative extraction of hummock landforms in a debris avalanche deposits formed by volcanic sector collapse. Polygons of hummocks derived from manual reading of aerial photographs are more similar to those from object-oriented image analysis than from elevation scale change.

I. Introduction

Hummocks are characteristic landforms formed on debris avalanche deposits (DADs) after catastrophic sector collapse of volcanoes [1,2], being a key morphology to estimate the characteristics of DADs. While identification of such hummocky landforms has often been performed manually using stereo-paired aerial photographs with support of field investigations [3-9], quantitative and quick extraction of hummock landforms from topography itself using digital elevation models (DEMs), which shall be useful particularly in remote areas, is a challenging theme. Here we perform comparative analysis of manual and automatic methods of the identification of hummock landforms.

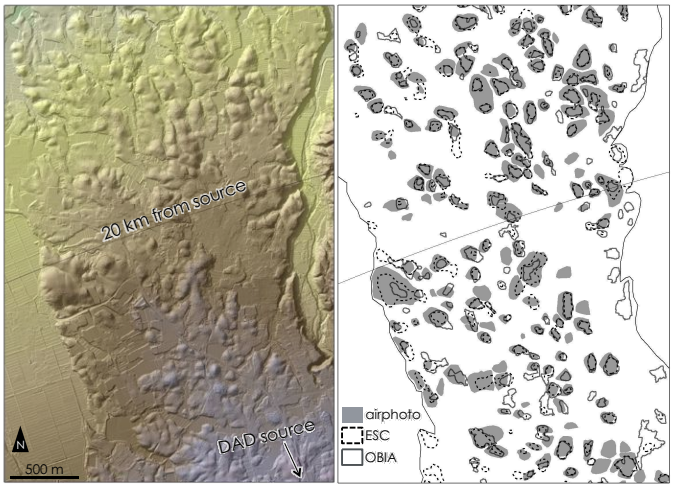


Figure 1. Hillshade image of the central part of the study site by 2-m resolution airborne laser scanning DEM, and hummock polygons extracted by the three different methods; light-gray-filled: manual airphoto reading, dashed black outline: ESC; solid dark-gray outline: OBIA

II. Study Area and Methods

We investigate the Sasagawa DAD (<400-300 ka, 50 ± 30 x10^8 m^3) located at northern side of the Mt. Gassan volcano in northwestern Japan. DEM with a resolution of 2 m derived from airborne laser scanning is used for the automatic extraction methods.

As a reference, we use polygon data of hummocks manually extracted from stereo-paired aerial photographs taken in 1990s by means of stereopsis ("airphoto reading"). Two other automatic methods are proposed. One utilizes scale-dependent changes in elevation with increasing buffer lengths (10–150 m by a 10-m step) for each cell of DEM ("ESC"; elevation scale change). Local bulges with relatively higher elevations within the search scales can be identified by this method, which is similar to the algorithm to identify locally steep sections in rivers (knickzones) by slopes [10]. The other applies object-based image analysis ("OBIA") [11]. A multiresolution segmentation (MRS) was performed on a residual relief layer, computed as a difference between the original DEM and a smoothed surface. Classification of segments considered mean layer values, segment geometry, and context.

III. Results and Discussion

More than two hundred polygons are investigated in the study area. The area properties of the polygons derived from the different three methods indicate that the OBIA method is more

In: Geomorphometry for Geosciences, Jasiewicz J., Zwoliński Zb., Mitasova H., Hengl T. (eds), 2015. Adam Mickiewicz University in Poznań - Institute of Geoecology and Geoinformation, International Society for Geomorphometry, Poznań

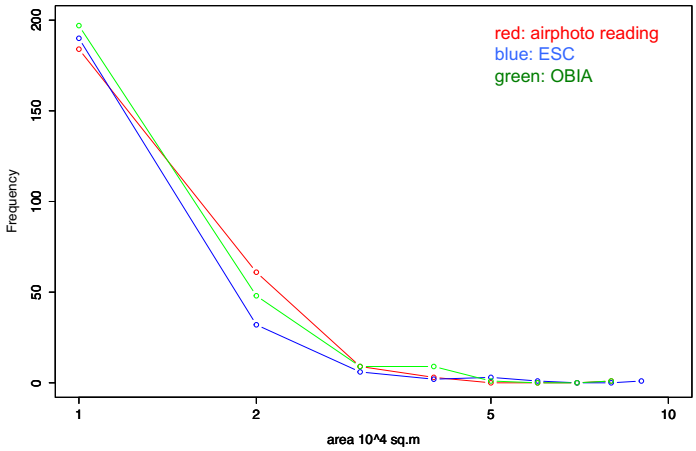


Figure 2. Histograms of polygon area of hummocks for the different extraction methods.

comparable to the airphoto reading in terms of polygon number and size (Table I, Fig. 2), while the ESC method often gives unexpected mounds particularly along the eastern edge of the DADs (Fig. 1). Although the actual extent of hummock edges would need to be validated in the field, the good agreement of airphoto reading and the OBIA methods method shows much potential of identifying numerous hummocks of DADs in remote areas.

IV. Concluding Remarks

The comparative analysis of different approaches for hummock extraction in DADs was performed in this study as a case of a Japanese volcano. An object-oriented methodology was found suitable to extract hummocks in a way that closely replicates human interpretation. Based on this, such approaches will be further assessed in other regions including Japan and pan-Pacific areas. Examinations with different DEM resolutions and object scales are also important for worldwide comparisons.

TABLE I. Comparison of polygon sizes by the different methods

	airphoto reading	ESC	OBIA
number of polygons	258	235	265
mean area (m^2)	8331.65	6931.30	8432.70
maximum area (m^2)	71174.43	85501.58	73584.50
minimum area (m^2)	1074.20	5.48	1092.00

Acknowledgment

This study is funded in part by JSPS KAKENHI Grant Number 25702014. Digital elevation models by Kokusai Kogyo CO. are used as the CSIS Joint Research #255 using spatial data provided by Center for Spatial Information Science, The University of Tokyo.

References

[1] Siebert, L., 1984. "Large volcanic debris avalanches: characteristics of source areas, deposits, and associated eruptions". J. Volcanol. Geotherm. Res. 22, 163–197.

[2] Ui, T., Takarada, S., Yoshimoto, M., 2000. "Debris avalanches". In: Sigurdsson, H., Houghton, B.F.,McNutt, S.R., Rymer, H., Stix, J. (Eds.), Encyclopedia of Volcanoes. Academic Press, San Diego, 617–626.

[3] Glicken, H., 1996. "Rockslide-debris avalanche of May 18, 1980, Mount St. Helens volcano, Washington". USGS Open-file Report 96-677, 1–90.

[4] Yoshida, H., 2012. "Evaluation of the 1888 sector-collapse volume of Bandai volcano, Japan, in terms of the size–distance distribution pattern of debris avalanche hummocks". Trans. Jpn Geomorphol. Union 33, 45–60 (in Japanese with English abstract).

[5] Yoshida, H., 2013a. "Reexamination of volume loss due to the catastrophic sector-collapse causing the Okinajima debris avalanche of Bandai volcano, Japan". Trans. Jpn Geomorphol. Union 34, 1–19 (in Japanese with English abstract).

[6] Yoshida, H., 2013b. "Decrease of size of hummocks with downstream distance in the rockslide-debris avalanche deposit at Iriga volcano, Philippines: similarities with Japanese avalanches". Landslides 10, 665–672.

[7] Yoshida, H., 2014. "Hummock alignment in Japanese volcanic debris avalanches controlled by pre-avalanche slope of depositional area". Geomorphology, 223, 67–80.

[8] Yoshida, H., and Sugai, T., 2010. "Quantitative examination of hummock alignment in debris avalanche deposits: Zenkoji debris avalanche, Usu volcano, Japan". Geogr. Rev. Jpn. Ser. B 83, 64–72.

[9] Yoshida, H., Sugai, T., Ohmori, H., 2012. "Size–distance relationship for hummocks on volcanic rockslide-debris avalanche deposits in Japan". Geomorphology 136, 76–87.

[10] Hayakawa, Y., and Oguchi, T., 2006. "DEM-based identification of fluvial knickzones and its application to Japanese mountain rivers" Geomorphology 78, 90–106.

[11] Dragut, L., and Blaschke, T., 2006. "Automated classification of landform elements using object-based image analysis". Geomorphology 81, 330–344.

The Salerno University Geomorphological Informative Mapping System: the Licosa polygentic case study (Cilento European Geopark, southern Italy).

Guida D., Cuomo A.
Department of Civil Engineering
Salerno University
Fisciano Campus, Italy

Cestari A., Siervo V.
C.U.G.RI- interUniversity Consortium for Prevision and Prevention of Great Risks,
Fisciano (SA), Italy

Dramis F.
Department of Geological Science,
Roma Tre University,
Rome, Italy

Palmieri V.
ARCADIS - Campanian Agency for Soil Defence,
Naples

Abstract— **The paper presents a specific application to a typical Mediterranean landscape (Punta Licosa headland) based on an advanced procedure of the hierarchical, multi-scale, object-based geomorphological mapping system in use at the Salerno University (Italy). The study area is a wide valley head characterized by shallow landslides and active stream erosion affecting Pleistocene landforms produced by diffusive processes (hollows, side-slopes, and noses). Based on simple geomorphometric parameters, from object-based geomorphological map obtained by supervised automatic landforms recognition, spatial analyses on target areas of the landscape have been performed. Results of the above analyses highlighted superposition landform components related to two distinctive morphogenetic controls. The proposed procedure allows the quantitative reconstruction of geomorphic events and scenarios in polygenetic/poly-chronologic landscapes, useful to assessing landslide and erosion hazard in a dynamic way.**

I. INTRODUCTION

Traditional geomorphological mapping, based exclusively on extensive field surveys, aerial photo analysis and symbol-based representation, is generally unable to provide a complete representation of landscape complexities at different scales and, therefore, is inadequate to fulfill all the scientific and practical needs of the modern society [1]. On the other hand, multiscale mapping, managed by Geographical Information System (GIS) [2] are easily readable and applicable to multidisciplinary landscape studies, such as geo-hazard zoning for risk mitigation, land conservation, inventory of geo-sites, soil mapping, hydrology, landscape ecology, environmental engineering, forestry and agronomy. Current advances in automated terrain analysis are based on geo-statistical and geo-morphometric concepts and procedures [3] [4] using both satellite imagery and Digital Elevation Models (DEMs), processed by GIS [5]. Automatic landform recognition is based both on supervised and unsupervised approaches. Supervised approach calibrates grid- or object-oriented mapping procedure by expert-judgement on training areas and extends the calibrated rules to the target areas [6] [7]. The unsupervised procedure can be based exclusively on grid segmentation and classification techniques, allowing the partitioning of DEMs or remotely sensed imagery by specific rule-sets into non-overlapping regions (segments), representative of geomorphic entities [8] [9]. Object-oriented geomorphological mapping is increasingly used both in the automatic and semi-automatic definition of landforms, with particular reference to those connected with hillslope and fluvial processes. The capacity of overcoming the 'a-dimensional' limitations related to symbol-oriented methods has progressively induced a widespread diffusion of this context [1] [9]. However, the transition to a full use of object-oriented geomorphological mapping is not simple and immediate. In fact, before reaching the goal of a reliable automatic recognition of landforms from DEM or remote sensing imagery, the 'traditional' symbol-oriented mapping system will continue to be used at least as the first operative step of the object-oriented methodology. DEMs are frequently used to extract surface morphology from elevation derivatives such as slope angle, plan and profile curvature, aspect, local drainage direction and upslope area [3] [10]. The basic concept in the automatic recognition and mapping of DEM-based landform is

In: Geomorphometry for Geosciences, Jasiewicz J., Zwoliński Zb., Mitasova H., Hengl T. (eds), 2015. Adam Mickiewicz University in Poznań - Institute of Geoecology and Geoinformation, International Society for Geomorphometry, Poznań

that each landform should be associated to a distinctive geomorphometric signature, as a specific combination of elevation derivatives [3] [11]. In theory, a known training set of *geomorphometric signature dictionary'* could be used to compare extracted terrain objects with standard 'discrete landforms' for their spatial automatic recognition and classification [12]. Actually, however, most landscapes are the result of a polygenetic and poly-chronologic geomorphic evolution. Frequently, younger landforms due to active geomorphic processes may transform, at least in part, discrete terrain landforms into new features: *i.e*, a colluvial hollow stemming from diffusive soil transport during the last glacial period may be modified by post-glacial / periglacial erosional processes or superimposed by new landforms [13]. This implies that the statistical information provided by present-day land features may be also 'inherited' from earlier land features. Fuzzy classification of objects belonging to more than one class can be used to overcome this problem. This may lead to geomorphological maps linked to a spatial geodatabase in a GIS, as proposed by [14] and [15]. These proposals represent an advanced approach on how we can represent and organize geomorphological objects, but they do not overcome the issue of the spatial super-position of objects and then their temporal succession as morphogenetic events, both in the same and in different morpho-climatic regimes. In [1] is illustrated a new GIS-based, full-coverage, object-oriented geomorphological mapping system. This system, named "Geomorphological Informative System_Salerno University" (GmIS_UniSa), is in use at the Department of Civil Engineering and the CUGRI (Great Risks inter-University Consortium, Salerno University) for application in several engineering, landscape ecology and hydro-geomorphology projects [16]. Currently, are being introduced improvements in GmIS_UniSa in order to perform the automatic space-time recognition of landform typology and evolution. This will allow a 'non-subjective' and repeatable delineation of the landform changes in order to better pursue dynamic landscape analyses and support environmental scenarios. The paper discusses this issue.

II. Case Study of the Salerno University Geomorphological Informative Mapping System

In order to enhance the above improvements in a real landscape, has been carried out an application on the Licosa Headland study area (Cilento European Geopark), a coastal landscape of the southern Tyrrhenian borderland (Fig. 1). Our aim was to recognize the space superposition and time succession of landforms in this typical Mediterranean polygenetic landscape by applying further geomorphometric procedures to the GmIS_UniSa [1]. The attention was focused on the objective landform mapping produced by present-day processes acting on Pleistocene landforms, such as active channels and shallow landslides on terraced alluvial fans, marine terraces, talus slopes and colluvial hollows.

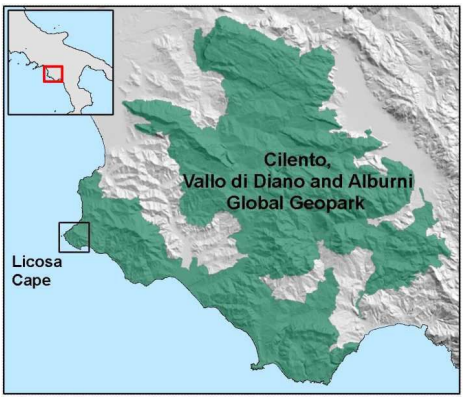


Figure 1. Location of the study area.

The new procedure includes an expert-driven spatial analysis on the traditional four steps of the GmIS_UniSa [1]. Step 1 concerns the 'traditional' field-surveyed, symbol-based geomorphological mapping and Step 2 "translates" the previously mapped landforms into a bounded, full coverage geomorphological map, delimiting and coding the geomorphological features as geomorphological units in a geodatabase. At the end of Step 2, specific "training landform units" are been selected among the most representative polygenetic landforms in the landscape. Step 3 manages the "training landform units" of Step 2 using a recursive procedure by rule-sets in a usual grid-based landform recognition, starting from a 5x5 m DEM and obtaining a new map by a first objective spatial validation of the previous subjective boundaries (Fig. 2). Step 4 performs the object-based procedure by *e-Cognition* package (Trimble Inc.) using the same 5x5 m DEM. The procedure includes: 1. grid-based pre-processing (Fig. 2a) of significant parameters (i.e. curvature, slope, flow accumulation, etc.; 2. segmentation of objects based on discriminant parameters with different weights (Fig. 2b); 3. supervised classification of the training landform components (Fig. 2c) and, finally, 4. fuzzy membership classification on target landform components having maximum likelihood in respect to the training ones (Fig. 2d). In order to improve the spatial relationships of the above illustrated objective mapping of over-posed landforms with different ages (herein event-based mapping), a sample procedure has been applied to the zero order basins or ZOB's (Fig. 3a), located as Fig. 2d. A distributed statistical analysis has been performed by using the plan and profile curvature as discriminant geomorphometric parameters, on the ZOB's components over the entire study area: hollow,

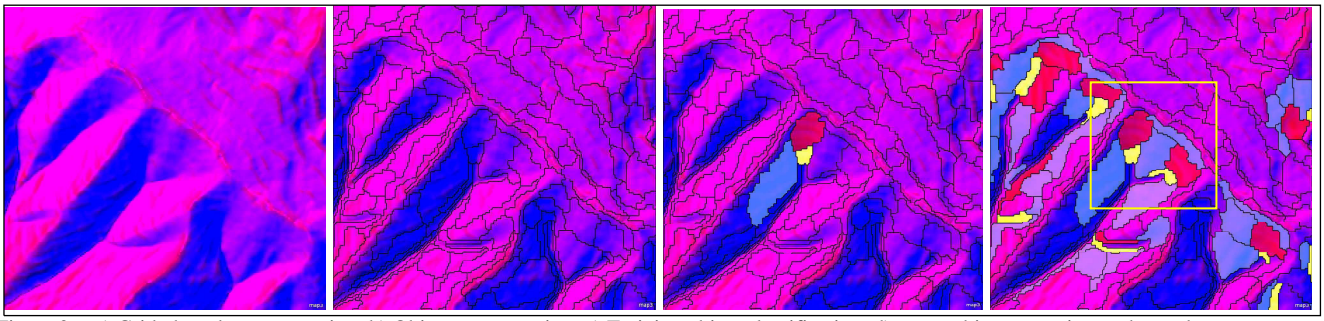


Figure 2. a) Grid –based pre-processing; b) Object segmentation; c) Training object classification; d) target object extension to the study area.

transient channel, first order channel and side slope. In the plot of Fig. 3b the results of the analyses are shown and two main fields can be clearly observed, each representing the geomorphometric signature of landform components due to two distinctive morphogenetic controls.

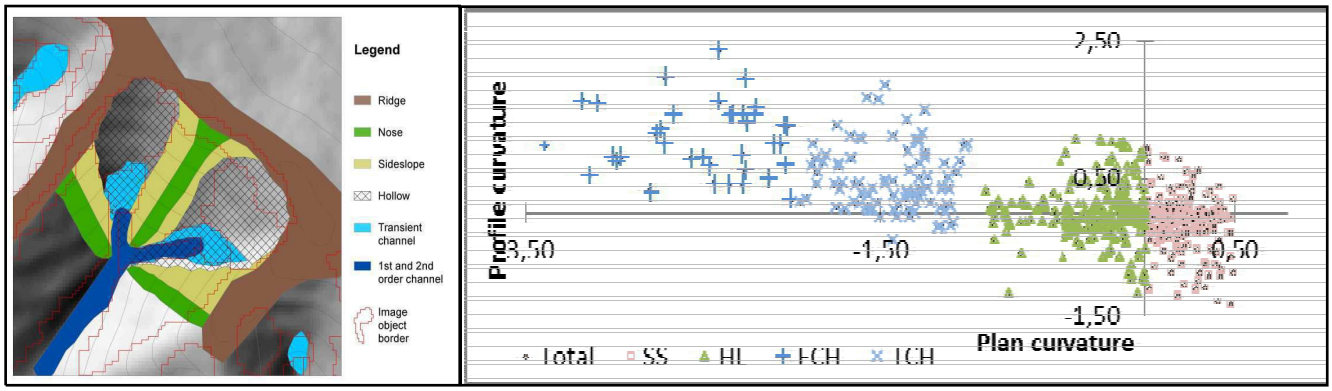


Figure 3. a) ZOB Landform Component map by automatic (red lines) and expert recognition; b) Plan vs Prof Curvature plot showing, on the right, the geomorphometric signature of landform components resulting from Pleistocene dominant diffusive processes (Side-slope – SS- and Hollow – HL); the left field shows landform components produced by Holocene dominant advective processes: transient channel – TCH - and first-order channel – FCH.

On the right, a very dense cluster of points defines both side slope (SS as pink squares), having PlanCurvature values > 0 and ProfCurvature values spanning between 1.00 and -1.00, and hollow (HL, green triangles) having PlanCurvature <0 up to -1.0 and the ProfCurvature having the same values intervals of SS. On the left, a more sparse cluster having a PlanCurvature < -1.0, spreads toward positive values in ProfCurvatures. The first field indicates the geomorphometric signature of the landform components resulting from diffusive hillslope processes, dominant during late Pleistocene stadial and inter-stadial stages. The second one results from dominant Holocene advective processes, as sapping erosion in the transient channel (TCH) and gully erosion along the first-order channel (FCH), both involved in debris flow initiation and transport, where boundary conditions are prone to trigger these processes.

III Discussion and Conclusion

Object-based spatial analyses performed by the GmIS_UniSa on the study area demonstrate their capability to perform the quantitative reconstruction of geomorphic events in polygenetic and poly-chronologic landscapes. Detailed field surveys confirmed the consistence between geomorphometric distribution of landforms and their long-term geomorphic evolution, revealing a mid-term geomorphic competition at the hollow toe, between gully retreat and colluvial filling by soil creep from side slopes. Downstream, the V-shaped channel indicates that the upstream collected runoff causes the initial and subsequent, progressive incision of the gully. This geomorphic path can evolve into flow-like transport, where saturation of colluvial soil and associated sapping erosion induces multiple, shallow soil slips, represented by narrow, elongated U-shaped scars. Finally,

the reconstruction of the pre-existent hollow boundaries, modified by Holocene linear erosion, was obtained by means of specific geomorphometric rule-sets based on flow accumulation, topographic wetness index and flow direction, having down-valley terminations at the first to second order channel junctions (gridded in Fig 3a). Objective space-time discrimination between present-day erosional and gravitational hillslope processes, acting on previous landforms could be definitely useful for both objective and dynamic assessment of geomorphological hazards, such as landslides and erosion.

In conclusion, the procedure applied to the zero order basins seems to demonstrate an effective capacity of improving the time-spatial relationship of landforms in the object-based mapping procedure. Moreover, the topological relations of superposition and substitution between geomorphological objects, introduces the perspective of transforming the present-day object-based mapping into event-based mapping.

ACKNOWLEDGMENT

Authors are grateful to CUGRI for technical and Cilento Geopark for financial support to research activities.

REFERENCES

[1] Dramis, F., Guida, D. and Cestari, A. (2011). Nature and Aims of geomorphological mapping. In: Smith, M.J., Paron, P. and Griffiths J.S. (Eds.), Geomorphological mapping: Methods and applications, pp. 39-73, Elsevier, Amsterdam.

[2] Mark, D. and Smith, B. (2004). A science of topography: from qualitative ontology to digital representations. In: Bishop, M. and Shroder J. (Eds.), Geographic Information Science and Mountain Geomorphology, pp. 75-100,, Springer-Verlag, Berlin.

[3] Mìnar, J. and Evans, I. (2008). Elementary forms for land surface segmentation: The theoretical basis of terrain analysis and geomorphological mapping. Geomorphology, 95, 236-259.

[4] Smith, M.J. (2011). Digital mapping: visulisation, interpretation and quantification of landforms. In: Smith, M.J., Paron, P. and Griffiths J.S. (Eds.), Geomorphological mapping: Methods and applications, pp. 225-251, Elsevier, Amsterdam.

[5] Oguchi, T., Hayakawa, Y. and Wasklewicz, T. (2011). Data sources. In: Smith, M.J., Paron, P. and Griffiths J.S. (Eds.), Geomorphological mapping: Methods and applications, pp. 189-224, Elsevier, Amsterdam.Pike, R., Evans, I. and Hengl, T. (2008). Geomorphometry: a brief guide. In: Hengl, T. and Reuter, H.I. (Eds.), Geomorphometry: Concepts, Software, Applications, pp. 1-28, Elsevier, Amsterdam.

[6] Molenaar, M. (1989). Single valued vector maps. A concept in Geographic Information Systems. GIS, 2(1), 18-26.

[7] Schmidt, J. and Hewitt, A. (2004). Fuzzy land element classification from DTMs based on geometry and terrain position. Geoderma, 121(3-4), 243-256.

[8] Drăgut, L. and Blaschke, T. (2006). Automated classification of landform elements using object-based image analysis. Geomorphology, 81, 330-344.

[9] Anders, N., Seijmonsbergen, A. and Bouten, W. (2011). Segmentation optimization and stratified object-based analysis for semi-automated geomorphological mapping. Remote Sensing and Environment, doi:10.1016/j.rse.2011.05.007.

[10] Pike, R., Evans, I., & Hengl, T. (2008). Geomorphometry: a Brief Guide. In T. Hengl, & H. I. Reuter, Geomorpho-metry: Concepts, Software, Applications. (Vol. 33, p. 1-28). Elsevier.

[11] Wood, J.K. (1996). The geomorphological characterisation of digital elevation models. PhD thesis, Department of Geography, University of Leicester, Leicester, UK, (http://www. soi.city.ac.uk/~jwo/phd/). Accessed 12th September 2008.Gallant, J.C., and M. F. Hutchinson, 2009. “A Differential Equation for Specific Catchment Area”, In Geomorphometry 2009 Conference Proceedings, Edited by: Purves, R., Gruber, S., Straumann, R. and T. Hengl, University of Zürich, Zürich.

[12] Anders, N. and Seijmonsbergen, A. (2008). Laser altimetry and terrain analysis. A revolution in geomorphology. GIM international, 36-39.

[13] Guida, D. (2003). The role of Zero-Order basins in flowslides-debris flows occurrence and recurrence in Campania (Italy). In: Picarelli, L. (Ed.), Conference on Fast Slope Movements-Prediction and Prevention for Risk Mitigation, vol. 2, pp. 255-262. Napoli, Patron Editore, Bologna.

[14] Van Asselen, S. and Seijmonsbergen, A. (2006). Expert-driven semi-automated geomorphological mapping for a mountainous area using a laser DTM . Geomorphology, 78, 309-320.

[15] Gustavsson, M. and Kolstrup, E. (2009). New geomorphological mapping system used at different scales in a Swedish glaciated area. Geomorphology, 110, 37-44.

[16] Cuomo, A. (2012). The contribution of hydro-geomorphology in the evaluation of flood discharge in the Campania region. PhD Thesis, University of Salerno, Italy.

Making the invisible visible – the DTM modelling in complex environments

Piotr Wężyk
Laboratory of Geomatics, DFMGFE, IFRM
Faculty of Forestry, University of Agriculture in Krakow
Krakow, Poland
p.wezyk@ur.krakow.pl

Abstract- **Mapping of forested areas and water bodies was very limited in the past. Access to such areas with traditional survey techniques (total station, GNSS etc.), analogue/digital photogrammetry or radar technologies was very limited because of the dense and multilayer vegetation, very complex topography, swamps, narrow beach and steep cliffs, deep water, etc. Gathered data by survey or remote sensing, were used for generation of digital terrain models (DTM, sometimes with unknown accuracy. Implementation of airborne laser scanning technology (ALS; LiDAR - Light Detection and Ranging) to monitor complex environments which are very hard to see by human eye or other instruments in 3D space - opens new opportunities to identify precisely the vertical and horizontal structures, objects and magnitudes. Use of precision DTM based on ALS point clouds, is now a widely deployed method in many environmental applications including: morphometry analyses, landslide monitoring, geomorphological and hydrological modelling etc. Dense forest crown cover and undergrowth is limiting the penetration of laser beams but now the ground (DTM) can be "seen" very detailed if using high density of ALS data performed with narrow nadir-off angle and using full waveform as well. The bathymetric scanners operating with green light, can penetrate the sea or river water and can be used for bed mapping. Also the terrestrial laser scanning technology (TLS) can be used for 3D point cloud collection and modelling of underground structures (e.g. caves) and later integrated with ALS data to generate continuously surfaces of the DTM and some new "underground DTM's".**

I. INTRODUCTION

Forests and water areas are the basic environments presented on maps since the early days of cartography, but because of their high complexity, they are very difficult for detailed and real mapping. The wooded areas, especially those covered by multi-layer evergreen dense tree and shrub vegetation are a challenge for detailed modelling of digital terrain models, because of the lack of the survey data referring to the true ground. The traditional photogrammetry approach and the GNSS survey are very limited due to the dense canopy, undergrowth and multipath signal errors. Water bodies like: sea, lakes or rivers cause serious problems with the measurement of the bottom. Therefore the need of the development on state-of-the-art technologies for precision mapping and 3D modelling of wide-areas still exist. Nowadays various Remote Sensing technologies like: aerial and satellite stereo-photogrammetry, radar and especially the Airborne (ALS) and Terrestrial Laser Scanning (TLS) technology are used for the national-wide, regional and local mapping. The precise DTM models besides their role in: geomorphology, archaeology or landslide monitoring are crucial for the quality of the generation of ALS derived products like normalised Digital Surface Models (nDSM). Those models (called also Crown Height Model) are very important e.g. for: foresters, ecologists and landscape planers. DTM mapping of river and sea bottom using bathymetric scanners can deliver very important information concerning the natural environment and different hazards especially when the integration of multi-source information leads to continuous DTM data. Also the using of TLS and handy scanners opens new possibilities to capture and make 3D models of underground surfaces such as caves or mines that can be integrated with DTM based on ALS and spectral information gathered by airborne cameras.

II. COMPLEX ENVIRONMENTS: FOREST AND WATER

A. DTM in wooded areas

Modelling of the ground surface in the forest areas has always been difficult due to the visibility limitations for traditional

In: Geomorphometry for Geosciences, Jasiewicz J., Zwoliński Zb., Mitasova H., Hengl T. (eds), 2015. Adam Mickiewicz University in Poznań - Institute of Geoecology and Geoinformation, International Society for Geomorphometry, Poznań

measurement methods such as levelling, total stations or even airborne and terrestrial photogrammetry. Only in clear-cuts, deforested areas, post-fire or areas without tall trees alongside the roads and other logging routes and trails it was possible to establish surveying control lines and refer to them with further, more detailed measurements (mass points, soft and hard break lines, barriers etc). In the forest areas triangulation towers were also constructed as important parts of height measurements networks. Gradually the traditional methods of getting information on digital terrain model (DTM) were supplemented by GNSS techniques, but these, due to the specifics of forest areas (negative influence of dense crown cover, wood biomass on the propagation of signal; multipath errors) they could not provide precise information compared to open areas [1]. The accuracy ($RMSE_{XYZ}$) of marking co-ordinates with GNSS method under the canopy of oak-pine tree stand (age 140 years; H=28m, dense crown cover) ranged between 0.10m (receiver CHC-900) trough 0.28m (Trimble 6000 GeoXR) to as much as 1.94m (TOPCON GRS-1) at RTK observations [2]. The reference control line in this tree stand was marked with a total station series with a very high accuracy referring to the points measured in the open area in a GNSS measurement session lasting many hours (post-processing stations ASG-EUPOS; [3]). The limitations in airborne photogrammetry have existed since its beginning and did not disappear with the appearance of airborne digital cameras or the increase of their resolution (ground, spectral or radiometric). Even in the situation of making photogrammetric measurements in the "leaf-off" season, the airborne pictures of deciduous forests are difficult for the collection of points on the ground and used in generation of DTM. This is because the shadows made by the trunks and branches of trees very negatively influence the perception of the operator of the photogrammetric station or the work of the algorithm responsible for the matching airborne stereo-images [4]. Only in the situations of disasters (deforestation of large areas with removal of all the trees) it was possible to use airborne photogrammetry in precise DTM for a few years, until a young generation of forest covered the ground densely. Some solution in DTM generation for large forest areas, was the application of radar technology (Shuttle Radar Topography Mission - SRTM in 2000), e.g. model DTED-2 (3 arc) or the new global data TanDEM-X and TerraSAR-X. Unfortunately the DTED-2 (SRTM) model in the forested areas often runs above the true ground, which results from the influence of biomass of dense old-growth stands on radar propagation. The studies showed that the errors of DTED-2 model took place in Central European forest areas, sometimes reach to the half of the tree stand height [5]. The Airborne Laser Scanning (ALS) certainly became an innovative technology in the studies of forest environment. This technology was awaited for dozens of years. At first ALS system represented a profiler, which was basically a static laser telemeter put aboard the plane, but with the appearing of technology NAVSTAR-GPS and inertial navigation systems (INS) a technology was made, owing to which ALS point cloud is made, covering large areas in a short time [6]. Forest ecosystem is, however, a very complicated terrestrial ecosystem limiting the penetration of the laser beam during its way to the ground [7]. The registration of subsequent laser returns in a tree stand depends on a very large number of factors. The number of registered returns in the height profile of the tree stand, and first of all these reaching the surface of the ground, results first of all from the type of the tree stand. Almost all the evergreen coniferous tree species during the whole vegetation season, basically do not show large differences between all returns and first returns, or last returns. Thus for the whole year in coniferous tree stands, almost the same density of the number of points reaching the ground while preserving the same scanning density – and in the same way – similar quality of DTM models can be expected. In case of deciduous stands (beech stands - *Fagus sylvatica* L.) covered by ALS flights during the vegetation season (May 2012, Ojcow National Park; OPN; South Poland, Fig. 1) leaves significantly limit the penetration of the laser beam in the relation to the ALS ISOK project flights performed at the end of the growth season (“leaf-off”; 24. Oct. 2012; Fig. 2). The vegetation period, however makes possibility to generate digital surface model (DSM; Fig. 1) of a proper quality, which also does not remain without the meaning for the examined forest ecosystems. Upper layers of canopy have higher number of the individual returns of the laser, which causes the limitation of the echo of the signal on the ground caused sometimes high errors in approximated DTM (Fig. 3; “leaf-on” conditions). About 20-30% laser impulses reaching the ground under forest canopy (“leaf-on”), make good input for DTM modelling when properly choose of ALS point cloud density is done concerning to specific type of relief and vegetation (Fig. 4; “leaf-off” conditions). Often dense undergrowth layer cause that the last ALS returns are registered generally not from the real ground but from surface of vegetation what influence DTM with certain elevation error. A particularly difficult case is dense vegetation occurring on the rocks, which causes problems for the algorithm looking for the lowest LiDAR returns. In this case the problem with the right approximation of DTM appears (Fig. 3) where the rocks (“Krakow Gate”; Fig. 6) are classified as high vegetation (Fig. 5) and are not taken to approximation of the ground surface. The maximum DTM RMSE between the “leaf-off” (Fig. 3) and “leaf-on” (Fig. 4) arrived over 20m in the height even when the

point cloud density in vegetation errors was 3 times higher (12 pts/m^2).

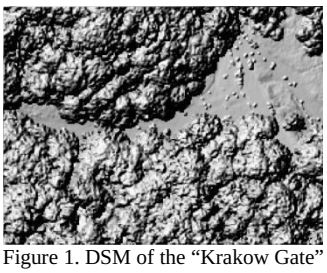


Figure 1. DSM of the "Krakow Gate" in Ojców NP (May 2012; OPN_ALS: 12 pts/m^2).

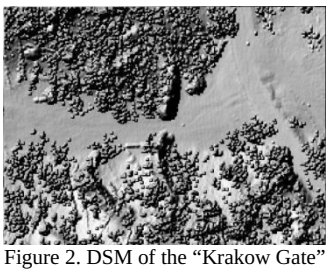


Figure 2. DSM of the "Krakow Gate" in Ojców NP (Oct. 2012; ISOK_ALS 4 pts/m^2).

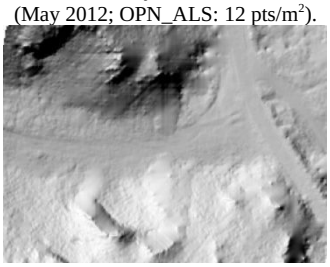


Figure 3. DTM of the "Krakow Gate" in Ojców NP with errors. (May 2012; OPN_ALS: 12 pts/m^2).

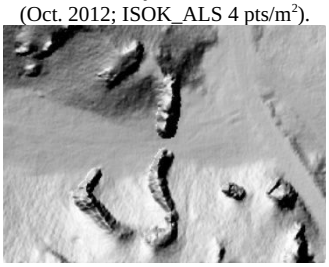


Figure 4. Correct DTM of the "Krakow Gate" in Ojców NP (Oct. 2012; ISOK_ALS 4 pts/m^2).

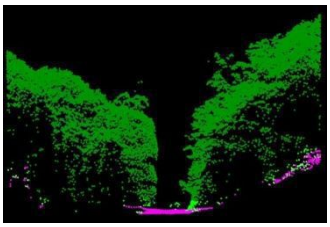


Figure 5. Wrong rock/ground classify-cation. OPN_ALS point cloud (May 2012; 12 pts/m^2).

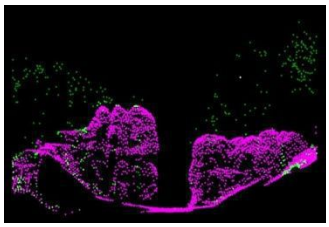


Figure 6 . Cross section through correct classified ISOK_ALS point cloud. (Oct. 2012; 4 pts/m^2).

Other authors in HIGH-SCAN project (point density 10 pts/m^2) reported RMSE in wooded areas on the level between 22 and 40 cm. Also the crown density was a crucial factor influencing the DTM RMSE showing the 14 cm in clear cut areas, 18 cm for lightly thinning forest and 29 cm for uncut old-growth forests [8].

Additionally factors influencing the DTM quality in the wooded areas can be: the lying dead wood, dense crown cover or windthrow areas after the hurricane disaster. It happens that the lying stems due to round shapes of trunks and tree crowns lead to the error in the ground detection algorithm and are counted to the triangles of TIN and as a result to DTM.

Horizontal and vertical crown cover of subsequent forest storeys results from preserving the natural character of the ecosystem (nature reserves) or silviculture treatments applied by the foresters. The crown cover is determined mainly by light requirements of the species and the mutual impact of the trees fighting for the space to live. In the situation of a great defoliation of trees (the fall of the LAI value), which is connected with their health status, the generated DTM are theoretically more accurate, but in some situations the growing access of light to the bottom tree stand causes the appearance of a dense layer of the ground cover or the undergrowth, making it more difficult to model the ground. To generate precise DTM models, ALS technologies in the deciduous stands should be perform in late autumn or winter (if there is no snow cover under trees). Other elements influencing the limitation of the number ALS points reaching the ground and their correct detection are: the nests of birds colonies, mistletoes, lichens, cones, acorns, clusters of fruit (in particular in the years of the abundance of seeds) or the occurrence of trunks and branches broken after hurricanes (microstructure). Single rocks or stones and their clusters can often make problems with generating proper DTM, which first of all results from the systematic approach to the approximated ground, and, on the other hand, make the work of algorithms detecting the ground more difficult, because of the shapes (e.g. round rocks in the river bed). The remaining elements or objects connected with DTM modelling in the forest areas are firmly connected with archaeology and the military remains (soil-made defence constructions: trenches, bunkers, war cemeteries, mass graves, remains after Nazi death camps etc.). It is estimated that in forest areas in Poland there are at least several thousand still undiscovered archaeological sites including: kurgans, hill forts, which are usually the element of DTM modelled from ALS data.

B. Underground

Another space invisible for the human eyes, even with the application of ALS are the objects under the surface of the ground or DTM. They can include: caves and cavities after the exploitation of resources (coal, silver, gold, salt etc.). Contemporary technologies of terrestrial laser scanning (TLS) and surveying (total stations + GNSS) not only allow getting full precise information, i.e. 3D cloud of TLS points, but also their integration with the ALS data. Due to this we obtain a continuous surface of „ground" under the real ground, which makes certain problems, even with the professional nomenclature. The example of such ALS integration can be both mobile laser scanning (MLS) or TLS data of underground car parks under the buildings or in rocks, tunnels in the mountains, but also caves (e.g. the "Łokietek Cave" in the Ojców NP). The integration very accurately allows non-invasive volumetric

measurements or making profiles and first of all defining in the distances between subsequent galleries or chambers of mines or caves in 3D, including their distance to the real ground. Such a precise information obtained by the integration with ALS in the same system of co-ordinates gives the possibility of not only wonderful visualization for the needs of tourist information or the plans of protective tasks, but also undertaking all the rescue operations by respective services (e.g. making a rescue corridor).

C. The bottom of the water bodies

Until recently the only way to know and visualize the sea bed was the application of sonar technologies. Today there is however an alternative of using airborne laser scanning i.e. so-called bathymetric scanners. They vary technologically in the length of the applied light (green e.g. 532nm like VQ-880-G from RIEGL) from typical topographic scanners used to obtain information of the objects on the ground (close NIR; e.g. 1550 nm like LMS-Q680i from RIEGL). Bathymetric scanners usually are able to penetrate up to the depth of several dozen metres (max. 40-50 m). Of course, many conditions have to be fulfilled, such as: proper water transparency (connected with the suspension, presence of: waves or water foam, algae or plankton or even fish – to allow the laser beam reach the bottom and return to the detector aboard the aircraft or helicopter. Such solution gives wonderful possibilities of generating a continuous DTM runs through bank, cliff [9] and near shore which so far has been rather difficult to verify in the water bodies

ACKNOWLEDGMENT

Special thanks to the Director of the Ojców National Park (Poland) for the free access to the ALS point cloud data from May 2012 and to the Main Office of Geodesy and Cartography (GUGiK in Warsaw, Poland) for free of charge access to ALS data (point cloud, DTM, DSM) preformed in frame of the ISOK project.

REFERENCES

[1] Ordóñez Galána C., Rodríguez-Pérezb J.R., Martínez Torresc J., García Nietod P.J., 2011. “Analysis of the influence of forest environments on the accuracy of GPS measurements by using genetic algorithms”, In Mathematical and Computer Modelling. Mathematical models of addictive behaviour, medicine & engineering. Volume 54, Issues 7–8, October 2011, pp. 1829–1834.

[2] Szostak M. and Wężyk P., 2013. “GNNS measurements in forest environment using various receivers and measurement modes”, In Archive of Photogrammetry, Cartography and Remote Sensing, Vol. 25, pp. 217-231.

[3] Wężyk P., 2012. The integration of the Terrestrial and Airborne Laser Scanning technologies in the semi-automated process of retrieving selected trees and forest stand parameters. Ambiencia, Vol. 8; 4: 533-548, Unicentro, Parana, Brasil.

[4] White, J. et al., 2013. The Utility of Image-Based Point Clouds for Forest Inventory: A Comparison with Airborne Laser Scanning. Forests, 4(3), pp. 518–536.

[5] Wężyk P., de Kok R., Świąder A., 2005. Empowered forest GIS – cross validation of SRTM and optical data. Remote Sensing of Environment. [In:] Olsson H. (Ed.) Rapport 8b. ForestSat 2005 in Boras. National Board of Forestry, Sweden: 91-96.

[6] Renslow M. S., 2014. Manual of Airborne Topographic LiDAR.

[7] Heritage G., Large A., 2009. Laser scanning – evolution of the discipline. In: Heritage G., Large A., (Eds.) 2009. Laser Scanning for the Environmental Sciences. Blackwell Publishing Ltd.

[8] Hyppä J., Hyppä H., Yu X., Kaartinen H., Kukko A., Holopainen M., 2008. Forest inventory using small-footprint airborne LiDAR. In: Shan J., Toth C.K. (Eds.) 2008. Topographic Laser Ranging and Scanning: Principles and Processing. CRC Press.

[9] Dudzińska-Nowak J., Wężyk P., 2014. Volumetric changes of a soft cliff coast 2008-2012 based on DTM from airborne laser scanning (Wolin Island, southern Baltic Sea). In: Green, A.N. and Cooper, J.A.G. (eds.), Proceedings 13th International Coastal Symposium (Durban, South Africa), Journal of Coastal Research, Special Issue No. 66, pp. 59-64.

Geometrical parameters of TLS-based DEM acquisition for a small Arctic catchment (Svalbard SW)

Waldemar Kociuba
Faculty of Earth Sciences and Spatial Management
Maria Curie-Sklodowska University
Lublin, Poland
E-mail: waldemar.kociuba@umcs.pl

Abstract. **The article presents an example of application of the Terrestrial Laser Scanning (TLS) technology in high definition surveys and recording results of geomorphical events, as well as in the assessment of the dynamics of transformations of the small paraglacial Tyvjobekken Stream valley. The field works involved the application of a Leica Scan Station C10 and GPS RTK global positioning system. The Tyvjobekken Stream is a paraglacial tributary catchment typical of the Arctic morphoclimatic zone. It is located in the NW part of the Wedel-Jarlsberg Land (Spitsbergen, Svalbard). A complex survey of the main part of catchment (central and lower part of the valley) was carried out from 24 interrelated measurement sites. 3D scanning at each of the sites resulted in a point cloud of 5 million points [M pt.]. The resulting cloud of 170 M pt. of data was used to create a digital elevation model [DEM] of the river valley with a length of more than 1.2 km and width of up to 0.45 km. The DEM developed based on the TLS survey, featuring high point density, permitted the determination of the basic hypsometric parameters of the analysed part of the catchment and valley floor, and comparison of the parameters of the asymmetric slopes of the valley's mouth section. The high accuracy of the obtained model permitted precise identification of the geometry of the main slope and valley floor landforms, as well as the identification and inventory of ephemeral rills and braided channels.**

I. INTRODUCTION

In the conditions of modern rapid transformations of the Arctic environment, the quantitative and qualitative assessment of the dynamics of the processes requires the application of new research strategies and precise measurement tools (1). The application of Terrestrial Laser Scanning [TLS] for monitoring transformations of slope (mass movements, solifluction, mud-debris runoffs, debris flow) and valley landforms (changes in the channel pattern, lateral erosion, scroll ridges) subject to continuous dynamic transformations permits the assessment of the rate of the occurring processes, and the identification of potential threats of occurrence of catastrophic phenomena (2). In contrast to the increasingly commonly applied data from aerial scanning [ALS] (3,4), the application of TLS in research on Arctic areas is still rare (5,1,6). In the case of the applications to date, the importance of selection of the relevant measurement strategy has been emphasised. This particularly concerns the applied methods of reference (7,2,1), and the implementation of normalised methods of area and volume analysis for the purpose of obtaining better comparability of results (8,1,5,6).

The primary objective of this paper was to evidence the effectiveness of TLS as a universal tool of spatial analyses in the environment of small Arctic catchments, and to develop a strategy of application of TLS in research on the dynamics of transformations o non-glaciated Arctic catchments.

II. RESULTS

A. *Study area*

The research involving the application of TLS in the cold climate environment covered the Tyvjobekken Stream catchment located in the NW part of the Wedel-Jarlsberg Land, in the Bellsund Region of Spitsbergen (Fig. 1). The paraglacial valley of the stream dissecting the area of elevated marine terraces (called the Calypsostranda) drains the eastern forefield of the Renard glacier, and the slopes of the Bohlinryggen massif. The sources of the stream with nival-permafrost alimentation regime, developing a catchment with an area of 1.3 km^2, are located at the forefield of the Bohlinryggen massif. The paraglacial Tyvjobekken Stream valley stretches from WSW to ENE along approx. 1.2 km, reaching a mean inclination of approx. 4.1% (9).

The valley floor relief includes three clearly distinguishable parts. The upper part has a character of an extensive, weakly developed basin covering the area between the moraine zone of the north-eastern forefield of the Renard glacier and the eastern slopes of the Bohlinryggen massif. From the side of the forefield of the Renard glacier, the Tyvjobekken Stream is fed by a bifurcating stream using the former routes of outwash plain runoff.

In: Geomorphometry for Geosciences, Jasiewicz J., Zwoliński Zb., Mitasova H., Hengl T. (eds), 2015. Adam Mickiewicz University in Poznań - Institute of Geoecology and Geoinformation, International Society for Geomorphometry, Poznań

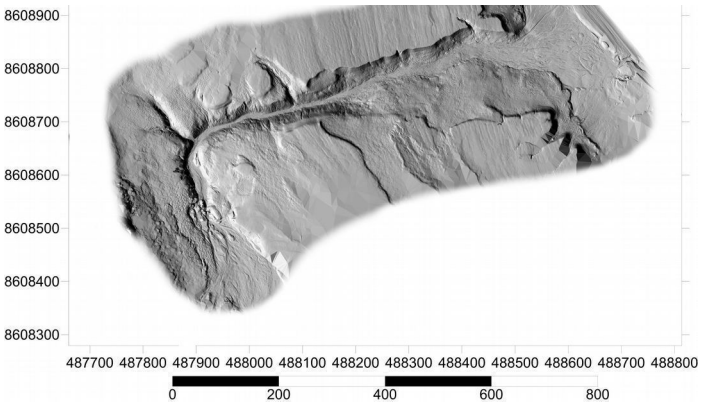


Figure 1. Digital elevation model of the scanned part of the Tyvjobekken Stream catchment (gridding method: Triangulation with Linear Interpolation, spacing: 0.1 m).

In its middle section, the stream develops a gorge with a depth of up to 25 m, extended along 0.8 km of the edge of the elevated marine terrace (9,10). The section is distinguished by a narrow erosional valley developed by the braided system. In this part, the stream is fed by small, periodically functioning tributaries with nival-permafrost regime. The slopes of the middle part of the valley have a character of an erosional scarp dissected by shallow erosional cuts, periodically modelled by cryogenic and solifluction processes and slight debris flow (e.g. 5). The floor with inconsiderable denivelations is modelled by a system of shallow channels (1,11).

In its lower course, below the gorge, the river causes aggradation of the alluvial fan inherited from the former outflow from the Renard catchment. The low amounts of water and sediments load transported by the Tyvjobekken Stream result in periodical lack of surface inflow of the river to the fjord, and contribute to the development of a micro lagoon separated from the fjord waters with a coastal berm (12,11).

B. Methods

The field research was conducted at the turn of July and August 2013. The applied model of terrestrial scanner Leica ScanStation C10 provides measurement of 3D location (accuracy of 3D point location to 6 mm) at a rate of up to 50,000 points per second by means of green pulse laser with wavelength of 532 nm. The measurements covered an area of 480,000 m^2, i.e. 37% of the catchment area. The measurements were performed from 24 measurement sites during three days. The predefined resolution of the survey determined the number of points. In this case, medium resolution was applied (0.1/0.1 m per 100 m), permitting obtaining an average of approximately 5 M pt.at each of the measurement sites.

The final DEM quality depends on both the technical possibilities of the device, and the applied field survey strategy (1,5). The survey involved the application of the modified target point [TP] method (5), i.e. measurement of a point with known coordinates oriented to the network of permanent control points with known coordinates [KC]. The measurement based on a network of points with known coordinates required prior permanent marking of points of the planned location of the scanner, as well as reference points (they were applied interchangeably). The determination of the location of the KC point network was based on satellite positioning by means of the GPS RTK TopCon Hipper II system. Although the KC methods required a precise (accuracy of 1 mm) determination of the location of the scanner at the measurement site, the orientation of the scanner was only based on one reference point. As a result of the application of the KC measurement strategy, each of the measured points already had geographic coordinates during the scanning process. Such organisation of measurements largely reduced the time of interpretation of results. The Leica Cyclone 8.0 software used for DEM integration automatically combines georeference model spaces obtained by means of this method into one 3D model (Fig.1).

C. Results. Catchment characteristics

The data (point clouds) transformed to a DEM model permit geomorphometric analyses of land surface, including the estimation of the area or volume, and detailed measurements of the geometry of selected landforms at various spatial scales (1), or analysis of changes in the shape of cross-sections and longitudinal sections (e.g. 13). The measurements resulted in a DEM model obtained from the integration of 24 “model spaces”, comprising approximately 170 M pt. The obtained model covered approx. 37% of the catchment area, including the entire erosional valley and subcatchments of the main tributaries. For the purpose of comparison of the analytical and interpretative possibilities of the obtained DEM, multiscale objects were selected for the detailed analyses. The macroscale object was the erosional valley with a length of approximately 1.18 km and width from 0.01 km to 0.44 km (13% of the catchment area), dissecting the elevated marine terrace (14-30 m a.s.l.). Along the section, the valley has a character of a gorge with a length of almost 800 m and width of 15-60 m (Fig. 1, Table 1).

TABLE I. PARAMETERS OF THE TYVJOBEKKEN STREAM EROSIONAL VALLEY

erosional valley parameters	direction	NS	WE		all
	part / units	upper	central	lower	
area	m^2	27,265.4	97,124.3	43,209.9	167,599.6
length	*m*	345	630	200	1,175
valley width / min.-max.	*m*	60-102	45-175	178-436	45-436
valley bed width / min.-max.	*m*	15-60	10-60	60-316	10-316
max. valley bed elev.	*m a.s.l.*	32.0	21.7	2.4	0.3
min. valley bed elev.	*m a.s.l.*	21.7	2.4	0.3	0.2
max. terrace elev. N/S [part]	*m a.s.l.*	37.9	37.9/32.7	----	37.9
min. terrace elev. N/S [part]	*m a.s.l.*	32.7	14.2/13.5	----	13.5
lifted terrace slope N/S [part]	$m\ m^{-1}$	0.02	0.04/0.03	----	0.06/0.03
valley bed slope	$m\ m^{-1}$	0.03	0.03	0.01	0.03

The denivelation between the valley floor in the area of the stream sources and its mouth to the fjord amounts to less than 32 m, and that of the dissected surfaces of the elevated marine terrace 24 m (N part) and 19 (N part), respectively. The comparison with the reference area (level of the elevated marine terrace) permitted the estimation of the volume of the erosional valley for 1,011,588 m^3. The valley slopes in the zone of the gorge have a character of an erosional scarp, and are intensively modelled by mass and solifluction processes. The narrowing of the valley floor to 10 m forces the concentration of braided channels. Below the gorge zone, along approximately 200 m, the valley widens to 440 m, and its floor occupies the alluvial fan at its mouth (Fig. 1, Table 1).

The mesoscale object was constituted by the asymmetric slopes of the mouth sections of gorge valleys, typical of the valleys of this part of the Wedel Jarlsberg Land, modelled by mass (slumps, breaking, solifluction) and erosional processes. The effects of the processes are microscale objects, including shallow erosional cuts and small debris flow dissecting the N slope and solifluction terraces on the S slope. A difference by 1.6 in volume was recorded between the N part of the mouth section (185,932 m^3) primarily modelled by erosional processes, and the S part (305,469 m^3) particularly modelled by solifluction processes.

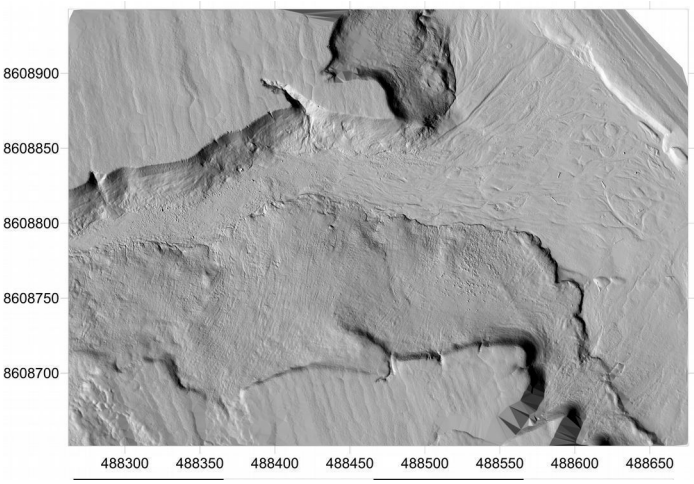


Figure 2. Digital elevation model of the lower part of the erosional valley. View on the asymmetric slopes transformed by erosional (N part) and periglacial (S part) processes (gridding method: Triangulation with Linear Interpolation, spacing: 0.1 m).

D. Final remarks and conclusions

Research on modern transformations occurring in the Arctic environment increasingly focuses on the detailed morphometric characteristics of the study object. Precise 3D modelling of multiscale objects such as catchments, valley floors, and valley or slope landforms, considerably facilitates solving research problems in the dynamically changing environment of the Arctic. Traditional measurement techniques are very time-consuming. In the case of cold climate environments, they are also strenuous for the researchers. Due to the varied degree of detail of the output materials, the existing DEM models of the analysed terrain, integrating information from aerial photographs, orthophotomaps, topographic maps, geodesic measurements, or GPS, have not permitted detailed analyses of landforms at meso- and microscale so far (1, 5). TLS is a universal tool possible to replace the currently applied methods. It provides precise data for land relief modelling and the quantitative assessment of spatial and temporal changes. TLS permits better understanding of the course of processes developing small proglacial catchments (1).

The TLS measurements in the Tyvjobekken Stream valley were analysed in the context of their usefulness for modelling landforms with varied size and origin. The application of TLS was evidenced to offer the possibility of multiscale analyses based on one universal DEM model. The performed detailed spatial analyses of the surface of the valley floor and slopes confirmed the high precision and efficiency of the tool. The applied strategy of measurements and high accuracy of output data provided obtaining a DEM with features permitting

multiparameter analyses adjusted to the size and importance of the analysed objects. This allowed for detailed analyses of the morphology of the catchment area, and the determination of the volume of selected parts of the erosional valley. The relevant selection of DEM parameters permits the determination of the degree of connectivity of the slope and valley subsystems, the estimation of the volume of material deposited in the valley floor (e.g. 14,1,5), and even a detailed analysis of the geometry of small erosional forms (e.g. 1,5).

ACKNOWLEDGMENT

The field research was conducted during the 25th Maria Curie-Sklodowska University Polar Expedition. The study was supported by the scientific project of the National Science Centre 2011/01/B/ST10/06996 “Mechanisms of fluvial transport and sediment supply to channels of Arctic rivers with various hydrological regimes (SW Spitsbergen)”. The author is grateful for the field and technical assistance from Ph.D. Grzegorz Gajek and M.Sc. Lukasz Franczak.

REFERENCES

[1] Kociuba, W., Kubisz, W. and P. Zagórski, 2014. „Use of terrestrial laser scanning (TLS) for monitoring and modelling of geomorphic processes and phenomena at a small and medium spatial scale in Polar environment (Scott River — Spitsbergen).” Geomorphology, 212, 84-96.

[2] Kenner, R., Philips, M., Danioth, C., Denier, C., Thee, P. and A. Zgraggen, 2011. “Investigation of rock and ice loss in a recently deglaciated mountain rock wall using terrestrial laser scanning: Gemsstock, Swiss Alps.” Cold Regions Science and Technology 67, 157-164.

[3] Bamber, J.L., Krabill, W., Raper, V., Dowdeswel, J.A. and J. Oerlemans, 2005. “Elevation changes measured on Svalbard glaciers and ice caps from airborne LiDAR data.” Annals of Glaciology 42, 202-208.

[4] Arnold, N.S., Ress, W.G., Devereux, B.J. and G.S. Amable, 2006. “Evaluating the potential of high resolution airborne LiDAR data in glaciology.” International Journal of Remote Sensing 27, 1233-1251.

[5] Kociuba, W., 2014. “Application of Terrestrial Laser Scanning in the assessment of the role of small debris flow in river sediment supply in the cold climate environment.” Annales UMCS B 69, 1, 79-91.

[6] Kääb, A., L. Girod, and I. Berthling, 2014. “Surface kinematics of periglacial sorted circles using structure-from-motion technology.” Cryosphere, 8, 1041–1056.

[7] Abbelán, A., Jaboyedoff, M., Oppikofer, T. and J.M. Vilaplana, 2009. “Detection of millimetric deformation using a terrestrial laser scanner: experiment and application to a rockfall event.” Natural Hazards and Earth System Sciences 9, 365-372

[8] Lichti, D., M. Stewart, M. Tsakiri and A. Snow, 2000. “Benchmark Testing on a Three-Dimensional Laser Scanning System”, Geomatics Research Australasia, 72, 1-235

[9] Bartoszewski, S., 1998. „Reżim odpływu rzek Ziemi Wedel Jarlsberga (Spitsbergen).” Wydawnictwo UMCS, Lublin. 167.

[10] Bartoszewski, S., Chmiel, S. and Z. Michalczyk, 2013. „ Hydrography.” In: The Geographical Environment of NW Part of Wedel Jarlsberg Land (Spitsbergen, Svalbard), Edited by: Zagórski, P., Harasimiuk, M. and J. Rodzik, Wydawnictwo UMCS, Lublin, 192-211.

[11] Kociuba, W. and G. Janicki, 2013. “Fluvial Processes.” In: The Geographical Environment of NW Part of Wedel Jarlsberg Land (Spitsbergen, Svalbard), Edited by: Zagórski, P., Harasimiuk, M. and J. Rodzik, Wydawnictwo UMCS, Lublin, 192-211.

[12] Harasimiuk, M. and T. Król, 1992. “The dynamics of morphogenetic and sedimentary processes in the estuary segments of river valleys in the Recherche Fiord (Western Spitsbergen).” In: Spitsbergen Geographical Expeditions, Arctic natural environment problems, Edited by: Repelewska-Pękalowa, J. and K. Pękala, MCSU Press, Lublin, 59–66.

[13] Kociuba W., Janicki G. and J. Rodzik, 2014. „3D laser scanning as a new tool of assessment of the dynamics of development of forested loess gullies based on the example of Kolonia Celejów (Lublin Upland).” Annales UMCS B 69, 1, 107-116.

[14] Bremer, M. and O. Sass, 2012. “Combining airborne and terrestrial laser scanning for quantifying erosion and deposition by a debris flow event.” Geomorphology 138, 49–60.

DEM based geomorphometric analyses of karst surface in the Republic of Macedonia

Marjan Temovski
SK Zlatovrv
Prilep, Republic of Macedonia
temovski_m@yahoo.com

Ivica Milevski
Institute of Geography,
Skopje, Republic of Macedonia
ivica@iunona.pmf.ukim.edu.mk

Abstract— **Karst terrains in the Republic of Macedoniacover 12 % of its territory, generally as a number of separate karst areas with various sizes, most of which are located in the western and central parts of the country. Karst rocks are represented mostly by Triassic limestones and Precambrian marbles, with also parts composed of Paleozoic marbles and carbonate schists, Jurassic and Cretaceous limestones, Pleistocene tufa, tufaceous limestones and travertines and also Cretaceous gypsum and anhydrite. General morphometric characteristics of the karst surface were analyzed, with hypsometry, slope inclination and type, and aspect analyzed for both total karst surface and different karst rocks. Average elevation of karst terrains is 1100.4 m, reflective of the extension of karst terrains generally in mountainous regions, with limestone and marble having higher average elevations. As youngest rocks, tufaceous limestones, tufa & travertines are located mainly at lower elevations. Average slope (20.6°) is also significantly higher than mean slope of the entire country (15.4°), reflecting generally deeply incised fluvio-karstic landscapes and well preserved tectonic structures within the karst surface. Aspect analysis of karst surface shows generally even distribution between classes. Regarding slope type, large areas have linear downhill slope, especially in regards to the plan curvature. Beside that, convex terrains prevail with 28.9% for plan and 38.6% for profile curvature (with positive values for both). These results represent first attempt to analyze the general morphometric characteristics of the karst surface in Republic Macedonia. The outcome reveals certain specific characteristic of the karst surface, especially between different karst lithologies.**

I. INTRODUCTION

In the last few decades, aside from the specific study on karst characteristics and development, spatial extent of karst areas in Macedonia has been analyzed. The resulting data are based on traditional area measurementof karst rock outcrop extension from geological maps. Thus, according to Andonovski [1], karst area in the country occupies 9.6% from the total, while for Kolčakovski &Boškovska[2] it is 10.4%. Very recently, Temovski [3] calculated the extent of karst area in Macedonia in fine scale by vectorization of all types of karst rocks, at 12% as a final result. These studies deal only with extension of karst rock outcrops, with no other aspects of the karstic surface analyzed. Thus, until now no geomorphometric study was made on the whole karstic surface. This study presents first attempt to analyze the general morphometric characteristics of the karst surface in Republic Macedonia.Karst is a significant landscape feature in this country, with karst water resources representing important part of the water supply system in the country. Karst terrains in Macedonia are found inmore or less isolated, generally smaller areas (so called "karst oases" [4]), most of which are in the western and central parts of the country.They have numerous doline and karren features, few active karst poljes, large fluvio-karstic areas, numbers of karst beveled surfaces andmore than

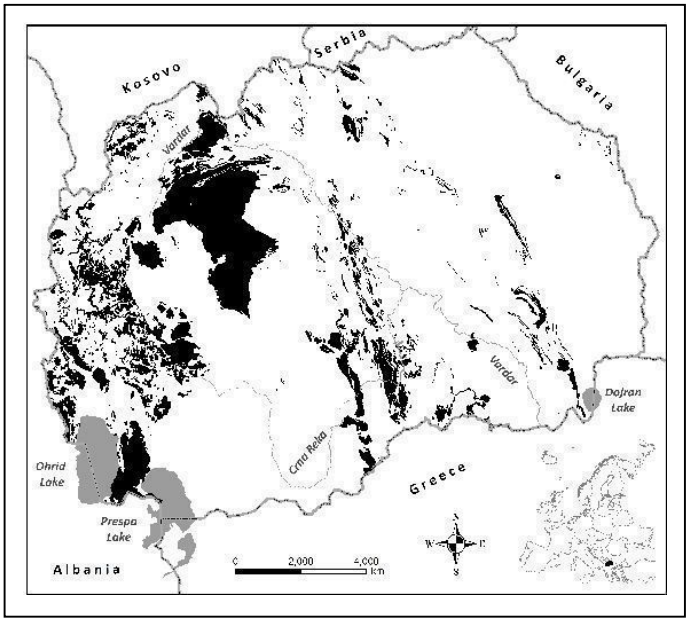


Figure 1.Extension of karst (black shade) in the Republic of Macedonia.

In: Geomorphometry for Geosciences, Jasiewicz J., Zwoliński Zb., Mitasova H., Hengl T. (eds), 2015. Adam Mickiewicz University in Poznań - Institute of Geoecology and Geoinformation, International Society for Geomorphometry, Poznań

400 documented caves. Karst rocks are represented mostly by Triassic limestones and Precambrian marbles, with also parts composed of Paleozoic marbles and carbonate schists, Jurassic and Cretaceous limestones, Pleistocene tufaceous limestones, tufa and travertines and also Cretaceous gypsum and anhydrite [3].

II. Methodology

Morphometric analyses were performed on vector data obtained by digitalization of karst rock outcrops from 100k General Geological Map of Macedonia. Map sheets containing karst rockswerefirstlygeo-referenced in national (Gauss Krugger)coordinate system. Digitalization of polygons was done in Global Mapper v.12 software, with database containing 11 fields for attributes of which 7 were extracted from the geological map (description, map source, symbol and 4 fields for age attributes), 3 were created with digitalization (area, island area, perimeter) and 1 was given according to the general classification of the karst rocks (limestone; marble; limestone, tufa & travertine; carbonate schist & marble; and gypsum & anhydrite). The obtained data, for the purpose of morphometric analysis, was later converted into UTM with WGS84 datum.

As a base for the geomorphometric analyses, 15m DEM of the Republic of Macedonia was used. This model is interpolated from 5m TIN-like detailed DEM of AREC-RM (Agency for Real Estate and Cadastre of the Republic of Macedonia), because of smoother surface and smaller file size. Currently, this is the best quality available DEM for the entire country with horizontal and vertical accuracy of +/- 2.2 m [5, 6].

Morphometric analyses of hypsometry, slope and aspect were performed using Spatial Analyst Tool in ArcGIS 10.1, and slope typein SAGA GIS v.2 modules.

III. Results and Discussion

Hypsometry

Average elevation of karst surface is 1100.4 m, with lowest value of 74.6 m and highest of 2743.9 m (Tab.1). The average elevation of the karst surface is well above the average elevation of the country at 829 m [7]. Distribution of elevation by 100 m classes shows major concentration between 500 and 1500 m, which is reflective of the extension of karst terrains generally in mountainous regions (Fig.2).

Analysis of hypsometry of various karst rock types shows that the distribution curve is mainly influenced by the major karst rocks, marble (51%) and limestone (43%), with peaks in classes of 800-900 and 900-100 m in marbles and classes of 1400-1500 and 1500-1600 m in limestones (Fig.2). Limestones have slightly higher average elevation (1192.1 m) than marbles (1045.4 m), generally found in mountainous areas in the western parts of the country. Marbles also cover mountainous areas in the western and central parts, but can also be found at lower elevations in the southern and eastern parts of the country.

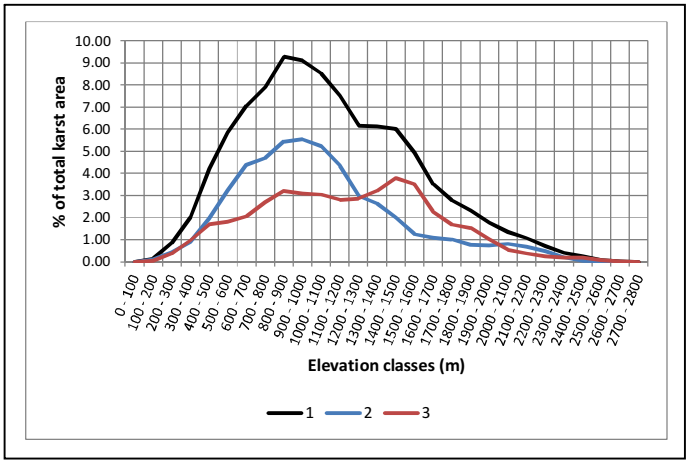


Figure 2.Area distribution by 100 m elevation classes of karst surface (1), marble outcrops (2) & limestone outcrops (3).

The other karst rocks cover much less surface (Fig. 3). Tufaceous limestones, tufa and travertines are the youngest karst rocks in Macedonia and are generally found at lower elevation, with lowest average elevation (593.7 m). Gypsum and anhydrites have the smallest area and can only be found along the deeply incised valley of Radika River, in the western part of the country. Carbonate schists & marbles and dolomites have wider vertical distribution, with average elevation of 1024.3 m and 1151 m respectively.Vertical distribution of the karst surface is a result of tectonic evolution of the area, with most of the karst rocks of Precambrian, Paleozoic and Mesozoic age, uplifted generally as part of horst structures. The tufaceous limestones, travertines and tufa are of Neogene and Quaternary age, deposited as continental deposits, mostly in lacustrine environments, and generallyare found at lower elevations, slightly elevated during the Quaternary.

TABLE 1.MAIN PARAMETERS (AREA, ELEVATION, SLOPE) OF KARST ROCKS.

Karst rocks	*% of total karst area*	*Elevation (m)*			*Slope (°)*		
		min.	*max.*	*avg.*	*min.*	*max.*	*avg.*
Marble	51.05	90	2607	1045.4	0	88.7	20.1
Limestone	43.36	74	2743	1192.1	0	88.7	20.5
Carbonate schist & marble	2.89	451	1965	1024.3	0	66.0	19.2
Tufaceous limestone, tufa & travertine	1.91	170	1057	593.7	0	51.1	9.7
Dolomite	0.76	368	1702	1151.0	0.12	52.6	23.2
Gypsum / anhydrite	0.07	577	1199	775.9	0	59.0	29.7
KARST	100.00	74	2743	1100.4	0	88.7	20.1

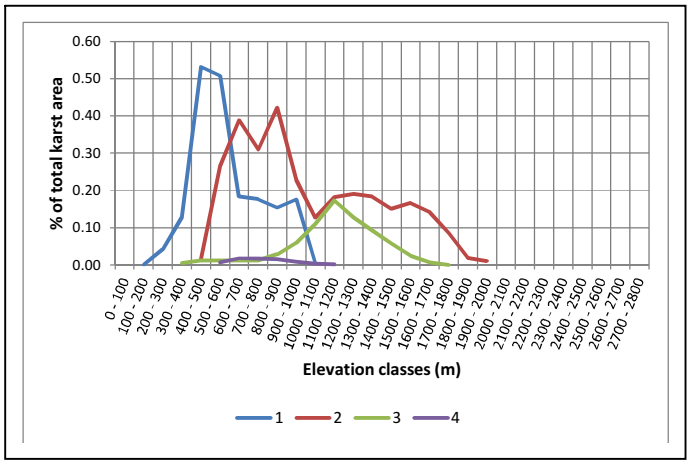


Figure 3. Area distribution by 100 m elevation classes of tufaceous limestone, tufa & travertine outcrops (1); carbonate schist & marble outcrops (2); dolomite outcrops (3); and gypsum & anhydrite outcrops (4).

In Macedonia, the amount of precipitation rises with altitude from about 500 mm on the lowest areas to 1200-1300 mm in high mountain parts (above 1500 m). It is opposite with temperatures which fall from 14°C to about 2-3°C. Thus, the karst weathering significantly increases especially above 1500 m, where limestone and marbles cover 591.5 km^2 or 16.2% of total karst area.

Slope

Average slope of the karst terrain in Macedonia is 20.6° or significantly higher than mean slope of the entire country which is 15.4° [5]. Only 35% of karst area has slope less than 20°, reflecting generally deeply incised fluvio-karstic landscapes and well preserved tectonic structures within the karst surface (Fig.4).

Marble and limestone have almost the same average slope with 20.1° and 20.5° respectively, while carbonate schist & marble have similar values at 19.2°. Gypsum & anhydrite and dolomite have the highest average slopes at 29.7° and 23.2°, generally due to deeply incised valleys. Tufaceous limestone, tufa and travertine have the lowest average slope inclination at 9.7°, which is mostly result to depositional low slopes, as most of these rocks are of lacustrine origin, have not been tectonically disturbed, and due to the karstic drainage have preserved their low slope surface.

Interestingly, the mean slope of karst terrains only slightly increase with altitude (unlike the overall terrain in the country) from 20.4° for areas under 1500 m to 21.3° for altitudes above 1500 m up to 2743 m. It is remarkable that highest values for slope angle have limestone and marble terrains (88.7°), while other rock types have more gentle peak slopes (up to 66°).

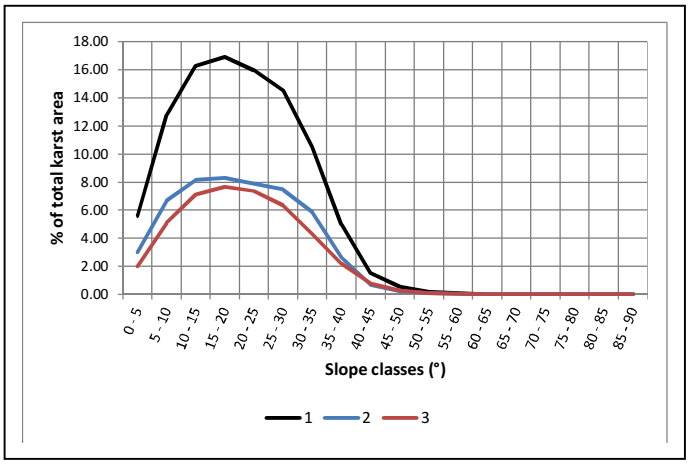


Figure 4. Area distribution by 5° slope classes of karst surface (1), marble outcrops (2) & limestone outcrops (3).

Also the area of slopes above 50° is much larger for limestone and marbles, mostly because of its hardness in comparisons to other, more erodible types of karst rocks. However, almost 1/3 of the karst terrain is flat or has slope under 15°, representing karst planation areas, karst polje bottoms etc. When compared with detailed 5m local DEM's, on these almost flat areas, small to medium-scale sinkholes frequently appear.

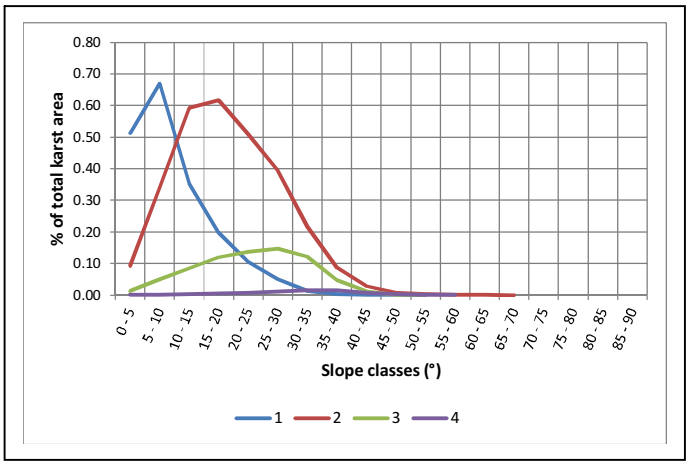


Figure 5. Area distribution by5° slope classes of tufaceous limestone, tufa & travertine outcrops (1); carbonate schist & marble outcrops (2); dolomite outcrops (3); and gypsum & anhydrite outcrops (4).

Aspect

Aspect analysis of karst surface shows generally even distribution between classes, with eastern (67.5-112.5°) and western (247.5-292.5°) expositions having slightly higher percentage.

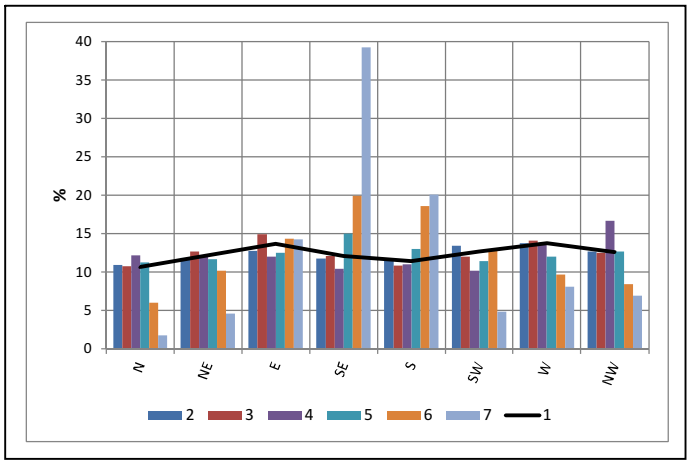


Figure 6.Area distribution of karst surface by 45° aspect classes: 1 – total karst area, 2 – marble, 3 – limestone, 4 – tufaceous limestone, tufa & travertine, 5 – carbonate schist & marble, 6 – dolomite, 7 – gypsum & anhydrite.

Similar distribution is found for most of the karst rocks, except dolomite and especially gypsum & anhydrite, where southern and southwestern expositions prevail. This is due to the local extension of these outcrops, mostly on valley sides with southern and southwestern aspect. As they represent less than 1% of the karst rock outcrops, this is not reflected on the total karst terrains aspect distribution.

When generalized to only north and south aspects, these two have exactly 50% each. However, small differences by altitude appear, where in lower karst terrains up to 1500 m, northern aspects prevail (50.3 %), while in higher terrains, southern aspects dominate (50.9%).Similar small differences are found in relation of aspects to the slope classes. Thus, terrains with steep slope (higher than 30°) are more inclined to south (50.7%), especially toward south-west and south-east. As a result, they are more exposed to temperature amplitudes and mechanical weathering.

Plan and profile curvature

Plan and profile curvature are calculated in SAGA GIS software, where negative values indicate concave slopes and positive values correspond to the convex terrains (peaks, ridges etc.). Values near zero indicate linear slopes [8]. As results in Table 2 shows, in karst terrains large areas have linear downhill slope, especially in regard to the plan curvature. Except of that, convex terrains prevail with 28.9% for plan and 38.6% for profile curvature (with positive values for both). This is normal, because the karst terrains composed of hard rocks, usually outcrop into the landscape as a ridges, crests, large stones etc.

According to the calculations, in lower altitudes (up to 1500 m), concave curvature dominates, while in higher it is opposite.

TABLE 2. PLAN AND PROFILE CURVATURE OF KARST TERRAINS.

Plan curvature	*Area (%)*	*Profile curvature*	*Area (%)*
<-0.01	14.0	<-0.001	23.2
-0.01 to -0.005	9.3	-0.001 to -0.0005	9.5
-0.005 to 0.005	47.8	-0.0005 to 0.0005	28.7
0.005 to 0.01	15.0	0.0005to0.001	9.4
>0.001	13.9	>0.001	29.2

IV. CONCLUSION

This research represent first attempt to analyze the general morphometric characteristics of the karst surface in the Republic of Macedonia. The outcome reveals certain specific characteristic of the karst surface, especially between different karst lithologies. Slope can be an important indicator of karst surface, as dolines will not develop on steep hillsides with more than about 20° [9]. Hypsometry of karst surface can also provide correlation to climatic characteristics (ex. precipitation, temperature) that control karst development, with most of the karstic terrains in Republic of Macedonia found in mountainous areas.Furthermore, with combination of selected geomorphometric parameters, fine-scale automated classification of karst features can be made [10].

REFERENCES

[1] Andonovski T., 1981. “Survey of underground karst forms in the SR of Macedonia”. 8th Yugoslav Congress of Speleology, Belgrade, 207-213.

[2] Kolčakovski D., Boškovska G., 2007. “Extension and age of carbonate rocks in the Republic of Macedonia”. Bulletin of Physical Geography, No.3-4, Skopje, 77-82.

[3] Temovski M., 2012. “Extension of karst rock outcrops in Republic of Macedonia”. Geographical Reviews, Skopje, 46, 21-35

[4] Manakovik D., 1980. “L’hydrographiekarstique en formed’oasis en Macedoine”. CongresYougoslave de speleology 7, Titograd, 293-309

[5] Milevski I., 2014. “Slope Values Accuracy vs Resolution of the Digital Elevation Models (Example of the Republic of Macedonia)”. Proceedings of 5th ICC-GIS Conference; Eds: Bandrova T &Konecny M., Vol. 2, Varna, 568-575.

[6] Milevski I., Gorin S., Markoski M., Radevski I., 2013. “Comparison of Accuracy of DEM’s Available for the Republic of Macedonia”. Proceedings from the 3rd International Geographic Symposium - GEOMED 2013, Antalya, 165-172

[7] Andonovski T., 1995. “Characteristics of relief in the Republic of Macedonia”, Geographical Reviews, Skopje, 30, 5-12.

[8] Dikau, R., 1989. “The application of a digital relief model to landform analysis”. In: Raper, J.F. (Ed.). Three dimensional applications in Geographical Information Systems. Taylor and Francis, London, pp. 51–77.

[9] Ford & Williams, 2007. “Karst hydrogeology and geomorphology”. 2nd ed., Wiley, 562 pp.

[10] Liang, F., and Y. Du., 2013. "An automated method to extract typical karst landform entities from contour lines on topographic maps". Geomorphometry 2013. Nanjing, China.

Mapping and geomorphometric analysis of 3-D cave surfaces: a case study of the Domica Cave, Slovakia

Michal Gallay, Ján Kaňuk, Jaroslav Hofierka, Zdenko Hochmuth
Institute of Geography, Faculty of Science
Pavol Jozef Šafárik University in Košice
Košice, Slovakia
michal.gallay@upjs.sk

John Meneely
School of Geography, Archaeology and Palaeoecology
Queen's University in Belfast
Belfast, United Kingdom
j.meneely@qub.qc.uk

Abstract—**Recent development in the laser scanning technology has provided new tools and methods for a very accurate and cost-effective way of mapping complex volumetric landscape features such as caves. In the presented case study, we use the laser scanning point cloud data representing over 1,500 meters of the Domica Cave in Slovakia to demonstrate the methodology of reconstructing the 3D digital cave surface at a high-level of detail. The digital 3D model was generated for a particular section of the cave. The model was used to analyze mean curvature of the cave surface at multiple levels of scale. The approach was performed in open-source software.**

I. INTRODUCTION

Caves represent specific underground landscape features which have a longer geomorphological memory than the superficial landforms. Studying their morphometry and genesis often provides clues for explaining also the evolution of the above-surface landscape [10]. Traditionally, the caves were mapped with mine surveying tools based on tacheometric principles and levelling [15]. With these approaches, the main principle is relatively straightforward to measure the general azimuth, slope angle, length and size of the underground corridors every few meters. The methods are applicable even in very narrow and difficultly accessible parts. However, the survey requires long time and physical effort of the surveying team. Also capturing the detail of the corridors and domes was based on expert manual drawings and sketches which potentially leads to inaccuracies.

Recent development in the laser scanning technology enabled rapid and accurate mapping of caves with an unprecedented level of detail. Terrestrial laser scanners (TLS) acquire millions of points in a single scan resulting in a three-dimensional (3-D) point cloud within a few minutes. TLS has been used in previous studies to obtain accurate three dimensional models of caves. These studies were motivated by the need for improved cartographic visualization and geomorphological analysis [5, 6]. Others have used TLS for archaeological and zoological research [1] and for heritage management and tourism [4, 23]. Some recent studies go further and combine the TLS data with other spatial data, for example, cave photography [18], orthotermography [3] or data from the surface above the cave [16].

The main challenge is in processing such a large amount of point measurements and generating 3D surfaces from them [16, 19, 20]. A good choice of software tools exists for rapid visualization of point cloud data and their basic processing (e.g., LAStools[1], lidarview[2], Bentley Pointools[3]). The tools enable efficient visualization and basic measurements of the cave 3D geometry such as the length, width, and height of a corridor, relative height of corridors, cross-sectional profiles which was explored in several studies. However, more complex analysis of the cave system requires digital reconstruction of the 3D cave surface and its integration with superficial data [16, 20, 21]. The concept of geographic information systems (GIS) is well suited for this purpose as it enables handling various geospatial data and naturally comprises tools for their analysis including geomorphometry.

Contemporary methods of digital geomorphometry are based on analyzing 2.5 surface models generated preferentially in a raster format (i.e. rectangular grid) [14]. While this approach is sufficient to handle most of the superficial landforms it poses constraints in handling landforms of a complex 3D shape such as caves. Such objects need to be modelled in 3D in different software and afterwards they can be imported into GIS. Examples of tools enabling the 3D visualization comprise NVIZ in GRASS GIS [12] or ArcScene in ArcGIS [9]. However, limited options are available in terms of analyzing the shape of a 3D surface in GIS packages and other software has to be

1 http://rapidlasso.com/lastools/
2 http://lidarview.com/
3 http://www.bentley.com/en-US/Promo/Pointools/pointools.htm?skid=CT_PRT_POINTOOLS_B

In: Geomorphometry for Geosciences, Jasiewicz J., Zwoliński Zb., Mitasova H., Hengl T. (eds), 2015. Adam Mickiewicz University in Poznań - Institute of Geoecology and Geoinformation, International Society for Geomorphometry, Poznań

explored to perform the analysis, for example, Meshlab[4], Blender[5], Geomagic Studio[6].

In this paper, we show preliminary results of reconstructing a 3D digital cave surface model and analysis of the 3D surface morphometry based on data acquired within terrestrial laser scanning of the Domica Cave in Slovakia. The research is conducted within the national research project titled: New methods of spatial modelling with laser scanning data and 3-D GIS (Nr. APVV-0176-12[7]).

II. STUDY SITE

The study area comprises the Domica Cave situated at the south-western edge part of the Slovak Karst near the state border of Slovakia and Hungary (Fig. 1). The total length of the cave is almost 5400 metres, however, its further continuation into the Hungarian Aggtelek Karst (the Baradla Cave) generates a multi-level single genetic cave system as long as 25,000 metres. The Domica cave evolved within several levels ranging between 318 - 341 meters a. s. l. It is the beginning part of the cave system formed by corrosive-erosive action of fluvial waters and temporary streams which sink underground at the contact of the Middle Triasic white limestones and the Pontian fluvio-lacustrine gravel-sand-clay sediments [2, 8]. The cave was inhabited by the Neolithic people but after a natural blockage of the entrance the cave was rediscovered by Ján Majko in 1926. The showcave part is accessible since 1932 and presently it is over 930 metres long. The cave was thoroughly mapped in 1960s by [8] and the last surveying was done by the Geological Survey, national enterprise, Spišská Nová Ves in 1976. The cave system named Domica-Baradla is a listed UNESCO Natural Heritage Site since 1997. Laser scanning of the cave provided non-disturbing means for highly detailed parameterisation of the cave corridors enabling to study specific landforms such as fluvial channels carved into the ceiling, faults, and abundant shapes of speleothems.

III. LASER SCANNING THE CAVE

The data used in the presented study were acquired with a terrestrial laser scanner in combination with RTK-GPS surveying within a 5 days mission in March 2014 in the Domica Cave, Slovakia. FARO Focus 3D scanner was used to scan around 1,500 metres of the cave from 328 scanner positions within 40 hours in total. The scanning density point spacing was set to 20 millimetres at 10 metres. The scans were oriented relative to each and with respect to the Slovak national coordinate system (S-JTSK) in SCENE[8], proprietary software by FARO. The final point cloud contained almost 12 billion of points representing the entire show cave and some parts inaccessible by public (Fig. 2). The total accuracy of registration of the scans was 4-5 millimetres. Georeferencing of the registered point cloud in the national grid achieved accuracy of 12 millimetres measured as the total RTK-GPS positioning error. The survey is thoroughly described in [11]. The point cloud provides a very high detail which enables viewing even small geomorphological features such as speleothems (Fig. 2). Visualisation of the point cloud allows for basic measurements of the cave morphometry but it is not applicable for defining morphometric parameters such as curvature or orientation for which a 3D volumetric surface is needed [20].

IV. GENERATING THE 3D SURFACE MODEL

In the current stage of the research presented by this paper, we are testing different approaches to handle such a massive dataset in order to derive a 3D surface model at different levels of detail. For now, we selected a part of the cave (Fig. 2, 3) to reconstruct its volumetric body to demonstrate the methodological approach. The acquired TLS point cloud provided a discontinuous (point) representation of the cave

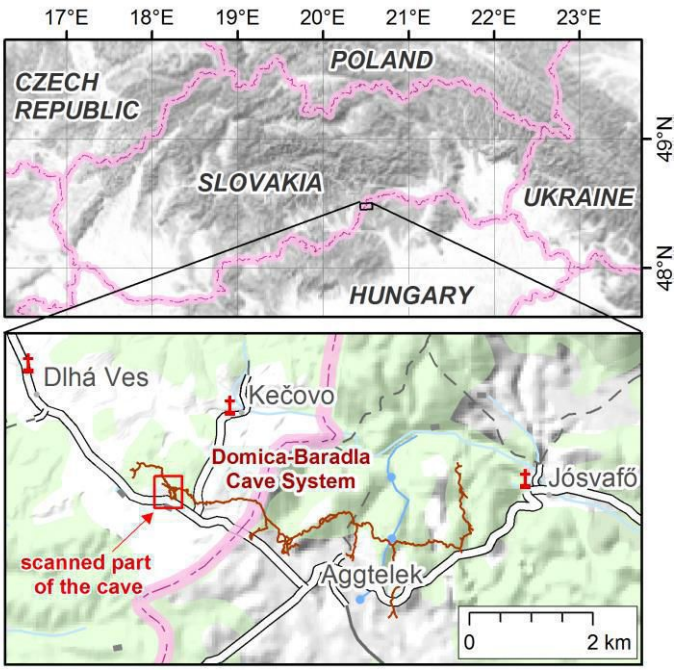


Figure 1. Location of the scanned part of the Domica Cave.

4 http://meshlab.sourceforge.net/
5 http://www.blender.org/
6 http://www.geomagic.com
7 http://spatial3d.science.upjs.sk/
8 http://www.faro.com/faro-3d-app-center/stand-alone-apps/scene

surface and for this reason it is necessary to generate a surface model. Computational representation of 3D surfaces is a widely studied problem in computer graphics and disciplines where 3D surface is the concern of research (e.g., biology, medicine, physics, geology). Surfaces are usually represented as a polygonal mesh which comprises a collection of vertices, edges and faces defining the shape of a polyhedral object [22]. In this work, we adopted a triangular 3D-mesh consisting of triangular faces. Each facet is defined by a set of three vertices and its orientation (the angle of azimuth and slope) is defined by a vector normal to the facet. Usually, it is meaningful to reduce the input point cloud before these steps are performed to test the methodological approach. Therefore, we decimated the point cloud of the sample cave section in the SCENE software to extract only 1 percent (268,720 points) of the original set. The Meshlab software [7] was used to generate the 3D triangular mesh. Meshlab is free and open-source software for mesh processing and editing capable of working with numerous 3D file formats. Generation of a 3D surface model in Meshlab involves several steps: In the first step, normals for the points (future mesh vertices) are estimated based on a defined neighbourhood of points for which a plane is fitted and its normal is calculated. Also viewing position has to be set for a correct orientation of the normals.

After computing the normals, the surface model (mesh) can be reconstructed using several algorithms. We tested the Poisson surface reconstruction approach by [17]. A similar study was conducted by [21] who modelled the surface of a cave chamber and identified stalactites based on local minima of the 3D surface. The authors also designed a web interface for viewing the model in 3D. The reconstruction of the 3D surface is based on the observation that the normal field of the boundary of a solid can be interpreted as the gradient of the solid's indicator function. Therefore, given a set of oriented points sampling the boundary of a solid, a 3D-mesh can be obtained by transforming the oriented point samples into a continuous vector field in 3D. This is performed finding a scalar function whose gradients best match the vector field, and extracting the appropriate isosurface. A thorough definition of the Poisson surface reconstruction can be found in [17]. It is important to mention that the vertices of the reconstructed triangular 3D meshes do not coincide with the points of the survey. With this algorithm, the octree depth is a key input parameter controlling the level of surface detail. It is the maximum depth of the tree that will be used to define the neighbourhood of points for fitting the indicator function reconstructing the 3D surface. The number of faces and vertices comprised in the resulting 3D mesh increases with the higher value of the octree depth as it is shown in TABLE 1.

After reconstructing the 3D mesh (Fig. 3), further processing and surface analysis can be performed, for example, filling the

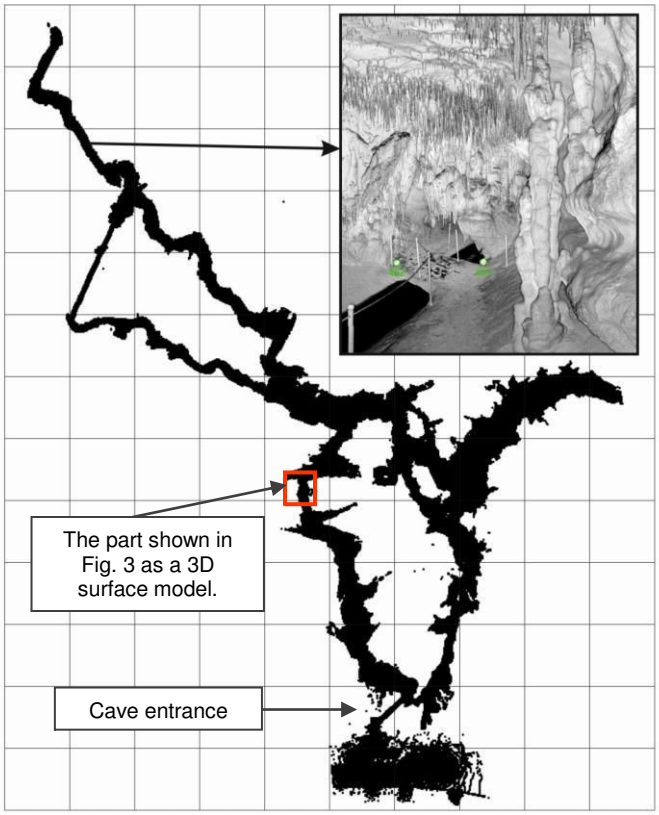


Figure 2. Top view of the entire point cloud representation of the Domica Cave containing 12 billion of points oriented towards north. The scale is given by the reference grid of 50 metres cell size. The picture in the upper right visualizes a perspective view of the cloud demonstrating the acquired level of detail in a paved corridor with the channel of the Styx River (black areas of no laser reflectivity).

holes, decimation of the mesh, or mesh parameterization. We explored the multi-scale parameterization of the mean surface curvature. Computation of the mean curvature requires points or mesh faces equipped with oriented normal [13]. The mean curvature is a measure of the surface convexity/concavity analogous the mean curvature of a 2.5 digital elevation model which is commonly analysed in GIS. As a result, peaks (stalactites, stalagmites) have positive mean curvature values and sinks have negative values (Fig 3).

V. RESULTING 3D SURFACE AND MORPHOMETRIC ANALYSIS.

The reconstructed 3D surface model of the part of the Domica cave is shown in Fig. 3. Table 1 reports the settings of the Poisson surface reconstruction approach and the time

TABLE I. PARAMETERS OF THE POISSON SURFACE RECONSTRUCTION

Dataset	Octree depth	Processing time [sec]	Number of vertices in the mesh
Cave corridor	6	0.5	4,310
	8	5.4	6,712
	9	13.8	140,631
Cave ceiling	10	3.5	28,091
	12	9.1	58,577
	13	25.5	66,025

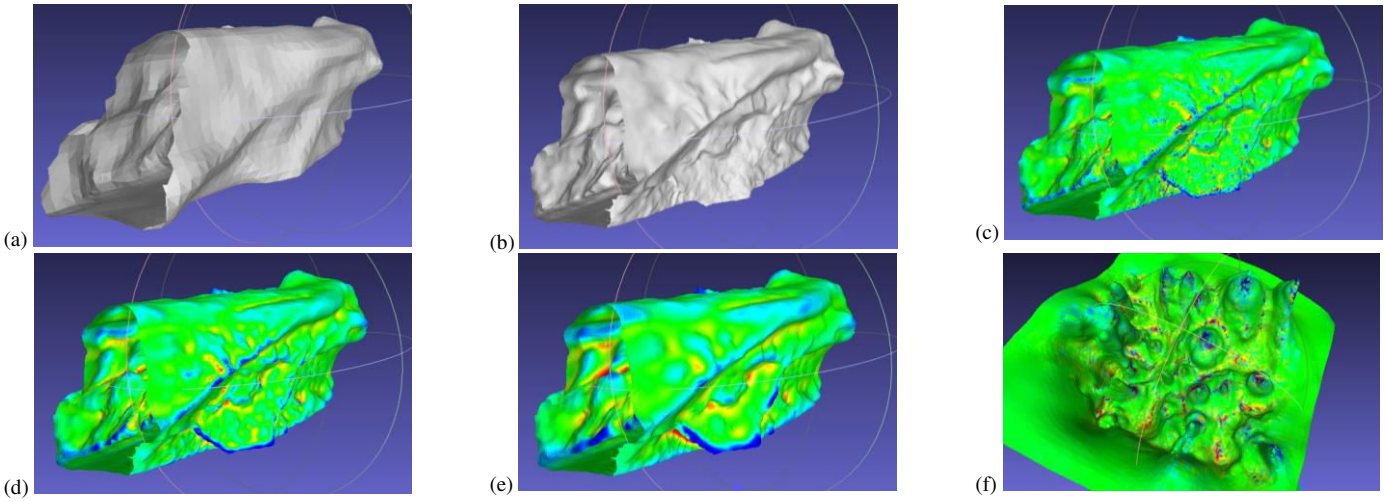


Figure 3. 3D cave surface reconstructed for a selected part of the Domica cave (10 meters long, 4 meters high) located in Fig. 2. Reconstructed 3D triangular mesh using the Poisson surface reconstruction with the octree depth of 6 containing 4,310 vertices (a), and with the depth of 9 containing 140,631 vertices (b). Mean surface curvature on multiple levels of scale was calculated for the surface (b) based on 5 neighbours (c), 10 neighbours (d), 20 neighbours (e). A part of the cave ceiling (1 m sq.) reconstructed with the octree depth of 12 rendered with the mean curvature based on 20 neighbours.

required for processing. Setting of the algorithm is user and data dependent. In order to reconstruct the surface of the corridor lower octree depths are sufficient while if more detail of the 3D surface model is required higher octree depths are needed, as in the case of the detailed model of the cave ceiling (Fig. 3f). The mean curvature of the model of the corridor analysed at multiple levels of scale distinguishes large and small features of the cave walls (Fig. 3a-e) and ceiling (Fig. 3f). Such a 3D approach provides means of quantification and parameterisation of speleoforms which was not possible with traditional 2.5D concept of contemporary tools used in geospatial analysis.

VI. CONCLUSION

This paper outlined a methodological approach of a 3D cave surface modelling in order to parameterise the 3D surface model. Such a task is analogous to the geomorphometric analysis of a 2.5 surfaces available in GIS software which is well suited for a more complex analysis of geographical data. However, tools for modelling 3D volumetric surfaces and their parameterisation do not exist in GIS. Therefore, combining the analysis of a 3D surface with 2.5 DEMs representing the land surface above the caves is a difficult task. We demonstrated the cave surface 3D modelling approach using a sample of the laser scanning point cloud of a cave section of the Domica Cave in Slovakia. The preliminary results show that Poisson surface reconstruction is a suitable approach. The level of detail controlled by the octree depth should be tested for particular modelling case and required level of detail. Scale-dependency of the resulting surface was explored with mean curvature. Further research will focus on efficient processing of much larger datasets to reconstruct a 3D model of the entire point cloud with on multiple-levels of scale. Such a model will be applicable for (i) studying relations between different parts of the cave system and also for (ii) inferring the relationship between environmental processes acting underground and on the above-surface.

ACKNOWLEDGMENT

The research presented in this paper originated within the scientific projects APVV-0176-12, funded by the Slovak Research and Development Agency, and VEGA 1/0473/14, funded by the Slovak Research Grant Agency. This paper is also the result of the Project implementation: University Science Park TECHNICOM for Innovation Applications Supported by Knowledge Technology, ITMS: 26220220182, supported by the Research & Development Operational Programme funded by the ERDF.

REFERENCES

[1] Azmy S.N., Sah S.A.M., Shafie N.J., Ariffin A., Majid Z., Ismail M.N.A., and Shamsir M.S., 2012. "Counting in the dark: Non-intrusive laser scanning for population counting and identifying roosting bats." Scientific Reports, 2 (524).

[2] Bella, P., Braucher, R., Holec, J., Veselský, M., 2014. "Burial age of cemented quartz gravel in the upper level of the Domica Cave, Slovakia", In Book of abstracts, 8th Scientific Conference of the Association of Slovak Geomorphologists at Slovak Academy of Sciences, Snina, Slovakia 6 – 8 October 2014, pp.10-11

[3] Berenguer-Sempere F., Gómez-Lende M., Seranno E., and de Sanjosé-Blasco J.J., 2014. "Orthothermographies and 3D modeling as potential tools in ice caves studies: the Peña Castil Ice Cave (Picos de Europa, Northern Spain)." International Journal of Speleology, 43: 35-43.

[4] Buchroithner M.F. and Gaisecker T., 2009. "Terrestrial Laser Scanning for the Visualization of a Complex Dome in an Extreme Alpine Cave System." Photogrammetrie Fernerkundung Geoinformation, 4: 329-339.

[5] Buchroithner M.F., Milius J., and Petters, C., 2011. "3D Surveying and Visualization of the Biggest Ice Cave on Earth". In Proceedings of 25th International Cartographic Conference, 8-11 July 2011, Paris.

[6] Canevese E.P., Forti P, Naseddu A., Ottelli L., and Tedeschi, R., 2011. "Laser scanning technology for the hypogean survey: the case of Santa Barbara karst system (Sardinia, Italy)." Acta Carsologica, 40 (1): 65-77.

[7] Cignoni, P., Corsini, M., and Ranzuglia, G., 2008."MeshLab: an Open-Source 3D Mesh Processing System". Ercim News - ERCIM , 2008/73.

[8] Droppa, A., 1972. "A contribution to the development of the Domica Cave (In Slovak)". Československý kras, 22: 65-72.

[9] ESRI. ArcGIS Desktop. http://www.esri.com/software/arcgis/arcgis-for-desktop

[10] Ford, D., Williams, P. D., 2013. "Karst Hydrology and Geomorphology". John Wiley & Sons, 576 p.

[11] Gallay, M., Kaňuk, J., Meneely, J., Hochmuth, Z., and Hofierka, J. "Large-scale and high-resolution 3-D mapping of caves by terrestrial laser scanning: a case study of the Domica Cave, Slovakia." International Journal of Speleology, submitted

[12] GRASS Development Team, 2015. "Geographic Resources Analysis Support System (GRASS) Software", Version 7.0. Open Source Geospatial Foundation. http://grass.osgeo.org

[13] Guennebaud, G., Gross, M., 2007. "Algebraic point set surfaces", ACM Transaction on Graphics, Proceedings of ACM SIGGRAPH 2007, 26/3, Article 23.

[14] Hengl, T., Reuter, H.I. (eds), 2008. "Geomorphometry: Concepts, Software, Applications". Developments in Soil Science, vol. 33, Elsevier. 796 p.

[15] Hochmuth, Z., 1995. "Cave mapping (in Slovak)". Slovenská speleologická spoločnosť, Liptovský Mikuláš, Slovakia, 80 p.

[16] Hoffmeister, D., Zellmann, S., Kindermann, K., Pastoors, A., Lang, U., Bubenzer, O., Weniger, G.-C., Bareth, G., 2014. "Geoarchaeological site documentation and analysis of 3D data derived by terrestrial laser scanning", ISPRS Ann. Photogramm. Remote Sens. Spatial Inf. Sci., II-5, pp. 173-179,

[17] Kazhdan, M. M., Bolitho, M., Hoppe, H., 2006. "Poisson surface reconstruction." In Symposium on Geometry Processing, ser. ACM International Conference Proceeding Series, A. Sheffer and K. Polthier, Eds., vol. 256. Eurographics Association, 2006, pp. 61–70.

[18] Lerma J.L., Navarro S., Cabrelles M., and Villaverde V., 2009. "Terrestrial laser scanning and close range photogrammetry for 3D archaeological documentation: the Upper Palaeolithic Cave of Parpalló as a case study." Journal of Archaeological Science, 37(3): 499-507.

[19] Mitasova H., Barton M., Ullah I., Hofierka J., Harmon, R.S., 2013. "GIS-Based Soil Erosion Modeling", In Treatise on Geomorphology, Edited by John F. Shroder, 3, San Diego: Academic Press, pp. 228-258.

[20] Roncat, A., Dublyansky, Y., Spotl, C., Dorninger, P., 2011. "Full-3D surveying of caves: A case study of Marchenhohle (Austria)", In Proceedings of the International Association for Mathematical Geosciences, September 5-9, 2011.

[21] Silvestre, I., Rodrigues, J.I., Figueiredo, M.J.G., and Veiga-Pires, C., 2013. "Cave Chamber Data Modeling and 3D Web Visualization", In 17th International Conference on Information Visualisation (IV), 16-18 July 2013, pp.468-473.

[22] Tobler, R. and Maierhofer, R., 2006. "A mesh data structure for rendering and subdivision." Proceeding of the International Conference in Central Europe on Computer Graphics, Visualization and Computer Vision, 2006, pp. 157–162.

[23] Zlot R. and Bosse M., 2014. "Three-dimensional mobile mapping of caves." Journal of Cave and Karst Studies, 76 (3): 191–206.

Surface geophysical surveys and LiDAR DTM analysis combined with underground cave mapping – an efficient tool for karst system exploration: Jaskinia Niedźwiedzia case study (Sudetes, SW Poland)

Marek Kasprzak
Institute of Geography and Regional Development
University of Wrocław
Wrocław, Poland
marek.kasprzak@uni.wroc.pl

Artur Sobczyk
Institute of Geological Sciences
University of Wroclaw
Wrocław, Poland
artur.sobczyk@ing.uni.wroc.pl

Szymon Kostka, Anna Haczek
Wrocław Caving Section
Wrocław, Poland
szymon@stopptak.com.pl

Abstract—**The paper presents results of last studies in karst area of Kleśnica valley in the Sudetes (SW Poland), known for spectacular discoveries of new cave passages in 2012–2014. We used airborne laser scanning data (LiDAR based DTM 1×1 m) and geophysical measurements (ground penetrating radar and 2-dimensional electrical resistivity tomography), combined with detailed underground mapping, representing a new multi-facet approach focused on the examination of karst voids distribution in Kleśnica valley. The confrontation and comparison of spatial data from different measurement techniques allowed us to determine the range of crystalline limestones and distribution of karst voids, including the voids previously unknown and not explored by speleologists.**

I. INTRODUCTION

Niedźwiedzia (Bear) Cave with entrance location at 50°14'03"N, 16°50'03"E, discovered on 14th October 1966, belongs to one of the biggest cave in Poland, at the same time being a leading one within the Sudetes Mts. (SW Poland). Since the 1983 middle level of karst voids might be reached by tourists, and its surrounding is protected within a natural reserve. For last tens of years, Kleśnica basin and Niedźwiedzia Cave within, have been a subject of intensive geological, geomorphological, hydro-geological and geophysical research, e.g. [1, 2, 3, 4, 5, 6]. Last few years have brought new facts, being an impulse for a new chapter in cave area research. During the years, 2012–2014 speleologists from the Wrocław Caving Section explored 1979 metres of new cave passages, with some spectacular speleothems inside (e.g. *Mastodont Hall* and *Humbaki Hall*). In this period underground cave passages were re-examined, resulting in new high-precision cave map [7, 8]. Simultaneously since 2013 land surface airborne laser scanning (ASL) data are available for Poland and distributed by Documentation Centre of Geodesy and Cartography. The LiDAR data with density of 4–6 points per square metre and vertical accuracy ≤ 0.15 m allow building digital terrain model (DTM) with a resolution of 1×1 m, making field work precise and convenient. Moreover new geophysical equipment is available, which gives an opportunity for leading a high-resolution near surface surveys. With this study, we present a new multi-facet approach focused on the examination of karst voids distribution in Kleśnica valley (Śnieżnik Massif). We combined electrical resistivity tomography (ERT), high--resolution DTM data and cave underground mapping.

II. METHODS

Geophysical ERT works done during spring and autumn seasons 2014, have been preceded by ground penetrating radar (GPR) study, which is commonly applied approach, e.g. [9, 10, 11, 12, 13]. Shallow GPR sounding of geological basement was made with 250 MHz shielded antenna for eight profiles located perpendicularly to the ridge axis of Mt. Stroma (1166 m a.s.l.). Next, we conducted 8 ERT profiles, 5 of them oriented perpendicularly to Kleśnica valley, last three lengthwise to this axis (Fig. 1). Profiles length range from 265 to 596 metres made with Wenner-Schlumberger electrode array and 5 m spacing between electrodes. ERT measurements were led over known karst voids, newly discovered parts as well as further to the south in the area of unknown underground structure.

We referenced all geophysical profiles with two GPS receivers and precision of 3–5 m and 0.5–1.5 m respectively

In: Geomorphometry for Geosciences, Jasiewicz J., Zwoliński Zb., Mitasova H., Hengl T. (eds), 2015. Adam Mickiewicz University in Poznań - Institute of Geoecology and Geoinformation, International Society for Geomorphometry, Poznań

(differential GPS). Subsequently we used high-resolution LiDAR based DTM image for crystalline limestone identification (Fig. 2), which form unobvious slope micro features, mainly in the contact zone of mica schist and karstic rocks [14]. Topography data also allowed integration with ERT measurements and latter spatial interpretation. We computed geophysical data with RAMAC Ground Vision 2 (MALÅ Geoscience) and RES2DINV (Geotomo) software for GPR and ERT respectively. We applied SAGA GIS (by O. Conrad) and MicroDEM (by P. Guth, PETMAR Trilobite Breeding Ranch) software for DTM analysis, and Voxler 3 (Golden Software) for three-dimensional visualising of geophysical and topography data. We used electronic cave surveying device (Leica Disto) with millimeter accuracy laser measurements feature for underground mapping, with magnetic declination correction included [8].

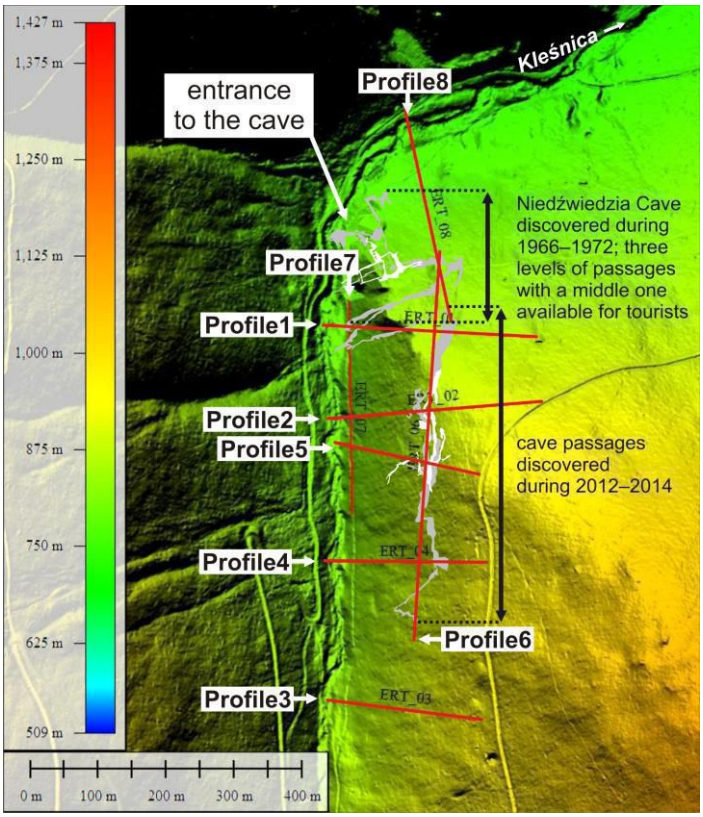


Figure 1. Electrical resistivity tomography profiles in the Kleśnica valley.

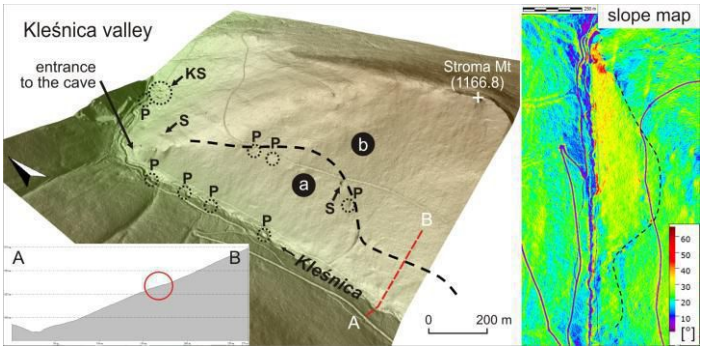


Figure 2. DTM analysis for detection crystalline limestones range on slope surface in the Kleśnica valley: a – crystalline limestones, b – mica schists and paragneisses, KS – karst spring, P – ponor zone [1], S – sinkhole.

III. RESULTS & RESEARCH PERSPECTIVES

Geophysical tomograms revealed existence of three levels of karst voids in the Niedźwiedzia Cave, being in accordance with previously reported data (Fig. 3). First horizon appears at the reference level of modern Kleśnica river valley floor. Second one, located higher and further to the east, is located 30–60 m above river floor (a.r.f.), latter one ranging from 70 to 80 a.r.f respectively. Above-mentioned values are of approximate meaning. Furthermore, crystalline limestone lens contains numerous minor karst voids, building highest underground level with still undiscovered passages therein. ERT profiling reached several recently discovered prominent underground features: *Zdzichu Gangway* and *Mastodont Hal*l (profile 1), *Piętrowa Hall* (profile 2), *Humbaki Hall* (profile 5) and *Kutaśnik* (profile 4). On the profile no. 3, located furthest to the east, we unequivocally confirmed existence of unknown karst voids, representing Kleśnica upstream continuation of the Niedźwiedzia Cave system (Fig. 4). Reported passages remain still undiscovered for speleo-

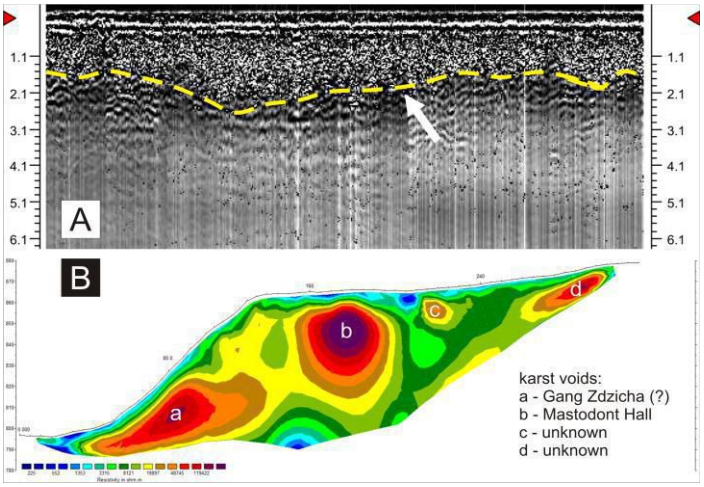


Figure 3. Examples of crystalline limestones imaging by ground penetrating radar (A) and 2-dimensional electrical resistivity tomography (B) – profile 1. Yellow line shows a boundary between solid and weathered rocks.

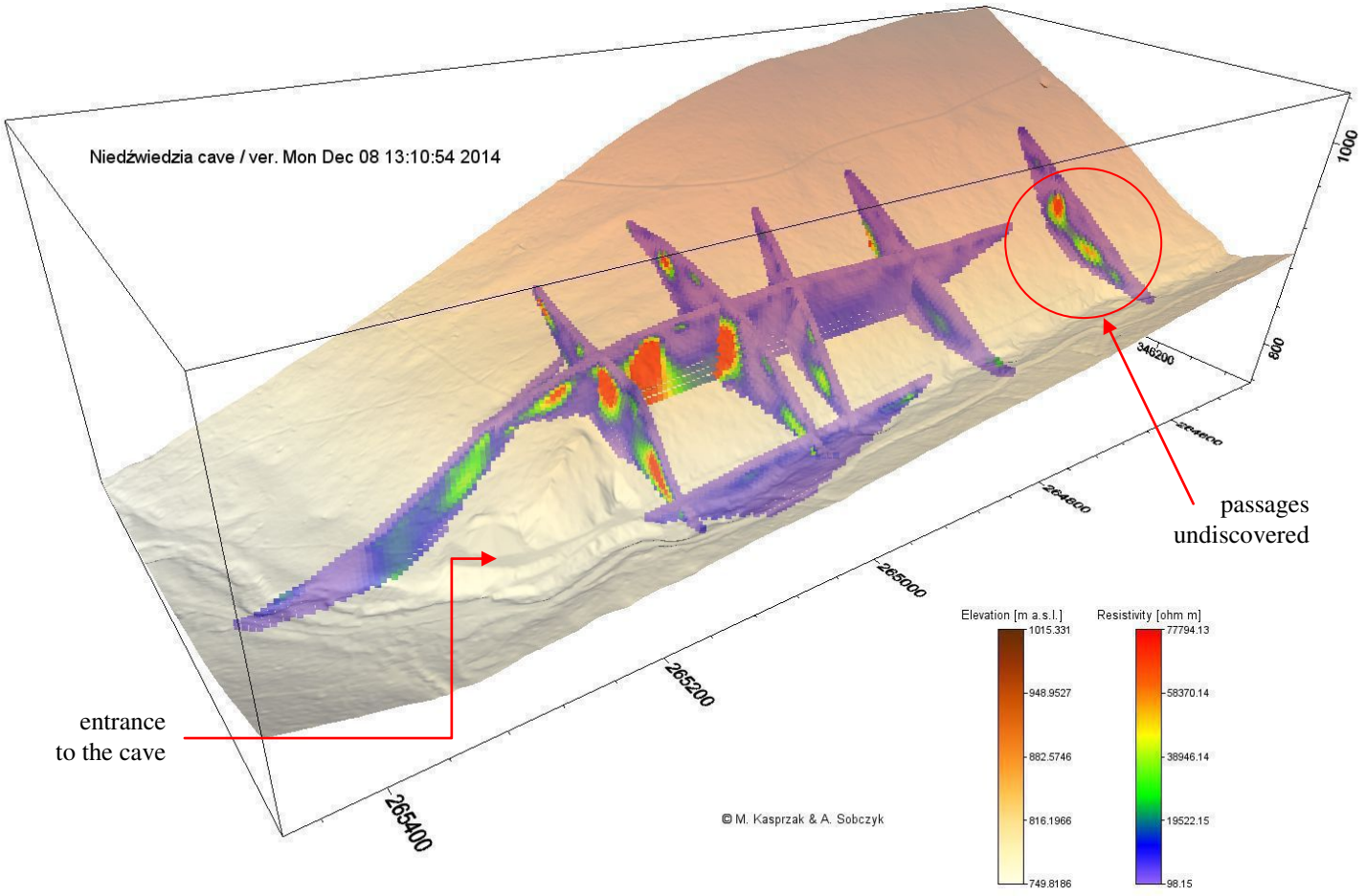


Figure 4. 3-dimensional image of karst voids detected by electrical resistivity tomography in the Kleśnica valley. Fields in ERT profiles, marked with "warm" colors, indicate a location of high resistivity areas – karst voids.

logists. According to tomograms performed, we reached the limestone lens floor, suggesting total thickness below 100 m. Moreover, we suggest its spatial distribution to be re-examined since we investigated the existence of crystalline limestone further to the east and south, out of mapped outcrops known from available geological maps [15, 16]. Presented initial remarks on Niedźwiedzia Cave system supported by multi-facet study, prove theirs high potential in a detailed study of karst areas. Nevertheless further works coupling geophysical methods, geomorphology and underground speleological explorations, should allow better understand origin and evolution of the Śnieżnik Massif in wider regional context [17]. The greatest difficulties of this research are an exploration and mapping inside the cave and slope $\geq 30°$ during surface geophysical surveys.

ACKNOWLEDGMENT

Fieldworks were partially supported by the project *Rozpoznanie systemu pustek krasowych w dolinie Kleśnicy (Masyw Śnieżnika) przy pomocy tomografii elektrooporowej,* award no 2170/M/IGRR/14, financed by statutory funds for the development of young scientists of Faculty of Earth Sciences and Environmental Management, University of Wrocław. Authors are grateful for the Regionalny Dyrektor Ochrony Środowiska we Wrocławiu for a permission to work in the nature reserve *Jaskinia Niedźwiedzia w Kletnie*. We would like to inform, that

LiDAR data used for this study, have been purchased and used with academic license DIO.DFT.DSI.7211.1619.2015_PL_N, according to the Polish law regulations in the administration of Główny Urząd Geodezji i Kartografii.

REFERENCES

[1] Ciężkowski, W., 1989. ”Badania hydrogeologiczne obszaru krasowego Masywu Śnieżnika”, In A. Jahn, S. Kozłowski, T. Wiszniowska (eds.), Jaskinia Niedźwiedzia w Kletnie. Badania i udostępnianie, Ossolineum, Wrocław, pp. 180–201.

[2] Don, J., 1989. ”Jaskinia na tle ewolucji geologicznej Masywu Śnieżnika”, In A. Jahn, S. Kozłowski, T. Wiszniowska (eds.), Jaskinia Niedźwiedzia w Kletnie. Badania i udostępnianie, Ossolineum, Wrocław, pp. 58–79.

[3] Jodłowski, S., 1989. ”Badania geofizyczne otoczenia Jaskini”, In A. Jahn, S. Kozłowski, T. Wiszniowska (eds), Jaskinia Niedźwiedzia w Kletnie. Badania i udostępnianie, Ossolineum, Wrocław, pp. 147–156.

[4] Kozłowski, S., 1989. ”Budowa geologiczna otoczenia jaskini”, In Jahn, A., Kozłowski, S., Wiszniowska, T., (eds) Jaskinia Niedźwiedzia w Kletnie. Badania i udostępnianie, Ossolineum, Wrocław–Warszawa–Kraków–Gdańsk–Łodź, pp. 80–118.

[5] Bosàk, P., 1995. ”Paleokarst of the Bohemian Massif in the Czech Republic: an overview and synthesis”, International Journal of Speleology 24, 1, pp. 3–39.

[6] Migoń, P., 1997. ”Zarys rozwoju morfologicznego Masywu Śnieżnika”, In A. Jahn, S. Kozłowski (eds), Masyw Śnieżnika – zmiany w środowisku przyrodniczym, Polska Agencja Ekologiczna SA, Warszawa, pp. 35–46.

[7] Kostka, S., 2012. ”Przepraszamy, to przez przypadek” In Ciężkowski, W., (ed.) Jaskinia Niedźwiedzia w Kletnie w 45-lecie odkrycia, Wrocław–Kletno, pp. 97–114.

[8] Kostka, S., Data, D., Haczek, A., and M. Markowski, 2014. ”Najnowsze odkrycia w Jaskini Niedźwiedziej oraz perspektywy udostępnienia”, Materiały 48. Sympozjum Speleologicznego, Kletno, 16–19.10.2014 r., Sekcja Speleologiczna Polskiego Towarzystwa Przyrodników im. Kopernika, p. 83.

[9] Beres, M., Luetscher, M., and R. Olivier, 2001. ”Integration of ground-penetrating radar and microgravimetric methods to map shallow caves”, Journal of Applied Geophysics 46, pp. 249–262.

[10] Mochales, T., Casas, M., Pueyo, L., Pueyo, O., Román, M.T. Pocoví, A., Soriano, M.A., and D.Ansón, 2008. ”Detection of underground cavities by combining gravity, magnetic and ground penetrating radar surveys: a case study from the Zaragoza area, NE Spain”, Environmental Geology 53, pp. 1067–1077.

[11] Brown, W.A., Stafford, K.W., Shaw-Faulkner, M., and A. Grubbs, 2011. ”A comparative integrated geophysical study of Horseshoe Chimney Cave, Colorado Bend State Park, Texas”, International Journal of Speleology 40 (1), pp. 9–16.

[12] Kaufmann, G., Romanov, D., and R. Nielbock, 2011. ”Case History. Cave detection using multiple geophysical methods: Unicorn cave, Harz Mountains, Germany”, Geophysics 76, 3, pp. 71–77.

[13] Martínez-Moreno, F.J., Pedrera A., Ruano, P., Galindo-Zaldívar, J., Martos-Rosillo, S., González-Castillo, L., Sánchez-Úbeda, J.P., and C. Marín-Lechado, 2013. ”Combined microgravity, electrical resistivity tomography and induced polarization to detect deeply buried caves: Algaidilla cave (Southern Spain) ”, Engineering Geology 162, pp. 67–78.

[14] Pulina, M., 1977. ”Zjawiska krasowe w Sudetach Polskich”, Dokumentacja Geograficzna IGiPZ PAN, 2–3, 116 p.

[15] Teisseyre, A.K., 1973. ”Szczegółowa Mapa Geologiczna Sudetów” 1:25,000, sheet *Międzygórze*, Państwowy Instytut Geologiczny, Warszawa.

[16] Don, J., Skácel, J., and R. Gotowała, 2003. “The boundary zone of the Eastand West Sudetes on the 1:50 000 scale geological map of the Velké Vrbno, Staré Město and Śnieżnik Metamorphic Units”, Geologia Sudetica, 35 (1), pp. 25–59.

[17] Sobczyk, A., and M. Kasprzak, 2014. ”Nowoodkryte partie Mastodonta w Jaskini Niedźwiedziej w świetle badań geologicznych i pomiarów geofizycznych ERT/GPR – wyniki wstępne oraz dalsze perspektywy badawcze”, In Materiały 48. Sympozjum Speleologicznego, Kletno, 16–19.10.2014, Sekcja Speleologiczna Polskiego Towarzystwa Przyrodników im. Kopernika, pp. 114–116.

Size and shape of glacial cirques: comparative data in specific geomorphometry

Ian S. Evans
Department of Geography, Durham University
Science Laboratories, South Road,
Durham City DH1 3LE, England
i.s.evans@durham.ac.uk

Nicholas J. Cox
Department of Geography, Durham University
Science Laboratories, South Road,
Durham City DH1 3LE, England
n.j.cox@durham.ac.uk

Abstract — **When comparably defined, cirque size and shape vary modestly but significantly between regions. Differences in vertical dimensions (height range, amplitude, wall height) are greater than those in horizontal dimensions. A broader set of data from various authors shows greater variability, especially in mean values, for which there are several possible explanations.**

I. INTRODUCTION

Studies of the morphometry of landforms normally deal with single regions. When regions are compared, differences can be attributed both to subjective differences between authors in their understanding of definitions, and to differences in source material and methods, as well as to real differences. Scientific progress in specific geomorphometry has thus been held back by the vagueness of definitions, leading to data sets produced by different authors lacking comparability. We require precise, repeatable operational definitions permitting replicable closed outlines to be drawn around each land-form. Ardelean et al. [1] showed that the considerable differences between different authors can be reduced if a common precise definition is applied. An attempt is being made, for glacial cirques, to produce a series of data sets based on the same definition [2] [3]. Initial results are reported here, and comparisons with differently produced data sets are made.

We consider the distributions of cirque size and shape especially for nine well-studied regions. A particular question in the development of cirques by glacial erosion is whether there is an upper limit on cirque size: Evans [4] suggested that cirques are scale-specific, with upper and lower limits to their size. Another is whether the form of glacial cirques is produced essentially by deep-seated rock avalanches [5]. A third question is the variation of shape with size and age: Evans [6] reported work confirming the static allometry of glacial cirques in several European and British Columbian areas.

II. DATA

Here we test for differences in cirque size and shape between nine regions with complete inventories: three divisions of Romania, three in Britain (Wales and England), and three adjacent ranges in south-west British Columbia. The first six data sets were produced by Evans, while the Romanian coverage was produced by Marcel Mîndrescu following the same definitions, with checks by Evans [7]. The Lake District (England) data are from Evans and Cox [3], but with two deletions; those for the two divisions of Wales are from Evans [8]; and the British Columbian data were used in Evans [4]. Each data set is based on detailed fieldwork, air photo interpretation, and large-scale topographic maps. We thus have a cluster sample, with complete coverage of Romania, of Wales and the Lake District, and of three contiguous mountain ranges in British Columbia (Cayoosh, Bendor and Shulaps). Wales is divided into the old volcanic and metamorphic terrain of the northwest ('Snowdonia') and the mainly sedimentary or weakly metamorphosed terrain of central, southern and eastern Wales. In Romania, the threefold division is achieved by separating the largest glaciated range, the Făgăraş Mountains, from the mountains to the west, and from those to the east and north.

III. SIZE ANALYSES

Median values for the two horizontal dimensions (length and width), and for three ways of defining the vertical dimension, are given in Table I. As all these size variables are positively skewed, the median is more representative than the mean (which is always higher) (Fig. 1). The effects of skewness are avoided by performing all further analyses on logarithms of these size variables, reducing skewness (per region) to between −0.75 and +0.63 (from initial values between +0.52 and +4.30).

In: Geomorphometry for Geosciences, Jasiewicz J., Zwoliński Zb., Mitasova H., Hengl T. (eds), 2015. Adam Mickiewicz University in Poznań - Institute of Geoecology and Geoinformation, International Society for Geomorphometry, Poznań

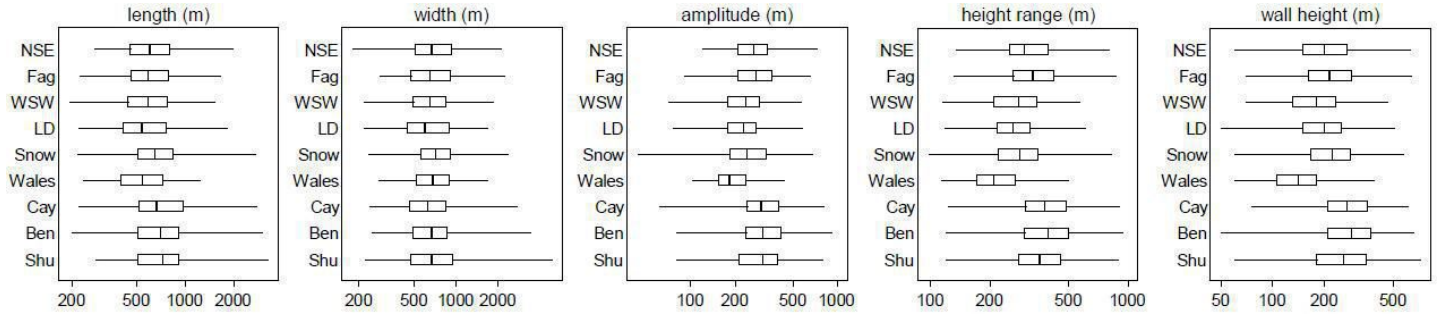


Figure 1. Box plots of five morphometric measures on logarithmic scale. The plots show minimum, quartiles and median (central box) and maximum. These measures are all commutative with logarithmic scale as (e.g.) median of logarithms is logarithm of median.

Note that length is greatest for the three British Columbian regions, and least for the Lake District and 'Wales C., S. and E'. Width is greatest for Snowdonia and least for the Lake District. Vertical dimensions are strongly inter-correlated, and much more variable between regions. All three vertical variables are greatest in British Columbia and least in Wales (C, S & E).

Analysis of variance between and within the nine regions produced highly significant differences ($P < 0.0001$) for all size dimensions except width ($P = 0.1452$) (Table II). Judging by either F ratio or R^2, between-region contrasts were greatest for vertical dimensions, especially height range. Similar results were obtained with and without logarithmic transformation.

IV. Shape and Gradient Analyses

Table III gives median values for gradient and shape variables. The gradient and closure variables are almost unskewed (−0.47 to +1.00 per region) and means are not far from medians: but medians are given for compatibility with the two ratios (skews +0.49 to +1.65) and with Table I. Profile closure is controlled mainly by maximum gradient: Snowdonian cirques are best developed (with especially gently-sloping floors), followed by Lake District and Cayoosh, while 'North and southeast Romania' has the poorest. It may be that Romanian gradients are distorted by relatively poorly-contoured maps, mainly at 1:25,000, with contours interrupted at cliff symbols. In plan, Făgăraş has the best-developed cirques, and Shulaps plus 'Wales central, southern and eastern' have the poorest. Wales (C, S & E) has the highest W/L and L/H ratios, while the British Columbian ranges have the lowest, accompanied by Făgăraş for L/H. This reflects the poor showing of Wales (C, S & E) on length and especially on height range.

Analysis of variance demonstrated highly significant differences between regions (Table II) for all seven shape variables (gradient, closure and ratio variables). Differences, as shown by F ratio and R^2 values, are greatest for gradient variables and thus for profile closure, and for the Length/Height ratio which is an inverse gradient measure.

TABLE I. Median dimensions (m) and numbers of cirques, per region.

Region	*Number*	*Length*	*Width*	*Amplitude*	*Height range*	*Wall height*
N & SE Romania	132	610	666	270	300	200
Făgăraş	206	592	652	280	330	215
W & SW Romania	293	591	644	240	280	180
Lake District	156	545	600	230	261	200
Snowdonia	143	655	720	242	285	222
Wales C, S & E	117	550	685	185	210	140
Cayoosh	198	670	625	305	381	270
Bendor	222	705	670	312	395	285
Shulaps	126	730	670	310	360	260
TOTAL	**1593**	**625**	**656**	**260**	**310**	**210**

TABLE II. Analysis of variance results for variance accounted for the division into nine regions. All except width are highly significant ($P<0.0001$). The *SD* (overall standard deviation) is given for comparison with the *RMSE* (root mean square deviation) within regions. Logarithms are used for the first five variables (dimensions).

Variable	*F*	R^2	*Adjusted* R^2	*rmse*	*SD*
Length	9.37	.045	.040	.188	.192
Width	1.52	.008	.003	.192	.192
Amplitude	26.77	.119	.115	.166	.177
Height range	48.39	.196	.192	.155	.172
Wall height	42.10	.175	.171	.182	.200
Max gradient	80.51	.289	.285	8.97	10.62
Min gradient	20.71	.095	.090	5.39	5.65
Plan closure	9.67	.047	.042	48.11	49.15
Profile closure	55.80	.220	.216	11.40	12.87
Axial gradient	13.39	.063	.059	6.51	6.71
Width/length	12.82	.061	.056	.365	.375
Length/height range	24.73	.111	.106	.643	.681

TABLE III. MEDIAN GRADIENT AND SHAPE VARIABLES (°, EXCEPT LAST TWO) AND NUMBERS OF CIRQUES, PER REGION. 'GRAD' = GRADIENT.

Region	*Number*	*Max grad*	*Min grad*	*Plan closure*	*Profile clos.*	*Axial grad*	*Width/Length*	*Length/Height*
N & SE Romania	132	48	10.2	137	37.6	23.8	1.10	2.04
Fagaras	206	55	8.7	145	46.5	24.6	1.03	1.81
W & SW Romania	293	51	7.5	134	42.3	22.5	1.11	2.10
Lake District	156	63	7.1	123	56.0	22.7	1.10	2.09
Snowdonia	143	65	3.5	121	61.5	20.6	1.07	2.29
Wales C, S & E	117	56	5.2	110	50.0	20.0	1.27	2.52
Cayoosh	198	68	9.7	135	55.6	25.4	0.91	1.88
Bendor	222	63	8.2	124	50.6	24.4	0.97	1.79
Shulaps	126	53	7.3	100	45.4	23.3	0.97	2.01
TOTAL	**1593**	**57**	**7.7**	**128**	**49.2**	**23.1**	**1.05**	**2.03**

The size and shape variables may thus be ranked in order of inter-regional contrast, measured by *F* in Table II, as: Maximum gradient; Profile closure; Height range; Wall height; Amplitude; (Length/Height range) ratio; Minimum gradient; Axial gradient; (Width/Length) ratio; Plan closure; Length; Width. The first six all include a vertical dimension, and it is clearly this that varies most between regions. Minimum gradient and shape measures come next, followed by Length and (insignificant) Width.

TABLE IV. MEAN CIRQUE SIZE DATA (m) FROM OTHER AUTHORS (* MEAN AMPLITUDE).

Region	*Number*	*Length*	*Width*	*Height range*	*Source*
Kintail-Affric-Cannich, W. Scotland	231	625	586	(276*)	[16] (simple cirques)
N. Scandinavia transect	537	845	888	400	[17]
High Tatra	116	570	550	311	[18]
Bohemia	27	788	700	272	[19]
Maritime Alps	432	672	663	355	[20]
E. Pyrenees	1071	489	482	(223*)	[10]
C. Pyrenees	206	519	691	364	[13]
SW. Asturias	70	487	594	255	[12]
W. Picos de Europa	59	295	467	294	[12]
NE. USA	49	1687	954	442	[21]
W.-C. Yukon	331	802	736	214	[22]
Kamchatka	3520	868	992	421	[11]
Fiordland, N.Z.	1296	855	882	463	[14]
Westland, N.Z.	480	1069	961	580	[14]
Ben Ohau Ra., N.Z.	90	489	536	216	[15]
N. Greece	166	530	737	289	[23]
S. Greece	99	376	460	173	[23]

V. FURTHER DATA

As the three clusters were selected as study areas for their feasibility and accessibility, they are obviously not representative of cirques globally. They cover intrusive, old volcanic, metamorphic and sedimentary rock areas in old crystalline massifs and young orogenic belts, but not young volcanic areas or the highest-relief mountains.

It might be expected that cirques around the world's highest mountain have been eroded vigorously for a considerable time period, and should thus be larger than those in areas of more marginal local glaciation. There are difficulties due to the presence of thick glaciers masking cirque floors, but these do not hinder measurement of cirque width and length. Preliminary measurements from the 1: 50,000 'National Geographic' 1986 map of Everest show that the mean width of 35 cirques around Mount Everest is 2.23 km (median 2.0 km). The largest cirque, with Lhotse Glacier, is 4.6 km wide, followed by the Western Cwm at 3750 m: both are 3.9 km long. This is not out of line with the largest cirques elsewhere: what are lacking, on this highest terrain, are small cirques. 22 cirques on the lower Nuptse-Dingboche ridge average 727 m wide (median 625 m), comparable to the nine regions in Table I. It seems that widths and lengths around 4 km are the limiting dimensions for mid-latitude glacial cirques, developing from previously fluvial topography.

Antarctica is a special case, where very long-continued glaciation may have developed larger cirques. Thus the 56 mapped in the 'Dry Valleys' by Aniya and Welch [9] have a mean length of 2116 m, mean width of 1679 m, and mean height range of 849 m: they dominate compiled graphs of cirque size, as in Delmas et al. [10].

Barr and Spagnolo [11] tabulated cirque size means from various authors, for 16 areas, although 5 of these had less than 40 cirques. These further data sets show a greater range of sizes (see also Table IV) than the nine comparable regions. Excluding Antarctica, those with more than 40 ranged in mean length from 295 to 1687 m, more than five-fold, and much more varied than the 577 to 798 m (545 to 730 m in medians) here in Table I. Their mean widths varied from 467 to 954 m, two-fold and considerably more than the 681 to 797 m (600 to 720 in medians) here. Mean height ranged from 236 to 442 m (their 209 m refers to wall height): this is somewhat greater than the 225 to 419 m (210 to 395 m in medians) here. Barr and Spagnolo's tabulated ranges for individual cirques were 100 to 4000 m in length (191

to 3280 here), 125 to 3100 m in width (180 to 4870 here), and 57 to 1328 m (97 to 953 here) in height range. The greatest subjectivity probably concerns recognition of cirques 100 to 200 m long or wide, and those < 100 m in height.

In Table IV, cirques in the western Picos de Europa [12], have a remarkably low mean length (295 m), the same as their 294 m mean height range. These are steeper than cirques elsewhere, possibly because this is a high-relief limestone massif. Garcia-Ruiz et al. [13] also have some very steep cirques, as high as long, in the central Spanish Pyrenees.

The greater contrasts between regions in Table IV might be because a greater variety of regions has been included. However, the three greatest height ranges come from studies based on satellite imagery [11] or automatic cirque identification [14]: Richter [14] included only features > 0.1 km^2 in area, giving 35 cirques in the Ben Ohau Range where Brook et al. [15] found 90. Fieldwork and use of higher-resolution DEMs or maps identifies smaller cirques and reduces average sizes.

VI. CONCLUSIONS

Three clear conclusions emerge from this analysis. When a clear, consistent operational definition is applied, differences in cirque size and shape are small between regions, compared with the variation within each region. Nevertheless the differences between regions in length, all vertical dimensions, gradients and closures are highly significant; only width does not differ significantly between regions. Second, differences are greatest for vertical dimensions, due more to differences in tectonic setting than in geology. Third, means of cirque populations can be compared where measured by the same author, but those from different authors cannot as yet be taken as real differences between regions. It is hoped that the results in Tables I and III provide a starting point for a consistent multi-regional data set to which future measurements of cirques can be related.

ACKNOWLEDGMENTS

We thank Marcel Mîndrescu for providing the Romania data set and Ovidiu Csillik for formatting.

REFERENCES

[1] Ardelean, F., Drăguţ, L., Urdea, P., Török-Oance, M., 2013. Variations in landform definition: a quantitative assessment of differences between five maps of glacial cirques in the Ţarcu Mountains (Southern Carpathians, Romania). Area 45, 348–357.

[2] Evans, I.S., Cox, N.J., 1974. Geomorphometry and the operational definition of cirques. Area 6, 150–153.

[3] Evans, I.S. & Cox, N.J., 1995. The form of glacial cirques in the English Lake District, Cumbria. Zeitschrift für Geomorphologie, N.F. 39, 175-202.

[4] Evans, I.S., 2010. Allometry, scaling and scale-specificity of cirques, landslides and other landforms. Transactions of the Japanese Geomorphological Union 31 (2), 133-153.

[5] Turnbull, J.M., Davies, T.R.H., 2006. A mass movement origin for cirques. Earth Surface Processes and Landforms 31, 1129–1148.

[6] Evans, I.S., 2009. Allometric development of glacial cirques: an application of specific geomorphometry. In: Geomorphometry 2009, Edited by R. Purves, S. Gruber, R. Straumann and T. Hengl. University of Zurich, Switzerland, 248-253.

[7] Mîndrescu, M., Evans, I.S., 2014. Cirque form and development in Romania: Allometry and the buzz-saw hypothesis. Geomorphology 208, 117–136.

[8] Evans, I.S., 2006. Allometric development of glacial cirque form: geological, relief and regional effects on the cirques of Wales. Geomorphology 80 (3-4), 245-266.

[9] Aniya, M., Welch, R., 1981. Morphometric analyses of Antarctic cirques from photogrammetric measurements. Geografiska Annaler A 63 (1/2), 41-53.

[10] Delmas, M., Gunnell, Y., Calvet M., 2014. Environmental controls on alpine cirque size. Geomorphology 206, 318-329.

[11] Barr, I.D., Spagnolo,M., 2013. Palaeoglacial and palaeoclimatic conditions in the NW Pacific, as revealed by a morphometric analysis of cirques upon the Kamchatka Peninsula. Geomorphology 192, 15–29.

[12] Ruiz-Fernández, J., Pobleta-Piedrabuena, M.A., Serrano-Muela, M.P., Martí-Bono, C., García-Ruiz, J.M., 2009. Morphometry of glacial cirques in the Cantabrian Range (northwest Spain). Zeitschrift für Geomorphologie N.F. 53, 47–68.

[13] García-Ruiz, J.M., Gómez-Villar, A., Ortigosa, L.,Martí-Bono, C., 2000. Morphometry of glacial cirques in the C. Spanish Pyrenees. Geografiska Annaler A 82, 433–442.

[14] Richter, D., 2006. Morphometric Analysis of Cirques in Fiordland, New Zealand. Dresden University of Technology. Diploma, 74 pp.

[15] Brook, M.S., Kirkbride, M.P., Brock, B.W., 2006. Cirque development in a steadily uplifting range: rates of erosion and long-term morphometric change in alpine cirques in the Ben Ohau Range, New Zealand. Earth Surface Processes and Landforms 31, 1167–1175.

[16] Gordon, J., 1977. Morphometry of cirques in the Kintail-Affric-Cannich area of NW Scotland. Geografiska Annaler A 59, 177–194.

[17] Hassinen, S., 1998. A morpho-statistical study of cirques and cirque glaciers in the Senja–Kilpisjärvi area, northern Scandinavia. Norsk geografisk Tidsskrift 52, 27-36.

[18] Křížek, M., Mida, P., 2013. The influence of aspect and altitude on the size, shape and spatial distribution of glacial cirques in the High Tatras (Slovakia, Poland). Geomorphology 198, 57–68.

[19] Křížek, M., Vočadlová, K., Engel, Z., 2012. Cirque overdeepenings and their relationship to morphometry. Geomorphology 139–140, 495–505.

[20] Federici, P.R., Spagnolo, M., 2004. Morphometric analysis on the size, shape and areal distribution of glacial cirques in the Maritime Alps (Western. French-Italian Alps). Geografiska Annaler A 86, 235–248.

[21] Davis, P.T., 1999. Cirques of the Presidential Range, New Hampshire, and surrounding alpine areas in the NEn. United States. Geographie Physique Et Quaternaire 53 (1), 25-45.

[22] Nelson, F.E.N., Jackson, L.E., 2003. Cirque forms and alpine glaciation during the Pleistocene, west-central Yukon. In: Yukon Exploration & Geology 2002, Emond, D.S. & Lewis, L.L. (Eds.), Indian & Northern Affairs Canada, 183-198.

[23] Bathrellos, G.D., Skilodimou, H.D., Maroukian, H., 2014. The spatial distribution of Middle and Late Pleistocene cirques in Greece. Geografiska Annaler A 96, 323–338.

Understanding landscape evolution by using DEM analysis, low order channels gradient and Asymmetry Factor: the case study of the upper Scrivia river basin (Northern Apennines, Italy).

Andrea Mandarino, Francesca Ferraris, Marco Firpo
Department of Earth, Environment and Life Sciences
University of Genova
Genova, Italy
andrea.mandarino.fiumi@gmail.com

Abstract—**The main aim of this study is to detect morpho-tectonic elements by using geomorphometry tools and GIS analysis to investigate and describe recent changes of the Earth surface relief. In particular, we search geomorphic evidences of active tectonics throughout active tectonics and classic morphometric indices.**
The upper Scrivia river basin is located along the Adriatic side of the Northern Apennines and shows peculiar landforms often controlled by both tectonics and lithology. Geologically this is a really interesting area, just to the East of the Sestri-Voltaggio Line, the boundary between the Ligurian Alps and the Northern Apennines.
After a general characterization and a zoning of the study area with respect to channels order, we used GIS software to calculate the Asymmetry Factor and its distribution and to analyze the second order channels gradient, both connected to active tectonics.
We recognized a general prevalence of regional tectonics on local tectonics. The gradient map of second order channels suggests recent uplift in the SE sector. The high second order channels gradient values near to the mouth of the studied sector may be connected, on the contrary, to the base level changes related to the Quaternary network evolution of the Po plain.
Preliminary results underline the importance of morphometry to detect large-scale information about landscape evolution and its applicability in different contests. The low order channels gradient may also give useful information about natural hazard assessment.

I. INTRODUCTION

The upper Scrivia river basin is located along the Adriatic side of the Northern Apennines, just to the E of the Sestri-Voltaggio Line that divides them from Ligurian Alps (Fig. 1). The study area spreads over 293 km2 and shows particular landforms often controlled by tectonics and lithology: wide valleys characterize areas with a clayey bedrock (Mignanego Mudstone, Montanesi Mudstone and Ronco Fm), while, on the contrary, steep slopes and narrow valleys form on the marly limestones of the 'Monte Antola Formation' and on the Oligocene conglomerates of the Tertiary Piedmont Basin (Savignone conglomerates and Molare Formation). The main trunk channel is drawn upon the Scrivia fault and the Scrivia-Fontanabuona Line [1]. This region shows a transition from Mediterranean to continental climate with hot summers, cold winters and absence of arid season (maximum rainfall registered in autumn).

Aim of this research is to investigate the basin anomalies and morphotectonic evidences by using GIS analysis and geomorphometry tools, in order to reconstruct the recent evolution of the area and, eventually, of the entire region.

II. MATERIALS AND METHODS

GIS analysis started with the Horton-Strahler hierarchization of streams, working on the digitalized network deriving from 1:10000 topographic maps (CTR Liguria, 2007). We used both Quantum GIS 1.8 and 2.4 (QGIS) © and Arc GIS 9.2 ® investigating both the compatibility and the potentialities of the different tools. A geological map (Fig. 2) has been derived from the available maps (1:100.000 Carta Geologica d'Italia and CARG - Genova, Bargagli - 1:50.000) [2,3]. An high resolution DEM (cell size 5 m: Cartographic office of the Liguria Region) has been used to perform a detailed terrain analysis in QGIS starting from classic slopes maps, aspect and gradient maps (Fig. 3). Ultimately, rectified aerial photographs (open data from Geoportale Nazionale) were used to map the main morpho-structural lineaments.

In: Geomorphometry for Geosciences, Jasiewicz J., Zwoliński Zb., Mitasova H., Hengl T. (eds), 2015. Adam Mickiewicz University in Poznań - Institute of Geoecology and Geoinformation, International Society for Geomorphometry, Poznań

To perform detailed analyses the upper Scrivia basin has been divided in smaller sectors, corresponding to the hydrographic basins of fifth order channels. Each of these sixteen basins has been processed with the QGIS plugin "Zonal Statistics" and average slope and elevation have been derived, as well as drainage density [4] and the main indices related to the basins shape (i.e. circularity ratio) [5]. Considering the well known connection between asymmetrical extension of right and left slopes of a river basin and regional tilting phenomena [6] we computed the Asymmetry Factor for the entire basin and for each one of the sixteen sub-basins (Fig. 4), using the equation

$$AF = 100\ (Ar/At), \quad (1)$$

with Ar as right area and At as total area. AF > 50 implies tilt down to the left of basin (looking downstream).

Lastly, we analyzed the low order channels gradient, known in literature to be connected to relative tectonic activity of mountains fronts [7,8]. Low order channel gradients are the aptest to register changes due to long-term uplift, increasing streams order the channels gradients are less altered by tectonics [6]. During rapid uplift, in fact, streams are rejuvenated and stream gradient increase. While larger streams are able to maintain their profile forms by incising rapidly enough to adjust to lower base level, smaller tributaries are unable to rapidly readapt, hence, they accumulate the effect of base level fall and have steepest profiles in the areas of highest uplift rates [9 and references therein]. In this study we used second order channel gradients because first order channels deriving from the utilized maps were just traces of incision. The slope of second order channels have been computed in ArcGIS (Easy calculate, free on line tool, www.ian-ko.com) as the ratio between the difference in elevation from the head to the mouth and the stream's total length. Slopes values are returned as attributes of a points shapefile; each point is located in the centre (with respect to elevation) of the related stream.Throughout the data interpolation tool, using the Inverse Distance Weighted (IDW) method, a thematic map of gradient's trend have been created (Fig. 5,6).

III. Results

Fifth order basins as well as the entire study area are characterized by an irregular shape, first sign of rejuvenating factors affecting the landscape evolution.

Drainage density values are strictly related to bedrock types: high values are linked to clayey lithotypes while lower ones are generally connected to marly limestones. The AF distribution (Fig. 4) does not show particular trend for the 16 analysed sub-basins. On the contrary, we can observe a strong asymmetry for the entire study area (AF = 64,9%). Regional tilting seems therefore to affect the area more than local tectonics; nevertheless, the presence of major tectonic lineaments does not allow to completely exclude this element.

Maps comparison (Fig. 2,3,6) gives relevant information: the outcropping bedrock and its structural characteristics are clearly related to slopes gradient. Marly limestones, typically liable for steep slopes, show an anomalous behaviour in the centre of the study area, along a NNE-SSW lineament, where a wide and gentle topographic surface is recognizable. According to the authors [10 and references therein] this structure may be related 1) to the presence of an anticline, 2) to the load of the overlying conglomerates or, 3) to the relict of an ancient hydrographic network.

The slopes gradient map and the low-order channels map show different trends. Within large sectors relief evolution seems to be decoupled from incising waters and linked to mass movements: this is clearly evident in the central zone, where the Savignone Conglomerates widely outcrop. The low-order channels map shows several areas of correlation with respect to lithology, nevertheless areas of random distribution of channels gradient are present too. Decoupled from the geological context this parameter can be linked to tectonic forcing. On this base, a SSW-NNE band possibly undergoing recent uplift has been isolated in the SE sector of the study area; this zone, located eastward of a morphologic lineation, has uniform bedrock with various attitude and presents several faults. Lastly, the high second order channels gradient values registered near to the mouth of the studied sector seem to be connected to the base level changes related to the Quaternary network evolution of the Po plain.

IV. Conclusions

In the study area landscape evolution has been heavily driven by tectonics. This research implements the geomorphological knowledge about the Scrivia river basin, convalidating, on the one hand, the existing theories on the region evolution, and offering, on the other one, new data for further analyses.

Morphometric approach for searching data about landscape evolution and for recognizing morphotectonic evidences plays an important role in this research sector.

Low order channels gradients, compared to slope and geology evaluations seems to be a useful tool that may be used with success also for natural hazard assessment in mountain areas.

A. *Figures and Tables*

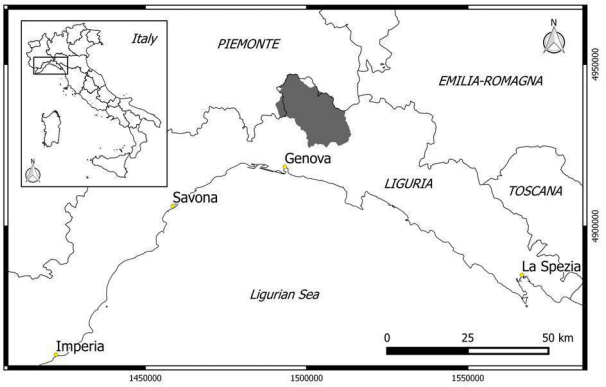


Figure 1. Study area

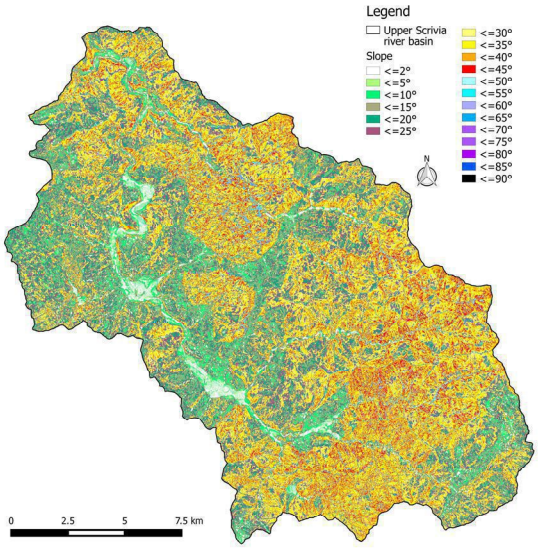


Figure 3. Slopes gradient map

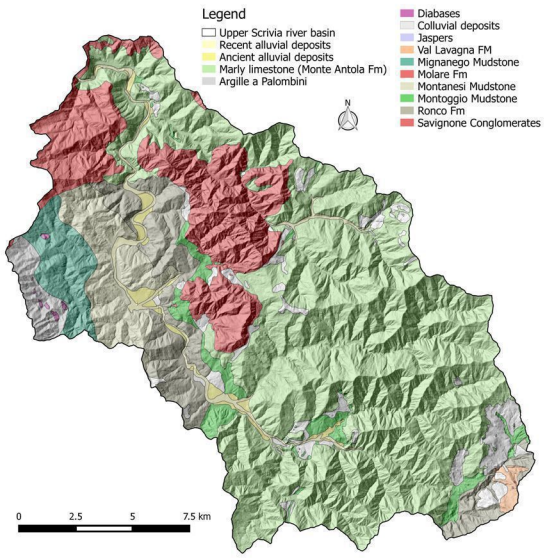


Figure 2. Geological map

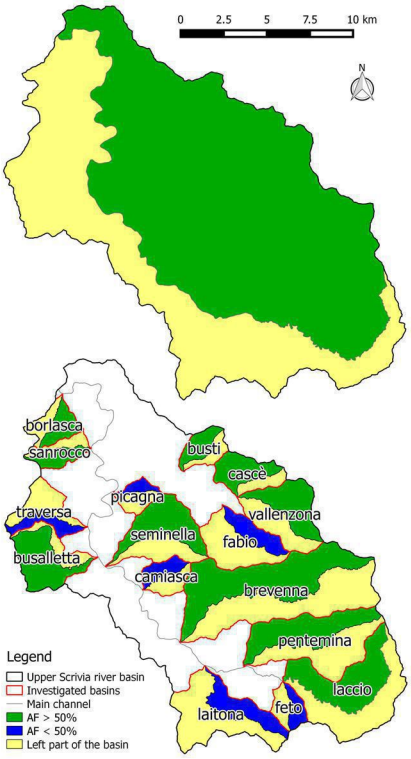


Figure 4. AF map

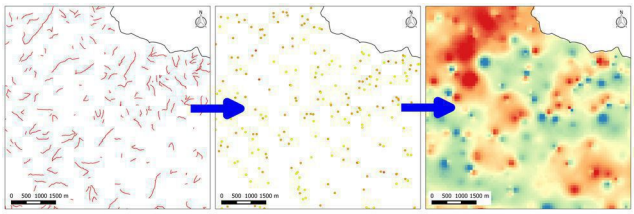


Figure 5. Phases to obtain Fig. 6

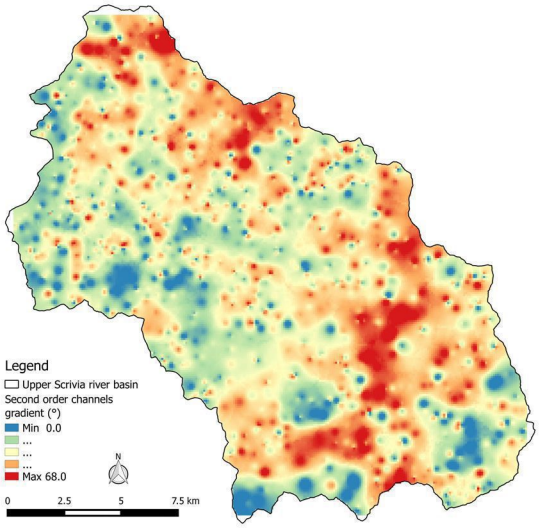


Figure 6. Second order channels gradient map

REFERENCES

[1] Capponi, G., Crispini, L., Federico, L., Piazza, M. and L. Amandola, 2009. "Late alpine tectonics in the Ligurian Alps: constraints from the TPB Conglomerates". Geological Journal, 44, 211-224 p.

[2] Boni, A., Braga, G., Conti, S., Gelati, R., Marchetti,G. and L. Passeri, 1969. "Note illustrative alla Carta Geologica d'Italia, Fogli 83 Rapallo e 94 Chiavari". Servizio Geologico d'Italia, Roma, 89 pp.

[3] ISPRA, "Note illustrative della Carta Geologica d'Italia alla scala 1:50.000, Foglio 214 Bargagli". Edited by Elter P., Marroni M. e Pandolfi L. – Servizio Geologico d'Italia, in press.

[4] Horton, R. L., 1945. "Erosional development of streams and their drainage basins; hydrophysical approach to quantitative morphology". Geol. Soc. Am Bull., 56, 275-370 p.

[5] Strahler, A.N., 1964. "Quantitative geomorphology of drainage basins and channel networks". In: Handbook of Applied Hydrology, edited by V.T.Chow, 4, -40-74, McGraw-Hill, New York.. 200

[6] Keller, R.A., and N. Pinter, 1996. "Active tectonics, earthquakes, uplift, and landscape". Prentice-Hall Inc., Upper Saddle River, New Jersey.

[7] Frankel, K., and F.J. Pazzaglia, 2005. "Tectonic geomorphology, drainage basin metrics and active mountains front". Geogr. Fis. Dinam. Quat., 28, 7-21 p.

[8] Merritts, D., and K. Vincent, 1989. "Geomorphic response of coastal streams to low, intermediate, and high rates of uplift, Mendocino triple junction region, northern California". Geol. Soc. Am. Bull., 101, 1373-1388 p.

[9] Ferraris, F., Firpo, M. and F. Pazzaglia, 2012. "DEM analyses and morphotectonic interpretation: The Plio-Quaternary evolution of the eastern Ligurian Alps, Italy". Geomorphology, doi:10.1016/j.geomorph.2012.01.009

[10] Sacchini, A., 2012. "Dinamica geomorfologica con particolare riferimento alle deformazioni gravitative profonde di versante in alta valle Scrivia (Appennino Ligure)". Ph-D thesis, University of Genova, 277 p.

Slope landscape change in a simulated watershed

Fayuan Li
School of geography
Nanjing Normal University
Nanjing China
lifayuan@njnu.edu.cn

Mingwei Zhao
Institute of Geographic Sciences and Natural Resources Research, CAS
Beijing, China

Abstract — **An artificial loess watershed is adopted to investigate the variation in slope landscape structure with loess watershed evolution. The evolution of the simulated loess watershed was driven by the exogenetic force of artificial rainfall. Quantitative indices of the slope landscape structure varied regularly following the evolution of the simulated loess watershed. Mean patch area (AREA_MN), and Patch Cohesion Index (COHESION) kept increasing following the evolution of the simulated watershed, while Perimeter-Area Fractal Dimension (PAFRAC), and Interspersion and Juxtaposition Index (IJI) showed an opposite trend. All the indices change actively in the early and active development periods, but changed slowly in the stable development periods.**

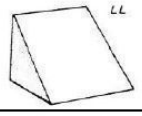
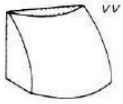
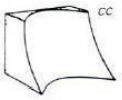
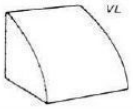
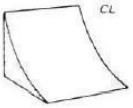
I. INTRODUCTION

Quantificational analysis of loess terrain is a key subject in the research of the loess plateau [1-7]. Tang et al (2008) proposed slope spectrum to quantitatively describe loess landforms [8], Zhou et al (2010) discussed the spatial pattern of loess landform based on loess positive and negative terrain [9]. However, their research cannot properly describe the spatial structure of loess slopes. In this paper, we investigate loess landforms from the landscape ecology point of view. Firstly, we classified slope into six types as table 1. Then, each map-patch of slope type was taken as an independent functional patch from the view point of landscape. Particularly, each map-patch of slope type is the patch of the landscape, all map-patches belonging to the same slope type constitute the class of the landscape, and all the classes constitute an integrated landscape. Then the slope map patch could be used to depict the patch's spatial structural features, such as relative size, shape, aggregated degree, connectivity degree, etc. Therefore, based on the loess terrain and landscape features, the theory and methodology of landscape ecology could be applied to study the spatial structure of slope distribution.

II. MATERIAL

A simulated loess watershed, where the loess material and relief properly represent the true loess surface, is adapted to investigate the variation in slope landscape with loess watershed evolution. The evolution of the simulated loess watershed was driven by the exogenetic force of artificial rainfall. For a period of three months, twenty artificial rainfall events with different intensities and durations were carried out. In the process, nine DEM data sets, each with 10 mm grid resolution, were established by the method of close-range photogrammetry [10]. The slope types were then classified base on these DEMs with the way of object oriented classification (Fig.1) [10, 11]. Then five landscape indices, including Mean patch area (*AREA_MN*), Perimeter-Area Fractal Dimension (*PAFRAC*), Interspersion and Juxtaposition Index (*IJI*), Patch Cohesion Index (*COHESION*), are applied to quantify the slope landscape.

TABLE I. GEOMETRIC FEATURE OF SIX SLOPE TYPES (ND MEANS NO DEFINITION)

Slope form		Geometric feature		
		plane curvature	profile curvature	Slope gradient
LL slope		±0	±0	ND
VV slope		>0	>0	ND
CC slope		<0	<0	ND
VL slope		±0	>0	ND
CL slope		±0	<0	ND
flat slope		ND	ND	⩽3

In: Geomorphometry for Geosciences, Jasiewicz J., Zwoliński Zb., Mitasova H., Hengl T. (eds), 2015. Adam Mickiewicz University in Poznań - Institute of Geoecology and Geoinformation, International Society for Geomorphometry, Poznań

III. RESULT AND DISCUSS

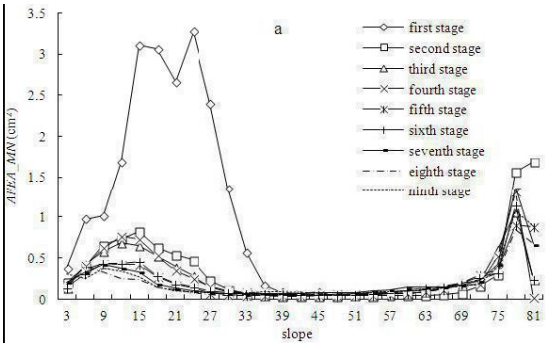
Fig. 1 shows the distribution of the slope map-patch indices at different stages at class level, which can depict the spatial structure of the patches for different slope classes.

1) Relative size and shape of patches:

AREA_MN of the slope patch was found to have a sudden decrease with continuing rainfall. The peak value of the curve falls in the interval between 0.8 and 3.5 cm^2, which reveals a high sensitivity of original loess surface to irreversible accelerated erosion. Overall, Fig. 1-a shows that the relative size of the patches is rather small, while the heterogeneity degree is high. *PAFRAC* at different stages varies from 1.17 to 1.83. Following the increase of the slope, *PAFRAC* of the simulated watershed shows the same trend, as does the complexity of the patches. The aforementioned variation of the slope patches indicates that once the rainfall erosion began, the original smooth loess surface became more complicated, i.e., the increasing surface roughness and gully enlargement accelerated headward erosion.

2) Spatial structure of patches:

An *IJI* value approaching 0 indicates that the target patch type is spatially adjacent to only one other patch type, and that the number of patch types increases. An *IJI* value equal to 100 represents spatially adjacent patch types that are equal in length, i.e., the possibility of adjacent patches is equal. *IJI* at slope gradients of 27- 60° are bigger than at other slope classes, showing that slope patches in hillslope areas are more dispersed than in flat areas, e.g., valley areas and interfluve areas. This reveals the phenomenon that gully headward erosion enlarges the degree of fragmentation in the simulated watershed. *COHESION* of all stages almost changes from 70-100%. To most stages, the minimum values appears at slope 39-54°which shows that in high relief areas, the degree of slope patch fragmentation and dispersion are high. This indicates that the continuity of the origin loess surface will change quickly following the watershed evolution driven by rainfall erosion.



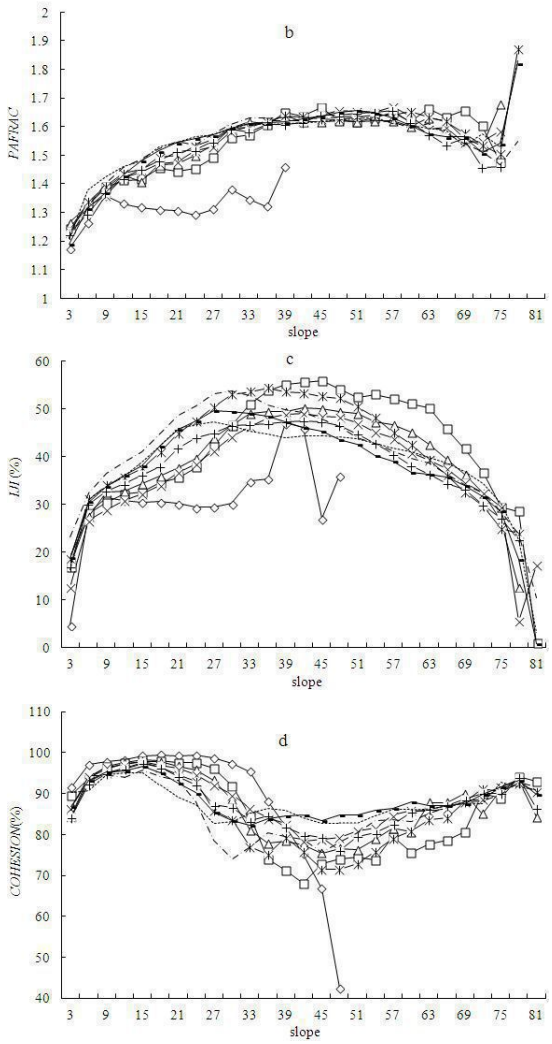
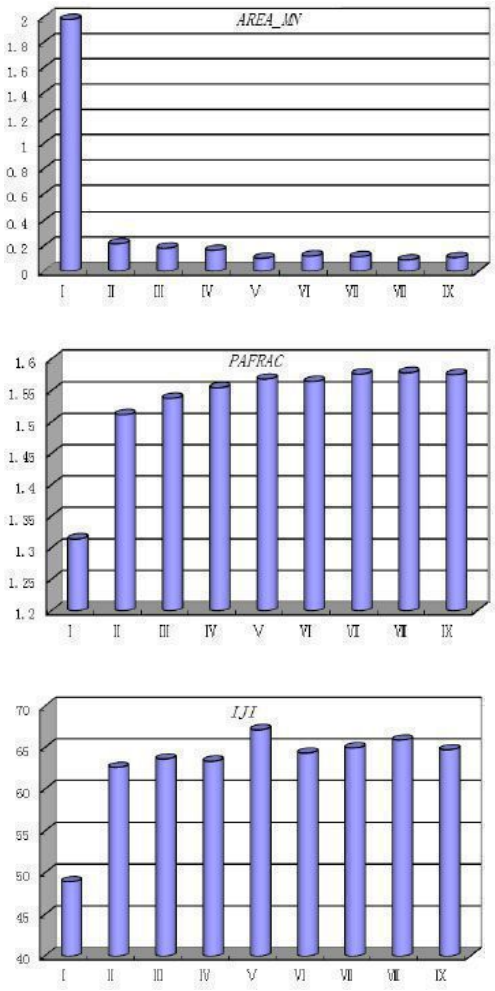


Figure 1. Comparison of slope landscape indices in different stages

Fig.2 shows slope patch structure of different stages at landscape level. Four indices show different variation patterns that could be classified into two groups. One group includes *PAFRAC* and *IJI*, which shows rising tendency on a global level following the evolution of the simulated watershed. Another group, including *AREA_MN*, and *COHESION*, shows opposite trend with the first group. The *PAFRAC* and *IJI* in the early period are smaller than in the later period, while the *AREA_MN* and *COHESION* in the early period are greater than in the later period. This suggests that, in the early period of simulated watershed, fragmentation of the patches of slope class

is rather small, the slope patches distribution is consecutive, and the patch shape is more regular than in the later period. The loess surface in the early period is smooth, so the *AREA_MN* is larger than in the later stage. This also suggests that, in the early period, fragmentation of slope patches is large, the patches distribute connectively, and the patch shape is more regular than in the later stage. Actually, *PAFRAC* at different stages show little difference (ranging from 1.314–1.576), which indicates comparability of the patch shapes in general. This is the same as the indices at class level. All the indices vary following the evolution of the simulated watershed.



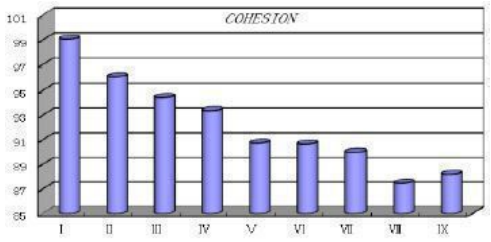


Figure 2. Slope landscape indices at landscape lever

ACKNOWLEDGMENT

Thanks for financially support from the National Natural Science Foundation of China (No.41171299).

REFERENCES

[1] Zhang Z.H. Regional geologic and physiognomy characteristic as well as contemporary erosion process of loess plateau. Acta geologic sinica, 1981, 55(4), pp.308 – 319.

[2] Chen W.N. Statistical analysis of gepmorphic conditions effection loess erosion in loess ridge-hill gully region. Scientia Geographical Sinica, 1988, 8(4), pp.323-329. 143

[3] Li Q., Lu Z.C., Yuan B.Y. Quantitative study of the stage of geomorphological evolution. Acta geographica sinica, 1990, 45(1), pp.110-120.

[4] Ma X.Z., Lu Z.C., Jin D.S. Evolution and pissipative structure in the drainage-geomorphic system. Acta geographica sinica, 1993, 48(4), pp.367-376.

[5] Jin D.S. Experiment and simulation in geomophology. Beijin, Earthquake 150 Press, 1995. 151

[6] Zhang L.P. and Ma Z.Z. The research on the relation between gully density and cutting depth in different drainage landform evolution periods. Geographical research, 1998, 17(3), pp.273-278.

[7] Xiao X.N., Cui L.Z., Wang C., et al. Analysis of spatial data for simulating the development process of topographic feature of watershed. Scientia geographical sinica, 2004, 24(4), pp.439-443.

[8] Tang G.A., Li F.Y, Liu X.J. et al. Research on the Slope Spectrum of the Loess Plateau. Science in China Series E: Technological Sciences, 2008, 51(Supp.1), pp.175-185.

[9] Zhou Y., Tang G.A., Yang X. et al. Positive and negative terrains on northern Shaanxi Loess Plateau. Iournal of geographical sciences, 2010, 20(1), pp.64-76.

[10] Cui L Z (2002). The Coupling Relationship between the Sediment Yield from Rainfall Erosion and the Topographic Feature of the Watershed. Doctoral dissertation of Northwest Agriculture & Forest University, Yanling (in Chinese)

[11] Dragut L. and Blaschke T. Automated classification of landform elements using object-based image analysis. Geomorphology, 2006, 81, pp.330-344.

[12] Zhao Mingwei, Li Fayuan, Tang Guo'an. Optimal Scale Selection for DEM Based Slope Segmentation in the Loess Plateau. International Journal of Geosciences, 2012, 3(1): 37-43

Improvement of Slope Angle Models Derived from Medium to Fine-Scale DEMs
Key study: Skopje area

Ivica Milevski
Institute of Geography,
Skopje, Republic of Macedonia
ivica@iunona.pmf.ukim.edu.mk

Anita Milevska
Trimaks Kartografija,
Skopje, Republic of Macedonia
anitamilevska@yahoo.com

Abstract - **Apart from freely available global to near-global medium-resolution DEMs (1-3"SRTM, 1"ASTER), for the territory of the Republic of Macedonia, three additional high quality DEMs are available. They are as follows: 20m and 5m DEM of the Agency of Real Estate and Cadastre (AREC) and 15m DEM filtered from original 5m DEM. For general purposes, horizontal and vertical accuracy of all of those models (even the freely available ones) is acceptable. But in fine-scale terrain applications and modellings, slope accuracy is much more sensitive and uncertain. Instead of assessment only, some kind of DEM-related slope accuracy correction and improvement is very useful. An example of such a procedure is presented in the current paper.**

I. INTRODUCTION

In the last decade, several good quality DEMs with a global or almost global coverage and medium to high spatial resolution were released for the public domain. These include free 3"SRTM DEM (90m) realized in 2004 (with later improvements up to version 4.1), and 1"ASTER GDEM (30m) released in 2009 and upgraded to version 2 in 2011. There were many analyses and studies as to which of the said free models is better because 1"ASTER GDEM has a higher resolution, but a lower overall quality [6, 13]. Normally, both models were widely used dependent on the needs and expected results. Only recently, with realization of 1"SRTM DEM (from which 3"DEM was formerly thinned for most of the world) before the aforementioned dilemma was probably over because 30m SRTM is much better than 30m ASTER GDEM. The latest high resolution global DEM released in 2014 is 12m WorldDEM, produced from image stereo pairs of TerraSAR-X and TanDEM-X mission. From the freely accessible WorldDEM DSM (Digital Surface Model) samples (1 degree tiles), we were unable to perform a detailed assessment of its accuracy compared to the other models due to the myriad of surface artifacts (DTM samples are not available yet). However, judging by the numerous indications and preliminary analyses, this is the highest quality global DEM available to date [7]. Aside from that, this product is commercial and currently at a relatively high price per km^2.

Besides the free global or near-global 3"SRTM, 1"ASTER and 1"SRTM DEMs, and the commercial 12m WorldDEM, other two DEMs are available for the area of the Republic of Macedonia. They have been prepared from aerial stereo-photos and ortho-photos by the Agency of Real Estate and Cadastre (AREC) of the Republic of Macedonia with a 20 m (2006), and 5 m (2010) resolution. Actually, the former has been provided as a vector layer with point grid (20 m) datasets in .shp format, from which 20m DEM has been generated. The latter (5 m resolution) has originally been rendered as a 5m DEM. Both DEMs (especially 5m) are of much better quality and accuracy than the aforementioned free global DEMs [11]. Nonetheless, our detailed tests demonstrate a few drawbacks of these models in the form of certain shifts and large artifacts in 20m DEM and small triangular TIN-like artifacts in 5m DEM. Because of that, the better and newer 5m DEM is filtered in SAGA GIS v2.1 and Global Mapper v15 software, and reinterpolated to smooth-surface 15m DEM.

Owing to the fact that there are six DEMs with medium to high resolution (from 90 m to 5 m) currently available for the Republic of Macedonia, a problem arises concerning the selection and usage of the most appropriate DEM for topographic modellings and other applications. In our previous work, a detailed assessment of 3"SRTM DEM for the area of the Republic of Macedonia was conducted, showing that the average horizontal and vertical accuracy is ±5 m, with maximum errors up to ±15 m [10, 11]. Such height inaccuracies are generally due to the resolution and location of DEM points around the prominent peaks. In addition, a detailed comparison of the real resolution and the vertical accuracy of 5 m, 15 m, 20 m (AREC), and 30 m and 90 m (SRTM, ASTER) DEM's has been done [11].

However, it is recognized that for precise modelling of some topographic-related processes such as natural hazards (soil

In: Geomorphometry for Geosciences, Jasiewicz J., Zwoliński Zb., Mitasova H., Hengl T. (eds), 2015. Adam Mickiewicz University in Poznań - Institute of Geoecology and Geoinformation, International Society for Geomorphometry, Poznań

erosion, landslides, hydrological models etc.), slope accuracy is crucial [12]. A number of studies have attempted to establish direct, simplified linkages between DEM resolution, data quality, and modelling uncertainty [1, 17, 2, 16, 15, 10, 3, 11]. Most of these authors have generally concluded that as cell size increases, slope gradients tend to decrease, ranges in curvatures decrease, flow-path lengths tend to decrease, and the accuracy of terrain attributes at particular locations tends to decrease [13]. When comparing different DEMs, several things must be considered. First, the exact locations of grid points that are to be compared may not coincide at different spatial resolutions. In this situation, spatially aggregated comparisons of data resolutions are inappropriate, especially in rugged mountainous landscapes where terrain characteristics often display an enormous variation over short horizontal distances. Second, the population of grid points is small at a coarse resolution, implying unstable statistics. Third, spatial autocorrelation between neighboring sample points may be stronger at fine resolutions because of close sample distances [15].

II. Methodology

Analysis of slope accuracy of previously mentioned available DEMs covering the area of the Republic of Macedonia has been conducted on a carefully selected test site – a rectangular area (20x20 km or 400 km^2) with very diverse topography (plains and valleys to steep mountains). The site is in the western part of Skopje Basin with an elevation range from 232 m to 1,378 m and a mean of 456.6 m. Four slope parameters have been analyzed: the maximal slope, mean slope, standard deviation of slope values and the terrain-slope profile. Also, the entire terrain has been divided into slope classes of 0-10°, 10-20° and higher than 20°. The results have been compared with 5m DEM, used as a reference and the most accurate model available, previously validated with 1 : 25 000 topographic and 1 : 5000 geodetic maps. According to our tests, this model is currently the closest to real topography with a very high horizontal and vertical accuracy (+/-1 m mean; +/-4 m max). For analyses, SAGA GIS v2.1 software is used with several corresponding modules (Terrain Morphometry; Grid Calculator etc.).

III. Results and discussion

The analyses indicate that the maximal slope values have the highest differences compared to the mean slope. In correlation with spatial resolution, the highest slope differences of analyzed DEMs show 3"SRTM, whereas the mean slope value for the entire test area is only 8.8° compared to 11.0° of the 5 m reference DEM (Table 1).

TABLE 1. SLOPE VALUES OF THE TESTED DEMS COMPARED TO THE 5 M REFERENCE DEM

Resol.	Type	Slope values / degree			File size Mb	
		max	*mean*	*stDEV*	*test ar.*	*country*
5 m	**AREC-RM**	**81.2**	**11.0**	**10.2**	**61.0**	**5,500**
15 m	FILTER	72.0	10.8	10.0	6.7	630
20 m	AREC-RM	64.0	10.8	9.6	5.4	350
30 m	SRTM	61.1	10.1	8.7	2.6	76
30 m	ASTER	65.5	10.7	8.8	2.6	75
90 m	SRTM	54.8	8.8	8.0	0.4	16

It is peculiar that, at first sight, 1"ASTER GDEM shows better results than 1"SRTM DEM, not due to higher quality but due to many artifacts with pseudo-slopes in the model as such. When an artifacts removing tool in SAGA GIS with Mesh Denoise module [14] is used (with Threshold 0.5), slope deviations have increased significantly (60.2° for maximal and 9.9° for a mean slope).

The newly available 1"SRTM DEM shows very tolerable deviations from the reference DEM in regard to the mean slope (values lower by 8 %) but greater inaccuracies for maximal slopes (25%). In essence, the maximal slope value shifts indicate fine-scale slope refinement, which is necessary for precise landscape modelling.

For spatial distribution of slopes derived from the analyzed DEMs, all slopes have been divided into 10-degree slope classes, bar the class with slopes above 30°. Afterwards, the area of each class has been calculated and compared to other DEMs (Table 2). In DEMs with coarser resolution (30-90m), flats and gentle slopes (0-10°) cover larger area compared to the reference 5m DEM. The opposite is the case with steep-slopes, whose areas significantly decrease with a reduced DEM resolution. Thus, slopes with 20-30° and above 30° cover 180% and 210% larger area in 5m DEM compared with 3"SRTM DEM.

TABLE 2. AREA COMPARISONS OF SLOPE CLASSES DERIVED FROM THE TESTED DEMS

Resol.	Type	Area of Slope Class in %				Total
		0-10°	*10-20°*	*20-30°*	*>30°*	*of 400km^2*
5 m	**AREC-RM**	57.3	24.5	11.8	6.3	100.0
15 m	FILTER	57.7	25.0	11.3	5.9	100.0
20 m	AREC-RM	57.6	25.5	11.2	5.6	100.0
30 m	SRTM	59.6	26.7	9.1	4.5	100.0
30 m	ASTER	60.5	26.4	8.9	4.3	100.0
90 m	SRTM	66.7	23.9	6.6	3.0	100.0

Similar trends show a graph of slopes along the selected topographic profile 4.0 km in length and an elevation range from 301 to 711 m (Fig. 1). It is evident that 1"ASTER GDEM has large shifts and jumps compared to the reference 5m DEM, for which this model in slope related analysis is very uncertain.

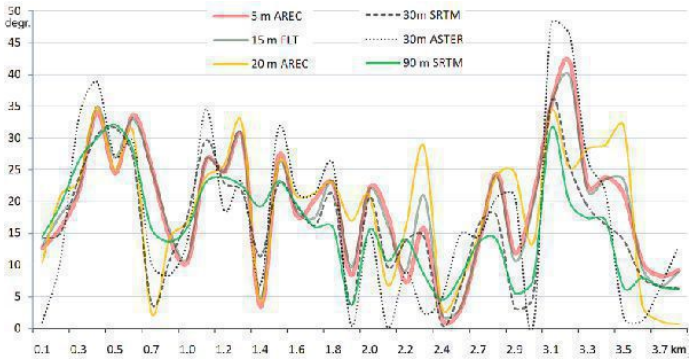


Figure 1. Graph of slope angle values (in degree) through the topographic profile of analyzed DEMs.

With detailed comparisons of the 5m DEM and other analyzed DEMs through the series of scatterplots, the appropriate regressions have been calculated and presented in Table 3.

Regressions and the correlation coefficient R^2 have confirmed that of the freely available DEMs, 1"ASTER GDEM has very uncertain slope angle values in relation to 5m-15m DEM and even to 1"-3"SRTM DEM. Without mesh denoise and/or other filtering, this DEM leads to unreliable results in earth processes modelling, as indicated in the number of works [12]. Pertaining to the other DEMs, the presented regressions are beneficial for correcting the slope values to a certain extent.

For further identification of the presented slope value accuracy, 400 points with 1km spatial resolution have been selected in the test area. For each point and DEM, the slope angle has been calculated. The results indicate a gradual increase of errors with the resolution decrease and the slope angle increase (Table 4.). The average correction index in connection with 5m AREC DEM is 1.25 for 1"SRTM and 1.45 for 3"SRTM for slopes >15° (for slopes of 5-10°, the values are almost identical). These values indicate that "coarse" justification of slope angle accuracy is possible with simple equations in the following form: *a*(1.25-1.25/a)* for 1"SRTM DEM and *a*(1.45-1.45/a)* for 3"SRTM DEM, where *a* is the slope angle in degrees [10, 11]. The former is partially applicable for 1"ASTER GDEM after filtering.

TABLE 3. SLOPE ANGLE REGRESSIONS OF ANALYZED DEMS IN REGARD TO THE REFERENCE 5 M AREC DEM

Resol.	Type	Regression	R^2
			%
5 m	**AREC-RM**	**-**	**-**
15 m	FILTER	0.090156+1.01253*a	98.6
20 m	AREC-RM	0.411494+0.97683*a	84.9
30 m	SRTM	0.732062+1.00231*a	83.2
30 m	ASTER	0.446229+0.98867*a	72.8
90 m	SRTM	1.037035+1.13559*a	81.1

TABLE 4. SLOPE ANGLE COMPARISONS FOR 400 PREDEFINED POINTS WITH 5 M AREC DEM AS A REFERENCE

Slope	5mAREC	15mFIL	20mAREC	1"SRTM	1"AST	3"SRTM
0-5°	100.0	101.4	78.8	63.2	49.9	94.5
5-15°	100.0	100.7	103.9	110.1	110.0	123.1
15-30°	100.0	103.7	105.7	117.1	116.9	137.7
30-45°	100.0	103.4	109.1	120.4	121.8	136.9
>45°	100.0	105.3	125.0	137.9	137.6	164.7
Avr>15°	**100.0**	**103.8**	**112.9**	**122.7**	**122.2**	**144.3**

As regards the 15-20m DEMs for country area, the rendered regressions are very accurate and applicable to most of the terrain situations, except in areas where 20m AREC DEM have large artifacts and irregularities.

Correcting Slope Artifacts and Pseudo-slopes in Flats

During terrain analyses and modellings, the problem of step-like slopes and artifacts in otherwise flat or almost-flat areas (plains, flats, valley bottoms) commonly emerges. They occur in all of the DEMs used in the current study but with a different shape and extent. It is clear that these "steps" are closely related with the production of DEMs (in both DSM-like and DTM models), and it is advisable to correct them. That is mostly the case with hydrological modelling, assessment of flood, erosion, landslide and other risk areas etc. One of the better procedures is easily performed in SAGA GIS software through the Multiresolution Index of Valley Bottom Flatness - MRVBF [4]. This index classifies terrains into the following: no bottom flat areas (<0.5), small valley bottom flats (0.5-1.5), larger flats (1.5-2.5) etc. With inverse MRVBF values reclassification within the range from 0-0.5 (flats and almost flats) to 1 (other terrains) and then its multiplication with slope angle values (a raster model), acceptable corrections are yielded. Thus, flat areas with unusual or unnecessary artifacts and slopes become "real flats" with near to or zero degree slope angle (Fig. 2).

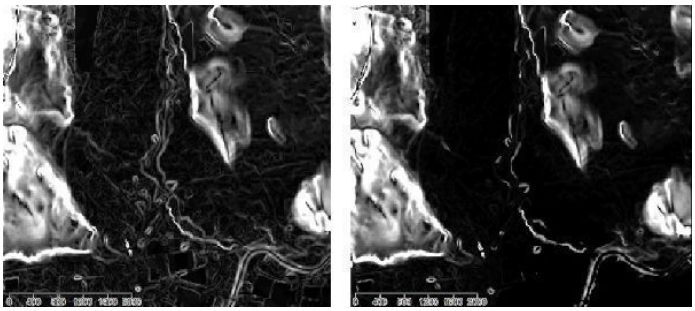


Figure 2. Corrections ("flattening") of slope artifacts (left) with MRVBF index (right) in SAGA GIS.

Discussion

The results of our analyses point to significant differences and a degree of inaccuracy, which increase from fine-scale to coarse scale DEMs and from flat to step-slope areas. In terms of slope accuracy, for the used test area, 3"SRTM DEM is generally better than 1"ASTER GDEM (v2), which itself has issues with high noise, many artifacts and pseudo-slopes. This issue is partially resolved with mesh denoise software modules in SAGA GIS. As for slope accuracy, both DEMs are behind 1"SRTM DEM, and far behind the 5m AREC-RM DEM, and 15m filtered DEM. Notwithstanding this fact, because of the size of 5m AREC DEM for country area (5.5 gigabytes) and the small TIN-like artifacts, an interpolated and filtered 15m DEM is a much better option to resort to (650Mb). It will probably be an upper limit for a reasonable terrain modelling and processing of areas larger than 100-200 km^2 to bear in mind the good spatial cover and the amount of data cells for processing. The 20m AREC DEM has a good overall horizontal, vertical and even slope accuracy but the number of rectangular artifacts significantly decreases its usability. Moreover, the two AREC DEMs (5 m and 20 m) are of commercial value, with the current price standing at 0.25 euro per km^2.

It is for those reasons that when high-resolution AREC DEMs are unavailable, 1"SRTM DEM is the best free compromise when availability, comparability, quality and spatial resolution for the entire country (as well as for other worldwide areas) are considered. In the extent (latitude) of Macedonia, the 1"SRTM DEM cell size is 22m*30m, which is sufficient for medium-scale modelling at a country level. The initial assessment demonstrates approximately 20-25% better horizontal and vertical accuracy (mean: ±3.5 m, max: ±11 m) with respect to 3"SRTM (mean: ±5 m, max: ±15 m). There are substantial shifts in the aspect of decreased values for steep slopes but with a correction equation $a*(1.25-1.25/a)$, where a is the slope angle, slope values may be acceptable.

In certain applications, such as erosion modelling, even a minor increase of slope accuracy implies improvement of the final results [18]. Thus, with prior empirical corrections, it is feasible to greatly improve slope along with model accuracy.

REFERENCES

[1] Chang, K., and B. Tsai, 1991. The effect of DEM resolution on slope and aspect mapping. Cartography and Geographic Information Systems. 18., 69-77.

[2] Chaplot, V., Walter, C., and P. Curmi, 2000. Improving soil hydromorphy prediction according to DEM resolution and available pedological data. Geoderma 97, 405–422.

[3] Deng, Y., Wilson P.J., and B.O. Bauer, 2007. DEM resolution dependencies of terrain attributes across a landscape. International journal of Geographical Information Science, Vol. 23, Nos. 1-2, 187-213.

[4] Gallant, J.C., and T.I. Dowling, 2003. A multiresolution index of valley bottom flatness for mapping depositional areas. Water Resources Research, Vol. 39, No. 12, 1347, DOI:10.1029/2002wr001426

[5] Guth, P.L. 2010. Geomorphometric comparison of ASTER GDEM and SRTM. A special joint symposium of ISPRS Technical Commision IV&AutoCarto in conjuction with ASPRS/CaGIS 2010 Fall Specialty Conference, Orlando, Florida, 1-9

[6] Hengl, T., and H. Reuter, 2011. How accurate and usable is GDEM? A statistical assessment of GDEM using LiDAR data. In Hengl, T., Evans, S. I., Wilson, P. J., Gould, M., eds. Geomorphometry 2011 - Proceedings (Redlands, CA, USA, 7–11

[7] Huber, M., Gruber, A., Wendleder, A., Wessel, B., Roth, A. and A. Schmitt, 2012. The Global TANDEM-X DEM: Production status and first validation results. International Archives of the Photogrammetry, Remote Sensing and Spatial Information Sciences, Volume XXXIX-B7, 2012 XXII ISPRS Congress, 25 August – 01 September 2012, Melbourne, Australia

[8] Jarvis, A., H.I. Reuter, A. Nelson, and E. Guevara, 2008. Hole-filled SRTM for the globe Version 4, available from the CGIAR-CSI SRTM 90m Database (http://srtm.csi.cgiar.org).

[9] Keeratikasikorn, C. and I. Trisirisatayawong, 2008. Reconstruction of 30m DEM from 90m SRTM DEM with bicubic polynomial interpolation method. The International Archives of the Photogrammetry, Remote Sensing and Spatial Information Sciences. Vol. XXXVII. Part B1. Beijing 2008

[10] Milevski, I., 2005. Using 3"SRTM DEM for geomorphometrical analysis. In Stamenkovic, S., ed. Proceedings: Serbia and modern processes in Europe and World. Faculty of Geography, University of Belgrade, Serbia, 825 – 832. (in Serbian).

[11] Milevski, I., Gorin, S., Markoski, M., and I. Radevski, 2013. Comparison of Accuracy of DEM's Available for the Republic of Macedonia. Proceedings from the 3rd International Geographic Symposium - GEOMED 2013, Antalya, 165-172

[12] Milevski I., Dragicevic S., and A.Georgievska, 2013. GIS and RS-based modelling of potential natural hazard areas in Pehchevo municipality, Republic of Macedonia. Journal of the Geographical Institute Jovan Cvijic, SASA, Belgrade, 95-107

[13] Rexer, M.; Hirt, C., 2014. "Comparison of free high-resolution digital elevation data sets (ASTER GDEM2, SRTM v2.1/v4.1) and validation against accurate heights from the Australian National Gravity Database.". Australian Journal of Earth Sciences 61

[14] Sun, X., Rosin, P.L., Martin, R.R., and F.C. Langbein, 2007. Fast and effective feature-preserving mesh denoising. IEEE Transactions on Visualization and Computer Graphics, Vol.13, No.5, 925-938.

[15] Thompson, J.A., J.C. Bell, and C.A. Butler. 2001. Digital elevation model resolution: effects on terrain attribute calculation and quantitative soil-landscape modeling. Geoderma 100:67-89.

[16] Wilson, J.P, Repetto, P.L., Snyder, R.D., 2000. Effect of data source, grid resolution, and flow routing method on computed topographic attributes. In: Wilson, J.P., Gallant, J.C. (Eds.), Terrain Analysis: Principles and Applications. John Wiley & Sons, New York, 133–161.

[17] Zhang, W., Montgomery, D.R., 1994. Digital elevation model grid size, landscape representation, and hydrological simulations. Water Resour. Res. 30, 1019–1028.

[18] Zhang, Z., 2012. The Comparison of Slope Angle Algorithms for Soil Erosion Based on Grid Digital Elevation Model. Advances in Technology and Management. Advances in Intelligent and Soft Computing Volume 165, 2012, pp 61-66

A new least impact approach for hydrological conditioning of DEMs

Markus Metz
Department of Molecular Biology
Fondazione Edmund Mach (FEM)
San Micheleall'Adige, Italy
markus.metz@fmach.it

Abstract—**Digital elevation models (DEMs) are the primary source for 2D hydrological modelling. Most approaches require a sink-free DEM, because standard flow tracing methods stops at the bottom of sinks. Sinks are commonly removed by sink filling, raising elevation values in the sink to the spill point. This is equivalent to filling a sink with water until the water overflows. The modifications introduced to the DEM by sink filling can be substantial. Sink filling assumes that elevation values are too low, and raises elevation values until the DEM is completely drained. DEMs obtained with remote sensing (radar, LiDAR, stereo imagery) have systematically too high and not too low values. Thus selected elevation values should be lowered rather than raised in order to drain a DEM completely. This method is known as carving, where a channel is carved into the DEM. The minimum impact approach investigates each sink and determines the impact of filling and carving. Each sink is then removed with the method causing less modifications. Here we present a new minimum impact approach that further reduces the amount of modifications. Each sink is removed by a combination of filling and carving. The best combination for a given sink is the combination of filling the sink up to a certain level and carving out a channel from that level that causes the least modifications to the DEM. Flow directions for carving are determined with a least cost path search. We compare the amount of modifications introduced by different methods and the resultant surface flow accumulations. The new method is implemented in the GRASS GIS module r.hydrodem. The hydrologically conditioned DEM can be used with any hydrological modelling software.**

I. Introduction

2D hydrological modelling provides the base for commonly used terrain parameters such as flow direction, basin delineation, surface flow accumulation, and stream network extraction. These parameters are in turn used for Hortonian analysis of drainage networks [1]. 2D hydrological modelling typically uses a Digital Elevation Model (DEM) with optional additional data to fine-tune the modelling. Most DEMs used nowadays are derived from remote sensing data (radar, LiDAR, stereo imagery). DEMs are not a true representation of the terrain, but a simplified model based on spatial samples. Due to the characteristics of data acquisition, any errors in these data result in systematically too high elevation values. For example, the bottom of narrow valleys can not be detected with viewing angles that are not exactly vertical (which is not possible for stereo DEMs), and none of the methods can penetrate vegetation (LiDAR can penetrate leaves but not wood). For 2D hydrological modelling, an important consequence of these simplified models containing a certain amount of errors is that artificial sinks are introduced. 2D Hydrological modelling commonly assumes that surface waterflow stops at the bottom of sinks, therefore these sinks need to be removed if the study area should be completely drained.

The first and still most commonly used method to remove sinks is known as sink filling [2], where each sink is filled up to the level of the spill point. Sink filling is thus raising elevation values. An alternative is carving [3, 4], where a channel is carved out from the bottom of the sink through the obstacle. Depending on the size of the sink and the size of the obstacle, either sink filling or carving might cause less modifications. The minimum impact approach of [5] investigates each sink and determines the impact of filling and carving. The method causing less modifications is then used to remove the sink.

II. Least impact sink removal

A. Theory

Here we present a new method that further reduces the impact of sink removal on the DEM. Each sink is removed with a combination of carving and filling. The best combination for a given sink is determined as the combination of filling the sink up

In: Geomorphometry for Geosciences, Jasiewicz J., Zwoliński Zb., Mitasova H., Hengl T. (eds), 2015. Adam Mickiewicz University in Poznań - Institute of Geoecology and Geoinformation, International Society for Geomorphometry, Poznań

to a certain level and carving out a channel from that level that causes the least modifications to the DEM. The drainage directions from the bottom of a sink to its spill point are determined with a least cost path search [6], as implemented in the GRASS GIS [7] modules *r.watershed* and *r.stream.extract*. Using a least cost path search algorithm, a DEM can be full drained without prior hydrological conditioning of the DEM. Since most other hydrological modelling software does not use least cost path search to determine drainage directions, the new tool *r.hydrodem* is provided to improve the result of hydrological modelling [6]. The new tool is implemented such that also very large datasets can be processed without causing out-of-memory errors. A limit on how much memory should be used can be set as an option for the tool.

B. *Examples*

The new least impact approach was tested on a LiDAR DEM with 1 meter resolution and a total of 525,000 grid cells (Fig. 1). Sink filling required modification of 6,299 cells, whereas the least impact approach modified only 331 cells (5% of the sink filling method).

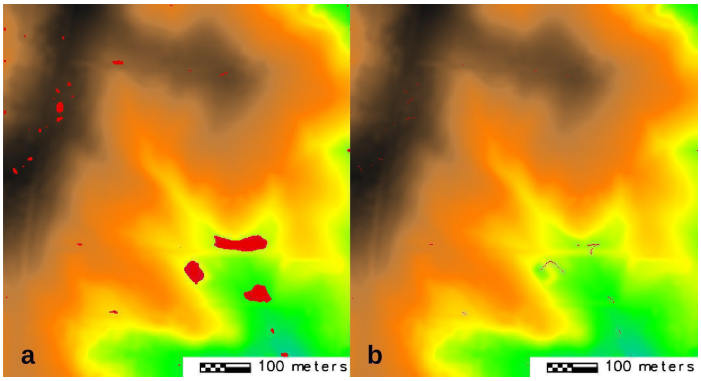


Figure 1. Amount of modifications (red)on a LiDAR-based Digital Elevation Model with a) sink filling and b) least impact approach.

Another test was performed on a radar-based DEM with 30 meter resolution and a total of 225,000 grid cells (Fig 2). Sink filling required modification of 12,066 cells, whereas the least impact approach modified only 5,218 cells (43% of the sink filling method).

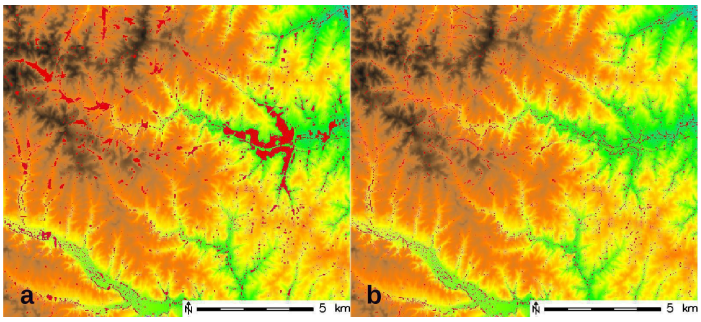


Figure 2. Amount of modifications (red) on a radar-based Digital Elevation Model with a) sink filling and b) least impact approach.

III. Conclusions

The new least impact approach to remove sinks requires much less modifications than traditional sink filling. As shown by [6], the least cost path search results in more realistic stream network extraction than sink filling. Differences in stream networks to the minimum impact approach of [5] were marginal. Automated hydrological conditioning of a DEM serves two purposes: 1) make them DEM more similar to the (unknown) ground truth, 2) enable 2D hydrological modelling to drain the study area completely unless the existence and location of real sinks is known. Therefore a method that minimizes modifications to the DEM is preferable.

Acknowledgment

The author thanks Jarek Jasiewicz for valuable comments and suggestions during the development and refinement of the tool.

References

[1] Jasiewicz, J, and M. Metz, 2011. “A new GRASS GIS toolkit for Hortonian analysis of drainage networks”, Computers & Geosciences 37, 1162-1173.

[2] Jenson, S. K., and J. O. Domingue, 1988. “Extracting topographic structure from digital elevation data for geographic information system analysis”, Photogrammetric Engineering and Remote Sensing 54(11), 1593–1600.

[3] Rieger, W., 1998. “A phenomenon-based approach to upslope area and depressions in DEMs” Hydrol. Process., 12, 857–872.

[4] Martz, L. W. and J. Garbrecht, 1998. “The treatment of flat areas and depressions in automated drainage analysis of raster digital elevation models” Hydrol. Process., 12, 843–855.

[5] Lindsay, J. B., and F. Creed, 2005. “Removal of artefact depressions from digital elevation models: towards a minimum impact approach”, Hydrological Processes, 19, 3113–3126.

[6] Metz, M., Mitasova, H., and R. S. Harmon, 2011. “Efficient extraction of drainage networks from massive, radar-based elevation models with least cost path search” HESS 15, 1–12.

[7] Neteler, M., Bowman, H., Landa, M., and M. Metz, 2012. “GRASS GIS: A multi-purpose open source GIS” Environmental Modelling & Software 31, 124–130.

Hydrological forecasting in real time: an experimental integrated approach

Tomasz Niedzielski, Bartłomiej Miziński
Department of Geoinformatics and Cartography
University of Wrocław
Wrocław, Poland
tomasz.niedzielski@uni.wroc.pl

Dapeng Yu
Department of Geography
Loughborough University
Loughborough, United Kingdom
D.Yu2@lboro.ac.uk

Abstract—**One of the roles of geosciences is to provide the society with efficient tools that may diagnose or predict various environmental hazards. Floods are among such events, and hence there is an ongoing need to develop and improve hydrological models. However, especially in mountainous catchments which respond quickly to extreme rainfall, the need covers not only predictive models but also real-time systems that produce and publish up-to-date predictions with sub-hour update frequency. This includes forecasting both the hydrograph and inundation. The objective of the paper is to present a novel approach that integrates the real-time system for forecasting hydrograph, known as HydroProg, with the following two elements: the real-time inundation model that simulates the flood extent on the top of the Digital Elevation Model (DEM), referred to as FloodMap, and the on-demand monitoring of inundation using the Unmanned Aerial Vehicle (UAV). Although skills of the hydrograph prediction models are relatively easy to assess, the problem arises when we want to evaluate the performance of inundation models. This can be done as a near real-time procedure, initiated automatically when the HydroProg and the associated FloodMap produce flood alert, making use of the UAV for oblique photogrammetry. The UAV-taken aerial photographs enable production of orthophoto images which are utilized to check the accuracy of spatial predictions of water extent. The prototype of the comprehensive integrated system is presented, and the results are based on the experimental implementation of the HydroProg system in the upper Nysa Kłodzka River basin (SW Poland).**

I. INTRODUCTION

The objective of this paper is to show how real-time hydrologic prediction systems may be combined with inundation models in order to compute a real-time prognoses of flood extent. The presentation is based on a recently designed and implemented hydrologic prediction system, known as HydroProg [1,2], which serves as a tool for issuing warnings against hydrologic hazards. Integrated with HydroProg is the FloodMap model [3,4,5,6], which allows one to carry out spatial simulations of inundation with several methodological approaches. The integration in question meets a key criterion of the real-time solutions, namely it works in an online fashion and offers predictions of inundation which are very frequently re-calculated and updated, following frequent calibration of hydrograph models. Unlike hydrograph predictions, inundation prognoses cannot be easily verified against true data. Hence, in order to check the correctness of the real-time inundation forecast, it is necessary to employ Unmanned Aerial Vehicles (UAVs) to produce ortophoto images that capture patterns of overbank flow [7]. Thus, the following elements may act in concert in a consecutive fashion: HydroProg-based real-time hydrograph predictions → FloodMap-based mapping of real-time hydrograph predictions into the spatial domain in order to produce real-time inundation prognoses → UAV-based verification of real-time inundation prediction.

Apart from HydroProg, there are numerous real-time hydrologic prediction systems and services. For instance, in the USA there exists the Advanced Hydrologic Prediction System [8], and for the Alpine region the MAP D-PHASE system has been deigned [9]. Although such systems serve a purpose of forecasting water levels or discharges, the above-mentioned integration of hydrograph real-time prediction with real-time inundation simulations, equipped with the UAV as a real-time verification tool, has not been developed so far.

The very initial test of the integration will be discussed in this paper, and the case study will focus on: (1) a single site of Gorzuchów located along the river of Ścinawka (left tributary of Nysa Kłodzka river in SW Poland) and (2) a single moderate peak flow event on 29 May 2014 – 2 June 2014. As there has been no flood since the launch of the HydroProg experiment for the upper Nysa Kłodzka river basin, herein we focus on high flow rather than inundation itself. However, even with such a limitation, we present a step-by-step concept of how HydroProg and FloodMap may be combined.

In: Geomorphometry for Geosciences, Jasiewicz J., Zwoliński Zb., Mitasova H., Hengl T. (eds), 2015. Adam Mickiewicz University in Poznań - Institute of Geoecology and Geoinformation, International Society for Geomorphometry, Poznań

II. METHODS

A. HydroProg and HydroProg-Kłodzko prototype

HydroProg is the acronym of a novel system – elaborated and designed at the University of Wrocław, Poland – which aims to issue warnings against hydrological hazards, such as peak flows. The system [1] integrates hydrometeorological gauging networks with numerous hydrologic models in order to produce hydrograph predictions based on individual models and on their multimodel ensemble. The prognoses are subsequently published online in an external web map service, and they are also used to issue warnings when peak flow is forecasted. The entire system may be called a rapid service as it works in real-time and offers predictions as well as the associated warnings which are calculated quickly, i.e. with the 15-minute update.

The general HydroProg infrastructure has been experimentally implemented for the upper Nysa Kłodzka river basin (SW Poland). This implementation, known also as the HydroProg-Kłodzko prototype, uses the real-time access to hydrometeorological data of the Local System for Flood Monitoring (Lokalny System Osłony Przeciwpowodziowej, LSOP) of Kłodzko County, Poland. Thus, HydroProg serves as an integrator of three elements: (1) the unique automatic gauging network installed in the mountains (LSOP), (2) a few hydrologic models, and (3) the web map service. The HydroProg-Kłodzko prototype generates predictions every 15 minutes, and this time step is used for: re-calibration of models, prediction update based on the newly calibrated models. The maximum lead time is equal to 3 hours, but intermediate prediction horizons are 15,30,…,180 minutes. The HydroProg-Kłodzko prototype has been launched on 1 August 2013, and since that time has been uninterruptedly working in a real-time fashion. Recent studies show that the HydroProg-Kłodzko prototype works well and is able to produce skillful real-time predictions of water level [2].

B. FloodMap

A well-established hydrodynamic model, known as FloodMap [3,4,5,6], was used to derive the dynamics of flood inundation. River flow is modelled by the full solution of the 1D Saint-Venant equations. The 2D flood inundation model is raster-based and solves the inertial form of the 2D Shallow Water Equations. At the river/floodplain boundary, the model is tightly coupled by considering the mass and momentum exchange between the river flow and floodplain inundation. The 1D river flow model is based on the fixed bed model of Abbott and Basco [10]. The model solves the one-dimensional St. Venant equations for unsteady flow using the Preissmann Scheme (as reported in [11]), also known as an implicit box scheme because of the way it approximates hydraulic variables. The details of the model structure have been described in [3]. The 2D flood inundation model (FloodMap-Inertial) takes the same structure as the inertial model of Bates et al. [12], but with a slightly different approach to the calculation of time step. Neglecting the convective acceleration term in the Saint-Venant equation, the momentum equation becomes:

$$\frac{\partial q}{\partial t} + \frac{gh\partial(h+z)}{\partial x} + \frac{gn^2q^2}{R^{4/3}h} = 0, \quad (1)$$

where q is the flow per unit width, g is the acceleration due to gravity, R is the hydraulic radius, z is the bed elevation, h is the water depth and n is the Manning's roughness coefficient. Discretizing the equation with respect to time produces:

$$\frac{q_{t+\Delta t} - q_t}{\Delta t} + \frac{gh_t\partial(h+z)}{\partial x} + \frac{gn^2q_t^2}{h_t^{7/3}} = 0. \quad (2)$$

To further improve this, one of the q_t in the friction term can be replaced by $q_{t+\Delta t}$ and this gives the explicit expression of the flow at the next time step:

$$q_{t+\Delta t} = \frac{q_t - gh_t\Delta t(\frac{\partial(h_t+z)}{\partial x})}{(1+gh_t\Delta tn^2q_t/h_t^{10/3})}. \quad (3)$$

The flow in the x and y directions is decoupled and take the same form. Discharge is evaluated at the cell edges and depth at the centre. To maintain model stability and minimize numerical diffusion, the Forward Courant-Freidrich-Levy Condition (FCFL) approach described in [6] for the diffusion-based version of FloodMap is used in the inertial model to calculate time step.

C. UAV

There are numerous techniques for mapping inundation. Along with terrestrial methods, such as for instance surveying citizens who witnessed the event or observing geomorphological consequences of overbank flow, there are many remote sensing methods suitable for such purposes. They can be based either on satellite remote sensing [13] or aerial photography [14]. Recent advances in unmanned aerial systems open new possibilities for observing flood extent, and this is due to both the unprecedented spatial resolution of UAVs as well as a feasibility to react quickly to fly over the flooded terrain.

Among numerous UAVs there are ones classified as micro UAVs which – being lightweight and often revealing flexibility to take off and land in a complex terrain – offer an opportunity to carry out aerial survey over areas of considerable sizes. They serve a purpose of demonstration missions, but their bigger equivalents may do the same job over larger areas, and in the operational way. To carry out research reported in this paper, we

use the micro fixed-wing UAV, swinglet CAM, manufactured by senseFly. Swinglet CAM is a flexible system that allows to take photographs with a pre-defined overlap with spatial resolution reaching 3 cm/px when the flight altitude is approximately 100 m above the take-off site. If there are no weather-related constraints, the flight time can be as high as 30-35 minutes. The UAV can be easily launched without special infrastructure, and this makes the device very suitable for geographical field research. Along with photo acquisition the UAV records numerous flight parameters, ranging from technical ones, through navigation-related values, to a few meteorological parameters. The UAV-acquired photographs can be geo-tagged, and hence both the Digital Surface Model (DSM) as well as orthophoto images may be generated using the Structure-from-Motion (SfM) procedure [15].

D. Integration

The calibrated FloodMap model can be used to produce inundation predictions based on the HydroProg-generated water level prognoses, and the integration can work in real time. Firstly, when a new and up-to-date prediction of water level at a given gauge is produced by HydroProg, the HydroProg infrastructure sends the CSV file consisting of the forecasted hydrograph to the external FloodMap server. This happens automatically at fixed times. Hence, when there is a delay in the system, the older file (but, due to 15-minute update time, the file is usually still up-to-date) is utilized. Second, the predicted hydrograph is assumed as an input to the FloodMap model which is automatically run at fixed time intervals. The calculations of water depth in the spatial domain in the vicinity of the gauge (reach of a few hundred meters either side of the gauge) must be completed before the next 15-minute interval begins so that inundation predictions are up-to-date, as the hydrograph prognoses are. The UAV team can be requested to carry out field survey when inundation is predicted.

III. CASE STUDY

A. Data

The concept of integrating HydroProg with FloodMap, with its verification using UAV, is presented herein in the case study. We consider one site, i.e. the gauge in Gorzuchów (50.4853˚ N, 16.5714˚ E) located along the Ścinawka river (SW Poland), and we focus on the inundation along a 300 m reach at the gauging site, during a single peak flow event that occurred between 29 May 2014 and 2 June 2014 (Fig. 1A). As noted above, there has been no significant floodplain inundation since the launch of the

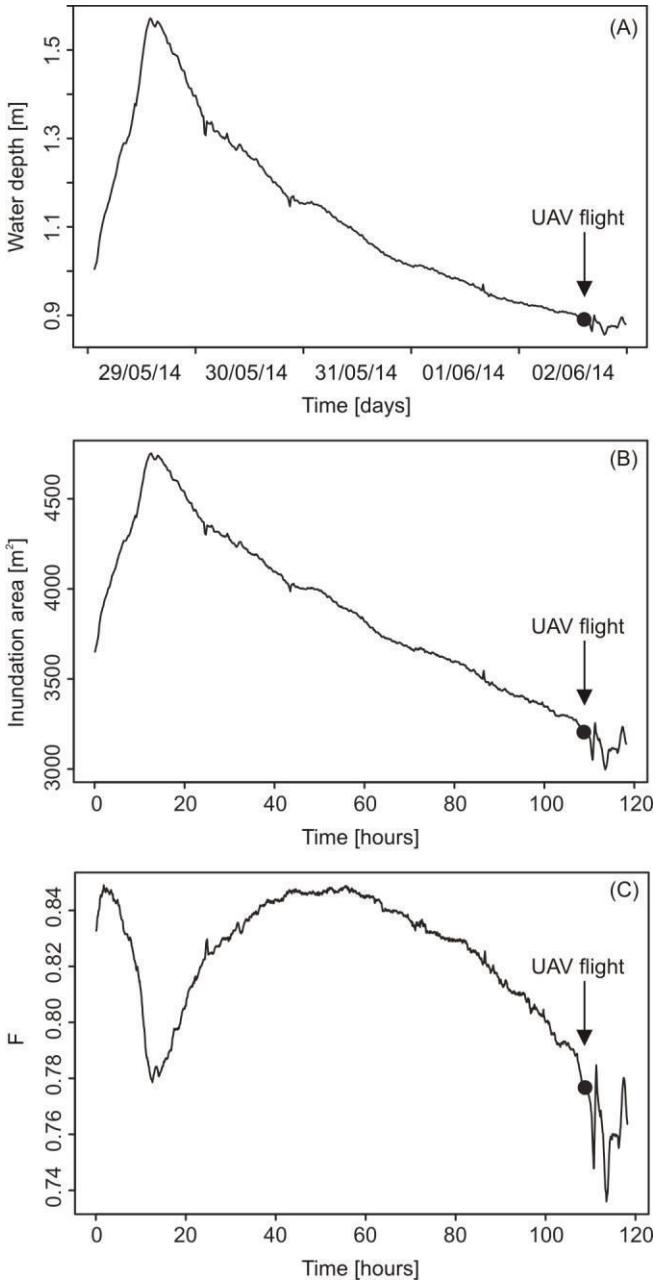


Fig. 1. Observed water depth at the Gorzuchów gauge between 29/05/2014 and 02/06/2014 (flow input to FloodMap) (A), total inundation area over time (B), time series of *F* statistics calculated against the UAV-derived inundation area at 14:30:00 UTC on 2 June 2014 – 109 hrs into the simulation (C).

.

HydroProg-Kłodzko prototype. Thus, our exercise is limited to the HydroProg-FloodMap integration in the high flow situation. For the purpose of this paper, we show the FloodMap application using both the observed and predicted data as inputs.

The following datasets are inputs to the FloodMap model: HydroProg-based 3-hour predictions of water level in Gorzuchów, Digital Elevation Model (DEM) with the resolution of 1 meter based on processing of the Light Detection and Ranging (LiDAR) data, bed elevation data at the gauging station. The verification of the approach is based on orthophoto image for the Gorzuchów site, the production of which was based on the UAV survey carried out on 2 June 2014 (two flights at 07:11:29–07:41:49 UTC and 14:14:12–14:36:01 UTC; areas in the vicinity of the gauge were surveyed in the second flight; the average time of observation was assumed to be 14:30:00 UTC). The 2D version of the model is used in the simulation. A uniform water surface elevation is used to represent river flow. Given the mild slope of the site (~0.004) and length of the reach, this is considered as a valid assumption. The next section presents the results of model verification.

B. Initial results

The total inundation area over time is presented in Fig. 1B. Although there is no significant floodplain inundation, the total area predicted to be wet follows the pattern of observed water depth at the gauging station. As water depth increases, more areas adjacent to the main river channel get inundated.

Fit statistics (F) is used to evaluate the degree of agreement between model prediction and observation, calculated as the ratio between the area both observed and predicted to be wet, and the total area either observed or simulated to be wet. The time series of F is shown in Fig. 1C. The F value of 77% is achieved for the validation point when UAV image was obtained, suggesting a good level of predictive ability. The lowest F was found to be corresponding to the peak flow, which is likely due to larger extent found during the peak.

Fig. 2 shows the model simulated water extent at 14:30:00 UTC on 2 June 2014, superimposed on the UAV observation of terrain. The simulated extent agrees well with the UAV-based orthophoto image. The presence of trees and bushes along the bank makes the determination of flooded area uncertain in places. In order to show where the comparison is reliable, we sketched red lines in places where it was possible to unequivocally determine the river bank (hence, where presence of vegetation or orthophoto artifacts did not cover the true water signal). It is also apparent from Fig. 2 that the simulations correctly predicted the episode of flooding the bar in the vicinity of the bridge.

In addition, Fig. 2 presents the predicted water extent, calculated using the HydroProg-FloodMap integration approach.

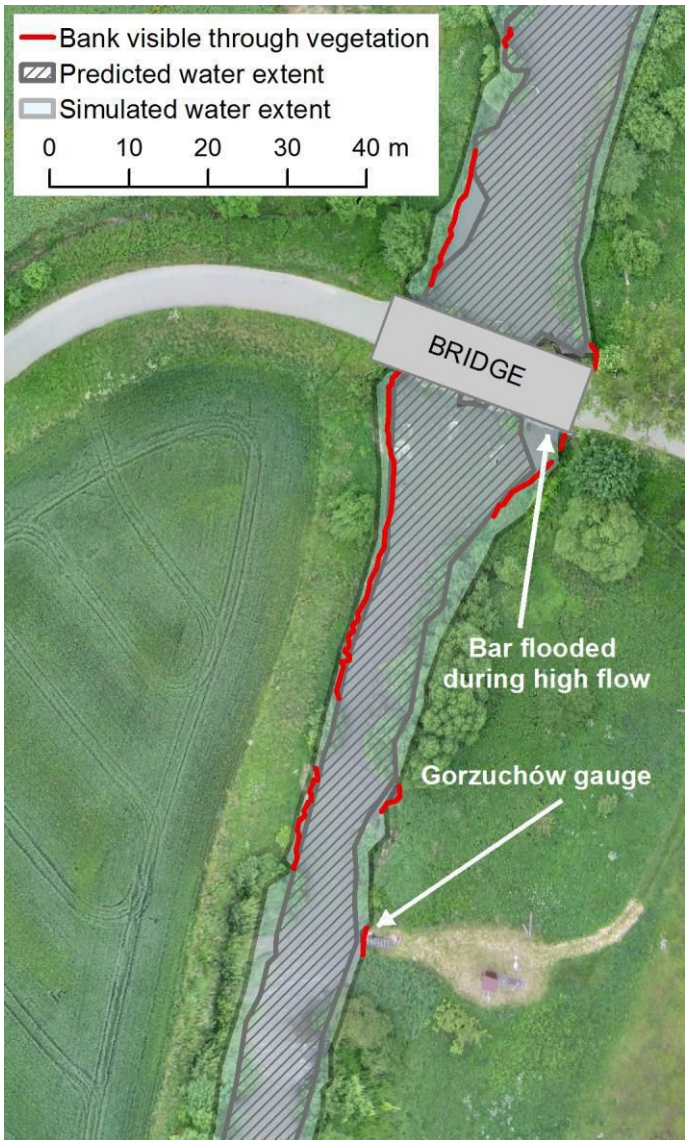


Fig. 2. Simulated water extent at 14:30:00 UTC on 2 June 2014 and predicted water extent (HydroProg-FloodMap) from 11:30:00 UTC into 14:30:00 UTC on 2 June 2014, both superimposed on the UAV-based orthophoto image serving as real observation (~14:30:00 UTC on 2 June 2014).

The HydroProg predictions of water level at the Gorzuchów gauge, calculated from 11:30:00 UTC into 14:30:00 UTC using the Vector Autoregressive (VAR) hydrologic model [16], became inputs to FloodMap, leading to the computation of 3-hour inundation prediction. The visual analysis of Fig. 2 leads to the conclusion that the predicted water extent is more accurate than

the simulated one, particularly along the linear banks, however the prediction does not resolve the flooding of the bar in the vicinity of the bridge.

IV. CONCLUSIONS

We presented the concept of integrating HydroProg with FloodMap in order to generate inundation predictions in real time. As it is difficult to evaluate the skillfulness of the inundation prediction, we believe that UAVs are able to serve a purpose of verifying the performance of such spatial hydrologic prognoses. The entire concept – hence the consecutive application of HydroProg, Floodmap and UAV – was shown herein to be feasible. Indeed, we presented the case study, based on one site and one peak flow event, which confirmed the usefulness of the approach. In particular, simulating high flow in the study site of Gorzuchów (along Ścinawka river, SW Poland) was successful, and the simulations were found to offer the 77% fit to the UAV data. The model was also able to reproduce site-specific episodes, such as flooding a bar. Forecasting high flow with the HydroProg-FloodMap approach was also found to be promising. Within this setup, water extent was predicted 3 hours ahead, leading to bigger agreement with linear banks observed by the UAV than in the case of water extent simulations. However, the HydroProg-FloodMap predictions of water extent failed to forecast flooding of the bar.

ACKNOWLEDGMENT

The research has been financed by the National Science Centre, Poland, through the grant no. 2011/01/D/ST10/04171 under leadership of Dr hab. Tomasz Niedzielski, Professor at the University of Wrocław, Poland. The authors are grateful to the authorities and staff members of the County Office in Kłodzko for partnership, professional advice and access to the LSOP data. We also thank Matylda Witek, MSc, for producing the orthophoto image used in this paper. The LiDAR data, used as the input to hydrological models presented in this paper, have been purchased and used in accordance with the academic license, following the Polish law regulations in the administration of Główny Urząd Geodezji i Kartografii. The engine of the HydroProg-Kłodzko prototype is based on R, PostgreSQL and MySQL.

REFERENCES

[1] Niedzielski, T., B. Miziński, M. Kryza, P. Netzel, M. Wieczorek, M. Kasprzak, W. Kosek, P. Migoń, M. Szymanowski, J. Jeziorska, and M. Witek, "HydroProg: a system for hydrologic forecasting in real time based on the multimodelling approach." Meteorology Hydrology and Water Management, submitted.

[2] Niedzielski, T., and B. Miziński, "Use of a novel multimodel hydrologic ensemble prediction system – Part 1: Real-time hydrograph modelling." Journal of Hydrology, submitted.

[3] Yu, D., 2005. "Two-dimensional diffusion wave modelling of structurally complex floodplains" PhD Thesis, School of Geography, University of Leeds, UK.

[4] Yu, D, and S.N. Lane, 2006a. "Urban fluvial flood modelling using a two-dimensional diffusion wave treatment, part 1: Mesh resolution effects." Hydrological Processes 20: 1541-1565.

[5] Yu, D, and S.N. Lane, 2006b. "Urban fluvial flood modelling using a two-dimensional diffusion wave treatment, part 2: Development of a sub grid-scale treatment." Hydrological Processes 20: 1567-1583.

[6] Yu., D., and S.N. Lane, 2011. "Interaction between subgrid-scale resolution, feature representation and grid-scale resolution in flood inundation modelling." Hydrological Processes 25: 36-53.

[7] Witek, M., J. Jeziorska, and T. Niedzielski, 2014. "An experimental approach to verifying prognoses of floods using an unmanned aerial vehicle." Meteorology Hydrology and Water Management 2: 3-11.

[8] Mcenery, J., J. Ingram, Q. Duan, T. Adams, and L. Anderson, 2005. "NOAA'S Advanced Hydrologic Prediction Service: Building Pathways for Better Science in Water Forecasting." Bulletin of the American Meteorological Society 86: 375-385.

[9] Zappa, M., M.W. Rotach, M. Arpagaus, M. Dorninger, C. Hegg, A. Montani, R. Ranzi, F. Ament, U. Germann, G. Grossi, S. Jaun, A. Rossa, S. Vogt, A. Walser, J. Wehrhan, and C. Wunram, 2008. "MAP D-PHASE: real-time demonstration of hydrological ensemble prediction systems." Atmospheric Science Letters 9: 80-87.

[10] Abbott, M.B., and D.R. Basco, 1989. "Computational Fluid Dynamics: an Introduction for Engineers." Longman Scientific and Technical Ltd, London, pp. 440.

[11] Liggett, J., and J. Cunge, 1975. "Numerical Methods of Solution of the Unsteady Flow Equations", In Unsteady Flow in Open Channels, Edited by Mahmood, K. and Yevjevich, V., Vol. I, Chap. 4., Water Resource Pub., Fort Collins, CO, USA, pp. 102.

[12] Bates, P.D., and A.P.J. De Roo, 2000. "A simple raster-based model for flood inundation simulation." Journal of Hydrology 236: 54-77.

[13] Smith, L.C., 1997. "Satellite remote sensing of river inundation area, stage, and discharge: a review." Hydrological Processes 11: 1427-1439.

[14] Schumann, G. J.-P., J.C. Neal, D.C. Mason, and P.D. Bates, 2011. "The accuracy of sequential aerial photography and SAR data for observing urban flood dynamics, a case study of the UK summer 2007 floods." Remote Sensing of Environment 115: 2536-2546.

[15] Westoby, M.J., J. Brasington, N.F. Glasser, M.J. Hambrey, J.M. Reynolds, 2012. "'Structure-from-Motion' photogrammetry: A low-cost, effective tool for geoscience applications." Geomorphology 179: 300-314.

[16] Niedzielski, T., 2007. "A data-based regional scale autoregressive rainfall-runoff model: A study from the Odra River." Stochastic Environmental Research and Risk Assessment 21: 649-664.

Conditional hydrological simulations as a tool for analysis of denudational transformation of post-glacial plains

Jarosław Jasiewicz
lInstitute of Geoecology and Geoinformation
Adam Mickiewicz University
Poznan, Poland
jarekj@amu.edu.pl

Jolanta Czerniawska
lInstitute of Geoecology and Geoinformation
Adam Mickiewicz University
Poznan, Poland
jolczer@amu.edu.pl

Abstract—**We propose here a new method of presentation and analysis of the morphometry of river basins developed on the postglacial lowlands. We use advanced conditional simulations based on the new tool designed to fast modeling of autocorrelated error surface and GRASS GIS hydro-geomorphological tools. We present two basins: Łupawa basin which represent very young postglacial area and Prosna basin which represent older surface, developed under preiglacial conditions. Preliminary studies show that morphometric characteristics of those two basins developed over the very similar substratum differ radically due to different developemnet conditions: Łupawa basin inherits fresh nature of postglacial surface while Prosna river has changed radically morphometry of its basin under periglacial condition during Weichselian.**

I. INTRODUCTION

Fluvial erosion is one of the most important processes which shapes the face of the Earth's surface. Unfortunately computer algorithms designed for hydro- and hydro-geomorphological modeling are designed to work on elevated areas already transformed by fluvial processes [1], leaving aside lowlands, especially the youngest surfaces which remained after last glaciations. Post-glacial lowlands, especially those in Central Europe consist of at least two types surfaces of different age: younger surface created during the last ice advance (ca. 22-14 ka BP), and older glacial surfaces originating from previous advances, remodeled under periglacial conditions [2,3] during last glacial period (ca. 110-14 ka BP). Those surfaces, developed over thick but soft glacial sediments, offer unique possibility to observe rapidly evolving lowland plains at different stages of their evolution. The morphometric characteristics will be presented as a relationship between existing channel network and extra-channel subsystem.

Despite years of research an accurate and universal method of distinguishing the overland-flow subsystem from stream-flow discharge one has not been developed. Extraction of drainage networks on lowlands is particularly difficult due to low diversity of the land surface which leads to high uncertainty of simulated models. On such areas threshold-based models usually produce equally-dense networks which arise from the fractal nature of river systems [4]. More complex methods that also utilize geomorphological components [5,6] are not sufficiently robust against small changes of the free parameters of applied models. Poor legibility of terrain forms on lowlands leads to considerable fluctuations in the drainage pattern even in the case of minor changes of input parameters. Moreover, the youngest surfaces have a very dense irregular pattern of small convex and concave forms created by sub-glacial processes. Algorithms designed to model drainage networks on mature areas usually confuse local convexity with channel heads which leads to unrealistic, very dense networks (see: [7]).

II. STUDY AREA

This paper presents a preliminary results of morho-hydrological modeling used to analyze of transformations post-glacial morainic plateaus. In order to demonstrate differences between young and old post-glacial plains, we have chosen two different drainage basins: one drains the youngest morainic plateau, and the other one has been evolving since Eemian interglacial. The first one, Łupawa River (98 km long), drains the youngest morainic plateau (Słupsk Plateau) which emerged after the main stage of the last glaciation, and has not been transformed under periglacial conditions. The second one, Prosna River (216 km long, Kalisz plateau), has a more complex history. While the first phases are identical to Łupawa's (short periglacial period at the end of Saalian Glaciation and normal cycle during

In: Geomorphometry for Geosciences, Jasiewicz J., Zwoliński Zb., Mitasova H., Hengl T. (eds), 2015. Adam Mickiewicz University in Poznań - Institute of Geoecology and Geoinformation, International Society for Geomorphometry, Poznań

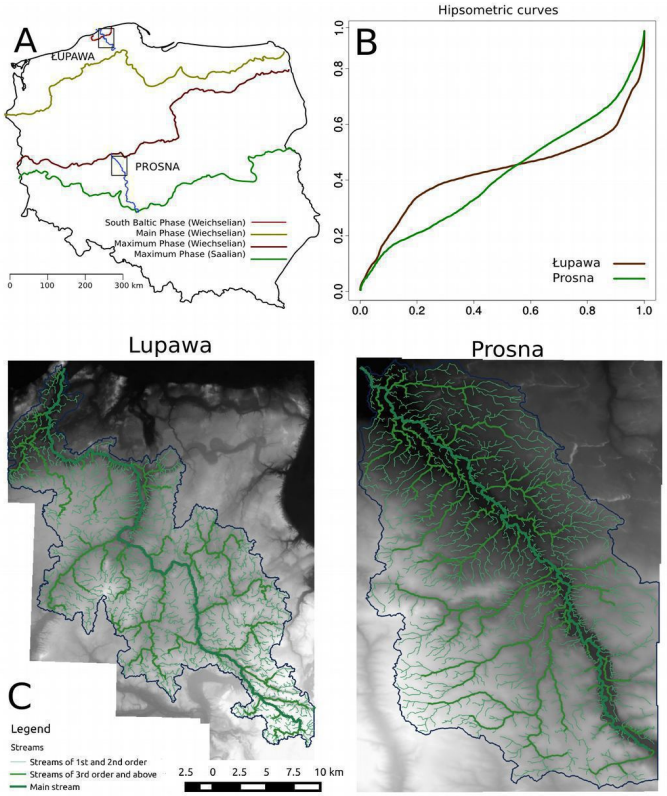


Figure 1. Study area: A) Location of testing areas; B) Hypsometric curves (area/altidude); C,D Łupawa and Prosna basins with stream network

Eemain interglacial), the main erosional phase took place under periglacial conditions during 100 ka years of Weichselian Glaciation. Analyzes were limited only to the ca. 50 km sections of both rivers which pass directly through morainic plateaus. The elevation ranges on investigated areas are also of the same order: 4-99 m a.s.l (locally up to 133 m.a.s.l) for Łupawa river and 74-160 m.a.s.l for Prosna. We assume that both rivers developed after the retreat of respective main ice sheet advances, under the same initial conditions: stable tectonic areas and thick glacial deposits underneath. For analysis we used two 5 m resolution DEM 5000x8000 cells each, created by manual digitization of 1:10000 topographic maps. Both areas are covered by more than 50 sheets of 5x8km extent.

III. METHODS

Horton's statistics is a popular and mature tool designed to quantitative description of drainage networks but, not for summarizing its geomorphometric properties of entire basin including slope subsystem. The simplest method of summarizing the geomorphology of drainage basins are hypsometric curves [8]. This method is often too general (see Fig. 1B). A usual approach to obtain more detailed information is to extract local transverse cross-sections through main axis of the basin. Unfortunately, it is difficult to generalize such data and use them to compare two (or more) separate basins. To avoid the mentioned limitations, we introduce a new approach where the overall morphometry of the investigated area is presented as average stream profile along the all watercourses which lead to the local erosional base. To obtain a network which consists of all the recognizable channel forms, including those without active flow on the terrain with high uncertainty, we employed conditional simulations that are widely applied to assess uncertainty of DEMs [9,10]. Stochastic simulations assume that the DEM uncertainty is propagated into terrain forms with manipulation of terrain data [9]. The addition or subtraction of elevation bias affects the terrain surface. If a channel form is distinct, small error (we used 1m) shall do not alter its geometry, so the channel course will remain unchanged. If a channel is poorly marked in the terrain or is just conformed, elevation bias will change the local morphometry and the stream line will be modeled at a somewhat different course. Conditional simulations require the surface error to be autocorrelated (see: [9] for in-depth discussion). The commonly used cell-swapping algorithm (Fisher, 1998) works in polynomial time. Considering at least 400 realizations for every area, it means a very long calculation time. To speed up this process, we decided to create a new GRASS GIS module: **r.random.corr** which adopts the concept from [11] designed to calculate a long-range correlation for large systems in Fourier space. It has reduced ~60 times the time needed to calculate Gaussian autocorrelated for 5000x8000 cells DEM and 30 cells autocorrelation range, in comparison with the mentioned cell swapping method.

If DEM is altered by autocorrelated error surface produces by default numerous closed depressions which are required by most of algorithms to be filled or removed. This process causes the loss of the DEM's local convexity and runs streamlines in one of eight main directions. GRASS GIS **r.watershed** [12,13] module (and following it r.stream toolbox – [7]) use an original least-cost path algorithm which do not require DEM conditioning so the error surface generally do not affect terrain convexity. At each step of the simulation we model the network with a relatively small flow accumulation threshold (25000m2), and add the result of a simulation to the probability map. After 400 realizations we have obtained a layer showing the probability (between 0 and 1) of the existence of any-order stream at a given cell (Fig. 2B).

Final networks were extracted using GRASS GIS r.stream.extract module. We have modeled networks using a product of flow accumulation map and probability map to

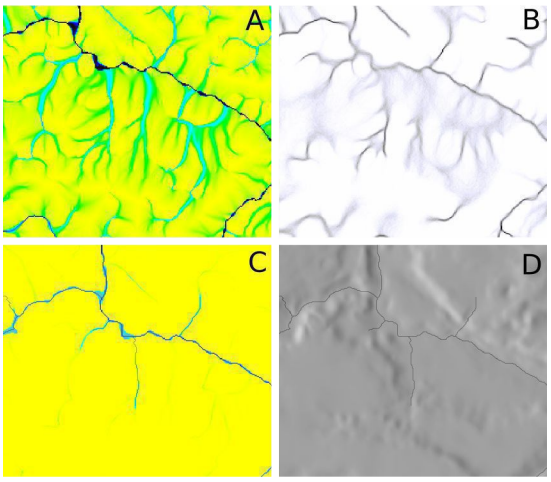


Figure 2. Steps of network modeling: A) Flow acumulation map; B) stream probablilty map; C) initiation map; D modeled streams over shaded relief

initialize channel heads while drainage system was determined using both flow accumulation and elevation surfaces (see: [7] for details). This way doubtful or fake “channels” are attenuated while those which are clearly marked in terrain remain unchanged. Using the same accumulation threshold as for probability map we reduced impact of surface specificity and extracted final networks (Fig. 1CD). Finally, with r.stream.order module, both networks were divided into three subsets: 1) first and second order streams which represents forms usually without or with limited active flow; 2) third order and above channels but without a main channel representing tributaries with active flow; and 3) main channel which represents erosional base for entire basin.

In order to produce vertical/horizontal distance profiles we calculated appropriate maps for every subset of the network using **r.stream.distance** tool. Pairs of numbers representing horizontal and vertical distance were assigned into 20m wide bins of horizontal distance while vertical distance was averaged (Fig. 3) for every bin.

IV. Discussion and conclusions

All profiles show that Łupawa and Prosna have completely different characteristics. In Łupawa basin channels of 1st and 2nd order streams are narrow (up to 200 m) and clearly incised into terrain up to 5 meters deep. Averaged profile gains maximum convexity at 400 m and shows a smooth character up to 800 m from the channel, which can be interpreted as an average extend of denudational transformation in the vicinity 1st and 2nd order channels. On the other hand 1st and 2nd order channels in Prosna basin are not marked as distinguishable terrain forms.

Different morphometric characteristics appear at the level of tributaries to the main stream (3rd order and higher). For Łupawa basin the extent of the denudational profile reaches 2000 m, due to the inclusions of subbasins of lower order. The profile in the part of the distance from stream longer than 2000 m reveals unsuitability as a result of specific properties of post-glacial surface that has not been included into the global surface discharge system yet. On the contrary, Prosna basin shows regularity up to 6000 m from stream lines. Prosna tributaries are located in shallowly incised (up to 3 m) narrow valleys which turns into a gently inclined smooth waste plain.

Profiles above the main channels show overall comparison of both basins. In Łupawa basin the main channel consists of a narrow (up to 500m) deeply incised (25m) valley, which clearly becomes an irregular moranic plateau. Local flattenings visible at the plateau (at ca. 2-3km; 4-5km; 8-10km distance from the stream) represent fragments of the older, pro-glacial outwash system adopted later by modern Łupawa, which is still well visible in terrain relief. The rest of the profile is completely random and is typical for fresh post-glacial surfaces. Prosna profile is divided into three parts: 1) main valley, 2-2.5km wide; 2) smooth, gently inclined terrace system up to 15 km range from the main channel along the watercourse; and 3) upper terraces and plateau plain. Profiles for Łupawa and Prosna converge at the distance of ~15km which allows to compare these curves to show a huge scale of transformation which took place during the periglacial period.

These preliminary, yet promising, results do not allow to draw more general conclusion about differences between young and old glacial plains now. It is required to test the proposed

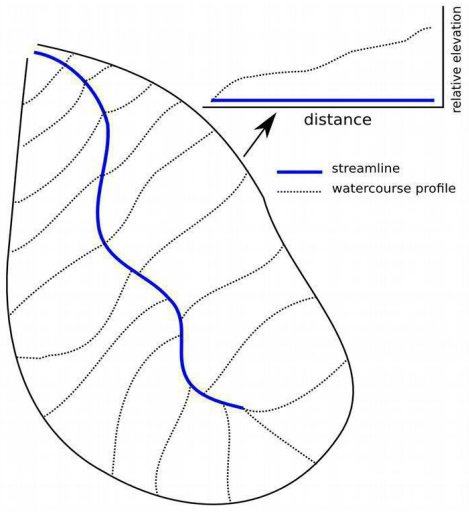


Figure 3. Stream channel and water-course profiles averaged into one resultant profile

method on a larger set of basins developed on post-glacial lowlands.

REFERENCES

[1] Mark, D. M. 1975. Geomorphometric Parameters: A Review and Evaluation. Geografiska Annaler. Series A, Physical Geography, 57, 165-177.

[2] Dylik, J., 1952. "The concept of the periglacial cycle in Middle Poland". Bull. Soc. Sci. Lettr., 3(5), 29.

[3] Rotnicki, K., 1974. "Slope development of Riss Glaciation end moraines during the Würm; its morphological and geological consequences". Questiones Geographicae, 1, 109–139.

[4] Rodriguez-Iturbe, I., Rinaldo, A., 1997. "Fractal River Basins: Chance and Self- Organization". Cambridge University Press, Cambridge, 547pp.

[5] Montgomery, D.R., Dietrich, W.E., 1992. "Channel initiation and the problem of landscape scale". Science 255, 826–830.

[6] Molloy, B.I., Stepinski, T.F., 2007. "Automated mapping of valley networks on Mars". Computers & Geosciences 33, 728–738.

[7] Jasiewicz, J., & Metz, M. 2011. "A new GRASS GIS toolkit for Hortonian analysis of drainage networks". Computers & Geosciences, 37, 1162–1173.

[8] Strahler, A.N., 1952. "Hypsometric (area-altitude) analysis of erosional topography". Geological Society of America Bulletin, 63(11), 1117.

[9] Fisher, P.F., 1991, "First experiments in viewshed uncertainty: the accuracy of the viewable area". Photogrammetric Engineering and Remote Sensing, 57, pp. 1321–1327.

[10] Lindsay, J.B., 2006. "Sensitivity of channel mapping techniques to uncertainty in digital elevation data". International Journal of Geographical Information Science 20 (6), 669–692.

[11] Makse, H., Havlin, S., Schwartz, M., & Stanley, H., 1996. "Method for generating long-range correlations for large systems". Physical Review. E, Statistical Physics, Plasmas, Fluids, and Related Interdisciplinary Topics, 53(5), 5445–5449.

[12] Ehlschlaeger, C. 1989. "Using the AT search algorithm to develop hydrologic models from digital elevation data". In: Proceedings of International Geographic Information Systems (IGIS) Symposium ’89, Baltimore, MD, pp. 275–281.

[13] Metz, M., Mitasova, H., Harmon, R.S., 2011. "Efficient extraction of drainage networks from massive, radar-based elevation models with least cost path search". Hydrol. Earth Syst. Sci. 15, 667–678

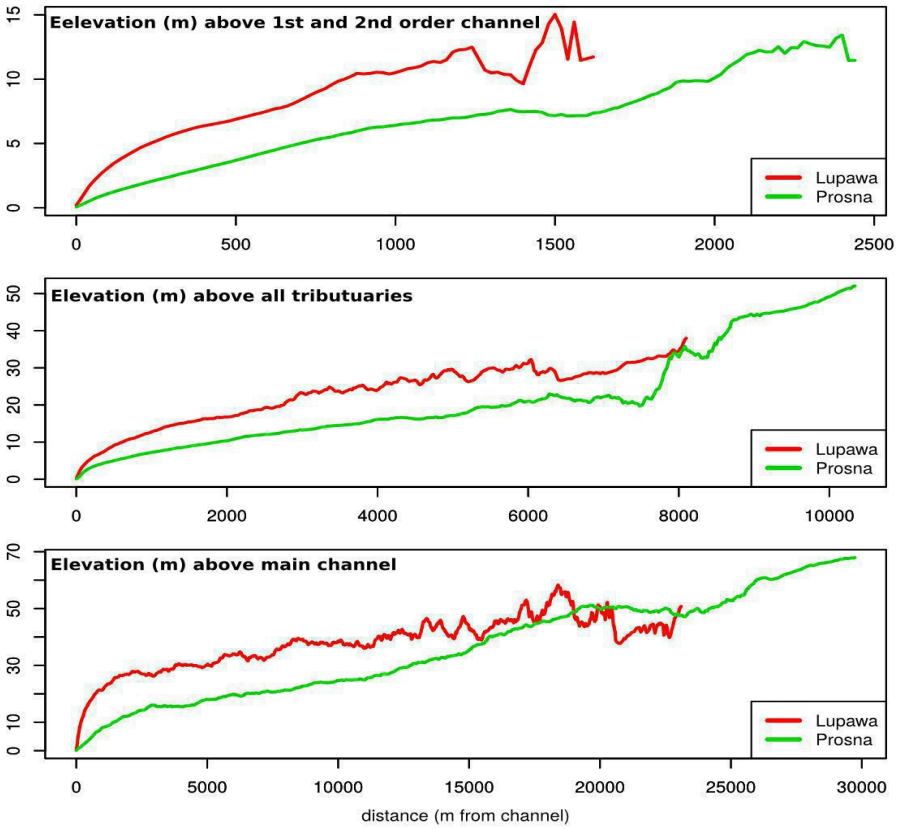


Figure 4. Profiles showing relative elevation (vertical axis) of basin surface over the streams of given order at the distance from stream calculated along watercourses.

Geomorphometry for studying the evolution of small basins: an example in the Italian Adriatic foredeep

Laura Coco, Viviana Cestrone, Marcello Buccolini
Department of Engineering and Geology
University "G. d'Annunzio"
Chieti, Italy
lauracoco@libero.it

Abstract—**The present work focused on the influence of pre-erosion slope morphometry on the arrangement and evolution of small basins in the Periadriatic belt of central Italy. *MSI* (Morphometric Slope Index) was considered as general index for slope morphometry and tested as geomorphometric driver of fluvial erosion processes. Using two DEMs with different resolution (30 m cell-size ASTER Global DEM and 10 m cell-size Italian TINITALY DEM) and *TauDEM* toolbox within ArcGIS, we automatically extracted watersheds and stream networks. We firstly proved their validity through visual investigation and statistics, and analyzed the effect of the different resolution on the morphometric parameters. Subsequently, we analyzed the influence of *MSI* on both drainage network and eroded volume through Regression Analysis and t-Student Statistics using the DEM which was proved to be the most correct. We reached the following main outcomes: (i) the slope morphometric features combined in *MSI* strongly influenced the amount of eroded material since the inception of fluvial erosion process, (ii) the drainage density was linked to *MSI* by a logarithmic trend, and (iii) this relation directly depended on lithological features of the basins due to different lithotechnical behavior of clay and conglomerate on which they were set. We proposed a further advancement of this research focused on geomorphological hazards, considering *MSI* as predictor, e.g., of landslides, and developing a model for landslides susceptibility.**

I. INTRODUCTION

Classical methods for analyzing hydrographical basins include the morphometric analysis of drainage networks and catchments through numerical indexes which consider basin area and stream length, following in the Horton's footsteps since 1945 [1]. The most used parameter for drainage networks is drainage density (*D*, as the ratio between total drainage length and basin area), which describes their evolutionary stage: a basin with high *D* is well organized therefore is at an advanced evolutionary stage in which the drainage network is fully developed, and vice versa.

As demonstrated in numerous studies, the development and setting of drainage systems are strongly influenced by the initial slope topography. Laboratory experiments demonstrated that the final arrangement of a basin is considerably different not only by varying the slope gradient [2] [3], but also its form [4]. The studies on natural basins revealed the complex relation between drainage and slope parameters. In fact, *D* can vary positively or negatively with slope gradient depending on the dominant erosion process in the watersheds (fluvial incision or landslide, respectively) [5] [6] [7] [8]. Moreover, the greater the source area, the more complex is the drainage network [9]. These studies, however, considered the slope parameters individually, resulting in partial relations with morphogenetic processes and losing the overall effect of their interactions.

In our studies [10] [11] [12] [13], we focused on the role of general slope morphometry on the erosion processes. We introduced a unique reference index for basin morphometry, named *MSI* (Morphometric Slope Index), which includes both areal and linear features, such as size, shape, inclination, length and width. It was applied on the entire drainage basin considering the initial topography prior to erosion, which was reconstructed using the heights of watershed divide by filling the fluvial incision. Its formula is:

$$MSI = R_c \cdot L \cdot A_{3D} / A_{2D} \qquad (1)$$

where R_c is circularity ratio, L is slope length, A_{2D} and A_{3D} are plane and surface area, respectively. We tested *MSI* on *calanchi* (Italian badlands) because they represent miniature models of catchments but have lithological and climate homogeneity that allows isolating morphometric factors. We demonstrated its effectiveness in determining the arrangement of stream network, the type of erosion processes and the amount of erosion.

The present work introduced the first application of *MSI* to small basins, and was aimed at revealing the influence of slope morphometry on their evolution. We chose small basins set on clayey slopes in the Adriatic foredeep of Central Italy, because they are more sensitive to the transformations of physical environment, in particular their drainage networks, but have

In: Geomorphometry for Geosciences, Jasiewicz J., Zwoliński Zb., Mitasova H., Hengl T. (eds), 2015. Adam Mickiewicz University in Poznań - Institute of Geoecology and Geoinformation, International Society for Geomorphometry, Poznań

quite homogenous geological and climatic characteristics. Combining GIS technologies and advanced statistics, we analyzed the role of general slope morphometry summarized in *MSI* on the current arrangement of drainage network and the eroded volume since the basin inception, comparing two different DEMs.

II. Geological and Geomorphological Setting

The Periadriatic belt of central Italy lies in the Plio-Pleistocene foredeep succession composed of clays in which are interposed clastic deposits with lenticular geometry and is closed on the Adriatic coast by a powerful deposit of sands, gravels and conglomerates of fluvial-deltaic or coastal environment [14]. These deposits are arranged in a NE vergence monocline as consequence of the compressive phase and the subsequent uplift started since the Pleistocene and still active [15]. This created an extensive coastal morphostructure cut from W to E by the main (cataclinal) watercourses whose corresponding valley floors are often filled by fluvial deposits [16]. Climatically, this area belongs to a temperate sub-littoral regime with scarce annual rainfall, mainly autumnal, dry summer and medium temperatures [17] that favor intense erosion processes.

III. Materials and Methods

We chose 37 small basins directly flowing in the Adriatic sea, 18 in the Abruzzo Region and 19 in the Marche Region (Tab. I). All of them were handled within ArcGIS 9.3 using two DEMs with different resolution: ASTER Global DEM (GDEM) [18] and the Italian DEM from National Institute of Geophysics and Volcanology (TINITALY) [19] [20]. The former was 30 m cell-size, while the latter was 10 m. The data were successively compared in order to analyze the effect of the different resolution on the morphometric parameters and their relations.

We extracted the drainage features of each basin for both GDEM and TINITALY using *TauDEM* (Terrain Analysis Using Digital Elevation Models) tools developed by Prof. Tarboton and freely downloadable from his website [21] [22]. We used the *Single Watershed Model* which automatically delineates stream network and watershed following a sequence of tools starting from the DEM and the outlet point shapefile. The final products were the hydrological correct stream network and watershed shapefiles, of which we calculated *D*.

For each watershed we built the pre-erosion DTM inserting the heights of current divide as Point Values in the *Topo-to-Raster* interpolation tool (Fig. 1) [11] and, on it, we calculated the pre-erosion 3D area (A_{3D}). After measuring A_{2D}, L and R_c, we calculated *MSI* using (1). Subtracting, through *Cut/Fill* tool, the current DEMs from the pre-erosion ones, we estimated the volume of eroded material (V) in each basin and computed its average value by dividing it by A_{2D} (V/A_{2D}).

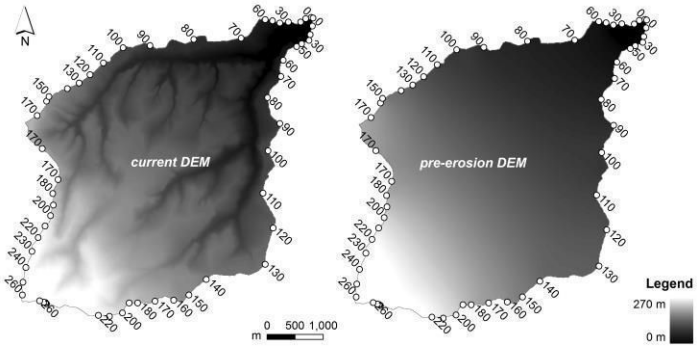


Figure 1. Example of current and pre-erosion DEMs of Acquachiara basin from TINITALY. White dots indicate some of the heights of the drainage divide used for the pre-erosion surface reconstruction through *Topo-to-Raster* tool.

Using SPSS Statistics Desktop V22.0 – trial packages, we firstly compared the two DEMs in order to test their validity and analyze the effect of different resolution on the morphometric parameters. Successively, we investigated the relations among the parameters using the DEM which was proved to be the most correct.

IV. Results

For testing the validity of the features obtained from *TauDEM* tools, we used two approaches: visual investigation and statistics. The former consisted in comparing the *TauDEM* stream networks and divides with Regional Topographic Maps (CTR). TINITALY derived features were almost perfectly coincident with CTR ones and the main nodes could be superimposed, but also GDEM gave satisfactory results although not perfectly superimposing and being reduced (i.e. shorter streams). The latter approach consisted in comparing the values of *D*, *MSI* and V/A_{2D} for the two DEMs using t-Student Statistics that showed the differences between the mean values of the variables. The one variable that showed significant differences between GDEM and TINITALY derived data was *D* ($t = 5.11$, $p < 0.05$), while *MSI* and V/A_{2D} did not show any significant differences (respectively, $t = 0.96$ and $t = 0.48$, $p > 0.05$).

In order to analyze the influence of slope morphometry on both the drainage network and the eroded volume, we performed the Regression Analysis between the morphometric variables. The interpolation functions and relative statistical quality index (R^2) were reported in Tab. II. They revealed a significant relation between V/A_{2D} and *MSI* for both GDEM ($R^2 = 0.54$) and TINITALY ($R^2 = 0.40$) derived data, as expected from the validation procedure.

TABLE I. DATABASE. THE ASTERISK (*) INDICATES BASINS WITH MAINLY CONGLOMERATE LITHOLOGY, WHILE THE OTHERS WERE MAINLY CLAYEY.

BASINS	TINITALY			GDEM		
	MSI (m)	*D* (m^{-1})	V/A_{2D} (m)	*MSI* (m)	*D* (m^{-1})	V/A_{2D} (m)
ABRUZZO						
Acquachiara *	3098	0.0017	12.39	2654	0.0020	11.57
Arielli *	3244	0.0012	20.89	2204	0.0017	21.43
Borsacchio	1730	0.0053	42.80	1573	0.0012	37.64
Buonanotte *	2337	0.0009	42.28	2026	0.0013	36.44
Calvano	3771	0.0021	88.42	3788	0.0011	82.61
Cerrano *	2272	0.0032	81.11	2139	0.0009	82.10
Feltrino *	5200	0.0013	43.19	3797	0.0015	43.47
Giardino *	1541	0.0069	27.92	1107	0.0012	27.31
Grande *	3863	0.0013	16.35	2718	0.0019	17.88
Lebba *	2765	0.0022	15.83	1905	0.0019	16.21
Mazzocco *	1487	0.0044	33.53	1274	0.0011	30.81
Moro	4744	0.0024	74.50	3500	0.0012	68.67
Osento	4833	0.0016	59.85	4260	0.0013	60.23
Piomba	4742	0.0026	106.55	3975	0.0010	95.85
Riccio *	2572	0.0022	13.81	2034	0.0020	13.05
Salinello	6209	0.0021	104.20	5161	0.0013	101.22
Vallelunga *	1552	0.0024	36.60	1418	0.0013	33.24
Vibrata	5087	0.0014	37.44	4755	0.0017	41.84
MARCHE						
Albula *	3240	0.0021	96.48	2858	0.0009	87.73
Arzilla	5362	0.0029	80.11	5374	0.0012	73.58
Asola	3285	0.0053	73.76	3022	0.0012	73.92
Bellaluce	1690	0.0069	31.47	1842	0.0014	25.22
Canale *	1460	0.0084	47.93	1487	0.0016	42.37
Caronte *	1744	0.0077	39.81	1549	0.0013	36.58
Molinetto *	1071	0.0051	44.78	1091	0.0015	40.36
Tavole *	574	0.0081	14.53	444	0.0031	11.79
San Biagio *	1542	0.0040	43.21	1474	0.0017	42.44
Sant'Egidio *	2519	0.0022	35.00	2513	0.0018	32.04
Ete Vivo	6807	0.0019	109.03	6272	0.0013	95.13
Genica	2249	0.0048	57.52	2061	0.0014	47.52
Menocchia	5387	0.0019	101.96	5155	0.0012	106.54
Petronilla	1179	0.0092	34.05	983	0.0017	28.88
Ragnola *	1726	0.0033	54.76	1870	0.0011	46.90
Rubiano	2475	0.0077	26.30	2076	0.0016	29.52
no-name *	1578	0.0065	31.74	1325	0.0013	30.53
Tesino	4666	0.0027	107.37	4478	0.0012	104.73
Valloscura	1629	0.0023	46.29	1434	0.0011	46.38

The relation between *D* and *MSI* was significant for only TINITALY derived data (R^2 = 0.48). Considering TINITALY, in the regression plot chart (Fig. 2) we individuated two main logarithmic trends, both with higher statistical significance, that corresponded to different lithological conditions: basins whose surface mainly lied on clays belonged to the upper interpolator (R^2 = 0.81; black in Fig. 2), while basins whose surface mainly lied on conglomerates belonged to the lower interpolator (R^2 = 0.60; grey in Fig. 2). The clayey basins had higher *MSI* mean value (M = 4013 m) while conglomeratic basins had lower *MSI* mean value (M = 2269 m) that were statistically different (t = 3.71, $p < 0.05$), but *D* was not statistically different (t = 0.04, $p > 0.05$). There was only one outlier (Valloscura basin) that could be included in the conglomerates series but was mainly clayey.

TABLE II. REGRESSION BETWEEN *D* AND *MSI* AND V/A_{2D} AND *MSI* FOR GDEM AND TINITALY DATA.

	INTERPOLATION FUNCTION	R^2
GDEM	$D = -0.0003 \ln(MSI) + 0.0038$	0.18
	$V/A_{2D} = 0.01\ MSI + 11.42$	0.54
TINITALY	$D = -0.003 \ln(MSI) + 0.0266$	0.48
	$V/A_{2D} = 0.01\ MSI + 17.05$	0.40

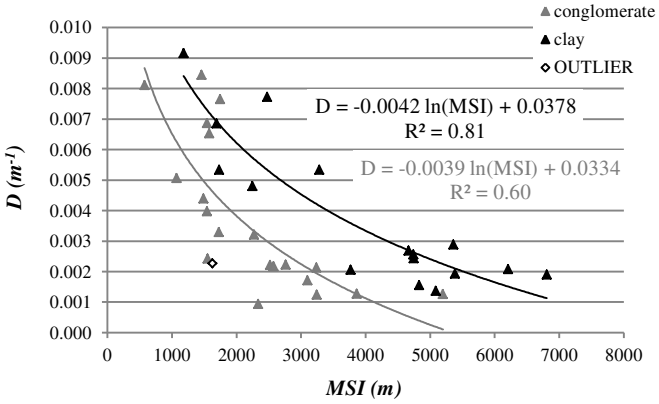


Figure 2. Regression between *D* and *MSI* of TINITALY data with distinction of basins' lithology (manly conglomerate in grey, mainly clay in back).

V. DISCUSSION AND CONCLUSION

The first application of *MSI* to small basins introduced in the present work aimed at investigating the influence of slope morphometry on their arrangement and evolution.

We used *TauDEM* toolbox, implemented for ArcGIS, to automatically derive stream networks and divides, and tested their validity. The validation procedure strengthened the effectiveness of this method for streams and divides automatic delineation, on the one hands, and the greater correctness of TINITALY for deriving stream network, on the other hands. This was mostly due to the TINITALY DEM building methods since it was built from Regional Topographic Maps that made it more precise and detailed [20]. The difference between GDEM and TINITALY derived *D* was expected considering the different DEMs' cell size in accordance with the observation made just above, while the lack of difference for *MSI* and V/A_{2D} highlighted the validity of both DEMs for deriving slope morphometric data.

The Regression Analysis between V/A_{2D} and *MSI* pointed out the influence of general slope morphometry on the amount of eroded material since the inception of fluvial erosion process. Moreover, assuming that slope morphometry influenced the erosion

processes and that their efficacy with respect to the amount of eroded material was a function of their duration, this positive relation might indicate that the basins activated approximately in the same time [12]. This issue, however, needs to be further investigated.

Furthermore, the Regression Analysis between *D* and *MSI* allowed many considerations. Firstly, although *D* was generally influenced by *MSI* regardless the lithology, the lithological characteristics had a great effect on this relation, in particular depending on the different lithotechnical behavior of clay and conglomerate. Basins set on clayey slopes had more developed drainage networks (higher drainage length) but also wider surface (higher A_{2D}) not resulting in higher *D*; moreover, they had more gentle morphology (higher *L* and lower inclination) [10] and wider surface (higher *A* and R_c) resulting in higher *MSI*. Otherwise, basins set on conglomeratic slopes had less developed drainage network (lower drainage length) but also smaller surface (lower A_{2D}) not resulting in higher *D*; moreover, they had steeper morphology (lower *L* and higher inclination) and smallest surface (lower *A* and R_c) resulting in lower *MSI*. Secondly, the Regression Analysis showed that *D* and *MSI* were linked each other by a logarithmic trend directly dependent on the lithological features of the basins, indicating that small increasing (decreasing) of *MSI* produced high decreasing (increasing) of *D*.

In conclusion, we can stress the effectiveness of *MSI* not only as general index for slope morphometry, but also as morphometric driver of fluvial processes as it represented and summarized the main slope morphometric features. It determined both the arrangement of drainage networks and the amount of soil erosion, and allowed to reconstruct the geomorphological evolution of small basins. Further advancement of this research could focus on geomorphological hazards, studying the effect of *MSI* as predictor, e.g., of landslides. At present, we are trying to develop a model for landslides susceptibility taking into account the outcomes of our present and previous researches.

REFERENCES

[1] Horton, R.E., 1945. "Erosional development of streams and their drainage basins: hydrophysical approach to quantitative morphology." Bulletin of Geological Society of America 56, 275–370.

[2] Parker, R.S., 1977. "Experimental study of drainage basin evolution and its hydrologic implications." PhD dissertation. Colorado State University, Fort Collins.

[3] Schumm, S.A., Mosley, M.P., and Weaver, W.E., 1987. "Experimental Fluvial Geomorphology." Wiley, New York, p. 413.

[4] Pelletier, J.D., 2003. "Drainage basin evolution in the Rainfall Erosion Facility: dependence on initial conditions." Geomorphology 53, 183–196.

[5] Oguchi, T., 1997. "Drainage density and relative relief in humid steep mountains with frequent slope failure." Earth Surface Processes and Landforms 22, 107–120.

[6] Tucker, G.E., and Bras, R.L., 1998. "Hillslope processes, drainage density, and landscape morphology." Water Resources Research 34 (10), 2751–2764.

[7] Talling, P.J., and Sowter, M.J., 1999. "Drainage density on progressively tilted surfaces with different gradients, Wheeler Ridge, California." Earth Surface Processes and Landforms 24, 809–824

[8] Lin, L., and Oguchi, T., 2004. "Drainage density, slope angle, and relative basin position in Japanese bare lands from high-resolution DEMs." Geomorphology 63, 159–173.

[9] Montgomery, D.R., and Dietrich, W.E., 1989. "Source Areas, Drainage Density, Channel Initiation." Water Resources Research 25 (8), 1907–1918.

[10] Buccolini, M., and Coco, L., 2010. "The role of the hillside in determining the morphometric characteristics of "calanchi": the example of Adriatic Central Italy." Geomorphology 123, 200–210.

[11] Buccolini, M., Coco, L., Cappadonia, C., and Rotigliano, E., 2012. "Relationships between a new slope morphometric index and calanchi erosion in northern Sicily, Italy." Geomorphology 149-150, 41–48.

[12] Buccolini M., and Coco L., 2013. "MSI (morphometric slope index) for analyzing activation and evolution of calanchi in Italy." Geomorphology 191, 142–149.

[13] Cappadonia, C., Coco, L., Buccolini, M., and Rotigliano, E., "From slope morphometry to morphogenetic processes: an integrated approach of field survey, GIS morphometric analysis and statistics in Italian badlans." Land Degradation & Development, *submitted*.

[14] Bigi, S., Cantalamessa, G., Centamore, E., Didaskalou, P., Dramis, F., Farabollini, P., Gentili, B., Invernizzi, C., Micarelli, A., Nisio, S., Pambianchi, G., and Potetti, M., 1995. "The Marche-Abruzzo Periadriatic belt from middle Pliocene to the present times: tectonic-sedimentary and geomorphological evolution." Camerti Geological Studies, Special Volume, 37–49. [La fascia periadriatica Marchigiano-Abruzzese dal Pliocene medio ai tempi attuali: evoluzione tettonico-sedimentaria e geomorfologia." Studi Geologici Camerti, Volume Speciale, 37–49.]

[15] Cantalamessa, G., and Di Celma, C., 2004. "Sequence response to syndepositional regional uplift: insights from high-resolution sequence stratigraphy of the late Early Pleistocene strata, Periadriatic Basin, central Italy." Sedimentary Geology 164, 283–309.

[16] Buccolini, M., Gentili, B., Materazzi, M., Aringoli, D., Pambianchi, G., and Piacentini, T., 2007. "Human impact and slope dynamics evolutionary trends in the monoclinal relief of Adriatic area of central Italy." Catena 71, 96–109.

[17] Fazzini, M., and Giuffrida, A., 2005. "A new proposal of quantitative rainfall patterns in the territory of Italy: first results." Urban Climate, City and Architecture, Acts XVIII International Symposium of Climatology, pp. 361–365. ["Une nouvelle proposition quantitative des regimes pluviometriques dans le territoire de Italie: premiers resultats." Climat Urbain, Ville et Architecture, Acts XVIII Colloque Internationale de Climatologie, pp. 361–365.]

[18] http://gdem.ersdac.jspacesystems.or.jp/

[19] http://tinitaly.pi.ingv.it/

[20] Tarquini, S., Isola, I., Favalli, M., Mazzarini, F., Bisson, M., Pareschi, M.T., and Boschi, E., 2007. "TINITALY/01: a new Triangular Irregular Network of Italy." Annals of Geophysics 50 (3), 407–425.

[21] http://hydrology.usu.edu/taudem/taudem5/index.html

[22] Tarboton, D.G., 1997. "A new method for the determination of flow directions and upslope areas in grid digital elevation models." Water Resources Research 33 (2), 309–319.

Relationships of attributes of gullies with morphometric variables

Libor Burian
Department of Physical Geography and Geoecology
Comenius University
Bratislava, Slovakia
libor.burian@uniba.sk

Andrey Vladimirovich Mitusov
Institut für Ökosystemforschung
Christian-Albrechts-Universität
Kiel, Germany
amitusov@ecology.uni-kiel.de

Jean Poesen
Division of Geography
KU Leuven
Leuven, Belgium
Jean.Poesen@ees.kuleuven.be

Abstract— **Investigations were conducted on a sample of 439 gullies at Hronská pahorkatina Hill Land in the Slovak Republic. The size of gullies was described by their area and perimeter. Morphometric variables such as altitude, slope steepness, maximal catchment area as well as maximal, minimal, mean, horizontal and vertical curvatures were determined at the start and end points of gullies. The analysis of correlation between area and perimeter of gullies has revealed the linear trend between these variables, which is the result of the definition of a shape of a gully. The frequency distribution of morphometric variables in a specific points of land surface has discovered the different behavior of morphometric variables in these points from those on land surface in general.**

I. INTRODUCTION

The issue of gully erosion stands on the border between soil science and geomorphology. The main reason of this status is that gully is a form of the land surface formed by the process of soil erosion. The process is dangerous for man and society. Therefore the cognition of the gully erosion process is crucial for restricting negative influences.

Formation and behavior of gully erosion processes and consequently formation of gullies are influenced by a group of five factors (topography, precipitation, land cover, physical characteristics of material, and linear predispositions). Topography is a limiting factor, so in case of inappropriate configuration of land surface, gully erosion does not occur. Topography is described by morphometric variables. The system of morphometric variables consists of a relatively limited group of commonly used morphometric variables (*e.g.* slope, aspect, horizontal curvature, *etc.*) and of a larger group of not so commonly used morphometric variables.

A wide range of studies is focused on the analysis of correlation between ephemeral gullies on one side and morphometric variables of slope and maximal catchment area on the other (*e.g.* [1], [2]. Numbers of studies are aimed on the use of a wide range of morphometric variables as inputs into regression modeling, *e.g.* [3], [4]. Another group of studies is aimed on the analysis of thresholds of initial conditions for gully formation. The most advanced approach is the use of morphometric variables as inputs into analytical models of gully erosion [5], [6].
Morphometric variables are usually represented in the format of raster. One of the most important attributes of this format is grid spacing. Increase of size of a smallest element means decrease in a volume of information on land surface and change in values of altitude derivatives. The latter is defined as a change of scale [7], [8]. Dependence between morphometric variables and a grid spacing is analyzed in a number of studies,*e.g.* [9], [10]. The majority of the works takes into account only morphometric variables derived from the first and second directional derivatives or the catchment area with almost identical results [11]. The dependence between grid spacing and results of analytical models is analyzed only in a limited number of works, *e.g.* [12]. The majority of works considered only the change of grid spacing in several resolutions, not in a continuous scale. This paper aims on analysis of change of values of morphometric variables in dependence on different grid spacing, which is examined in start and end points of gullies as a specific points of land surface.

The main objective of the work is to study dependence between attributes of gullies and the wide range of morphometric variables. Partial objectives are:

* Analysis of correlation between area and perimeter of gullies on larger datasets.

** Analysis of morphometric variables in start and end points of gullies and differences between attributes of land surface in these positions.

*** Analysis of dependence between morphometric variables and grid spacing in start and end points of gullies.

**** Analysis of dependence between slope and maximal catchment area in incision (start) point of gully.

In: Geomorphometry for Geosciences, Jasiewicz J., Zwoliński Zb., Mitasova H., Hengl T. (eds), 2015. Adam Mickiewicz University in Poznań - Institute of Geoecology and Geoinformation, International Society for Geomorphometry, Poznań

II. METHODS

The area of investigations, the Hronská pahorkatina Hill Land, is located in the southern part of the Slovak Republic (fig. 1). It is on the contact between a neogene quaternary river basin and a chain of hills in the north-eastern part. On the shallow base fluvial and colluvial material with different thickness can be found. The mean annual temperature of the region is 8 – 10°C, average year precipitation is 500 – 600 mm. According to Stehlík [13] the present gully formation in this region is inactive.

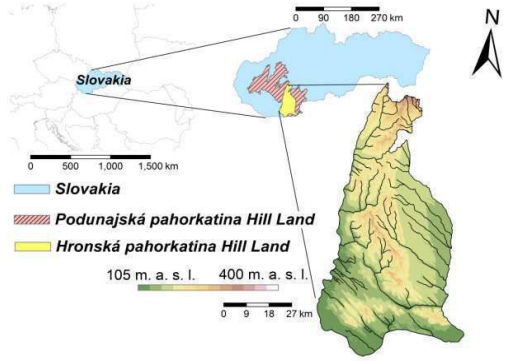


Fig. 1. Location of Hronská pahorkatina Hill Land

For the investigations the modern topographic map of the Slovak Republic 1:10 000 was used. Contour lines of this map were digitized using ArcGIS 10.0 and in the next step interpolated into a digital elevation model (DEM) with a grid spacing of 10 m. Interpolation was carried out using the algorithm *v.surf.rst* in GRASS GIS. DEMs with lower resolution were generated by eliminating rows and columns from the grid using GIS ECO [14]. For example, if grid spacing w = 10 m was to be changed to grid with spacing w = 20 m, every other row and column was removed. Totally, DEMs with a resolution from 10 m up to 100 m in a 10-meter interval were computed. Morphometric variables were computed from the generated DEMs using GIS ECO [14].

The Military topographic map 1:10 000 constructed between years 1957 – 1971 was used for construction of a database of gullies. Based on this map, gullies were digitalized using ArcGIS 10.0 into a polygon layer. Topographic information contained in this map is not as precise as topographic information contained in the topographic map of the Slovak Republic 1:10 000. Thus, the integration of all spatial datasets into one GIS system showed a positional error between the Military topographic map and the constructed digital elevation model from the topographic map of the Slovak Republic. Therefore, position of each gully was checked and corrected on the base of the DEM constructed from the topographic map. Gully positions were verified on the basis of isolines of altitude and thalwegs derived from the Military map and the digital elevation model.

The gully database was coupled into two datasets. Firstly, to the merged dataset, where complex gullies were merged into a single shape. Characteristics such as area (m^2), perimeter (m) and ratio between them were the same for the whole complex gully. Secondly, to the split dataset, where complex gullies were split and recorded as a set of simple gullies. Characteristics such as area (m^2), perimeter (m) and ratio between them were not the same for the whole complex gully. In the final datasets gullies were represented by their start and end points, see fig. 2.

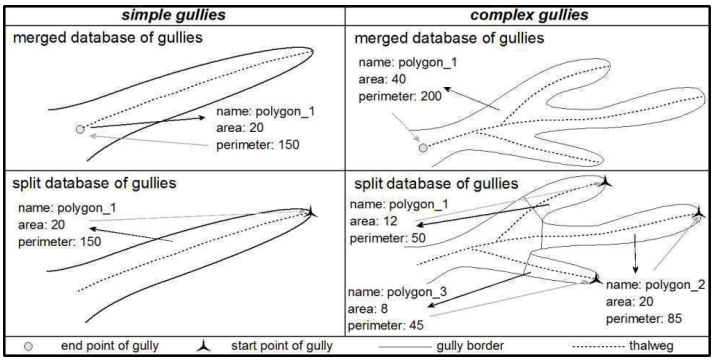


Figure 2. Differences between merged datasets and split datasets in case of simple and complex gullies.

Correlation between them was taken into account as statistically significant at $p \leq 0.05$.

Dependence between slope and maximal catchment area was analyzed using the methodology of Poesen [15]. Start (incision) points of gullies were set on a logarithmic scatter plot of slope and maximal catchment area. Cloud of points is represented by exponential function approximated on the basis of the lowest values located in the upper left part of the scatter plot.

III. RESULTS AND DISCUSSION

The ratio between perimeter and area of gullies is described by a linear trend with relatively high value of R^2 (fig. 3). Dependence between area and perimeter of gully is only mediated dependence between wide and length of gully. In the lower right part of the cloud narrow and long gullies can be found. In the upper left part wide and short gullies are located.

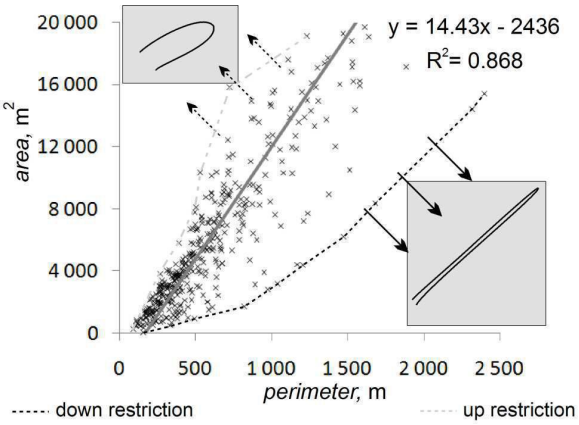


Figure 3. Ratio between perimeter and area of gullies on example of end points of gullies with additional potential shapes for extreme values. Down / up restriction is defined by the lowest / highest values of the area.

In fig. 3. is pointed out on example of dependence between area and perimeter of gully on dataset of end point of gullies. Linear trend in this figure represents the average ratio between area and perimeter, which represents the shape of a gully. Consequently, the linear trend in fig. 3 represents the potential ideal shape of a gully in the Hronská pahorkatina Hill Land. Coefficient of determination in case of trend line constructed from the database of (incision) start points of gullies is 0.80 and in case of end points 0.87. It can be assumed that this trend is dependent on the location of sampling points and the location of the database itself. There exist two possibilities of explanation.

*The common approach with another characteristic was used for many landforms as landslides [16], underwater landslides [17] or glacial cirques [18]. In this studies it was proven that correlation between some different quantitative characteristics of landforms exists. These correlations are close to a linear, logarithmic or exponential trend.

**A gully is the only form of land surface which stands between ephemeral gully and valley. Ephemeral gully is transformed to gully, which changes into valley. Both transitions are caused by erosion. Is it possible that trend will disappear in case that ephemeral gullies and valleys will be incorporated into the scatter plot. Therefore the trend is only result of a definition of shape and size of gully.

The restriction line in the lower part of the plot is conditioned by a minimal width of the gully. This minimal width depends on the gully area. But this is the only an indirect dependence between minimal width and length of the gully. It can be assumed that the lower restriction is represented by a strict border. On the other hand, the upper restriction is just a diffuse area.

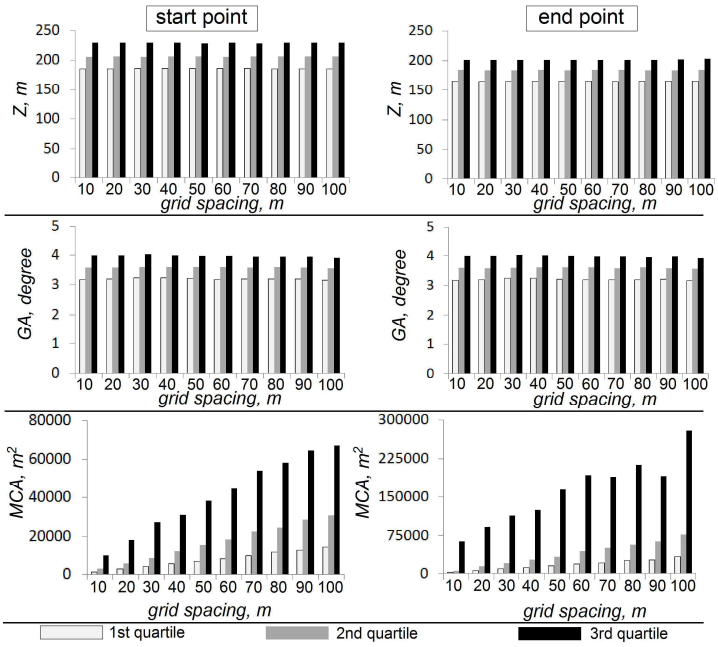


Figure 4. Quartiles for sets of morphometric variables on DEMs with different grid spacing for the dataset of start points and end points on Hronská pahorkatina Hill Land. Left – values for start point of gullies, right – values for end points of gullies, Z - altitude, GA – slope, MCA – maximal catchment area.

Only specific points of the land surface are represented by the datasets of start and end points of gullies, thus some statistical attributes of morphometric variables are different in comparison with a common land surface. On the basis of work by Shary [19] altitude and slope are scale-dependent morphometric variable and maximal catchment area is scale-free morphometric variable, which is not in an accordance with our results. It can be assumed that this is caused by the specific position of gullies on land surface in this area when gully is situated on smooth slopes with constant values of slope or in flat part of land surface, thus value of slope and altitude is almost constant for different grid spacing. Reason for increase of maximal catchment area depending of grid spacing is still unclear, however it can be assumed that this fact is caused by change of position of divide line due to change of grid spacing.

An example of the analysis of dependence between a maximal catchment area and a slope in start and end points of gullies using scatter plot is in fig. 5. The approximated line in the scatter plot provides information about resistivity of the study area against gully formation.

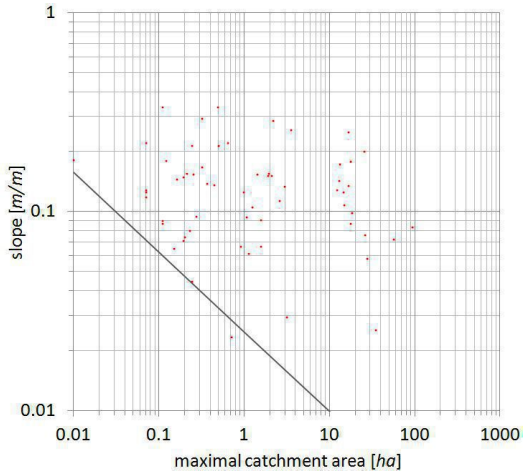


Figure 5. Example of the scatter plot of dependence between maximal catchment area [*ha*] and slope [*m/m*] for catchments forested less than 50 % for start (incision) points located in Hronská pahorkatina Hill Land. Each point represents one start point of gully. Gully located below the line is an outlier of the dataset.

During this analysis it is crucial to take into account differences between land use classes in catchments, thus resistivity of the area against gully formation varies in dependence on land use of the catchment area. This approach can be directly used for prediction position of start (incision) point of gully under different land use classes.

IV. CONCLUSION

According to the results, correlation between perimeter and area of gullies was discovered, but it can be assumed that this correlation is just a result of your definition of gully. Frequency distribution of morphometric variables in specific points of land surface is influenced by different rules than statistical distribution of morphometric variables on whole land surface. We have proven this fact only for a change of values of morphometric variables in dependence from grid spacing, however it can be assumed that there exists a higher number of similar phenomena. It was proven that the potential position of the start point of gully can be predicted using dependence between maximal catchment area and slope.

ACKNOWLEDGMENT

This work was supported by the Slovak Research and Development Agency under the contract No. APVV-0625-11.

REFERENCES

[1] Desmet, P. J. J., Poesen, J., Govers, G., and Vandaele, K. 1999. "Importance of slope gradient and contributing area for optimal prediction of the initiation and trajectory of ephemeral gullies". Catena, 37(3-4), 377–392.

[2] Daggupati, P., Sheshukov, A. Y., and Douglas-Mankin, K. R. 2014. "Evaluating ephemeral gullies with a process-based topographic index model". Catena, 113, 177–186.

[3] Conoscenti, C., Angileri, S., Cappadonia, C., Rotigliano, E., Agnesi, V., and Märker, M. 2014. "Gully erosion susceptibility assessment by means of GIS-based logistic regression: A case of Sicily (Italy)". Geomorphology, 204, 399–411.

[4] Gutiérrez, Á. G., Schnabel, S., and Lavado Contador, J. F. 2009. "Using and comparing two nonparametric methods (CART and MARS) to model the potential distribution of gullies". Ecological Modelling, 220(24), 3630–3637.

[5] Semmens, D. J. 2008. "KINEROS2 and the AGWA modeling framework". In: Wheater, H. S. Hydrological modeling in arid and semi-arid areas. Cambridge University Press, Cambridge, pp. 41 – 48.

[6] Cerdan, O., and Souchere, V. 2001. "Incorporating soil surface crusting processes in an expert-based runoff modeł Sealing and Transfer by Runoff and Erosion related to Agricultural Management". Catena, 46, 189 – 205.

[7] Shary, P. A., Sharaya, L. S., and Mitusov, A. V. 2002. "Fundamental quantitative methods of land surface analysis". Geoderma, 107, 1 – 32.

[8] Fan, W. U. 2003. "Scale-Dependent Representations of Relief Based on Wavelet Analysis", Geo-spatial information science, 5(1), 66–69.

[9] Chang, K., and Tsai, B. 1991. "The effect of DEM Resolution on Slope and Aspect Mapping". Cartography and Geographic Information Systems. 18(1), 69 – 77.

[10] Quinn, P., Beven, K., Chevallier, P., and Planchon, P. 1991. "The prediction of hillslope flow paths for distributed hydrological modeling using digital terain models", Hydrological processes, 5, 59 – 79.

[11] Thompson, J. a., Bell, J. C., and Butler, C. 2001. "Digital elevation model resolution: effects on terrain attribute calculation and quantitative soil-landscape modeling". Geoderma, 100(1-2), 67–89.

[12] Thieken, A. H., Lücke, A., Diekkrüger, D., and Richter, O. 1999. "Scaling input data by GIS for hydrological modelling". Hydrological processes, 13, 611 – 630.

[13] Stehlík, O. 1981. "Development of soil erosion in ČSR". Studia Geographica, 72, 5 – 22.

[14] Shary, P. A. 2005. "Geomorphometry and analytical GIS Eco, software description and demonstrative version". Available online at: www.giseco.info, /29. 10. 2007/

[15] Poesen, J., Torri, D. 2014. "A review of topographic threshold conditions for gully head development in different environment". Earth science reviews, 130, 73–85.

[16] Kalderon-Asael, B., Katz, O., Aharov, E., and Marco, S. 2008. "Modeling the relation between area and volume of landslides". In Report for Steering Comittee for Earthquakes, Jerusalem, Israel

[17] Hühnerbach, V., and Masson, D. G. 2004. "Landslides in the North Atlantic and its adjacent seas: an analysis of their morphology, setting and behaviour". Marine Geology, 213(1-4), 343–362.

[18] Mîndrescu, M., and Evans, I. S. 2014. "Cirque form and development in Romania: Allometry and the buzzsaw hypothesis". Geomorphology, 208, 117–136.

[19] Shary, P. A. 1995. "Land surface in gravity points classification by a complex system of curvatures". Mathematical Geology, 27(3), 373 – 390.

Reinterpretation of morphometry of headwater areas using LiDAR data in homoclinal flysch mountain ridge modelled by landslides. Case study of the Babia Góra Mt., the Western Carpathians

Adam Łajczak
Institute of Geography
Pedagogical University
Krakow, Poland
alajczak@o2.pl

Barbara Czajka, Ryszard J. Kaczka
Faculty of Earth Sciences
University of Silesia
Sosnowiec, Poland
barczajka@wp.pl, ryszardjkaczka@gmail.com

Abstract—**Basing on the data of Airborne Laser Scanning (LiDAR) the reinterpretation of relief and morphometry of headwater areas in Babia Góra homoclinal flysch mountain ridge (1725 m a.s.l.) modelled by landslides was made. The newest information source made it possible to determine the distribution of gentle relief landforms indicating the former and/or present directions of transport of colluvia. Four ways of changes in relief of headwater areas followed by changes in their morphometry were analysed. Deposition of huge volume of colluvial material in the bottoms of headwater areas increases the hazard of valley landslide movement. The development of landslides on the slopes of headwater areas is connected with headward erosion in the areas and includes – unlike other areas in the flysch Carpathians – wide range of Babia Góra ridge slope hight. This insures an extremely large load of colluvial deposits which re-model the relief of slopes and bottoms of headwater areas. The data from LiDAR made it possible to distinguish such elements of relief of headwater areas which so far have been neglected in the Polish geomorphological literature.**

I. INTRODUCTION

The aim of the paper is reinterpretation of morphometry of headwater areas at the slopes of the Babia Góra ridge (the flysch Western Carpathians) modelled by deep-seated landslides basing on the data of Airborne Laser Scanning (LiDAR) carried out in September 2012. The basis of investigations was a geomorphological map at the scale 1:5000 made in the period 1997-2007. The range and configuration of landslide tongues and lobes of various size entering the headwater areas from the higher located parts of the ridge slopes were analysed. The newest information source applied in these investigations made it possible to determine precisely the distribution of gentle relief landforms indicating the former (or present) directions of transport of colluvia. The airborne laser scanning was conducted with the accuracy of 6 points per 1 m^2 to the order of the Management of Babiogórski National Park and then available for the Authors. Basing on this information source provided by ESRI ArcGIS 9.3 software, a Digital Terrain Model was generated with resolution 1x1 m as well as a map of slope inclinations and a hillshade model map.

II. RESULTS

Babia Góra (1725 m a.s.l.) is the highest mountain ridge in the flysch Western Carpathians formed as a homoclinal asymmetric ridge 10 km long showing W-E orientation and reaching 1100 m of relative altitude. The main ridge is joined with some lower lateral

In: Geomorphometry for Geosciences, Jasiewicz J., Zwoliński Zb., Mitasova H., Hengl T. (eds), 2015. Adam Mickiewicz University in Poznań - Institute of Geoecology and Geoinformation, International Society for Geomorphometry, Poznań

ridges. The part of the ridge located above 1000 m a.s.l. is built of Magura sandstone layers dipping towards the south whereas the lower part is built of folded and less resistant sub-Magura layers. Within the northern and southern parts of the slopes, much below the ridge axis, up to 300 m deep headwater areas occur. In the northern slope the headwater areas are located below a steep cuesta of average inclination 40^o (locally 70^o) usually at the height 1100 m a.s.l. (locally 1400 m a.s.l.). In the southern slope inclined at 20^o most of the headwater areas occur at the height of 1300-1400 m a.s.l. The inclination of the headwater areas is in the range of 30^o-40^o and the inclination of their bottoms accounts to 10^o-20^o. Below the headwater areas, 150-300 m deep valleys occur which cut the mountain ridge foot.

As a result of large energy of the relief of Babia Góra and relatively poorly resistant flysch bedrock, numerous large deep-seated landslides developed which result from gravitational tectonics of highly uplifted ridge. The deep-seated landslides model the slopes of the upper part of the mountain ridge built of thick layers of Magura sandstones. The landslides represent Holocene forms of Pleistocene foundations which contemporarily do not show any activity (with some minor exceptions). The development of these landslides is controlled by the distribution of fissures in the massif of the directions NW-SE and SW-NE. The elements of landforms which commonly occur within the deep-seated landslides include ridge and slope trenches, and below, within the escarpment slopes there are rock walls and rock recesses. Below these forms the slopes are covered by thick layer of debris and block colluvia locally reaching 30 m of thickness. In such places, ramparts and irregular hummocks occur which are distributed similarly to contour-lines. Apart of them there are tongues and wide lobes distributed perpendicularly to the latter ones which go down to headwater areas. The landslide lobes in the further course of valley headwater sections function as valley landslides.

The headwater areas developed at the contact of sub-Magura layers and Magura sandstones and are located in highly located ridge slopes. These forms are present at the height where the intensity of groundwater outflow to the surface is the highest (large number of springs). Therefore in the whole area of Babia Góra ridge, the density of watercourses is the highest in the headwater areas. Slow movement of colluvia deposits in the higher located fragments of the ridge slopes as well as deepening of channels of watercourses in the bottoms of headwater areas cause local activation of landslides on the slopes of headwater areas. At present debris colluvial mantles of small thickness (about 2 m) are the most mobile, whereas thicker colluvial mantles do not show clear mobility. Morphology of landslide lobes and valley landslides, despite their contemporary dynamics, is differentiated which may indicate young age of these forms and also large hazard of landslide movements in the spring headwater sections of the valleys. There is no however any evidence which would confirm these fears apart of large landslides in two headwater areas which have activated since the 1860s.

Changes of morphology of headwater areas followed by changes in their morphometry occur as a result of dislocation of colluvial deposits in the following way:

(a) formation of narrow landslide tongues on the slopes of headwater areas → filling the bottom of headwater areas with colluvial deposits → development of narrow valley landslides → change of V-shaped cross-section of headwater areas into the cross-section of convex bottom → large hazard of further dislocation of colluvial deposits,

(b) formation of wider landslide tongues on the slopes of headwater areas → filling the fragments of bottoms of large headwater areas with colluvial deposits → development of valley landslides →

change of V-shaped cross-section of headwater areas into a cross-section of convex bottom → smaller than in (a) hazard of further dislocation of colluvial deposits,

(c) formation of wide landslide lobes on the slope of headwater areas visible as a system of connected smaller tongues → filling the entire bottom of headwater areas with colluvial deposits → development of valley landslides visible as connected landslide lobes → formation of cross-section of headwater areas with convex bottom → smaller than in (a) and (b) hazard of further dislocation of colluvial deposits,

(d) formation of two landslide tongues going down to the bottom of headwater areas from the opposite slopes → blocking up the outflow from headwater areas and filling them with slope wash deposits → cutting the landslide barrier and removing the deposited material → transport of material to further distances → formation of valley landslide → change of V-shaped cross-section of headwater area into a cross-section of flat bottom above the landslide barrier and of convex bottom below this barrier → lack of hazard of further dislocation of slope wash masses to further distances.

Only in situation (a) the landslide headwalls retreating up the hill cross the timberline, which makes the limit of snow avalanches larger and activate debris flows in large area. Deposition of material in the bottoms of headwater areas increases therefore the hazard of landslide movements in the further course of valleys. Basing on different sources of information, the process of changes in morphology of headwater areas was reconstructed.

The mechanism of development of landslides in headwater areas of Babia Góra ridge reflected in their morphology is typical for landslides from other areas described from the flysch Carpathians and other mountains. The development of landslides on the slopes of Babia Góra ridge is connected with headward erosion in headwater areas. Because of the fact that headwater areas in this ridge are located much lower than the upper range of slopes, the development of landslides includes – unlike other areas in the flysch Carpathians – wide range of slope height. This ensures an extremely large load of colluvial deposits which re-model the relief of bottoms of headwater areas. This feature of the relief of Babia Góra emphasises a unique morphology of this ridge in the flysch Western Carpathians. The data from LiDAR in the analysis of morphology and morphometry of headwater areas made it possible to distinguish such elements of the relief of headwater areas, which so far have been neglected in geomorphological literature.

ACKNOWLEDGMENT

The study was carried out as part of the grant from the Ministry of Science and Higher Education, No. NN306070640 *"Natural and anthropogenic conditions of the distribution of the upper timber limit in Babia Góra massif and its dynamics in the last 200 years"*. The authors wish to thank the Babiogórski National Park for the access given to the LiDAR survey data.

REFERENCES

[1] Łajczak, A., 2014. "Relief development of the Babia Góra massif, Western Carpathians", Quaestiones Geographicae, 33(1), p. 89-106.

[2] Łajczak, A., Czajka, B., and R.J. Kaczka , 2014. „The new features of landslide relief discovered using LiDAR. Case study from Babia Góra massif, Western Carpathian Mountains", Quaestiones Geographicae, 33(3), p. 73-84.

Automated transformation of slope and surface curvatures to avoid long tails in frequency distributions

Ovidiu Csillik
Department of Geography
West University of Timişoara
Timişoara, Romania
cskovi@yahoo.com

Ian S. Evans
Department of Geography
Durham University
Durham City, England
i.s.evans@durham.ac.uk

Lucian Drăguţ
Department of Geography
West University of Timişoara
Timişoara, Romania
lucian.dragut@fulbrightmail.org

Abstract — **Automated procedures are developed to change scales so that long tails in frequency distributions of morphometric variables are avoided. They minimize the skewness of slope gradient frequency distributions, and modify the kurtosis of profile and plan curvature distributions towards that of the Gaussian (normal) model. Box-Cox (for slope) and arctangent (for curvature) transformations are tested on nine digital elevation models (DEMs) of varying origin and resolution, and different landscapes, and shown to be effective. Our results show considerable improvements over those for previously recommended slope transformations (sine, square root of sine, and logarithm of tangent). By avoiding long tails and outliers, they permit parametric statistics such as correlation, regression and principal component analysis to be applied, with greater confidence that requirements for linearity, additivity and even scatter of residuals (constancy of error variance) are likely to be met. It is suggested that such transformations should be routinely applied in all parametric analyses of long-tailed variables. Our Box-Cox and curvature automated transformations are based on a Python script, implemented as an easy-to-use script tool in ArcGIS.**

I. INTRODUCTION

For most types of statistical analysis, it is important to check the shape of the frequency distribution of each variable. Many statistical approaches assume that the variables are normally distributed, and a violation of this assumption can lead to errors in analysis. 'Long tails' of values at either extreme or both are the main problem. This is tackled by changing (transforming) the measurement scale. Unfortunately, many environmental science publications overlook the need to apply transformation in this way.

Most slope frequency distributions have the mean and mode usually closer to 0° than to the upper limit of 90°. The lower tail is limited and the upper tail is commonly more extended, giving widespread positive skew. This is common also because, even in mountain or hill regions consisting mainly of slopes, deposition in fans, floodplains and lakes produces extra areas of low gradient, 'fattening' frequencies below the mean. Where these features are absent, however, distributions may be symmetrical or, where high relief pushes gradient toward a limiting value for slope stability, negatively skewed – with a tail extending toward lower values.

Given this natural diversity between regions, there have inevitably been different transformations proposed to rectify slope skewness [1] [2] [3]. Evans [4] favoured no single transformation, but later he inclined to use of the square root of sine [5].

For real-world DEMs, the distribution of curvatures measured in degrees per unit length is always strongly peaked at the mode of zero, and both tails are very long. The presence of extremely positive and negative values makes calculations extremely sensitive to outliers. There is less work on transformation to rectify kurtosis than on skewness: transformation of curvatures to normality is difficult, but can be achieved using a two-sided function such as the arctangent [6].

We propose general solutions to the transformation of surface derivatives, specifically slope gradient and curvatures, so that estimates of statistics such as correlation, regression, analysis of variance and principal component analysis will not be distorted by extreme values. Automated procedures are described for reducing skewness and kurtosis to the parameters of a normal, Gaussian distribution.

II. DATA AND METHODS

A. *Data used*

Tests were conducted on 9 Digital Elevation Models (DEMs) differing in spatial resolution, extent, altitude range, type and landscape. Spatial resolutions ranged from 1m to 90m. The

In: Geomorphometry for Geosciences, Jasiewicz J., Zwoliński Zb., Mitasova H., Hengl T. (eds), 2015. Adam Mickiewicz University in Poznań - Institute of Geoecology and Geoinformation, International Society for Geomorphometry, Poznań

TABLE I. DEM CHARACTERISTICS.

Test Area	Name	Spatial resolution	Method	Scene size (pixels)	Altitude range (m)	Mean altitude (m)	Region	Courtesy of
A	**Slovinec**	1 m	Photogrammetric	306 x 300	141 - 244	187	Slovakia	University of Bratislava
B	**Fishcamp**	2.5 m	LiDAR	638 x 318	1443 - 1833	1658	USA	USGS National Map seamless server
C	**Boschoord**	5 m	LiDAR	1108 x 1079	2 - 20	6	Netherlands	Universiteit van Amsterdam
D	**Țarcu Mountains**	10 m	Topo	905 x 871	1045 - 2195	1706	Romania	
E	**Ebergotzen**	25 m	Topo	398 x 398	159 - 429	272	Germany	State Authority for Mining, Energy and Geology, Germany
F	**Baranja Hill**	25 m	Topo	145 x 147	85 - 244	158	Croatia	Croatian State Geodetic Department
G	**Zlatibor**	30 m	Topo	148 x 98	851 - 1174	991	Serbia	Geodetic Governmental Authority of Serbia
H	**Apuseni Mountains**	90 m	SRTM	412 x 411	404 - 1824	1054	Romania	USGS – Shuttle Radar Topography Mission
I	**Banat Plain and Hills**	90 m	SRTM	1185 x 604	65 - 588	106	Romania	USGS – Shuttle Radar Topography Mission

spatial extent of test areas ranged between 306 × 300 m and 106.7 × 54.4 km. DEM types include photogrammetric, LiDAR, SRTM and those derived from topographic maps (Table 1). Landscape and geomorphologic characteristics vary from very low relief, mixed plain and hilly landscape, hilly areas to mountainous areas.

B. Automated normalization of LSVs

Box-Cox transformation [7] is one of the most widely used methods to transform data to approximate the bell-shaped normal (Gaussian) frequency distribution model. It identifies an exponent (lambda, λ) to which all the values should be raised in order to acquire the above-mentioned shape. This is in line with Tukey's 'ladder of transformations'. Note that for λ = 0 slope values are not raised to the power of 0 (because this would be 1 for every value) but a logarithmic transformation is applied (Table 2).

TABLE II. BOX–COX TRANSFORMATIONS: LAMBDA (λ) VALUES USED TO TRANSFORM INITIAL VALUES OF SLOPE (x, IN DEGREES) INTO POSSIBLY NORMALIZED SLOPE (*y*).

λ	−2	−1	−0.5	0	0.5	1	2
y	$1/x^2$	$1/x$	$1/\sqrt{x}$	$\log x$	$\sqrt{x}$	x	x^2

Applying the Box-Cox transformation for slope angle, the initial skewness (with λ = 1) was compared with that for λ equal to 2 or 0.5. Further, we kept the lowest skewness and compared this iteratively with the next λ value in the Box-Cox transformation scale. Thus we selected the λ to be used in the normalization of slope. To avoid an indeterminate logarithm (λ =0) or division by 0 (λ <0) we added a constant value, (1− *min*), to each value of slope prior to applying the transformations, where *min* is the minimum value of slope. This moves the minimum value of the distribution to 1°, changing only the mean, while keeping standard deviation, skewness and kurtosis.

In order to deepen the analysis, we computed three other slope rasters using formulas available in the literature (eq. 1 – [3]; eq. 2 – [6]; eq. 3 – [4]) and compared the results with those of the Box-Cox transformation:

$$\text{TransformedSlope} = \sin(\text{slope}) \quad (1)$$

$$\text{TransformedSlope} = \text{sqrt}(\sin(\text{slope})) \quad (2)$$

$$\text{TransformedSlope} = \ln(\tan(\text{slope})) \quad (3)$$

For both profile and plan curvature, the formula proposed by Evans [7] was applied:

$$\text{TransformedCurvature} = \arctan(k \times \text{curvature}) \quad (4)$$

where k is a parameter to give normalized curvature with kurtosis close to 0. Arctangent transformation preserves the sign and positive, zero and negative curvatures remains such. Long tails are pulled in symmetrically, depending on the value of k: the higher the k is, the more pulling in. The selection of k values is still a trial-and-error approach and differs from one dataset to another, depending on their characteristics. The automated workflow to select the appropriate value of k starts from $k = 0.1$. If kurtosis of transformed curvature is less than the initial kurtosis, the iteration continues until a value of k producing kurtosis close to 0 is found.

III. RESULTS

In terms of skewness, the Box-Cox transformation gave the least skewed result for all test areas except one where sine transformation gives skewness of 0.006 instead of 0.224, but here no transformation is needed any way. The log-tangent (Eq. 3) seriously over-transformed seven areas, producing negative skewness. The sine (Eq. 1) is a weak transformation and usually makes little difference. The square-root of sine (Eq. 2) over-transformed the four distributions with skewness < 0.4, but it did improve distributions for two test areas. All slope gradient distributions had |skewness| < 0.28 after Box-Cox transformation, so this can be recommended for general use even if it is not quite optimal in two test areas (Fig. 1).

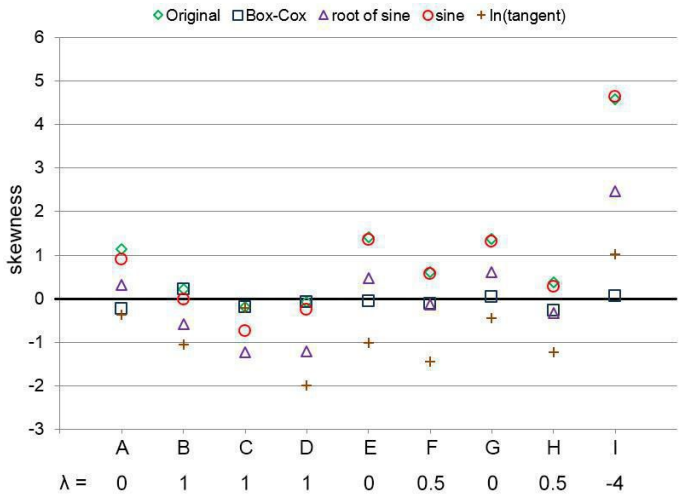


Figure 1. Comparison of skewness (vertical axis) of original slope and transformations according to different formulas for test areas A to I. Lambda (λ) values detected for Box-Cox are displayed below each test area.

For profile curvature, the initial kurtosis varies between 2.46 and 46.24: the higher the kurtosis, the sharper the mode around 0 and the longer the tails. The arctangent transformation brings in both tails, giving finite values mainly between −1.5 and +1.5. All the transformed distributions now have kurtosis values between −0.14 and 0.01, negligibly different from normality, suggesting that the automatically identified *k* values are meaningful (Fig. 2). This does not necessarily make them optimal, as other aspects of histogram shape should be considered. Use of 2*k* and *k*/2, however, showed much worse results both in kurtosis (Fig. 2) and in other aspects of shape: judged by visual inspection of histograms, the automatically selected *k* values seem optimal. The skewness is acceptable.

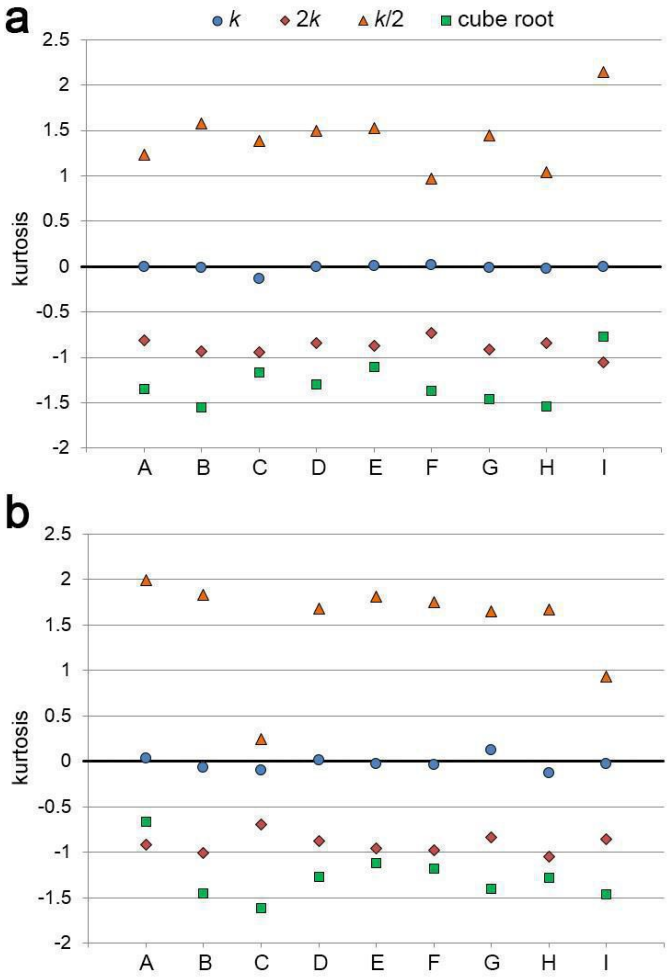


Figure 2. Kurtosis for (a) profile curvature and (b) plan curvature: values after transformation using *k* and (for comparison) after transformation using 2*k*, *k*/2 and cube root.

Depending on the size, spatial resolution and relief characteristics of each test area, the values of *k* varied between 0.6 and 46.4. Cox [8] suggested that a cube root transform would reduce kurtosis while avoiding the need to select a *k* value. For these DEMs, however, it produced bimodal histograms with negative kurtosis (Fig. 2).

Plan curvature histograms have longer tails and initial kurtosis ranges from 0.43 to 82.99. As for profile curvature, the arctangent transformation reduced the range of values to between −1.5 and +1.5, the mode is around 0 and only one test area presents important secondary modes. All the transformed histograms of frequency distribution are more nearly Gaussian, with kurtosis between −0.13 and 0.13 with *k* values between 0.1

and 3.2 (Fig. 2). The higher the kurtosis, the higher the *k* value needed for normalization.

IV. DISCUSSION AND CONCLUSIONS

We developed a Python tool to perform the transformation of slope gradient and curvatures to near-Gaussian distribution shapes. This study showed that Box-Cox transformation is effective in identifying the appropriate transform of slope gradient in a given area, so that slope skewness can be automatically rectified. The algorithm for arctangent transformation of curvatures is based on the formula proposed by Evans [6], and replaces a trial-and-error determination of a data-dependent parameter *k*, by an iterative tuning towards kurtosis close to 0. Thus, we provide a 'push-the-button' solution to prepare these surface derivatives for statistical (parametric) analysis. Use of a tool such as this is important in any terrain-based environmental analysis where slope gradient and curvatures are statistically related to other variables using parametric techniques (e.g. correlation or regression).

For further information about transformation (normalization) of slope gradient and surface curvatures, please refer to Csillik et al. [9]. The ArcGIS toolbox is available on the page: http://research.enjoymaps.ro/downloads.

ACKNOWLEDGMENT

This work was supported by a grant of the Romanian National Authority for Scientific Research, CNCS - UEFISCDI, project number PN-II-ID-PCE-2011-3-0499. We are very grateful to Nicholas J. Cox for numerous insightful comments on a draft.

REFERENCES

[1] Strahler, A.N., 1950. "Equilibrium theory of erosional slopes approached by frequency distribution analysis; Part II". American Journal of Science, 248(11), 800-814.

[2] Chorley, R.J., 1966. "The application of statistical methods to geomorphology", In: G.H. Dury (Ed.), Essays in Geomorphology. Heinemann, London, pp. 275-387.

[3] Speight, J.G., 1971. "Log-normality of slope distributions". Zeitschrift für Geomorphologie, 15, 290-311

[4] Evans, I.S., 1975. "The Effects of Resolution on Gradients Calculated from an Altitude Matrix", Department of Geography, University of Durham.

[5] Evans, I.S., 1977. "Frequency Distributions of Gradient", Department of Geography, University of Durham.

[6] Evans, I.S., 1984. "Properties of the Wessex Land Surface: An Investigation of Dimensionality and the Choice of Key Variables", Department of Geography, University of Durham.

[7] Box, G.E.P., and D.R. Cox, 1964. "An analysis of transformations". Journal of the Royal Statistical Society. Series B (Methodological), 26(2), 211-252.

[8] Cox, N.J., 2011. "Stata tip 96: cube roots" Stata J. 11 (1), 149–154.

[9] Csillik, O., Evans, I.S., Drăguţ, L., 2015. "Transformation (normalization) of slope gradient and surface curvatures, automated for statistical analyses from DEMs". Geomorphology, 232, 65-77.

The Influence of DEM Resolution on the Extraction of Terrain Texture

HUANG XiaoLi
Key laboratory of Virtual Geographic Environment, Ministry of Education
Nanjing Normal University
Nanjing, China
Xiaoli_yanyee@vip.163.com

Liu Kai
Key laboratory of Virtual Geographic Environment, Ministry of Education
Nanjing Normal University
Nanjing, China
lklkymym@163.com

Abstract—**Terrain texture is the important basis to distinguish different landform. Terrain texture analysis based on DEM has become one of the important parts of digital terrain analysis. However, the scale effect of DEM data on the terrain texture extraction has been mostly ignored in recent researches. In this paper, 6 sample areas from different landform types of Shaanxi Province were selected to make scale-effect analysis on the terrain texture by Gray level co-occurrence matrix (GLCM) model. The result shows that the parameters of slope data and hill-shading data are insensitive with the change of data resolution. Angular Second Moment (ASM) and Contrast (CON) have the strongest ability to distinguish different types of landforms.ASM is suitable for recognizing the detail terrain texture and CON is suitable for recognizing wide-range terrain texture in contrast. Our results could deepen the understanding of DEM based terrain texture and the scale effect of some other texture models will be investigated in the further study.**

I. INTRODUCTION

Terrain texture is an important type of natural texture. The existing literatures mainly focus on the terrain texture from Remote sensing data, which have been widely used for improving the methods in features extraction and land type classification. Recently, the terrain texture derived from DEM has drawn more attention, due to its purity in representing terrain surface morphology and its derivability in terrain analysis. Shruthi et al. [1] thought texture measure based on flow direction could be applied for gully identification. Tao et al. [2] proposed an improved 3D Lacunarity model based on DEM for quantifying spatial structure characteristics of terrain surface. Liu et al. [3] used the GLCM model to quantize the terrain texture from DEM in different area, and then made the landform recognition using BP neural network. It is obvious that, the terrain texture from DEM could be regarded as an important index on macro scale analysis, which overcomes the shortcomings of common pixel-based index. Furthermore, the texture analysis shows the special potential in recognition of geomorphic signatures and landform classification.

It should be noted that digital elevation model (DEM) and terrain analysis based on DEM is scale-dependent. Scale effect is a basic problem in DEM based terrain analysis and application, such as DEM error investigation, land surface parameters extraction and hydrological modeling [4-8]. However, litter research has focused on the scale effect in terrain texture analysis, in which the influence of DEM resolution could not be neglected.

The aim of this paper is to investigate the scale effect of the terrain texture extraction from DEM. In this paper, 6 parameters of gray level co-occurrence matrix model were chosen as the quantitative indices, meanwhile DEM data from 6 sample areas representing different landform types were regarded as the study data.

II. Materials and Methods

Materials

6 sample areas, with 25m cell size of DEM data representing different landform types of Shaanxi Province, China, were selected as the test area to investigate the scale effect of terrain texture extraction. The DEM data was resampled to different cell sizes ranging from 25m to 325 m with an interval of 50m using the method of bilinear interpolation in ArcGIS. The experiment datasets contain the DEM and its derivatives (slope, hill-shading and roughness). The existing research proved that the derivations parameters from DEM could also be applied for terrain analysis, hence, the datasets in this study contain not only the DEM but also its three kinds of derivations i.e., slope, hill-shading and roughness. Figure 1 shows the test datasets.

In: Geomorphometry for Geosciences, Jasiewicz J., Zwoliński Zb., Mitasova H., Hengl T. (eds), 2015. Adam Mickiewicz University in Poznań - Institute of Geoecology and Geoinformation, International Society for Geomorphometry, Poznań

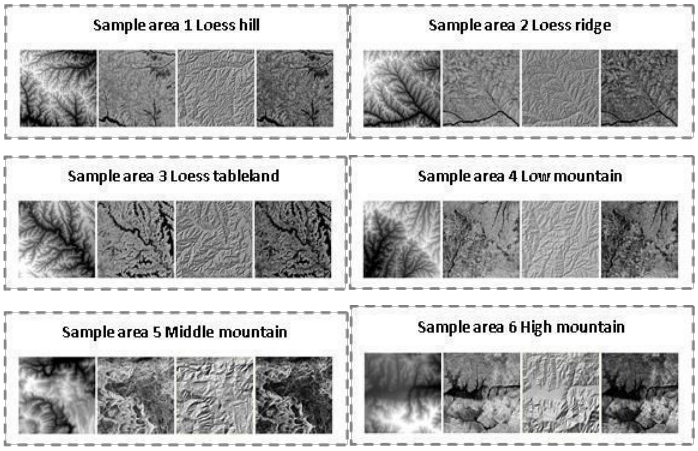


Fig.1 The test datasets of different landform types

Methods

The GLCM (Gray-level co-occurrence matrix) is a common technique in statistical image analysis that is used to estimate image properties related to second-order statistics. GLCM considers the relation between two neighboring pixels in one offset, as the second order texture, where the first pixel is called reference and the second one the neighbor pixel. GLCM is the two dimensional matrix of joint probabilities $P_{d,\theta}(i, j)$ between pairs of pixels, separated by a distance d in a given direction θ. Haralick defined 14 statistical features from gray-level co-occurrence matrix for texture classification [9] In this paper, we choose the most commonly used 6 statistical features as indices. They are Angular Second Moment (ASM), Contrast (CON), Variances (VAR), Inverse Difference Moment (IDM), Entropy (ENT) and Difference Variance (DFV). Meanwhile, according to previous researches[10], 5-pixels is chosen as the analytic distance of GLCM model, and use mean values of 4 different directions of NE, SE, SW and NW as the values of statistical features.

III. RESULTS

（1）When considering single sample area, the change rates of texture parameters with variation of the resolution are calculated. The result shows that overall mean of parameters of slope data and hill-shading data are the 2 smallest among the 4 parameters. That means slope data and hill-shading data are more insensitive with change of data resolution relatively. Table 1 shows the results.

Tab.1 Rates of texture parameters with the variation of the resolution

DEM	ASM	CON	VAR	IDM	ENT	DOV	**Overall mean**
S1	0.220	1.185	0.001	0.079	0.135	0.268	
S2	0.143	0.441	0.002	0.057	0.063	0.153	
S3	0.100	0.314	0.003	0.047	0.043	0.106	
S4	0.109	0.256	0.028	0.042	0.042	0.085	
S5	0.062	0.194	0.008	0.037	0.023	0.066	
S6	0.023	0.150	0.004	0.028	0.015	0.058	
Average	**0.109**	**0.423**	**0.008**	**0.048**	**0.053**	**0.123**	**0.128**
Slope	ASM	CON	VAR	IDM	ENT	DOV	**Overall mean**
S1	0.149	0.172	0.044	0.055	0.033	0.073	
S2	0.187	0.227	0.084	0.057	0.063	0.110	
S3	0.086	0.115	0.0004	0.038	0.027	0.050	
S4	0.013	0.010	0.033	0.005	0.003	0.012	
S5	0.029	0.039	0.016	0.014	0.008	0.020	
S6	0.062	0.039	0.035	0.004	0.016	0.041	
Average	**0.088**	**0.100**	**0.036**	**0.029**	**0.025**	**0.051**	**0.055**
Hill-shading	ASM	CON	VAR	IDM	ENT	DOV	**Overall mean**
S1	0.105	0.014	0.024	0.057	0.035	0.079	
S2	0.237	0.176	0.015	0.040	0.059	0.150	
S3	0.193	0.162	0.013	0.037	0.054	0.131	
S4	0.053	0.055	0.020	0.004	0.022	0.049	
S5	0.107	0.075	0.007	0.023	0.029	0.075	
S6	0.004	0.005	0.006	0.002	0.001	0.003	
Average	**0.116**	**0.081**	**0.014**	**0.027**	**0.033**	**0.081**	**0.060**
Roughness	ASM	CON	VAR	IDM	ENT	DOV	**Overall mean**
S1	0.318	0.408	0.287	0.056	0.249	0.151	
S2	0.373	0.746	0.480	0.096	0.331	0.201	
S3	0.109	0.240	0.125	0.037	0.078	0.087	
S4	0.019	0.031	0.009	0.002	0.0006	0.010	
S5	0.013	0.087	0.032	0.009	0.0206	0.037	
S6	0.059	0.030	0.045	0.009	0.022	0.018	
Average	**0.148**	**0.257**	**0.163**	**0.035**	**0.117**	**0.084**	**0.134**

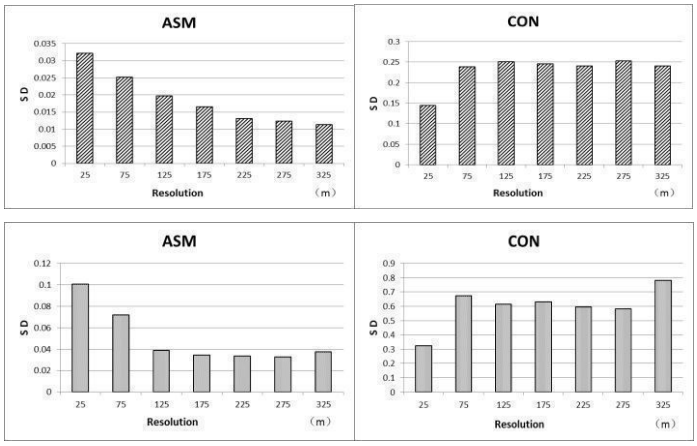
(2) While considering different types of sample areas, according to above statistics, we use variation coefficient as the index to measure original DEM data and roughness data's ability of recognition of different types of landform. The result shows the variation coefficients of ASM and CON are the 2 biggest among the 6 parameters. Table 2 shows the results.

Tab.2 Variation coefficients of texture parameters with the variation of resolution.

DEM	ASM	CON	VAR	IDM	ENT	DOV
25	0.249	0.485	0.183	0.077	0.079	0.231
75	0.268	0.414	0.202	0.094	0.066	0.185
125	0.240	0.337	0.205	0.086	0.052	0.148
175	0.216	0.281	0.206	0.076	0.046	0.124
225	0.182	0.242	0.205	0.068	0.039	0.110
275	0.182	0.226	0.209	0.065	0.038	0.109
325	0.171	0.199	0.208	0.060	0.032	0.099
Average	**0.216**	**0.312**	**0.203**	**0.075**	**0.050**	**0.144**
Roughness	ASM	CON	VAR	IDM	ENT	DOV
25	0.431	0.464	0.274	0.103	0.220	0.234
75	0.483	0.514	0.328	0.148	0.205	0.308
125	0.401	0.328	0.561	0.123	0.142	0.255
175	0.302	0.369	0.244	0.115	0.114	0.213
225	0.310	0.327	0.233	0.115	0.108	0.211
275	0.300	0.315	0.231	0.111	0.102	0.191

Average	**0.366**	**0.391**	**0.312**	**0.120**	**0.147**	**0.234**

(3)Additional, we calculated the standard deviations of ASM and CON with change of data resolution. The result shows below (Figure.2)



(The above 2 pictures are results of DEM; the under 2 pictures are the results of roughness)

Fig.2 Standard deviations of ASM and CON with change of data resolution

IV. CONCLUSIONS

(1) The result shows that parameters of slope data and hill-shading data are the most insensitive with change of data resolution. That means the texture characteristics of these two kinds of data are enhanced compared with original DEM data to some extent, therefore strengthen the structural features of the image and make them relatively not easily affected by the change of resolution.

(2) The value of variation coefficient of ASM and contrast are the biggest among the six parameters in the model, showing that ASM and contrast have the strongest ability to distinguish different types of landforms.

(3) ASM has relatively high scale-dependent and its distinguish ability declines dramatically with the change of data resolution (the values of standard deviation change from 0.032 to 0.011 and 0.101 to 0.038), which means ASM is suitable for recognizing the detail terrain texture. On the contrary, the ability of CON to distinguish landforms experienced an increase trend from 25 m to 325 m resolution (the values of standard deviation change from 0.145 to 0.241 and 0.325 to 0.783), and it has relatively low scale-dependent indicating its better adaptability in coarse resolution.

ACKNOWLEDGMENT

This work was supported by the National Natural Science Foundation of China (41171320, 41401440) and the Foundation of Graduate Innovation Plan of Jiangsu Province (KYLX_0701). The authors express their great thanks to everyone who have helped in the writing of this article.

REFERENCES

[1]Shruthi, R.B.V., Kerle, N., Jetten, V. Object-based gully feature extraction using high resolution imagery. *Geomorphology*. 2011(134), 260–268.

[2]Tao, Y., Tang, G., J. Strobl, et al. Detecting spatial pattern characteristics of terrain texture based on 3D Lacunarity Model. *Chinese Geographical Science*, 2012, 22(1):88-96.

[3]Kai Liu, Guoan Tang, Shen Jiang. Research on the classification of terrain texture from DEMs based on BP neural network[C], *Geomorphometry 2013*, Nanjing, 2013.

[4]Jun L. Spatial-scaling Effect of DEM on the Simulation of Spatial Distribution of Temperature in Mountain Area[J]. *Journal of Mountain Science*, 2012.

[5]TANG Guo'an ,LIU Xuejun, FANG Liang, et al. A review on the scale issue in DEMs and digital terrain analysis[J].*Geomatics and Information Science of Wuhan University*. 2006, 31(12): 1059-1066.

[6]LIU Xue-jun,LU Hua-xing,REN Zheng.et al. Scale issues in digital terrain analysis and terrain modeling[J].*Geographical Research*. 2007,26(3): 433-442.

[7]Chow, T. Edwin, and Michael E. Hodgson. Effects of lidar post-spacing and DEM resolution to mean slope estimation. *International Journal of Geographical Information Science* 23.10 (2009): 1277-1295.

[8]Barrios, M., and F. Francés. Spatial scale effect on the upper soil effective parameters of a distributed hydrological model. *Hydrological Processes* 26.7 (2012): 1022-1033.

[9]Haralick R M. Statistical and structural approaches to texture[J].*Proceedings of the IEEE*.1979,67(5):786-804.

[10]Ulaby F T, Kouyate F, Brisco B, et al. Textural infornation in SAR images[J]. *IEEE Transactions on Geoscience and Remote Sensing*, 1986, 24(2): 235-245.

Relief Index (RI) as a simple tool for geomorphometry

Bartłomiej Szypuła
University of Silesia, Faculty of Earth Sciences,
Department of Geomorphology
Bedzinska 60, 41-200 Sosnowiec, Poland
e-mail: bartlomiej.szypula@us.edu.pl

I. INTRODUCTION

Common availability of LiDAR data - high-quality digital elevation data, with a vertical accuracy of approx. 0.15 m and horizontal resolution of approx. 0.5 m makes, that very precise geomorphometric calculations of the relief (or microrelief) of different areas becomes possible. This work is part of the current research tendency related to find some kind of indicator which can quantitatively describe the diversity of the surface relief. Sometimes in geomorphology were used terms as relief intensity or energy of relief (Szczepankiewicz 1948, Szumowski 1967, Grygorenko 1973, Richling 1973, Kaulfuss 1974, and others) or elevation-relief ratio (Pike, Wilson 1971) based mainly on the relative heights, slopes, or the number of depressions. Relief Index (RI) is a simple mathematical tool which characterizes the quantity of relief. This index is based on the ratio of the summary length of the contour lines and the surface area at which they occur.

II. DATA MATERIAL AND METHODS

The primary research material were ASCII GRIDs data with 1m horizontal resolution, which are derived from LiDAR data types. From these ASCII GRIDs 1m-contour lines were generated, and then results were filtered by removing the contour lines of less than 3m length (3m is the length threshold of the biggest circle in 1m x 1m square - accurately 3.12 m). The basic calculation field was a square of 10m x 10m. The results represented the average total length of contour lines per each $1m^2$ of the basic field area ($100m^2$). The total length of the contour lines pays attention to two aspects of the relief: 1. relative heights (the number of contour lines and the distance between them), 2. horizontal curvatures (length of the contour lines and sinuousity connected with it). The results show the degree of diversification (or complication) surface relief, ie. character of the surface.

III. STUDY AREAS

Application of Relief Index was describing using three areas of variable relief. Each study place had area of approx. 47 km^2 (6.7 km x 7.0 km).

Interest has covered three different areas, which were analysed: the Silesian Upland, Czestochowska Upland and the Tatra Mountains. Silesian Upland is a typical upland landscape, with gentle ridges and hills of 30-70 m (building of middle-triassic dolomites) and broad river valleys (filled with pleistocene sands and gravels). Czestochowska Upland is a karst area (formed by the upper-jurassic limestones and holocene sands and clays) with numerous karst outliers on the surface. Tatra Mountains are alpine high-mountains landscape, with large relative altitudes (> 1000 m) and very steep walls (> 80°), built of paleozoic granitoids and quaternary sands, gravels and rock rubbles.

IV. RESULS

Results show that in areas of low relief (Silesian Upland - height st.dev <20m) Relief Index takes values from 0.0 to 1.5 and mean value about 0.1. Relief Index results are very homogeneous (st. dev. 0.10). It nearly corresponds with slopes and local relief - so it seems be good quantity measure which describes diversification of surface relief. As one can see in TAB. 1 - Relief Index values rise with local relief and slope values. For high-mountains relief (Tatra Mountains) values of Relief Index are very high - almost 30 (sic!). This large effect is for places with slope values more than 80 degrees. Moreover these results of Relief Index also refer to slopes: correlation coefficient for the Silesian Upland was amounted to 0.64, for Czestochowska Upland to 0.54 and for Tatra Mountains to 0.82.

Basic morphometric statistics (for hyspometry, slopes, and the Relief Index results) shows the TAB. 1.

In: Geomorphometry for Geosciences, Jasiewicz J., Zwoliński Zb., Mitasova H., Hengl T. (eds), 2015. Adam Mickiewicz University in Poznań - Institute of Geoecology and Geoinformation, International Society for Geomorphometry, Poznań

TABLE 1. Statistics of heights, slopes and Relief Index values of study areas

Study Area	Heights [m a.s.l.]				Slopes [°]				Relief Index [m/m^2]			
	min	*max*	*mean*	*SD**	*min*	*max*	*mean*	*SD*	*min*	*max*	*mean*	*SD*
Silesia Upland	238.4	381.5	272.9	14.6	0.0	37.2	2.7	2.8	0.0	1.35	0.09	0.10
Częstochowska Upland	329.2	457.9	389.8	24.4	0.0	54.2	4.4	3.1	0.0	3.91	0.10	0.09
Tatra Mountains	1021.0	2388.4	1694.6	246.2	0.0	83.6	30.0	15.0	0.0	29.48	0.71	0.58

SD - standard deviation

V. CONCLUSIONS

Relief Index is a simple and good quantitative measure shows the degree of differentiation surface relief of the area. The total length of the contour lines occured on the surface unit (here: 1m^2) clearly reflects the nature of the surface. In addition, Relief Index has a high correlation with slopes (from 0.54 to 0.82), especially in the areas with the high altitude, where the slopes are the dominant morphometric feature of the landscape. Relief Index can be used to compare the amount of the relief of different areas with each other or in the same area for different time moments (if we only provided with suitable reference material). Elementary data for Relief Index indicator must be given the highest quality elevation data (from the laser scanning LiDAR), because only such data provide adequate quality (mainly vertical accuracy). Relief Index indicator can also be used in presently glaciated areas because the glacier is a system with dynamically changing of the surface geometry.

REFERENCES

[1] Grygorenko W., 1973. Numerical criteria of assessment of cartographical image value. Polski Przegląd Kartograficzny 5, 3: 117–125. [in polish]

[2] Kaulfuss W., 1974. Darstelungsmetode und Anwendungsmoglichkeiten eines Kartogramms Reliefenergie fur den Bezirk Dresden. Petermanns Geogr. Mitteilungen. Dresden. Heft 4, 13.

[3] Pike R.J., Wilson S.E., 1971. Elevation − relief ratio, hypsometric integral and geomorphic area − altitude analysis. Geol.Soc.Am.Bull. vol.82. p.1079-1084.

[4] Richling A., 1973. About of ways of relief showing in young-glacial areas. Przegląd Geograficzny XLV, 1: 109–117. [in polish]

[5] Szczepankiewicz S., 1948. Relief intensity of Wałbrzych landscape. Prace Wrocławskiego Towarzystwa Naukowego, ser. B, 8: 23 pp. [in polish]

[6] Szumowski A., 1967. Development of main trends in morphometry. Czasopismo Geograficzne XXXVIII,1: 37–54. [in polish]

A Method of Automatic Topographic Recognition Based on Slope Spectrum

Liu Shuanglin
Key laboratory of Virtual Geographic Environment, Ministry of Education
Nanjing Normal University
Nanjing, China
liuslin28@163.com

Li Fayuan
Key laboratory of Virtual Geographic Environment, Ministry of Education
Nanjing Normal University
Nanjing, China
li_fayuan@sina.com

Abstract—**Slope spectrum is an effective method of reflecting macro terrain feature with the quantitative micro-terrain-factor, slope, which has been attracting more and more attentions in the geomorphology research area. In this paper, a method of automatic topographic recognition based on slope spectrum was proposed. First, characters of slope spectrum derived from DEM is extracted as quantitative factors to describe terrain feature. And then, this method using BP neural network model to automatically recognize landforms from DEM data quickly and accurately, according to characters of slope spectrum. In this paper, eight sample areas from different landform types of Shaanxi Province in China are selected to test this method. As is shown in experimental results, the recognition rate is 70% on average and the best combination of terrain feature factors are found out in sample areas, which shows a great potential in landform recognition.**

INTRODUCTION

Automatic topographic recognition play an important role in the landscape classification and recognition research. Compared with the traditional artificial recognition methods, the accuracy of automatic topographic recognition is more stable without the influence of prior knowledge and work experience. The method is widely used in geomorphology indexing, digital cartography, massive data filtering and other fields. Previous studies have developed many recognition and classification method over times. Hammond [1] and Collins [2] discussed different algorithms that recognize landforms with slope and aspect. And these algorithms were implemented automatically by Dikau [3], because of the development of computer technology, Brabyn [4] and Morgan [5] reprogrammed his work latter. Some methods are proposed to recognize specific landforms. For example, Barbanente [6] developed a method for automatically recognizing ravines and cliffs. Later, the Digital Elevation Models (DEMs) as the major information source in describing morphological surfaces, is widely applied in the automatic topographic recognition. Many researchers extracted some parameters of landform from DEMs and put forward some new algorithms to extract more complex landforms [7,8,9].

Slope spectrum is an effective method which can well describe terrain feature of loess landforms in China based on the micro quantitative terrain factors, slope. Some prior research works [10, 11] show that every landform could find its corresponding slope spectrum, which is unique and is capable of reveling corresponding landform type. Based on former research, slope spectrum is investigated in automatic topographic recognition.

In this paper, back-propagation (BP) neural network is applied to automatically recognize different types of geography based on slope spectrum. The outline of the article is as follows: Section 2 introduces the study area and the method of landform recognition. In section 3 the paper provide the experimental results and analysis. Finally, Section 4 summarizes the work and concludes the paper.

MATERIALS AND METHODS

Study areas and data

Eight sample areas from different landform types of Shaanxi province in China are selected to test the new method proposed in this paper. Each study area is divided into eight basins as test sample areas. DEM data in this research is from the contours of 1:50000 topographical maps and produced by the National Geomantic Center of China with a spatial resolution of 25m. Shaanxi province 1:300 million landform zoning map is selected as a landform type reference. The study area is shown in Figure 1.

In: Geomorphometry for Geosciences, Jasiewicz J., Zwoliński Zb., Mitasova H., Hengl T. (eds), 2015. Adam Mickiewicz University in Poznań - Institute of Geoecology and Geoinformation, International Society for Geomorphometry, Poznań

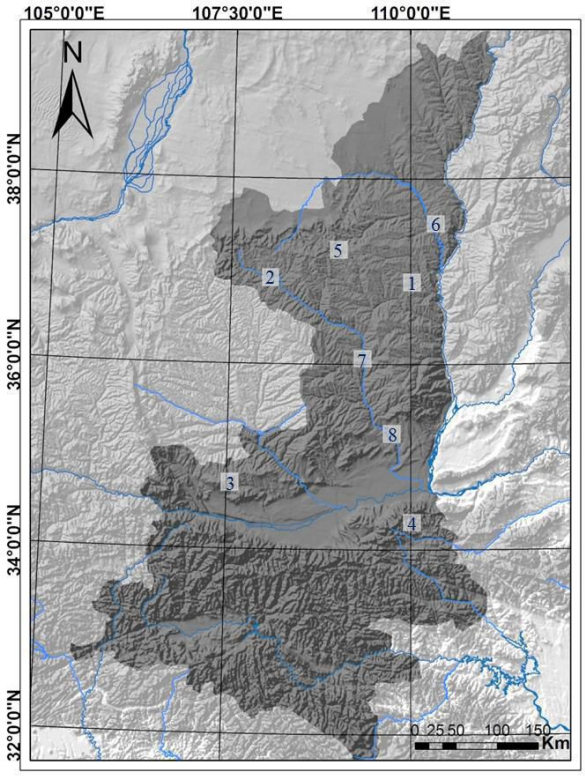


Figure 1. Study areas (1. Loess Flat-topped Ridge 2. Loess Ridge 3. Low Mountain 4. High Mountain 5. Loess Hilly-gully 6. Loess Hill-ridge 7. Loess Tableland 8. Loess Terrace)

Methods

1. Extraction of slope spectrum based on DEM

The slope spectrum is defined as a statistic graph or a mathematical model with its X-axis denoting the numerical value of the slope factors and its Y-axis is the corresponding area on the ground in a specific statistic area. The study area is in the loess plateau in China where terrain is mainly sharped by runoff erosion. And the basin is a hydrologic unit formed naturally where the exchange of energy and information is relatively independent. As a result, the graphical feature is similar inside the basin. It is advantaged to be used as a statistic area in slope spectrum for its geographical self-similarity. The method is implemented via the following steps. First, extracting basin and calculating basin area. Ten of them are selected as sample areas, each one of which is larger than thirty square meters. Second, equal interval classification of three degree is used to analysis of slope statistics in basin based on previous works.

2. Quantitation of slope spectrum

Slope spectrum parameters are acquired by quantifying slope spectrum, which are the basis of further research. The features of slope spectrum are quantified from four aspect, including information theory, statistics, morphology and landscape ecology. Not only does the quantitative characteristics describe the relations of slope combination, but also reveals the relations of space structure. As shown in Table 1, the parameters and the physical significance is redefined according to slope spectrum.

Table 1. Slope spectrum parameter

Parameter	Formula	Physical Significance
Slope Spectrum Information Entropy	$H = -\sum_{i=1}^{m} P_i \ln P_i$	Describe the degree of frequencies difference of each group of data.
Slope Spectrum Skewness	$S = \sqrt{\frac{1}{6n}\sum_{i=1}^{n}\left(\frac{P_i - \bar{P}}{\sigma}\right)^3}$	Describe the asymmetric distribution of the slope data.
Mean Slope Spectrum	$X = \frac{\sum_{i=1}^{n} X_i}{n}$	Describe the average value of slope spectrum.
Slope Spectrum Standard Deviation	$\sigma = \sqrt{\frac{1}{N}\sum_{i=1}^{N}(X_i - \mu)^2}$	Describe the dispersion degree of slope spectrum.
Termination Slope	$P_{max} = MAX(P_1, P_2 \ldots)$	Describe the maximum achievable of slope spectrum.
Patch Density	$PD = n_i * 10000 * 100/A$	Describe the fragmentation slope grading and composition.
Mean Patch Area	$AREA_{MN} = \sum_{j=1}^{n} a_{ij}/n_i$	Describe the complexity of slope classification patch shape.
Slope spectrum Aggregation Index	$AI = \left[\frac{g_{ii}}{max \rightarrow g_{ii}}\right] * 100$	Describe the reunion degree of slope spectrum in different slope classification.

3. Establishment of BP model

BP network is basically a gradient decent algorithm designed to minimize the error function in the weights space. During training of the neural network, weights are adjusted to decrease the total error. In principle, it has been proved that any continuous function can be uniformly approximated by BP network model with only one hidden layer. So a three-layer BP model is employed in our study. In this paper, the input neurons are slope spectrum parameters and the corresponding geomorphic types. The output neurons numbers are eight which depends on the classification categories.

EXPERIMENT AND ANALYSIS

In this paper, BP neural network is applied to recognize the topographic categories. Each study region contains 10 sample area in which six sample areas are selected as training sample areas to construct the recognition network. The rest four sample areas are chosen to combine with others as the test samples. This experiment includes three tests. Test 1 is consist of eight study areas, which mixed 32 sample areas, and separately identified each landform. Test 2 and Test 3 are used seven study areas, loess hilly-gully and loess hill-ridge are respectively excluded.

By using the above method to construct the automatic topographic recognition, the accuracy is shown in Table2. The accuracy means the percentage of correctly identified sample of total number of samples. The result shows that accuracy is 70% (kappa of 67.9%) in total samples, but loess hilly-gully and loess hill-ridge have poor recognition accuracy. The other two experiments are used to verify the poor recognition accuracy caused by the similarity between loess hilly-gully and loess hill-ridge, which show better result. The recognition accuracy is up to 85.7% and 92.8% respectively, and kappa coefficient is about 87%.

Table 2. Recognition accuracy

Type \ Accuracy	Test 1	Test 2	Test 3
Loess Tableland	100%	100%	100%
Loess Terrace	75%	100%	100%
Loess Flat-topped Ridge	100%	100%	100%
Loess Ridge	75%	25%	100%
Loess Hilly-gully	25%	--------	50%
Loess Hill-ridge	0%	75%	--------
Low Mountain	75%	100%	100%
High Mountain	100%	100%	100%
Total	70%	85.7%	92.8%

Recognition varies with parameter changes. The accuracy reaches the peak when using six parameters (slope spectrum information entropy, slope spectrum skewness, mean slope spectrum, slope spectrum standard deviation, termination slope、patch density) and it could be regarded as the optimal parameter combination.

CONCLUSIONS

The method of automatic topographical recognition was proposed in this paper to solve the problem of automatic identification of loess landform types. Slope spectrum and BP neural network are used in this method. It reduces the influence of subjective factors in landscape identification and proves the good correspondence between slope spectrum and loess landform. Accuracy of this experiment is 70%, but it increased to 80% when loess hilly-gully and loess hill-ridge are respectively excluded. Loess tableland and loess flat-topped ridge get the highest recognition accuracy landform in this experiment. Slope spectrum is hard to describe the difference between loess hilly-gully and loess hill-ridge under the conditions of this experiment scale. The average correction rate of recognition in test1 is lower than which in test2 and test3 because the recognition model can't distinguish loess hilly-gully and loess hill-ridge. The result shows that slope spectrum can effectively describe and recognize the characteristics of terrain surface. This method could be seen as a new trial for the quantification and recognition of landforms. Considering the complexity of actual terrain, remote sensing data and other multiple geo-data will be used to improve the landform recognition with this method in the future research.

ACKNOWLEDGMENT

The research is supported by National Natural Science Foundation of China (Key Project NO. 41171299, 41271438). The authors express their great thanks to everyone who have helped in the writing of this paper.

REFERENCE

[1] Hammond E H, 1964. Analysis of Properties in Land form Geography: an Application to Broad‐Scale Land Form Mapping. Annals of the Association of American Geographers. 54(1): 11-19.

[2] Collins S H, 1973. Terrain parameters directly from a digital terrain model. Publication of: American Congress on Surveying and Mapping.

[3] Dikau R, Brabb E E, Mark R M, 1991. Landform classification of New Mexico by computer. US Department of the Interior, US Geological Survey.

[4] Brabyn L, 1998. GIS analysis of macro landform. Proceedings of the spatial information research center's 10th colloquium.35-48.

[5] Morgan J M, Lesh A M, 2005. Developing landform maps using ESRI'S Model-Builder. ESRI International User Conference.

[6] Barbanente A, Borri D, Esposito F, et al.1992. Automatically acquiring knowledge by digital maps in artificial

intelligence planning techniques. Theories and Methods of Spatio-Temporal Reasoning in Geographic Space. Springer Berlin Heidelberg. 379-401.

[7] Jun X，Yueting Z，Fei W,2003. Recognition and Retrieval of 3D Terrain Based on Level of Detail and Minimum Spanning Tree. Journal of Software. 15(04): 1955-1963.

[8] Zengpo Z，Weiming C，Chenghu Z, et al,2009. Extraction of Volcanic Landform Information Basedon DEM Data. Journal of Geo-Information Science. 31(04): 773-777.

[9] Weichao C，Heping T, Kong Bo Liu，A Yuquan Road, et al,2011. Topographic Automatic Recognition Based on Optimal Topography Feature Space—Taking Southwest China as an Example. 36(11): 1376-1380.

[10] Fayuan L, Guoan T, Qini J, et al, 2007. Scale Effect and Spatial Distr ibution of Slope Spectrum' s Information Entropy. Geo-Information Science. 9(04): 13-18.

[11] Chun W, Guoan T, Fayuan L, et al, 2007. Fundamental Conditions of Slope Spectrum Abstraction and Application. Scientia Geographica Sinica. 27(04):587.

Finding the Best Combinations of Terrain Attributes and GIS software for Meaningful Terrain Analysis

Vincent Lecours, Alvin Simms, Rodolphe Devillers, Evan Edinger
Department of Geography
Memorial University of Newfoundland
St. John's, Canada
vlecours@mun.ca

Vanessa Lucieer
Institute for Marine and Antarctic Studies
University of Tasmania
Hobart, Australia

Abstract—**Tools that derive terrain attributes from digital elevation models are common in geospatial software. Their accessibility permits applying geomorphometric techniques to a wide range of applications. These tools however, can be considered "black boxes" where the analysis and comparison of the internal workings of the technique are vague and cannot be assessed. Selecting the most effective set of tools for a given task can thus be challenging. This work presents a method for selecting an optimal set of terrain attributes that can help non-expert GIS users make the best use of geomorphometry. The selection of terrain attributes aims to remove redundancy between attributes and maximize the amount of information given on a surface. We derived 230 terrain attributes from an artificial surface using 11 software. This approach is twofold: a pre-selection based on the ranking of attributes was first established using stepwise multicollinearity measures, followed by a final selection of attributes from a principal components analysis (PCA). The results show that using 13 independent terrain attributes can explain up to 83% of the variance for that particular surface: the combination of common attributes that are available in most GIS (i.e. aspect, basic curvatures, slope and a measure of rugosity) can explain 67% of the surface variance. The method proved efficient to reduce a high-dimensional list of terrain attributes to identify combinations of 13 attributes or less that can be used by non-expert GIS users.**

I. INTRODUCTION

Tools allowing geographic information systems (GIS) users to derive terrain attributes from digital elevation models (DEM) are increasingly available in GIS software. These attributes can be used for a wide range of purposes, such as explanatory variables or indicators in biological and ecological studies [1]. The algorithms implemented by the different software are not always specified and can often leave users with little choice of the appropriate algorithm and specific parameters to use. Since different algorithms can produce significantly different results [2], and that few studies outside of the field of geomorphometry report the methods used for the computation of terrain attributes [3], comparisons between studies can be misleading. Users are left with a large number of options and without guidance are often tempted to select a random or sub-optimal set of terrain attributes for their study using the GIS they are familiar with.

Using a random selection of terrain attributes or all the available attributes from a specific software might result in outcomes that are not representative of the observed phenomenon, failing to capture the key properties of a terrain. For instance, being all derivatives from a same surface (the DEM), terrain attributes are likely to show a certain level of covariation [4]. Covariation between variables is known to influence performance of regression analyses [5] and other statistical models [4]. Since multicollinearity makes it difficult to distinguish the influence of individual drivers on a response variable [6], it is important to carefully select the terrain attributes in order to reduce that covariation. Analysts rarely assess multicollinearity between independent variables used in a regression analysis [7].

This study aims to test a method that determines sets of terrain attributes that can (1) minimize multicollinearity between the selected attributes and (2) maximize the variance of the terrain explained by the selected attributes. Such sets of attributes could be used by GIS users to help create more robust models.

II. METHODS

A. *Terrain Attributes*

A 1x1m resolution artificial surface covering an extent of 106x106m was created using the spectral synthesis method in Landserf 2.3 (Figure 1). 230 terrain attributes were derived

In: Geomorphometry for Geosciences, Jasiewicz J., Zwoliński Zb., Mitasova H., Hengl T. (eds), 2015. Adam Mickiewicz University in Poznań - Institute of Geoecology and Geoinformation, International Society for Geomorphometry, Poznań

from this surface using different software packages (Table I). Since some of the software only allow using a 3x3 window of analysis, all analyses were performed using this size of window to allow the inclusion of as many attributes as possbile. The terrain attributes tested are from general geomorphometry, i.e. are computed continuously across a surface, and include both local geometric and statistical attributes. Selected software include both commercial and open source software. To eliminate edge effects, the outer 6m were clipped, resulting in 100x100m surfaces. Each terrain attribute was tested against the others to identify those giving strictly identical results, and thus likely to be using a same algorithm. Since the algorithms should only be accounted for once, only one attribute was kept for each set of duplicates.

A. *Pre-Selection –Dimensionality Reduction*

Several methods exist to detect multicollinearity among variables, and three were selected to examine how all the attributes vary with the others: the Variable Inflation Factor (VIF) [8], the Mutual Information (MI) [9] and the minimum redundancy (W_c) [10]. A known limit of multicollinearity measurements is the lack of meaningful threshold to distinguish values characterized as collinear from values representing the absence of multicollinearity [11]. Some methods, such as the VIF, use arbitrary values as threshold. This makes it difficult to objectively select subsets of terrain attributes based solely on these three measures of multicollinearity. However, variable ranking is often used in machine-learning as a pre-processing step [10] which, even when non optimal, is computationally efficient and statistically robust in preventing over fitting [12]. It was thus possible to rank the terrain attributes based on their level of co-association with the others, without defining any threshold.

Since the levels of co-association vary as soon as one of the variables is removed from the datasets, stepwise measures of VIF, MI and W_c were computed using the statistical software R 3.1.1. The stepwise algorithms (1) calculate the values of the measures for each terrain attribute, (2) rank the terrain attributes based on these values, (3) remove the most collinear or least informative attribute, (4) save it in a list, and (5) repeat the process until all the attributes are ranked in this list. The process is the same for the three measures of multicollinearity. An average of the three rankings was then performed for each terrain attribute, and the 40% top-ranked attributes were kept for further analysis.

B. *Selection and Grouping – Principal Component Analysis (PCA)*

The remaining terrain attributes measurements were imported in the IBM SPSS Statistics software v.22. Principal Component Analysis (PCA) is one of the most common techniques used to reduce multicollinearity in a dataset [4]: a stepwise PCA using a Varimax orthogonal rotation was performed. The PCA grouped terrain attributes in independent groups (called components) of highly correlated attributes. An orthogonal rotation allows components to be uncorrelated, hence removing multicollinearity between the groups. Varimax is the most commonly used method for orthogonal rotation and maximizes the variance of component loadings [13].

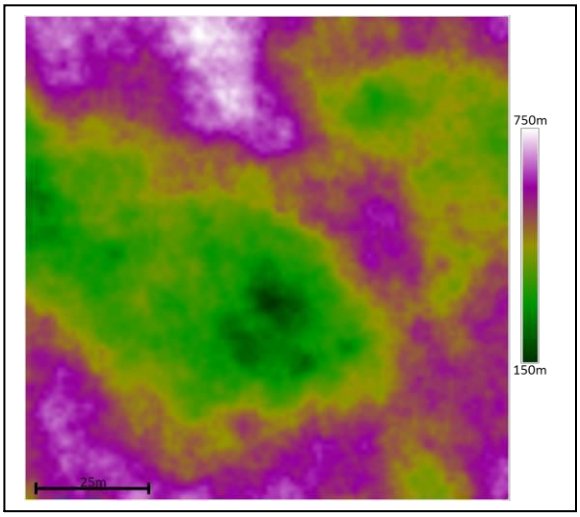


Figure 1. Artificial surface used to derive the 230 terrain attributes

For each iteration of the PCA, the attributes that loaded equally on two or more components were identified and removed: when a variable was found in more than one group, it was considered redundant, not contributing to the model [13]. Iterations ended once the computation of the PCA ceases to isolate any further redundant attributes. The optimal number of components to be retained was then found in SPSS using a parallel analysis [14] on the remaining attributes. PCA was then performed using the number of components obtained from the tests, and the attributes that did not load on any the components were removed before running a final PCA. Since the first step of the analysis consisted in subjectively removing one attribute over an identical one and that we did not want to favour a software over another, the identical attributes were added back to the final solution under the assumption that if one of the attributes reached the final solution, an identical one would have too.

III. RESULTS AND DISCUSSION

Removal of identical terrain attributes reduced the list of spatial geomorphology derivatives from 230 attributes to 182.

The pre-selection reduced that list further to 73. The iterative PCA removed the redundant attributes in 7 iterations. The 73 attributes of the initial PCA loaded on 17 components, and the seventh iteration left 59 attributes loading on 14 components. The optimal number of components given by three of the four tests was 13. When the PCA was re-run with 13 components, two of the 59 attributes did not load on any of the components and were thus removed. The final solution had therefore 57 terrain attributes loading on 13 components. By adding back the identical attributes, the solution used for interpretation had 67 attributes (Table I).

The percentage of variance explained by each component and the cumulative percentage of the variance are indicated in Table II. The final solution shows a clear association between the type of terrain attributes and the components. The interpretation of the components presented in Table II is based on the terrain attributes that contributed the most to each component. The first four components and the seventh had only one type of terrain attributes in them. For instance, the first component includes only measures of easterness from different software and computed using different algorithms. Other components (5-6, 8-9, 11-13) had a combination of two types of terrain attributes, with one primary and one secondary type. For example, the fifth component had 5 measures of slope and one measure of local fractal dimension. Only the tenth component had three different types of terrain attributes. They were however all from the same software, which might indicate that the algorithms used by Whitebox GAT to measure curvatures are significantly different from those of other software. A general interpretation of the results indicates that a combination of attributes of first (i.e. aspect and slope) and second derivatives (i.e. plan and profile curvatures), which are

TABLE I. SOFTWARE USED, NUMBER OF TERRAIN ATTRIBUTES GENERATED USING EACH OF THEM, AND NUMBER AND PROPORTION OF ATTRIBUTES IN THE FINAL SOLUTION

Software and Versions	Number of Attributes Computed	Number in Final Solution	Proportion Retained
ArcGIS 10.2.2 with Python 2.7.8	22	3	14%
ArcGIS 10.2.2 with DEM Surface Tools (v.2.1.399)	17	4	24%
ArcGIS 10.2.2 with Benthic Terrain Modeler 3.0 rc3	12	0	0%
Diva-GIS 7.5.0	7	1	14%
Idrisi Selva 17.0	7	2	29%
Landserf 2.3	12	3	25%
Quantum GIS 2.4.0 Chugiak	13	1	8%
SAGA GIS 2.0.8	96	26	27%
TNTmips Free 2014 (MicroImages)	25	21	84%
uDig 1.4.0b	9	2	22%
Whitebox GAT 3.2.1 Iguazu	10	4	40%
TOTAL:	**230**	**67**	**29%**

TABLE II. TOTAL OF VARIANCE EXPLAINED BY EACH COMPONENT AND INTERPRETATION

Component	Percentage of Variance	Cumulative Variance	Number of Attributes	Interpretation (Primary / Secondary)
1	15.07%	15.07%	12	Easterness
2	12.92%	28.00%	11	Northerness
3	8.60%	36.60%	5	Plan Curvature
4	8.52%	45.12%	5	Profile Curvature
5	5.88%	51.00%	6	Slope / Local Fractal Dimension
6	5.87%	56.86%	4	Tangential / Plan Curvatures
7	5.25%	62.12%	4	Vector Ruggedness Measure
8	4.57%	66.69%	3	Longitudinal / Profile Curvatures
9	4.33%	71.02%	7	Local Maximum / Slope
10	4.17%	75.19%	3	Curvatures (from Whitebox GAT)
11	3.43%	78.61%	3	Total Curvature / Slope Variability
12	2.46%	81.07%	2	Plan / Profile Curvatures (from Saga GIS)
13	2.42%	83.49%	2	Representativeness / Mean of Residuals

the most common terrain attributes implemented in GIS software, accounts for 51% of the variance of the surface alone (Table II). The addition of other measures of curvature, rugosity and statistical attributes increases the variance explained.

Since all the terrain attributes within each component load almost equally high, they are considered equivalent in importance: PCA regroups highly correlated attributes that also interact with attributes from other components in the same way, therefore making each attribute very similar to all the others within the same component. An optimal combination of terrain attributes would thus consist of one terrain attribute from each component. This indicates that an optimal combination of terrain attributes would have between 5 and 13 attributes.

The algorithm used to derive some of the terrain attributes does not seem to matter much for that particular surface: some algorithms loaded higher than others on each component, but not in a significant manner. TNTmips was the software that had the highest percentage of its surface attributes kept in the analysis (Table I). In addition, at least one attribute from TNTmips is included in each of the five first components, indicating that 51% of the variance can be explained using this software alone (Table II).

The method proved to be efficient in reducing the number of terrain attributes to measure and to provide combinations of terrain attributes to capture the most variance on the surface. More tests will however be necessary to refine the method and test it on natural surfaces, at different scales, and on surfaces of different complexity levels.

IV. Conclusion

This contribution presented a new method to reduce a high-dimensional list of terrain attributes in order to select optimal combinations of terrain attributes to be used by non-expert GIS users. The method reduces multicollinearity and maximizes the variance of the surface that is explained. The proposed method proved to be efficient for the surface on which it was tested and reduced a list of 230 terrain attributes to a list of 67. From these 67 attributes, only 5 were needed to explain 51% of the variance and 13 to explain 83% of it. PCA allowed a meaningful statistical grouping of terrain attributes presenting similar characteristics. Using the results from the final PCA, one can use only one attribute per component and be sure that multicollinearity is removed and that a significant amount of variance is explained. Since principal components will reflect the surface used, future analyses will be conducted using a range of natural and artificial surfaces.

Acknowledgment

Thanks to Dr. Arnaud Vandecasteele for helping with programing, and to the Canadian Natural Sciences and Engineering Research Council (NSERC) for their financial support.

References

[1] Rengstorf, A.M., Grehan, A., Yesson, C., and C. Brown, 2012. Towards high-resolution habitat suitability modeling of vulnerable marine ecosystems in the deep-sea: resolving terrain attribute dependencies. *Marine Geodesy* 35, 343-361.

[2] Dunn, M., and R. Hickey, 1998. The effect of slope algorithms on slope estimates within a GIS. *Cartography* 27, 9-15.

[3] Dolan, M. F. J., and V. L. Lucieer, 2014. Variation and uncertainty in bathymetric slope calculations using geographic information systems. *Marine Geodesy*, 37 (2), 187-219.

[4] Dormann, C. F., Elith, J., Bacher, S., Buchmann, C., Carl, G., Carré, G., Gracía Marquéz, J. R., Gruber, B., Lafourcade, B., Leitão, P. J., Münkemüller, T., McClean, C., Osborne, P. E., Reineking, B., Schröder, B., Skidmore, A. K., Zurell, D., and S. Lautenbach, 2013. Collinearity: a review of methods to deal with it and a simulation study evaluating their performance. *Ecography* 36, 27-46.

[5] Hijmans, R. J., 2012. Cross-validation of species distribution models: removing spatial bias and calibration with a null model. *Ecology* 93, 679-688.

[6] MacNally, R., 2000. Regression and model-building in conservation biology, biogeography and ecology: the distinction between – and reconciliation of – "predictive" and "explanatory" models. *Biodiversity and Conservation* 9, 655-671.

[7] Graham, M. H., 2003. Confronting multicollinearity in ecological multiple regression. *Ecology* 84, 2809-2815.

[8] Belsley, D. A., Kuh, E., and R. E. Welsch, 2004. Regression diagnostics: Identifying influential data and sources of multicollinearity. *Wiley*, 292 p.

[9] Song, L., Langfelder, P., and S. Horvath, 2012. Comparison of co-expression measures: mutual information, correlation, and model based indices. *BMC Bioinformatics* 13, 328

[10] Ding, C., and H. Peng, 2005. Minimum redundancy feature selection from microarray gene expression data. *Journal of Bioinformatics and Computational Biology* 3, 185-205.

[11] Kohavi, R., and G. John, 1997. Wrappers for feature selection. *Artificial Intelligence* 97, 273-324.

[12] Guyon, I., and A. Elisseeff, 2003. An introduction to variable and feature selection. *Journal of Machine Learning Research* 3, 1157-1182.

[13] Tabachnick, B. G., and L. S. Fidell, 2014. Using multivariate statistics, Sixth edition. *Pearson Education Limited*, 1056 p.

[14] O'Connor, B.P., 2000. SPPS and SAS programs for determining the number of components using parallel analysis and Velicer's MAP test. *Behavior Research Methods, Instruments, & Computers* 32, 396-402.

Longitudinal Elevation Profiles of Rivers: Curve Fitting with Functions Predicted by Theory

Scott D. Peckham
University of Colorado
Boulder, Colorado USA
Scott.Peckham@colorado.edu

***Abstract*—This paper provides a concise review of three different derivations for the shapes of longitudinal elevation profiles in rivers. These are then briefly compared to an observed elevation profile for Beaver Creek, Kentucky, as extracted from a 1-arcsecond DEM.**

I. Introduction

Longitudinal elevation profiles in rivers are generally concave down for a short distance from the drainage divide and are then concave up over the rest of the profile. This has generally been interpreted as due to a change in process dominance between essentially diffusive processes near divides and fluvial processes that dominate once discharge values become large enough. There have been many efforts to explain the shapes of these profiles from physical and empirical laws. This paper provides a concise review of three different derivations for the shapes of longitudinal profiles and then briefly compares them to observed profiles for Beaver Creek, Kentucky.

II. Longitudinal Profiles from an Idealized Steady-State Fluvial Landform Model

To explore connections between function and form in fluvial landscapes, Peckham (1999, 2003a, 2003b, 2003c) studied a partial differential equation intended as a simplified model for steady-state fluvial landforms. This equation is derived by combining three assumptions for the *steady-state* flow of water over a landscape: (1) mass conservation for water, (2) 2D flow direction given by the antigradient of the water's free surface and (3) a power-law relationship between unit-width discharge, q, and free surface slope, S. These can be expressed mathematically as: (1) $\nabla \cdot \underline{q} = R$, (2) $\underline{q} = -q\,(\nabla z / S)$ and (3) $|\underline{q}| = q = q_1 S^{\gamma}$. The third assumption comes from combining two well-known empirical equations of downstream hydraulic geometry (Leopold et al., 1995): $S \propto Q^{\alpha}$ and $w \propto Q^{b}$, where $Q = q\,w$ is volumetric discharge, q is unit-width discharge, $S = S(x,y) = |\nabla z| = (z_x^2 + z_y^2)^{1/2} \geq 0$ is the slope at the point (x, y), and w is channel width. This implies that $\gamma = (1 - b)/\alpha < 0$, and $\gamma \approx -1$ for typical α and b values. Together, these equations lead to a nonlinear, 2nd-order PDE for the free water surface, $z(x, y)$:

$$\nabla \cdot \left(S^{\gamma - 1} \nabla z \right) = -R^{\star} \tag{1}$$

where, $R^{\star} = R/q_1$. Here R is a *geomorphically effective rainrate* (assumed steady and spatially uniform) and q_1 is the unit-width discharge that corresponds to unit slope ($S = 1$). R is viewed as an extreme and geologically rare rainfall rate that produces flows with extreme shear stresses that can reshape the landscape. It is assumed to last long enough that shear stresses on the reshaped landscape drop to subcritical levels everywhere as a result of readjustment (e.g. wider channels, higher sinuosities, redistribution of roughness elements and formation of bedforms). Erosion caused by lesser rainfall rates is assumed to be insignificant by comparison. Sediment transport is not represented directly; the idea is to seek a landscape that has adjusted so that runoff rates less than or equal to R are insufficient to exceed the critical shear stress required to initiate significant sediment transport. While Peckham (1999, 2003) obtained numerous results for the 2D version of this equation, the 1D version (taking $z = z(x)$) is given by:

$$\left(S^{\gamma - 1} z'(x) \right)' = -R^{\star} \tag{2}$$

Since $z(x)$ is a decreasing function and $S(x) \geq 0$, we have $S(x) = -z'(x)$, so (2) simplifies to $(S^{\gamma})' = R^{\star}$. Integrating with respect to x and rearranging terms we have

$$z'(x) = -\left[S_0^{\gamma} + R^{\star}\,(x - x_0) \right]^{\frac{1}{\gamma}}, \tag{3}$$

In: Geomorphometry for Geosciences, Jasiewicz J., Zwoliński Zb., Mitasova H., Hengl T. (eds), 2015. Adam Mickiewicz University in Poznań - Institute of Geoecology and Geoinformation, International Society for Geomorphometry, Poznań

where $S_0 = -z'(x_0)$. In the case where $\gamma \neq -1$, a second integration yields the general solution:

$$z(x) = z_0 + \frac{1}{p_\gamma R^\star}\left\{S_0^{\gamma+1} - [S_0^\gamma + R^\star(x - x_0)]^{p_\gamma}\right\} \quad (4)$$

where $p_\gamma = (\gamma + 1)/\gamma$. Note that $p_\gamma \leq 0$ for $\gamma \in [-1, 0)$ and is positive otherwise. In the case where $\gamma = -1$, the second integration of (3) gives:

$$z(x) = z_0 - \frac{1}{R^\star}\left\{\ln\left[1 + S_0\, R^\star(x - x_0)\right]\right\}. \quad (5)$$

In (4) and (5) we have $z(x_0) = z_0$ and $z'(x_0) = -S_0$.

III. Steady-state Longitudinal Profiles from a Sediment Transport Law and Hack's Law

A generalized and widely-used sediment transport law – which contains several other transport laws for specific choices of m and n – is given by

$$Q_s = KQ^m S^n. \quad (6)$$

The coefficient, K, is usually called the *erodibility* and the exponents m and n are both typically taken to be between 1 and 2. Assuming that the long-term average runoff rate, R is spatially uniform, we have $Q = RA$, where A is the total contributing area above a given river outlet. Assuming a steady, spatially uniform rate of tectonic uplift, U, that exactly balances the rate of fluvial erosion (sometimes called "dynamic equilibrium"), we must similarly have $Q_s = UA$. Combining these with (6), we therefore find

$$S_{eq} = [U/(KR^m)]^{1/n}\, A^{(1-m)/n} \quad (7)$$

where S_{eq} is the steady-state or equilibrium slope at any point and R is a uniform runoff rate (Tucker and Bras, 1998). This agrees with an empirical law called Flint's Law (Flint, 1974), often written as $S = cA^{-\theta}$, where the exponent $\theta > 0$ is typically close to $1/2$. The prediction here is that $\theta = (m - 1)/n$, and $\theta > 0$ since $m > 1$. As shown by Whipple and Tucker (1999), an empirical law known as Hack's Law, given by

$$A = k_h\, x^h \quad (8)$$

can be inserted into (7) to express slope in terms of x, the flow distance downstream from a drainage divide. The Hack exponent is typically close to $3/5 = 0.6$, so its reciprocal, h, is close to $5/3 = 1.67$. This results in the equation: $S(x) = -z'(x) = Cx^{p-1}$, which can be integrated to get a functional form for the longitudinal profile. This gives

$$z(x) = \begin{cases} z_0 - (C/p)\,(x^p - x_0^p), & \text{if } p \neq 0 \\ z_0 - C\ln(x/x_0) & \text{if } p = 0, \end{cases} \quad (9)$$

where $p = 1 - \theta h$ and $C = [U/(KR^m)]^{1/n} k_h^{-\theta}$. For $\theta = 1/2$ and $h = 5/3$ we have $p = 1/6$. Note that $z(x_0) = z_0$ and $z'(x_0) = -S_0$, where $S_0 = Cx_0^{p-1}$. These functional forms are somewhat similar to those predicted from the idealized steady-state fluvial landform model, as given by (4) and (5). However, here $p > 0$ and there, $p_\gamma < 0$. Also, here we need $x_0 \neq 0$ to avoid an infinite slope at x_0. Despite these differences, their plots look very similar for typical values of their parameters.

IV. Longitudinal Profiles from a Sediment Transport Law and Similarity Solutions

Smith et al. (2000) developed a theory of graded streams that is based on conservation of sediment and the generalized sediment transport law

$$q_s = Cx^\gamma S^\delta \quad (10)$$

where q_s is unit-width sediment discharge, x is downstream distance from a divide, C is a constant and $S = -z_x > 0$. While Smith et al. (2000) gave results for both (transport-limited) alluvial channel profiles and (detachment-limited) bedrock channel profiles, which obey different sediment conservation laws, here we restrict attention to alluvial channel profiles. For alluvial channels, conservation of sediment mass can be expressed as

$$z_t = \nabla \cdot [-q_s\,(\nabla z/S)] \quad (11)$$

which in the 1D case, after inserting (10) becomes

$$z_t = -C\left[x^\gamma\,(-z_x)^\delta\right]_x. \quad (12)$$

Similarity solutions to (12) are sought by inserting

$$z(x,t) = \tau^\alpha\, F\left(x/\tau^\beta\right) \quad (13)$$

and solving the resulting ODE for $F(\eta)$, where $\eta = x/\tau^{\beta}$ is called the *similarity variable* and $\tau = \tau_0 + \omega t$. The resulting solutions have an initial elevation of $z_0 = z(0,0)$ at the upstream end where $x = 0$ and descend to $z = 0$ at the downstream end where $x = X(t)$. An expression for $X(t)$ can be obtained by solving $z(X,t) = 0$ for X. The initial x-position is denoted by $X_0 = X(0)$.

Not including a tectonic uplift term in (12) allows similarity solutions to be found. However, if $z(x,t)$ is a similarity solution to (12), then it is easy to check that $z(x,t) + \int_0^t U(t)dt$ is a solution to (12) with $U = U(t)$ added to its right-hand side, where $U(t)$ is a spatially uniform uplift rate. The resulting solution will no longer be a similarity solution. For steady uplift, $U(t) = u_0$, and the solution is $z(x,t) + u_0 t$.

Smith et al. (2000) showed how these similarity solutions for alluvial channel profiles can be divided into four classes, each with a different physical interpretation. In all cases, *admissible* solutions require $\delta > 1$ and $0 < \gamma < \delta + 1$. These are briefly summarized in the following four sections.

1) Fans and Pediments: $\alpha + \beta = 0$.
These solutions are characterized by zero net sediment loss, so that the mass of material under the profile does not change over time. They are always concave upwards and there is no net loss of material through the lower boundary, which advances downstream over time. Solutions are interpreted as representing a spreading fan of material, as occurs in internal basins such as those in arid and semi-arid regions of the western U.S..

$$z(x,t) = z_0\, G(\omega t)\, \{1 - [(x/X_0)\, G(\omega t)]^{p_1}\}^{p_2} \tag{14}$$

$$G(\omega t) = (1 + \omega t)^{1/(\gamma - 2\delta)} \tag{15}$$

$$\omega = -C\,(\gamma - 2\delta)\left(\frac{1 - \gamma + \delta}{\delta - 1}\right)^{\delta} \frac{z_0^{\delta - 1}}{X_0^{1 - \gamma + \delta}} \tag{16}$$

where $p_1 = (1 - \gamma + \delta)/\delta$, and $p_2 = \delta/(\delta - 1)$. Admissible solutions have $(0 < p_1 < 1)$ and $p_2 > 1$.

2) Hanging Valleys: $\alpha = 0$.
These solutions are characterized by unconstrained sediment removal. The elevation at their upstream end is fixed for all time; that is, $z(0,t) = z_0$ for all t. Profiles are concave upwards for $\gamma > 2$, linear for $\gamma = 2$ and convex upwards for $\gamma < 2$. Slopes decrease over time if the profile is concave upwards and increase over time if it is convex or linear. $X(t)$ is a decreasing function, so the lower boundary moves upstream over time. Sediment discharge at the lower boundary remains constant over time. After a time, $t = \tau_0$, profiles approach a vertical "cliff" at $x = 0$.

$$z(x,t) = z_0\,[1 - G(\omega t)\,(x/X_0)^p] \tag{17}$$

$$G(\omega t) = (1 + \omega t)^{1/(1-\delta)} \tag{18}$$

$$\omega = -C\,(2\delta - \gamma)\left(\frac{1 + \delta - \gamma}{\delta - 1}\right)\frac{z_0^{\delta - 1}}{X_0^{1 + \delta - \gamma}} \tag{19}$$

where $p = (1 + \delta - \gamma)/(\delta - 1) > 0$.

3) Fixed Lower Boundaries and Base Levels: $\beta = 0$.
These solutions are applicable to rivers that drain to a large water body with a fixed elevation. The x-position of their downstream end is fixed for all time; that is, $X = X_0$ and $z(X_0, t) = 0$ for all t. The solutions are *separable*, so that $z(x,t) = F(x)T(t)$, where

$$T(t) = [(\delta - 1)C\lambda\, t + 1]^{\frac{1}{1-\delta}} \tag{20}$$

$$\left[x^{\gamma}\,(-F_x)^{\delta}\right]_x = \lambda F. \tag{21}$$

Note that $\lambda > 0$, $T(0) = 1$ and $z(x,0) = F(x)$. However, the ODE for $F(x)$ must be solved numerically. Hypsometric curves for these solutions are time-invariant.

4) Steady-State Profiles and Tectonic Motion: $\alpha = 1$.
These solutions are characterized by $z_t = -L$, where L is a spatially uniform rate of downcutting. That is, solutions are curves that rise or lower at a constant rate and they are always upward concave, with

$$z(x,t) = z_0\,[(1 + \omega t) - (x/X_0)^p] \tag{22}$$

$$\omega = (-C/z_0)(z_0\, p\, X_0^{-p})^{\delta} < 0 \tag{23}$$

where $p = 1/\beta = (1 + \delta - \gamma)/\delta$ and $0 < p < 1$. When the effect of steady, uniform uplift is included by adding $u_0 t$ (as explained previously), the terms $u_0 t$ and $z_0\,\omega t$ can be grouped, $z_t = -L = u_0 + z_0\,\omega$ and the result is still a similarity solution. In the special case where $u_0 = -\omega z_0$, we have $L = 0$ and the profile is a *steady-state* solution. This is a type of *dynamic equilibrium*, as discussed earlier.

V. Fitting Curves to Longitudinal Profiles

RiverTools 4.1 is a software toolkit for terrain analysis. It includes tools for extracting longitudinal elevation profiles from DEMs and finding best-fit parameters for a variety of functional forms using nonlinear least-squares regression. *Downstream profiles* from any cell in the DEM can be extracted, in addition to *upstream* or *main channel profiles*. The latter are defined by repeatedly moving upstream toward the D8 neighbor cell with the largest total contributing area until reaching a drainage divide. Figure 1 shows the best fit of equation (4) to the main channel profile for Beaver Creek, Kentucky. This function provides the smallest standard error of any of those tested ($\epsilon = 4.55$), with $\gamma = -0.70$ and $R^\star = 0.0035$. Note that $x_0 = 0$, $z_0 = 668.33$ and $S_0 = 0.462$ were held fixed. If we take $q_1 = 0.007$ $[m^2/s]$ (Leopold et al., 1995), this implies $R = 87.2$ $[mmph]$. This is a very large, but not unrealistic value. A rate of 435 $[mmph]$ was sustained for 42 minutes in Holt, Missouri (Lott, 1954). As explored by Peckham (2003c), this suggests a method for deducing the magnitude of landscape-shaping rainfall events from elevation data.

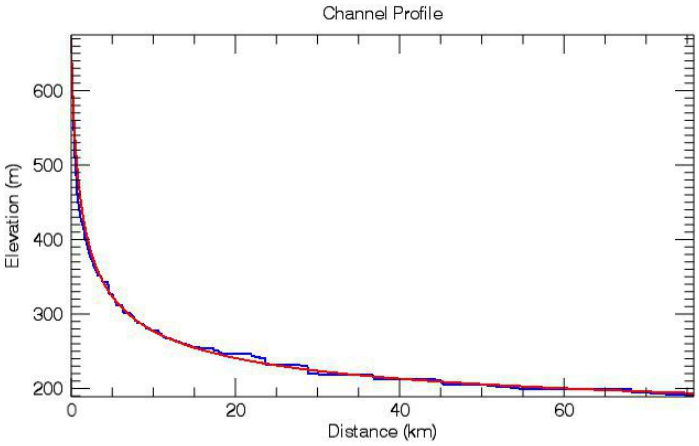


Fig. 1. Best fit of (4) to the main channel profile of Beaver Creek, KY.

Figure 2 shows the best fit of the power-law (9) to the main channel profile for Beaver Creek, Kentucky. This curve has $p = 0.133$, $C = 14.71$ (x_0 and z_0 again fixed). The standard error, $\epsilon = 15.93$, is 3.5 times larger. The best fit of the power-law (22) is identical, since $x_0 = 0$, with the same p and ϵ (steady case). An exponential curve constrained to go through (x_0, z_0) provides an extremely poor fit (not shown), with $\epsilon = 123.33$. An unconstrained, 3-parameter exponential curve, also poor, has $\epsilon = 15.49$.

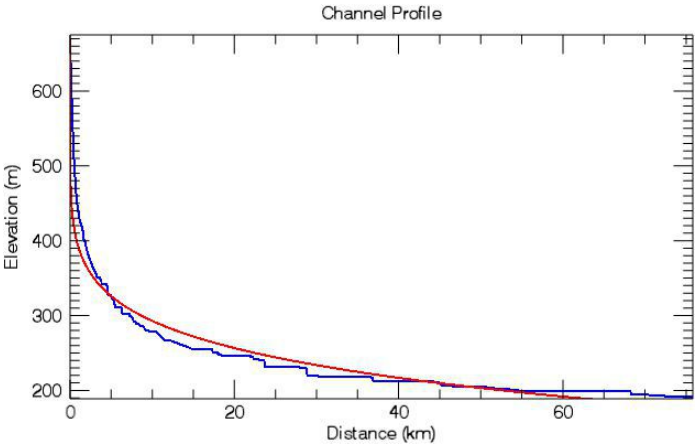


Fig. 2. Best fit of power-laws (9) and (22) to the main channel profile of Beaver Creek, KY. Standard error $= 15.93$ and $p = 0.133$.

References

Flint, J.J. (1974) Stream gradient as a function of order, magnitude and discharge, *Water Resour. Res.*, 10(5), 969–973.

Hack, J.T. (1957) Studies of longitudinal stream profiles in Virginia and Maryland, *U.S. Geological Survey Professional Paper*, 294-B, 97.

Leopold, L.B., M.G. Wolman and J.P. Miller (1995) *Fluvial Processes in Geomorphology*, Dover, New York (first published 1964).

Lott, G.A. (1954) The world-record 42-minute Holt, Missouri, rainstorm, *Monthly Weather Review*, 82(2), 50–59.

Peckham, S.D. (1999) Solutions to nonlinear partial differential equations: A geometric approach, In: *Proc. of the Conference on Geometry in Present-Day Science*, edited by O.E. Barndorff- Nielsen and E.B. Vedel Jensen, World Scientific, New Jersey, 165–186.

Peckham, S.D. (2003a) Mathematical modeling of landforms: Optimality and steady-state solutions, In: *Concepts and Modelling in Geomorphology: International Perspectives*, Eds. Evans, I.S., Dikau, R., Tokunaga, E., Ohmori, H. and Hirano, M., 167-182.

Peckham, S.D. (2003b) Fluvial landscape models and catchment-scale sediment transport, *Global and Planetary Change*, 39, 31–51.

Peckham, S.D. (2003c) Estimating geomorphically effective rainrates from elevation data, *Eos Trans. AGU*, 84(46), p. 263, Fall Meet. Suppl., H41A-07.

Smith, T.R., G.E. Merchant and B. Birnir (2000) Transient attractors: Towards a theory of the graded stream for alluvial and bedrock channels, *Comp. & Geosci.*, 26, 541–580.

Tucker, G.E. and R.L. Bras (1998) Hillslope processes, drainage density, and landscape morphology, *Water Resour. Res.*, 34, 2751–2764.

Whipple, K.X. and G.E. Tucker (1999) Dynamics of the stream-power river incision model: Implications for height limits of mountain ranges, landscape response timescales, and research needs, *J. Geophys. Res.*, 104(B8), 17,661–17,674.

Doing Geomorphometry with Pattern Analysis

Tomasz F. Stepinski[1], Jaroslaw Jasiewicz[2,1], Pawel Netzel[3,1], Jacek Niesterowicz[1]
[1]University of Cincinnati, USA; [2]Adam Mickiewicz University, Poland; [3]University of Wroclaw, Poland

Abstract—**We have developed a concept of pattern-based analysis of land-surface where a basic unit of analysis is a pattern of landform elements defined over an arbitrary local region referred to as a scene. The DEM is subdivided into a regular grid of scenes reducing its effective dimension by orders of magnitude. Scenes are described by histograms of local pattern primitive features and similarities between scenes are calculated using histogram distance measures. With scene histograms as cell attribute and histogram distance as a metric the grid-of-scenes can be analyzed much like the ordinary DEM including its segmentation and classification. The result is a framework for efficient and robust automatic classification of topography on continental or global scales using extensive DEM archives. The framework also supports spatial search for similar landscapes. The concept of pattern-based analysis is described and an example pertaining to automatic delineation of physiographic units in Poland is presented. In addition, a GeoWeb application for spatial search of landscapes in Poland is also discussed. To facilitate pattern-based analysis we have developed GeoPAT – a toolbox of GRASS GIS modules intended as a platform for experimentation with the pattern-based analysis of DEMs and other spatial datasets.**

I. Introduction

Geomorphometry is the science of quantitative land-surface analysis. A significant portion of this analysis focuses on surface classification, or more specifically on DEM (digital elevation model) classification as DEM is the most commonly used quantitative representation of the surface. Classification converts DEM into a thematic map of semantically meaningful classes. Landform elements – elementary forms characterized by constant values of morphometric variables – are the most popular target classes of classification [1,2,3]. This stems from a traditional geomorphologic interest in relating land-surface form to physical process. Increased availability of continental and global scales DEMs led to an additional, different rationale for performing DEM classification – an objective algorithmic delineation of different types of topography. This is in-line with interest in other disciplines of geosciences in providing global, objective delineations of geospatial variables such as, for example, land cover or land cover types classes [4] or climate classes [5].

An original approach to algorithmic classification of global topography [6] utilized a cell-based methodology with classification algorithm assigning class labels to individual cells in a DEM. Note that this is fundamentally different from how a human interprets a visualization of a DEM by perceiving the coherence of different landforms on multiple scales simultaneously and assigning a topographic class label to extended tracts (not an individual cell) of the surface on the basis of pattern of different landforms. Therefore cell-based classification algorithms suffer from poor performance especially if applied to high resolution DEMs, where individual cells correspond to small elements of surface and their associated numerical attributes are not sufficient to recognize the topographic class, or, if applied to very large DEMs where the goal of analysis is to retrieve generalized topographic classes (physiographic units).

Object-based classification of topography was developed [7] to alleviate the problems associated with cell-based classification. In the object-based method the DEM is first segmented into "objects" – tracts of surface homogeneous with respect to cell-based morphometric variables – which in turn are classified into topographic classes. Object-oriented algorithms get closer to the way an analyst interpret a DEM but they still suffer from a number of shortcomings First, segmentation itself is a complex and computationally expensive process and there is no single method that performs consistently well (does not under-segment or over-segment portions of a DEM). Second, because objects are, by definition, homogeneous segments of the surface, current object-oriented methods can only classify DEM into very general topographic classes (see [7]) as they are not able to take advantage of the information contained in the pattern of landform elements constituting a landscape.

To get a more robust means of classifying topography from a DEM we have developed a pattern-based method that has proven to be fast and effective on even the largest datasets. In our method a DEM is divided into a regular grid of local blocks of cells (referred to as local scenes) thus converting a large DEM into much smaller grid-of-scenes at very small computational cost. The core ingredients of the method are the mathematical description of a topographic pattern in each scene and a function that calculates a degree of similarity between the patterns. With pattern representation and similarity function defined, the grid-of-scenes can be segmented and classified in a manner similar to an ordinary DEM but at a small fraction of computational cost and at significantly higher degree of information generalization.

In: Geomorphometry for Geosciences, Jasiewicz J., Zwoliński Zb., Mitasova H., Hengl T. (eds), 2015. Adam Mickiewicz University in Poznań - Institute of Geoecology and Geoinformation, International Society for Geomorphometry, Poznań

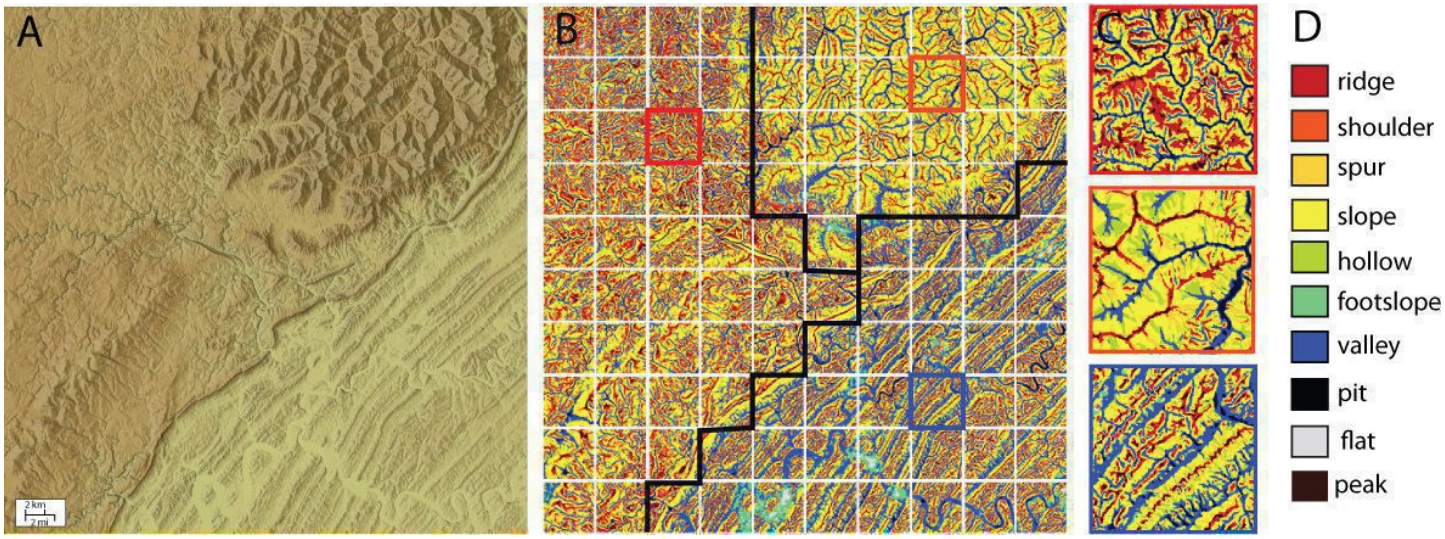


Figure 1. (A) Hillshade rendition of the 2000×2000 cells DEM. (B) Cell-based classification of the DEM into ten landform elements and its sub-division into a grid-of-scenes. (C) Examples of three scenes representing three different physiographic regions present in the region. (D) Landform elements legend.

II. METHODOLOGY

Fig.1 illustrates the concept of pattern-based analysis of DEM. Fig.1A shows a hillshade rendition of a 2000×2000 cells DEM. In the depicted region one can observe at least three distinct physiographic units. The DEM cells are first classified into ten landform classes (Fig.1D) using the geomorphons method [3]. The result of this classification is shown in Fig.1B. The region is then divided into a regular 10×10 grid of hundred scenes (Fig.1B) with each scene containing 4×10^4 cells forming a local, block-bounded pattern of landforms.

To delineate the three physiographic units as seen in the DEM the method segments and/or classifies the coarse grid-of-scenes in a way that is in general analogous to how a cell-based algorithm would perform these tasks on the entire DEM. Significant technical differences in performing these operations on scenes vs. cells stem from differences in mathematical representations of patterns vs. numbers, and from differences in the definitions of a distance between patterns vs. distance between vectors.

Three scenes representative of three different physiographic units are selected from the grid and highlighted by red, orange, and blue frames, respectively. Fig.1C shows close-ups of these scenes showing distinct patterns of landform elements in each scene. Either unsupervised (clustering and/or segmentation) or supervised methods can be used to delineate the three physiographic provinces from the grid-of-scenes. This is schematically shown by black lines on Fig.1B.

To perform pattern-based analysis of DEMs (and other datasets) we have developed the Geospatial Pattern Analysis Toolbox (GeoPAT) - a collection of GRASS GIS modules that integrates the various tools necessary for pattern-based analysis of DEMs including a classification task as described above. GeoPAT integrates into the GIS system procedures for pattern description, pattern similarity, and the search and retrieval of similar patterns. These concepts were originally developed for working with natural images in the context of Content-Based Image Retrieval (CBIR) systems [8] but are now utilized by GeoPAT for the purpose of geospatial analytics. GeoPAT works with DEMs of all sizes but it is designed to be especially effective when applied to giga-cell and larger DEMs. In addition to segmentation and classification GeoPAT supports tasks such as spatial search and scene-by-scene comparison of two grids. GeoPAT is available at http://sil.uc.edu/.

A. Pattern representation

The input to the pattern-based method is not an original DEM but a categorical grid of the same size as the DEM. This grid is a result of classifying cells of the DEM into landform elements. We use the geomorphon method [3] to achieve this pre-processing step but other methods (for example, [6]) can also be used. A concise mathematical description of categorical pattern

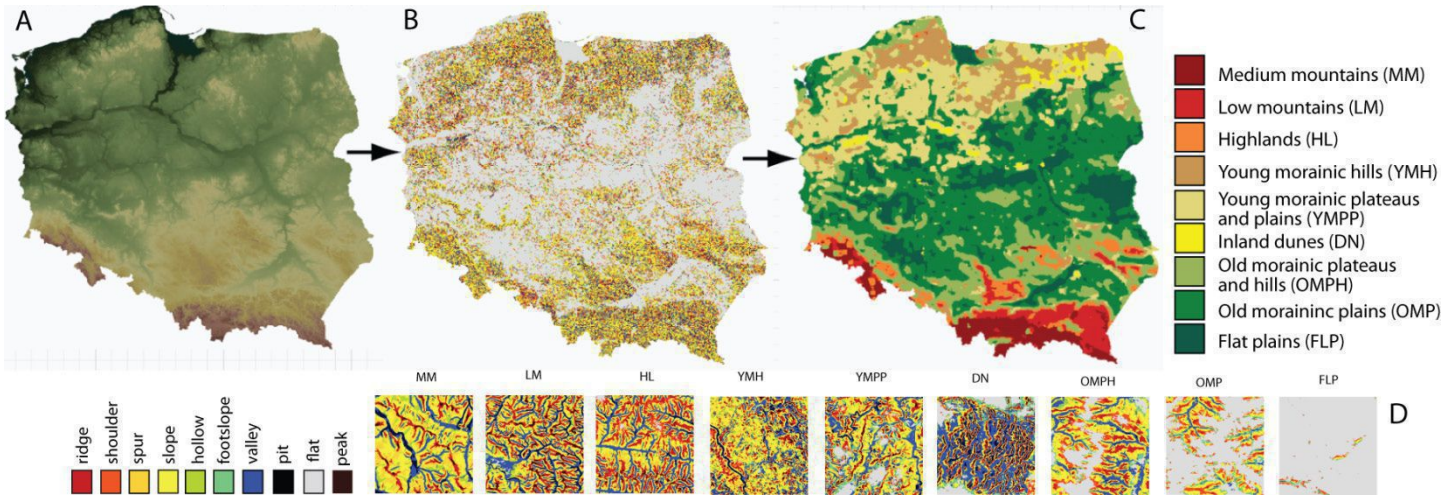


Figure 2. (A) DEM of Poland with 30m resolution. (B) Ten-categories map of landform elements with 30m resolution. (C) Results of pattern-based supervised classification of grid-of-scenes into nine physiographic units. (D) Examples of characteristic patterns of landforms for the nine physiographic units.

of landform elements in a scene is a histogram of pattern "primitive features." Primitive features are simple local elements of a pattern. GeoPAT implements several popular methods of representing pattern by a histogram of primitive features, a co-occurrence method is recommended for working with patterns stemming from topographic data.

The co-occurrence method is a variant of the Gray-Level Co-occurrence Matrix (GLCM) [9] with gray-scale values replaced by landform element classes. Co-occurrence method uses a single primitive feature - a pair of landform elements classes assigned to two neighboring cells. When the DEM is classified by the geomorphons method into 10 landforms elements the co-occurrence histogram has (10 × 10)/2 +5=55 bins. Thus, a pattern in each scene is encapsulated by 55 numbers describing the composition of different landforms and their relative spatial configuration.

B. Pattern similarity/distance

"Distance" between two scenes assesses the degree of dissimilarity between them, it is the opposite of similarity. In our method a distance between scenes is a distance between histograms representing the scenes. When the value of distance is equal to zero identical histograms are indicated, and thus scenes have identical or very similar patterns, whereas large values of the distance indicate very different histograms and scenes having significantly different patterns. Over 40 possible histogram distance measures have been proposed [10]. For topographic data and co-occurrence signature the normalized Wave Hedges distance metric is recommended.

III. EXAMPLES

We apply pattern-based methodology to delineate physiographic unit in the country of Poland using supervised approach [11]. The input is the 30m DEM with the size of 21,696 × 24,692 cells (Fig.2A). This DEM is classified using the geomorphons method (Fig.2B). The region is subdivided into grid-of-scenes with 433 × 493 coarse cells each having size of 50 × 50 cells (1.5 km scale) and being a center of 15 × 15 km scene resulting in a significant overlap between scenes.

The territory of Poland exhibits a number of physiographies and we decided, based on the prior knowledge, to map nine selected physiographic units (see legend to Fig.2C). For each of these units a number of representative scenes have been selected as examples; one example for each unit is shown in Fig.2D. The pattern of all scenes was encapsulated using the co-occurrence signature and the Wave-Hedges distance function was used to calculate dissimilarity between scenes. The nearest neighbor supervised classification was used to assign one of nine labels to each cell in the grid-of-scenes. The resultant map shown in Fig.2C is comparable to a manually developed physiographic map of Poland [12].

Another application of pattern-based method is web-based landscape search which enables the discovery of locations having landscapes similar to a specified landscape of interest. Given a query – landscape (topography) of the site of interest – landscape search returns the similarity map which visually shows a degree of similarity to a query at all location throughout the entire study. Similarity map provides much more information than a non-spatial list of top matches to a query. By utilizing spatial organization it simultaneously shows similarity relations between

the query and all scenes in the database. Thus, it allows an analyst to concentrate on revealed geomorphic phenomena rather than on similarity between specific scenes. For the Poland data we have implemented the landscape search as TerraEx-PL http://sil.uc.edu/webapps/terraex_pl/ (see Fig.3).

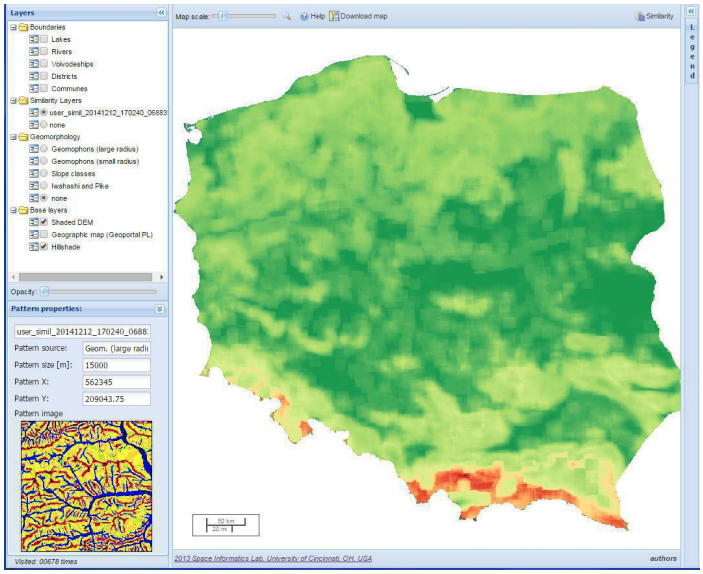


Figure 3. Screenshot of TerraEx-PL GeoWeb application for performing spatial searches for landscapes similar to a user-selected query. The query is shown in the bottom-left corner and the output is the similarity-to-query map with colors red-to-green indicating decreasing similarity of local landscapes to the landscape of the query.

IV. SUMMARY

Our pattern-based approach analyses the land-surface at the high level of generalization with the basic unit of analysis being a local landscape rather than more basic landform element. Such approach works best with very large DEMs and when the object of analysis is exploration or large-scale mapping of topography. The concept of pattern-based analysis of DEMs is new and will require much more work to mature. In particular, the key issues of scene signature and scene distance/similarity needs more study. We have developed the GeoPAT – toolbox of GRASS GIS modules intended as a convenient platform for experimentation with the pattern-based analysis of DEMs and other spatial datasets including datasets having giga-cell and larger sizes. In addition to classification, our pattern-based approach yields itself to spatial search function that can be implemented as web application.

ACKNOWLEDGMENT

This work was supported partially by the National Science Foundation under Grant BCS-1147702, by the National Science Centre (NCN) under Grant DEC-2012/07/B/ST6/01206, and by the University of Cincinnati Space Exploration Institute.

REFERENCES

[1] Wood, J., 1996. "The geomorphological characterisation of digital elevation models". Ph.D. Thesis, PhD Thesis Department of Geography, University of Lancaster, UK.

[2] Dikau, R.; Brabb, E. & Mark, R. Morphometric landform analysis of New Mexico Zeitschrift für Geomorphologie, 1995, Supplement 101, 109-126

[3] Jasiewicz, J., Stepinski, T.F 2013. "Geomorphons -a pattern recognition approach to classification and mapping of lanforms." Geomorphology 182, pp. 147-156.

[4] Jin, S., Yang, L., Danielson, P., Homer, C., Fry, J., and Xian, G. 2013. "A comprehensive change detection method for updating the National Land Cover Database to circa 2011". Remote Sensing of Environment, 132, 159 – 175.

[5] Metzger, Marc J., Robert GH Bunce, Rob HG Jongman, Roger Sayre, Antonio Trabucco, and Robert Zomer. 2013 "A high‐resolution bioclimate map of the world: a unifying framework for global biodiversity research and monitoring." Global Ecology and Biogeography 22, no. 5, 630-638.

[6] Iwahashi, J., Pike, R., 2007. "Automated classification of topography from DEMs by an unsupervised nested-means algorithm and three-part geometric signature." Geomorphology 86, 409-440.

[7] Dragut, L., Eisank, C., 2012. "Automated object-based classification of topography from SRTM data."Geomorphology 141-142, 21--23.

[8] Datta, R., Joshi, D., Li, J., Wang, J.Z. 2008. "Image Retrieval: Ideas, Influences, and Trends of the New Age." ACM Computing Surveys, 40,1—60.

[9] Haralick, Robert M., Karthikeyan Shanmugam, and Its' Hak Dinstein. 1973. "Textural features for image classification." IEEE Transactions on Systems, Man and Cybernetics, 610-621.

[10] Cha, S.-H. 2007. "Comprehensive survey on distance/similarity measures between probability density functions. "International Journal of Mathematical Models and Methods in Applied Sciences, 1(4), 300-307.

[11] Jasiewicz, J., Netzel, P., Stepinski, T.F. 2014. "Landscape similarity, retrieval, and machine mapping of physiographic units". Geomorphology 221, pp.104-112

[12] Kondracki, J., 2002. "Geografia regionalna Polski." 3rd Edition. Wydawnictwo Naukowe PWN, Warszawa.

Hybrid implementation of evaluation of primary topographic parameters using GPU-accelerated clusters

Przemysław Stpiczyński, Dominik Szałkowski
Department of Computer Science, Institute of Mathematics
Maria Curie-Skłodowska University, Lublin, Poland
przem@hektor.umcs.lublin.pl, dominisz@umcs.lublin.pl

Leszek Gawrysiak, Łukasz Chabudziński
Department of Earth Sciences and Spatial Management
Maria Curie-Skłodowska University, Lublin, Poland
leszek.gawrysiak@umcs.pl, lchabudzinski@gmail.com

Abstract—**The aim of this paper is to present an efficient method for parallelizing computations of primary topographic parameters like aspect, slope, and curvature for very large data sets using clusters with GPU-accelerated nodes. We outline the implementation and discuss the results of experiments, which justify the use of such computer architecture.**

I. INTRODUCTION

Topographic parameters and indicators are the essential part of the spatial data analyses, which are used to show dependencies between various components of the natural environment. The parameters, which are obtained from the digital elevation model (DEM), are also used to describe terrain properties in a quantitative way. Parameters like slope, aspect, and curvature are called primary topographic parameters and they are directly computed from the DEM. The topographic position index, topographic wetness index, stream power index, and roughness are called secondary topographic parameters and they are derived from the primary ones. The values of the parameters represent important properties of the surface, which in turn determines the behavior of hydrologic, geomorphologic, and ecologic processes.

For the last twenty years the size of the GIS data to process have been constantly growing together with the complexity of computations needed to perform spatial analyses (Healey et al., 1997). There are some papers concerning the use of standard multiprocessor architectures for GIS related tasks (Huyaji W. et al., 2011, S. H. Han, 2009, F. Huang, 2011, X. Guan, 2009) as well as surveys of utilizing parallel capabilities of new architectures of general purpose GPUs (Graphics Processing Unit) (Osterman, 2012). However, there are no studies that take into account the hybrid nature of contemporary multiprocessor architectures consisting of various types of computing units, i.e. many-core CPUs and multicore GPUs. Today, this approach should be used to fully exploit the true power of high performance computers. In order to efficiently deal with very complex spatial analyses, it is necessary to develop new kinds of algorithms and computational techniques, which are based on an effective use of all processing devices (CPU and GPU cores) available within the nodes of computer clusters.

II. NEW HYBRID ALGORITHM

In this paper, we show how to use hybrid node clusters to compute primary topographic parameters like aspect, slope, and curvature for very large data sets, which exceed the computational resources of one node. We show how to store the data in cluster distributed memory and how to use different types of computational devices.

The general outline of the data processing scheme for large DEM files is as follows:

1. Divide the DEM file into overlapping horizontal stripes and write them into separate files.
2. Distribute the files among the nodes of the cluster.
3. Start the parallel program on the cluster to process distributed data. Each process running on a single node is responsible for distributing work among all available computational devices (CPU and GPU cores).
4. Locally, compute necessary primary topographic parameters (e.g. slope, aspect, curvature) in parallel using CPU and GPU cores.
5. Retrieve the processed data from all nodes.
6. Merge separate output files containing results into one large DEM file.

Although, we have considered the use of MPI (*Message Passing Interface*) for distributing the work among nodes of the cluster (Step 2 and 5), it can be simply implemented using a shell script spawned on nodes. We use routines provided by GDAL library for splitting and merging DEM files (Step 1 and 6).

In: Geomorphometry for Geosciences, Jasiewicz J., Zwoliński Zb., Mitasova H., Hengl T. (eds), 2015. Adam Mickiewicz University in Poznań - Institute of Geoecology and Geoinformation, International Society for Geomorphometry, Poznań

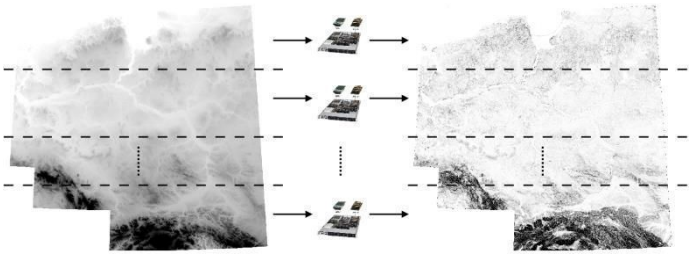


Figure 1. Data distribution scheme



Figure 2. Local computations on a single node

Data distribution scheme among available nodes is presented in Figure 1. A large input data file (presented on the left hand side) is divided into horizontal stripes (one stripe for each cluster node) with overlapping border of 1 pixel. Such a border is required due to nature of used algorithms (to compute the result for one grid cell we need its neighbours, see Figure 3). All stripes are processed in parallel. Then the results of computations are merged into one big file (right hand side of the figure).

On each node, all CPU and GPU devices are used. The data are divided into two (or three) horizontal stripes. Two stripes are always processed by two GPUs. In case of large amount of data (exceeding the size of GPU memory) the third stripe is assigned to CPU cores. This approach is presented in Figure 2.

III. DATA FILES

For our numerical experiments we use ten DEM files with properties presented in Table 1. These files contain elevation data of Poland area with various cell sizes which result in file sizes. Figure 4 shows the memory occupation of the devices used for processing the data.

TABLE 1. PROPERIES OF DEM FILES

File	Columns	Rows	Total memory (MB)	GPU0 memory (MB)	GPU1 memory (MB)	CPU memory (MB)
DTED2_31%	9954	9239	350	175	175	0
DTED2_44%	14129	13114	706	353	353	0
DTED2_54%	17340	16094	1064	532	532	0
DTED2_63%	20230	18777	1449	724	724	0
DTED2_70%	22478	20863	1788	894	894	0
DTED2_77%	24726	22949	2164	1082	1082	0
DTED2_83%	26652	24738	2515	1257	1257	0
DTED2_89%	28579	26526	2891	1445	1445	0
DTED2_94%	30185	28016	3225	1499	1499	227
DTED2_100%	32112	29805	3651	1499	1499	653

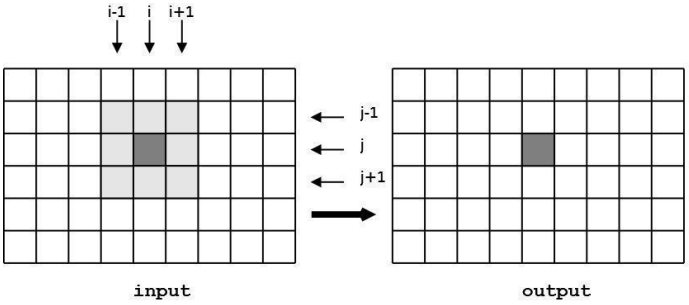


Figure 3. Using a data cell and its neighbours

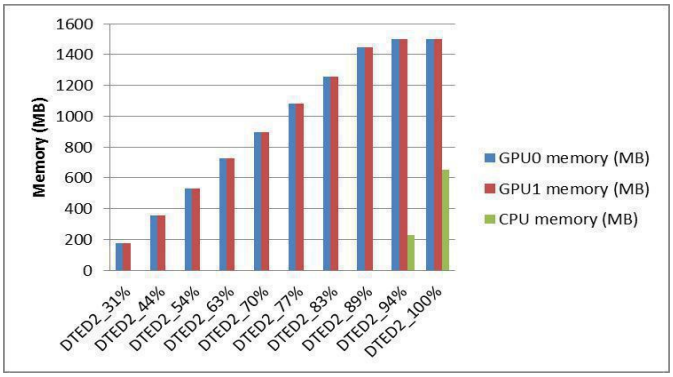


Figure 4. Memory occupation during processing

IV. SOFTWARE, HARDWARE AND RESULTS

Our software is a library of C/C++ functions for computing primary topographic parameters (slope, aspect, curvature, insolation). Inside a single node we use OpenMP and CUDA interfaces for parallel programming. This approach allows using many CPU and GPU cores at the same time, which increases the total performance of the computations. Our software also uses the widely known GDAL/OGR open source library for dealing with GEOTIFF files.

Tests were run on our Solaris cluster, which consists of 32 hybrid nodes. In each node, there are two Intel Xeon X5650 processors (6 cores each with hyper-threading, 2.67 GHz) and two NVIDIA Tesla M2050 cards (448 CUDA cores, 3 GB GDDR5 RAM with ECC off). The nodes are connected using 40 Gbit/s Infiniband. Programs were compiled using NVIDIA CUDA Toolkit version 5.5 and Intel Cluster Studio version 2013. Debian GNU/Linux operating system was used.

A comparison of the calculations performed this way with the results obtained using well known GIS programs (ArcGIS 10.1, GRASS 6.4.3, GDAL 1.10.1 and QGIS 2.0.1) on a PC with processor i7 (2.93 GHz, 4 GB RAM) shows that the algorithms are accurate and very efficient, especially in case of large data sets (see Figures 5-7).

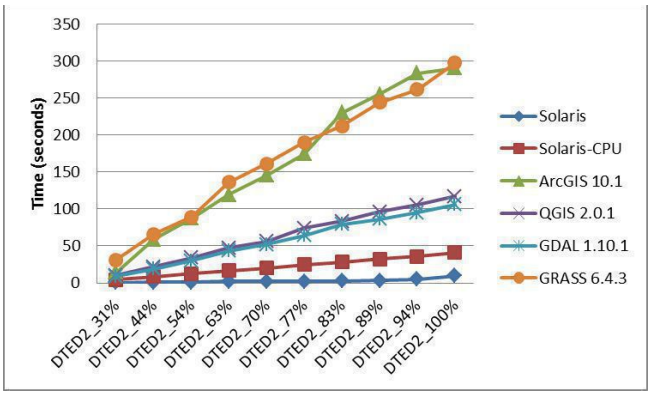


Figure 5. Execution time for slope

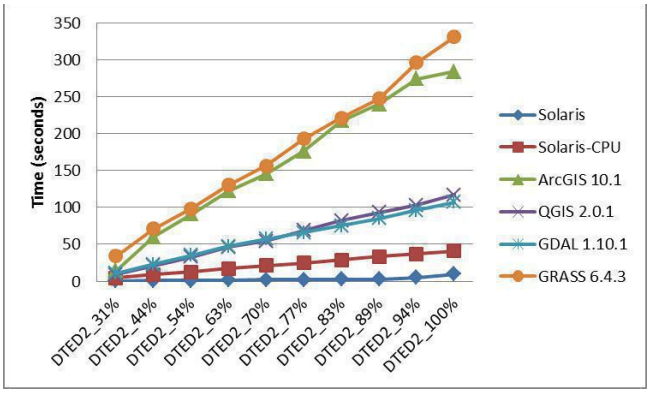


Figure 6. Execution time for aspect

Figure 8 and Table 2 present the scalability of our implementation. We can observe that the speedup grows with the increasing number of nodes. The best performance is achieved when only GPUs are used. The use of CPU cores results in the performance degradation, however it is necessary for larger data files when the amount of data to be processed by a single node exceeds the memory capacity of both GPUs.

TABLE 2. EXECUTION TIME (SECONDS) FOR VARIOUS NUMBER OF NODES

Nodes	Aspect	Aspect-CPU	Slope	Slope-CPU	Curvature	Curvature-CPU
1	9,76	41,93	9,43	40,66	5,76	17,29
2	1,83	20,36	1,88	19,98	1,81	8,74
3	1,22	13,40	1,27	13,16	1,23	5,65
4	0,94	9,92	0,93	9,59	0,89	4,23
5	0,72	7,75	0,75	7,49	0,72	3,35
6	0,54	6,02	0,62	5,76	0,59	2,64
7	0,51	4,51	0,53	4,32	0,51	1,98
8	0,44	3,58	0,46	3,47	0,45	1,58

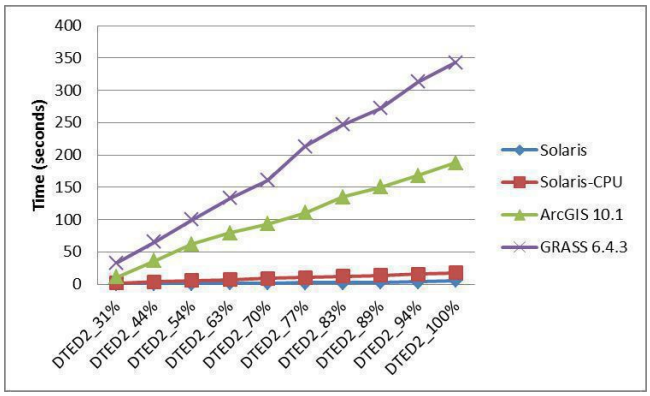


Figure 7. Execution time for curvature

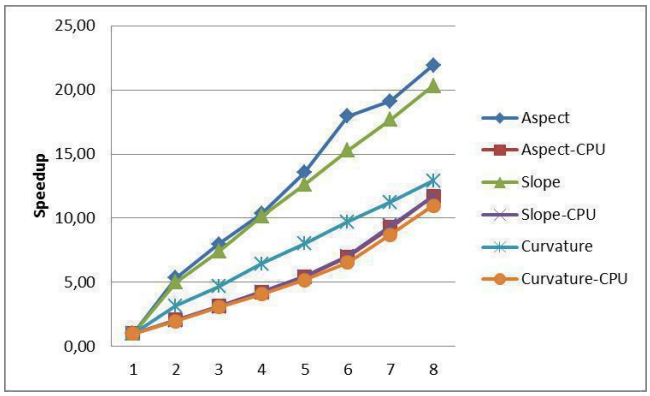


Figure 8. Speedup for various number of nodes

REFERENCES

[1] Fang Huang, Dingsheng Liu, Xiaowen Li, Lizhe Wang, Wenbo Xu: 2011: Preliminary study of a cluster-based open-source parallel GIS based on the GRASS GIS. Int. J. Digital Earth 4(5): 402-420

[2] Healey R.(ed.), Dovers S.(ed.), Gittings B.(ed.), Mineter M.J.(ed.), 1997: Parallel Processing Algorithms For GIS. Taylor&Francis

[3] Huayi Wu, Xuefeng Guan, Jianya Gong, 2011: ParaStream: A parallel streaming Delaunay triangulation algorithm for LiDAR points on multicore architectures. Computers & Geosciences 37(9): 1355-1363

[4] Osterman A., 2012: Implementation of the r.cuda.los module in the open source GRASS GIS by using parallel computation on the NVIDIA CUDA graphic cards. Elektrotechniski Vestnik 79(1-2): 19–24

[5] Soo Hee Han, Joon Heo, Hong Gyoo Sohn and Kiyun Yu, 2009: Parallel Processing Method for Airborne Laser Scanning Data Using a PC Cluster and a Virtual Grid. Sensors 9

[6] Xuefeng Guan, Huayi Wua, 2009: Leveraging the power of multi-core platforms for large-scale geospatial data processing: Exemplified by generating DEM from massive LiDAR point clouds. Computers and Geosciences 36

Geomorpho: a methodology for the classification of terrain units

Sergio Camiz
Department of Mathematics "Guido Castelnuovo"
Sapienza University of Rome
Institute of Acoustics and Sensors "O.M. Corbino"
CNR – National Research Council
Rome, Italy
sergio.camiz@uniroma1.it

Maurizio Poscolieri
Institute of Acoustics and Sensors "O.M. Corbino"
CNR – National Research Council
Rome, Italy
maurizio.poscolieri@idasc.cnr.it

Abstract—**In order to perform a thorough quantitative analysis of the morphology of an area, a methodology has been developed, able to deal with a Digital Elevation Model (*DEM*), that classifies the *DEM* pixels starting from the eight topographical gradients, computed as differences between each pixel and the eight surrounding ones, and provides for each class a complete set of statistics of terrain attributes, including elevation, slope, and aspect. In addition, a thematic colour map may be built, with hue and saturation attributed according to both mean aspect and slope of each class, respectively. As an example, Mount Soratte in Italy has been analysed in two different ways.**

I. Introduction

The study of the terrain morphology is based on the identification of the morphometric parameters of each terrain unit within the study area. In particular, altitude, aspect, and slope, are within the most used topographic attributes to take into account [1][2][3]. In this respect, the analysis of Digital Elevation Models (*DEM*) significantly helps this investigation, since through their processing it is possible to obtain a quantitative description of the relief. Several studies have been carried out so far, in order to automatically extract most information from *DEM*s [4][5][6][7][8][9].

The classification of terrain units, considering morphological attributes, was performed since long in literature [1][2][3][4][5][6][7][10][11][12]. Our approach, based on Parchiaridis *et al.* [13], distinguishes from the others since it avoids to use slope, aspect, and other terrain attributes, calculated through procedures that may lead to different results, depending on the analysis procedures and the different weighing of the characters in the classification process. Instead, in agreement with [13], we propose to create an 8-layers stack of the topographic gradients, measured along the 8 azimuth orientations of each *DEM* pixel neighbourhood. This is obtained by computing, for each pixel, its differences in elevation values with respect to the eight closest neighbours. Such a simple approach, allows to quickly estimate the spatial distribution of different types of slope steepness, so that the studied area may be partitioned into classes with similar local terrain attributes [14][15][16][17]. Hence, changes in shape, orientation, and steepness are highlighted.

The partition may be performed in several ways, providing a set of classes, whose relevant statistics may be studied in order to both understand and describe the different terrain units that may be found in the study area. In addition, if appropriate colours may be attributed to each class, the thematic map, obtained by colouring this way the pixels, may provide an immediate overview of the area structure and maybe even approach a 3-dimensional vision Error: Reference source not found.

Here, we present a methodology, fully implemented in a Fortran 95 program (not yet available for distribution), that starts from the *DEM* of a study area, performs a classification of the pixels based on the eight gradients, and provides both a complete set of statistics of the main land surface parameters, and a basis file for a thematic map, in which the pixels are coloured according to the mean aspect and slope of the class of belonging.

II. Theoretical aspects

The aim of the methodology is to partition the set of pixels that compose the area under study in homogeneous geomorphometric classes. Considering that they usually form a nearly continuous pattern, the partition may not be *natural*, in the sense that usually discontinuities do not appear in the pattern itself that suggest the existence of isolated natural classes. Thus, we consider that the adopted *Tandem* technique may be a good explor-

In: Geomorphometry for Geosciences, Jasiewicz J., Zwoliński Zb., Mitasova H., Hengl T. (eds), 2015. Adam Mickiewicz University in Poznań - Institute of Geoecology and Geoinformation, International Society for Geomorphometry, Poznań

atory method to partition the set of pixels in a nearly optimal way for the purpose.

The methodology starts with a submitted *DEM* file, in which the non-interesting part has been filled with zeros. This allows to limit attention and computation only to the selected part of the *DEM*. Then, for each pixel eight gradients are computed, as its elevation differences with the eight contiguous ones, along *NW, N, NE, E, SE, S, SW*, and *W* directions. A positive difference means that the central pixel is higher than the neighbour. At the same time, both slope and aspect values are computed [10][11][12][15][16][17].

Then the program runs a classification of the pixels according to the *Tandem Analysis* (*TA*, [19]), that consists in a *Principal Component Analysis* (*PCA*, [20][21]) followed by a classification performed on the coordinates issued by *PCA*. *TA* is largely used in exploratory studies, in which a partition is sought to better understand and describe a data structure, in particular when no natural structure in classes exists. The *PCA* used before a classification allows to better control the variables at hand, since the principal components are uncorrelated. This reveals useful to equilibrate the data variability, usually larger along the direction of highly correlated original variables and reduced along the non-correlated ones.

PCA is performed on the eight gradients, since the use of slope and aspect as input variables is not convenient, *i)* because their computation in different ways would give different results [10][11][12]; *ii)* because the aspect is circular: this means that there is no way to take into account the identity between the extreme values 0º and 360º, not even the use of sine and cosine of aspect may be appropriate here. A large number of preliminary applications of *PCA* to topographic gradients showed that usually the first two principal components summarize, in a relative weighed way, most of the data variability (always over 90%) and their spanned plane corresponds, up to reflections and a rotation, to the rose diagram. In addition, the third one, that summarizes most of the remaining variability, usually opposes peaks to pits. Thus, it is up to the researcher to decide to limit the following classification to the first two or three principal components: the use of standardized coordinates for the classification reduces on one side the differences in variability among the first two principal components, so that the obtained classes would be distinguished according only to slope and aspect; on the other side, the use of three factors would dramatically enhance the variability along the third one, so that local elevation maxima and minima may be better put in evidence.

After *PCA*, a classification, based on the Euclidean distances among pixels in the two- or three-dimensional space spanned by the principal components, is performed in four steps: *i)* a first *K-means* algorithm ([22][23]) is run, to create 100 homogeneous classes; *ii)* a *Hierarchical Ascendant Classification* (*HAC*, [23][24]) is performed on the 100 classes, through the *minimum variance clustering* method [25]; *iii)* a partition in *k* classes is chosen, according to the suggestions of two different methods; *iv)* a second *K-means* procedure is run on this chosen classification. All methods' objective functions aim at minimizing the within-classes variability and maximize the between-classes one. The first step of the clustering algorithm is used to get the procedure faster, the second to get information concerning the most suitable number of classes, and the third to optimize the chosen partition by minimizing the within-classes variability. To select the best partition, the Calinski and Harabász method [26] is adopted, considered the best by Milligan and Cooper [27] for this purpose, together with the identification of the partitions followed by a larger increase of within-classes variability. This second method was introduced since the first one, albeit more reliable, may not always suggest a partition in the range 10-25 classes that we consider the most appropriate to describe terrain attributes.

Once defined the partition, for each class means and standard deviations are calculated for both the eight gradients and the three geomorphometric characters height, slope, and aspect. It must be pointed out that for the aspect, measured by an angle, special circular statistics based on trigonometric functions [28] were considered, in order to avoid misleading values for some class [28][29]. The problem is particularly important for a class whose mean value is close to 0º = 360º, since the deviation from the mean would appear highest, only due to the (wrong) difference between 1º and 359º that, without this care, would appear of 358º and not only 2º.

The statistics are useful to characterize the classes: this is achieved by arranging them in a table in which each class is described according to the given statistics. Eventually, colours are set for each class, according to the Hue-Saturation-Lightness (*HSL*) colour modelling [30], by transforming the respective mean aspect and slope into hue and saturation values, whereas lightness is kept fixed (average) for all classes. All these results are reported by the program both in text and *ENVI* format, the latter to be used in Geographical Information System environments for a fast building of graphics.

III. An Application: Mount Soratte

As case study, an application to Mount Soratte is shown. Soratte is a *NW-SE* stretching, isolated, medium relief carbonate massif within the Italian Latium region [16]. The used *DEM* has 551×623 pixels, each one measuring 10×10 meters, in which all pixels not belonging to the relief were masked. Two geomorphometric classifications were performed, based on the coordinates of two and three factors issued by *PCA*, in 10 and 15 classes, respectively.

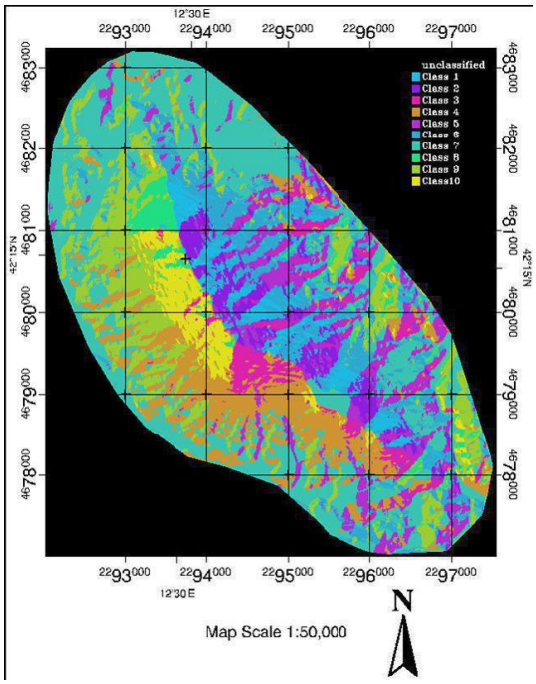


Fig. 1 - Thematic map of Mount Soratte coloured according to the 10 classes partition based on the first two *PCA* factors.

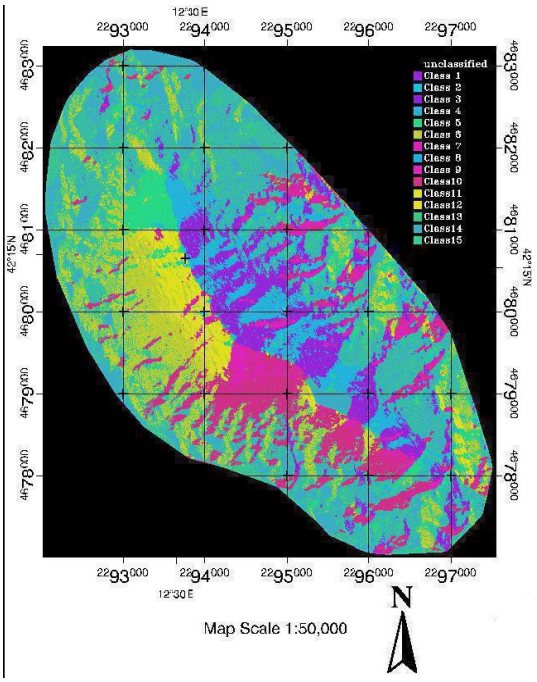


Fig. 2 - Thematic map of Mount Soratte coloured according to the 15 classes partition based on the first three *PCA* factors.

The corresponding maps are displayed in Figs. 1 and 2 and may be compared with the shaded relief of the same area, displayed in Fig. 3. The results of the two classifications are in part similar, and show the differences of the Soratte's main landforms according to both slope and aspect values of terrain units. In addition, the classification based on three factors yielded three pair of classes very similar according to these mean values, but highly different according to the local topographic gradients settings, that result concave in one case and convex in the other. Moreover, other three classes, of mostly flat areas, represent respectively local pits, peaks and real plains. This separation does not appear in the two factors classification, in which these peculiar classes are merged in one class only. In this respect, the classification based on three factors provides some extra characterization to the landforms. To get a better comparison among the two partitions, in Fig. 4 a rose diagram is shown in which all classes' mean and standard deviation of both slope and aspect are displayed. This way, it is easy to see the agreement of the classes of the two partitions.

Acknowledgment

The work of Camiz was carried out in the framework of its association with the *CNR*-Institute of Acoustics and Sensors.

References

[1] Evans, I.S., 1972. “General geomorphometry, derivatives of altitude, and descriptive statistics”. In: Spatial Analysis in Geomorphology, Edited by: Chorley, R.J., Methuen, London, pp. 17– 90.

[2] Evans, I.S., 2013. “Land surface derivatives: history, calculation and further development”. Geomorphometry 2013, pp. 1-4. http://geomorphometry.org/system/files/Evans2013geomorphometry.pdf

[3] Mark, D.M., 1975. “Geomorphometric parameters: a review and evaluation”. Geografiska Annaler 57A, pp. 165–177.

[4] Florinsky, I.V., 2012. “Digital terrain analysis in soil science and geology”. Elsevier, London.

[5] Hengl, T. and Reuter, H.I. (Ed.), 2008. “Geomorphometry: Concepts, Software, Applications”. Developments in Soil Science, 33, Elsevier, London.

[6] Pike, R.J., 2002. “A bibliography of terrain modelling (geomorphometry), the quantitative representation of topography”, U.S. Geological Survey, Open-File Report 02-465.

[7] Wilson, J.P., and J.C. Gallant, 2000. “Terrain Analysis: Principles and Applications”, Wiley, New York.

[8] Grosse, P., van Wyk de Vries, B., Euillades, P.A., Kervyn, M., Petrinovic, I.A., 2012. “Systematic morphometric characterization of volcanic edifices using digital elevation models”. Geomorphology, 136, pp. 114–131.

[9] Jordan, G., 2007. “Digital terrain analysis in a *GIS* environment. concepts and development”. In: Digital Terrain Modelling Development and Applications in a Policy Support Environment, Edited by: Peckham, R.J., Jordan, G., Springer, Berlin, pp. 1-44.

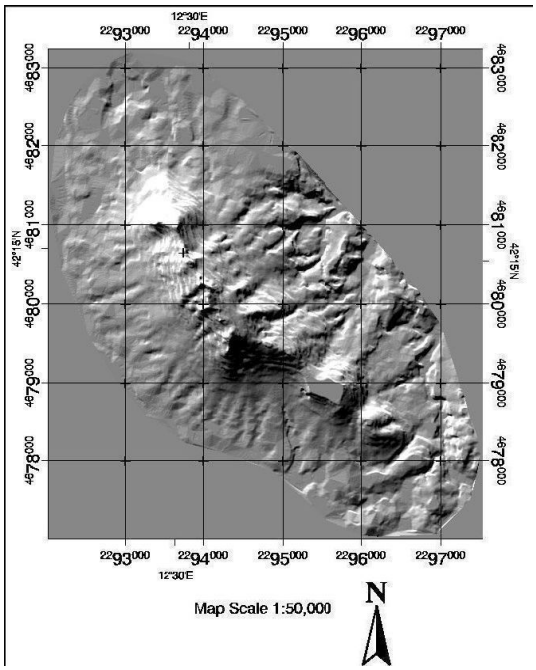


Fig. 3 – The shaded relief of Mount Soratte.

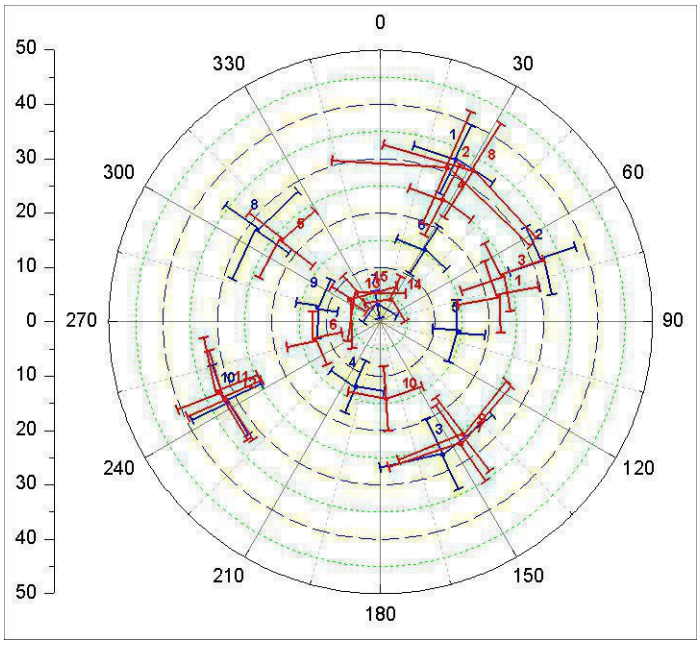


Fig. 4 – Rose diagram showing the mean and standard deviations of both mean and aspect of each class of the two partitions of Mount Soratte. Blue: partition in 10 classes based on two *PCA* factors; red: partition in 15 classes based on three *PCA* factors.

[10] Guth, P., 1995. "Slope and aspect calculations on *DEM*s", Zeitschrift für Geomorphologie, Neue Folge, Supplementband 101, pp. 31-52.

[11] Florinsky, I.V. 1998. "Accuracy of local topographic variables derived from digital elevation models". International Journal of Geographical Information Science 12 (1), pp. 47-61.

[12] Onorati, G., Poscolieri, M., Ventura, R., Chiarini, V., Crucilla, U., 1992. "Analysis of the Digital Elevation Model of Italy for quantitative geomorphology and structural geology", Catena, 19, pp. 147-178.

[13] Parcharidis, I., Pavlopoulos, A., Poscolieri, M., 2001. "Geomorphometric analysis of the Vulcano and Nysiros island: clues of the definitions of their volcanic landforms". In: Proceedings of International Workshop The Bridge Between Big Bang and Biology, Stromboli, Italy, 13–17/9/1999, Edited by: F. Giovannelli, *CNR* President's Bureau pub., Roma, pp. 310–320.

[14] Poscolieri, M., 2010. "Geomorphometry as a value added to land analysis". Proceedings of the *E-ICES 5*. *CNEA*, Buenos Aires, pp. 236–244.

[15] Adediran, A.O., Parcharidis, I., Poscolieri, M., Pavlopoulos, K., 2004. "Computer assisted discrimination of morphological units on north central Crete (Greece) by applying multivariate statistics to local relief gradients". Geomorphology, 58, pp. 357-370.

[16] Abbate, G., Cavalli, R.M., Pascucci, S., Pignatti, S., Poscolieri, M., 2006. "Relations between morphological settings and vegetation covers in a medium relief landscape of Central Italy". Ann. Geophys. 49(1), pp. 153–165.

[17] Camiz, S, Poscolieri, M., Roverato, M., 2014. "Morpho-Structural Comparison of Latin-American Volcanoes". Proceedings of *E-ICES* 9. *CNEA*, Buenos Aires, pp. 46-64.

[18] Chiba, T., Kaneta, S., Suzuki, Y., 2008. "Red Relief Image Map: new visualization method for three dimensional data". The International Archives of the Photogrammetry, Remote Sensing and Spatial Information Sciences 37, pp. 1071-1076. http://www.isprs.org/proceedings/XXXVII/congress/2_pdf/11_ThS6/08.pdf

[19] Arabie, P., Hubert, L., 1994. "Cluster analysis in marketing research". In Advanced methods of marketing research, Edited by: R.J. Bagozzi, Blackwell, London, pp. 160–189.

[20] Jolliffe, I.T., 2002. "Principal Component Analysis", Springer, Berlin.

[21] Lebart, L., A. Morineau, and M. Piron, 1997. "Statistique exploratoire multidimensionnelle". Dunod, Paris.

[22] MacQueen, J.B., 1967. "Some Methods for classification and Analysis of Multivariate Observations". In: Proceedings of 5-th Berkeley Symposium on Mathematical Statistics and Probability, University of California Press, Berkeley, 1, pp. 281-297 .

[23] Gordon, A.D., 1999. "Classification". Chapman and Hall, London.

[24] Hartigan, J.A., 1975. "Clustering Algorithms". Wiley, New York.

[25] Ward, J.H.Jr., 1963, "Hierarchical Grouping to Optimize an Objective Function", JASA, 58(301), pp. 236-244.

[26] Calinski, R.B., Harabász, J., 1974. "A Dendrite Method for Cluster Analysis", Communications in Statistics 3, pp. 1-27.

[27] Milligan, G.W., Cooper, M.C., 1985. "An examination of procedures for determining the number of clusters in a data set", Psychometrika 50(2), pp. 159-179.

[28] Mardia, K.V., Jupp, P.E., 1999. "Directional Statistics". Wiley, New York.

[29] Fisher, N.I., 1993. "Statistical Analysis of Circular Data". Cambridge University Press, Cambridge (*UK*).

[30] Agoston, M.K., 2005. "Computer Graphics and Geometric Modeling: Implementation and Algorithms", Springer, London.

Terrain misclassification problem – analysis using pattern simulation approach

Jarosław Jasiewicz, Alfred Stach, Jakub Nowosad
Institute of Geoecology and Geoinformation
Adam Mickiewicz University
Poznań, Poland
jarekj@amu.edu.pl

Abstract– **We present the results of a numerical experiment aiming at explaining reasons for classification errors when using an automatic pattern-based terrain classifications algorithm proposed by Jasiewicz et. al. [3]. We use composition of landform elements from incorrectly classified areas, and we use texture pattern from example areas to synthesize a new "terrain" which inherits properties from both sources. Using a new Pattern Analysis Toolbox (GeoPAT, [4,5]) we found that classification errors come from convergence of landscape properties: after replacing texture in misclassified areas with texture as indicated by an example area a new synthetic area shows higher degree of similarity to the landscape class from which it inherits texture. It allow to draw conclusion that short-range textural properties is that feature which at that moment best describes diversity of landscapes for automatic classifications.**

I. INTRODUCTION

One of the goals of geomorphometry is an automatic classification of terrain. Automatic classification is much faster than manual mapping (a significant advantage when working with big data sets) and the results are based on clearly defined rules. On the other hand automatic algorithm does not possess human "knowledge" about numerous hidden relations between entities in the data which leads to classification errors. Algorithm performance is based on assessment of classification error and is usually based on confusion matrix which compares amount of correctly classified examples with those which were classified incorrectly. Performance describes the quality of classifier and its real usefulness for automatic mapping. In classical machine learning performance is calculated using a test set – a set of objects for which a class is assigned by an analyst.

With classification of landscapes [1] the problem of performance assessment is more complex. The assignment of a landscape to a particular landscape class is based not only on the information available in the data but also on a knowledge not described by a mathematical description of a landscape, such as location, relation to neighborhood, distance, direction and shapes of objects on several spatial scales. In addition, in geomorphometry, like in other natural sciences, we face the problem of the convergence. Surfaces created by different processes may have similar properties at the level of the data, thus cannot be correctly classified without additional information which is not a part of topographic data.

In terrain classification errors appear for three reasons: (a) selection of inappropriate classifier, (b) lack of clear distinction between classes, and (c) gap between the information available in the data and the knowledge needed to make a correct classification. The third reason is rarely considered when performing automatic terrain classification.

Jasiewicz and Stepinski [2] published a method for classification of landform elements from DEM data; their method, called geomorphons, uses computer vision approach rather than land-surface parameters to classify landform elements into ten types. A local landscape can be considered of a mosaic of landform element types.

Recently, Jasiewicz et al. [3] demonstrated how to classify entire local landscape into landscape types (Fig. 1) using supervised learning methodology. In [3] a 30 m resolution DEM of the entire country of Poland was first transformed into a categorical map of landform elements using the geomorphons algorithm. This categorical map was then divided into a grid of overlapping square areas (300*300 cells each) and for every node in the grid a signature of a local landscape (pattern of landform element types) was calculated as a histogram of features where each feature is one of 55 possible connections between 10 existing landform element types (see [3], [4] and [5] for details). Thus signature contains information on both, the composition of landform elements in the landscape, and their relative configuration (short-distance texture of the terrain). Based on the

In: Geomorphometry for Geosciences, Jasiewicz J., Zwoliński Zb., Mitasova H., Hengl T. (eds), 2015. Adam Mickiewicz University in Poznań - Institute of Geoecology and Geoinformation, International Society for Geomorphometry, Poznań

expert knowledge 9 landscape types were selected to best describe variability of geomoprhological landscapes in Poland and example areas for these types were given. As similarity measure between local landscapes a modified Wave-Hedges measure was used which calculated weighted intersection between two signatures representing two landscapes. By default every local landscape can be similar to more than one landscape type because of aforementioned landscape convergence problem. The final single label for each local landscape was assigned using the most similar landscape type. Performance of the method proposed by Jasiewicz et. al. [3] gained 70% against the classification of landscapes in Poland made manually by Kondracki [6].

Our goal here is to investigate the reasons for misclassifications at the level of data description. Using a complex texture-composition signature (see [3]) we want to check what information affects the misclassification: general long-range (of the order of kilometers) composition of the whole area or short-range (order of tens of meters) textural properties. To solve the problem we run 2304 conditional simulations where as the source of information about the long-range composition we used misclassified areas and as a source of short-term texture we used examples of areas which were classified correctly. Simulation will change the texture of the area but will keep its general composition. The similarity between new simulated "landscape" and landscape types used as a source for composition component and texture component will answer which of those two elements plays more important role during classification process.

II. DATA AND METHOD

A. Study area

To analyze the problem we use post-glacial developed areas across the central-European lowlands. One of them is a young, immature surface which preserves the original features remained after regression of the last glaciation. Those features are very slightly or even not changed by further denudation. The second is an older surface and include area which was not covered by ice during the last glaciations; its original postglacial features were transformed into a new assemblage under periglacial conditions [7]. The extension of last glaciation is well defined (Fig. 1), and we used only landscapes which represents class "moranic plateau" so an identification and selection of misclassified areas do not rise doubts.

Areas within the reach of last glaciation (we will use the term "young glacial" in the rest of the paper) stands out by inclined slopes along narrow valleys, domination of undulated plains and numerous closed depressions alternated with small isolated hills; all together forms a very irregular pattern (See fig. 2, TP_04). On the other hand postglacial lowlands outside the extend of the last glaciation ("old glacial" in the rest of the paper) are due to substantial denudation under periglacial conditions characterized by smooth, wide and gently inclined slopes; channels with dendrite pattern, vast plains and lack of closed depressions. (see fig. 2, TN_10). The differences between those areas are expressed both in short-range textural properties represented by connection between individual cells and more general long range composition which is represented by amount and size of given terrain forms in the entire sample area.

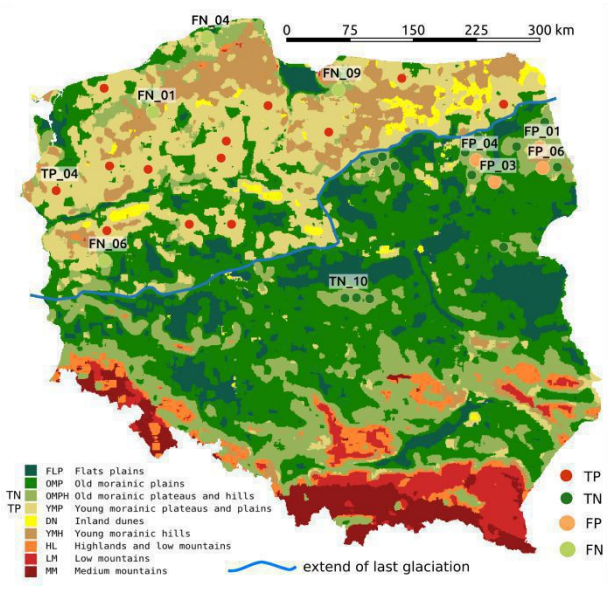


Figure 1. Location of learning and testing areas. True Positives (TP): areas classified as young glacial plateaus and located inside the extent of last glaciation; True Negatives (TN): areas classified as old glacial plateaus and located outside the extend of last glaciation; False Positives (FP): areas classified as young glacial but located outside the extend of last glaciation; False Negatives (FN): areas classified as old glacial but located inside the extend of last glaciation. Labels on misclassified areas and these two correctly classified areas used as examples on fig. 2.

B. Data

To address our problem we selected 3 areas which were used as training examples in [3] both for young and old moraine plateaus. We defined them as True Positive (TP) and True Negative (TN) respectively (fig. 1). Also we choose 8 areas which undoubtedly are located on young and old areas but were classified inversely. We defined them as False Positive (FP) and False Negative (FN) respectively (fig. 1).

C. Processing steps and implementation

To simulate landscape patterns we used FILTERSIM algorithm [8], [9] implemented in the SGeMS software [10]. This

is an intermediate solution between the pixel and object-oriented simulations. Its essence is to use a reference image that is divided into small pieces. The algorithm classifies these pieces, and then assembles the image to fit the measurement data and previously arranged parts. The best analogy is perhaps that of building a puzzle. Resulting image should be as similar as possible to the reference (training) image, while keeping the data coming from the sample. The algorithm can be used to generate a desired set of simulations, whose variability is the result of different, random paths defining the stacking order of the pieces of which creates a whole.

In our experiments we sampled composition from incorrectly classified surfaces (FN and FP), and used the patterns from surfaces of TP and TN previously used to train classifier (fig. 2). Each of the 8 selected misclassified surfaces (4 FP and 4 FN) of 300*300 cells size has been subjected to 4 levels random stratified sampling (0.1, 0.2, 0.5, and 1% of whole data). These data was used as the source of texture during the simulations. For the evaluation of the simulations variability arising from the use of different random paths each one was repeated 3 times. One of the most important parameters that affect the quality of the result, is the size of the pieces (template size) which a master image is divided into. To assess its importance calculation was performed for the four sizes: 11, 15, 19 and 23 cells. Other parameters of the algorithm were left to the default settings [10]. In summary, for each tested FP and FN surface 288 simulations was performed (6 training images × 4 sampling levels × 4 template size × 3 repetitions), which gives a total of 2304 simulated surfaces (fig. 2).

All 2304 simulated areas were imported to GRASS GIS and used to calculate the similarity/distance matrix using GeoPAT software [4,5] using identical parameters for signature and similarity measure as described by Jasiewicz et. al. [3]. Similarity matrix was used to present results in a form of Sammon's map (fig. 3) which is a form multidimentional scaling which tries to map distance between objects in multidimentional space into the two dimentional plane.

III. RESULTS

On Fig. 3A we see two distinct groups of samples, one representing correctly classified young glacial samples (red, True Positive), the second correctly classified "old glacial" (green, True Negative). Misclassified old glacial and young glacial areas are marked as FP and FN respectively and show higher similarity to the different group than the area where they are really located. Samples which results form series of conditional simulations (Fig 3B) show a much higher similarity to those areas from which sort-term pattern was taken, rather those which were provided as a source of long-range composition.

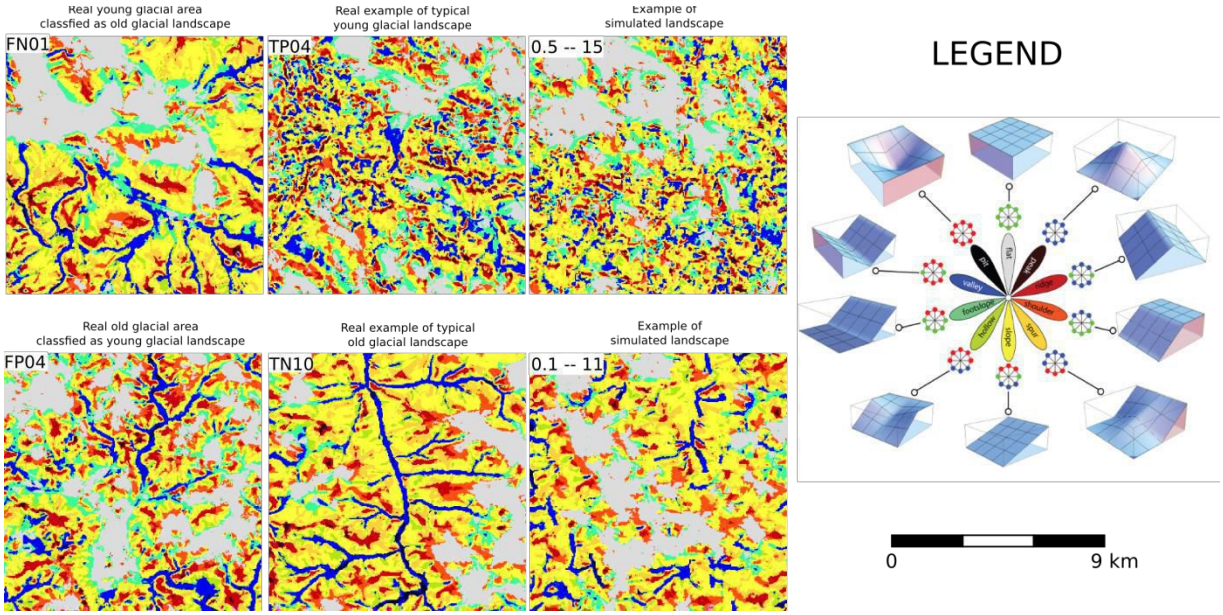


Figure 2. Example of simulations: misclassified young glacial area (upper row) old glacial area (lower row) with appropriate example of patterns used to simulate expected results. See text for details.

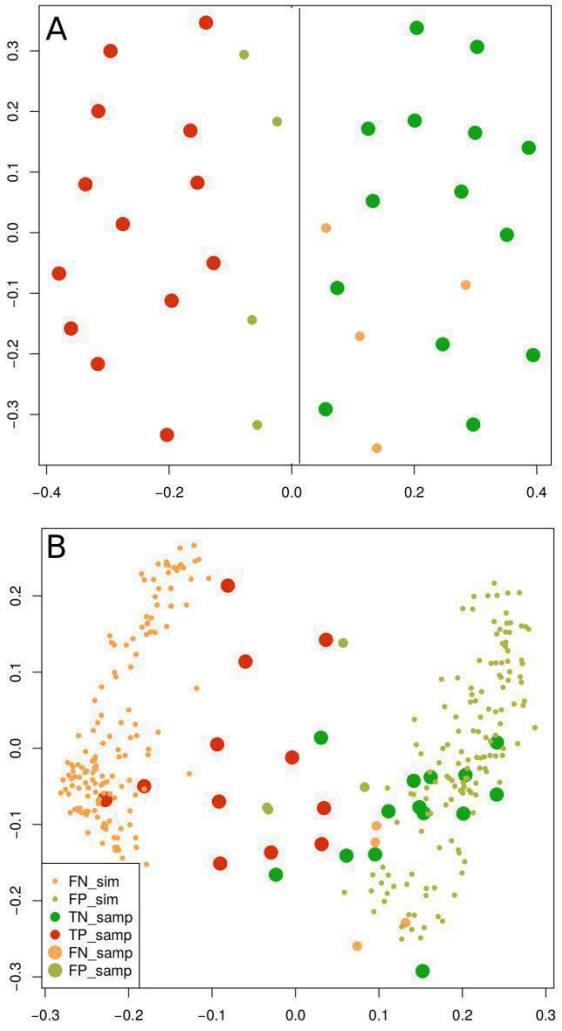


Figure 3. Classification of simulated areas on Sammon's map. Top panel (A) shows similarity between correctly and incorrectly classified samples (real). Bottom panel (B) show similarity between real samples and simulated examples. Both group of simulated areas are more similar to the group of samples from which short-range pattern is taken rather than to the group used as a source for long-range composition. Differences between location of real samples on left and right panels are results of the properties of multidimensional scaling. The values on the axes represent the dimensionless distance (objects similarity).

IV. Conclusions and Outlook

We found that misclassification error comes from convergence of landscape properties: after replacing texture in misclassified area with texture taken from correctly classified example new simulated area showed higher similarity to that landscape class from which it inherits texture than general composition. It allow to draw conclusion that short-range textural properties is that feature which best describes diversity of landscapes for automatic classifications.

V. Acknowledgments

This work was supported by NCN Grant DEC-2012/07/B/ST6/01206. The authors would like to thank Dr. T. Stepinski for helpful comments and linguistic corrections in the text.

References

[1] Minar, J., Evans, I., 2008. "Elementary forms for land surface segmentation: the theoretical basis of terrain analysis and geomorphological mapping". Geomorphology 95: 236–259.

[2] Jasiewicz, J., Stepinski, T.F., 2013. "Geomorphons — a pattern recognition approach to classification and mapping of landforms". Geomorphology 182: 147-156.

[3] Jasiewicz, J., Netzel, P., Stepinski, T.F., 2014. "Landscape similarity, retrieval, and machine mapping of physiographic units". Geomorphology 221: 104-112.

[4] Jasiewicz, J., Netzel, P., Stepinski T.F., 2014. "Retrival of pattern-based information from giga-cells categorical rasters - concept and new software." IGARSS 2014, 1785-1788.

[5] Jasiewicz, J., Netzel, P. Stepinski, T.F., 2015. "GeoPAT: A toolbox for pattern-based information retrieval from large geospatial databases." Computers & Geosciences, 80: 62-73.

[6] Kondracki, J., 2002. „Regional geography of Poland". 3rd edition. Wydawnictwo Naukowe PWN, Warszawa. (In Polish)

[7] Dylik, J., 1952. "The concept of the periglacial cycle in middle Poland". Bull. Soc. Sci. Lett. 3: 5–29.

[8] Zhang, T., 2006. "Filter-based training pattern classification for spatial pattern simulation". Ph.D. Dissertation, Stanford University, Stanford, CA, 137pp. (http://pangea.stanford.edu/departments/ere/dropbox/scrf/documents/Theses/SCRF-Theses/2000-2009/2006_PhD_Zhang.pdf, last accessed 30 April 2015)

[9] Wu, J., Zhang, T., Journel, A., 2008. "Fast FILTERSIM Simulation with Score-based Distance". Mathematical Geosciences 40: 773–788.

[10] Wu, J., Boucher, A., Zhang, T., 2008. "A SGeMS Code for Pattern Simulation of Continuous and Categorical Variables: FILTERSIM". Computers & Geosciences 34(12): 1863-1876.

Visualizing morphometric changes in a piping system using DEM and GIS analysis: the Bieszczady Mts., Poland

Anita Bernatek
Institute of Geography and Spatial Management
Jagiellonian University
Krakow, Poland
anita.bernatek@uj.edu.pl

Abstract— **This paper presents the morphometric changes in a selected piping system in the Tyskowa catchment in the Bieszczady Mts. (Eastern Carpathians) in Poland. The detailed geodesic measurements were made twice a year – in spring and in autumn – in 2013-2014. The Topcon Hiper II (base and rover) with the FC-250 field controller were used. The high resolution elevation model and additional maps were prepared using ArcGIS 10.2 software with ArcScene for 3D visualization. The positive and negative openness index were calculated in Saga GIS 2.1.4 software. The morphometric changes were calculated using Algebra map in ArcGIS 10.2. The different ways of the piping system visualization allow emphasizing the position of pipes in the slope-valley system. The concavity above the existing gully with the surface traces of pipe collapsing indicate the influence of piping in the gully formation and in its future development. The morphometric changes in the piping system enables to present erosion and accumulation zone within the piping system.**

I. INTRODUCTION

Piping is a subsurface process which leads to the formation of underground channels (pipes) by concentrated flowing water [1], [2]. From geomorphological point of view, the role of piping may be crucial, because the pipe collapse can result in the formation of discontinuous gully, and after regular gully. Therefore, the question about morphometric changes in a piping system thus dynamics of its possible development into gullies is worth of research.

Most research on piping is dedicated to the role of piping in relief development [3], particularly gully development (e.g. [4], [5]) and the factors controlling pipes development (e.g. [6], [7], [8]). The piping dynamics is considered mostly in terms of the soil erosion rates (e.g. [9], [10]).

Therefore, the aim of this study is to present the piping dynamics in different way – by visualizing the morphometric changes in a piping system using high resolution elevation model (0.25 m) and GIS analysis. The detailed objectives are: (1) to present the selected piping system in different maps to extract the information of its position in a slope-valley system; (2) to analyze the elevation data using terrain analysis indexes (positive and negative openness index); (3) to present the vertical differences in the ground level within the piping system in 2013-2014.

II. STUDY AREA

A. *Tyskowa catchment*

The analyzed piping system is located in the Tyskowa catchment in the Polish Bieszczady Mts., which are part of the Eastern Carpathians (Fig. 1). The Bieszczady Mts. are mainly formed of the Carpathian Flysch characterized by thick-bedded sandstones alternating with shales, where on the slopes developed silty-clay cover beds. It is a mid-mountain region, with altitudes ranging from 573 m to 894 m a.s.l. on the highest point. The climate is temperate with a mean annual temperature ranges from 4.0°C to 5.0°C [11] and a mean annual precipitation of 1000-1300 mm [12].

In: Geomorphometry for Geosciences, Jasiewicz J., Zwoliński Zb., Mitasova H., Hengl T. (eds), 2015. Adam Mickiewicz University in Poznań - Institute of Geoecology and Geoinformation, International Society for Geomorphometry, Poznań

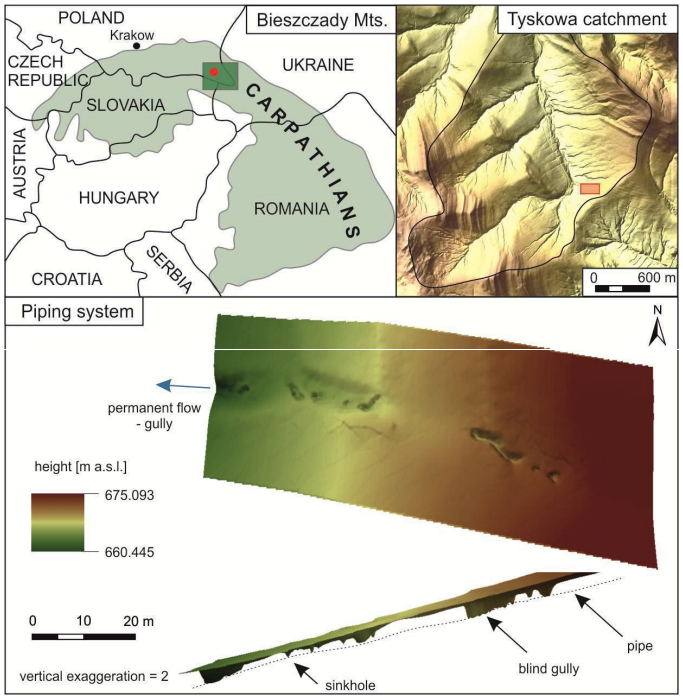


Figure 1. Location of study area with the 3D image of analyzed piping system.

B. *Piping system*

Piping system is a complex of piping forms, which are associated with one or more combined pipes [13], [14], [15]. The studied piping system constitutes of 4 sinkholes and 3 blind (discontinuous) gullies. It is located in the upper part of the catchment, on the slope of W aspect and average gradient of 10° to 15°. The majority of piping system is developed in grassland and the pipe outlet is in the forest in the channel head of the gully.

III. MATERIALS AND METHODS

The elevation data were collected in the field using the Topcon Hiper II (base and rover) with the FC-250 field controller. The detailed geodesic measurements were made twice a year – in spring (early April, after snow melting) and in autumn (late October – early November, after summer rainfalls, before snowfalls) in 2013-2014. The individual surface piping forms were additionally measured with a measuring tape.

The digital elevation model (DEM) and additional maps of 0.25 m resolution were prepared using ArcGIS 10.2 software with ArcScene for 3D visualization. The positive and negative openness index were calculated in Saga GIS 2.1.4 software. The morphometric changes were calculated using Algebra map in ArcGIS 10.2. According to the observer error (estimating 0.05 m), the root mean squared error (RMSE) was calculated (RMSE = 0.07 m).

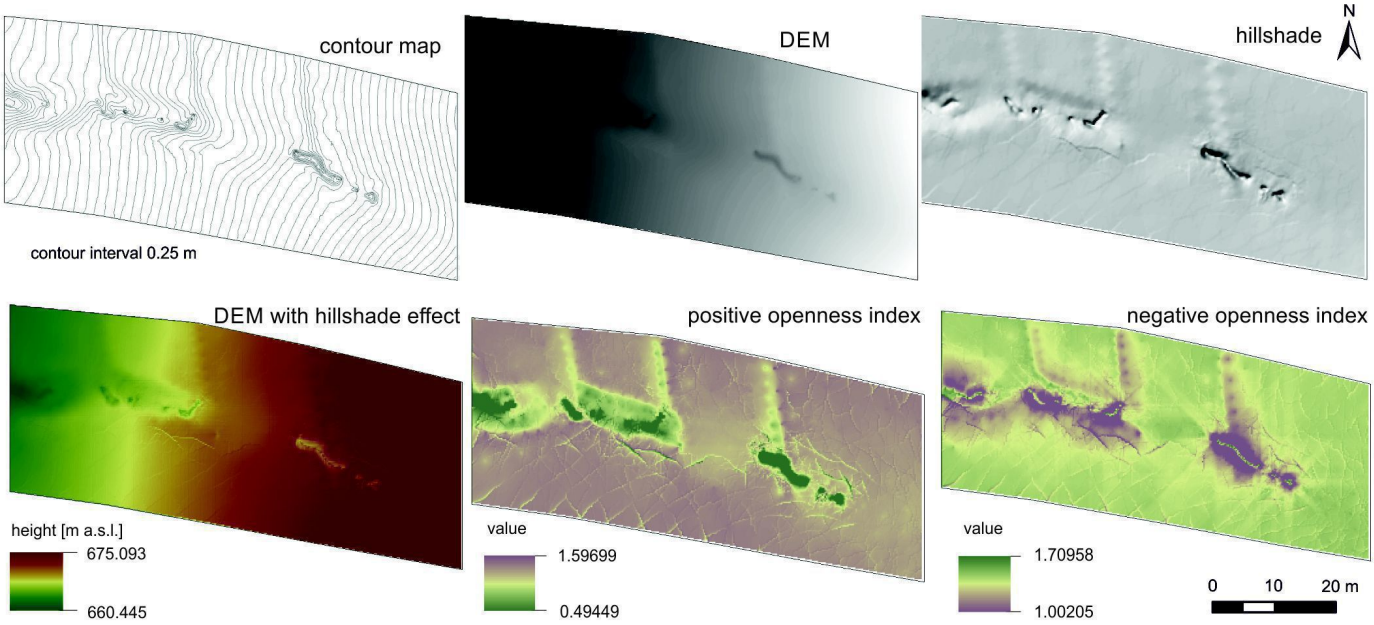


Figure 2. The different way of visualizing elevation data of the piping system.

IV. RESULTS

The depth of sinkholes in the study area ranges from 0.50 to 1.00 m, which is also the depth at which pipes developed, since the bottom of a sinkhole is the bottom of a pipe. The blind (discontinuous) gully reaches maximum 1.50 m of the depth, 11.25 m long and 1.50 m wide in the maximum point.

The piping system can be visualized by distinguishing the surface traces of collapsed pipes (sinkholes, blind gully etc.). It can be done by creating the contour map with appropriate contour interval (Fig. 2). To extract the concavity of these piping forms in DEM is helpful to use a hillshade effect or 3D images (Fig. 1, 2). The positive and negative openness index marks the places of concavities, but also emphasizes abandoned agricultural terraces (perpendicular to the system). The negative openness index reflects also the flat bottom of the blind (discontinuous) gullies (Fig. 2).

The visualization of morphometric changes in the piping system allows to distinguish areas where prevails erosion and accumulation within the collapsed pipe(s). In the upper part of the piping system dominates accumulation, because of the blind gully and sinkhole walls failure. In the lower part, the erosion area in the pipe inlet is noticed. This may indicate the linkage of side pipe to the principal pipe (E-W direction). It requires further research, for instance geophysical investigations which can present the subsurface network of pipes.(Fig. 3).

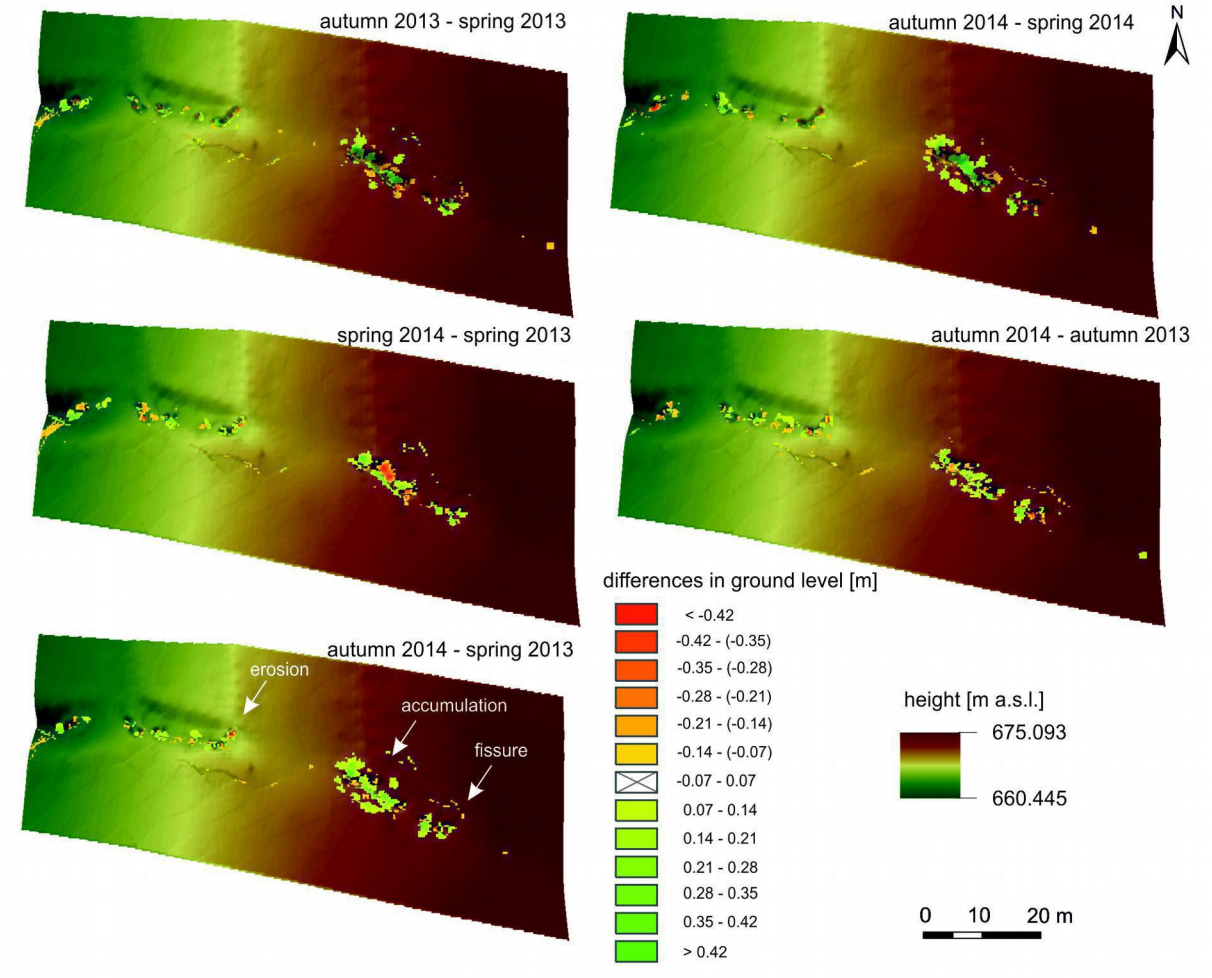


Figure 3. The morphometric changes in the piping system in 2013-2014.

V. Conclusions

In recent years piping is increasingly considering as one of the geomorphological processes that impacts the relief. This paper presents the different ways of visualizing piping system to emphasize its position in a slope-valley system. On the one hand, the noticeable concavity above the existing gully with the surface traces of pipe collapsing indicate the influence of piping in the gully formation and in its future development. On the other hand, the dominance of accumulation zones underlines that these piping forms are ephemeral and after collapsing they will be filled in. However, the seasonal variation shows that the erosion occurs mainly in winter time (snow melting) – according to comparison of spring measurements, and accumulation prevails in summer time (summer rainfalls are not enough to create morphological effective flow in the piping system). It can be also a result of the vegetation cover, which is quite dense even in the end of autumn, so the field measurements can be disturbed.

Moreover, the openness and closeness indexes are appropriate and useful to visualize and identify the places where piping occurs.

This paper presents the preliminary results and conclusions, which need to be continued and expanded.

Acknowledgment

This study is part of the project "The role of piping in relief development (the Bieszczady Mts., the Eastern Carpathians)" supported by the National Centre of Science, Poland – grant no DEC-2012/05/N/ST10/03926. I would like to express my gratitude to Michał Jakiel for his invaluable assistance in the fieldwork, Prof. Kazimierz Krzemień and Dr. Dominika Wrońska-Wałach for their constructive remarks that helped me in improving this paper.

References

[1] Jones, J.A.A., 1994. “Soil piping and its hydrogeomorphic function”. Cuaternario y Geomorfología 8 (3-4), 77–102.

[2] Jones, J.A.A., 2004. “Pipe and piping”, In Encyclopaedia of Geomorphology, Edited by: Goudie, A.S., Routledge, 784–788.

[3] Bryan, R.B., Jones, J.A.A., 1997. “The significance of soil piping processes: inventory and prospect”. Geomorphology 20, 209–218.

[4] Frankl, A., Poesen, J., Deckers, J., Haile, M., Nyssen, J., 2012.” Gully head retreat rates in the semi-arid highlands of Northern Ethiopia”. Geomorphology 173–174, 185–195.

[5] Faulkner, H., 2013. “Badlands in marl lithologies: A field guide to soil dispersion, subsurface erosion and piping-origin gullies”. Catena 106, 42–53.

[6] Gutiérrez, M., Sancho, C., Benito, G., Sirvent, J., Desir, G., 1997. “Quantitative study of piping processes in badland areas of the Ebro Basin, NE Spain”. Geomorphology 20, 237–253.

[7] Botschek, J., Krause, S., Abel, T., Skowronek, A., 2002. “Piping and erodibility of loessic soils in Bergisches Land, Nordrhein-Westfalen”. Journal of Plant Nutrition and Soil Science-Zeitschrift für Pflanzenernahrung und Bodenkunde 165, 241–246.

[8] Verachtert, E., Maetens, W., Van Den Eeckhaut, M., Poesen, J., Deckers, J., 2011. “Soil loss rates due to piping erosion”. Earth Surface Processes and Landforms 36, 1715–1725.

[9] Rodzik, J., Furtak, T., Zgłobicki, W., 2009. „The impact of snowmelt and heavy rainfall runoff on erosion rates in a gully system, Lublin Upland, Poland”. Earth Surface Processes and Landforms, 34, 1938–1950.

[10] Verachtert, E., Van Den Eeckhaut, M., Poesen, J., Govers, G., Deckers, J., 2011. “Prediction of spatial patterns of collapsed pipes in loess-derived soils in a temperate humid climate using logistic regression”. Geomorphology 130, 185–196.

[11] Michna, E., Paczos, S., 1972. „Zarys klimatu Bieszczadów Zachodnich” (The outline of climate of Western Bieszczady Mts.). Lubelskie Towarzystwo Naukowe, Zakład Narodowy im. Ossolińskich, Wydawnictwo PAN, 72 p. [in Polish].

[12] Nowosad, M., 1995. “Zarys klimatu Bieszczadzkiego Parku Narodowego i jego otuliny w świetle dotychczasowych badań” (The outline of climate of Bieszczady National Park and its buffer zone shown by the previous studies)”. Roczniki Bieszczadzkie 4, 163–183 [in Polish].

[13] Czeppe, Z., 1960. “Zjawiska sufozyjne w glinach zboczowych górnej części dorzecza Sanu” (Suffosional phenomena in slope loams of the Upper San drainage basin). Biuletyn Instytutu Geologicznego, Z badań czwartorzędu 9, 297–324 [in Polish].

[14] Beckedahl, H.R., 1996. “Subsurface soil erosion phenomena in Transkei and Southern Kwazulu – Natal, South Africa”. PhD thesis, University of Natal, Pietermaritzburg (manuscript), 224 p.

[15] Bernatek, A., 2015. “The influence of piping on mid-mountain relief: a case study from the Polish Bieszczady Mts. (Eastern Carpathians)”. Carpathian Journal of Earth and Environmental Sciences (In Press).

CAUTION DUST STORMS DO EXIST (and so do mountains): Modeling dust source suitability within an object-oriented geoecology

Charles P. Jackson
Department of Geography
New Mexico State University
Las Cruces, USA
charliej@nmsu.edu

Abstract—**GIScience has long been dominated by the naturalistic and scientistic ontological constraints championed by Willard Van Orman Quine. This has relegated dust storms and even mountains to the so-called slum of possibles that Quine had sought to clear in favor of a more aesthetic desert landscape. Paradoxically, mountains and dust storms often are real constituents of Earth's deserts and semi-arid regions. The New Mexico Department of Health (NMDOH) is studying air quality and its impact on human health in the U.S.-Mexico border region. Emissions of fine particulate matter (PM_{10}) from the Pleistocene pluvial Lake Palomas basin in the Chihuahuan Desert are a primary concern. Through Graham Harman's object-oriented philosophy and rejection of the abiotic and biotic as ontologically distinct realms, "species" distribution models (SDMs) generated in Maxent become possible with just a small number of dust source presences located in MODIS visible band imagery. The first models from 2013 used multiple geoecologically relevant terrain objects to replace the geographically uncertain point sources. Although the terrain objects had been segmented with eCognition® from only two of the three ASTER GDEM parameters used, the early SDMs nevertheless suggested that dust storms are accessible on geomorphometric terms alone. Wind directions were derived in 2014 using dust plume image objects segmented from the MODIS thermal band translations of three dust storms. Three 'wind-related terrain attributes' were then generated for each storm in Whitebox GAT from the SRTM DEM to complement the new SRTM terrain objects. When comparably biased multi-object "background data" also replace the 10,000 pixel-level background samples in Maxent, the model AUCs decrease expectedly but still remain high enough for the SDMs to be potentially useful. The probability distributions are now "projected" over the same extents to the successively lower object and pixel levels in this novel and geographically scalar approach.**

I. INTRODUCTION AND BACKGROUND

Dust storms and the emissions of fine particulate matter (PM_{10}), airborne particles with aerodynamic diameters less than 10.0 µm, have been studied across many of Earth's endorheic basins and dry plains. Most of the studies oriented towards the sources of PM_{10} have typically focused on geomorphological settings, soil types, anthropogenic factors, land cover, climatic and meteorological drivers of atmospheric dust loading or, in some cases, the discernment of dust plumes in satellite imagery. In addition, some recent studies have turned to the sub-basin scale and even include attempts at locating individual dust sources in MODIS imagery [1], [2]. However, until now, none has approached dust storms as unified and ephemeral objects with component parts in a geomorphometric and geoecological context.

The development of an object-oriented maximum entropy approach for modeling dust source suitability distributions began in 2013 as an attempt to utilize what was previously done by [1] and [3]. [1] located close to 150 individual dust sources from the distinct plumes visible in the U.S.-Mexico border region and on the U.S. southern High Plains in a "true color" enhancement of the MODIS translation of the 15 December 2003 dust storm. [3] developed a method for locating dust sources in NOAA GOES and POES satellite imagery that translated five synoptically-forced dust storms in the border region during 2002 and 2003. Of the five dust storms in [3], only three have samples with at least 15 presences located in the higher spatial resolution NOAA POES AVHRR imagery to take advantage of the 'hinge features' in the presence-only maximum entropy modeling software known as Maxent [4]. As was expected, the preliminary model that used the MODIS presences from the border region in [1] outperformed those using the far more geographically uncertain AVHRR presences from [3].

Species distribution models (SDMs) are important for determining the distribution of suitable conditions for a species or, in this case, objects. Geographic bias in sampling can be especially problematic for presence-only or presence-background

In: Geomorphometry for Geosciences, Jasiewicz J., Zwoliński Zb., Mitasova H., Hengl T. (eds), 2015. Adam Mickiewicz University in Poznań - Institute of Geoecology and Geoinformation, International Society for Geomorphometry, Poznań

models [4], [5]. Sampling satellite imagery for dust source occurrences has its own peculiar forms of bias associated with it. First, because discovery is constrained by the spatial resolutions of the imagery, we cannot say that there are, in fact, any true absences. Second, the dust plumes can sometimes obscure additional underlying sources and plumes [1] resulting in an upwind concentration at or near the 'plume head' [2]. Third, the object-oriented ontology used here for replacing the geographically uncertain point sources introduces a new bias and its own subsequently novel and geographically scalar solution.

One consequence of the *anti*-object-oriented naturalism and ontological scientism established by [6] and endorsed by [7] is the reduction of geomorphometric data to "ancillary" status in service to a more primary optical remote sensing. Despite the many object-based and object-oriented approaches and some noteworthy attempts to unify them with field-based models, none have been object-oriented in the ontological sense. That is, entities, objects and fields are typically either reduced downward to supposedly more fundamental elements or processes or reduced upward to events, appearances, aggregates, bundles of qualities, effects or relations [8], [9]. Contra anthropocentric philosophy, all forms of access are indirect and take place on the interior of a containing relation-object [10]. Not even mountains are reducible to mere conceptualizations or specific aggregates of molecules, as they are for [11], but are indeterminate and real objects in their own right that remain susceptible to translation by humans, glaciers, air parcels and the asthenosphere.

II. Methods and Materials

A. Terrain attributes

A 3-arc-second CGIAR-CSI post-processed Shuttle Radar Topography Mission (SRTM) DEM mosaic was projected in the UTM projection with a 90 meter spatial resolution and filtered in Whitebox GAT. Two geoecologically relevant terrain attributes were generated in Whitebox GAT for use in Maxent along with elevation. The first is the statistical parameter measuring local vertical complexity in the DEM generated with a three by three neighborhood application of the 'standard deviation filter' [12], [13]. It is referred to here as 'local variability' (LV). [14] used 'local variance' (also LV) to refer to a statistical procedure for describing the variability over an entire image, and [15] were correct in later renaming it as 'average local variance' (ALV). Because the local variability of any parameter can be a quality of objects at any spatiotemporal scale including the image as a whole, the use of LV as local variability is retained here for the sake of simplicity.

The second terrain parameter approximates the asymmetrical heating of the land surface in the northern hemisphere [16]. This simple estimation of the anisotropic diurnal heat (H_α) distribution (referred to here as ADHD) is generated through a seven-step process involving the local slope aspect and angle of the DEM as they appear in the following formula:

$$H_\alpha = \cos(\alpha_{max} - \alpha) \cdot \arctan(\beta)$$

where α_{max} is the slope aspect of maximum total heat surplus in the northern hemisphere (202.5°), α is slope aspect and β is the slope angle [16]. The ADHD index effectively approximates relative available soil moisture, possible changes in soil type and even possible changes in ecological community structure and function, especially when it is coupled with vertical complexity and elevation in terrain segmentations within an object-oriented ontology. Use of the biophysically and geoecologically relevant ADHD parameter also circumvents the problem encountered by [17] when attempting to segment terrain objects from surrogates like slope aspect [5].

B. Wind-related terrain attributes

Due to the absence of surface meteorological observations, surface wind azimuths were approximated using the directions of long and narrow 'microplume' objects. The reprojected 1 km spatial resolution MODIS thermal infrared (TIR) surface/cloud temperature bands (23, 32 and 31) were segmented and classified in eCognition® after a histogram equalization was applied to highlight and intensify the dust plumes (Fig. 1). The 'main direction' of the microplumes were averaged and reversed by 180° for the wind azimuths. The 'directional relief', 'fetch analysis' and 'relative aspect' were then generated in Whitebox GAT using the hypothetical azimuths for each storm [18].

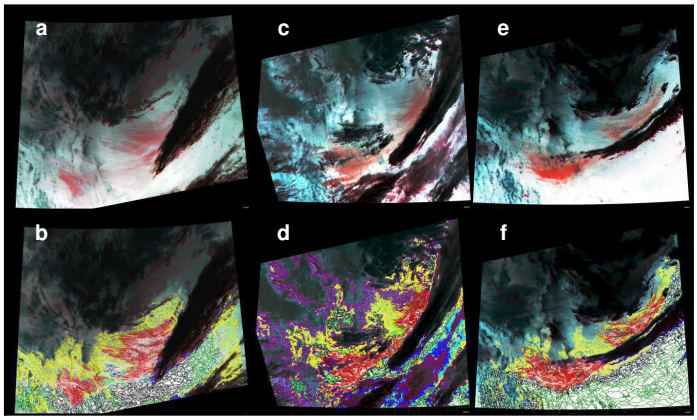


Fig. 1. The 1 km spatial resolution MODIS thermal infrared (TIR) surface/cloud temperature bands 23, 32 and 31 (red, green and blue (RGB), respectively) after reprojection and histogram equalization (top row). Border region (left) and High Plains region (right) dust plumes appear red in these TIR translations of the 15 December 2003 (a&b), 19 February 2004 (c&d) and 27 November 2005 (e&f) dust storms. The classified objects appear in the bottom row. Wind azimuths were derived from the white microplume objects within the red 'macroplumes'.

C. Terrain segmentations

Multiresolution terrain segmentations were completed for three subsets in the U.S.-Mexico border region containing the dust source presences so as to minimize presence-background bias [4], [5], [19]. A 'scale parameter' of four was used and the 'shape' and 'compactness' homogeneity criteria were set at 0.1 and 0.7, respectively. Only the LV and ADHD attributes were used and a double weight was applied to the ADHD layer to ensure a higher degree of geoecological relevance. This results in terrain objects locally determined by both the variability in elevation and the estimated topo-climatic heating of the terrain. The 39,590.2 km^2 subset containing the 15 December 2003 dust storm presences in the Lake Palomas basin yielded 46,887 objects with a mean of 104.2 pixels (SD: 97.5) or mean area of 84.4 hectares. The smaller but more topographically complex 14,290.6 km^2 subset for the 19 February 2004 dust storm is located on the eastern slope of the Sierra Madre Occidental in Mexico where a total of 33,886 terrain objects with a mean of 52.1 pixels (SD: 53.4) or mean area of 42.2 hectares were segmented. The 73,429.5 km^2 subset of the 27 November 2005 model area in the Lake Palomas basin yielded 128,511 objects with a mean of 70.5 pixels (SD: 77.7) or mean area of 57.1 hectares. Each of the presences and 10,000 background points was given a 1 km radius uncertainty buffer following the stated confidence that the points were within one or two kilometers of the actual dust source [20]. The means for each of the six parameters were then calculated from the objects intersecting the uncertainty buffers and compiled as 'samples with data' (SWD) for use in Maxent.

III. Results

The Maxent models used cross-validation with 10 replicates for each of the four presence-only samples from the three dust storms. The logistic outputs of the Maxent distributions (Fig. 2) were "projected" to the successively lower terrain object and pixel levels within the presence subsets. The [1] sample of the 15 December 2003 dust storm had the highest test and training AUCs (areas under the receiver operating characteristic [ROC] curves) (Table 1). Furthermore, each of the four presence samples produced potentially useful models with average test AUCs above 0.75 [4]. However, the 10-replicate cross-validation model runs that are well-suited for small sample sizes also exhibit considerable variability (Fig. 3).

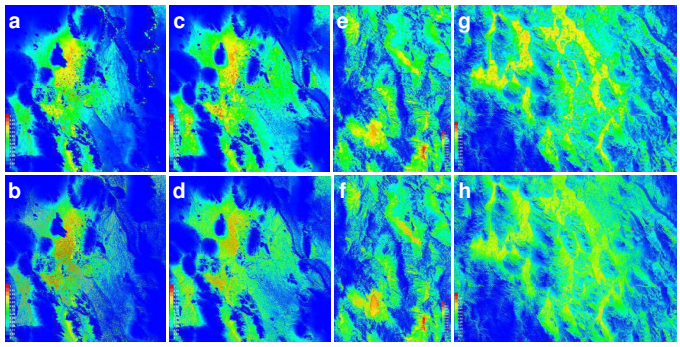


Fig. 2. The logistic outputs of the Maxent 10-replicate average suitability distributions "projected" to the successively lower object level (top row) and pixel level (bottom row) for the 15 December 2003 (a-d; a&b come from the [1] sample), 19 February 2004 (e&f) and 27 November 2005 (g&h) dust storms. Typical presences have values near 0.5 (green) [4].

TABLE I. RESULTS OF THE 10- REPLICATE MODEL RUNS IN MAXENT USING CROSS-VALIDATION.

Dust Storm Day (DSD)	Presences (*n*) and average area under the ROC curves (AUC)		
	# of dust source presences: Training n (Test n)	*Training AUC*	*Test AUC*
15 Dec 2003 [1]	29 or 30 (4 or 3)	0.9142	0.8804
15 Dec 2003	62 or 63 (7 or 6)	0.8717	0.8315
19 Feb 2004	53 or 54 (6 or 5)	0.8624	0.7920
27 Nov 2005	56 or 57 (7 or 6)	0.8315	0.7976

IV. Discussions

A novel and geographically scalar approach for modeling suitability distributions for dust sources during major dust storms has been introduced. This object-oriented geoecological strategy provides a necessary and coherent foundation that uses geomorphometric terms alone. The early SDMs generated in Maxent in 2013 demonstrated that the obscuration of downwind dust sources by the dust plume(s) might be overcome in this way. The addition of three Whitebox GAT wind-related terrain attributes has resulted in improved models with AUCs high enough to consider them as being potentially useful. More importantly, by properly accounting for geographically uncertain, and therefore biased, presence samples, the Maxent suitability

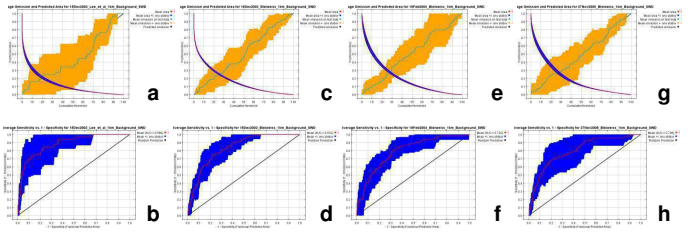


Fig. 3. Average omission and predicted area (top row) and test ROC curves (bottom row) for the four 10-replicate model runs for the 15 December 2003 (a-d; a&b come from the [1] sample), 19 February 2004 (e&f) and 27 November 2005 (g&h) dust storms. One SD of omission is shown in orange and one SD of variability in the ROC curves is shown in blue.

distributions are now able to be projected to the successively lower object and pixel levels.

In doing so, we effectively go below the MODIS spatial resolutions through "displacement" to the spatial resolution of the geomorphometric terms while simultaneously retaining pixels as objects. That is to say, the suitability distributions have more or less been "transferred" to the lower scalar levels over the same spatial extents without privileging spectral remote sensing over and above geomorphometry. Not only does an object-oriented geoecology put the abiotic and biotic on equal ontological footing, it has also allowed, through a geographically scalar application of the maximum entropy principle, for dust sources to be either vagile or non-vagile objects.

This approach can now be further improved with additional land-surface parameters and a more thorough investigation of the wind-related terrain attributes used here, and others including the 'channelling/deflection index' (CDI) [18]. Analysis of specific dust storm characteristics is also required. For instance, the lower AUCs for the 19 February 2004 and 27 November 2005 dust storm models might be explained by the greater variability in the orientations and morphologies of the microplume objects and estimated wind directions. The 15 December 2003 dust storm models benefit from the many distinct microplumes of relatively uniform direction and shape. Additional geomorphometric analyses are also required for the region as a whole, especially with respect to the hydrology of the many playas and their associated agricultural uses. Finally, terrain objects like these can now be "encrusted" with the appropriate spectral data and further segmented for more comprehensive analyses.

ACKNOWLEDGMENTS

This project was initially funded by the New Mexico Department of Health (NMDOH) and made possible by atmospheric scientist and New Mexico State Climatologist, David W. DuBois, PhD. I would like to thank Max P. Bleiweiss for kindly providing dust source samples of these and many more dust storms. The segmentations were all completed through the use of the eCognition® software license which the Jornada Experimental Range, and Jim Lenz in particular, thankfully made possible. Thank you, Janet Greenlee, Andrew Martinez, Shelby Van Arnam and Curtis Atherton, for your support and insights while employed at the Spatial Applications and Research Center (SpARC). Finally, this application of a non-holistic geography is entirely the author's own and in no way does it reflect the views held by anyone in either the NMSU Department of Geography or the Jornada Experimental Range.

REFERENCES

[1] Lee, J.A., Gill, T.E., Mulligan, K.R., Dominguez Acosta, M., Perez, A.E., 2009. "Land use/land cover and point sources of the 15 December 2003 dust storm in southwestern North America". Geomorphology 105: 18-27.

[2] Baddock, M.C., Bullard, J.E., Bryant, R.G., 2009. "Dust source identification using MODIS: A comparison of techniques applied to the Lake Eyre Basin, Australia". Remote Sensing of Environment 113: 1511-1528.

[3] Rivera Rivera, N.I., Gill, T.E., Bleiweiss, M.P., Hand, J.L., 2010. "Source characteristics of hazardous Chihuahuan Desert dust outbreaks". Atmospheric Environment 44: 2457-2468.

[4] Phillips, S.J. and Dudík, M., 2008. "Modeling of species distributions with Maxent: New extensions and a comprehensive evaluation". Ecography 31: 161-175.

[5] Phillips, S.J., 2008. "Transferability, sample selection bias and background data in presence-only modeling: A response to Peterson et al. (2007)". Ecography 31: 272-278.

[6] Quine, W.V.O., 1964. "From a Logical Point of View: 9 Logico-Philosophical Essays". 2nd ed., rev., Harvard University Press, 184 p.

[7] Zhang, J. and Goodchild, M.F., 2002. "Uncertainty in Geographical Information". CRC press, 266 p.

[8] Harman, G., 2011. "The road to objects". Continent 3(1): 171-179.

[9] Harman, G., 2011. "The Quadruple Object". Zero Books, 148 p.

[10] Harman, G., 2010. "Time, space, essence, and eidos: A new theory of causation". Cosmos and History: The Journal of Natural and Social Philosophy 6(1): 1-17.

[11] Smith, B. and Mark, D.M., 2003. "Do mountains exist? Towards an ontology of landforms". Environment and Planning B 30(3): 411-428.

[12] Lu, H., 2008. "Modelling terrain complexity". In: Zhou, Q., Lees, B., Tang, G. (Eds.), "Advances in Digital Terrain Analysis". Springer, 462 p.

[13] Olaya, V., 2009. "Basic land-surface parameters". In: Hengl, T. and Reuter, H.I. (Eds.), "Geomorphometry: Concepts, Software, Applications". Developments in Soil Science Vol. 33, Elsevier, 796 p.

[14] Woodcock, C.E. and Strahler, A.H., 1987. "The factor of scale in remote sensing". Remote Sensing of Environment 21: 311-332.

[15] Bøcher, P.K. and McCloy, K.R., 2006. "The fundamentals of average local variance—part I: Detecting regular patterns". IEEE Transactions on Image Processing 15(2): 300-310.

[16] Böhner, J. and Antonić, O., 2009. "Land-surface parameters specific to topo-climatology". In: Hengl, T. and Reuter, H.I. (Eds.), "Geomorphometry: Concepts, Software, Applications". Developments in Soil Science Vol. 33, Elsevier, 796 p.

[17] Drăguţ, L. and Blaschke, T., 2006. "Automated classification of landform elements using object-based image analysis". Geomorphology 81: 330-344.

[18] Lindsay, J.B. and Rothwell, J.J., 2008. "Modelling channelling and deflection of wind by topography". In: Zhou, Q., Lees, B., Tang, G. (Eds.), "Advances in Digital Terrain Analysis". Springer, 462 p.

[19] Phillips, S.J., Anderson, R.P., Schapire, R.E., 2006. "Maximum entropy modeling of species geographic distributions". Ecological Modelling 190: 231-259.

[20] Lee, J.A., Baddock, M.C., Mbuh, M.J., Gill, T.E., 2012. "Geomorphic and land cover characteristics of aeolian dust sources in West Texas and eastern New Mexico, USA". Aeolian Research 3: 459-466.

Regional quantification of rock glacier movement in Austria using governmental GIS data

Viktor Kaufmann
Institute of Remote Sensing and Photogrammetry
Graz University of Technology
Graz, Austria
viktor.kaufmann@tugraz.at

Andreas Kellerer-Pirklbauer
Department of Geography and Regional Science
University of Graz
Graz, Austria
andreas.kellerer@uni-graz.at

Abstract—**This paper demonstrates (1) how the kinematics of rock glaciers can be monitored at a regional scale using multi-temporal governmental GIS data, such as digital orthophotos and digital elevation models, and (2) how this geometric information can be exploited in climate change studies. Research was carried out in a 125 km² mountain area in Central Austria characterized by widespread permafrost and active rock glaciers. Our main conclusions are: (1) rock glacier monitoring using governmental GIS data is possible, with certain restrictions in the significance level due to reduced data quality and limited data availability, (2) flow velocities have increased significantly within the observation period, and (3) temporal change of flow velocity is correlated with temperature although mean annual rates computed by averaging velocities over several years mask high inter-annual variations in climatic conditions.**

I. INTRODUCTION

Active rock glaciers are creep phenomena in high-relief environments under permafrost conditions moving slowly down-valley or downslope. Morphologically, rock glaciers are commonly characterized by distinct flow structures with ridges and furrows at the surface [1, 2]. Permafrost is defined as perennially frozen ground with a seasonally unfrozen surface (active layer). According to [3], the global permafrost area is about 16-21 × 10^6 km² including Antarctic and sub-sea permafrost. Flow velocities of active rock glaciers are typically in the range of a few centimeters up to several meters per year. The magnitude of the creep/flow velocity and its spatio-temporal change is influenced by different parameters, such as air and ground temperature, topography, ice content, and hydrology [1, 4, 5].

Inactive rock glaciers do not move at present but are still under widespread permafrost conditions. Active and inactive rock glaciers are jointly termed as intact rock glaciers [1] because a lack of adequate data makes it difficult to judge whether a rock glacier is moving or not. In contrast, relict rock glaciers are no longer under permafrost conditions and are considered as non-moving, paleo-permafrost indicators.

II. STUDY AREA

The study area (125 km^2) is located in the central part of the Schober Mountains, Hohe Tauern Range, Central Austria (Fig.1). According to a recently elaborated rock glacier inventory [6], 64 intact and 35 relict rock glaciers are located within the area of interest. Permafrost is a widespread thermal phenomenon in this region as shown by numerous intact rock glaciers, local ground temperature monitoring [7], and regional permafrost models [8] indicating a possible lower limit of permafrost at c. 2200 m a.s.l..

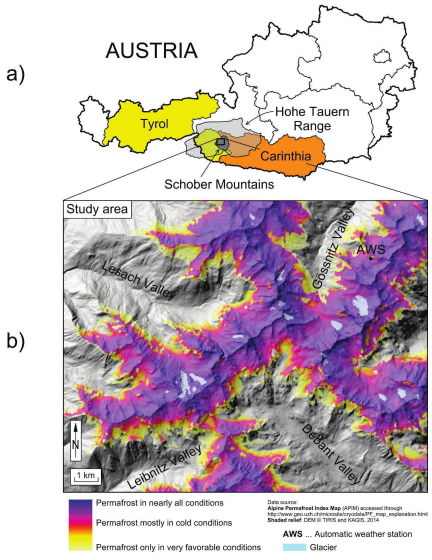


Figure 1. a) Location of the study area in the central Schober Mountains, Hohe Tauern Range, Austria. b) Permafrost distribution in the study area. AWS-automatic weather station; Data source: [8]; TIRIS and KAGIS (GIS data providers).

In: Geomorphometry for Geosciences, Jasiewicz J., Zwoliński Zb., Mitasova H., Hengl T. (eds), 2015. Adam Mickiewicz University in Poznań - Institute of Geoecology and Geoinformation, International Society for Geomorphometry, Poznań

III. MATERIALS AND METHODS

A. Multi-temporal digital orthophotos

Digital orthophotos of three different epochs (2002, 2009, 2012) covering the area of interest were made available by the authoritative GIS data providers of the regional governments of Tyrol and Carinthia (Fig. 1, Tab. 1). Image data was provided as tiled jpg-compressed files, with each tile covering an area of 6.25 km^2. All tiles of each epoch were mosaicked together to assemble a large image file. A common ground sampling distance (GSD) of 50 cm was chosen to limit file sizes and thus computational work load. Local analyses, however, were carried out with 20 cm GSD for several test sites. RGB data was converted to grayscale for subsequent use in the image matching software. Image data of 2012 was low-pass filtered using a Gaussian kernel to approximate smoothness of the 2002 and 2009 image data.

TABLE I. MULTI-TEMPORAL DIGITAL ORTHOPHOTOS USED

Date	Original GSD (cm)	Spectral bands	Type of camera
Sept. 18, 2002	25	RGB	Analog
Sept. 7, 2009	25	RGB	Analog
Aug. 25, 2012	20	RGB NIR	Digital

B. Multi-temporal digital elevation models

The GIS data providers also made available digital elevation models (DEMs) derived from airborne laser scanner (ALS) data with a grid spacing of 10 m for the whole study area and 1 m for selected test sites. Due to administrative reasons, the DEM data of Austrian provinces is strictly confined by provincial boundaries, however with a small overlap to the neighboring province. Elevation data from the Tyrolean and Carinthian part of the study area dates from August/September 2009 and the year 2012, respectively. The precise dates of ALS data acquisition were not available . The overlapping zone of the two grids in the border area is approximately 700 m in width. This part was then used in our change detection analysis.

C. Computation of displacement vectors

Information about the geometric change of the Earth's surface can be derived by different measuring techniques. Remote sensing techniques from air or space are highly appropriate to efficiently retrieve such information on a regional scale, e.g. for a whole mountain group. In this study we applied multi-temporal orthophotos and DEMs. The computation of horizontal displacement vectors using orthophotos of at least two different acquisition dates has been reported for many earth science applications (e.g. [4]). Image matching is preferably carried out using the normalized cross-correlation coefficient as a similarity measure for searching homologous points [9].

We have implemented our software in Matlab R2012b. In order to uniformly measure surface displacement over a larger area, a variable grid of measuring points can be defined. For the purpose of efficiently screening the given study area we chose a grid spacing of 12.5 m. This setting provides sufficient geometric resolution for all rock glaciers of the inventory. The size of the correlation window is crucial and has been set to 31 by 31 pixels, which relates to an areal coverage of 15.5 m by 15.5 m.

A threshold of greater than 0.4 for the correlation coefficient defines potential good solutions. Furthermore, sub-pixel accuracy in image registration is achieved by parabolic interpolation. All prospective matches are cross-checked by back-matching using the same procedure as outlined above. Special emphasis was put on automatically detecting any remaining outliers in the final result. In order to detect these outliers we have defined a small set of rules of exclusion. These rules are primarily based on the smoothness assumption of the overall deformation and slope information derived from the DEMs. The rules turned out to be very useful in attaining an automatic procedure without significant loss of correct measurements. All rules are bound to the general significance level of the computed displacements. More dense and accurate displacement vector fields were computed for several other test sites within the study area following the workflow outlined above. Due to both the small areal extent and the general higher measurement precision, the displacement vectors computed for stable areas outside the rock glacier were used to detect small systematic offsets of the orthophotos involved and to quantify the attainable precision. In a few incidences a significant horizontal shift of the orthophotos was detected and corrected for.

Three-dimensional displacement vectors can also be derived from multi-temporal DEMs. The small overlapping area of the two DEMs (grid spacing of 1m) was used to validate any potential movement detected by means of orthophoto comparison in this area. In principle, the same image matching technique was applied as above. Height or gradient values (kind of shaded relief) may serve as gray values in the matching process. Our example is numerically based on the direct use of height values. Grid spacing was set to 5 m and the correlation window was 21 pixels, providing high spatial correlation. Stable areas around the suspected mass movement were analyzed to quantify maximum attainable precision.

D. Meteorological data

An automatic weather station (AWS) was installed in the study area in 2006. The station is located 2655 m a.s.l. in close vicinity to a highly active rock glacier (Fig. 1). We used air

temperature data for the period September 2006 to September 2012. Data gaps were closed by using correlation analysis and temperature data from the meteorological observatory Hoher Sonnblick (SON) located 15 km northeast of AWS. Due to the high correlation of mean monthly air temperature data between AWS and SON, mean monthly values for AWS were furthermore estimated for the time period October 2002 to August 2006. See [4] for further methodological details. No ground temperature data were used in this study due to the lack of continuous ground temperature data between 2002 and 2012.

IV. RESULTS

Two thematic maps were produced showing the mean annual horizontal flow velocity of all rock glaciers of the study area for the two consecutive time periods 2002-2009 and 2009-2012. Figure 2 displays the map for the first period. Twelve intact rock glaciers revealed significant movements in both periods. The rock glaciers with the highest flow velocities (labeled as 1, 2 and 3 in Fig. 2) show mean horizontal flow velocities of up to 440 cm/a. The comparison of the two periods shows a general trend of higher velocities during the second period (by a factor of 1.4 to 1.8).

As an example of additional large-scale studies conducted in the study area, results from the Tschadinhorn rock glacier are depicted in Fig. 3. The maximum velocity of this rock glacier increased from 117 cm/a during the first period to 177 cm/a during the second period. The kinematics of an additional, previously unknown mass movement (label 4 in Fig. 2) detected outside the rock glacier areas was re-evaluated using the two DEMs of 2009 and 2012. Maximum flow velocities of up to 69 cm/a were calculated for this mass movement. This result

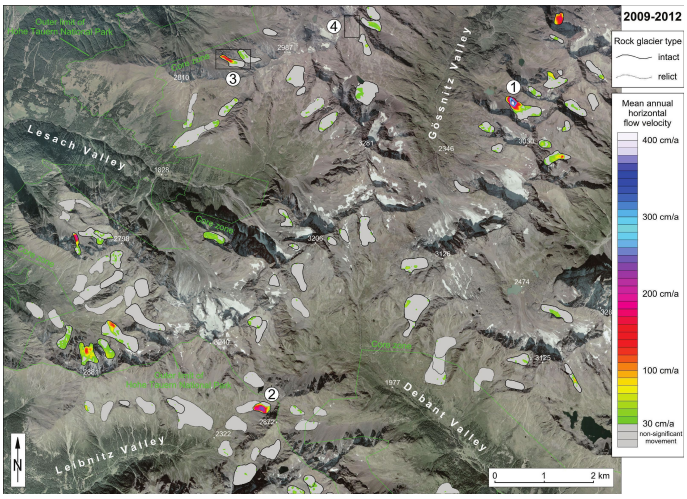


Figure 2. Thematic map showing the mean annual horizontal flow velocity of rock glaciers located in the study area for the time period 2009-2012.

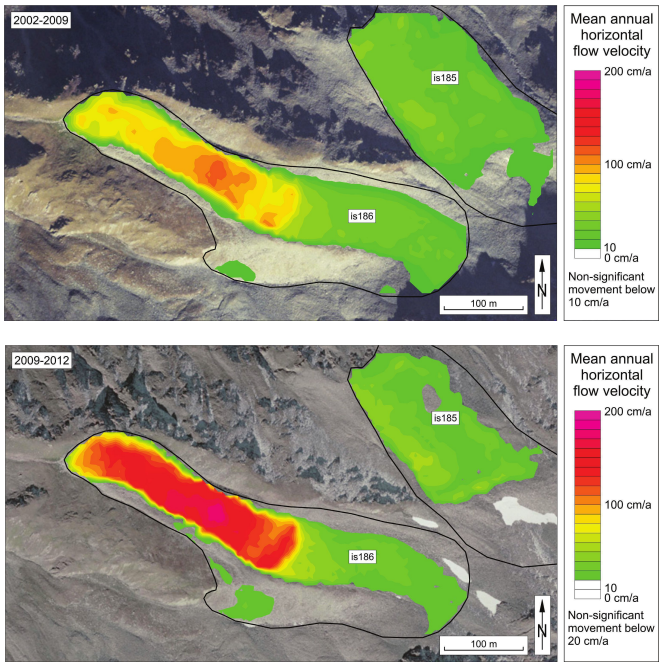


Figure 3. Mean annual horizontal flow velocity of Tschadinhorn rock glacier (is186) for the time period 2002-2009 (top) and 2009-2012 (bottom). For location see Fig. 2, label 3.

confirms the orthophoto-based deformation analysis.

Mean annual air temperature (MAAT) values at AWS were calculated for each hydrological year between 2002 and 2012. All hydrological years indicate a negative mean annual value. 2006-2007 (-0.1°C) was by far the warmest year, followed by 2011-2012 (-0.9°C), whereas the coldest year was 2003-2004 (-2.3°C). Apart from the values of 2002-2003 (rather warm), 2006-2007 (very warm), and 2009-2010 (rather cold) one might see a warming trend during the 10-year period. Furthermore, the mean annual value for 2002-2009 is 0.2°C lower than for 2009-2012, despite the "outliers" of the three hydrological years mentioned above. This observation further suggests a warming trend in the area.

V. DISCUSSION AND CONCLUSIONS

A. Data availability and accuracy

Multi-temporal orthophotos are available for the study area from governmental GIS data providers for at least three different epochs at GSDs of 50 cm, 25 cm and 20 cm. High spatial and also high radiometric resolutions can only be expected from recent digital orthophotos which are derived from aerial photographs taken with digital aerial cameras. Accuracy analysis

of the orthophotos used has shown that geometric quality is generally high. Animated GIFs of orthophoto time-series and also calculated displacement vectors suggest, however, that the geometric quality of the orthophotos is mostly reduced by erroneous or low-resolution DEMs used in the rectification process. It was found that the orthophoto geometry was quite poor in some local areas. As a rule of thumb we can expect a mean relative registration error of ±60 cm for any two orthophotos taken at different times. Assuming a time interval of 3 years, the mean annual flow velocities computed would have an accuracy of approx. ±20 cm/a (1σ), which means that this kind of image data (3-year interval) do not allow detection of slow moving rock glaciers. The significance level can, however, be increased dramatically by using contemporary DEMs derived from the aerial photographs themselves or by at least using the high resolution DEMs derived from ALS data. Anticipated accuracies are in the range of a few cm/a as shown in other pilot studies, e.g. [10].

The current availability of multi-temporal governmental DEMs is limited. Nonetheless, this kind of data offers great potential in change detection.

B. Rock glacier speed-up and climate relationship

This study shows that almost all fast moving rock glaciers in the study area have increased their mean annual velocities between the two time periods despite the fact that the multi-annual averaging (7 and 3 years, respectively) masks inter-annual changes. This multi-annual trend is also confirmed by field-based (total station and RTK-GNSS) annual movement measurements at some of the rock glaciers in the study area. As shown by published [5] and unpublished data, rock glaciers in the study area showed slower movement in 1999-2002, higher rates in 2002-2005, deceleration and lower values in 2005-2009, and continuous speed-up since then. The field-based movement measurements revealed a 1.5 fold increase between the first (2002-2009) and the second (2009-2012) period. This is in accordance with the regional signal revealed in this study (1.6 times between the first and second period). This regional signal is also confirmed on an Alpine-wide scale. Reference [11] reported comparable relative velocity changes of a large number of rock glaciers in the European Alps supporting the climatic dominance of rock glacier velocity changes. This study and some previous studies [e.g. 5, 12] indicate that warmer temperatures favor higher velocities of rock glaciers. However, this reaction might have a time lag of several months or even years reflecting the delay in propagation of the temperature signal deeper into the rock glacier body. Furthermore, higher temperatures cause higher deformation rates of the ice contained in the rock glacier body and might influence the quantity of liquid water lubricating rock glacier movement.

ACKNOWLEDGMENTS

The financial support by OeAV-Patenschaftsfonds Nationalpark Hohe Tauern is kindly appreciated. The AWS was financed through the project “ALPCHANGE – Climate Change and Impacts in Southern Austrian Alpine Regions” funded by the Austrian Science Fund (FWF) through project no. FWF P18304-N10.

REFERENCES

[1] Barsch, D., 1996. “Rockglaciers: indicators for the present and former geoecology in high mountain environments”, Springer Series in Physical Environment, 16, 331 p.

[2] Haeberli, W., Hallet, B., Arenson, L., Elconin, R., Humlum, O., Kääb, A., Kaufmann, V., Ladanyi, B., Matsuoka, N., Springman, S., and D. Vonder Mühll, 2006. “Permafrost Creep and Rock Glacier Dynamics”, Permafrost and Periglacial Processes, 17, 189-214.

[3] Gruber, S., 2012. “Derivation and analysis of a high-resolution estimate of global permafrost zonation”, The Cryosphere, 6, 221-233.

[4] Kääb, A., 2005. “Remote Sensing of Mountain Glaciers and Permafrost Creep. Schriftenreihe Physische Geographie”, 48, Department of Geography, University of Zurich, 264 p.

[5] Kellerer-Pirklbauer, A., and V. Kaufmann, 2012. “About the relationship between rock glacier velocity and climate parameters in central Austria”, Austrian Journal of Earth Sciences, 105(2), 94-112.

[6] Kellerer-Pirklbauer, A., Lieb, G.K., and H. Kleinferchner, 2012. “A new rock glacier inventory of the eastern European Alps”, Austrian Journal of Earth Sciences, 105(2), 78-93.

[7] Kellerer-Pirklbauer, A., 2013. “Ground surface temperature and permafrost evolution in the Hohe Tauern National Park, Austria, between 2006 and 2012: Signals of a warming climate?”, In 5th Symposium for Research in Protected Areas - Conference Volume, 10 to 12 June 2013, Mittersill, Austria, 363-372.

[8] Boeckli, L., Brenning, A., Gruber, S., and J. Noetzli, 2012. “Permafrost distribution in the European Alps: calculation and evaluation of an index map and summary statistics”, The Cryosphere, 6, 807-820.

[9] Debella-Gilo, M., and A. Kääb, 2011. “Sub-pixel precision image matching for measuring surface displacements on mass movements using normalized cross-correlation”, Remote Sensing of Environment, 115, 130-142.

[10] Kaufmann, V., and R. Ladstädter, 2002. “Monitoring of active rock glaciers by means of digital photogrammetry”, Proceedings of the ISPRS Commission III Symposium "Photogrammetric Computer Vision", Graz, Austria, IAPRS, Vol. 34, Part 3B, 108-111.

[11] Delaloye, R., Perruchoud, E., Avian, M., Kaufmann, V., Bodin, X., Hausmann, H., Ikeda, A., Kääb, A., Kellerer-Pirklbauer, A., Krainer, K., Lambiel, Ch., Mihajlovic, D., Staub, B., Roer, I., and E. Thibert, 2008. “Recent Interannual Variations of Rock Glacier Creep in the European Alps”, In Proc. Ninth Int. Conf. on Permafrost, Institute of Northern Engineering, University of Alaska, Fairbanks, Vol. 1, 343-348.

[12] Kääb, A., Frauenfelder, R., and I. Roer, 2007. „On the response of rockglacier creep to surface temperature increase”, Global and Planetary Change, 56, 172-187.

Thermal satellite scenes in modelling soil humidity for single event modelling of wind erosion

Rafal Wawer, Artur Lopatka, Eugeniusz Nowocien
The Department of Soil Science Erosion Control and Land Protection. The Institute of Soil science and Plant Cultivation – State Research Institute, Pulawy, Poland
huwer@iung.pulawy.pl

Abstract— **Soil moisture remains one of the most important indices influencing soil resistance to the shear forces of dropping and flowing water or blowing wind. Physically based models as well as experiments at various spatial and time scales confirm that firmly. There is however a major obstacle in wide utilization of soil moisture information in wide-area erosion intensity monitoring - the availability of reliable data sources. The research described in that paper is aimed at finding a reliable methodology for the estimation of current moisture of the topsoil, which can be than used to estimate potential or actual erosion rates at given erosive factors' intensity and duration. Thermal satellite imagery was chosen as source of data for soil humidity. Algorithms were developed for combining scenes from different satellites were developed aiming at achieving maximum temporal and spatial resolution of the output data. A NDTI model for transforming the thermal band images into soil humidity rasters were developed basing upon thermal inertial model. The models were validated with manual on ground measurements of soil humidity using high accuracy TDR soil moisture meter, revealing relatively good fit of the developed models with correlation coefficient at the level of R^2=0,41. A simple wind erosion model was chosen to demonstrate the usage of the soil moisture data overlaid with soil and land use maps. However the method of estimating the temporal soil moisture has a bigger application potential, eg. in single event soil erosion models, plant water deficit estimations and defense.**

I. INTRODUCTION

Soil moisture remains one of the most important indices influencing soil resistance to the shear forces of dropping and flowing water or blowing wind. Physically based models [12] as well as experiments at various spatial and time scales confirm that firmly. The results of our experimental research, performed in controlled micro-plot conditions, show high correlations between soil humidity in its upper layer and the rates of both wind [16] and water erosion [17]. There is however a major obstacle in wide utilization of soil moisture information in wide-area erosion intensity monitoring - the availability of reliable data sources. In case of Poland, similarly to whole Northern Europe, where soil cover tends to be highly variable due to the spatial diversity of post-glacial soil substrates, measuring soil moisture physically is not a realistic option, especially as interpolation methods are not reliable enough considering low density soil moisture monitoring stations not covering a representative set of soil units. The monitoring of the dynamics of soil moisture induced by precipitation remains equally difficult. While the average distance between meteorological stations within Poland national weather monitoring grid is ca 70km, the size of an average storm cloud remains at the level of few kilometers, hence using a simple linear interpolation of even geostatistics do not provide results reliable enough for the soil moisture to be effectively modelled based upon the climatic water balance or other models of water balance. The potential solution for wide-area and relatively frequent monitoring of soil moisture remains satellite imagery. This paper will present an exercise of modelling soil moisture content based upon thermal satellite images and its use in the modeling of single event events of wind erosion.

II. SOIL MOISTURE MODEL FOR THERMAL SATELLITE IMAGERY

A. *Available models*

The models suitable for the estimation of soil humidity basing upon the thermal satellite images can be divided into two groups:

1. Thermal balance models utilizing the effect of stronger warming of areas with water deficit in soil caused by limited real evapo-transpiration (transpiration has cooling effect on the surface);
2. Thermal inertial models basing upon the fact, that wet areas warm up and cool down slower than dry areas, because of the water's large heat capacity, which corresponds to the daily amplitude of temperature being inversely proportional to soil humidity.

In: Geomorphometry for Geosciences, Jasiewicz J., Zwoliński Zb., Mitasova H., Hengl T. (eds), 2015. Adam Mickiewicz University in Poznań - Institute of Geoecology and Geoinformation, International Society for Geomorphometry, Poznań

For the thermal balance models the starting point of the equations is the thermal balance of the surface of crop cover as a consequence of the energy conservation principle in a time unit. These models can be divided into two categories differing in the representation of surface as one or two layer models [10]. In the one-layer models the surface of plant and soil is treated as a single uniform layer. Two-layer models the temperature of soil and plant cover is separated into two surfaces, dependent from each other.

In the one-layer category the most popular models are [10]: SEBS (Surface Energy Balance System) [13], SEBAL (Surface Energy Balance Algorithm for Land) [3, 4] and METRIC (Mapping EvapoTranspiration at high Resolution with Internalized Calibration) [1].

In the realm of two-layer models the most widely used models are [10]: TSEB - Two Source Energy Balance [5, 8], ALEXI – Atmosphere-Land EXchange Inverse [2] and DisALEXI – Disaggregated ALEXI [6, 9].

A separated group of models related to the thermal balance model, but based upon empirical observations are models based upon a cloud of points within a coordinate system of two axes: one is surface temperature (Ts) or its function and second is a vegetation index, eg. most frequently used NDVI (Normalized Difference Vegetation Index). Among this group, the most popular models are: triangular model (Ts/NDVI), NDTI (Normalized Difference Temperature Index), SWSI (Crop Water Stress Index) and S-SEBI (Simplified Surface Energy Balance Index (chart of Ts/albedo) [11].

Thermal inertial models are not that frequently used as thermal balance models. Their application as explanatory models for thermal satellite scenes has one large disadvantage. The models assess the dynamics of temperature change in two time intervals in a single day, eg. day and night, which is very hard to achieve in existing satellite systems, which have either frequent reacquisition time and low resolution or high resolution and long return time (see tab. I for free data source options).

TABLE I. SOURCES OF FREE SATELLITE IMAGES IN THERMAL BAND

Satellite	Sensor	Spectral resolution Number of TIR bands, wavelengths	Spatial resolution [m]	Temporal resolution [days]
Terra	ASTER	5 (8,5-11,6 µm)	90	16 on demand
Terra, Aqua	MODIS	16 (3,7-14,4 µm)	1000	2 (day and night) automatic
Landsat 8	TIRS	1 (10,3-12,5µm)	100	16 automatic
Landsat 7	ETM+	1 (10,4-12,2µm)	60 (od 31.05.2013 partially corrupted – 22% of a scene)	
NOAA	AVHRR/ 3	2/3 (3,5-12,5 µm)	4000	2 (day and night)
ENVISAT	AATSR	3 (3,7-12 µm)	1000	2 (day and night)
Meteosat 8, 9, 10	SEVIRI	8 (3,5-14,4 µm)	3000	0,01

As the combination of high spatial and temporal resolutions and in practice not possible to achieve in a single thermal satellite product an algorithm of combining scenes of high spatial and low temporal resolutions with ones with high temporal and low spatial resolutions. The refining algorithm bases upon a comparative analyses with archive and current precise scenes as reference and correction layers, the agricultural-soil map as the reference for spatial variability of soils' hydrological features and current low spatial resolution but frequent scenes.

B. Validation of the scene combination algorithm

The algorithm for the estimation of current soil humidity was validated on a sample are of Bystra river catchment in South-Eastern Poland. 23 locations for soil sampling were chosen: 12 on ploughland, 6 on grasslands, 1 on abandoned land and 5 in the forests. Urban areas , waters and water wastelands were not considered.

Soils investigated are: sands, loams, silts, rocks and organic peat.

The validation was done through comparison of soil humidity, measured with a TDR sensor with values predicted by the NDTI model applied on thermal satellite scenes disaggregated with the refining algorithm. The validation revealed relatively good fit between models and observed soil moisture values, where $R^2 = 0,41$ while there were no data filtering applied on extreme values. The results for satellite scenes are still higher than for the simple profiling soil moisture sensors widely used in practice eg. for irrigation management.

III. APPLICATION OF SATELLITE DERIVED SOIL MOISTURE DATA IN THE ESTIMATION OF EROSION INTENSITY

One single event was chosen as an example.

The calculations are basing upon empirical models developed in controlled conditions of simulated wind. The inputs were:

- Soil moisture layer based derived form a desegregated thermal scenes of MODIS;
- Soil texture derived from agricultural soil map 1:25000 and linked with the IUNG database of reference soil samples;
- Land use structure derived from a LANDSAT 7TM scene;
- Wind occurrence were derived from IUNG meteorological stations in Pulawy, Rogalow and Palikije.

Very simple model was chosen for this example. The equation for wind erosion in threshold wind speed was assessed using equation [17]:

$$D = 19{,}73 + 0{,}241998 \bullet Fp - 1{,}211924 \bullet W + 39{,}11221 + 0{,}1 \bullet Fp + 55{,}32836 \bullet W \quad (1)$$

where:

D-deflation [g•h•m -2];

Fp- content of sand fraction in soil [%];

W- initial soil humidity [%].

Soil agricultural map and land use map derived from Landsat 8 were used as a reference for the spatial distribution of sand content in soils and locations of land not being ploughed, which is excluded from the study. The event of March 2013 was chosen, where winds of 8m/s were blowing for 2,5 hours.

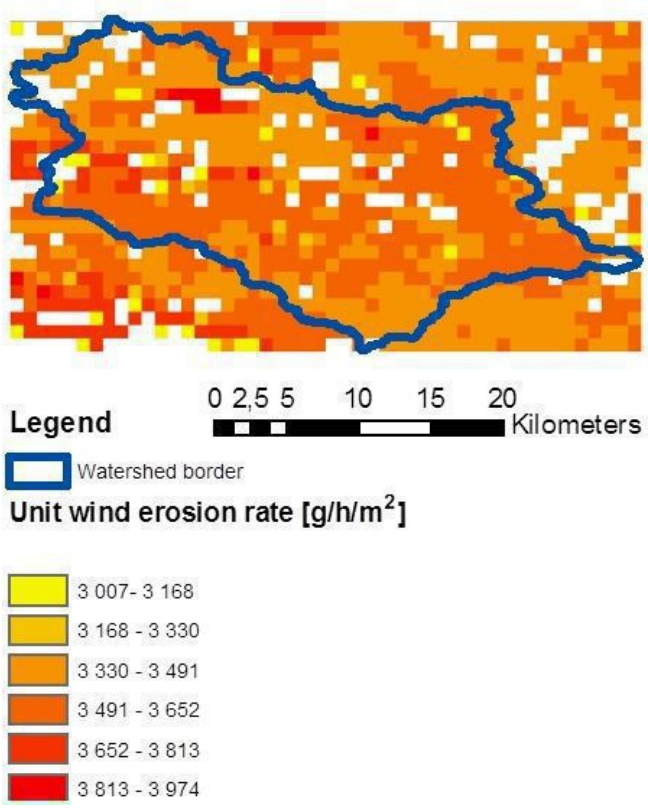


Figure 1. Unit deflation rates on agricultural ploughed land for the event on March 17th 2013

IV. CONCLUSIONS

The NDTI model to transform thermal satellite bands into the spatial datasets of soil humidity has underwent initial validation, revealing relatively high R square at the level of 0,41. The algorithm for combining various sources of thermal scenes into a source for NDTI calculation increases the spatial and temporal resolution of the data sources.

The method for remote estimation of current soil moisture has potentially a wide range of applications, going beyond the example wind erosion rate calculations. Many single event models addressing erosion and geomorphology [12, 14] utilize soil moisture information, which is usually hardly available for wider geographical extents. Another possible domains, where the algorithms of NDTI me be of use use are agriculture (calculation of plant water deficit) [7] and defence (estimating terrain trafficability through calculation of soil bearing capacity for military vehicles) [15].

ACKNOWLEDGMENT

The research was performed in two projects financed within the statutory research grants of the Institute of Soil science and Plant Cultivation – State Research Institute.

REFERENCES

[1] Allen R.G., Tasumi M., Morse A., Trezza R., Wright J.L., Bastiaansen W., Kramber W., Lorite I.J., Robison C.W., 2007. „Satellite-based energy balance for mapping evapotranspiration with internalized calibration (METRIC) - Applications." J. Irrig. Drain. Eng., 133(4), 395-406.

[2] Anderson M.C., Norman J.M., Diak G.R., Kustas W.P., 1997. "A two-source time Integrated model for estimating surface fluxes for thermal infrared satellite observations." Remote Sens. Environ., 60, 195-216.

[3] Bastiaanssen, W.G.M., M. Menenti, R.A. Feddes, A.A.M. Holtslag. A remote sensing surface energy balance algorithm for land (SEBAL): Part 1: Formulation. Journal of Hydrology 1998, 212 (213):213-229.

[4] Bastiaanssen, W. G. M., Pelgrum, H., Wang, J., Ma, Y., Moreno, J., Roerink, G. J., and van der Wal, T. (1998b). "The surface energy balance

algorithm for land (SEBAL), Part 2: Validation." J. Hydrol.,212-213, 213–229.

[5] French A., Schmugge T., Kustas W.P., 2002. „Estimating evapotranspiration over El-Reno, Oklahoma with ASTER imaginery." Agronomie, 22, 105-106.

[6] Kustas W., Norman J.M., Anderson M.C., French A.N., 2003. "Estimating subpixel surface temperatures and energy fluxes from the vegetation index-radiometric temperature relationship." Remote Sens. Environ., 85, 429-440.

[7] Lopatka A., Kozyra J., Wawer R. 2014. "Integrating wireless soil moisture and meteorological monitoring with numerical weather forecast into a comprehensive decision support system for irrigation management". 12 International Conference of Meteorology, Climatology and Physics of the Atmosphere, Heraklion 28 – 31 May 2014. E-book of proceedings ISBN-978-960-524-430-9. Vol 2, 147-152.

[8] Norman J.M., Kustas W.P., Humes K.S., 1995. "A two-source approach for estimating soil and vegetation energy fluxes in observations of directional radiometric surface temperature." Agric. For. Meteorol., 77, 263-293.

[9] Norman J.M., Anderson M.C., Kustas W.P., Frencz A.N., Męcikalski J., Torn R., Diak G.R. i inni, 2003. "Remote sensing of surface energy fluxes at 101-m pixelresolutions." Water Resour. Res., 39(8), 1221.

[10] Petropoulos G.P., 2014. "Remote sensing of Surface Turbulent Energy Fluxes." 49-84, in.: Remote sensing of Energy Fluxes and Soil Moisture Content. Taylor and Francis Group, Boca Raton.

[11] Roerink G., Su Z., Menenti M., 2000: S-SEB. "A simple remote sensing algorithm to estimate the surface energy balance." Phys. Chem. Earth, Part B, 25(2), 147-157.

[12] Schmidt J., 2000. "Soil Erosion – Application of Physically Based Erosion Models." Springer-Verlag Berlin: 1-307

[13] Su Z., 2002. "The Surface Energy Balance System (SEBS) for estimation of turbulent heat fluxes." Hydrol. Earth Syst. Sci., 6(1), 85-89.

[14] Wawer R., Nowocien E. 2003. "Application of Sinmap Terrain Stability Model in Grodarz Stream Watershed". Electornic Journal of Polish Agricultural Universities. Environmental Development Series. Vol. 6, issue 1, 2003[1]

[15] Wawer R., Nowocien E., Lopatka A. 2015. „An approach to dynamic trafficability mapping as a component of battle management systems" Proceedings of Estonian National Defence College, No 20, forthcoming.

[16] Wawer R., Nowocien E., Podolski B. 2013. "Sediment uptake rates under extreme rainfall in controlled conditions" Journal of Food Agriculture and Environment, Vol.11 (1): 1089-1093

[17] Wawer R., Nowocien E., Podolski B. 2013. "Wind erosion rates for ten soils under threshold wind speed in controlled conditions". Journal of Food Agriculture and Environment, Vol. 11 (2): 1432-1436

[1] http://www.ejpau.media.pl/volume6/issue1/environment/art-03.html

Mapping gradient fields of landform migration

Vaclav Petras, Helena Mitasova and Anna Petrasova
Department of Marine, Earth and Atmospheric Sciences and
Center for Geospatial Analytics, North Carolina State University
Raleigh, North Carolina, USA

Abstract **—Geospatial analytics techniques describing changes of unstable landscapes provide critical information for hazard management and mitigation. We propose a method for quantifying horizontal migration of complex landforms based on the analysis of contour evolution. When applied to a set of elevations this technique provides comprehensive information on magnitude and direction of landform migration at any point in space and time. The method is based on the concept of space-time cube combined with GIS-based analysis applied to spatio-temporal surface. The result of the analysis is a vector field representing the movement and deformation of contours. We also present several approaches to visualization of these vector fields as space-time gradient lines, vectors or dynamic "comets". We demonstrate the method on a laboratory model and an elevation time series capturing evolution of a coastal sand dune.**

I. Introduction

Natural hazards often involve significant changes in topography induced by coastal or stream channel erosion, aeolian sand transport, or gravitation forces on unstable hillslopes. Quantification of these changes, especially their evolution over time, is critical for hazard management and mitigation. Modern 3D mapping technologies such as lidar are now routinely used to monitor 3D landscape change at high spatial and temporal resolutions. Over the past decade new methods and techniques were developed to analyze these monitoring data and derive quantitative metrics of observed changes [1, 2]. DEM differencing, per cell statistics, as well as aggregated metrics such as total volume change can be computed using standard raster analysis tools [3]. Time series of DEMs can also be visually analyzed using dynamic 3D techniques implemented in GIS [4].

Horizontal migration rates of landforms which involve change in landform geometry (as is often the case with dunes and shorelines) are harder to quantify because the rates are spatially variable and involve change in both magnitude and direction. Standard techniques for assessment of line feature migration rates are based on transects approximatelly perpendicular to the direction of feature migration and on measurement of displacement along these transects [3, 5]. This approach is limited by the transect spacing and does not provide information on migration direction change. Also, dramatic changes in landform can make it difficult to generate valid transects.

We propose a method for quantifying horizontal migration of complex landforms based on the analysis of contour time series with the aim to generate a quantitative representation of magnitude and direction of landform evolution at any point in space and time.

II. Approach

Landscape evolution is often represented by a time series of DEMs derived from repeated 3D surveys, often using lidar technology. To analyze horizontal migration and deformation of landforms within a dynamic landscape we introduce the following concept. Given a time series of n DEMs we can represent the evolution of landscape in space time cube (STC) where the third coordinate is time t and the modeled variable is elevation z:

$$z = f(x, y, t). \tag{1}$$

Landform evolution at a given constant elevation $z = c$ can then be represented and visualized as an isosurface[1] derived from the STC representation (Fig. 1).

To quantify the rate and direction of contour horizontal migration we can segment the time series of contours $z_i = c,\ i = 1, ..., n$ into non-intersecting segments.[2] Each of these sets of contour segments then define a bivariate function g_c which represents time t as a function of contour position (x, y):

$$t = g_c(x, y). \tag{2}$$

[1]The mathematical definitions of contour and isosurface are the same since both are special cases of a level set which is defined as $f(x_1, \cdots, x_n) = c$ or more precisely as $L_c = \{(x_1, \cdots, x_n) \mid f(x_1, \cdots, x_n) = c\}$.

[2]There should be no other contour between two successive states of one contour, i.e. by following the surface in the direction of increasing time, we first get to a newer state of the contour we started from before any other contour. This is equivalent to segmentation of the isosurface in Fig. 1 into sub-surfaces which can be represented by bivariate functions.

This project was funded by the US Army Research Office, grant W911NF1110146

In: Geomorphometry for Geosciences, Jasiewicz J., Zwoliński Zb., Mitasova H., Hengl T. (eds), 2015. Adam Mickiewicz University in Poznań - Institute of Geoecology and Geoinformation, International Society for Geomorphometry, Poznań

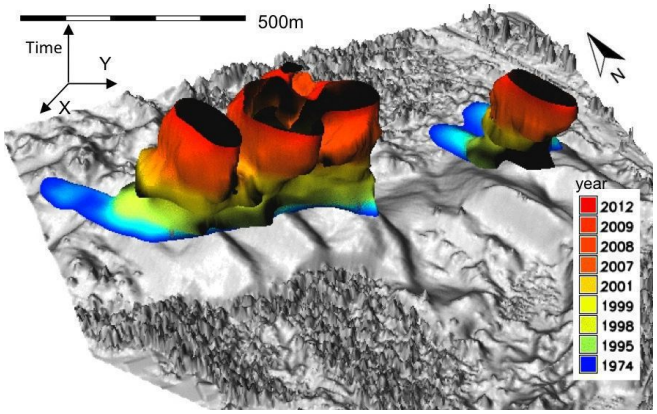


Figure 1. Jockey's Ridge dune: lidar based DSM (year 2009) and an isosurface showing evolution of 16 m contour for years 1974 through 2012.

Additionally, only the areas between the contours in successive times are considered and these areas must fulfill the following condition:

$$f(x, y, t_i) > c \triangle f(x, y, t_{i+1}) > c \tag{3}$$

where $\triangle$ is a symmetric difference of two sets defined as $A \triangle B = (A \cup B) \setminus (A \cap B)$.

The time series of contour segments which fulfill the above condition can then be interpolated using a suitable GIS-based interpolation to create a raster representation of the temporal function $g_c(x, y)$. This function then allows us to derive a vector field describing the movement of a contour by computing its gradient:

$$\nabla g_c = (g_x, g_y), \text{ where } g_x = \frac{\partial g_c}{\partial x}, \; g_y = \frac{\partial g_c}{\partial y}. \tag{4}$$

For visualization in GIS, it is convenient to represent gradient using its direction θ (aspect) and magnitude w (slope) components:

$$\tan\theta = \frac{g_y}{g_x}, \; w = \sqrt{g_x^2 + g_y^2} \tag{5}$$

The gradient vector field is then represented as two raster maps (w and θ). Since gradient magnitude $w[time/length]$ of the temporal function $t = g_c(x, y)$ is an inverse value of rate of change we compute the speed (rate) of horizontal migration $v[length/time]$ as:

$$v = \frac{1}{w}. \tag{6}$$

In other words, if two contours from two consequent time snapshots are spatially close to each other, this will lead to steep slope (large w) in g_c and a low horizontal migration speed.

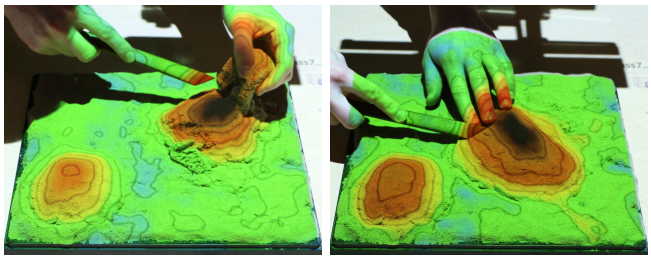


Figure 2. Physical laboratory terrain model at the initial and final state with projected elevation color map and contours derived from the model scan using Tangible Landscape [6].

Now we have a two-dimensional vector field which assigns a vector defined by direction θ and speed v to each position (x, y). This vector field represents the rate and direction of landform migration at given elevation c. We can derive such a vector field for a set of elevations representing the entire landform and obtain a 3D, spatially variable representation of its horizontal migration and deformation. We can also map locations of migration acceleration and rate of deformation by computing relevant metrics based on second order derivatives (divergence of the vector field or spatio-temporal "profile" curvature).

To support the presented concept, we have used and further developed visualization techniques for graphical representation of vector fields using gradient lines, arrow fields, and dynamic comet-like visualization [4]. The raster maps representing migration rates at multiple elevations can also be stacked into a 3D raster (voxel model) and areas of equal migration rates can be extracted and visualized as isosurfaces.

III. Applications

We are exploring application of the presented technique to the mapping of migration vector fields associated with various types of landscapes and processes. Here we present a test of the algorithm using laboratory models and a real-world application for analysis of a coastal sand dune migration.

A. Laboratory experiment

We have used a laboratory terrain model to test our methodology and algorithms in a fully controlled environment. Our tangible geospatial modeling system Tangible Landscape [6], allows us to create realistic terrain models from polymeric sand in a relatively intuitive way while providing real-time feedback about our model properties using contours, slope or flow pattern (Fig. 2).

The initial model and a sequence of its modifications was scanned and imported into GIS providing a series of DEMs suitable for testing the performance of our algorithms for different

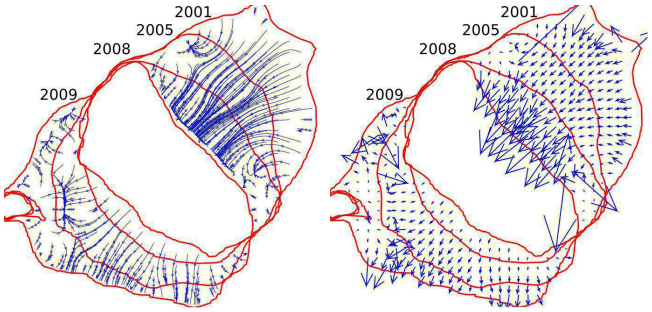


Figure 3. Contour time series with space-time gradient lines and vectors.

landform geometries. Our test case was designed in such a way that the hill migrated in one prevailing direction while changing its shape. For this type of migration, we can compute the vector field without segmentation of the contour time series.

The example illustrates the landform migration analysis using 4 different states with the assigned range of elevation values between 103 m and 128 m. The individual states were assigned the years 2001, 2005, 2008, and 2009 so the time interval varied from 1 to 4 years. The resulting migration rate and direction at the elevation $z = 110\ m$ was visualized by gradient lines, vector arrows (Fig. 3), and a comet-like visualization.[3] The comet-like visualization tool was modified so that the comets are generated and move only in relevant areas, while the 4 states of terrain represented by a series of elevation maps are periodically changing in background.

B. Jockey's Ridge sand dunes

We have applied the method to measure migration of the Jockey's Ridge sand dune field located in a state park on the North Carolina coast. The dunes have been migrating at variable rates with sand often transported outside the park boundaries, obstructing roads and threatening homes in neighboring communities. The approximate rate of migration was assessed for the first time several years ago from a series of DEMs by manually measuring distances between consecutive positions of dune crests [7]. The process was time consuming and to some extent subjective because the distance between the crests was highly variable as the dune has changed its shape and elevation.

We have used the presented method to analyze the spatial pattern of dune migration, including the dune windward side which was not measured previously using the crest-based method. We also measured and compared horizontal migration rates at

[3]Comet-like visualization is available online at `http://ncsu-osgeorel.github.io/spatio-temporal-contour-evolution`.

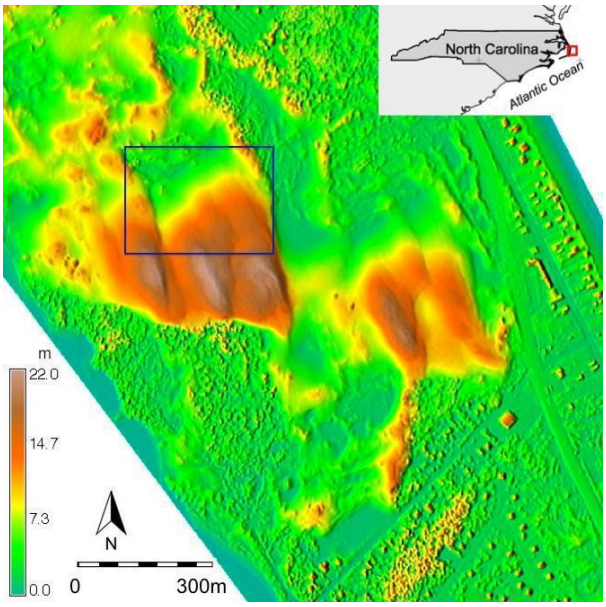


Figure 4. Jockey's Ridge (2008 DEM) with rectangle showing the test area. The size of the test area is approximately 280 m times 350 m.

different elevations—here we present the migration gradient fields at elevations 10, 12, 14 and 16 m based on a time series of DEMs representing the dunes in the 1974, 1995, 2001 and 2008 years (see [3] and [7] for description of data and processing including correction of registration errors). As expected, the resulting gradient field shows a more homogeneous pattern at lower elevation (10 m) compared to higher variability in both rates and direction at higher elevation (16 m). The analysis also reveals a relatively stable pivot point, around which the dune migration changes its direction. The migration rates presented here for the windward side of the dune are comparable to the values at the leeward side, estimated manually from the crests [7] but the vector field provides much more detailed information about the spatial variability of the migration and the mapping process is to a large extent automated.

IV. Discussion and Future Work

It is important to note that the migration vector field does not represent the physical transport of the soil or sand particles. Instead, it provides information how a landform geometry at the given elevation was transformed between the time snapshots due to the redistribution of its mass. Such information can be used not only for dune management but also to improve dune evolution simulations by deriving more accurate relationships between the elevation and sand transport [8].

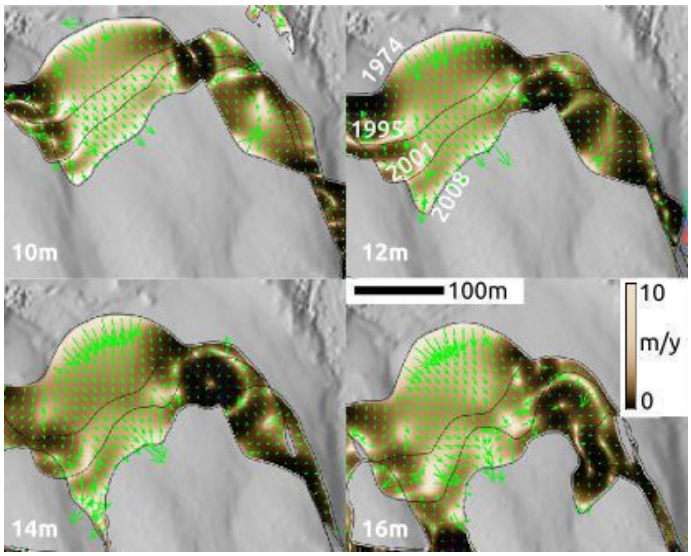


Figure 5. Migration speed and direction for north east part of Jockey's Ridge main dune at elevations 10, 12, 14, and 16 m, derived from the 1974, 1995, 2001 and 2008 DEMs.

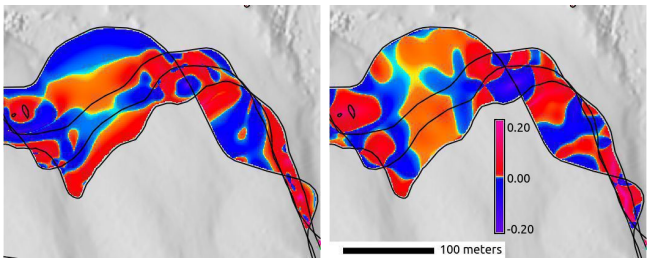


Figure 6. Curvature in the direction of the fastest temporal change (left) and in the perpedicular direction (right) derived from the spatio-temporal surface of 12 m contour evolution.

We have further explored properties of the spatio-temporal gradient fields, by deriving curvatures in the direction of fastest temporal change and in its perpendicular direction (Fig. 6), to assess acceleration and deformation rates, but more work is needed to provide full mathematical representation and interpretation of these derived fields. We will also discuss several additional experiments, such as extraction of a space-time gradient field from the 3D raster (voxel) representation of elevation time series.

The presented method is not limited to elevation contours, it can be applied to other evolving line features such as dune crests, eroding stream channels or shorelines as well as to dynamic processes, such as isochrones of observed fire spread or glacier melting.

V. Conclusion

We implemented the presented algorithm for the computation of horizontal migration vector fields from spatio-temporal sets of contours in a GRASS GIS module *r.contour.evolution*.[4] The module input is a series of DEMs and elevation values, the output is a set of raster maps which represent migration gradient field and its properties. The presented method further extends the set of tools for analysis of evolving topography outlined in [2, 3], by providing a more detailed and automated approach for assessment of horizontal migration of dynamic landforms.

References

[1] Teza, G., A. Galgaro, N. Zaltron, and R. Genevois, 2007, "Terrestrial laser scanner to detect landslide displacement fields: a new approach," International Journal of Remote Sensing 28.16, pp. 3425–3446.

[2] Starek, M. J., H. Mitasova, E. Hardin, K. Weaver, M. Overton, and R. S. Harmon, 2011, "Modeling and analysis of landscape evolution using airborne, terrestrial, and laboratory laser scanning," Geosphere 7.6, pp. 1340–1356.

[3] Hardin, E., H. Mitasova, L. Tateosian, and M. Overton, 2014, GIS-based Analysis of Coastal Lidar Time-Series, Springer Briefs in Computer Science, New York: Springer, p. 86.

[4] Petras, V., A. Petrasova, H. Mitasova, and J. G. White, "Spatio-temporal data visualization in GRASS GIS: desktop and web solutions," Transactions in GIS, submitted.

[5] Thieler, E., E. A. Himmelstoss, J. L. Zichichi, and A. Ergul, 2009, The Digital Shoreline Analysis System (DSAS) Version 4.0 - An ArcGIS Extension for Calculating Shoreline Change, tech. rep., U. S. Geological Survey No. 2008-1278.

[6] Petrasova, A., B. Harmon, V. Petras, and H. Mitasova, 2014, "GIS-based environmental modeling with tangible interaction and dynamic visualization," Proc. 7th International Congress on Environmental Modelling and Software, ed. by D. Ames, Q. N.W.T., and R. A.E., San Diego, CA, USA.

[7] Mitasova, H., M. Overton, and R. S. Harmon, 2005, "Geospatial analysis of a coastal sand dune field evolution: Jockey's Ridge, North Carolina," Geomorphology 72.1, pp. 204–221.

[8] Pelletier, J. D., H. Mitasova, R. S. Harmon, and M. F. Overton, 2009, "The effects of interdune vegetation changes on eolian dune field evolution: a numerical-modeling case study at Jockey's Ridge, North Carolina, USA," Earth Surface Processes and Landforms 34, pp. 1245–1254.

[4]GRASS GIS module *r.contour.evolution* is lable online at `http://github.com/ncsu-osgeorel/spatio-temporal-contour-evolution`.

Multidimensional approach to natural instabilities in mountain areas: how geomorphometry can improve both hazard modeling and risk perception

Marco Giardino
Earth Sciences Department and NatRisk Centre
University of Torino
Torino, Italy
marco.giardino@unito.it

Walter Alberto
ImaGEO srl
Spin off Company University of Torino
Torino, Italy
walter.alberto@imageosrl.com

Luigi Perotti
Visiting scientist at Earth Sciences Department
Simon Fraser University
Burnaby, Canada
luigi.perotti@unito.it

Sara Ratto
Centro Funzionale
Regione Autonoma Valle d'Aosta
Aosta, Italy
s.ratto@regione.vda.it

Abstract—**On going climatic and environmental changes have increasing impacts on infrastructure and human activities within mountain areas. Improvements are needed for both accurate hazards modelling and targeted risks management through diffusion of scientific results. By means of the application of a multidimensional approach (local, regional) to natural hazards and risks case studies of the European Alps, the paper shows the strategic roles played by geomorphometric tools and methods (accurate DEM derived data and targeted geomatics analytical tools) for both enhanced accuracy of models of diverse geoenvironmental processes and improved knowledge on natural hazards and awareness on natural risks in mountain areas.**

I. INTRODUCTION

Natural hazards and risks assessment in mountain areas is a challenging issue because of ongoing environmental changes associated with climate change and increasing impacts on infrastructure and socio-economic and cultural activities. Since behavior of mountain communities towards natural hazards is mostly influenced by "perceived risk" than "real risk", research should be addressed both to accurate hazards modelling and targeted applications of new technologies for diffusion of scientific results. This could improve the share of information among people, reaching for a larger and deeper corpus of knowledge about natural hazards and risk related policies [1]. By means of assessment of DEM derived data and selection of geomatics analytical tools, geomorphometry can be useful for both 1) enhanced accuracy of models of diverse geoenvironmental processes of mountain regions and 2) improved "targeted" knowledge on natural hazards and increased awareness on natural risks.

II. AIMS AND METHODS

A. Multidimensional Approach to natural hazards

A diversity of information on natural hazards is available for the Alpine region, including different types of data and models by contents, quality, and dimensions. Within our research, we updated geodatabases on natural instability phenomena of the Western Alps with new regional and local data, either by remote sensing or by field surveys. We applied geomorphometrical techniques, we interpreted data, then we summarized and redrawn results in order to create reports, base maps, models and/or more elaborated geothematic or statistical representations. Our challenges were not only to overcome technical difficulties of data management and interpretation, but also to make available new straightforward risk scenarios to decision-makers, and the citizens. For this purpose, a multiscale approach (Regional Geological, Local Morphodynamic) for collection, interpretation, and representation of data on natural hazards is here proposed.

1) Regional Geological Approach (RGA) focuses on mountain environmental systems as a whole, by addressing

In: Geomorphometry for Geosciences, Jasiewicz J., Zwoliński Zb., Mitasova H., Hengl T. (eds), 2015. Adam Mickiewicz University in Poznań - Institute of Geoecology and Geoinformation, International Society for Geomorphometry, Poznań

the analysis of large-scale, long-term features related to natural hazards; these represent general factors of instabilities in the mountain relief (geomorphological, lithological and structural factors). RGA allows interpretation of: 1) evolutionary stages of the mountain relief; 2) regional independent variables, offering a "static" conditioning to the mountain system (e.g. landslides: "internal" causes, lowering shear strength).

2) Local "Morphodynamic" Approach (LMA) focuses on single elements of the dynamic environmental system. It is the study of characteristic landforms and processes of natural instability of mountains, relevant for understanding mechanism of relief evolution and natural hazards. LMA allows to perform: 1) control on dynamic factors of natural instabilities (e.g. landslides "external" causes, increasing shear stress); 2) modelling of instability process and assessment of natural hazards.

B. Geomatics applications for Geomorphometry

In the last 10 years Geomatics opened up new methods for detailed Earth surface analysis and new potentials for data processing [2]: combining geodatabases and geomorphometry [3], geomorphosites identification, assessment and representation [4], geomorphological mapping [5] and remote sensing analysis of landforms within a GIS environment [6]. Our hypothesis is that the combination of geomatics with DEMs and LiDAR derived DTMs [7] can be successful for both geomorphometric studies on landforms within remote/inaccessible areas [8], and for 2.5D perspective views and simplified mapping of natural hazard studies in mountains. For this purpose, we aims to explore the scalability of data within multidimensional approaches. Even if both approaches need a reference DEM or DTM, RGA is focused on extension quality for good reference derived map for instabilities, while LGM needs best GSD and precision in order to derive real relief characteristics.

III. Applications and Results

A. Regional Geological Approach

The Aosta Valley is the smallest Italian region (area: 3.262 km^2) and one of the main alpine valley systems, whose elevations ranges from 400 m a.s.l. (valley's mouth into the Po Plain) to 4810 m a.s.l. (Mount Blanc, the highest peak of the European Alps). It is a relatively densely populated area, characterized by international transport corridors to France and Switzerland, high geodiversity content and tourist attractiveness, thus representing an ideal test area for natural hazards and risk studies.

In order to improve the understanding of landslide, debris flow and flood hazards in the Aosta Valley and to better face the risks they represent for this mountain area, a comprehensive study program (field researches, remote-sensing studies and historical data analysis) has been established by the Centro Funzionale and the Regional Geological survey of the Aosta valley. The University of Turin and Imageo organized a geodatabase, performed GIS mapping of monitored landslide at the regional and local scales. Neural network processing of high resolution hyperspectral MIVIS (Multispectral Infrared and Visible Imaging Spectrometer) images [9] produced orthoprojected maps of the whole Region for better definition of both lithotecnical properties (Figure 1) and geometry and state of activity of landslide (Figures 2 and 3). For the Regional Geological Approach to slope instabilities in the Aosta Valley, the DEM analysis has been coupled with interferometric assessment of terrain deformation by detection of permanent scatterers (PSInSAR techniques, [10].

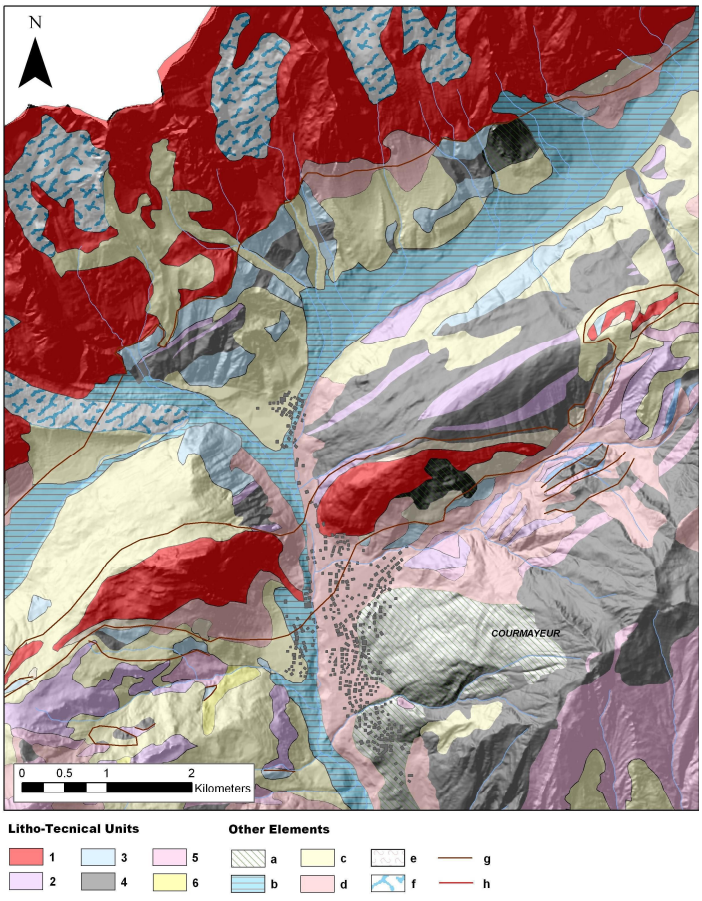


Figure 1 – A portion of the lithotechnical map of the Aosta Valley in the Courmayeur district area, on the photogrammetric generated DEM (Digital Elevation Model) of the Region. Lithotecnical Units: 1) Massive igneous and metamorphic rocks; 2) Marble and other carbonatic massive rocks; 3) Carbonatic schist; 4) Fine-grained schist), 5) Pelitic-arenaceous-conglomeratic rocks; 6) Evaporitic rocks). Other Elements: a) Landslide accumulation; b) Alluvial deposits; c) Glacial deposits; d) slope debris; e) DSGSD: Deep-seated Gravitational Slope Deformation; f) Glaciers; g) Thrusts; h) Faults.

Close analysis of the Quart-Croce Fana DSGSD (Figure 2; middle Aosta Valley) reveals: up to 13 mm / year displacements along an active major scarp (A1), extensional, lower PS velocities (up to 8 mm / year) at A2; and a small area (D) corresponding to an active landslide.

B. Local Morphodynamic approach

Other spatial analysis techniques (R.Sensing, Photogrammetry, GNSS monitoring and Laser Scanning) are suitable for mapping active landforms and modelling instability processes at a local scale. Our case studies ranges from km-long geomorphological features related to large slope instabilities to detailed monitoring of single m-long sectors of unstable rock walls.

At the foot of the Mont Blanc Massif, the Mont de la Saxe ridge (NW-Aosta Valley) is affected by extremely slow deep-seated gravitational slope deformations (DSGSD) and by a rapid landslide on its distal slope, towards the Courmayeur town. The combined application of high resolution LIDAR and DTM and orthophotos from aerial images allowed morphostructural characterization of the DSGSD. NW-SE trenches and closed depressions, scarps and counterslope scarps (Figure 3) affect limestone-marly limestone, black schist and calcschists (Figure 1). Block-flexural toppling on subvertical rock masses has been confirmed by both field monitoring [11] and remote sensing studies [9]. Part of the ridge is affected by a faster and shallower complex landslide (rock/earth flows rockslides), with a maximum

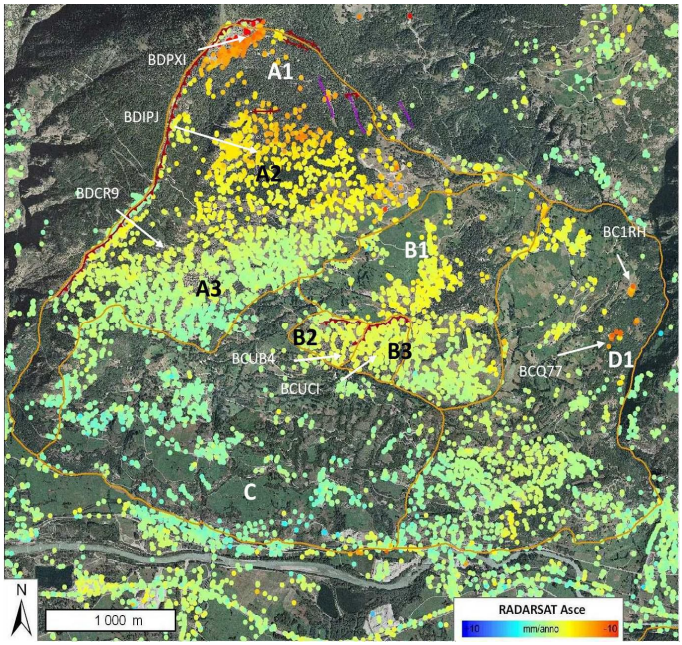


Figure 2 - State of activity of Quart-Croce Fana DSGSD, middle Aosta Valley. Yearly displacement rates (2001-2011) by SqueeSARTM analysis, RADARSAT ascendant dataset [12].

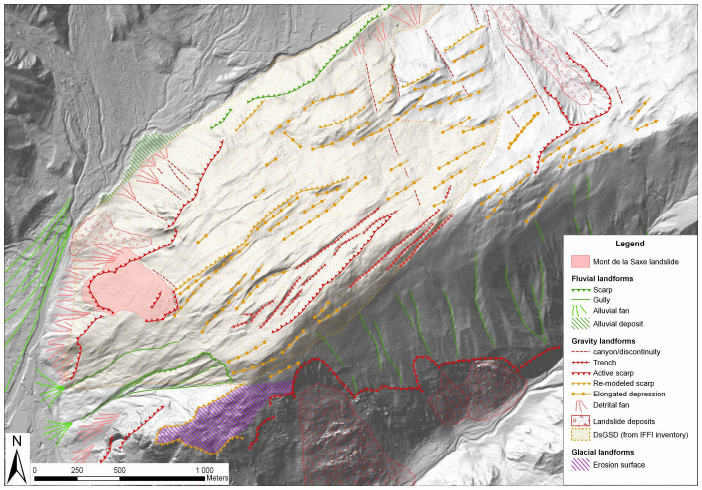


Figure 3 – Morphostructural map of the Mont de la Saxe ridge, by combined interpretation of high resolution LIDAR DTM and orthophotos.

estimated volume of a 8Mm^3 as estimated by detailed geotechnical modelling.

Very detailed investigation are needed when natural instabilities endanger infrastructures. In the case of Perrero (Germanasca Valley, Central Western Alps. [13]) an unstable rock wall collapsed during the intense rainfall event of autumn 2013, involving the provincial road and segregating the communities of the upper valley. Rapid characterizations of geomechanical and morphodyanamic properties were needed to determine suitable protection measures. Terrestrial laser scanning offered a 3D model of the 75 m long slope with cm-resolution data. Integration with Structure for Motion photogrammetric model allowed recognition of macroscopic characteristics of the slope, either qualitative (weathered and unstable materials) or quantitative (distances and angles of structural discontinuities, areas and volume calculations) (Figure 4).

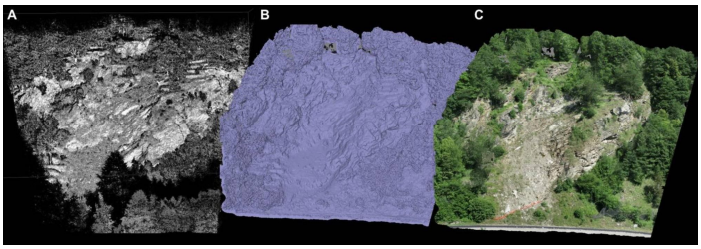


Figure 4 – Comparison of digital models of the Perrero Rockfall (Germanasca Valley): by laser scanner (A: point cloud) and UAV photogrammetric (B: grayscale; C: color RGB).

IV. Discussion and Conclusion

An innovative conceptual framework has been adopted for a multidimensional approach to natural hazards and risks on

mountain regions. Geomorphometric methodologies and geomatics technologies have been applied for both accurate hazards modelling and targeted risks management [14].

The results of the case studies in the Western Alps reinforced the validity of the interpretative key for an user-friendly classification of mountain hazards. Within the Regional Geological Approach (RGA), case studies of 10-100 km wide areas indicated satellite regional DEM/DTM (SRTM, ASTER) and related low to medium resolution multispectral images from optical sensors as the appropriate tools for assessing structural, lithological and geomorphological features as long term and large scale factors of natural hazards. Application of Differential Radar Interferometry techniques (PSInSAR) allowed to individualize areas of enhanced ground deformation; target monitoring, time series visualization and correlation to the regional context allowed better results in reconstructing the recent evolutionary stages of the mountain relief.

Following the spatial and temporal "sizes" of natural instabilities, it has been also possible to operate appropriate selections of geomatics techniques and geomorphometric products within the case studies related to the Local Morphodynamic Approach (LMA). Better results, both in hazard and risk assessments of 0,1-1 km geomorphological phenomena have been obtained by the application of LIDAR DTMs, hyperspectral and high resolution satellite images, close range photogrammetry and Laser Scanning.

Geomatics applications to geomorphometry go beyond the limit of classical geomorphological techniques. They both overcome the difficulty of quantitative analysis over large areas, and allow monitoring of small/slow instability markers; moreover, they can be efficient despite lack of direct field geomorphological evidences. This is of great importance in the knowledge about rates and distributions of instability phenomena.

Mountain regions have geological and geomorphological characteristics that make them very sensitive to climate changes. Moreover their geo-environmental characteristics are very attractive to tourism activities. Consequently, increased human "pressure" makes higher geomorphological risks, particularly related to slope instability phenomena.

REFERENCES

[1] Angignard, M., Garcia, C., Peters-Guarin, G., Greiving, S., 2014 "The relevance of legal aspects, risk cultures and insurance possibilities for risk management" In: Mountain risks: from prediction to management and governance. Edited by: van Asch, T., Coronas, J., Grieving, S., Malet, J.P., Sterlacchini, S., Springer, 327-340.

[2] Tarolli P., Arrowsmith J R., Vivoni E.R. 2009 "Understanding earth surface processes from remotely sensed digital terrain models". Geomorphology, 113: 1-3. doi:http://dx.doi.org/10.1016/j.geomorph.2009.07.005.

[3] Bolongaro-Crevenna A., Torres-Rodriquez V., Sorani V., Frame D., Ortiz D.M.A. (2005) - Geomorphometric analysis for characterizing landforms in Morelos State, Mexico. Geomorphology, 67: 407-422.

[4] Seijmonsbergen A.C., De Jong M.G.G., De Graaf L.W.S. (2009) - A method for the identification and assessment of significance of geomorphosites in Vorarlberg (Austria), supported by Geographical Information Systems. Geografi Fisica e Dinamica Quaternaria. Mem. Descr. Carta Geol. d It., LXXXVII, 163-172.

[5] Anders N.S., Seijmonsbergen A.C., Bouten W. (2009) - Multi-Scale and Object-Oriented Image Analysis of High-Res LiDAR Data for Geomorphological Mapping in Alpine Mountains. Proceedings of Geomorphometry. Zurich, Switzerland, 31 August -2 September, 2009

[6] Siart C., Bubenzer O., Eitel B. (2009) - Combining digital elevation data (SRTM/ASTER) high resolution satellite imagery (Quickbird) and GIS for geomorphological mapping: A multi-component case study on Mediterranean karst in Central Crete. Geomorphology, 112 (1-2): 106-121. doi: http://dx.doi.org/10.1016/j.geomorph.2009.05.010

[7] Corona P., Cartisano R., Salvati R., Chirici G., Floris A., Di Martino P., Marchetti M., Scrinzi G., Clementel F., Travaglini D., Torresan C. (2012) - Airborne Laser Scanning to support forest resource management under alpine, temperate and Mediterranean environments in Italy. European Journal of Remote Sensing, 45: 27-37. doi: http:// dx.doi.org/10.5721/EuJRS2012450.

[8] Lucchesi S., Giardino M., Perotti L. (2013) - Applications of high-resolution images and DTMs for detailed geomorphological analysis of mountain and plain areas of NW Italy. European Journal of Remote Sensing 46: 216-233. doi: http://dx.doi.org/10.5721/ EuJRS20134612.

[9] Giardino M., Borgogno Mondino E., Perotti L. (2004). MIVIS Images classification for the geomorphological characterization of large slope instabilities in Aosta Valley (Italian NW-Alps), in In: Ehlers, M. Posa, F., Kaufmann, H.J., Michel, U., De Carolis, G.: "Remote Sensing for Environmental Monitoring GIS applications and Geology", Proceeding of S.P.I.E., vol 5574, 331-340.

[10] Ferretti A., Prati C., Rocca F., (2001) Permanent Scatterers in SAR Interferometry. IEEE Trans. on Geoscience and Remote Sensing, Vol. 39, no. 1, pp. 8-20

[11] Deline P., Gruber S., Delaloye R., Fischer L., Geertsema M., Giardino M., Hasler A., Kirkbride M., Krautblatter M., Magnin F., McColl S., Ravanel L., and Schoeneich P., 2015- Ice Loss and Slope Stability in High-Mountain Regions. in Haeberli W. and Whiteman C. (Eds) 521-562. Snow and Ice-Related Hazards, Risks, and Disasters. http://dx.doi.org/10.1016/B978-0-12-394849-6.00015-9

[12] Ferretti A., Fumagalli A., Novali F., Prati C., Rocca F., Rucci A., (2011) A new algorithm for processing interferometric data-stacks: SqueeSAR. To be published on IEEE Trans. Geosciences and Remote Sensing.

[13] Allasia P., Audisio C., Baldo M., Cirio C.G., Lollino G., Giordan D., Godone F., Nigrelli G., Alpe F., Ambrogio S., Giardino M., Perotti L., Sambuelli L., De Renzo G., Fontan D., Barbero T., 2004 - P41 - Instrumented experimental sites for the control of landslide hazards in mountain environments: the Germanasca and Susa Valleys (NorthWestern Italy), In: Guerrieri, L., Rischia, I. & Serva, L. (Series Eds). Field Trip Guide Books, 32nd International Geological Conference, Florence 20-28 Agosto 2004, Memorie Descrittive della Carta Geologica d'Italia, Vol. LXIII (5), P - 41, APAT, Roma, 40 p.

[14] Giardino M., Perotti L., Lanfranco M., Perrone G. (2012) - GIS and geomatics for disaster management and emergency relief: a proactive response to natural hazards. Applied Geomatics, 4 (1): 33-46. doi: http://dx.doi.org/10.1007/s12518-011-0071-z.

High resolution satellite SAR multi-temporal interferometry for regional scale detection of landslide and subsidence hazards

Janusz Wasowski
National Research Council
CNR - IRPI
Bari, Italy
j.wasowski@ba.irpi.cnr.it

Raffaele Nutricato, Davide Oscar Nitti
GAP srl
c/o Politecnico di Bari
Bari, Italy
raffaele.nutricato@gapsrl.eu

Fabio Bovenga
CNR – ISSIA
Bari, Italy

Maria Teresa Chiaradia, Luciano Guerriero
Politecnico di Bari
Bari, Italy

Abstract—**Among a number of advanced satellite-based remote sensing techniques, synthetic aperture radar (SAR) multi-temporal interferometry (MTI) appears the most promising for fostering new opportunities in landslide and subsidence hazards detection and assessment. MTI is attractive to those concerned with terrain instability hazards because it can provide very precise quantitative information on slow displacements of the ground surface over huge areas with limited vegetation cover. Although MTI is a mature technique, we are only beginning to realize the benefits of the high-resolution imagery that is currently acquired by the new generation radar satellites (e.g., COSMO-SkyMed, TerraSAR-X). In this work we demonstrate the great potential of high resolution MTI for regular, wide-area detection of ground instability hazards by presenting results from two regions characterized by different geomorphic, climatic and vegetation conditions: densely populated metropolitan area of Port-au-Prince (Haiti), with the coastal areas and local slopes destabilized by the 2010 Mw 7.0 earthquake, and the remote high mountain region of Southern Gansu Province (China) prone to large slope failures. The interpretation and widespread exploitation of high spatio-temporal resolution MTI results can be facilitated by visualizing the scientific data using Google Earth™ tools or other web-based applications.**

I. INTRODUCTION

Ground instability hazards caused by landslides and subsidence can affect any country in the world and as such constitute a global problem. This and the growth of population, with urbanization of areas susceptible to ground failure, together with the climate change, call for the development of effective and more economically sustainable approaches to hazard assessment and reduction. We argue that the extensive exploitation of modern remote sensing technologies, with focus on early detection of small pre-failure ground deformations through long-term monitoring, represents one of the emerging options for scientists concerned with slope and subsidence hazards.

In particular, among different innovative remote sensing techniques capable of detecting and monitoring ground surface changes and deformations related to terrain instability e.g., air/terrestrial LiDAR [1], [2], or air/space-borne image matching [3], [4], the satellite MTI offers excellent surveying capabilities e.g., [5], [6], [7], [8]. The applications of MTI can rely on the following strengths of the technique:

- Wide-area coverage (tens of thousands of km^2) combined with high spatial resolution (up to 1 m for the new generation radar sensors such as COSMO-SkyMed and TerraSAR-X), and the possibility of conducting multi-scale investigations (from regional to site-specific);
- Systematic, high frequency (from few days to weeks) measurements over long periods (years);
- High precision of surface displacement measurements (mm-cm resolution) only little affected by bad weather conditions;
- Integration of monitoring based on new satellite imagery with retrospective studies (using archived imagery) to

In: Geomorphometry for Geosciences, Jasiewicz J., Zwoliński Zb., Mitasova H., Hengl T. (eds), 2015. Adam Mickiewicz University in Poznań - Institute of Geoecology and Geoinformation, International Society for Geomorphometry, Poznań

investigate ground failure history and long-term (years-decades) instability processes;

- Regional scale, regular update on ground stability conditions in inhabited areas or those to be urbanized (prevention and land use planning).

In this work we illustrate what kind of geospatial information relevant for ground instability hazard assessment the MTI technique can provide. This is done by considering regional-scale applications in two settings characterized by different geomorphic, climatic and vegetation conditions:

1) The densely populated metropolitan area of Port-au-Prince (Haiti), with the coastal areas and local slopes destabilized by the 2010 Mw 7.0 earthquake;

2) The remote mountain region of Southern Gansu Province (China) prone to large slope failures.

Even though MTI applications are considered cost-effective e.g., [7], [9], their potential is relatively less exploited in the geomorphologist community with respect to other innovative surveying techniques (e.g., LiDAR). This, and the capability of MTI to provide high quality geo-referenced information for process-based modeling of terrain instability hazards, further motivates our work.

II. Background information on MTI

MTI techniques rely on processing of long temporal series of radar images (usually >15) to remove the atmospheric disturbance, and on the identification of radar targets on the ground (mainly human-made structures, rock outcrops) that provide a backscattered phase signal coherent in time (e.g., [5], [7]). To perform distance measurements between the satellite sensor and the target, phase difference images (interferograms) are generated by using radar images acquired over the same area during successive satellite passes. For more details on space-borne interferometry and MTI the reader is referred to the above cited articles and the vast literature on radar remote sensing.

Regarding practical applications, the standard products of MTI include: i) position of radar target (lat., long., height); ii) map showing average annual displacement rates of targets; iii) displacement time series of each target.

One significant limitation of MTI is that it is usually impossible to detect strong non-linear deformations and high velocity displacements (e.g. exceeding few tens of cm/year). Furthermore, the displacements are measured in one dimension along satellite Line of Sight (LOS), with incidence angles varying between about 20°-50°, and it is nearly impossible to retrieve movements in the radar satellite flight direction (azimuth), i.e. approximately north-south.

III. Examples of high resolution wide-area MTI applications to ground instability detection

The two examples of regional scale MTI applications rely on processing of high resolution (3 m) X-band imagery acquired by the Italian constellation of radar satellites COSMO-SkyMed (CSK). In both cases the results were obtained by using the updated version of the SPINUA MTI algorithm [10]. The obtained results were ground checked. The quality and validation of SPINUA products is further discussed in [7].

A. Example of MTI application to coastal subsidence hazards in Port-au-Prince, Haiti

The example of Haiti is of interest, because it shows that MTI can furnish very useful data on terrain instability even in case of tropical regions characterized by dense and rapidly growing vegetation, as well as by significant climatic variability (two rainy seasons) with intense precipitation events. Regions with such environmental characteristics can be harsh for MTI applications, because of the coherence loss problems that can occur especially when exploiting shorter wavelength (X- and C-band) radar data.

Despite the unfavorable setting, MTI processing of over 100 high resolution (3 m) CSK mages (June 2011 - August 2013) led to the identification of a large number of radar targets (nearly 2,997,000), with full CSK frame (~1700 km^2 coverage) density exceeding 1700 radar targets/km^2 [11]. Thanks to the high resolution of CSK radar imagery and the presence of many human-made structures dispersed in heavily vegetated terrain, even some landslide prone rural areas had a density of targets suitable for ground deformation detection [8], [11].

Importantly, the extremely high density of radar targets in the metropolitan area of the Haitian capital (on the order of 10,000/km^2) resulted in the detection and clear spatial delimitation of significant subsidence phenomena affecting river deltas and coastal areas of the Port-au-Prince and Carrefour region (Fig. 1). The over two year long time series of radar target displacements show that the maximum rate of subsidence movements locally exceed few cm/yr. This implies increasing flooding (or tsunami) hazard, as well as risk, considering high population density in coastal areas.

B. Example of MTI application to slope hazards in mountains of Southern Gansu, China

This region, known to be affected by large magnitude (M7-8) earthquakes and catastrophic landslides, is characterized by steep slopes with elevations reaching 4000 m (Fig. 2). Vegetation cover is limited and rocks include Silurian and Carboniferous slates and phyllites, as well as Permian and Devonian metamorphosed limestones [12].

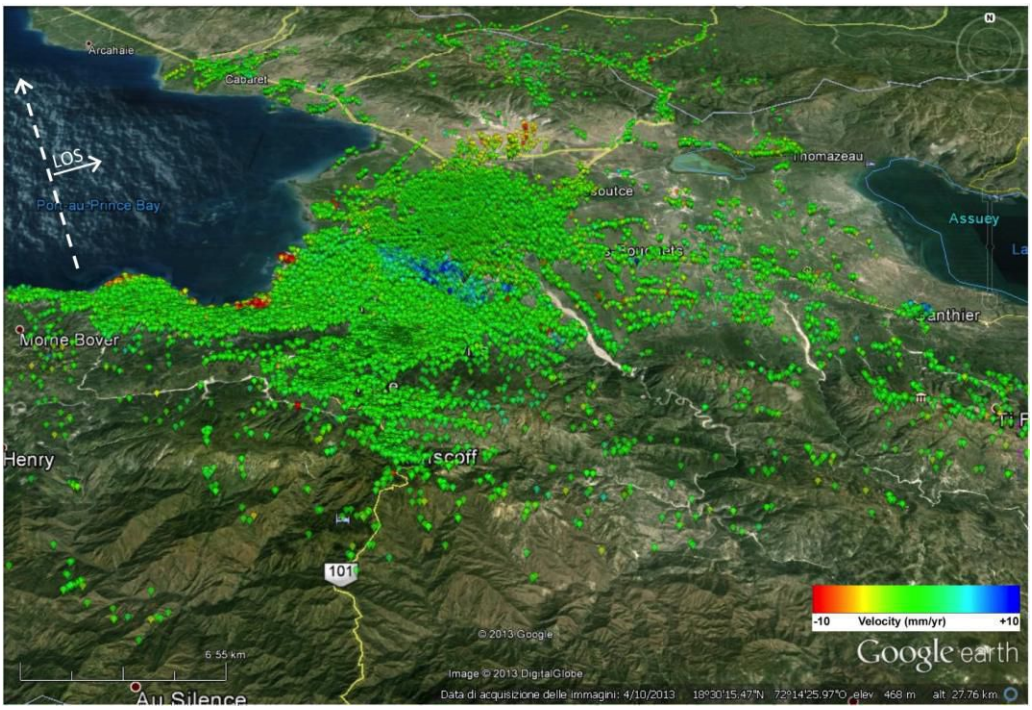


Figure 1. Distribution and average line of sight (LOS) velocity of radar targets (color dots) identified in the metropolitan area of Port-au-Prince, Haiti, and the surrounding regions; the targets are mainly human-made structures, rock outcrops, bare ground). Reddish to yellowish dots represent targets moving away from the satellite sensor and denote significant (up to few cm/year) subsidence affecting coastal areas. The background image is from Google Earth™.

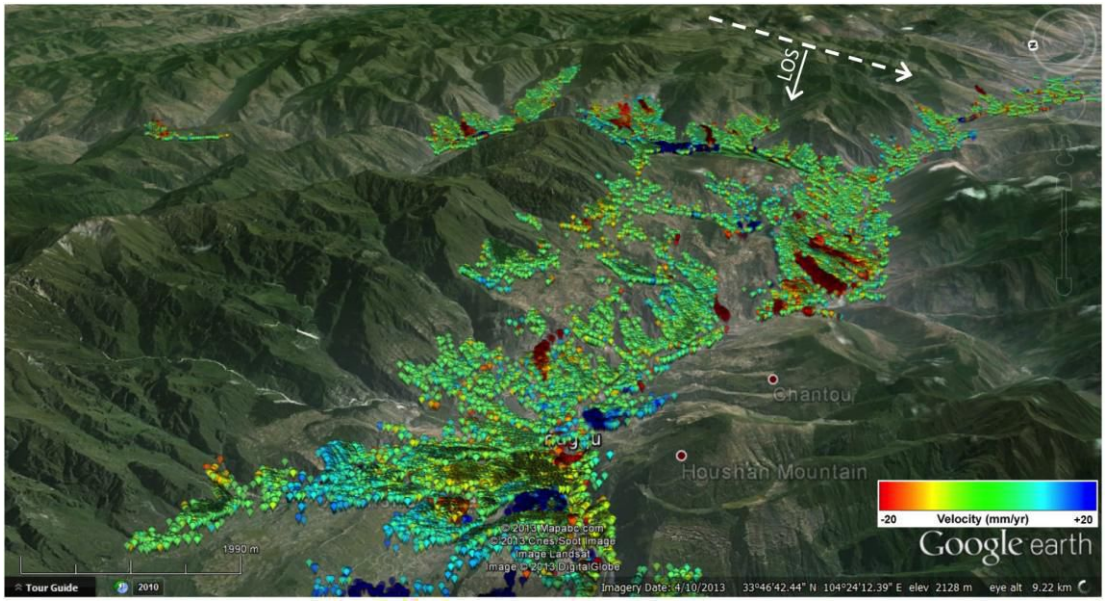


Figure 2. Distribution and average line of sight (LOS) velocity of radar targets in the Southern Gansu Mountains, China. Reddish and bluish dots represent targets moving, respectively, away from and toward the satellite sensor. The high density of targets, especially along the Bailong River valley, allowed the detection of numerous, large active landslides with average displacement rates exceeding 100 mm/year. The background image is from Google Earth™.

The initial MTI processing of 22 images (covering period January 2011-February 2012) focused on about 40 km^2 mountain terrain around the town of Zhouqu; this produced spatially dense information (more than 1000 radar targets/km^2) on ground surface displacements [7],[13]. A substantial portion of the radar targets showed significant displacements (from few to over 100 mm/yr), denoting widespread slope instability.

Here we present wide-area results from full CSK frame (~1700 km^2 coverage) processing, which lead to the identification of nearly 629,000 measurable radar targets. The average density of the targets (370/km^2) was suitable for the detection of numerous landslides (Fig. 2). In particular, the MTI results provided valuable information on the activity of several very large, very slow (<1.6 m/year) moving landslides that represent a persistent hazard to the local population and infrastructure, which are concentrated along the Bailong River valley. Indeed, in the past some of these landslides underwent periods of increased activity resulting in river damming and disastrous flooding [12].

IV. CONCLUDING REMARKS

The case study examples presented in this work demonstrate that thanks to the wide-area coverage of satellite imagery (tens of thousands of square km), combined with a high spatial resolution (1-3 m) and improved re-visit frequency (days-weeks) of the new radar sensors, the millimeter precision MTI surveying can generate an unprecedented quantity (and quality) of information about ground surface displacements occurring in areas susceptible to slope or subsidence hazards. Furthermore, with regular globe-scale coverage and freely available imagery, new radar satellite background missions such as the European Space Agency's Sentinel-1 (https://earth.esa.int/web/guest/missions/esa-operational-eo-missions/sentinel-1) will guarantee ever increasing and more efficient use of MTI in ground hazard investigations. The widespread exploitation of high spatio-temporal resolution MTI data for both science and societal applications (including visualization and analysis) can be facilitated by Google Earth™ tools with free acess to high resolution optical imagery [10], or by new types of web-based participatory approaches including the so-called CrowdSourcing (e.g., Voluntered Geographic Information applications such as OpenStreetMap).

ACKNOWLEDGMENT

Work carried out using CSK® Products© of the Italian Spatial Agency (ASI) delivered under the license to use by ASI. We benefited from the collaboration with the Centre National dell'Information Géo-Spatiale -CNIGS, Haiti and from comments provided by three reviewers.

REFERENCES

[1] Monserrat, O., and M. Crosetto, 2008. “Deformation measurement using terrestrial laser scanning data and least squares 3D surface matching”. ISPRS Journal of Photogrammetry and Remote Sensing 63: 142-154.

[2] Jaboyedoff, M., Oppikofer, T., Abellan, A., Derron, M.-H., Loye, A., Metzger, R., and A. Pedrazzini, 2012. “Use of LIDAR in landslide investigations: a review”. Natural Hazards 61: 5-28.

[3] Kääb, A. 2002. “Monitoring high-mountain terrain deformation from repeated air- and spaceborne optical data: examples using digital aerial imagery and ASTER data”. ISPRS Journal of Photogrammetry and Remote Sensing 57: 39–52.

[4] Raucoules D., de Michele, M., Malet, J.P. and P. Ulrich, 2013. “Time-variable 3D ground displacements from high resolution synthetic aperture radar (SAR): application to La Valette landslide (South French Alps)”. Remote Sensing of Environment 139: 198-204.

[5] Colesanti, C., and J. Wasowski, 2006. “Investigating landslides with space-borne Synthetic Aperture Radar (SAR) interferometry”. Engineering Geology 88(3-4): 173–199.

[6] Hooper, A., Bekaert, D., Spaans, K., and M.T. Arıkan, 2012. “Recent advances in SAR interferometry time series analysis for measuring crustal deformation”. Tectonophysics 514–517: 1-13.

[7] Wasowski J., and F. Bovenga, 2014a. “Investigating landslides and unstable slopes with satellite Multi Temporal Interferometry: Current issues and future perspectives”. Engineering Geology 174: 103–138.

[8] Wasowski J., and F. Bovenga, 2014b. “Remote Sensing of Landslide Motion with Emphasis on Satellite Multitemporal Interferometry”. In Landslide Hazards, Risks, and Disasters, Edited by: T. Davis and J. Shroder, Elsevier Inc., Chapter 11, pp. 345-403. http://dx.doi.org/10.1016/B978-0-12-396452-6.00011-2

[9] Tomás, R., Romero, R., Mulas, J., Marturià, J.J., Mallorquí, J.J., Lopez-Sanchez, J.M., Herrera, G., Gutiérrez, F., González, P.J., Fernández, J., Duque, S., Concha-Dimas, A., Cocksley, G., Castañeda, C., Carrasco, D., and P. Blanco, 2014. “Radar interferometry techniques for the study of ground subsidence phenomena: a review of practical issues through cases in Spain”. Environmental Earth Sciences 71: 163-181.

[10] Bovenga, F., Wasowski, J., Nitti, D.O., Nutricato, R., and M.T. Chiaradia, 2012. “Using Cosmo/SkyMed X-band and ENVISAT C-band SAR Interferometry for landslide analysis”. Remote Sensing of Environment 119: 272-285. doi: 10.1016/j.rse.2011.12.013.

[11] Nutricato, R., Wasowski, J., Chiaradia, M.T., Piard, B.E., and P. Mondesir, 2013. "Multi-temporal interferometric monitoring of ground deformations in Haiti with COSMO-SkyMed HIMAGE data (ID: 1808199)". AGU Fall Meeting 2013, Abstract NH13A-1589, San Francisco, California, USA, 9-13 Dec. 2013.

[12] Dijkstra, T.A., J.H. Chandler, J.H., Wackrow, R., Meng, X.M., Ma, D.T., Gibson, A.,Whitworth,M., Foster, C., Lee, K., Hobbs, P.R.N., Reeves, H.J., and J. Wasowski, 2012. “Geomorphic controls and debris flows - the 2010 Zhouqu disaster, China”, In the 11th International and 2nd North American Symposium on Landslides Proceedings - Landslides and Engineered Slopes, Edited by: Eberhardt, E., Froese, C., Turner, A.K., and S. Leroueil, CRC Press/Balkema, Leiden, The Netherlands, Vol. 1: pp. 287–293.

[13] Wasowski J., Bovenga F., Dijkstra T., Meng X., Nutricato R., and M.T. Chiaradia, 2014. “Persistent Scatterers Interferometry Provides Insight on Slope Deformations and Landslide Activity in the Mountains of Zhouqu, Gansu, China”, Edited by: K. Sassa et al., Landslide Science for a Safer Geoenvironment, Vol. 2: Methods of Landslide Studies, pp. 359-364. DOI 10.1007/978-3-319-05050-8_56, Springer International Publishing.

Very-high resolution monitoring of movement of surface material within a landslide

CLAPUYT François, VANACKER Veerle, VAN OOST Kristof
Earth and Life Institute, Georges Lemaître Centre for Earth and Climate Research
Université Catholique de Louvain
Louvain-la-Neuve, Belgium

SCHLUNEGGER Fritz
Institute of Geological Sciences
University of Bern
Bern, Switzerland

Abstract—**UAV-based aerial pictures processed with Structure-from-Motion algorithms provide an efficient, low-cost and rapid framework for remote monitoring of dynamic environments. This methodology is particularly suitable for repeated topographic surveys in remote or poorly accessible areas. The aim of the study is to assess differential movement of surface material within a landslide located in the northern foothills of the Swiss Alps based on a time series of digital surface models derived from the UAV-SfM framework. Based on two digital surface models reconstructed with aerial pictures taken within a 6-months time interval, first results show that the central part of the landslide is very dynamic with horizontal movements up to several meters.**

I. INTRODUCTION

The study and monitoring of mass movements require accurate and high-resolution representations of the earth surface. For this purpose, topographic surveys are typically conducted using real-time kinematic (RTK) global positioning system (GPS) [1], total stations [2], terrestrial laser scanning (TLS) [3] and aerial laser scanning (ALS) [4]. While these acquisition techniques are increasingly used in geomorphology and result in rich observational datasets, they are often time-consuming and costly. Recent developments in image processing, with the application of computer vision algorithms as *Structure-from-Motion* (SfM), and the availability of reliable, low-cost and lightweight unmanned aerial vehicles (UAVs), permit to overcome some of these drawbacks [5].

During the last years, exploratory research has shown that UAV-based image acquisition is suitable for environmental remote sensing and monitoring [6], [7]. Image acquisition with cameras mounted on an UAV can be performed at very-high spatial resolution (centimeter) and high temporal frequency in the most dynamic environments [8], [9]. Besides, the SfM technique allows reconstructing landform topography based on an unoriented set of pictures (i.e. without spatial orientation or georeferencing information) and taken with consumer grade uncalibrated cameras without having prior information on the location of the principal point, radial distortion, focal length or distance to the surveyed topography [10].

The UAV-SfM framework is now capable of providing digital surface models (DSM) which are highly accurate when compared to other very-high resolution topographic datasets and highly reproducible for repeated measurements over the same study area [11]. As DSM differencing automatically leads to error propagation, the approach requires both a high accuracy for topographic representation and consistency between measurements over time.

Based on a time series of digital surface models derived from the UAV-SfM framework, the aim of the study is to assess the differential movement of surface material within a landslide located in the Swiss Alps over a period of 6 months. In addition to this, very high-resolution topographic monitoring of the landslide will help understanding the sediment fluxes at short term and enable comparison with studies over the same area at different time scales.

II. STUDY AREA

The study area is the Schimbrig landslide located in the northern foothills of the central Swiss Alps. The landslide is part

In: Geomorphometry for Geosciences, Jasiewicz J., Zwoliński Zb., Mitasova H., Hengl T. (eds), 2015. Adam Mickiewicz University in Poznań - Institute of Geoecology and Geoinformation, International Society for Geomorphometry, Poznań

of the Entlen catchment whose outlet is located near the town of Entlebuch and its elevation is ranging between 1150 m and 1300 m above sea level. The landslide is located in Flysch terrain which promotes hillslope instability due to the low mechanical strength of this geological material. The landslide reactivation activity is mainly linked to precipitation events. [12].

Previous studies on the Schimbrig landslide activity were carried out at the decadal scale based on classic photogrammetry datasets [13] and at the centennial scale based on dendrogeomorphic data [14].

III. METHODOLOGY

To acquire aerial photographs over the study area, we equipped an eight-propeller drone with a standard reflex camera. The flight speed and altitude, the focal length and the acquisition rate were tuned to provide the best trade-off between image overlap, pixel resolution and efficiency of the field survey. Ground control points (GCP), consisting of white and orange targets, were regularly scattered over the study area for further point cloud georeferencing. The GCPs were surveyed with sub-meter accuracy GPS.

Then, the SfM algorithm was applied to airphoto datasets in order to derive unoriented 3D point clouds. Scene structure is rendered as a 3D sparse point cloud generated in an arbitrary coordinate system, lacking spatial scale and orientation. This cloud is then projected in a real-world coordinate system using ground control points that are visible in the point cloud and were surveyed with a GPS in the field. To this end, a 7-parameter Helmert transformation, with a single factor of scale, three factors of translation and three of rotation, is computed based on the GCP coordinates in both arbitrary and real-world coordinate systems. In a next step, the similarity transformation is applied to the entire set of 3D point arbitrary coordinates in order to have a properly georeferenced output.

Finally, each georeferenced point cloud was converted into a triangulated irregular network (TIN) and then linearly interpolated into a raster surface with a pixel resolution of 0.1m, in order to avoid the use of complex statistical interpolation methods to transform 3D points to raster format.

IV. RESULTS

Two datasets of aerial pictures of the Schimbrig landslide were acquired, i.e. (1) October 2013 and (2) June 2014, and used to reconstruct un-oriented 3D point clouds. Regarding the georeferencing step, 29 ground control points were used for the 2013 dataset and 32 for the 2014 dataset in order to compute the 7 parameters of the Helmert transformation.

The associated errors are the Root Mean Square Errors (RMSE) derived from the simple linear regression computed by comparing the coordinates measured with GPS receiver and SfM coordinates of the targets after georeferencing (Table 1). For both datasets, the horizontal error is ranging between 0.24 m and 0.31 m while the vertical error is slightly higher with a value of 0.44 m. Also, the average point density is about 120 points per square meter.

Based on the two very-high resolution digital surface models of the landslide at the two different time steps, e.g. the Fig. 1 showing the DSM of June 2014, we are able to compute the difference between both surfaces. The extent of the final study area, i.e. the intersection of both datasets, is 2.94 ha and cover the major part of dynamic section of the landslide. After removing differences of elevation smaller than the vertical error on the georeferencing, we obtain a map quantifying erosion and accumulation of sediments for the period of interest (Fig. 2).

Preliminary analysis shows that erosion and sedimentation occur in the landslide during the 6-month period of interest. However, the most remarkable result is that horizontal movements within the central part of the landslide are large. This can be inferred by the analysis of the pattern of erosion, i.e. negative values, and sedimentation, i.e. positive values, at various places within the central part of the landslide. These shapes are similar in form, size and intensity, and in fact represent vegetation, i.e. bushes and small trees, which move downward. The intensity of these horizontal movements is up to 8 meters.

TABLE I. ACCURACY ASSESSMENT OF HELMERT TRANSFORMATION FOR POINT CLOUD GEOREFERENCING.

Dataset		October 2013	June 2014
Nb of Targets		29	32
R^2 (GPS vs SfM)	*x*	1	1
	y	1	1
	z	0.9996	0.9996
RMSE (m)	*x*	0.3144	0.2499
	y	0.2448	0.2932
	z	0.4358	0.4411

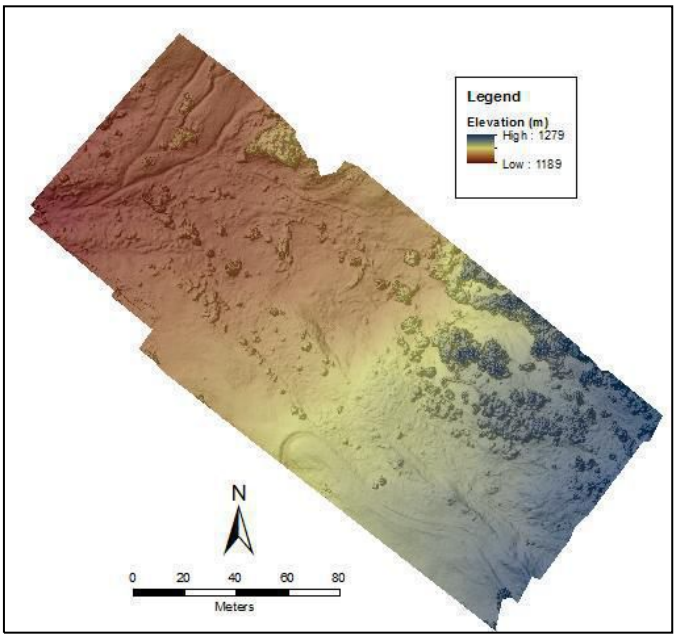


Figure 1. Digital Surface Model reconstructed based on the 2014 survey.

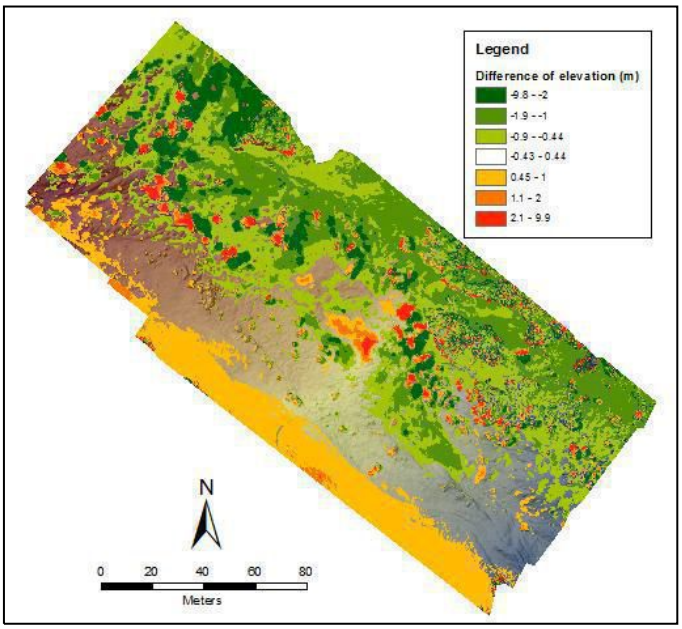


Figure 2. Difference of elevation between the digital surface models of October 2013 and June 2014. Negative values correspond to erosion and positive values to accumulation.

V. CONCLUSION

Based on aerial pictures taken by an UAV platform equipped with a standard reflex camera and the SfM algorithm, we reconstructed the topography of the Schimbrig landslide for two time steps: October 2013 and June 2014. The vertical accuracy of both datasets is 0.44 m, which could be improved for further surveys by using a RTK GPS for GCP georeferencing.

By DEM of difference, we highlighted large horizontal movements within the central part of the landslide up to several meters by detecting vegetation shifts downward.

ACKNOWLEDGMENT

The authors would like to thank Romain Delunel from Bern University for its precious help by setting up a GPS.

REFERENCES

[1] Squarzoni, C., Delacourt, C., Allemand, P., 2005. “Differential single-frequency GPS monitoring of the La Valette landslide (French Alps)”. Engineering Geology 79, 215–229.

[2] Moss, J.L., McGuire, W.J., Page, D., 1999. “Ground deformation monitoring of a potential landslide at La Palma, Canary Islands”. Journal of Volcanology and Geothermal Research 94, 251–265.

[3] Travelletti, J., Oppikofer, T., Delacourt, C., Malet, J., Jaboyedoff, M., 2008. “Monitoring landslide displacements during a controlled rain experiment using a long-range terrestrial laser scanning (TLS)”. The International Archives of the Photogrammetry, Remote Sensing and Spatial Information Sciences XXXVII, 485–490.

[4] Dewitte, O., Jasselette, J.-C., Cornet, Y., Van Den Eeckhaut, M., Collignon, A., Poesen, J., Demoulin, A., 2008. “Tracking landslide displacements by multi-temporal DTMs: A combined aerial stereophotogrammetric and LIDAR approach in western Belgium”. Engineering Geology 99, 11–22.

[5] Neitzel, F., Klonowski, J., 2011. “Mobile 3D mapping with a low-cost UAV system”. International Archives of the Photogrammetry, Remote Sensing and Spatial Information Sciences XXXVIII, 1–6.

[6] Dandois, J.P., Ellis, E.C., 2010. « Remote Sensing of Vegetation Structure Using Computer Vision”. Remote Sensing 2, 1157–1176.

[7] Westoby, M.J., Brasington, J., Glasser, N.F., Hambrey, M.J., Reynolds, J.M., 2012. ““Structure-from-Motion” photogrammetry: A low-cost, effective tool for geoscience applications”. Geomorphology 179, 300–314.

[8] D’Oleire-Oltmanns, S., Marzolff, I., Peter, K., Ries, J., 2012. “Unmanned Aerial Vehicle (UAV) for Monitoring Soil Erosion in Morocco”. Remote Sensing 4, 3390–3416.

[9] Lucieer, A., de Jong, S.M., Turner, D., 2014. “Mapping landslide displacements using Structure from Motion (SfM) and image correlation of multi-temporal UAV photography”. Progress in Physical Geography 38, 97–116.

[10] Snavely, N., Seitz, S.M., Szeliski, R., 2008. “Modeling the World from Internet Photo Collections”. International Journal of Computer Vision 80, 189–210.

[11] Clapuyt, F., Vanacker, V., Van Oost, K., 2014. “Reproducibility of UAV-based earth topography reconstructions based on Structure-from-Motion algorithms”. Geomorphology (submitted).

[12] Schwab, M., Läderach, C., Rieke-Zapp, D., Schlunegger, F., 2007. “Slip rates variability and sediment mobilization on a shallow landslide in the northern Swiss Alps”. Swiss Journal of Geosciences 100, 281–292.

[13] Schwab, M., Rieke-Zapp, D., Schneider, H., Liniger, M., Schlunegger, F., 2008. “Landsliding and sediment flux in the Central Swiss Alps: A photogrammetric study of the Schimbrig landslide, Entlebuch”. Geomorphology 97, 392–406.

[14] Savi, S., Schneuwly-Bollschweiler, M., Bommer-Denns, B., Stoffel, M., Schlunegger, F., 2013. “Geomorphic coupling between hillslopes and channels in the Swiss Alps”. Earth Surface Processes and Landforms 38, 959–969.

Evaluation of a terrestrial photogrammetry method to assess rock glacier dynamics

A study case in the Argentinean Andes of Mendoza

Xavier Bodin
Laboratoire EDYTEM
UMR 5204, CNRS / Université de Savoie
Le Bourget-du-Lac, France
xavier.bodin@univ-savoie.fr

Dario Trombotto
Instituto Argentino de Nivología, Glaciología y Ciencias Ambientales
IANIGLA, CCT- Mendoza, CONICET
Mendoza, Argentina

Abstract—**This paper investigates the potential and limits of terrestrial photogrammetry for studying rock glacier dynamics, and more especifically its interannual surface changes. Using a rather simple digital photogrammetric workflow, the restitution of two 3D-models was done thanks to multi-correlation of more than 100 images acquired in summers 2013 and 2014 on an active rock glacier in the Argentinian Andes. The quality of the output datasets is evaluated by comparing to GPS data, collected on artificial targets (XYZ) and along tracks (Z). Based on this results, we can consider ± 0.24 m as the margin of error that has to be taken into account to assess the surface changes between the two DEMs. Vertical differences affecting the rock glacier front over the one-year time lapse can then be quantified and interpreted in terms of geomorphological processes.**

I. Introduction

When compared to other available remote-sensing and ground-based technics, terrestrial photogrammetry can appear as an interesting option to measure relatively homogeneous surface displacements, such as those generally affecting rock glaciers [1]. With a reasonable cost in time and money, this approach allows to survey several ha and up to a few km² with an accuracy and a precision potentially high enough to get valuable insights into the spatial and temporal variations of surface characteristics (e.g. [2]). We evaluated this method on an active rock glacier in the semi-arid Andes of Argentina and we present in this paper the main results after comparison between the 3D models generated from 2 photography datasets (processed within a commercial software) and GPS measurements.

II. Study site and methodology

The Quebrada del Medio rock glacier is located on the Cordón del Plata, in the Argentinian Andes of the Mendoza Province. The landform is almost 3 km long, oriented N-S, has a glacigenic origin [3] and is characterized by steep lateral and frontal taluses and arcuate ridges and furrows evidencing the present activity of the deformation mechanisms [4]. The study area is limited to the lowest 600 m of the tongue, with a mean width of 200 m and elevations ranging between 3600 and 3400 m asl (Fig. 1). It benefits from a relatively easy access and is also surveyed with thermal and kinematic monitoring since April 2014.

The photogrammetric method uses several images of the same object taken with a sufficient overlapping between each ones to measure their relative orientations and to restitute 3-dimensional properties of the object. The apparition of digital photography and better hardware and software computational capacities have recently made the terrestrial, or ground-based, photogrammetry a powerful and affordable tool to generate high resolution models, extremely valuable for Geosciences applications, like 3D point clouds, Digital Elevation Model (DEM) and orthophotography (e.g. [5]).

In this work, two acquisition campaigns were carried out in May 2013 and August 2014 (Fig. 1), with two photographic devices sligthly different (Table 1), based on Nikon digital single lens reflex models (D7000 and D7100) equiped with fixed focal length lenses (respectively 27 and 36mm eq. 35mm, and with sensor size of 4928 x 3264 pixels and 6000 x 4000 pixels, respectively).

In: Geomorphometry for Geosciences, Jasiewicz J., Zwoliński Zb., Mitasova H., Hengl T. (eds), 2015. Adam Mickiewicz University in Poznań - Institute of Geoecology and Geoinformation, International Society for Geomorphometry, Poznań

TABLE I. CHARACTERISTICS OF THE PHOTOGRAPHIC DATASETS FOR THE TWO FIELD CAMPAIGNS

Date	Acquisition system	Number of images	Characteristics of the images			
			Size (pixel)		Time of shot	
			heigth	width	start	end
01/05/13	D7000 + 27mm	151	4928	3264	12h10	12h50
15/08/14	D7100 + 36mm	145	6000	4000	11h29	14h57

Date	Acquisition system	Characteristics of the terrain		
		Elevation (m asl)		Others
		min	max	
01/05/13	D7000 + 27mm	3307	3432	Only lower part
15/08/14	D7100 + 36mm	3478	3694	Snow remnants

A survey of 15 artificial targets (B&W cross printed on laminated canvas sheet, 10 targets of size 40 x 40 cm, and 5 targets of size 80 x 80 cm) was performed during the campaign of 15-Aug.-2014 with differential bi-frequency GPS (Trimble R5 used in PPK mode, with a computed precision of 0.01 m horizontally and 0.02 m vertically), in order to obtain accurate ground control points (GCP). A kinematic differential GPS survey (with the same device and a 5-second interval of acquisition) was also conducted the same day along two transversal tracks crossing the rock glacier, with an accuracy of ± 0.05 m (Trimble R5 factsheet).

In this work, two acquisition campaigns were carried out in May 2013 and August 2014 (Fig. 1), with two photographic devices sligthly different (Table 1), based on Nikon digital single lens reflex models (D7000 and D7100) equiped with fixed focal length lenses (respectively 27 and 36mm eq. 35mm, and with sensor size of 4928 x 3264 pixels and 6000 x 4000 pixels, respectively). A survey of 15 artificial targets (B&W cross printed on laminated canvas sheet, 10 targets of size 40 x 40 cm, and 5 targets of size 80 x 80 cm) was performed during the campaign of 15-Aug.-2014 with differential bi-frequency GPS (Trimble R5 used in PPK mode, with a computed precision of 0.01 m horizontally and 0.02 m vertically), in order to obtain accurate ground control points (GCP). A kinematic differential GPS survey (with the same device and a 5-second interval of acquisition) was also conducted the same day along two transversal tracks crossing the rock glacier, with an accuracy of ± 0.05 m (Trimble R5 factsheet).

After grouping the images according to the terrain they cover and eliminating those with wrong exposure, blurred or unnecessary coverage, the following steps were followed within the software Photoscan (© Agisoft): 1) aligning each groups of images (an additional optimization procedure was also performed to achieve better alignment results); 2) manual identification of the GCPs on each images; 3) dense cloud correlation; and 4) export of DEM and orthophotography at the best resolution (between 6 and 15 cm depending on the model).

For the GPS and photo campaign of 15-Aug.-2014, the mean positioning error based on 384 projections of 11 GCP is 0.154 m for X, 0.094 m for Y and 0.110 m for Z, corresponding to a mean overall error of 1.23 pixel after alignment optimization. Once generated, the 3D model of 15-Aug.-2014 was then used to georeference 1-May-2013 model by retrieving 7 new GCPs on fixed areas on both sets of images, achieving a mean error of 0.248 m.

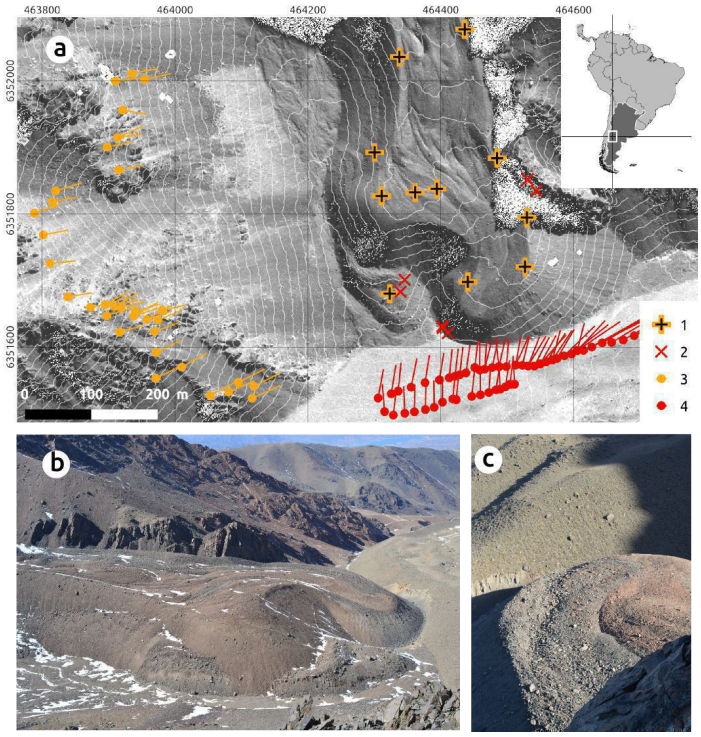


Figure 1. a) Map of the study area and location of the different photogrammetric elements. Legend: 1) target used for the GPS and photo campaign of 15-Aug.-2014; 2) GCP extracted from 2014's model to georeference 2013's models; 3) position of cameras and view angle of the photos for 2014's campaign; 4) position of camera and view angle of the photo for 2013's campaign. 10-m contour lines and background orthoimagery are from Pléiades images [6]; b) View from the West of the tongue of the rock glacier; c) View from the North of the terminus.

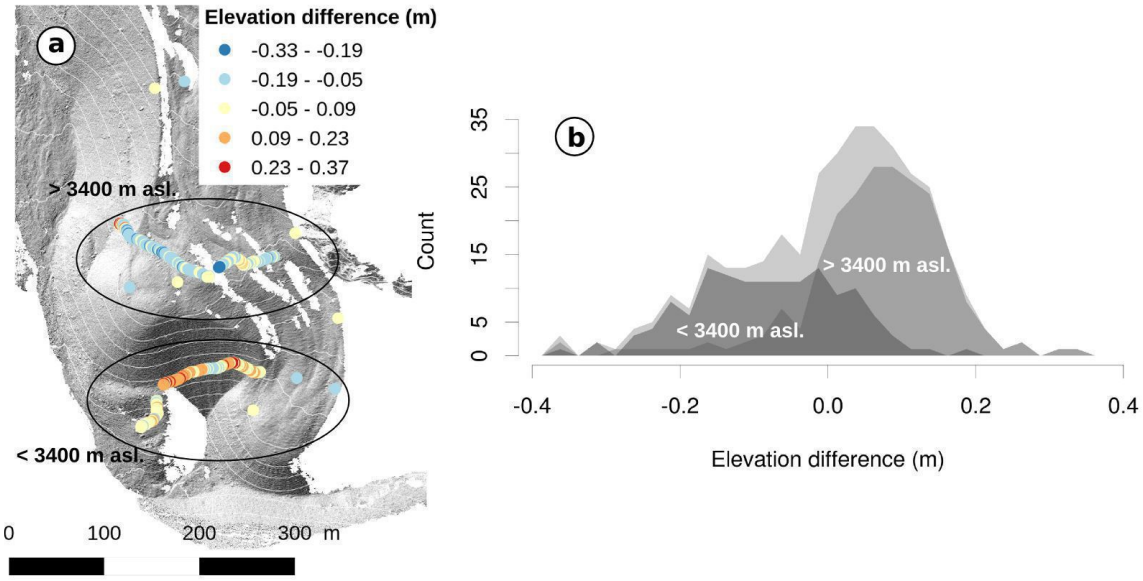


Figure 2. Comparison of the elevation values between 2014 DEM and 361 GPS measurements along two tracks on the rock glacier: a) Overall view of the DEM and location of the GPS points (areas above and below 3400 m asl. are distinguished); b) distribution of the error (difference in elevation between GPS value and corresponding DEM cell) for each area (above and below 3400 m asl.) and for the total.

III. Results and discussion

We compared the DEM produced with the 15-Aug.-2014 images with the kinematic GPS measurements performed the same day, by extracting in a GIS the DEM value corresponding to each of the 361 GPS points and then compute the difference in elevation (Fig. 2). Taking into account that an error of ± 0.08 m should be empirically added due to the movements of the antenna mounted on the top of the stick and hand-held along the tracks, the elevation differences between GPS and 2014's DEM are ranging from -0.371 to 0.326 m, with an RMSE of 0.123 m.

Two significantly different distributions of the errors are found on the two evaluation areas (roughly grouped according to the elevation, ie. above and below 3400 m asl), which is most probably related to unsolved alignment problems on the 3D models. A third campaign is planned in December 2014 with a greater number of large targets (80 x 80 cm) to try to better understand and hopefully solve this problem.

If we now consider 2σ (0.24 m) of the DEM-GPS elevation differences as a reasonnable error margin, then the differences between the 3D models of 15-Aug.-2014 and 1-May-2013 (Fig. 3) can be interpreted in terms of geomorphological dynamics that affect the Quebrada del Medio rock glacier. Due to the above mentionned alignment problem, the comparison has been only focused on the frontal part of rock glacier tongue, where numerous GCP better constrain the alignment between 2013 and 2014 3D models.

Over the 15-month time interval between the two campaigns, several phenomena are nicely imaged by this approach. First, a characteristic pattern of elevation difference observed here probably reflects the advance mechanism of the rock glacier: the advection of frozen debris to the front due to the creeping of the ice and debris mixture leads to higher horizontal displacements, which is reflected by a gain of elevation spread homogeneously on the upper part of the talus (see [7]). Most probably related to the same process, the fall of three pockets of debris is also evidenced by a loss of elevation on the upper part of the talus immediately followed below by a gain, where the fallen material accumulated.

IV. Conclusion

We evaluate the potential of a low-cost procedure to generate 3D models, from which high resolution DEMs and orthoimages can be easily derived, for studying rock glacier dynamics. The comparison between DEM and GPS measurements made in 2014 gives a margin of error of ± 0.24 m. Though unsolved problem of alignment between the 3D models limits the comparison between 2013 and 2014 DEMs, characteristic processes affecting the front of the rock glacier have been highlighted. This approach therefore appears as a very promising tools, as computational performance and optical quality of the digital cameras are still progressing.

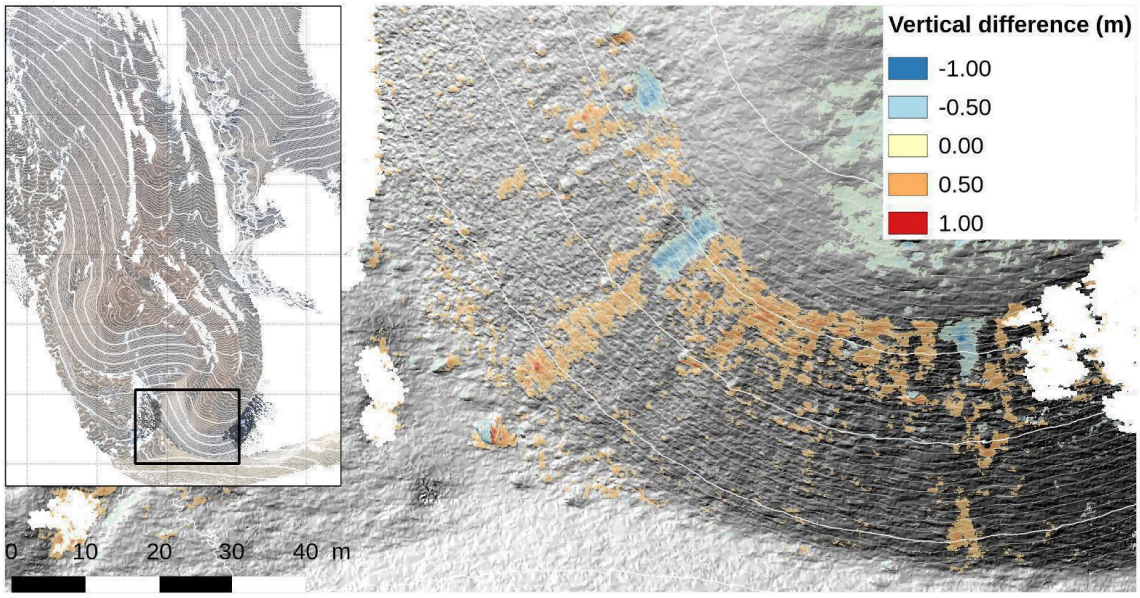


Figure 3. Vertical changes between 15-Aug.-2014 and 1-May-2013 DEMs on the frontal part of the Quebrada del Medio rock glacier (values between -0.24 and 0.24 m, corresponding to the error margin, have been set to transparent). Inset map shows the location of the zoomed area (background is the 2014 orthoimage overlaid with 1-m contour lines)

Acknowledgment

This work is part of the ANDALP project (“Geomorphological dynamics and permafrost in the Andes”), funded by the CMIRA program of the Région Rhône Alpes, France (COOPERA n°13.005522.01/02). The D7100 digital camera was acquired thanks to a grant from the AAP Université de Savoie 2014. The authors wish to thank Pepe Hernandez (IANIGLA) and Jean-Pierre Beck for their help in preparing the campaigns, Daniel Falaschi (IANIGLA), Michèle Vernay, Elise Beck (and Clément!), Gilen Anetas and Damien Bornet for their help during fieldwork. The stay of X. Bodin at IANIGLA (Mendoza, Argentina) during year 2014 was made possible thanks to the financial support of the Région Rhône Alpes (EXPLORA PRO). We thank the constructive comments of three anonymous reviewers.

References

[1] Barsch, D. 1996. Rockglaciers. Indicators for the permafrost and former geoecology in high mountain environments. Springer, Berlin. 331p.

[2] Kaufmann, V. 2012. “The evolution of rock glacier monitoring using terres- trial photogrammetry: the example of Äußeres Hochebenkar rock glacier (Austria)”. Austrian Journal of Earth Sciences, 105(2), 63–77.

[3] Trombotto, D. 2003. “Mapping of permafrost and the periglacial environments, Cordón del Plata, Argentina”. In 8th International Conference on Permafrost (pp. 161–163).

[4] Haeberli, W., Hallet, B., Arenson, L., Elconin, R., Humlum, O., Kääb, A., … Mühll, D. V. 2006. “Permafrost creep and rock glacier dynamics”. Permafrost and Periglacial Processes, 17(3), 189–214.

[5] Westoby, M. J., Brasington, J., Glasser, N. F., Hambrey, M. J., & Reynolds, J. M. 2012. “Structure-from-Motion photogrammetry: A low-cost, effective tool for geoscience applications”. Geomorphology, 179, 300–314. doi:10.1016/j.geomorph.2012.08.021

[6] Ruiz, L. and X. Bodin. Submitted. “Analysis and improvement of surface representativeness of high resolution Pléiades DEMs: examples from the Andes”. Geomorphometry conference 2015, Poznan, Poland

[7] Kääb, A., & Reichmuth, T. 2005. Advance mechanisms of rock glaciers. Permafrost and Periglacial Processes, 16(2), 187–193. doi:10.1002/ppp.507

Quantifying sediment transfer between the front of an active alpine rock glacier and a torrential gully

Mario Kummert
Dept. of Geosciences
University of Fribourg
Fribourg, Switzerland
Mario.Kummert@unifr.ch

Reynald Delaloye
Dept. of Geosciences
University of Fribourg
Fribourg, Switzerland
Reynald.Delaloye@unifr.ch

Abstract—**The present contribution describes results from the quantification of transferred sediment volumes between the front of an active rock glacier and a torrential gully. The focus is set on the methodological approach which combines terrestrial laser scanning (TLS) generated digital terrain models (DTM) and geodetic field surveys. The aim is to compare high resolution DTMs from different dates in order to calculate volume gain and loss in the system for different time intervals. As the object of the study is a fast moving landform, other sources of information such as geodetic measurements (GPS) were necessary to estimate the advance of the rock glacier during the same time intervals and to facilitate the interpretation of the TLS data. It was then possible to estimate sediment budgets in the whole scanned area for different time intervals. The results show an extensive erosion of the front (up to 5000 m^3/year) but also the presence of a temporary sediment storage area in the upper part of the torrential channel.**

I. INTRODUCTION

In alpine periglacial hillslopes, large volumes of rock debris originating from talus screes and moraines are transported downward by rock glaciers creep [1]. The movement of rock glaciers is a consequence of the deformation of the ice present in the porosity of the terrain under permafrost conditions. The ice content in the ground can be highly variable between sites. Active rock glaciers are usually delimited downward by a steep unstable front [2]. When located on steep slopes, the front of rock glaciers can act as the sediment source favoring the triggering of hazardous gravitational processes such as debris flows and rock falls [3]. Consequently, quantifying and monitoring the sediment transfer processes occurring at the front of active alpine rock glaciers could help the management of natural hazards in mountainous terrains.

In environmental sciences, terrestrial laser scanning (TLS) has been used to obtain high resolution digital terrain models (DTMs) since the beginning of the years 2000 [4]. The progresses made at a technical level over the years have induced an important increase in the amount of research projects using TLS in the last five years. Today, TLS devices offer the possibility to get high resolution terrain elevation data, allowing precise measurement and monitoring of geomorphological landforms to be made especially by the use of DTMs comparison techniques. There are only few applications of TLS on rock glaciers monitoring in the Alps (e.g.: [5]), and despite the influence of these landforms on the triggering of debris flow and rock fall, there are even less studies focusing on the sediment transfer dynamics at the front of rock glaciers [6]. However, while airborne methods tend to be costly (airborne LiDAR) or to show performance restriction linked to the steepness of the terrain (photogrammetry), TLS seems to be a suitable method to get high resolution DTMs in steep and remote mountain environments [7].

This contribution presents results from two years of TLS survey at the front of the Gugla-Bielzug rock glacier (western Swiss Alps). The aim is to discuss the interests and the limits of this method in the context of the monitoring of sediment transfer processes in such environments.

II. STUDY SITE

The Gugla-Bielzug rock glacier is located on the orographic right side of the Zermatt valley (western Swiss Alps, see Fig. 1). The front is directly linked to a torrential gully which shows traces of debris flow until the valley bottom. The rock glacier is currently in a destabilization phase, the surface velocities having drastically increased during the last ten years, reaching locally a maximum of 8 cm/day in June 2013. Another particularity of this rock glacier is the role it has been playing in the triggering of several debris flows in 2013 and 2014. The debris flows were

In: Geomorphometry for Geosciences, Jasiewicz J., Zwoliński Zb., Mitasova H., Hengl T. (eds), 2015. Adam Mickiewicz University in Poznań - Institute of Geoecology and Geoinformation, International Society for Geomorphometry, Poznań

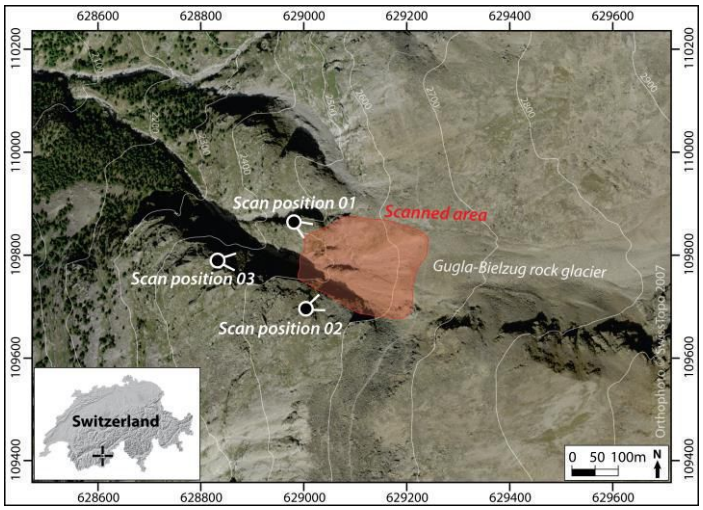


Figure 1. Location of the three scanning stations and the resulting scanned area at the Gugla-Bielzug rock glacier.

initiated beneath the front by snow-melt or rain fall events and reached the valley bottom near the village of Herbriggen (St Niklaus, VS, Switzerland).

III. METHODOLOGY

Five TLS campaigns were carried out at this site using a Riegl VZ-6000 long range scanner. The results are high resolution point clouds representing the surface of the terrain. We used three scanning positions to enhance the surface coverage and increase point clouds density (Fig. 1). Concerning the coregistration, we applied an Iterative Closest Point (ICP) algorithm on the RiscanPro software. Assumed stable areas (rock walls) were used to register point clouds from different dates. After the coregistration, the root-mean-square error (RMSE) in assumed stable areas is about 0.013m, and the resolution of the resulting point clouds is 0.1m. Given the high density of the point clouds we used a simple GIS natural neighborhood interpolation for the creation of DTMs [8].

In the context of sediment transfer studies, the interest of this method is to produce several high-resolution DTMs corresponding to different dates. It is then possible to compare the DTMs to calculate and map the vertical surface changes in the area:

DTM (date 2) – DTM (date 1) = vertical surface changes

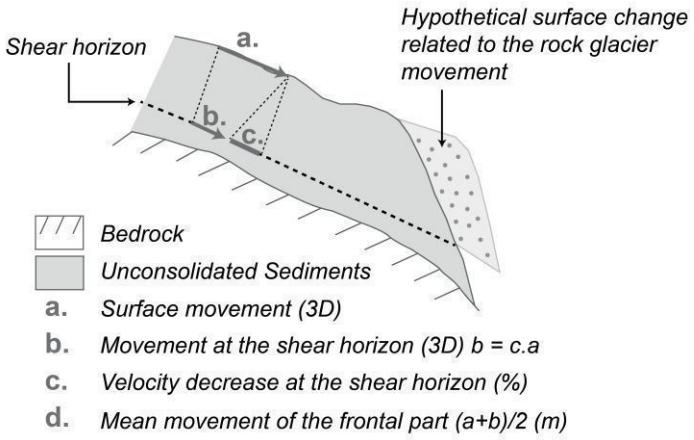


Figure 2. Schematic drawing explaining how the rock glacier movement impacts the volume gain and loss calculation. At Gugla-Bielzug, c. is assumed to be important (estimated at 50%) because of the presence of three shear horizons.

In our scanned area, two different zones can be distinguished (Fig. 4). The first zone is the gully where volume gain and loss calculated from the DTMs comparison can be interpreted respectively as accumulation and erosion of sediments. The second zone is the front of the rock glacier, located at the top of the gully and acting as the sediment source to the system. There, volume gain and loss results from erosion/accumulation processes but also from the movement of the rock glacier (Fig. 2). As the aim of the study is to quantify accumulation and erosion processes, it was important to remove the effect of the rock glacier movement on the calculated volumes. In order to complete that, movements measured by GPS on the surface of the rock glacier were used as explained hereafter:

1. First, the area affected by the rock glacier movement was delimited using the vertical difference map produced by DTMs comparison for a 2 week interval (Fig. 3).
2. In a second step, the position of several boulders was measured by GPS on the surface of the rock glacier at the dates of the scans. Boulders located near the front were selected to calculate for each time interval the mean 3D displacement at the surface of the rock glacier.
3. As the rock glacier velocity decreases in depth, a mean displacement for the whole frontal part was calculated using the formula described in Fig. 2 (point d.). The velocity at the shear horizon was estimated to be significantly lower than the surface velocity (about 50%) because of the presence of at least three different shear horizons, favoring the velocity decrease in depth.

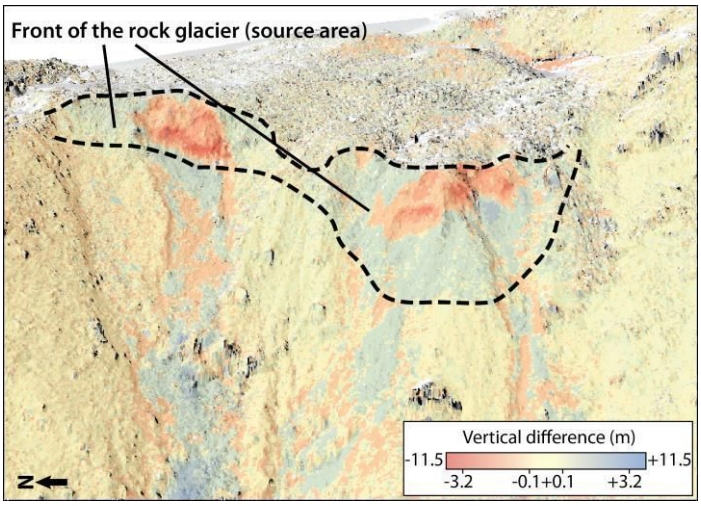


Figure 3. Limits of the front area detected on the surface changes between the 25.06.2013 and the 10.07.2013.

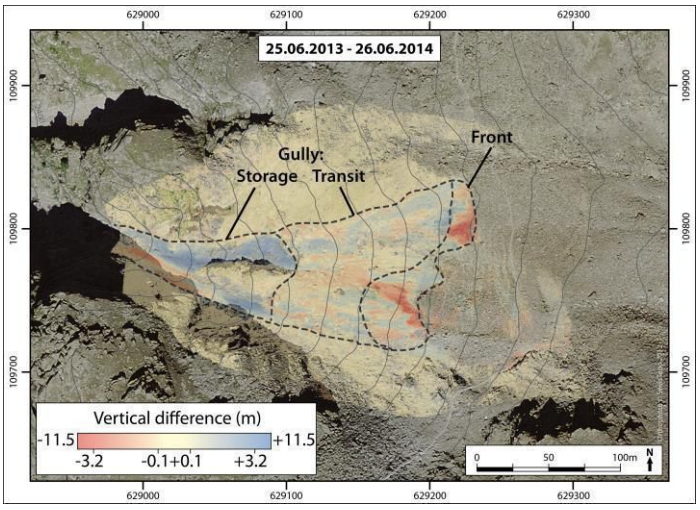


Figure 4. Example of a surface changes map for a one year period between June 2013 and June 2014.

4. Knowing the mean slope angle of the front (σ, calculated from the DTMs) and the mean horizontal (d_{xy}) and vertical (d_z) displacement (decomposition of the mean 3D displacement), the vertical differences related to the rock glacier advance (ΔH) were estimated for each time interval covered by the scans:

$$\Delta H = (\tan \sigma \, . \, d_{xy}) - d_z$$

The vertical differences (ΔH) related to the movement of the rock glacier were then subtracted from the vertical differences calculated by the DTMs comparison for the whole front area in order to obtain estimations of accumulated and eroded volume in this sector.

IV. Results

Five scanning campaigns were carried out at the Gugla-Bielzug rock glacier between the 25th of June 2013 and the 9th of October 2014, each campaign including three scanning positions. The results are five high resolution DTMs (0.1m) which were compared to obtain an overview of the evolution of sediment transfer processes in the system.

Fig. 4 presents an example of a surface changes map produced by DTMs comparison. The erosion areas are represented in red and the accumulation areas in blue. Changes too small to be significant are represented in pale yellow. The image shows a good coverage of our zone of interest, which is the interface between the front of the rock glacier and the upper part of the gully. The analysis of these maps shows that most of the erosion occurred at the front during the period covered by the scans. An important accumulation area is present in the lower part of the scanned area. These two sectors seem to be separated by a transit area, characterized by smaller eroded and accumulated volumes (Fig. 4).

Based on in situ observations of permafrost outcrops, the ice content of the rock glacier should not exceed by much the general porosity of the terrain, and is about 50%. This allows us to make a correspondence between the volumes eroded from the front (approximately 50% of sediments and 50% of ice) and the volumes accumulated in the gully (approximately 50% of sediments and 50% of air), and then to calculate a total sediment budget (the sum of volume gain and loss) in our entire scanned area. Budgets were also calculated separately for the two zones (the front and the gully). The results are presented in Table 1. They show plausible values given the velocity of the rock glacier and the geometry of the front. Important amounts of sediment were eroded from the front during the investigated period, and most of it was transported further down, sometimes after having been stored for a certain lapse of time in the gully.

V. Discussion

The methodology seems appropriate to the object of the study. It brings important information about the spatial behavior of the sediment transfer processes and especially quantitative data about erosion and accumulation. The repetition of the

TABLE I. CALCULATED VOLUMES (SEDIMENTS ONLY) FOR THE DIFFERENT TIME INTERVALS

Time interval	Budget at the front (m^3)	Budget in the gully (m^3)	Total budget (front & gully) (m^3)	Erosion rate at the front (m^3/day)
25.06.2013-10.07.2013 *(15 days)*	-394	*352*	42	26
10.07.2013-04.10.2013 *(86 days)*	-1163	1065	-98	14
04.10.2013-26.06.2014 *(265 days in which 124 days where the front is covered with snow)*	-2437	582	-1855	18
26.06.2014-09.10.2014 (105 days)	-2304	-2207	-4511	22

measurement supplies temporal variability data. However, the results need to be analyzed carefully. The methodology used to correct the influence of the rock glacier movement implies some simplifications and the calculated volumes give therefore an order of magnitude more than exact numbers. In addition, the interpretation of the surface changes map can be difficult depending on the time between two scanning campaigns. There is then a need for other sources of information. In this study, webcam images were used to link surface changes with the occurrence of sediment transfer processes.

There are also some limits associated to the measurement itself. For example, it is difficult to find stable terrains for the coregistration. This could induce some uncertainties that we did not quantify. In addition, the presence of snow in the gully between November and June reduces the potential scanning period. Finally, the method asks for a good coverage of the whole area of interest, which implies to have access to good scan positions at reasonable distances.

VI. CONCLUSION

TLS seems to be a well suited method the get quantitative data about surface changes and sediment transfer processes in steep and remote environments where aerial and satellite data are known to have performance restrictions [4]. However, the application of such a method on rock glacier fronts asks for additional data such as GPS measurements and images to help the interpretation of the results. In the case of the Gugla-Bielzug rock glacier, the combination of geodetic measurements, observations from high temporal resolution photographs and TLS have been proven to be a coherent method to get precise spatial and temporal information about the evolution of this system.

VII. ACKNOWLEDGEMENT

The work has been carried out in collaboration with the local authorities (municipality of St. Niklaus) and cantonal and federal offices (Cantonal Service for the Forests and Landscape and Federal Office for the Environment BAFU), that have to be acknowledged for their contribution. We also would like to thank all the people involved in the data collection and processing.

REFERENCES

[1] Delaloye, R., Lambiel, C. & Gärtner-Roer, I. (2010). Overview of rock glacier kinematics research in the Swiss Alps. Seasonal rhythm, interannual variations and trends over several decades. Geogr. Helv. 65: 2, 135–145.

[2] Barsch, D. (1992). Permafrost creep and rock glaciers. Pemafrost and Periglacial Processes, 3 (3), 175-188.

[3] Lugon, R. & Stoffel, M. (2010). Rock glacier dynamics and magnitude-frequency relations of debris flows in a high-elevation watershed : Ritigraben, Swiss Alps. Global and Planetary Change, 73, 202-210.

[4] Bauer, A., Paar, G. & Kaufmann, V. (2003). Terrestrial laser scanning for rock glacier monitoring. In: Eighth International Conference on Permafrost. Balkema: Lisse; 1, 55–60.

[5] Bodin, X., Schoeneich, P. & Jaillet, S. (2008). High-resolution DEM extraction from terrestrial LIDAR topometry and surface kinematics of the creeping alpine permafrost: The Laurichard rock glacier case study (southern French Alps). In: Kane, D.L. & Hinkel, K.M. (eds): Proceedings of the 9th International Conference on Permafrost, June 29-July 3, 2008, Fairbanks, Alaska, 1: 137-142.

[6] Avian, M., Kellerer-Pirklbauer, A., Bauer, A. (2009). LiDAR for monitoring mass movements in permafrost environments at the cirque Hinteres Langtal, Austria, between 2000 and 2008. Nat. Hazards Earth Syst. Sci., 9, 1078 – 1094.

[7] Kenner, R., Phillips, M., Danioth, C., Denier, C., Thee, P., Zgraggen, A. (2011). Investigation of rock and ice loss in a recently deglaciated mountain rock wall using terrestrial laser scanning : Gemsstock, Swiss Alps., Cold Regions Science and Technology, 67, 157-164.

[8] Scheidl, C., Rickenmann, D. & Chiari, M. (2008). The use of airborne LiDAR data for the analysis of debris flow events in Switzerland. Natural Hazards and Earth System Sciences, 8, 1113–1127.

An attempt to assess the influence of road network on flash flood wave parameters - the case study of the Carpathian Foothills

Kroczak Rafał
Institute of Geography
Pedagogical University of Cracow
Cracow, Poland
e-mail kroraf@gmail.com

Bryndal Tomasz
Institute of Geography
Pedagogical University of Cracow
Cracow, Poland
e-mail tbryndal@up.krakow.pl

The road network complements the natural drainage network and accelerates the water cycle in the catchment. In this study the methodology enabling for inclusion of a road network into a simple rainfall-runoff routing model was proposed. The road network was included into the surface drainage system and quantified as the Horton's ratios. The bifurcation (R_B), the length (R_L) and area (R_A) ratios increased when the road network was introduced to the surface drainage system. The Soil Conservation Service-Curve Number (SCS-CN) and Geomorphological Unit Hydrograph (GIUH) models were adapted to evaluate the influence of a road network on the flood wave hydrograph in the Zalasówka catchment (the Carpathian Foothills). Results revealed that the maximum flow is c.a. 20% higher, when the Horton's ratios include the natural river system and the road network. Moreover, the differences between the simulated and observed maximum flows were lower when the R_B, R_L, and R_A ratios included the road network as an element of the drainage system. It seems that including the road network in Horton's ratios improves the simulation of flash flood wave parameters in small catchments.

I. INTRODUCTION

The Carpathian Foothills have been significantly changed by agricultural development since the mid XIV century. Since the beginning of the XIX to the mid XX century there was so called "land hunger" due to a high birth rate and a lack of alternative livelihoods in this region. As a result of this, many small arable fields were established and settlements areas were scattered. These factors contributed to the development of a dense road network. The road network density reaches 9 $km \cdot km^{-2}$, and it is one of the highest in mountainous areas in the world.

The road network is treated as a "human-made element" that complements the natural drainage network and therefore modifies the path of the flow within the slope and accelerates the water cycle [1, 2, 3, 4]. Road networks may drain up to 30% of a catchment area [4].

Roads create favorable conditions for runoff formation, because they always have a higher value of the runoff coefficient than other types of land use. Unpaved roads have a runoff coefficient higher than 0.64, whereas roads covered by concrete and asphalt reach 0.95 [5]. Moreover, roads act as water collectors, in which high-speed concentrated flows occur. Overland flow velocity on a slope ranging from 10º to 17º may reach 8 – 9 $cm \cdot s^{-1}$ on grassland fields, 13 $cm \cdot s^{-1}$ on ploughed fields, but more than 1 $m \cdot s^{-1}$ on unpaved roads [6]. Froehlich and Słupik [7] proved that during a flood event the road network delivers c.a. 60% of rainfall water and the specific flow on the road is higher than those observed in the river channel. Higher stream density allows the landscape to drain more efficiently. More efficient drainage means that water moves into streams faster, causing peak flows to be larger and to occur sooner [2]. As a result of this floods occur more frequently and are more severe - turning into flash floods [1, 2, 4].

Flash floods usually affect small ungauged catchments. The only way to reconstruct flood wave hydrographs is to use hydrological models. As far as input data availability for small catchments is concerned, simple conceptual rainfall-runoff routings models may be considered as the best for flash flood hydrogram simulation [2].

Taking into account that the road network complements the river drainage system we made an attempt to include the road network "as part of the drainage network" and quantified it by using Horton's and Schumm's ratios [8, 9].

In: Geomorphometry for Geosciences, Jasiewicz J., Zwoliński Zb., Mitasova H., Hengl T. (eds), 2015. Adam Mickiewicz University in Poznań - Institute of Geoecology and Geoinformation, International Society for Geomorphometry, Poznań

The goals of this study were: 1) to develop a methodology enabling the inclusion of the road network into the hydrological model and 2) to evaluate the influence of road networks on flash flood wave parameters.

The research hypothesis assumed in this study is that the modelling of rapid surface runoff during flash flood events may be improved by incorporating hydrological measures that take into account the contributions of both natural and man made (road) features to the runoff characteristics of a catchment. In this context, the methodological approach presented in this study is novel.

II. THE STUDY AREA

The Zalasówka catchment (9.2 km^2) was chosen for detailed investigation (Fig. 1). The catchment may be considered fully representative for the Carpathian Foothills in terms of geology, relief, and land use. More than 60% of the catchment area has a slope gradient between 5°-15°. The river network density amounted to 1.6 $km \cdot km^{-2}$. The Zalasówka catchment represents a typical agricultural type of foothills catchment. More than 80% of its area is covered by agricultural lands. The fields are significantly fragmented, which means they have small areas. As a result of this, the road network is well-developed. The road network densities range between 7-9 $km \cdot km^{-2}$. Forest and settlement areas occupy 10%.

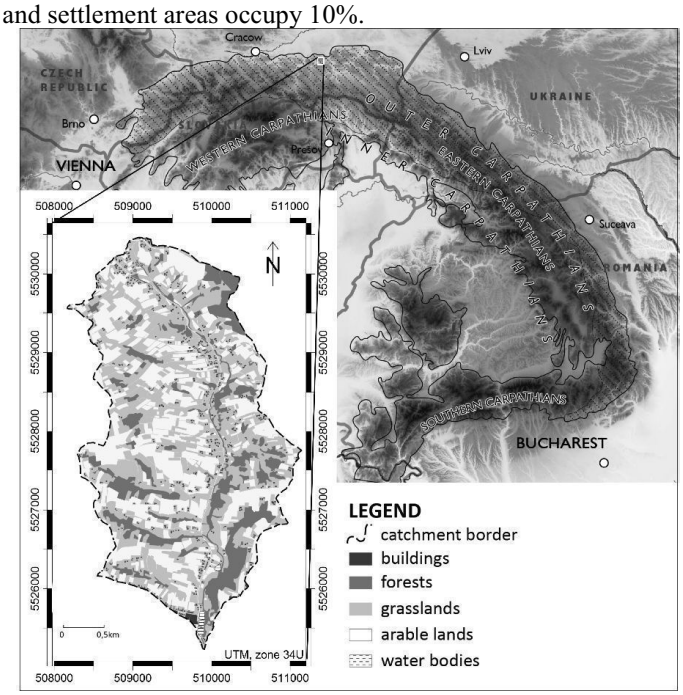


Figure 1. The study area and the structure of land use in the Zalasówka catchment.

III. MATERIALS AND METHODS

Incorporation of a road network to surface drainage system – the procedure

The first step was to develop the natural surface drainage system pattern. The digital terrain model DTM with a resolution of 5x5m and ILWIS software modules were used for this purpose (Fig. 2). Then, a Hortonian-type analysis was performed and the bifurcation (R_B), length (R_L) and area ratios (R_A) were calculated.

The second step was the incorporation of the road network into the surface drainage system. In order to reach this goal the contemporary road network (obtained from topographical maps at a scale of 1:10000) was "burned into" the DTM. Then the surface drainage system was generated again (Fig. 2B) and the Hortonian-type of analysis has been performed again. In this way the R_B, R_L and R_A ratios characterize quantitatively both natural and man made (road) features.

The influence of the road network on flash flood wave parameters – the assessment

The influence of the road network on flood wave parameters was evaluated using two hydrological models: the SCS-CN [10] and GIUH [11]. First model was adapted for the reconstruction of the transformation from rainfall into excess rainfall process, while the second model was used for the reconstruction of flood wave parameters. The GIUH model requires the R_B, R_L and R_A ratios which are the input data characterizing the drainage system. Flood hydrographs were developed for a flash flood event recorded in June 2005. Precipitation data was obtained from the raingauge station situated near the catchment border. The maximum flow was measured at the catchments outlet using the slope-area method.

The flood wave simulation taken into account had two scenarios: 1) the Horton's and Schumm's ratios describing the natural river system, 2) the Horton's ratios and Schumm's ratios describing the natural river system and road network system. The differences were evaluated by the relative errors between the maximum flows observed and those simulated by SCS-SC and GIUH models.

IV. RESULTS AND DISCUSSION

A road network as a part of surface drainage system. Natural and modified by road networks surface drainage systems are presented on Fig. 2. The road network significantly modifies the water flow from the slopes and a considerable part of a catchment is drained by road networks. These changes are reflected in the Horton's ratios (Table. 1). When the road network was included the R_B, R_L and R_A ratios increased.

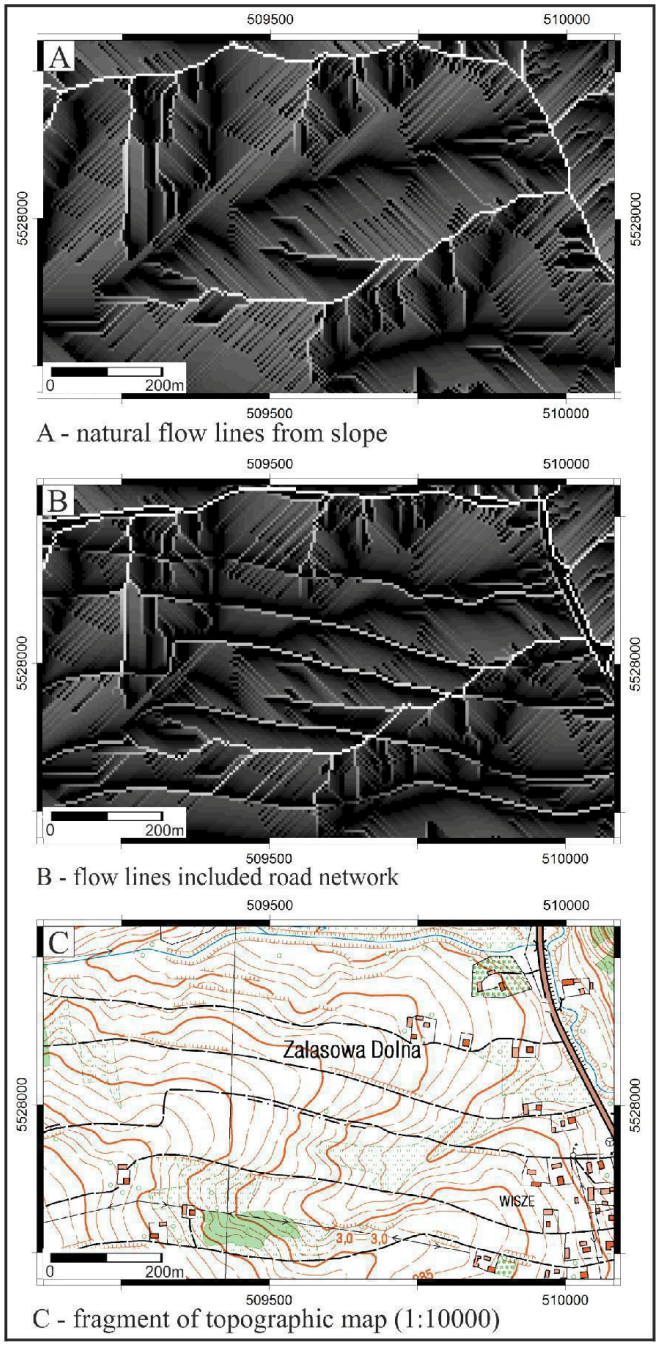


Figure 2. The natural – A and modified – B by road networks surface drainage systems in a part of the Zalasówka catchment. The lowermost part – C presents the topographical map ot this area.

TABLE I. THE HORTON'S RIVER NETWORK PARAMETERS IN THE ZALASÓWKA CATCHMENT

Source of the data	The Horton's ans Schumm's ratios		
	R_B	R_L	R_A
The river network	4.7	2.2	5.5
The river and road networks	5.4	4.8	6.4

The final pattern of a surface draining network (composed of natural and road network) is presented on Fig. 3. It is notable that the road network significantly modifies the water flow from the slopes and c.a. 1/3 of a catchment is drained by the road networks.

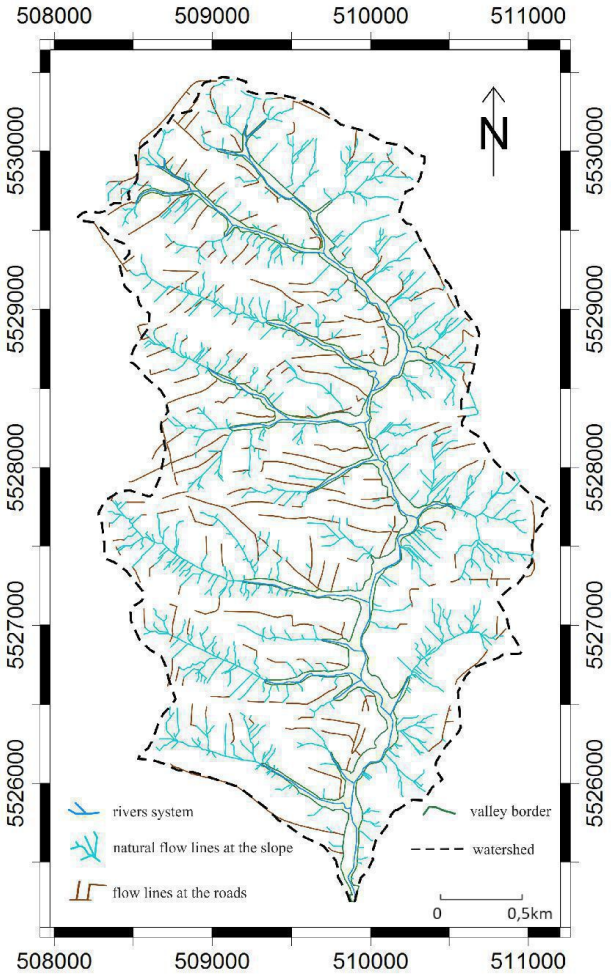


Figure 3. The surface drainage systems in the Zalasówka catchment.

The influence of road network on flash flood wave parameters

In order to evaluate the influence of the road networks, the hydrographs generated by short duration rainstorm event were developed (Fig. 4). Hydrographs revealed rapid responses of the catchment to heavy rainfall. The rising limb and recession limb were very steep and coincided with the course of rainfall. The maximum peak flow during the flood event on 5 July 2005 reached 10.2 $m^3 \cdot s^{-1}$. The simulated hydrographs revealed that the maximum flow is more consistent with the peak flow recorded during flood event when the R_B, R_L and R_A ratios characterize all (river and road) surface drainage networks.

The maximum flow is c.a. 20% higher, when the Horton's ratios include both the natural surface drainage and the road network.

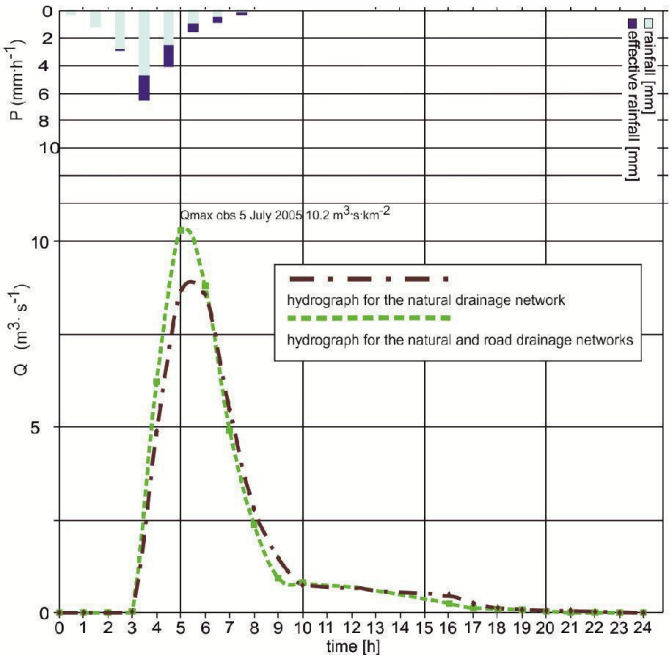


Figure 4. The hydrogrphs generated by a short duration rainstorm event on 5 of June 2005 in the Zalasówka catchment. Reconstruction by SCS-CN and GIUH models.

CONCLUSIONS

This paper proposes a methodology that enables the inclusion of the road network into the simple rainfall-runoff routing model. The road networks were included in the surface drainage system and quantified as the Horton's ratios. The results revealed that the bifurcation (R_B), length (R_L) and area (R_A) ratios increase when the road network is introduced into the surface drainage system.

The SCS-CN and GIUH models were adapted to evaluate the influence of a road network on the flood wave hydrograph in the Zalasówka catchment (the Carpathian Foothills). The results revealed that the maximum flow is c.a. 20% higher when the Horton's ratios include the natural river system and the road network. The differences between the simulated and observed maximum flows were lower when the R_B, R_L, and R_A ratios included the road network as an element of the drainage system.

The road network complements the natural drainage system and accelerates the water cycle in the catchment. It seems that the incorporation of a road network into the surface drainage system according to Horton's and Schumm's ratios improves the simulation of a flash flood wave in small catchments. The proposed methodology was not yet widely discussed in literature. This paper presents the preliminary results of our investigations as a case study for one catchment. The results seem to be encouraging, however, this approach needs further investigations.

REFERENCES

[1] Bryndal T., 2014. "A method for identification of small Carpathian catchments more prone to flash flood generation. Based on the example of south-eastern part of the Polish Carpathians, Carpathian". Journal of Earth and Environ Sciences 9(3):109-122

[2] Bryndal, T., Cabaj, W., Suligowski, R., 2010. "Hydro-meteorological analysis of flash floods in small basins located in headwater of Wielopolka river on the 25th of June 2009". Monografie Komitetu Inżynierii Środowiska PAN 69:81-91. (in Polish).

[3] Croke J, Mockler S, Fogarty P, Takken I., 2005. "Sediment concentration changes in runoff pathways from a forest road network and the resultant spatial pattern of catchment connectivity". Geomorphology 68(3-4):257-268.

[4] Kroczak R., 2010. "Geomorphological and hydrological effects of unmetalled road network functioning on the example of Ciężkowickie Foothills". Prace Geograficzne IGiPZ PAN 225:1-138. (in Polish with English summary).

[5] Radwan-Dębski R,. 1995. "Estimation of excess rainfall on the basis of sealing of surface". Gospodarka Wodna 12:315-320. (in Polish)

[6] Figuła K., 1955. "Preliminary assessment of erosion on the several districts of the Krakowskie province". Roczniki Nauk Rolniczych 1:1-80. (in Polish).

[7] Froehlich W, Słupik J., 1986. "The role of road in flow and erosion formation in the flysch Carpathian basins". Przegląd Geograficzny 58(1–4):67-85. (in Polish).

[8] Horton R. E., 1945. "Erosional development of streams and their drainage basins: hydrophysical approach to the quantitative morphology". Geological Society of America Bulletin 56: 275-370.

[9] Schumm S.,A., 1956. "Evolution of drainage systems and slopes in badlands and Perth Amboy, NY". Geological Society of America Bulletin 67: 597-646.

[10] *Soil Conservation Service*, 1972. "National Engineering Handbook, Section 4, U.S. Department of Agriculture", Washington, D.C. 544.

[11] Rodriguez-Iturbe I., Valdes J.B., 1979. "The geomorphologic structure of hydrologic Response". Water Resources Research 15: 1409-1420.

Automatic extraction of landslide flow direction using geometric processing and DEMs

Mihai Niculiță
Geography and Geology Faculty
Alexandru Ioan Cuza University
Iași
mihai.niculita@uaic.ro

Abstract—**Landslides are mass wasting landforms which occur due to various triggering factors, and generate a specific morphology. This morphology is governed by the flow of the material downslope. While the majority of the landslide have the length bigger than the width (flows, slides, deep-seated landslides), in certain topographic conditions, landslides with width larger than length can exist (slides and deep-seated landslides). We target such a case, by creating a methodology to automatically determine the direction of the flow, in such a way that the oriented bounding box polygon to be aligned downslope, and the length of the landslide polygon to be determined. After the application of the first step of the algorithm, in which the direction of landslide flow is assessed using the altitude range of the midpoints of the long (length candidates) and short (width candidates) sides of the landslide oriented bounding box (for a landslide to be long the altitude range between the opposite long sides need to be greater than the range for the opposite short sides), manual check was used to assess the results. This check showed that the majority of the landslides were correctly classified, either as long or wide, but in the long landslide class there are in fact wide class landslides which are situated on valley sides with steep channels. These landslides have the altitude range between the short sides smaller than the altitude range between the long sides, although the direction of the flow is along the short side. To correctly classify the flow direction for these landslides, we have used the slope length computed on the DEM patches of the landslide polygons. Where the slope length is greater than the landslide width determined in the first phase and the landslide is classified as long, the landslide class is changed to wide, and vice versa. By this approach we manage to correctly classify the landslides as long or wide in the landslide inventory of the Moldavian Plateau, Romania (24 263 landslides).**

I. INTRODUCTION

Landslides are natural phenomena which appear when a terrain mass is moving down a slope. A typical morphology appear as an effect of this process [1], [2]. Landslide geomorphometry is very important because can be used to assess the typology of the landslides and perform various geomorphologic analyses [3], [4], [5]. While the majority of the landslides are more long than wide, there are landform situations when the landslides are wider than longer [6], [7], [8] (for example on monoclinic structure, where cuesta hills develop, or on the banks of steep channels of gullies incised in hillslopes – Fig. 1). The present study show a methodology for geometric and geomorphometric processing of landslide polygons and DEMs, for obtaining the direction of the material flow and to get the downslope oriented length and the associated width.

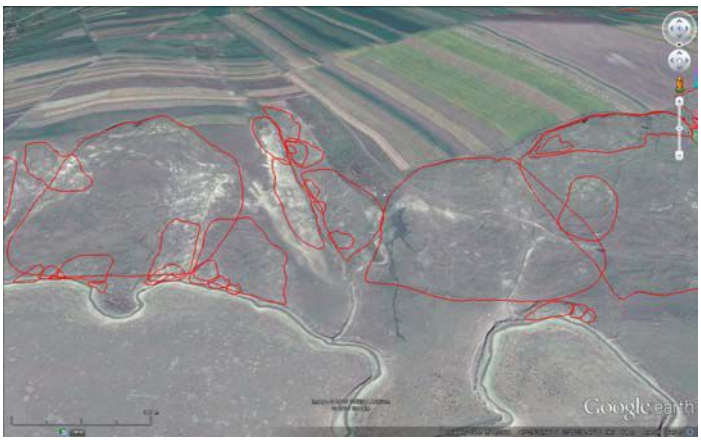


Figure 1. Cases of wider versus longer landslides in an area with monoclinic cuesta hillslopes and gully incision of cuesta scarp slope (Miletin village, Moldavian Plateau, Romania)

II. MATERIALS AND METHODS

A. *Materials*

The landslide inventory described by [9] was used to develop and test the method. The landslide inventory contains 24 263

In: Geomorphometry for Geosciences, Jasiewicz J., Zwoliński Zb., Mitasova H., Hengl T. (eds), 2015. Adam Mickiewicz University in Poznań - Institute of Geoecology and Geoinformation, International Society for Geomorphometry, Poznań

landslide polygons, extracted from high resolution aerial imagery and high resolution DEMs.

The altitude data used to determine the flow geometry was SRTM 1 DEM [10], because it covers all the inventory extent, but in the same time is easy to be manipulated using personal computers.

B. Methods

The landslide polygons were used to generate the oriented bounding box, with the ArcGIS function Minimum Bounding Geometry (RECTANGLE_BY_WIDTH geometry type). This method compute a bounding box which is oriented to the width and length of the polygon, and touch the polygon on all the four sides.

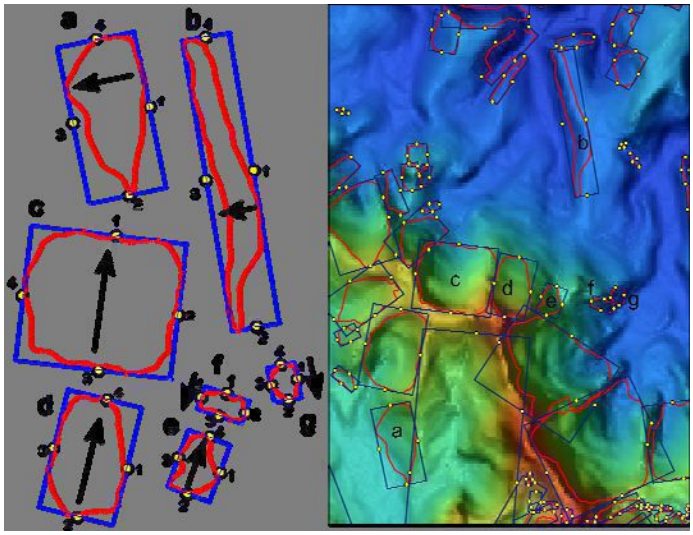


Figure 2. Geomorphometric context (shading from SRTM data - right) and geometry processing (left) of a snapshot of the landslide inventory; the position toward north is kept, but the landslide on the left were scaled, and a-g indicate the correspondence between the right and the left side; the arrows indicate the direction of landslide flow

The bounding box rectangle was then split in 4 lines, for every side in SAGA GIS, and a unique id of the polygon was given to the side lines. The construction of the bounding box polygons allowed also the numbering of the sides from 1 to 4, starting from the northernmost in a clockwise direction in such a way that the length sides of the rectangle are coded as 1 and 3, while the widths as 2 and 4 (Fig.). For every landslide bounding box rectangle, the midpoint of the bounding box rectangle side line was generated using ST_Line_Interpolate_Point(b.geom, 0.5) PostGIS function. The bounding box side lines midpoints were numbered also according to the line numbering, 1 and 3 being coded for the midpoints of the rectangle length sides, and 2 and 4 for the midpoints of the rectangle width sides.

For every landslide bounding box rectangle side midpoints the SRTM3 altitude was assigned. Then for every 1-3 (dzL) and 2-4 (dzW) pairs the difference in altitude (dz) was computed in R [11]. Root mean squared (RMS) values of the above differences were used to obtain the difference in altitude between the length and width side.

Using the altitude difference between the length and width sides, the landslides can be assessed as more wide (MW) or more long (ML) this way:

- If for a certain landslide the length side difference of altitude is smaller than the width side, then the landslide is considered to be more wide than long;
- If for a certain landslide the length side difference of altitude is greater than the width side, then the landslide is considered to be more long than wide.

This pass of the classification classify well only 2/3 of the more wide than long landslides, because some of these landslides are situated on hillslopes of steep first order valleys (Fig. 2). For correctly classifying these cases, the slope length (SL), computed in SAGA GIS using a D8 flow algorithm is used. The maximum slope length (maxSL) for the more long than wide landslides is compared with the length (L) of these landslides, and the wrong classified landslides are reclassified this way:

- If for a certain more long than wide classified landslide the maximum slope length is bigger than the landslide length, than the landslide is considered to be more long than wide;
- If for a certain more long than wide classified landslide the maximum slope length is smaller than the landslide length, than the landslide is considered to be more wide than long.

III. CONCLUSION

Using the specified data and methodology, the flow direction of landslides, along the width or the length of the geometric bounding box, and from here the “real” width and length were successfully determined. This approach can be useful when dealing with inventories where the morphometric variables of the landslide polygons are not computed (like in a semi-automatic derived landslide inventory [7]), if the wider landslides are a reality. The “correct” length and width of a landslides can be used for the separation of flows, slides and deep seated landslides and in susceptibility modelling.

A further step in this work would be to increase the validation dataset, and to validate the method on other datasets, from other areas, where the wider than longer landslides appear. Also, the general aspect (as north azimuth) of the landslide can be estimated after the direction of flow was determined.

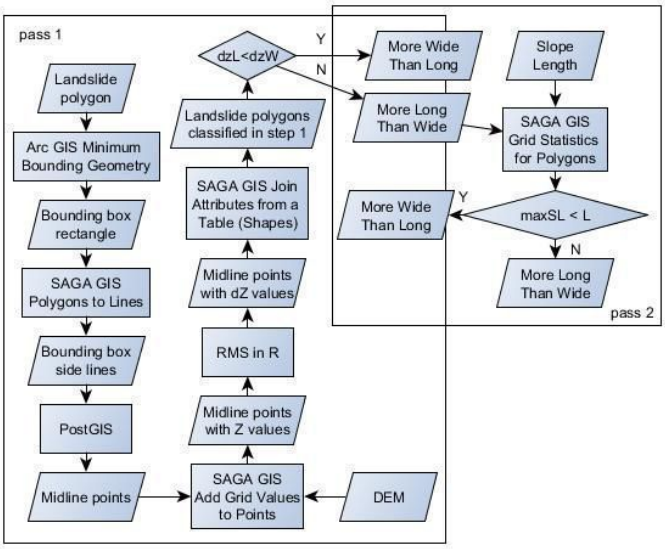


Figure 3. The workflow for landslide geometry classification

ACKNOWLEDGMENT

The authors gratefully acknowledge partial support by the European Social Fund in Romania, under the responsibility of the Managing Authority for the Sectoral Operational Program for Human Resources Development 2007-2013 [grant POSDRU/159/1.5/S/133391].

REFERENCES

[1] Cruden, D.M., Varnes D.J. 1996. Landslide type and processes, in eds. A.K. Turner, R.L. Schuster: Landslides investigation and mitigation, Special Report 247, Transportation Research Board, National Research Council, National Academy Press, Washington D.C.

[2] Cornforth, D.H., 2005. Landslides in practice. Investigations, analysis, and remedial/preventative options in soils, Wiley, 624 p.

[3] Carrara, A., Catalano E., Sorriso Valvo M., Reali C., Merenda L., Rizzo V., 1977, Landslide morphometry and typology in two zones, Calabria, Italy, Bulletin of the International Association of Engineering Geology, 16(1):8-3.

[4] Dewitte, O., Demoulin A., 2005, Morphometry and kinematics of landslides inferred from precise DTMs in West Belgium, Natural Hazards and Earth System Sciences, 5:259-265.

[5] Hattanji, T., Moriwaki H., 2009, Morphometric analysis of relic landslides using detailed landslide distribution maps: implications for forecasting travel distance of future landslides, Geomorphology, 103(3):447-454.

[6] Van Den Eeckhaut, M., Vanwalleghem T., Poesen J., Govers G., Verstraeten G., Vandekerckhove L., 2005. Prediction of landslide susceptibility using rare events logistic regression: A case-study in the Flemish Ardennes (Belgium), Geomoprhology, 76:392-410.

[7] Ardizzone, F., Cardinali M., Galli M., Guzzetti F., Reichenbach P., 2007, Idenitifcation and mapping of recent rainfall-induced landslides using elevation data collected by airborne Lidar, Natural Hazards and Earth System Sciences, 7:637-650.

[8] Van Den Eeckhaut, M., Kerle N., Poesen J., Hervas J., 2012, Object-oriented identification of forested landslides with derivatives of single pulse LiDAR data, Geomorphology.

[9] Niculiță, M. and M.C. Mărgărint, Landslide inventory for Moldavian Plateau, Romania, Proceedings of International conference Analysis and Management of Changing Risks for Natural Hazards, 18-19 November 2014, Padova, Italia.

[10] SRTM v2, 2005, http://dds.cr.usgs.gov/srtm/.

[11] R Development Core Team (2008). R: A language and environment for statistical computing. R Foundation for Statistical Computing, Vienna, Austria. ISBN 3-900051-07-0, URL http://www.R-project.org.

Development of GIS methods to assess glaciers response to climatic fluctuations: a Minimal Model approach.

Daniele Strigaro[1], Massimiliano Moretti[1], Matteo Mattavelli[1], Mattia De Amicis[1], Valter Maggi[1], Antonello Provenzale[2]
(1) Department of Earth and Environmental Sciences, University of Milano-Bicocca, Milan, Italy
(2) Institute of Atmospheric Sciences and Climate, CNR, Torino

Corresponding to: daniele.strigaro@unimib.it , m.moretti8@campus.unimib.it

Abstract

Theoretical work on glacier dynamics led to the construction of mathematical models for estimating glacier response to different climate change scenarios [2]. The aim of this work is to include a simple version of such models (the so-called Minimal Glacier Models [6]) within a GIS framework, to better understand, evaluate and reproduce the glacier response to climate fluctuations. Then, in this work three sections have been included: (I) the formulation of the Minimal Glacier Models, evaluating physical laws and numeric resolution; (II) the description of a GIS algorithm to calibrate and to validate the simulated results; (III) the application of GRASS – GIS module to obtain a spatial representation of glacier retreat.

I. MINIMAL GLACIER MODEL

This type of model tries to reduce the complexity of glacier dynamics to a very simple description based on basic physical laws. The glacier evolution is obtained from an integrated continuity equation over the entire volume, assuming that the glacier has a constant width and accepting a crude representation of the real glacier geometry. This starting point is:

$$\frac{dV}{dt} = \frac{d}{dt}\left(WH_m L\right) = W\left(H_m \frac{dL}{dt} + L\frac{dH_m}{dt} \right) = B_S \quad (1)$$

where V is the ice volume and B_s is the total surface balance rate. The volume is the product of the width W, the mean ice thickness H_m and the glacier length L.

Minimal Glacier Models assume perfect plasticity, an approximation of how the horizontal glacier flow line varies following the glacier thickness variations, and an instantaneous relationship between glacier length and thickness. Starting from these assumptions, H_m is given by [6]:

$$H_m = \frac{\alpha_m}{1+\nu\bar{s}} L^{1/2} \quad (2)$$

where $\bar{s}$ is the mean bed slope over the glacier length and α_m and ν are constants.

The scheme in Fig. 1 represents the iterative process of Minimal Glacier Model integration. The combination of eq. (1) and (2) describes the variation of glacier terminus along the flow-line direction, dL/dt, shown in Fig. 1 as the core of the algorithm.

Considering a linear balance profile, the surface balance B_S expression includes $\bar{b}$, the mean bed elevation, E, the Equilibrium Line Altitude (*ELA*, the line that divides the accumulation from the ablation areas), and β, the mass balance gradient along the glacier. This gradient is estimated from the annual net mass balance B_n, which is the most important driver of glacier behaviour and describes the amount of mass gained or lost in meters of water equivalent.

In this formulation, the input data are B_n and the ELA, which are determined by the climatic forcing: mainly, winter precipitation and summer air temperature (although in principle there is a contribution also from the net incoming solar radiation). Analysing the correlations between climatic variables and snout fluctuations of several glaciers [1] the most significant contributions come from the period November – March for winter precipitation and July – October for summer temperature. Then, we relate climate forcing to the model inputs by using a bivariate fit (Fig. 1, *Climate forcing*):

$$\dot{b}_i = aT_{s,i} + bP_{w,i} + c \quad (5)$$

In: Geomorphometry for Geosciences, Jasiewicz J., Zwoliński Zb., Mitasova H., Hengl T. (eds), 2015. Adam Mickiewicz University in Poznań - Institute of Geoecology and Geoinformation, International Society for Geomorphometry, Poznań

$$E_i = uT_{s,i} + vP_{w,i} + z \quad (6)$$

where i represents the *i-th* year, $T_{s,i}$ is the summer 2m air temperature and $P_{w,i}$ is the winter precipitation.

The glacier length, that is, the output variable, is then obtained by numerically integrating the equations described above [3]. The output length for a given year is an input data for the further cycle, so this is an iterative process.

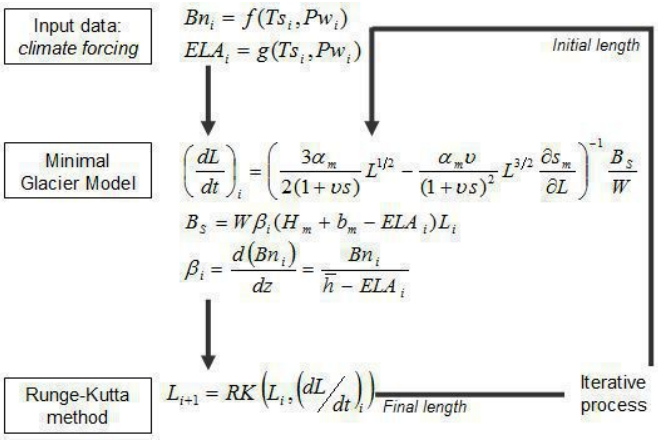


Figure 1. Minimal Glacier Model scheme.

II. Use of a GIS algorithm to calibrate the Minimal Glacier Model

A huge quantity of morphometric and morphologic parameters of several glaciers are collected by different remote sensing instruments, such as satellites and UAV, and by in-situ measurements. Such morphometric parameters provide detailed information to calibrate and validate glacier models.

To set the Minimal Model parameters and initial conditions, we determined the glacier geomorphology from a Digital Terrain Model using a GIS. Through DTMs, we reconstructed the evolution of glacier with a multi-temporal analysis and draw the flow lines that follow the accumulation-ablation dynamics, along which the model is applied. The algorithms were developed to extrapolate from DTMs, in a GIS environment, all the features needed to calibrate the Minimal Model (Fig. 2).

This algorithm is developed with QGIS tools, using several libraries and the interoperability of different open source software such as GDAL, GRASS, and SAGA. The procedure requires, as inputs, DTMs, POLYGONs and FLOW LINEs and we obtain all the morphological parameters and initial condition for the Minimal Model, such as maximum and minimum elevation, altitude range along the flow lines, mean slope and its variations, and flow line length.

These parameters are useful to start the iterative process (Fig. 1) and to calibrate the results on real values. Moreover, we validate the simulated results by comparing the numerical outputs with the flow line length values from past measurements.

In this way, the GIS analysis of glacier flow line could increase the accuracy of a Minimal Model (or of more refined glacier models). As shown in Fig. 3 for the Rutor glacier (western Italian Alps, Val d'Aosta), the accuracy of the simulated values obtained from the model calibrated with the DTM analysis (blue line) is much better than the accuracy obtained using bibliographical or standard parameters (red line).

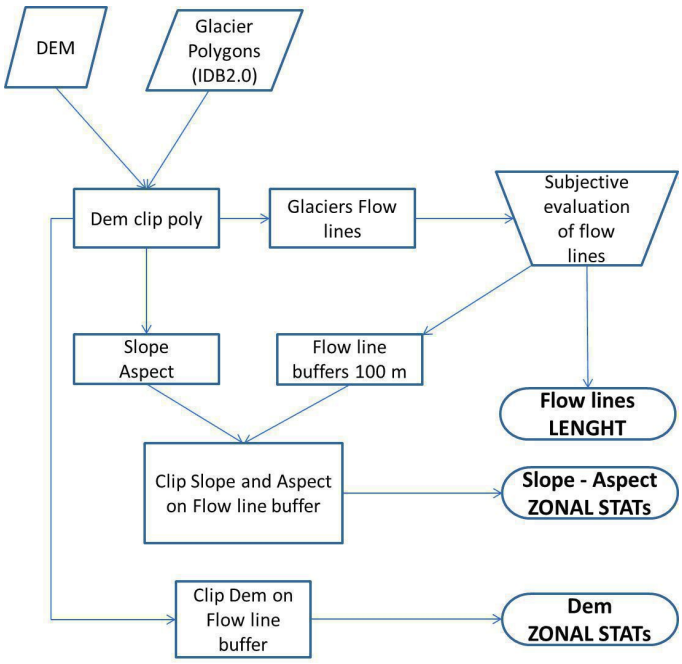


Figure 2. GIS algorithm used to calibrate Minimal Glacier Model boundary and initial condition.

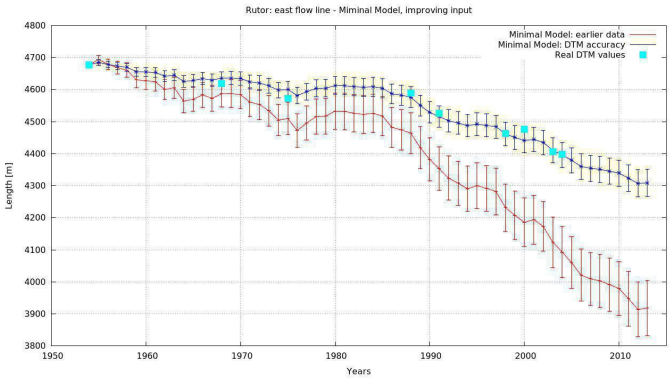


Figure 3. Comparison of model results. Light blue dots represent the flow line lengths measured by polygons on DEM, the blue line represents the simulated results, obtained from a model calibrated using the GIS algorithm, and the red line represents the simulated results with data from the databases of glaciers.

III. Application of a GRASS GIS module to the Minimal Glacier Model: r.glacio.model

The final step of this work is the integration of the Minimal Glacier Model with a GIS module, to obtain a spatial representation of the glacier retreat. The different reasons to create this GIS module are:

- the geospatial evaluation of flow line fluctuations;
- the formulation of a useful and simple tool for users;
- the development of an easy way to apply Minimal Models on large scale.

GRASS GIS [5] is an open-source software used for geospatial data management and analysis, image processing, graphics and maps production, spatial modelling and visualization. An easy and powerful development environment was set up, using Python language programming and GRASS GIS tools.

The result was the module r.glacio.model. The last formulation derives from a rigorous validation with different types of glaciers and the module will be released as a GRASS-addon under the GNU General Public License (≥ v.2).

The core of this algorithm is based on the equation in Fig.1, so it requires that some mandatory input data (as in Fig. 2) are included in the module: the glacier maximum altitude, the mean slope around the flow line, the length of flow line, the α_m constant for thickness, the mass balance and the ELA.

The first two parameters are derived from a DTM analysis, the third needs the flow lines and polygons as an input vector layer. The parameter α_m can be set by the user as a constant or it can be calculated from eq. 2, retrieving H_m through [4]:

$$H_m = \frac{\tau}{f \cdot \rho \cdot g \cdot \sin(\gamma)} \quad (7)$$

where f = 0.8 is the shape factor, related to the lateral drag on the glacier through friction at the valley walls and to the general form of the glacier cross section (Paterson, 1994), ρ = 900 kg m^{-3} is the mean ice density, g = 9.81 m s^{-1} is the gravity acceleration, γ is the glacier surface slope along the flow line and τ is the basal shear stress [4].

The climatic inputs of the Minimal Model are the annual mass balances, which are included in r.glacio.model to start the algorithm. To increase the module's usability and versatility, the ELA data are not included because it is often difficult to retrieve such data. Therefore, the equations are simplified.

We make an illustrative application of the r.glacio.model to the Rutor glacier, for which the algorithm was already calibrated. Fig. 4 shows the glacier retreat along the flow lines from 1954 to 2003.

Fig. 5 shows the initial mask of the module, where the user can insert the input raster, vector layer and the input climatic data.

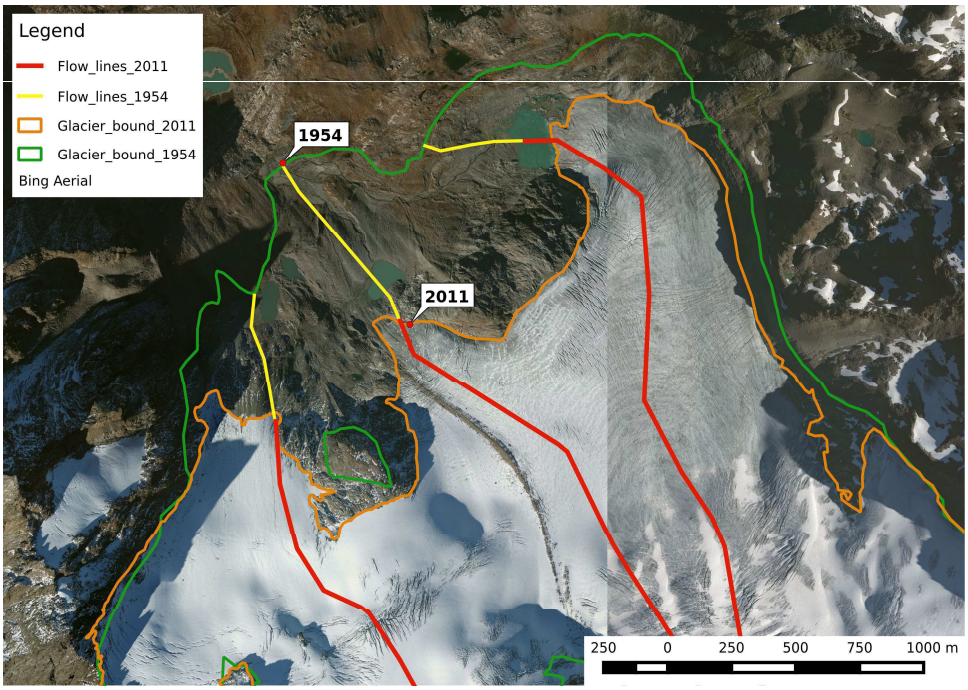


Figure 4. Glacier retreat along Rutor flow lines: results of the r.glacio.model. The yellow lines are the lengths at 1954, then the red lines are the estimated lengths at 2011 applying Minimal Glacier Model.

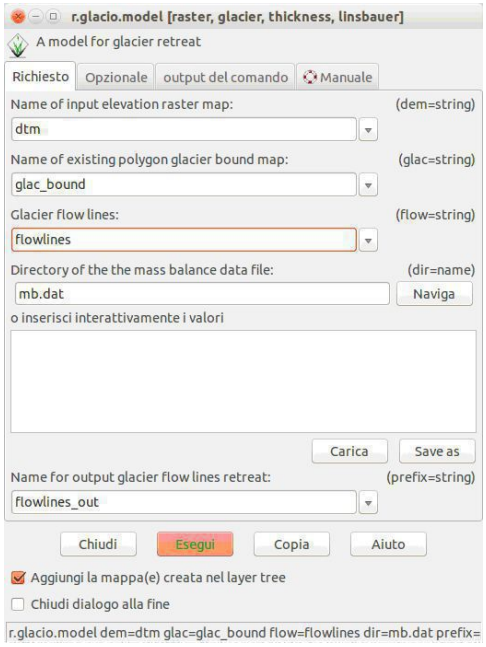


Figure 5. User mask of r.glacio.model. The inputs are the raster map (DTM), the polygon vector layer, the glacier flow line vector layer created by the user and the data file or the manual insertion of mass balance values for the years under consideration.

References

[1] Bonanno R., Ronchi C., Cagnazzi B. and Provenzale A., 2013. “Glacier response to current climate change and future scenarios in the northwestern Italian Alps”. Reg. Environ. Change. v.13, n.4.

[2] Haeberli W., Hoelzle M., 1995. “Application of inventory data for estimating characteristics of and regional climate-change effects on mountain glaciers: a pilot study with the European Alps”. Annals of Glaciol., 21, 206–212.

[3] Hamming R.W., 1986 “Numerical Methods for Scientists and Engineers”. Unabridged Dover, republication of the 2nd edition published by McGraw-Hill 1973.

[4] Linsbauer A., Paul F., Haberli W., 2012. “Modeling glacier thickness distribution and bed topography over entire mountain ranger with GlabTop: Application of fast and robust approach”. Journal of Geo. Res., Vol. 117, F03007, 2012.

[5] Neteler, M., Bowman, M. H., Landa, M., & Metz, M. (2012). GRASS GIS: A multi-purpose open source GIS. Environmental Modelling & Software, 31, 124-130.

[6] Oerlemans J., 2011. “Minimal glacier models”. Second print. Igitur, Utrecht Publishing & Archiving Services, Universiteitsbibliotheek Utrecht. ISBN 978-90-6701-022-1.

Case-based formalization of knowledge of digital terrain analysis

Cheng-Zhi Qin
State Key Laboratory of Resources and Environmental Information System, Institute of Geographic Sciences and Natural Resources Research, CAS
Beijing, China
qincz@lreis.ac.cn

Jing-Chao Jiang
State Key Laboratory of Resources and Environmental Information System, Institute of Geographic Sciences and Natural Resources Research, CAS
Beijing, China
jiangjc@lreis.ac.cn

Xue-Wei Wu
State Key Laboratory of Resources and Environmental Information System, Institute of Geographic Sciences and Natural Resources Research, CAS
Beijing, China
wuxw@lreis.ac.cn

A-Xing Zhu
Jiangsu Center for Collaborative Innovation in Geographical Information Resource Development and Application and School of Geography
Nanjing Normal University
Nanjing, China

Department of Geography
University of Wisconsin-Madison
Madison, Wisconsin, USA
azhu@wisc.edu

Yan-Jun Lu
State Key Laboratory of Resources and Environmental Information System, Institute of Geographic Sciences and Natural Resources Research, CAS
Beijing, China
luyj@lreis.ac.cn

Abstract—**Digital terrain analysis (DTA) in practical application is typically a workflow-building process which needs to organize the various DTA tasks properly and assign the algorithm (and its parameter settings) for each task. During this process it is crucial to use knowledge on specifying the proper algorithm and parameter settings for each DTA task according to the application context (such as the target task, the terrain condition of the study area, the DEM resolution, etc.), referred to as application-context knowledge. However existing DTA-assisted tools often cannot use application-context knowledge because this type of DTA knowledge has not been formalized to be available for inference in these tools. This is mainly because this type of DTA knowledge often exists in the minds of domain experts and is implicit in the text of case studies published in academic papers. This situation makes the DTA workflow-building process difficult for users, especially for non-experts. This study proposes a case-based formalization for application-context knowledge in the DTA domain and a corresponding case-based reasoning method. A preliminary experiment demonstrates the usability of the proposed case-based method.**

I. BACKGROUND

Digital terrain analysis (DTA) in practical application is typically a workflow-building process which needs to organize the various DTA tasks properly and assign the algorithm and its parameter settings for each task [1]. Tools to assist DTA have been developed to lighten the burden of this process on users (especially non-expert users). For this purpose, DTA-assisted tools not only need to integrate existing DTA algorithms, but also to use the formalized DTA knowledge [2].

The knowledge involved in DTA workflow-building can be classified into three types [2]:

1) task knowledge which describes the relationship between DTA tasks and their input/output;

2) algorithm knowledge which is the meta-data of a DTA algorithm and its parameters;

3) so-called application-context knowledge on how to specify the proper algorithm and its parameter settings for a DTA task according to the application context (such as application goals, characteristics of the study area, and DEM resolution) [3,4].

In: Geomorphometry for Geosciences, Jasiewicz J., Zwoliński Zb., Mitasova H., Hengl T. (eds), 2015. Adam Mickiewicz University in Poznań - Institute of Geoecology and Geoinformation, International Society for Geomorphometry, Poznań

Among the three types of DTA knowledge, both task and algorithm knowledge have been formalized by means of rule or semantic networks [2,4] and then used in exiting DTA tools. However, application-context knowledge, which is crucial for building a proper DTA model for specific applications and is more difficult for users to acquire than the other two types of knowledge, has no well-established formalization method for DTA tools. This study therefore focuses on formalizing application-context knowledge to aid in DTA workflow-building.

II. BASIC IDEA

Unlike task and algorithm knowledge which is explicit, application-context knowledge is often implicit in the case studies documented in articles about applying DTA to specific study areas. The case method is a suitable way to formalize this type of knowledge, after which a case-based reasoning method can use this knowledge to solve a new similar problem [5].

III. METHOD

A. Case representation

In this study, the case is initially designed to use the features shown in Table 1 to describe the DTA application context.

TABLE I. CASE REPRESENTATION FOR DTA APPLICATION

DTA application context	Feature	Formalized index
Application goal	DTA task type	DTA task enumeration
Data	DEM resolution	DEM grid size
	Data quality[a]	
Area characteristics	Position[a]	
	Area	Area (km^2)
	Terrain condition	Relief (m)
		Hypsometric curve
		Slope-relief histogram
	Other environmental conditions (such as climate, soil, and landuse) [a]	

[a.] Not used in current study

B. Case indexing

To enable case retrieval and comparison, indices were designed to formalize the features of a case (Table 1). Because the terrain condition of an area is crucial for choosing the DTA algorithm and its parameter settings, three indices were designed to describe the terrain condition of a study area:

- Relief.
- Hypsometric curve [6], which is widely used to characterize the stage of geomorphic development of a basin.
- Slope-relief histogram (the distribution of slope gradient for various relative elevation level), which is used to describe the configuration of the slope gradient as relief levels in a watershed. This is currently quantified by a two-dimensional frequency histogram with seven categories of slope gradient (0°–3°, 3°–8°, 8°–15°, 15°–25°, 25°–35°, 35°–45°, and 45°–90°) and ten categories of relief. Note that the effect of DEM resolution on slope gradient impacts the slope-relief histogram. However, this effect will be removed in later case-based reasoning because the index is taken into account when determining the DEM resolution. The equal classification of relief makes the resulting slope-relief histograms of different areas mathematically comparable. The design of this index ignores the relief difference between areas because the relief information is characterized by the "relief" index.

C. Case-based reasoning

Case-based reasoning for solving new DTA application problems is designed to compute the similarity between the new application problem and each case involving the same DTA task. The similarity computation is designed as follows:

Step 1. Compute the similarity for each index between each case (i) and the new problem (Table 2).

TABLE II. SIMILARITY COMPUTATION FOR EACH INDEX BETWEEN A CASE AND THE NEW APPLICATION PROBLEM

Index	Similarity computation on single index[a]
DEM grid size	$s_i = 2^{-\left(\left\|\lg r_{new} - \lg r_i\right\|/0.5\right)^{0.5}}$
Area (km^2)	$s_i = 1 - s_i^{'}/\max(s_i^{'}),\ s_i^{'} = \left\|\lg(Area_{new}) - \lg(Area_i)\right\|$
Relief (m)	$s_i = 1 - s_i^{'}/\max(s_i^{'}), s_i^{'} = \left\|Relief_{new} - Relief_i\right\|$
Hypsometric curve	$s_i = 1 - s^{'}_i/\max(1 - HypsoIntegral_{new}, HypsoIntegral_{new})$ $s_i^{'} = \left\|HypsoIntegral_{new} - HypsoIntegral_i\right\|$
Slope-relief histogram	$s_i = \frac{2\sum \min(SlpRlfHistogram_{new}, SlpRlfHistogram_i)}{\sum(SlpRlfHistogram_{new} + SlpRlfHistogram_i)}$

[a.] The subscript i means the i-th case; the subscript *new* means the application problem. r – DEM grid size; *HypsoIntegral* - integral value of the hypsometric curve; *SlpRlfHistgram* – slope-relief histogram.

Step 2. The similarity between a case and the new problem is calculated to be the minimum of the similarity on every index for this case.

Step 3. Among all cases the one with the highest similarity is retrieved as the solution case. The specific DTA algorithms and corresponding parameter-settings used in the solution case are then recommended for the new application. Currently, case adaptation is not included.

IV. EXPERIMENT

A. *Experimental design*

Taking as an example the determination of the catchment area (CA) threshold for extracting a drainage network, the authors prepared 12 cases from randomly-selected articles related to this task from journal in Chinese or English (Fig. 1).

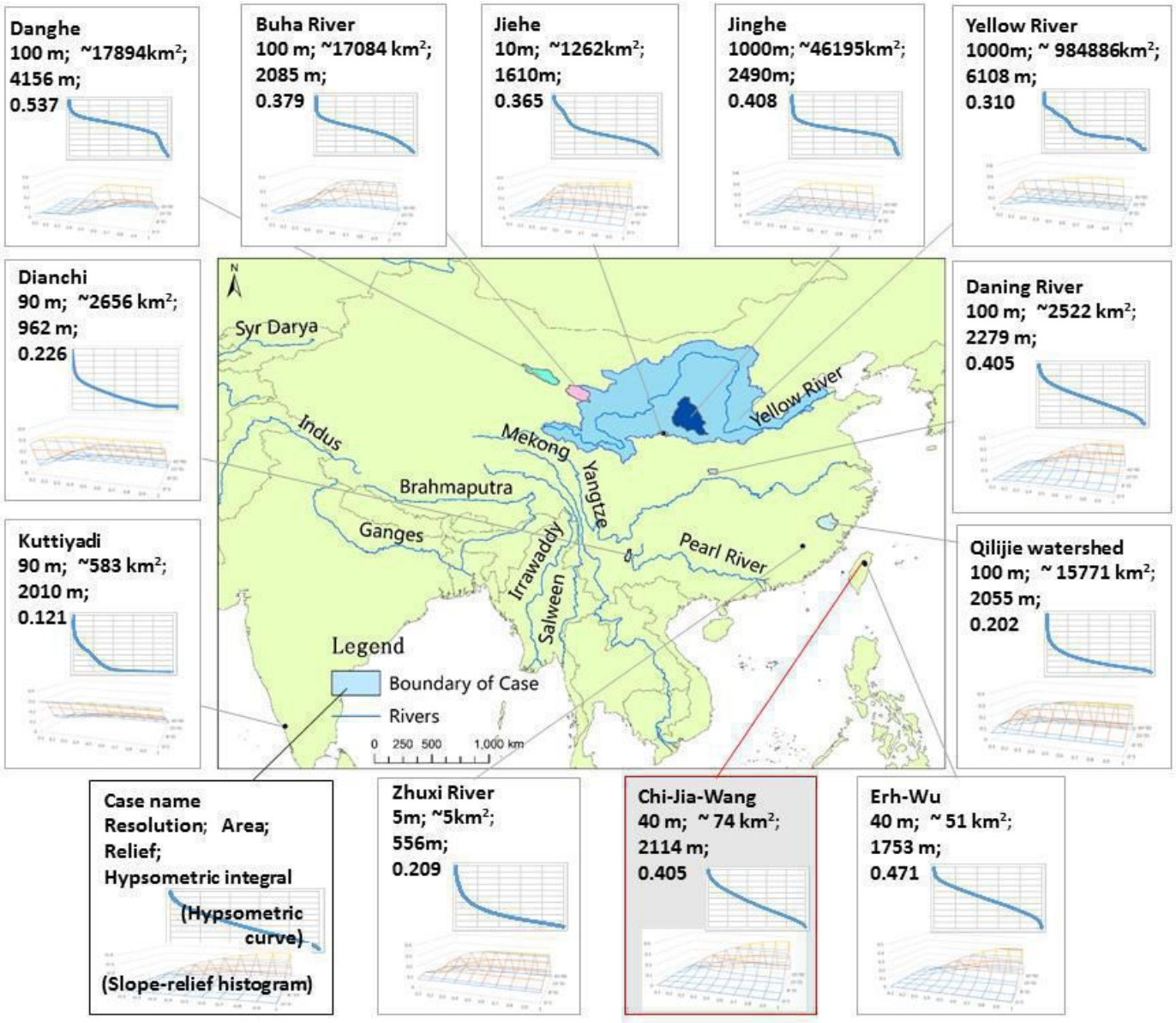


Figure 1. Case base in this study

It was assumed that the author(s) of each article set the CA threshold properly to match the study area. The 12 cases were manually prepared, whereas the reasoning process was automatic.

The case of the Chi-Jia-Wang watershed [7] was chosen as the new problem without determining the CA threshold. Then the proposed method was applied to the other cases to determine the CA threshold for the Chi-Jia-Wang watershed.

B. Experimental results and discussion

The similarity values between the Chi-Jia-Wang watershed and each case are shown in Table 3. The solution came from the case of the Erh-Wu watershed, in which the CA threshold was 0.232 km^2. Compared to the threshold values from other cases, this was the closest to that proposed in the case of the Chi-Jia-Wang watershed (0.344 km^2). Table 3 further shows that in general, the lower the similarity of a case, the larger will be difference between the CA threshold value of the case in question and that of the Chi-Jia-Wang watershed. This indicates that the proposed case-based method is reasonable for use in this application.

TABLE III. SIMILARITY VALUES BETWEEN THE CHI-JIA-WANG WATERSHED AND EACH CASE USING THE PROPOSED CASE-BASED REASONING METHOD

Case	CA threshold used in the case (km^2)	Similarity	Index with minimum similarity
Erh-Wu	0.232	0.89	Hypsometric curve
Daning River	10	0.54	Grid size
Qilijie Watershed	0.61	0.40	Slope-relief histogram
Jiehe	4	0.40	Slope-relief histogram
Zhuxi River	0.03	0.39	Grid size
Kuttiyadi	0.1215	0.33	Slope-relief histogram
Buha River	6.5	0.29	Slope-relief histogram
Danghe	41	0.25	Slope-relief histogram
Dianchi	60	0.23	Slope-relief histogram
Jinghe	100	0.04	Slope-relief histogram
Yellow River	1000	0	Area, Relief

V. SUMMARY

This study has proposed a case-based formalization for DTA application-context knowledge existing in journal papers. The corresponding case-based reasoning method was designed as an inference process for computing similarity. A preliminary experiment showed the usability of the proposed case-based method.

The proposed method can be implemented as an inference engine in a DTA modeling environment to provide the user with heuristic DTA modeling capabilities [4].

Ongoing research involves evaluating the feasibility of both the case indices and the similarity computation on each index in other DTA applications with different goals. Moreover, several questions raised by this preliminary research remain open. For example, if the solution case recommended by the case-based reasoning method based on the current case base has little similarity to the new application problem (which means that no case is similar enough to the new application problem), how should case adaptation be performed? To ensure an adequate number of cases in the case base, could an automatic method be developed to create relevant cases by crawling an article database?

ACKNOWLEDGMENTS

This study was supported by the National Natural Science Foundation of China (No. 41422109), and the National Science & Technology Pillar Program of China (No. 2013BAC08B03-4).

REFERENCES

[1] Hengl, T., and H.I. Reuter (Eds), 2008. "Geomorphometry: Concepts, Software, Application". Developments in Soil Science - Volume 33, Elsevier, 765 p.

[2] Qin, C.-Z., Y.-J. Lu, A.-X. Zhu, and W.-L. Qiu, 2011. "Software prototyping of a heuristic and visualized modelling environment for digital terrain analysis". In 11th International Conference on GeoComputation, July 20-22, University College London, UK.

[3] Lu, Y-.J., C.-Z. Qin, A.-X. Zhu, and W.-L. Qiu, 2012. "Application-matching knowledge based engine for a modelling environment for digital terrain analysis". In 20th International Conference on Geoinformatics, June 15-17, Chinese University of Hong Kong, China.

[4] Qin, C.-Z., J.-C. Jiang, L.-J. Zhan, Y.-J. Lu, and A.-X. Zhu, 2013. "A Browser/Server-based prototype of heuristic modelling environment for digital terrain analysis". In Geomorphometry'2013 Conference Proceedings, Edited by: Tang, G., Q. Zhou, T. Hengl, X. Liu, and F. Li, Nanjing Normal University.

[5] Watson, I., and F. Marir, 1994. "Case-based reasoning: a review". The Knowledge Engineering Review, 9(4), 327-354.

[6] Strahler, A. N., 1952. "Hypsometric (area-altitude) analysis of erosional topography". Geological Society of America Bulletin, 63, 1117-1142.

[7] Lin, W.-T., W.-C. Chou, C.-Y. Lin, P.-H. Huang, and J.-S. Tsai, 2006. "Automated suitable drainage network extraction from digital elevation models in Taiwan's upstream watersheds". Hydrological Processes, 20(2), 289-306.

Natural hazards mapping of mega waves on the NW coast of Egypt

Magdy TORAB[(1)],

[(1)] Prof. of Geomorphology, Geography Department, Damanhour University, Egypt.
Corresponding author: magdytorab@hotmail.com

Nora DALAL[(2)]

[(2)] Ph.D. student, Geography Department, Menoufia University, Egypt.
E-mail: soso_soso1734@yahoo.com

Abstract: **Some boulder fields were deposited by the sea waves during winter storms or by paleo tsunami mega waves and most of these boulders were uprooted from the marine platform and distributed within 90 m of the shoreline, are found up to 4 m above present mean sea level.**

The objective of this work is defining systematic characterisation of the high-energy depositional contexts working by storms or paleo tsunami deposit, and to reconstruct the history of mega block deposition along the study area, depends upon extensive field surveying and geomorphic mapping by using GIS and GPS techniques as well as statistical analysis of boulders in order to determine both extreme events using the significant wave height and period of maximum observed storms and historical tsunamis along the study area, as well as geomorphic hazard mapping and samples dating.

The results show that both possible processes (storm and tsunami waves) can deposit these boulders, it attested at Alexandria for example by the archaeological excavations and historical sources. Tsunami waves and storms cause the displacement of huge boulders from sea bottom and submersible marine terraces (platforms) to the beach due to its major power and ability of carving and graving it is also capable of pulling other boulders from the land and redeposit it on the beach or coastline.

1. INTRODUCTION

The study area forms a belt about 20 Km deep, which extends for about 500 Km of the NW coast of Egypt on The Mediterranean Sea between Alexandria City and El Sallum town near the borders with Libya "Fig.1".

The objective of this work is defining systematic characterisation of the high-energy depositional contexts working both on the type of storm or paleo tsunami deposit and the different geomorphological contexts, and to reconstruct the history of mega block deposition along the study area, using chronostratigraphy methodology, it will aid in evaluating the risk of submersion in an area that is affected by storms and tsunamis. The consequences on the occupation of the coastline are important, such as the destruction of Alexandria's ancient lighthouse, as well as dating of mega blocks characteristic of high-energy events (storms or tsunamis) using fixed marine bioconstructions, to evaluate sedimentological impacts and natural hazards associated with these events (submersion, coastal mobility, erosion, high-energy impacts).



Figure 1. Location map of the study area

2. SETTING

2.1. Geology

The coastal plain of the study area is consists of three Pleistocene calcareous ridges parallel to the coast and separated by flat-bottomed depressions. The ridges sediments are composed of well sorted medium grained aragonic ooids sands. The cliffs of the Middle Miocene table run parallel to the coast. A discontinuous series of dunes develops at a distance varying from the coast to 2 Km deep. There are some saline depressions and sabkhas in the lower part of the plain, some with outlets to the sea. The escarpment of the plateau is deeply cut by wadis.

2.2. Geomorphology

The previous geomorphologic studies of the northwest coastal plain of Marsa Matruh area as a part of the northwest coastal plain of Egypt show that the origin of the extended calcareous ridges could be grouped under three environmental conditions as follows:

- Continental environment (Hilmy, 1951).
- Marine environment (Anwar et al.,1981).
- Maine/ continental environment (El-Shazly et al., 1964 ; Selim, 1974 & Torab, 1984).

But sea waves were able to erode the first calcareous ridge in some parts of the study area and therefore the second ridge found on the coastline directly and affected by coastal erosion at the moment.

In: Geomorphometry for Geosciences, Jasiewicz J., Zwoliński Zb., Mitasova H., Hengl T. (eds), 2015. Adam Mickiewicz University in Poznań - Institute of Geoecology and Geoinformation, International Society for Geomorphometry, Poznań

2.3. Climate

Average annual wind directions graph "Fig. 2" indicates that most wind blow toward the NW coast of Egypt from NW & NNW directions. Offshore wind speed at 50 m a.g.l. of Egypt "Fig.3" show that The NW coast of Egypt is lies in the most offshore wind speed in the Mediterranean region, its speed range between 6-7 m/s (determined by meso scale modelling, Wind atlas of Egypt, by Mortensen, et al., 2006).

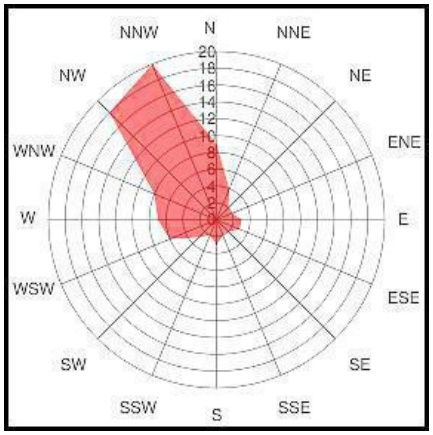


Figure 2. Average annual wind directions in Marsa Matruh city between 2001/2011
(Data source: www.windfinder.com)

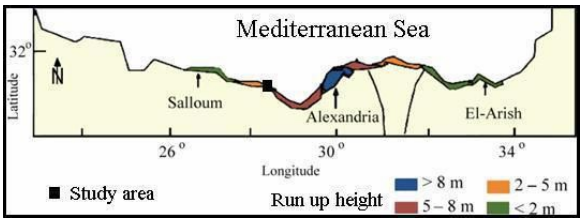


Figure 3. Run up height along the Egyptian Mediterranean sea coast (After: Hamouda, 2006)

3. METHODS

This paper depends upon detailed geomorphological field surveying, 578 boulders have been measured in eight selected sites of the study area, the boulders measurements were chosen on 11 elongated sectors "Tab.1& Fig.4".

TABLE.1. LOCATION OF SELECTED FIELD WORK SITE

Site#	Sector#	Location	Coordinates	
			Lat. (N)	Long. (E)
1	1.A	El Fyrouz Beach	31°22`01"	27°16`12"
2	2.A	Andalusia Beach	31°22`08"	27°17`49"
	2.B			
3	3.A	Alam El Rom Beach	31°22`18"	27°19`22"
	3.B			
	3.C			
4	4.A	Mina Hasheesh Beach	31°22`22"	27°19`46"
5	5.A	Ras El-Hekma west	31°13`43"	27°51`49"
6	6.A	Ras El-Hekma east	31°13`39"	27°52`27"
7	7.A	Ras Hossan	31°05`37"	28°06`32"
8	8.A	El-Dabaa	31°04`33"	28°28`24"

Each sector started from the coast line to the end of boulder field, including coordinates, the three boulders axis (a, b &c), elevation from coastline of the mean sea level and distance between each boulder and coastline by use GPS and tape. The boulders volume and weight have been calculated using the volumetric method as 2.2g/cm^3.

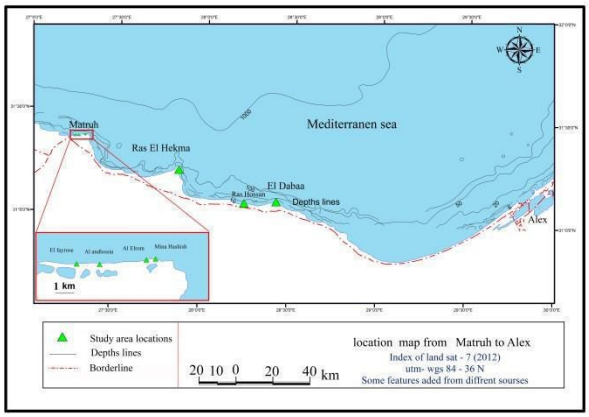


Figure 4. Location of selected field work sites

4.RESULTS

4.1. Distribution and dimensions of accumulated mega boulders:
The measured dimensions of accumulated boulders "Tab.2" and the field observation show that most boulders are rectangular, with sharp, broken edges, most blocks consist of limestone and sandstone fragments up to 14m^3 in volume and 43 ton in weigh, some of these blocks were observed by local people to have moved after strong winter storms. it shows that maximum mean size of accumulated boulder appears on site # 3c (Volume 2.25 m^3), and the maximum mean weight is 2.57 ton at the same site and also the maximum number of the boulder deposited on the site # 3.C (90 boulders), but the maximum mean distance between the coastline and the end of boulder field is (54.93 m) in site # 1.A .

TABLE 2. AVERAGE DIMENSIONS OF ACCUMULATED BOULDERS

S#	Bn	Average dimensions of boulders			D	L	V	W
		a(m)	b(m)	c(m)				
1.A	57	1.51	1.14	0.51	54.93	0.96	1.02	2.08
2.A	13	1.82	1.61	0.65	26.95	1	2.15	4.58
2.B	85	1.07	0.79	0.36	39.69	3.41	0.41	0.17
3.A	90	1.34	0.94	0.42	29.92	3.43	1.01	2.57
3.B	23	1.42	1.01	1.7	28.2	0	0.65	1.04
3.C	38	1.63	1.21	.47	21.63	3.60	2.25	7.96
4.A	81	1.22	0.94	0.41	9.49	1.2	0.56	0.89
5.A	38	1.45	0.97	0.40	10.67	0.95	0.74	1.46
6.A	55	1.36	0.97	0.33	14.46	.37	0.51	0.84
7.A	51	0.85	0.59	0.26	7.04	1.33	0.16	0.18
8.A	47	0.87	0.58	0.17	19.1	1	0.13	0.19
Oa	52.54	1.31	0.98	0.51	23.81	2.02	1.56	2.11

(After: Dalal, 2013)
S#: Sector #
Bn: Boulders number
D: Distance (m)
L: Level (m)
V: Volume (m^3)
W: Weight (t)
Oa: Overall average

4.2. Topographic profiles and geomorphological maps:

Eight topographic profiles have been surveyed and geomorphological maps on the selected sites; it shows the accumulated boulders morphology on beaches and coastal platforms as the following: it seems as random shape deposition at Alam El Rom and semi parallel to the coastline "Fig.5&6".

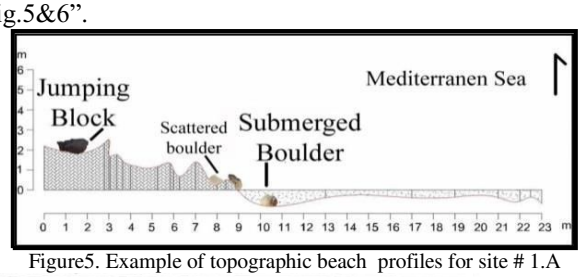


Figure5. Example of topographic beach profiles for site # 1.A

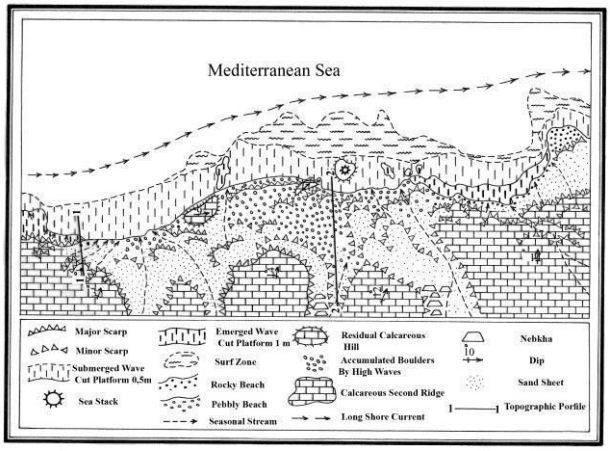


Figure.6: Geomorphological map for site #3 at Alam El Rom Beach

4.3. Boulders accumulation positions on the beaches

Boulders accumulation can be classified as many types such as the following example positions on the beaches depending upon field investigation:

4.3.1. Boulders accumulated horizontally on the coastal platforms by strong waves, and it always advance horizontally near the coastline « Fig.7».

4.3.2. Vertically accumulated boulders on the beach or settling vertically upon earlier boulders .

4.3.3. Buried boulders under aeolian sands on the back shore inside aeolian accummulated sands.

4.3.4. Crammed boulders inside high coastal notches (2-3 meters above sea level), as a result of high waves energy « Fig.8 ».

4.3.5. Sequential deposited rocks by powerful waves flowing consecutively



Figure7. Horizontally boulder deposits on site # 3 at Alam El-Rom



Figure8. Crammed boulders inside high coastal notches on site # 3

4.4. Estimation of storms and tsunami waves heights

Some equations have been used to estimate storms and tsunami wave heights depending upon boulders dimensions, volume, weight, moving distance on the platform (Williams D.& Halls, A., 2004) & (Pignatelli, C.et al., 2009) "Table 3", the first equation show that the minimum storms wave height is more than 10 m on sector 2.A and 6 m on sector 3B&C, and tsunami waves height about 2.7m (Sector 2.A) and 1.6 (Sector 1.A.,3.B&C).

TABLE 3. ESTIMATED HEIGHT OF STORMS AND TSUNAMI WAVES.

Sector #	**Boulder #**	**Estimated minimum wave height (m)**			
Equation		**Williams D.& Halls, A., 2004**		**Pignatelli, C.et al., 2009**	
Wave type		**HS(m)**	**HT(m)**	**HS(m)**	**HS(m)**
1.A	57	6.292	1.573	2.696	0.614
2.A	13	10.786	2.696	7.191	1.797
2.B	85	4.943	1.234	2.696	2.696
3.A	90	5.393	1.348	2.696	0.647
3.B	23	6.292	1.573	3.595	0.898
3.C	38	6.292	1.573	3.595	0.898
4.A	81	2.696	0.674	2.696	0.674
5A	38	5.842	1.460	2.696	0.674
6.A	55	5.393	1.348	2.696	0.667
7.A	51	4.044	1.011	2.39	0.449
8.A	47	3.146	0.786	1.779	0.440
OA	**52.54**	**5.556**	**1.388**	**3.156**	**0.;952**

(After: Dalal,2013)
HS: Storms wave height
Ht:Tsunami wave height
OA: Overall average

4.5. Boulders shells dating

Two samples of seashells were collected from accummulated boulders on site # 3B & 3C at Alam El-Rom has been dated. The results shows that the first sample was displaced from 60 years ago, as a result of an earthquake centered at the bottom of Mediterranean sea near the southern coasts of Cyprus Island near Limassol city, this earthquake took place on 10-9 1953 and caused tsunami waves that damaged about 135village and killed40 persons and 1000 others were became homeless(Guidoboni et al., 1994). The second sample back to 960 ±35 BP (1018 to 1088 AD) as evedence of other tsunami occurred in the eastern portion of The Mediterranean Sea "Table 4".

TABLE 4. DATING OF SEASHELLS WERE COLLECTED FROM SITE #3 AT ALAM EL-ROM

Sh #	S #	Dimensions of boulders			D	V	W	Dating BP
		A (m)	B (m)	C (m)				
1	3B	1.45	0.7	0.45	32.70	0.46	0.66	60 ± 4
2	3B	2.15	1	0.50	27.20	1.08	2.31	960 ±35

Sh#: Shell Sample number
S#: Sector number
D: Distance between boulder & coastline (m)
V: Volume (m^3)
W : Weight (ton)

4.6. Geomorphological Hazard map

The geomorphological hazard map « Fig.8 » has been produced for the study area using hazard index depending upon the following factors :

1. Coastline shape.
2. Angle of wave direction to the coastline.
3. Beach profile Slope.
4. Hardness of beach rocks.
5. Sea water depth.
6. Estimation of mega boulders accumulation by storms and tsunami.

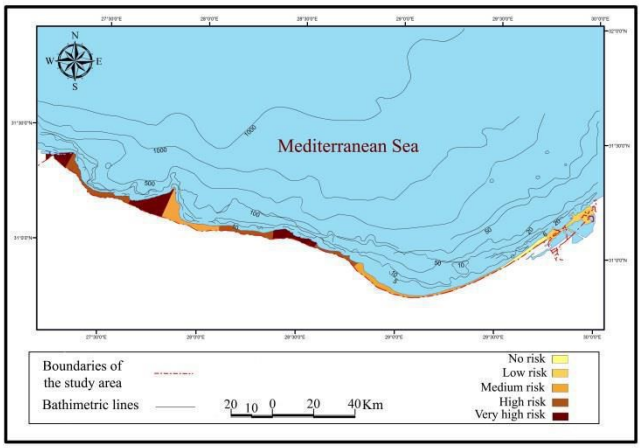


Figure8. Geomorphological hazard map of the study area.

5. CONCLUSION

The results show that both possible processes (storm and tsunami waves) can deposit these boulders, specially the NW coast of Egypt has recorded a number of seismic or tsunami events during the Holocene (tsunamis of 23 AD, 365 AD, 746 AD, 881 AD, 1202 AD, 1303 AD, 1870 AD and 1908 AD attested at Alexandria for example by the archaeological excavations and historical sources.

Tsunami waves and storms cause the displacement of huge boulders from sea bottom and submersible marine terraces (platforms) to the beach due to its major power and ability of carving and graving it is also capable of pulling other boulders from the land and redeposit it on the beach or coastline. The geomorphological hazard map of the study area shows that Alam El Rom and the western coast of Ras El-Hekma, then El Dabaa and El Fyrouz areas east of Mersa Matruh City of about 10 65, 135 and 2 km, is the most affected portions by hazards by estimated tsunami catastrophic in the NW coast of Egypt, and currently more affected recent storms depending on the results of the results of this study.

6. ACKNOWLEDGMENT

This study is financially supported by the Egyptian-Franco research program IMHOTEP (research project No. EGY/FR7-016) Titled: Effects of tsunami on the Egyptian Mediterranean coasts. Field work was supported by The Egyptian Society of Environmental Changes.

1. REFERENCES

1. Anwar,Y.M., M.A. El Askary, and S.M. Nasr (1981), Petrography and origin of the oolitic carbonate sediments of Arab' Bay, western part of the continental shelf of Egypt, N. *JB.Geol*. Palaont Mh.,2: 65-75.
2. Dalal,N., (2013), The Catastrophic Geomorphology of Some Chosen Parts of NW Coast Between Alexandria and Marsa Matruh in Egypt and Eastern Sicily, Italy, *MA. Degree Thesis*, Damanhour University, Egypt.
3. El Shazly, M.M., A.A. Shata and E.M. Farag, (1964), Lithology of the Neogene and Post-Neogene sediments in Marsa Matruh area.*J.Geol.,*UAR,Ciaro, 8:21-45.
4. Guidoboni E., A. Comastri, G. Traina, (1994), *Catalogue of Ancient Earthquakes in the Mediterranean Area up to the 10th Century*, Roma .
5. Hamouda.A,Z,(2006), Numerical computations of 1303 tsunamigenic propagation towards Alexandria, Egyptian Coast. *Journal of African Earth Sciences* 44 (2006) 37–44.
6. Hilmy, M.E., (1951), Beach sands of the Mediterranean coast of Egypt, *Jour. Sed. Petrology*, 21: 109-120.
7. Mortensen,N., Said,U.,Badger,J.,(2006), Wind Atlas for Egypt, Proceedings of the *2006 European Wind Energy Conference and Exhibition*, Athens, Greece, February 27 to March 2.
8. Pignatelli,C., Sansò,P ., Mastronuzzi.G.,(2009), Evaluation of tsunami flooding using geomorphologic evidence, *Marine Geology* 260 (2009) 6–18.
9. Selim, A.A., (1974), Origin and lithification of the Pleistocene carbonates of the Salum area, western Coastal plain of Egypt, *Jour. Sed. Petrology*, 44: 70-78.
10. Torab, M. (1984), Geomorphology of Um El Rakham aea, west of Marsa Matruh City, *MA. Degree Thesis*, Alexandria University, Egypt.
11. William,D,M., Hall,M,A.,(2004), Cliff-top megaclast deposits of Ireland, a record of extreme waves in the North Atlantic—storms or tsunamis, *Marine Geology* 206 (2004) 101–117.

Combining LiDAR data with field mapping and Schmidt-hammer relative age dating - examples from the Babia Góra range (Western Carpathians, Poland)

Piotr Kłapyta
Institute of Geography and Spatial Management
Jagiellonian University
Kraków, Poland
woytastry@gmail.com

Natalia Kolecka
Institute of Geography and Spatial Management
Jagiellonian University
Kraków, Poland
nkolecka@gis.geo.uj.edu.pl

Abstract—**The Babia Góra ridge (Outer Western Carpathians) exhibits one of the most complex landslide relief in the Carpathians. The aim of this research was to create a new interpretation of the Babia Góra range morphology, using the combined LiDAR data analysis, field mapping and the Schmidt hammer relative age dating. The general approach consisted of generation and automatic analysis of high-resolution DEM, interpretation of DTM-derived maps, manual vectorization of landforms and identification of ambiguous locations, in-situ investigation and Schmidt-hammer measurements, and completion of geomorphological data for the Babia Góra ridge. As a result, two generations of glaciofluvial levels were distinguished at the foothills of Diablak and Cyl, and for the first time three flow-like landforms were recognized at the foothills of the Sokolica peak. Above them the colluvial covers were located that formed two altitudinal complexes of landslide covers. In the uppermost Babia Góra slope section, the dominant features were sliding landforms, partially shaped by glacial and periglacial processes and debris flows activity.**

I. INTRODUCTION

Until recently, traditional geomorphological mapping has been based mainly on time consuming filed works. They have been occasionally aided by interpretation of aerial photographs and re-interpretation of the existing cartographic materials, often insufficient in details. With the increasing availability of Light Detection and Ranging (LiDAR), the new source of reliable spatial information occurred. Aerial laser scanning (ALS) has gained popularity in landslide research over large areas, in particular for landslide detection and characterization, hazard assessment, modelling, and monitoring [1]. One of the great advantage of the technology is that it provides detailed description of minor topographic features even under dense vegetation, thanks to the ability to penetrate through forest canopies [2,3]. LIDAR data can be fully integrated into geomorphological analyses. In particular, they provide a wider context of what we see in the field, which helps to readily identify large landforms and minimizes the ambiguity of what we see [4]. Nevertheless, description of spatial pattern and evolution of complex landforms is a great challenge. In this regard, the relative-age dating of various rock surfaces may assist [5]. A widely used method is Schmidt hammer (SH) measurement that provides the rebound values (R-values). The R-values tend to decline in response to rock-surface weathering and hence they reflect the time for which the rock surface has been exposed to subaerial processes [6]. Combination of LiDAR data analysis, field mapping and the Schmidt hammer relative age dating provides a rich information on landforms and their development.

The Babia Góra ridge (Outer Western Carpathians) exhibits one of the most complex landslide relief in the Carpathians. It has been subject to geomorphological and geological research since many decades [7]. Even though the geology and geomorphology of the range is regarded to be well known [7–9], the new high resolution LiDAR data create a unique perspective for detailed identification of landforms and their spatial patterns in this area. Additionally, relative chronology of various landslide landforms has not established so far. Therefore, the aim of this research was to create a new interpretation of the Babia Góra range morphology, using the combined LiDAR data analysis, field mapping and the Schmidt hammer relative age dating.

II. MATERIALS AND METHODS

A. Study Area

The Babia Góra ridge (1725 m a.s.l.) is located in the Outer Western Carpathians at the Polish-Slovak border and is the highest massif in the Western Beskidy Mts. On the Polish side the Babia Góra National Park exists, which covers 3392 ha. The landforms of the Babia Góra range are strongly controlled by the

In: Geomorphometry for Geosciences, Jasiewicz J., Zwoliński Zb., Mitasova H., Hengl T. (eds), 2015. Adam Mickiewicz University in Poznań - Institute of Geoecology and Geoinformation, International Society for Geomorphometry, Poznań

geological structure. The 10 km long monoclinal ridge is built of resistant Magura sandstones dipping southwards. The northern slopes of the Babia Góra Mts. form extensive cuesta, shaped by multi-phased mass movement activity, and periglacial and glacial processes during the Pleistocene [7,10]. However, the erosional and accumulational traces of glaciations are hardly distinguished from landslide features [11].

The investigated area covers ca.25 km^2, laying mainly on the northern slopes of the ridge, which have inclination of 40º-70º in the upper part, and less in the lower part. The slopes are difficult to access and densely vegetated: forest and dwarf pine reach up to app. 1390 m a.s.l. and app. 1650 m a.s.l., respectively.

B. Data

LiDAR point clouds were acquired in 2012 within the Babia Góra National Park project. The minimum point cloud density was 6 points / m^2, and vertical accuracy was 0.15-0.25 m. The point clouds were classified according to the American Society for Photogrammetry and Remote Sensing standards (ASPRS 2008) into: ground (class 2), low (3), medium (4) and high (5) vegetation, buildings (6), low points (7), model key-points (8), water (9) and others. The LiDAR data were used for generation of digital terrain model (DTM).

RGB orthophotomaps with a spatial resolution of 0.25 m that were generated from aerial images acquired in 2009 were used as auxiliary data for visual interpretation and landforms detection. They were received from CODGiK (Centralny Ośrodek Dokumentacji Geodezyjnej i Kartograficznej; Main Centre of Geodetic and Cartographic Documentation in Poland).

C. Methods

Our goal was to revise the geomorphology of the Babia Góra ridge. Thus, the general approach consisted of the following steps: (1) Generation of high-resolution DEM; (2) Automatic DTM processing and analysis; (3) Interpretation of DTM-derived maps, manual vectorization of landforms and identification of ambiguous locations; (4) Field works: verification of derived results, investigation and Schmidt-hammer measurements of the most significant or ambiguous locations; (5) Completion of geomorphological data for the Babia Góra ridge.

The DTM was interpolated from the LiDAR point clouds and had resolution of 1 m. It represented the mean elevation of the ground points. Using DTM, the following maps were derived: shaded relief, slope and curvature maps, Topographic Position Index (TPI) and slope position [12]. The shaded relief was the fundamental layer for landforms identification; however, the process was supported by the remaining DTM-derivatives. In the course of manual vectorization some locations of unclear character or difficult to interpret occurred. They were all marked and subsequently investigated in the field by direct observation and Schmidt-hammer measurements. The SH R-values were collected along 3 vertical transects (Sokolica transect – Sk, Diablak transect – B, Cyl transect – Cl) with BN-type Schmidt hammer at 18 sites (Fig. 1), where 150 impacts were recorded (Tab.1). Various types of landforms were investigated including: glaciofluvial cones, landslide tongues, slump fissures, debris flows and alluvia. Only the largest (0.5-1 m), stable, dry and near-horizontal boulders were tested. Moreover, the landforms identified on-screen were additionally verified in the field. In this way the geomorphological database for the Babia Góra ridge was completed.

III. RESULTS

Based on the on-screen interpretation of the LiDAR derivatives and field mapping, areal landforms, such as glaciofluvial cones, colluvial covers and mud flow deposits, as well as linear features, e.g. landslide niches and trenches, were delineated (Fig. 1). The glaciofluvial cones were located at the foothills of Diablak and Cyl, between 950 and 750 m a.s.l. Two generations of glaciofluvial levels were distinguished, namely the Sulowa Cyrhel level 70 m and the Słonowy level 20 m high. They formed gently inclined (5°) cones both built with gravels dominated by well-rounded Magura sandstone clasts (5-10 cm in diameter). The most distal part of the Słonowy glaciofluvial cone passed directly into the Würmian terrace of the upper Skawica river (20 m high). At the foothills of the Sokolica peak, three flow-like landforms were recognized for the first time. They formed extended tongues 0.5-1.5 km long with 20-25 m high steep fronts reaching 760-800 m a.s.l. They were built with mud flow deposits dominated by poorly sorted loamy sediments with angular clasts of Magura and Submagura sandstones.

Above the glaciofluvial cones and the mud flow deposits the colluvial covers were located. They formed two altitudinal complexes of landslide covers. The lower landslide complex (900-1100 m s.s.l.) was built with muddy and debris material, whereas the upper one (1300-1500 m a.s.l.) represented cataclasmic and sub-cataclasmic rock slope failures (*sensu* [13]) built with open-work blocks of Magura sandstones (up to 1.7 m in diameter) (Fig. 1, 2; Tab.1).

The dominant features in the uppermost Babia Góra slope section were sliding landforms including deep cracks, tension crevices, landslide scars and shallow fissures that framed the top side of the landslide hollows (Fig. 1). The landslide hollows in the Diablak area were partially shaped by glacial and periglacial processes and debris flows activity.

TABLE I. RESULTS OF THE SCHMIDT-HAMMER MEASUREMENTS. M - MEDIAN, N –NUMBER OF MEASUREMENTS, SD –STANDARD DEVIATION, V – COEFFICIENT OF VARIATION, SK -SKEWNESS

Site [a]	Characteristics							
	Land form [b]	*Altitude [m a.s.l.]*	*Mean R-value*	*M*	*N*	*SD*	*V*	*SK*
Sk-1	LC	990	33.4 ± 1.3[c]	33	63	5.2	27	0.3
Sk-2	LC	1025	35.2 ± 0.7	35.5	125	3.8	10.9	0.2
Sk-3	LC	1074	39.6 ± 0.8	40	125	4.4	11.3	-0.1
Sk-4	LC	1188	39.3 ± 0.8	39	125	4.3	10.9	0.1
Sk-5	LC	1284	36 ± 0.9 [d]	36	125	5.3	14.7	0.4
B-1	LC	1077	34.4 ± 0.8	34.5	125	4.5	13	-0.5
B-2	LF	1183	37.4 ± 0.7	37	125	4.2	11.3	0.05
B-3	RST	1097	39.1 ± 0.8	39	125	4.5	11.5	0.1
B-4	RST	1311	41.6 ± 0.8	41	125	4.4	10.6	0.6
B-5	RST	1300	35.5 ± 1.1 [d]	35	125	6.1	17.1	0.05
B-6	DFL	1285	42.2 ± 2.0 [c]	43	40	6.0	35	-0.6
B-7	RA	705	54 ± 0.7	55.5	125	4.2	7.8	-0.8
Cl-1	GC	820	27.1 ± 0.7	27	125	4.0	14.7	0.1
Cl-2	GC	860	29.4 ± 0.9	29.5	125	5.0	17	-0.1
Cl-3	LC	1011	29.6 ± 0.7	30	125	3.9	13.3	-0.02
Cl-4	LC	1111	32.3 ± 0.8	32.5	125	4.7	14.4	-0.2
Cl-5	LC	1265	38 ± 1.8 [c]	37.5	40	5.1	25	1.3
Cl-6	LC	1292	35 ± 1	34.5	125	5.7	16.2	-0.1

a. Sk – Sokolica transect, B – Diablak transect, Cl – Cyl transect;

b. LC - landslide colluvium, LF - landslide fissure, RST - rock slump tongue, DFL - debris flow levee, RA - recent alluvium, GC - glaciofluvial cone;

c. limited number of rock blocks available

d. effect of high rock moisture (removed from dataset)

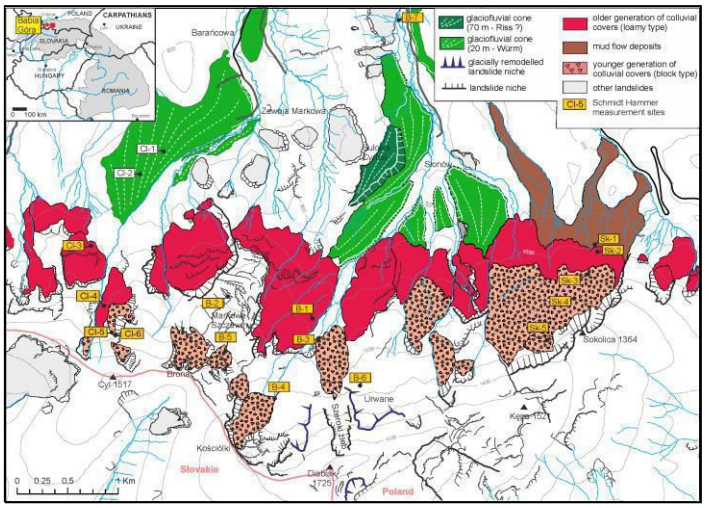


Figure 1. Landforms identified in the Babia Góra ridge and the Schmidt Hammer measurement sites.

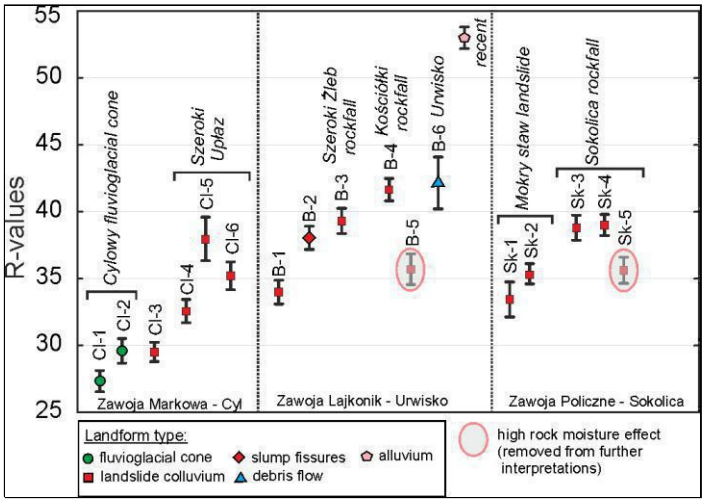


Figure 2. Results of the Schmidt Hammer measurements.

IV. DISCUSSION

The present study was designed to investigate the geomorphology of the Babia Góra ridge using the combined LiDAR data analysis, field mapping and the Schmidt hammer relative age dating. The LiDAR point cloud with nominal density of 6 points per 1 m^2 proved their suitability for detailed identification of landforms and their spatial patterns in mountainous vegetated area, which is normally difficult-to-access due to steep slopes and dense forest or shrub pine cover. The field mapping added information of landform sedimentological structure and allowed necessary verification of ambiguous

features identified on-screen. The SH measurements allowed relative age dating of the rocks, which was translated into development of the landforms.

Schmidt Hammer relative age dating indicated decreasing weathering rates and thus the overall younger age of landforms in up-slope direction of the Babia Góra.

Deposition of extensive water-laid gravel covers could be possibly linked with local glaciation in the highest parts of Babia Góra massif in the area of Mt. Diablak and Mt. Cyl during the last (Würm) and penultimate glaciation (Riss ?). This issue however is based on morphostratigraphy and requires further research in up slope area, where glacial sediments could be locally preserved [9].

Morphological relation confirmed by SH measurements indicate that accumulation of glaciofluvial gravels was replaced by intense gravitational slope deformations (mudflows, landslides, rock avalanches). Schmidt-hammer dating enabled us to distinguish two generations of individual landslide complexes, which point to two phased development of landslide relief. In contrast to previous research [10], no evidence of single giant rock slump on the northern slope was detected. This difference may be explained by the fact that until recently no highly detailed elevation model has been available.

A new LiDAR-based DEM revealed that the morphology of the middle and toe sectors of the northern Babia Góra slopes with a set of individual landslides are significantly more complex than assumed before. The investigation revealed the evidence of deep-seated gravitational slope failures, including: sackungs, translational slides (cataclasmic and sub-cataclasmic), large rock slumps and flow-like features (mud flow tongues), which cover the vast majority of the Babia Góra northern slopes (Fig. 1). The striking landslide morphology of Babia Góra range indicate a large scale slope instability, which could be potentially linked with climatic trigger (warming, thawing of permafrost and paraglacial processes). However, further research should be undertaken to determine the exact timing and cause of slope deformations. Cosmogenic nuclide dating of Babia Góra landslides is however recommended to determine the exact timing and cause of gravitational slope deformations.

ACKNOWLEDGMENT

FORECOM project (Forest cover changes in mountainous regions – drivers, trajectories and implications, PSRP-008/2010), supported by a grant from Switzerland through the Swiss contribution to the enlarged European Union.

REFERENCES

[1] Jaboyedoff, M.; Oppikofer, T.; Abellán, A.; Derron, M.-H.; Loye, A.; Metzger, R.; Pedrazzini, A. Use of LIDAR in landslide investigations: a review. Nat. Hazards 2010, 61, 5–28.

[2] Eeckhaut, M. Van Den; Poesen, J.; Verstraeten, G.; Vanacker, V.; Nyssen, J.; Moeyersons, J.; Beek, L. P. H. Van; Vandekerckhove, L. Use of LIDAR-derived images for mapping old landslides under forest. 2007, 769, 754–769.

[3] Migoń, P.; Kasprzak, M.; Traczyk, A. How high-resolution DEM based on airborne LiDAR helped to reinterpret landforms – examples from the Sudetes , SW Poland. 2013, 22, 89–101.

[4] Roering, J. J.; Mackey, B. H.; Marshall, J. a.; Sweeney, K. E.; Deligne, N. I.; Booth, A. M.; Handwerger, A. L.; Cerovski-Darriau, C. "You are HERE": Connecting the dots with airborne lidar for geomorphic fieldwork. Geomorphology 2013, 200, 172–183.

[5] Shakesby, R. a.; Matthews, J. a.; Owen, G. The Schmidt hammer as a relative-age dating tool and its potential for calibrated-age dating in Holocene glaciated environments. Quat. Sci. Rev. 2006, 25, 2846–2867.

[6] Matthews, J. a.; Owen, G. Schmidt hammer exposure-age dating: developing linear age-calibration curves using Holocene bedrock surfaces from the Jotunheimenâ□□Jostedalsbreen regions of southern Norway. Boreas 2010, 39, 105–115.

[7] Łajczak, A. Relief Development of the Babia Góra Massif, Western Carpathian Mountains. Quaest. Geogr. 2014, 33.

[8] Książkiewicz, M. The geology od the Babia Góra region. In National Park of the Babia Góra. Mt. Nature and Man; 1983; pp. 25–39.

[9] Wójcik, A.; Rączkowski, W.; Mrozek, T.; Nescieruk, P.; Marciniec, P.; Zimnal, Z. Babiogórski Park Narodowy w skali 1 : 13 000 2010.

[10] Aleksandrowicz, S. The northern slope of Babia Góra Mt. as huge rock slump. Stud. Geomorphol. Carpatho-Balcanica 1978, 12, 133–145.

[11] Ziętara, K.; Ziętara, T. O rzekomo glacjalnej rzeźbie Babiej Góry. Rocz. Nauk. WSP Kraków 1958, 8.

[12] Weiss, A. D.; Conservancy, T. N. Topographic Position and Landforms Analysis. 2000, 200.

[13] Jarman, D. Large rock slope failures in the Highlands of Scotland: Characterisation, causes and spatial distribution. *Eng. Geol.* **2006**, *83*, 161–182.

Geomorphometric analysis of glacial curvilineations (GCL) in Dobrzyń Lakeland, Central Poland

Aleksander Adamczyk, Marcin Sobiech, Agata Urbańska, Wojciech Wysota
Faculty of Earth Sciences
Nicolaus Copernicus University
Toruń, Poland
adams@doktorant.umk.pl

Abstract— **Morphometric analysis of forms of surface terrain is one of the main tasks facing the geomorphologists. This type of study is also using to describe landforms formed during the Pleistocene glaciations. So far, researchers analyzed morphometric characteristics of the tunnel valleys, drumlins, eskers and mega - scale glacial lineations.**

Recent study ongoing by Lesemann et al. [1, 2] have led to describe new forms eroded by subglacial meltwater - glacial curvilineations. The main aim of the authors is describe morphometric characteristics of these features.

I. INTRODUCTION

Dobrzyń Lakeland, located at the back of the maximum extent of the Scandinavian ice sheet (LGM) in central Poland (fig. 1), is characterizing by unique subglacial landscape [3]. Numerous tunnel valleys in Dobrzyń Lakeland (fig. 2) contain enigmatic bedforms that occur as fields of parallel, sinuous ridges separated by troughs [1]. For more than ninety years, these forms were determined as drumlins [4, 5, 6, 7, 8, 9, 10], although, their distribution and morphology are entirely different than typical. Recent studies suggest, that these features were formed due to subglacial meltwater erosion, so Lesemann et al. [1, 2] proposed quite new term to describe them as glacial curvilineations (GCL).

II. METHODS AND AIMS

Previous studies have been focused mainly on the internal structure of the ridges, while much less attention have been paid to the analysis of their morphology. Researchers generally analyzed specific parameters for drumlins, such as length, width and height or length / width ratio [i.e. 7, 8, 9, 10]. So far, morphometric and spatial relationships between ridges and troughs and outstanding, spatial regularity of these features have not been sufficiently analyzed. Availability of high resolution elevation data (LiDAR) and application of GIS tools to their analysis offer the possibility of a comprehensive morphostatistical study of these intriguing landforms. These researches could have big potential in new hypothesis about genesis of sinuous ridges in Dobrzyń Lakeland [1, 2] covered by the last continental ice sheet.



Figure 1. The study area on the background of maximum limit of the last Scandinavian ice sheet (LGM) in Poland

In: Geomorphometry for Geosciences, Jasiewicz J., Zwoliński Zb., Mitasova H., Hengl T. (eds), 2015. Adam Mickiewicz University in Poznań - Institute of Geoecology and Geoinformation, International Society for Geomorphometry, Poznań

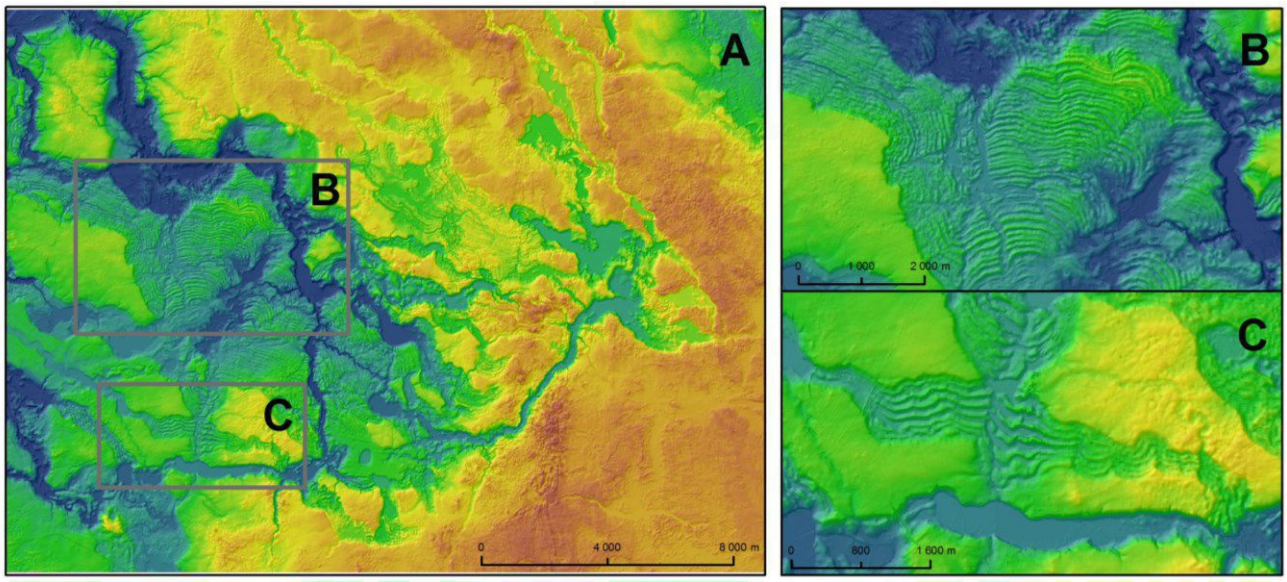


Figure 2. General view of study area (A), and two the most interesting locations of glacial curvilineations (B,C)

The main aim of the study is establishment in detail geomorphometric characteristics of ridges and depressions between them, especially: length, width, height / depth, sinuosity, orientation, development of the longitudinal profile and cross section spacing. High resolution digital elevation model will be used in the advanced ArcGIS analysis. Based on this data derivative shaded relief model, slope model and cross and longitudinal sections data will be created and statistically analyzed.

III. RESULTS

First results show large diversity in few morphometric parameters, especially in length and width of these forms. The longest landforms exceed 8 km, however the shortest ones have only 0,5 km. Diversity of length of these features depend on cross-cutting its by lineations and channels perpendicular to their. The average width of the individual forms ranges from 57 to 120 m, although in some places even exceed 200 m. The average tortuosity of the shaft is 1.15 while the development of the longitudinal profile is minimal – 1,002.

Obtained first results show that analyzed landforms (GCL) have morphometric similarities to other subglacial features as eskers or tunnel channels, examined in a lot of areas of the last glaciation. It could be one of the strongest argument in discussion about genesis of glacial curvilineations.

Results of the study will be useful in verification of ideas on glacial curvilineations genesis and modeling of processes of their formation within the Dobrzyń Lakeland subglacial landsystem.

REFERENCES

[1] Lesemann J.E., Piotrowski J.A., Wysota W., 2010, " 'Glacial curvilineations': New glacial landforms produced by longitudinal vortices in subglacial meltwater flows." Geomorphology 120, 153-161

[2] Lesemann J.-E., Piotrowski J.A., Wysota W., 2014, "Genesis of the 'glacial curvilineation' landscape by meltwater processes under the former Scandinavian Ice Sheet, Poland." Sedimentary Geology 312 (2014), 1-18

[3] Niewiarowski W., Olszewski A., Wysota W., 1995 "Role of subglacial features in glacial morphogenesis of the Kujawy-Dobrzyń subphase area in the southern and eastern part of the Chełmno-Dobrzyń Lakeland", Quaternary Studies in Poland, Spec. Issue, 13, 65–76.

[4] Nechay W., 1927, "Utwory lodowcowe Ziemi Dobrzyńskiej." Sprawozdania Państwowego Instytutu Geologicznego 4 (1-2), 61-144

[5] Jewtuchowicz S., 1956, "Struktura drumlinów w okolicach Zbójna.", Acta Geographica Universitatis Lodzensis 7, 1-74

[6] Lamparski Z., 1972, "Geneza form drumlinowych okolic Zbójna (Pojezierze Dobrzyńskie)" Acta Geologica Polonica 22 (1), 139-158

[7] Baranowski S., 1977, "Regularity of drumlin distribution and the origin of their formation." Studia Geologica Polonica 52, 53-68

[8] Wysota W., 1994, "Morphology, internal composition and origin of drumlins in the southeastern part of the Chełmno - Dobrzyń Lakeland." Sedimentary Geology 91, 345-364

[9] Olszewski A., 1997, "Drumlins of the northwestern Dobrzyń Moraine Plateau, location, structure and morphogenesis." Quaternary Studies in Poland 14, 71-83

[10] Głębicki P., Marks L., 2009, "The origin of drumlins at Zbójno, Central Poland", Geologija 51 (3-4), 131-138

Analysis and improvement of surface representativeness of high resolution Pléiades DEMs

Examples from glaciers and rock glaciers in two areas of the Andes

Lucas Ruiz
IANIGLA
CCT- Mendoza, CONICET
Mendoza, Argentina
lruiz@mendoza-conicet.gob.ar

Xavier Bodin
Laboratoire EDYTEM
UMR 5204 CNRS / Université de Savoie
Le Bourget-du-Lac, France
xavier.bodin@univ-savoie.fr

Abstract—**High spatial resolution Digital Elevation Models (DEMs) are fundamental datasets to understand the dynamics of Earth surface, such as recent change of the cryosphere, and especially in remote mountainous areas, like the Andes. Here we describe a methodological framework to improve the quality in terms of representativeness of terrain surface for high spatial resolution stereoscopic DEM obtained from Pléiades images. Using as example two DEMs from highly different regions from the Andes, we analyzed the different types of errors present in both DEMs. In order to improve the output DEM a post-processing scheme was designed, following those steps: (1) filling the gaps with a spline interpolation method; (2) elimination of the granular noise with a multidirectional Lee filter; and (3) elimination of the spikes with a slope-based DTM filter. Besides improving the representativeness of both DEMs in terms of terrain feature, the post-processing also improves the accuracy of DEMs in terms of absolute accuracy of elevations.**

I. INTRODUCTION

Glaciers, debris-covered glaciers and rock glaciers are very common cyrospheric landforms in the Andes, and represent important water storage for anthropic uses, such as agriculture, hydroelectric power generation and other industrial activities developed at the foot of the Argentinian Andes. Since a few decades, these cryospheric features are rapidly shrinking, mostly due to an increase in air temperature and a decrease in winter precipitation in the Andes range [1].

The recent availability of high spatial resolution DEMs, like those derived from Pléiades images (from the French spatial agency, CNES), represents a great advantage compared to previous sensors, as their resolution allows to measure volume change and surface characteristics of small glaciers and rock glaciers. Nevertheless, various errors could be propagated into the DEM calculation and limit the full exploitation of high resolution advantages [2]. Among the most common source of errors are speckle noise, anomalous artifacts and no data areas. The first one introduces non-real spatial variation to volume change measurements and higher standard deviation to typical morphometric parameters such as slope, aspect or elevation, which helps to characterize landforms. On the other hand, anomalous artifacts, like holes and/or spikes, could introduce a total anomalous pattern for volume change or in the statistical analysis of morphometric parameters. In the case of no data areas, the main drawback is the lack of information.

Here we introduce a post-processing procedure that intends to (1) assess the presence of different kinds of error, and (2) to use filtering scheme to eliminate the errors. We apply our method on two areas (Fig. 1), which differ in terms of elevation range, slope and surface cover, showing that, in both situations, the post-processing scheme of DEMs improves the representativeness of the surface and the elevation accuracy.

II. MATERIAL AND METHODS

A. DEM generation and GCP (ground control points)

Both DEMs were generated using the same methodology, with the triplets of Pléiades images taken on 21-April-2012 on Tronador and on 14-May-2014 for Vallecitos. We used PCI Geomatica (v2013) Ortho Engine module to construct the epipolar images and, then, to construct the DEMs. Output DEM with a 2-m resolution was generated from the pixel values with higher correlation scores between the three DEMs created from the different combinations of images (nadir-back, nadir-front, and back-front).

In: Geomorphometry for Geosciences, Jasiewicz J., Zwoliński Zb., Mitasova H., Hengl T. (eds), 2015. Adam Mickiewicz University in Poznań - Institute of Geoecology and Geoinformation, International Society for Geomorphometry, Poznań

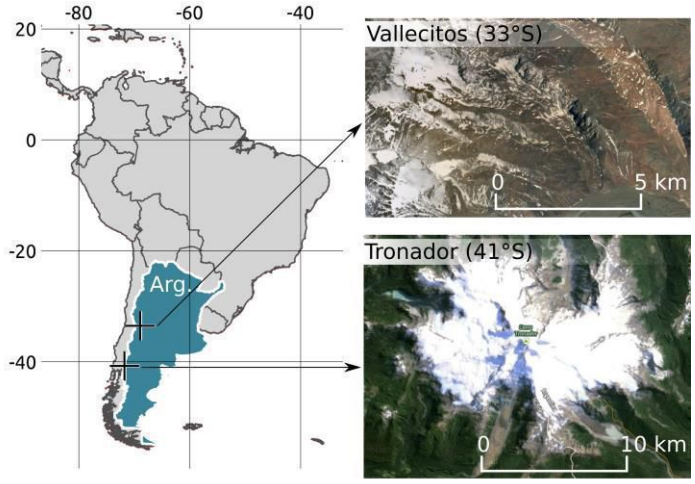


Figure 1. Location of the two study areas in the Argentinian Andes: the heavily glaciated Tronador summit (41°S) and the more rocky Vallecitos catchment (33°S). Imagery from Google Maps.

The first study area (Tronador) corresponds to the Monte Tronador (3475 m asl, 41°09′ S 71°53'W) an extinct volcano of the Wet Andes. Valleys of this region are deep glacial troughs, whereas the upper part concentrates the accumulation area of eight major valley glaciers, in both Argentina and Chile. There is a combination of debris covered glaciers and debris free glaciers, the first ones reach lower elevations (~600 m asl), meanwhile the last ones do not descend below 1500-1400 m asl. Five GCPs were selected to orthorectify the Pléiades images, measured with a Trimble GeoExplorer 6000 Series GNSS receiver on static mode. After differential correction, the horizontal and vertical accuracy of GCPs are 0.1 m and 0.2 m, respectively. Final RMSE (Root Mean Square Error) between the location of the GCPs in the images and on the ground was 0.28 m and 0.48m in X and Y coordinates, respectively. Additionally, 53 tie points with a RMSE of 0.12 m and 0.1 m in X and Y, respectively, were collected in the three images to refine the sensor model.

The second study area (Vallecitos) is a small catchment of the South-east facing flank of the Cordón del Plata, in the Argentinian Dry Andes (between 32°55 and 32°20'S). The altitude are mostly comprise between 3000 and 5400 m asl., and the terrain is characterized by rock surfaces, debris-free glaciers and large portions of debris-covered and rock glaciers [3]. Five GCPs were collected with a dual-frequency Trimble R5 GNSS receiver (horizontal accuracy: 0.015 m, vertical accuracy: 0.028 m). Final RMSE for GCP is 0.49 m and 0.58 m respectively for X and Y, whereas it reaches 0.37 m and 1.19 m in X and Y for the 30 tie points.

B. Representativeness

We consider here the representativeness as a measure of how good a particular DEM represents the different elements or characteristics of a particular region. Because this metric is difficult to quantify and may be confused with the accuracy of the elevation, we use a qualitative approach: this latter first assesses the representativeness of surface features by the output DEMs thanks to a visual inspection using a hill shaded surface model of each output DEM. We also compared the hill shaded model with Pléiades ortho images and terrain photos searching for visual discrepancies.

C. DEM elevation accuracy

To quantify the accuracy in elevation of output DEMs we measure the RMSE between DEM elevation values and several thousands of GPS elevation data collected over bare ground (no ice or forest cover areas) with the Trimble receivers (GeoExplorer 6000 for Tronador, and R5 model for Vallecitos) on dynamic mode. After differential correction, the horizontal and vertical precisions of these ground truth data (GTD) for both study areas are 0.1 m and 0.2 m, respectively.

We use 2301 and 858 GTDs for Tronador and Vallecitos, respectively. In order to avoid pseudo-replication due to the cell size of output DEMs (2m), GTD were resampled to the spatial size of each DEM. When more than one GTD falls inside one cell the mean value was used.

D. Post-processing scheme

To correct the errors found in the qualitative representativeness analysis (see section III; Figure 2 A) the following post process scheme is proposed; (1), filling the gaps (no data areas) with a spline interpolation method, (2) elimination of the granular noise with a multidirectional Lee filter [4]; and (3) elimination of the spikes with a slope based DTM filter [5]. All raster tools are included in the modules library of SAGA GIS (v 2.1). Figures 2 A-D show the improvements in the Pléiades Tronador´s DEM generated by each of the steps mentioned above.

III. Results and discussion

Although the Pléiades DEM reproduces with great details the surface of the glaciers and the rock glaciers, different kinds of errors were identified after the representativeness analysis (visual inspection): (1) holes (cells with no data in highly shadowed areas); (2) granular noise, typically of stereoscopically generated DEMs; (3) spikes (high elevation cells surrounded by lower elevation data) without any spatial correlation (Fig. 2 A).

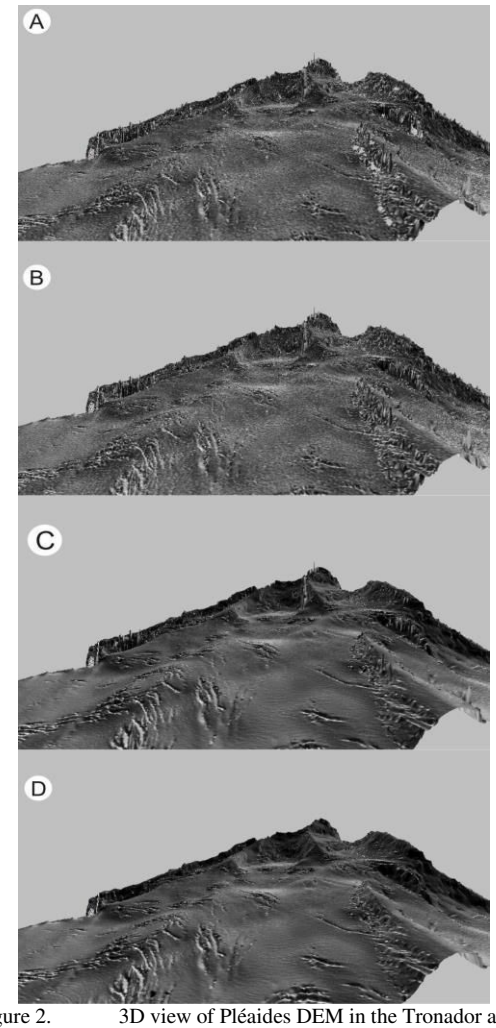


Figure 2. 3D view of Pléaides DEM in the Tronador area shown as a hill shade model: A) without post-processing (note the presence of gaps, granular noise and spikes); B) First step in post-processing, Pléiades DEM with gaps filled; C) Second step in post-processing, Pléiades DEM with speckle noise removed; D) Final Pléiades DEM without spikes, granular noise and gaps. Note the smoothness of ice surface and how well the crevasses are represented.

There are numerous methods to interpolate values in areas of no data, from the most time consuming one, like digitalizing on-screen contour lines, to the most automatic method using numerical interpolation. The best option depends on the objective and on the size of the holes: if the holes are small and do not interference with the region of interest a simple and rapid numerical interpolation methods it is always the best choice. In this context, spline interpolation is preferred to others interpolation methods, like inverse distance weight or nearest neighborhood, because it results in a smooth surface without modifying the original values of pixels adjacent to the voids (Fig. 2 B).

To reduce or eliminate the granular noise advanced filter techniques are required, which identify and eliminate the noise while saving the terrain geometry. The multidirectional Lee filter [6], search for the minimum variance in 16 directions and applies a local mean filter in the direction of minimum variance. The filter is therefore always right-angled to the slope and parallel to the valley system. Thus, the filter eliminates the noise without changing the position and elevation of sharp ridges and deep canyons [4]. The filter eliminates the speckles, preserving small surface features like crevasses or moraine ridges (Fig. 2 C).

Anomalous objects, like spikes, found especially in the Tronador DEM, were created during the generation of DEMs close to high slope areas, like cliff or ridges (Fig. 2A). The slope-based DTM filter we applied to correct this, is based on the observation that a large height difference between two nearby points is unlikely to be caused by a steep slope in the terrain. Although the spikes where already in high slope areas, the filter was able to eliminate it without modified the rest of the high slope areas (Fig.2 D).

When comparing with the GTDs, the elevation accuracy of the Tronador's post-processed DEM (RMSE of the difference between the DEM and the GPS measurements) is 1.08 m, which is slightly better than the one calculated from the only GCP-based raw DEM (1.20 m, Fig.3). In the case of Vallecitos, the RMSE shifts from 3.72 to 3.69 m, displaying a yet unexplained wide distribution of the errors (with three modes around -3, 3 and 5 m, that could be related to artefacts generated by dark pixels in shadow areas).

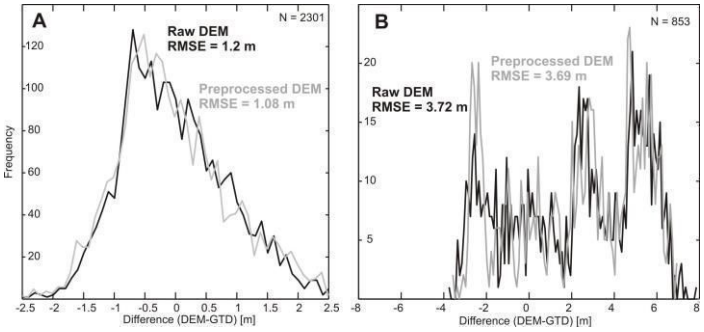


Figure 3. Histograms of differences between DEMs and GTD for Tronador (A) and Vallecitos (B) areas. Thick black line represents the error distribution of the raw (non processed DEM), grey line represents the error distribution of post-processed DEM.

IV. Conclusion

Using a combination of automatic filters we were able to eliminate different sources of error and to improve the elevation accuracy in our DEM by 5% in two very different types of high mountain environments (mostly debris-free glaciers in Tronador area, mostly debris-covered and rock glaciers in Vallecitos). The gain in representativeness, especially for glaciological and geomorphological studies, of such improved high resolution datasets will probably allow the development of many applications in the next years, among which the most promising could be accurate estimation of volume changes and of surface displacements.

Acknowledgment

The Pléiades images for Tronador area were provided at no cost by Airbus Defense and Space through the Pléiades User Group.. For the Vallecitos areas, the purchase of the Pléiades imagery was done thanks to the ANDALP project, funded by the CMIRA program of the Région Rhône Alpes, France (COOPERA n°13.005522.01/02). The PCI Geomatica software was donated to IANIGLA by Etienne Berthier. The constructive comments of three anonymous reviewers helped to improve the manuscript.

References

[1] Berthier, E., Vincent, C., Magnússon, E., Gunnlaugsson, Á. Þ., Pitte, P., Le Meur, E., … Wagnon, P. 2014. “Glacier topography and elevation changes derived from Pléiades sub-meter stereo images”. The Cryosphere, 8(6), 2275–2291. doi:10.5194/tc-8-2275-2014

[2] Bodin, X., Trombotto, D. and A. Soruco. Submitted. “Evaluation of a terrestrial photogrammetry method for the study of interannual high mountain dynamics. Quebrada del Medio rock glacier, Mendoza, Argentina”. Geomorphometry conference 2015, Poznan, Poland

[3] Rabatel, A., Francou, B., Soruco, A., Gomez, J., Cáceres, B., Ceballos, J. L., Wagnon, P. 2013. “Current state of glaciers in the tropical Andes: a multi-century perspective on glacier evolution and climate change”. The Cryosphere, 7(1), 81–102. doi:10.5194/tc-7-81-2013

[4] Selige, T., Böhner, J. and Ringeler. A. 2006 “Processing of SRTM X-SAR Data to correct interferometric elevation models for land surface process applications, Göttinger Geographische Abhandlungen, 115, 97–104.

[5] Vosselman, G. 2000. “Slope based filtering of laser altimetry data”. IAPRS, Vol. XXXIII, Part B3, 935-942. Amsterdam, The Netherlands.

[6] Lee, J.-S., K. P. Papathanassiou, T. L. Ainsworth, M. R. Grunes, and A. Reigber (1998), A new technique for noise filtering of SAR interferometric phase images, IEEE Transactions on Geoscience and Remote Sensing, 36(5), 1456–1465, doi:10.1109/36.718849.

A Method of Depression Filling with Consideration of Local Micro-relief Features

JIANG RuQiao
Key laboratory of Virtual Geographic Environment, Ministry of Education
Nanjing Normal University
Nanjing, China
jobryant@163.com

TANG GuoAn
Key laboratory of Virtual Geographic Environment, Ministry of Education
Nanjing Normal University
Nanjing, China
tangguoan@njnu.edu.cn

Abstract—**Depression filling is one of the most basic and time-consuming operation steps in the process of hydrological analysis based on digital elevation model (DEM). With the improvement of spatial resolution of DEM data, quicker method of depression filling plays a key role in the calculation of distributed hydrological model. The paper described a quick depression-filling algorithm which means Micro-relief Flood algorithm (MFF algorithm). This method takes local micro-topographical features into full consideration. In this method, redundant points, depressions and flats will be processed optimally, to achieve further promotion of efficiency in depression filling. And then, 70 DEM data with different sizes are used to test the new algorithm. A comparative analysis was also conducted to investigate the accuracy and efficiency between our modified algorithm and the widely used W&L algorithm and M&V algorithm. Experimental results show that the MFF algorithm can not only fill the depression accurately, but also reduce the computation time by 40.13% than that of W&L algorithm, on average. This method provides a new approach to highly-efficient hydrological analysis.**

INTRODUCTION

In recent decades, Digital Elevation Models (DEMs) have been widely used in the automatic hydrologic analysis of surface topography [1-4]. Depression filling is one of the most basic and time-consuming operation steps in the process of hydrological analysis based on digital elevation model (DEMs). Depression by error and other causes are prevalent in DEM data, and would seriously interfere with the accuracy of the results of flow algorithm [5-7]. Depression filling enables each grid cell flow to the correct position through a certain path, so as to ensure accurate and continuous extraction of drainage network [8, 9]. Nevertheless, time-consuming has always been a problem in former depression filling algorithms. With the trend that high-resolution DEM data gradually become the main analysis data, more rapid and efficient depression filling algorithms are required.

Due to the undesirable results caused by depression, the common practice is to remove depression in the DEM at the very first step of hydrologic analysis [4]. Various algorithms of depression removal have been proposed to discover and fill the depressions. Filter in a window were firstly used to remove depressions [10]. It help to eliminate a great deal of depressions and bring about a great improvement in continuity of extracted stream network. However, it alter the original data too much and cause the distortion of DEM. To overcome the shortcoming above, three types of depression removal algorithms are proposed under the definition of the depression-filling problem [11]. Among those algorithms, the J&D Algorithm developed by Jenson and Domingue is the best known one, which was applied to ArcInfo [12]. This algorithm enable all the depression to be removed with a minimum modification of DEM. Besides, Moran and Vezina proposed the M&V algorithm, which reduce the iteration to make a progress in time cost [13]. Garbrecht optimize the algorithm with elevating flatland to eliminate parallel flow [14]. Soille and Gratin firstly applied the concept of Priority-Flood to depression filling and proposed a more efficient method [15]. As the best known one in methods of depression filling with Priority Flood, W&L algorithm was described by Wang and Liu, which identify and fill depressions with Least-Cost Search algorithm, LC-Search. This method process only once without iteration and further increase the speed of depression filling. In this method, the efficiency of LC-Search algorithm play a key role in the speed of depression filling. Hence, more efficient LC-Search algorithms are continue to be proposed to accelerate W&L algorithm [16-20]. Some researchers have also adopted the method of parallel computing to improve the speed of depression filling computing in large scale, but it still needs a serial algorithm as the ideological foundation [21]. These methods can solve the basic problem of depression removal, however, it ignores the impact of local micro-topographical features on depression filling efficiency and redundant computation exists in the algorithm.

This paper analyzed the regular pattern of water flowing in local micro-relief and proposed Micro-relief Flood Fill algorithm

In: Geomorphometry for Geosciences, Jasiewicz J., Zwoliński Zb., Mitasova H., Hengl T. (eds), 2015. Adam Mickiewicz University in Poznań - Institute of Geoecology and Geoinformation, International Society for Geomorphometry, Poznań

based on W&L algorithm. The generation and elimination of redundant computation in depression filling were discussed to try to release the potentiality of local micro-topographical features for improving efficiency of depression filling algorithm.

METHODS

Basic Idea

Wang and Liu proposed W&L algorithm based on Least-Cost Search algorithm. In this method, each of the cells in DEM data only be accessed once. Most of the cells, however, remain in priority queue and result in the priority queue operating slowly. Interestingly, a large number of cells in priority have nothing to do with the depression filling result. If these redundant computations were able to be avoid, the efficiency of depression filling will be promoted largely. This paper hold the view that the redundant computations mentioned above are primarily due to the ignorance of influence from local micro-topographical feature to depression filling. Therefore, two optimal strategies are proposed to speed up W&L algorithm.

Optimal strategies

1. Redundant Points Elimination

Redundant point is defined as the point involved in the calculation, but not related with the calculation result. The generation of redundant point is associated with the spatial distribution of elevation in local micro-relief. If the topographical feature is in accord with the following elevation distribution in 3 × 3 window, the central cell must be redundant point. All adjacent cells of the central cell are able to bypass the central one, along the direction of maximum gradient (Figure 1). Two general recognition method for redundant are concluded from next 8 circumstance ().

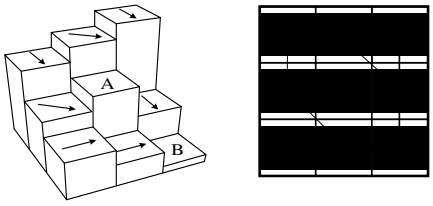


Figure 1.Flow direction in 3D and 2D

I. Diagonal position judgment method:

(1) Father point and pending point are in a diagonal position;

(2) Brother points is lower than pending point;

(3) Either one of the sub-points in orthogonal position is lower than pending point;

Then, the pending point must be a redundant point.

II. Orthogonal position judgment method:

(1) Father point and pending point are in an orthogonal position;

(2) Both of the brother points are lower than pending point;

Then, the pending point must be a redundant point.

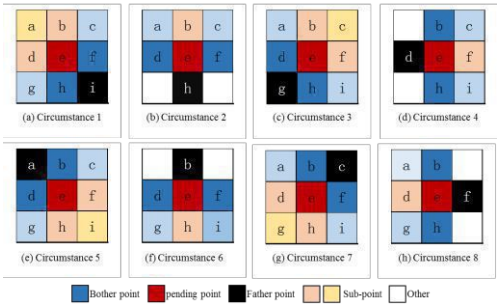


Figure 2.The judgment circumstances of redundant points

2. Faster Calculating for Flatland and Depression

The pending point is defined as flatland when its elevation is equal to one of its father point. Flatland has same priority level with its father due to their equal elevation. Thus, in this paper, the general queue as the fast calculating queue is used to calculate flatlands, for the reason that the time complexity of dequeuing operation in general queue are only O(1) much less than which in priority queue (O(logn)). Depression will be filled as flatland first, so it can also be treated as flatland. This strategy are able to calculate depression and flatland quickly and avoid them participating in the subsequent sorting calculation in priority queue (Figure 3).

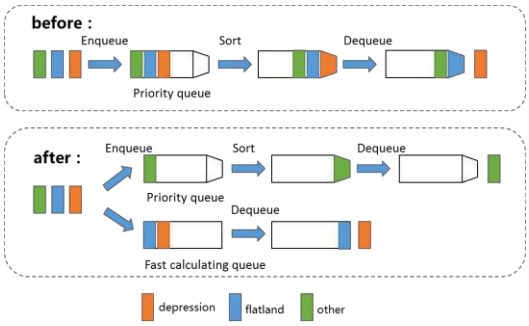


Figure 3.Fast calculating for flatland and depression

Algorithm

Micro-relief Flood Fill algorithm are proposed based on the above two optimal strategies and W&L algorithm. It is composed

of next five steps. Step1. Initialization; Step2. Minimum spill elevation searching; Step3. Depression and flatland fast calculating; Step4. Redundant elimination; Step5. Repeat step2 to step4 until both of the fast calculating queue and priority queue are empty; Pseudo-code of MFF Algorithm is shown below (Figure 4).

```
Algorithm  Micro-relief FloodFill
1:  Define DEM[] as the source data
2:  Define Flag[] as the mark matrix which has the same dimensions as DEM
3:  Define PriQueue as the priority queue
4:  Define AdvQueue as the normal queue
5:  Define IsRDPoint(cell, dir) as the function to check cell is a redundant point
6:  Initialize Flag[] to FALSE
7:  for all cell on the edge of DEM[] do
8:      PriQueue.Push(cell)
9:      Flag[cell] = TRUE
10:  while TRUE do
11:     if AdvQueue is not empty then
12:         cell = AdvQueue.Pop()
13:         for all neighbors n of cell do
14:             dir = Current Direction      //Position between pending point and father point
15:             if Flag[n] is FALSE then
16:                 maxElevation = Max( DEM[n], DEM[cell] )
17:                 if DEM[n] <= maxElevation then
18:                     DEM[n] = maxElevation
19:                     AdvQueue.Push(n)
20:                 else if call IsRDPoint(n, dir) == FALSE then
21:                     PriQueue.Push(n)
22:     else if PriQueue is not empty then
23:         cell = PriQueue.Pop()
24:         for all neighbors n of cell do
25:             dir = Current Direction
26:             if Flag[n] is FALSE then
27:                 maxElevation = Max( DEM[n], DEM[cell] )
28:                 if DEM[n] <= maxElevation then
19:                     DEM[n] = maxElevation
30:                     AdvQueue.Push(n)
31:                 else if call IsRDPoint(n, dir) == FALSE then
32:                     PriQueue.Push(n)
33:     else
34:         break while
```

Figure 4.Pseudo-code of MFF Algorithm

RESULTS

70 DEM data with different sizes are used to test the new algorithm in comparison with W&L and M&V. All the algorithms in the test produce identical results. Hence, this paper will discuss the difference between the three algorithms only from the aspect of time cost. The testing result is shown in Figure 5 and Figure 6. The results shows that two optimal strategies proposed in this paper is proved effective. Scatter in Figure 5 shows a linear relationship between the speed-up rate of MFF vs. W&L and the proportion of cells be optimized.

Speed-up Rate = (MFF Runtime – W&L Runtime) / W&L Runtime

The linear regression equation is $y=1.067x+0.002$(R^2=0.99), which means the optimal strategies have a good stability and cost performance. Figure 6 shows that difference of time cost between three algorithms increases with data size which means the cell count. The average runtime of MFF is 476s, the W&L being 820s and the M&V is 3536s when the data size goes to 5.29×10^8. It is clear that MFF has a greater advantage in dealing with large size data.

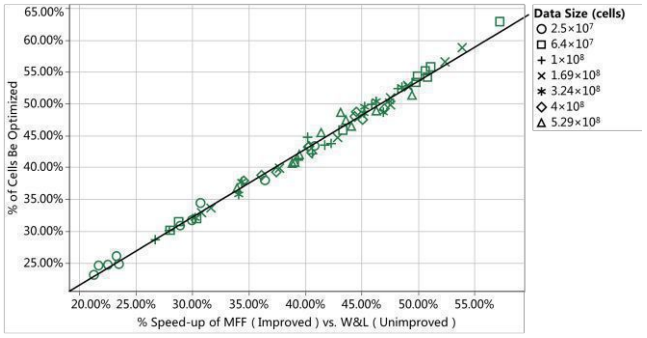


Figure 5.Scatter plot of proportion of cells be optimized and the speed-up rate of MFF vs. W&L.

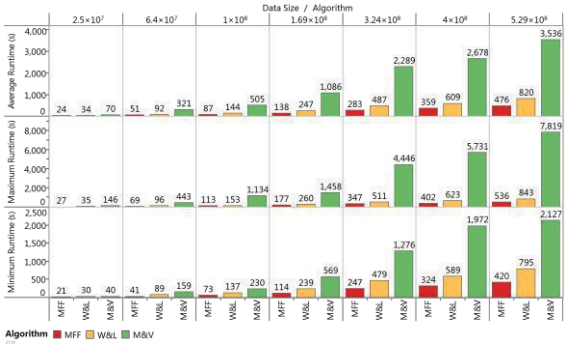


Figure 6.The comparison of runtime of MFF, W&L and M&V

CONCLUSIONS

This paper proposed Micro-relief Flood Fill algorithm to eliminate redundant computation during depression filling due to the fluctuation in local micro-relief. This method further reveals the influence of local micro-topographical feature on flow path in local micro-relief and make further efforts for releasing the potentiality of W&L algorithm.

By analyzing the regular pattern of water flowing in local micro-relief, this paper describe two optimal strategies to speed up depression filling. Testing results shows that MFF algorithm performed up to 57.21% faster than W&L algorithm at most and 40.13% on average.

ACKNOWLEDGMENT

The research is supported by National Natural Science Foundation of China (NO. 41171320, 41471316); Major Scientific Research Projects of Universities in Jiangsu Province (NO.13KJA170001); The authors express their great thanks to everyone who have helped in the writing of this article.

REFRENCES

[1] Band L E, 1999. Spatial hydrography and landforms. Geographic Information Systems. 1: 527-542.

[2] Moore I D, Turner A K, Wilson J P, et al, 1993. GIS and land-surface-subsurface modeling. Oxford University Press: 196-230.

[3] Garbrecht J, Martz L W, 2000. Digital elevation model issues in water resources modeling. Hydrologic and hydraulic modeling support with geographic information systems: 1-28.

[4] Wang L, Liu H, 2006. An efficient method for identifying and filling surface depressions in digital elevation models for hydrologic analysis and modelling. International Journal of Geographical Information Science. 20(2): 193-213.

[5] Yang Xiaoyun，Gu Liya，Cen Minyi, et al,2005. A Method Based Fitting of Moving Quadric Surface with Variable Windows for Detecting Gross Errors in Irregular DEM. Acta Geodaetica et Cartographica Sinica. 34(02): 148-153.

[6] Qin Chengzhi，Li Baolin，Zhu Axing, et al,2006. Multiple Flow Direction Algorithm with Flow Partition Scheme Based on Downslope Gradient. Advances in Water Science. 17(04): 450-456.

[7] Tarboton D G, Bras R L, Rodriguez-Iturbe I, 1991. On the extraction of channel networks from digital elevation data. Hydrological processes. 5(1): 81-100.

[8] Lu Guonian，Qian Yadong，Chen Zhongming,1998. Study of Automated Mapping of Channel Network in Hilly Loess Region. Acta Geodaetica et Cartographica Sinica. 27(02): 40-46.

[9] Zhu Qing，Zhao Jie，Zhong Zheng, et al,2004. The Extraction of Topographic Patterns Based on Regular Grid DEMs. Acta Geodaetica et Cartographica Sinica. 33(01): 77-82.

[10] O'Callaghan J F, Mark D M, 1984. The extraction of drainage networks from digital elevation data. Computer Vision, Graphics, and Image Processing. 28(3): 323-344.

[11] Planchon O, Darboux F, 2002. A fast, simple and versatile algorithm to fill the depressions of digital elevation models. CATENA. 46(2–3): 159-176.

[12] Jenson S K, Domingue J O, 1988. Extracting topographic structure from digital elevation data for geographic information system analysis. Photogrammetric engineering and remote sensing. 54(11): 1593-1600.

[13] Moran C J, Vezina G, 1993. Visualizing soil surfaces and crop residues. Computer Graphics and Applications, IEEE. 13(2): 40-47.

[14] Garbrecht J, Martz L W, 1997. The assignment of drainage direction over flat surfaces in raster digital elevation models. Journal of hydrology. 193(1-4): 204-213.

[15] Soille P, Gratin C, 1994. An efficient algorithm for drainage network extraction on DEMs. Journal of Visual Communication and Image Representation. 5(2): 181-189.

[16] Beucher S, Meyer F.1993. The morphological approach to segmentation: the watershed transformation. Mathematical morphology in image processing. 34, 433-481.

[17] Metz M, Mitasova H, Harmon R S, 2010. Accurate stream extraction from large, radar-based elevation models. Hydrology and Earth System Sciences Discussions. 7(3): 3213-3235.

[18] Luengo Hendriks C L, 2010. Revisiting priority queues for image analysis. Pattern Recognition. 43(9): 3003-3012.

[19] Gomes T L, Magalhaes, Andrade M V, et al, 2012. Computing the drainage network on huge grid terrains. ACM, New York, USA: 53-60.

[20] Barnes R, Lehman C, Mulla D, 2014. Priority-flood: An optimal depression-filling and watershed-labeling algorithm for digital elevation models. Computers & Geosciences. 62: 117-127.

[21] Jiang Ling，Tang Guoan，Song Xiaodong, et al,2014. Parallel DEM Preprocessing Algorithm with Granularity Control on Gridded Terrain Datasets. Geomatics and Information Science of Wuhan University. 39(12): 1457-1462.

Comparison of digital elevation models of riparian wetland generated from airborne laser scanning of different accuracy

Marcin Brach
Division of Hydrology and Water Resources, Dept. Water Engineering
Warsaw University of Life Sciences
Warsaw, Poland
m.brach@levis.sggw.pl

Jarosław Chormański
Division of Hydrology and Water Resources, Dept. Water Engineering
Warsaw University of Life Sciences
Warsaw, Poland
j.chormanski@levis.sggw.pl

Abstract— **In the last decade, the development of laser scanning allowed the widespread use of this technology in Poland. Currently, Airborne Laser Scanning (ALS) become the most reliable source of elevation data for large areas. It was selected as a main source of data in the project IT System of the Country's Protection against extreme hazards (ISOK), which provides LiDAR data for almost whole country. Despite progress in availability of accurate elevation data, there are specific areas were quality of the data collected in ISOK is not sufficient, e.g. Kampinoski National Park (KPN). The lower data quality can be expected in marsh ecosystems covered by dense vegetation in the floodplain and former river valleys. The aim of this work is to compare ALS Digital Elevation Models (DEM) collected with different scanning parameters, evaluate and determine causes of their quality degradation.**

I. INTRODUCTION

A. *IT System of the Country's Protection against extreme hazards (ISOK)*

The project "IT System of the Country's Protection against extreme hazards (ISOK)" is realized nowadays in Poland. Its aim is to create complex system for water management, especially flood protection [1] including accurate digital elevation model (DEM). As a main source of elevation data Airborne Laser Scanning (ALS) was selected. ALS mapping of Poland area was started in 2011 year. In the first stage of project realization (2011-2013) around 65% of the country area was scanned. In 2013 the second stage began and that aim was to collect additional LiDAR data for above 90% of the total country area. Data was collected in 2 standards. Standard I rural areas, points density 4 pts/sq. m (in special cases the density was higher – 6 pts/sq. m), standard II urban areas, points density 12 pts/sq. m [2].

B. *Nationwide LiDAR data in context of local scale (natural river valley case)*

Despite that the ISOK project provided dense, high quality data, it's nationwide character, in some particular areas like e.g. area with dense natural vegetation coverage or relatively wet area (natural river valleys, floodplains, wetlands) it's quality (especially DEM) could be not enough and generate significant errors in hydrodynamic modeling and estimating of the water storage capacity [3]. The problem concerns Kampinos National Park (KNP) located in central-eastern Poland. A numerous marshland habitats pose a problem for laser beam, as a result limits the possibility of beam reflection from the ground. An additional issue are communities of sedges', especially *Caricetum cespitosae* or *Caricetum appropinquatae* which form tussocks as a mixture of root system, organic and mineral muddy materials [4]. Sedge's tussocks influence a floodplain micro-topography, which in our opinion can be difficult for ALS technique to acquire and then process for extracting this structure from the vegetation.

C. *ISOK LiDAR data problems within the Kampinos National Park*

If we are interested on large natural area bigger than one ALS block the continuum of the natural objects and phenomena could be not kept on, what can strongly influence results. In the possible worst situation a part of the object is scanned in autumn and another part in spring two years later, by different instrument. The full area of the KNP was covered by ISOK system ALS mission. Its premises is divided by the border of four blocks, which indicates that, the data was acquired in different time ('Fig. 1'), and it's processing was done separately.

In: Geomorphometry for Geosciences, Jasiewicz J., Zwoliński Zb., Mitasova H., Hengl T. (eds), 2015. Adam Mickiewicz University in Poznań - Institute of Geoecology and Geoinformation, International Society for Geomorphometry, Poznań

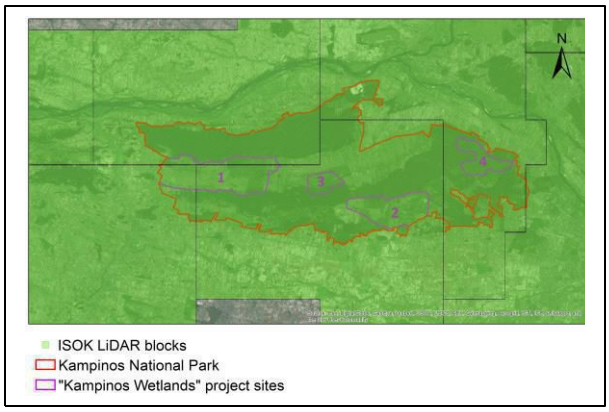


Figure 1. ISOK block borders in the Kampinos National Park. Four regions of "Kampinos wetlands" project realization: 1- Lower Łasica, 2- Zaborowski Canal, 3 – Żurawiowe, 4 – Wilcza Struga.

In extreme cases, like in the part of the KNP – Lower Łasica region (Region no. 1 on Fig.1)), the date of the ALS scanning missions differs in time by 1.5 year 'Fig. 2'. These gap for riparian ecosystems, with the high rate of vegetation variability between missions periods and the fact that the part of the data was acquired late spring and other in the autumn (different water regimes) in our opinion it's causing significant quality degradation.

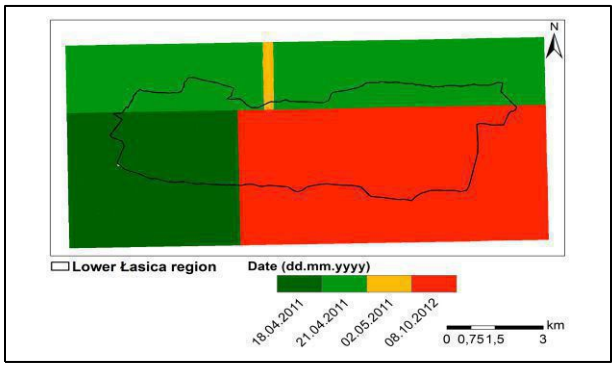


Figure 2. ISOK LiDAR data acquiring date based on the points "GPS Time" parameter.

II. STUDY AREA

Kampinos National Park (KNP) was established in 16 January 1959, for protection of the unique mosaic of landscape consisting of dunes, wetlands and forests. It covers a total area of 385.44 ha. It is located close to Warsaw agglomeration, a capitol of Poland. Intensive urbanization pressure from the Warsaw agglomeration has been considered to be an important cause for increasing groundwater degradation [5]. Groundwater table lowering and changes in the water balance are recognized as the main causes behind changes in the ecosystems in KNP [6,7] conducting to decrease of wetlands by 54% during the last 200 years [8]. KNP with its buffer zone is recognized by UNESCO as Kampinos Forest Biosphere Reserve and is an area of NATURA 2000. The purpose of the ALS data acquiring, was to generate accurate DEM, which will be later used for the hydrodynamic modeling of the reanaturisation works planned to realize within the LIFE+ project *"Kampinos Wetlands"*. We performed analysis for whole KNP area and selected the lower Łasica region for more detailed study.

III. METHODS

A. *Acquisition of the new LiDAR data*

The existing ISOK data has been collected.. In the 21 October of 2014, the new LiDAR data was acquired and analyzed. Aim of the measurements was to acquire whole area within short period of time (one day), while the water level is very low, outside the of vegetation season and with increased accuracy compared to ISOK data. The parameters of new mission (TABLE 1) were discussed according to the aim of scanning, budget, and selected based on the knowledge and experience of the company – responsible for the data acquisition (MGGP Aero sp. z o.o.) and they significantly differ from the ISOK standard. They were two standards of point density – 6 points per sq. m for whole KNP area and 12 points per sq. m for Lower Łasica (Fig 1).

TABLE I. ALS PARAMETERS

Parameters	**ALS collection**	
	ISOK	***"Kampinos Wetlands"***
Field Of View (FOV)	≤ +25º (in forest areas≤ +30º)	30º
Points density	4 pts/sq. m	6 and 12 pts/sq. m
Altitude above ground	900 m	700 m
Flight line overlap	20 – 30 %	50 %
Flight term	October to April (outside the vegetative period) years 2010 – 2012	21 October 2014 (low water states)

*Acquired only for lower Łasica region

B. *Terrestrial Laser Scanning of the tussocks*

First verification issue was to compare point clouds with of the real ground surface. The most difficult places were selected for that – area covered by sedge tussocks. In order to capture tussocks geometry we have chosen five testing fields with area around 25 sq. m (5 x 5m). The areas were chosen based on the tussocks shape, height and how densely they were arranged in the area. Before the measurements it was necessary to clear those areas from vegetation, leaving only tussocks. Collected data was later registered and filtered within Leica Cyclone software using methodology described in [3].

C. GNSS measurements

Second verification issue was comparison of DEM products. In order to compare quality of final DEMs derived from, the GNSS reference point network consists of 6250 points was measured (with 2475 on Lower Łasica region), predominantly in the autumn and winter in years 2014-2015. Two GRS-1 and two GR-3 TOPCON GNSS receivers were used for measurements performing. The geodetic service NAWGEO [9] was used for GNSS data correction in RTN (real time network) VRS (*Virtual Reference Station)* method with use of GPRS modules. In remote area, out of GPRS range we used a single base station (RTK) method with correction via radio. The measurements focused mostly on the areas of wet meadows (sedge, reed) but also forest managed and wild meadows. Locally total station and leveling instrument were used.

D. DEM and point cloud analysis

To estimate the DEM accuracy, the elevation error was calculate as mean error and absolute mean error using the GNSS RTN/RTK reference data. Mean error (ME) is a mean difference between DEM and GNSS reference points. It shows direction of the error (whether elevation values are overestimated - positive value or understated - negative value). Absolute mean error (AME) is an absolute mean difference between DEM and GNSS reference points. It indicates the general accuracy of the models. In order to verify differences between DEMs, differential analysis was performed, using "Kampinos Wetlands" DEM as reference. Aim of this is to capture regions with the greatest difference between both DEMs. Both ALS clouds were compared with TLS cloud as reference using Global Mapper profiling tool.

IV. Results

A. Digital Elevation Model accuracy

Figure 3 Shows error values for the whole KPN area, while Figure 4 shows errors on the Lower Łasica region (where the data were acquired in two densities (6 and 12 pts/sq. m).

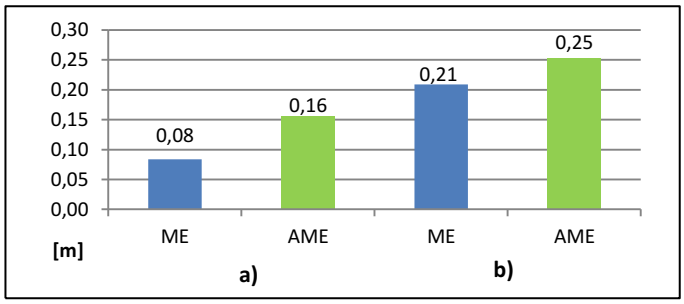


Figure 3. Elevations error of both DEMs, on whole Kampinos National Park. a) Kampinos Wetlands DEM – 6 pts/ sq. m; b) ISOK DEM – 4 pts/ sg.m

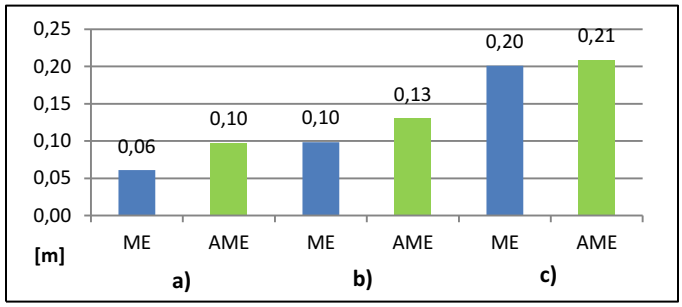


Figure 4. Elevations error of both DEMs, on Lower Łasica Region. a) Kampinos Wetlands DEM – 6 pts/ sq. m;. b) Kampinos Wetlands DEM – 6 pts/ sq. m; c) ISOK DEM – 4 pts/ sq. m.

Results are showing that DEM from "Kampinos Wetlands" data has higher accuracy. It also was observed that the higher point density, generates smaller errors. In order to observe which areas influenced the ISOK DEM accuracy the most, difference between two DEMS was calculated, using "Kampinos Wetlands" DEM as reference. It was observed that areas located near the river are much higher on the ISOK DEM, additionally the ISOK block boundary can be observed, showing that the data due not align with each other (Fig. 5).

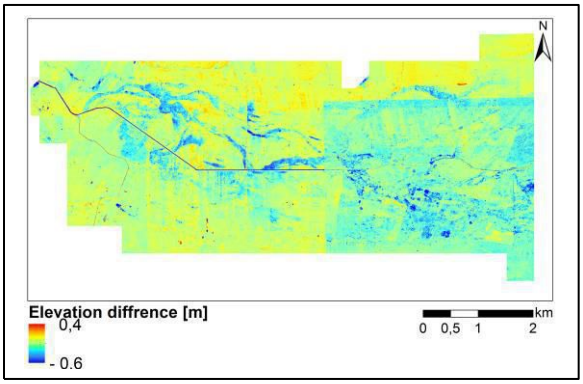
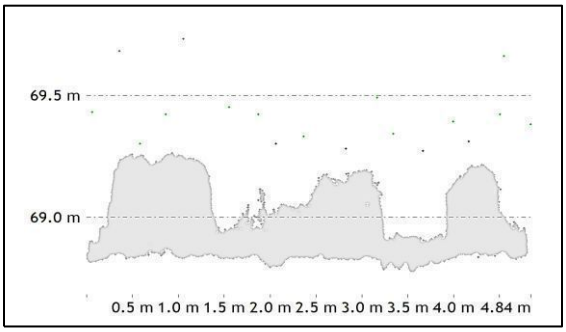


Figure 5. Elevation difference between both DEMs.

B. Tussocks detection and impact on DEM accuracy

The diameter of the tussocks is around 30 - 40 cm and their height from 20 up to 40 cm (depending on the stage of the sedges development). Their size causes difficulties while detecting them by the ALS. We used two types of fields to verify possibilities of detecting them, using ALS, mowed from vegetation and scanned just before ALS measurements (this only applies to "Kampinos Wetlands" data) and mowed after. While ISOK data are well above the ground and tussocks level (Fig. 6). The "Kampinos Wetlands" data points classified as Ground are on the level of tussocks' tips (Fig. 7).



ISOK profile through LiDAR and TLS point clouds, on the measurements field. Points legend: Gray – TLS, Brown – ALS ground, Green – ALS vegetation.

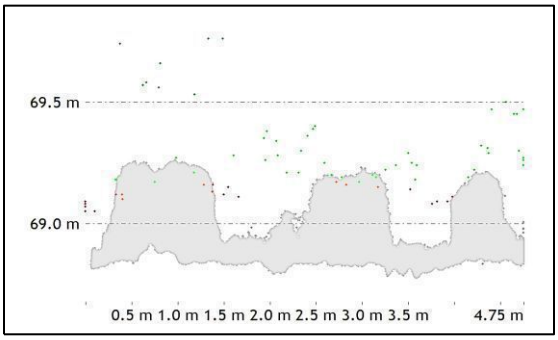


Figure 6. "Kampinos Wetlands" profile through LiDAR and TLS point clouds, on the measurements field. Points legend: Gray – TLS, Brown – ALS ground, Green – ALS vegetation.

Analyzing situation on field mowed before the ALS, the Ground points are on the center level of the tussocks (Fig. 8).

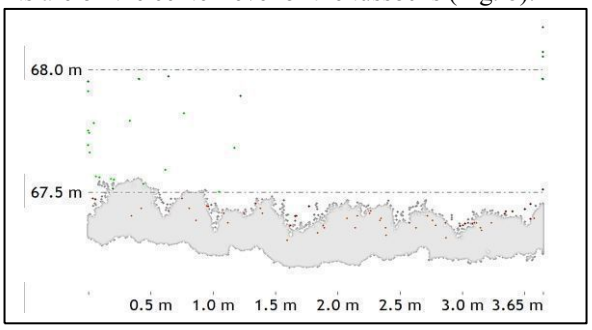


Figure 7. "Kampinos Wetlands" profile through LiDAR and TLS point clouds, on the mowed before flight field. Points legend: Gray – TLS, Brown – ALS ground, Green – ALS vegetation..

V. CONCLUSIONS

In this work we analyzed how accurate DEM derived from ALS is on the natural river valleys. It was observed that higher points density gave better results, this is due to that in dense vegetation it's harder to capture the ground points. Major problems with ISOK data is the date of the ALS mission. The high time gap between blocks affects the quality of data. Another problem is that the data was collected during wet period, which also affects its quality. Correctly selected parameters and appropriate term of the ALS measurements, are key to ensure the highest quality of data. Despite all the benefits that ISOK generated, there will always be the problems like the KNP. That's why it's important to make the necessary preparations of the data because if the errors will be located at this stage, there will be adequate time to eliminate them. This is important when we analyze water management and flood protection.

ACKNOWLEDGMENT

We would like to thank to: Academic circle – "GISowcy" from Warsaw University of Life Scicences for help during measurements and Waldemar Kubisz from Leica Geosystems Poland for the provision of the scanner for the measurements. The research was by the LIFE+ "Kampinos Wetlands" project.

REFERENCES

[1] ISOK – IT System of the Country's Protection. [URL:http://www.isok.gov.pl/en Accessed: 31 March 2015].

[2] Kurczyński,, Z., Stojek E., Cisło-Lesicka U., 2014. "Zadania GUGiK realizowane w ramach projektu ISOK". In: Wężyk P., (Ed.) Podręcznik dla uczestników szkoleń z wykorzystania produktów LiDAR. Warsaw, s. 22 – 5 ISBN: 978-83-254-2090-1

[3] Brach and Chormanski, 2015 Terrestrial Laser Scanning (TLS) as a detection method of the natural river valley microtopography – case study of the Upper Biebrza. Ann. Warsaw Univ. Life Sci. – SGGW, Land Reclam. 46 (4), 267–278

[4] Opdekamp W., Teuchies J., Vrebos D., Chormański J., Schoelynck J., van Diggelen R., Meire P., Struyf E., 2012 Tussocks: Biogenic Silica Hot-Spots in a Riparian Wetland. Wetlands (2012) 32:1115–1124

[5] Krogulec E. (2003) Hydrogeological conditions of the Kampinoski National Park (KNP) region. *Ecohydrology & Hydrobiology*. 3(3): 257-266

[6] Piniewski, M. Gottschalk L., Krasovskaia I., Chormański J. 2012: A GIS-based model for testing effects of restoration measures in wetlands: A case study in the Kampinos National Park, Poland. Ecological Engineering 44 (2012) 25– 35

[7] Kopeć D., Michalska-Hejduk D., Krogulec,E., 2013 The relationship between vegetation and groundwater levels as an indicator of spontaneous wetland restoration Ecological Engineering 57 (2013) 242–251

[8] Gutry-Korycka, M. (2003) Long-term tendencies of water circulation in the protected lowland Łasica river catchment. *Ecohydrology & Hydrobiology*, 3(3): 351-358.

[9] ASG – EUPOS. [URL:http://www.asgeupos.pl/ Accessed: 31 March 2015].

Extracting possible terrace surfaces from digital elevation models – methodological issues and case study from Hungary

Edina Józsa
Doctoral School of Earth Sciences
University of Pécs
Pécs, Hungary
edina.j0zs4@gmail.com

Abstract—**Terraces of the Danube is a mainstream research topic for Hungarian geomorphologists. The research group of Demoulin, A. developed a GIS-based algorithm to extract terrace surfaces, which proved the suitability of automated landform extraction to detect even small terrace remnants [1]. Further improvement of this method was carried out in the form of GIS model tools and R scripts to provide an automated approach to create consistent and repeatable results.**

Issues arising from the methods used for the terrace extraction were analysed using an artificial hillslope model. The effect of erosion processes were imitated by adding Gaussian noise to the data. Besides, the algorithm was tested on a contour-based DEM of the Danube tributaries in the Southeastern-Börzsöny, Northern Hungary, where small terrace remnants were expected.

In the first step the analysed catchment is cut into parallel sections and the relative altitude above streamline is plotted against the filtered slope values of every cell in the section. Afterwards the cells potentially belong to terrace surfaces are selected and the histogram of altitude values is created, also showing the mean slope and standard deviation of slope for every relative elevation value. This diagram helps to define a minimum area threshold and maximum mean slope value for the detection of possible terrace cells. As a final output a plot is created that shows the stream's long profile and marks at altitude of the selected cells and a map containing the terrace remnants cells. Based on these results, with the consideration of the neotectonic processes, it is possible to reconstruct the paleo-profile of the given valley and the terrace top-surfaces.

The biggest challenge of the proposed algorithm is the determination of the thresholds best adapted to the topography and the available DEM of a given study site, therefore further testing is necessary.

REFERENCES

[1] Demoulin, A., B. Bovy, G. Rixhon and Y. Cornet, 2007. "An automated method to extract fluvial terraces from digital elevation models: The Vesdre valley, a case study in eastern Belgium." Geomorphology 91(1–2), 51–64.

In: Geomorphometry for Geosciences, Jasiewicz J., Zwoliński Zb., Mitasova H., Hengl T. (eds), 2015. Adam Mickiewicz University in Poznań - Institute of Geoecology and Geoinformation, International Society for Geomorphometry, Poznań

Water resources assessment using GIS procedures: application in Ceará State (Brazil)

Ângelo Moura Araújo, Paulo Pereira, Renato Henriques, Diamantino Pereira

Institute of Earth Sciences
Pole of the University of Minho
Braga, Portugal
arangeo@gmail.com

Abstract—**A methodological approach and preliminary results on water resources assessment in large areas are described with the case study of Ceará State (Brazil). The methodology includes analysis and interpolation of climatic and hydrological data, Digital Elevation Model (DEM) production and interpretation, and GIS procedures. The present results include the distribution of historical rainfall and fluvial discharges and the definition of a 7-levels river and watershed hierarchy in the Ceará State. The highest rainfall and discharge average values are located in the northeastern sector of the state confirming the important role of climatic features in hydrological diversity. Water resources management must then consider technical tools for water resources assessment, in the line of other methods for quantitative assessment of natural features either biotic or abiotic..**

I. INTRODUCTION

Water must be understood as an environmental and social asset, an economical resource and a matter of extreme importance for all societies. Therefore water management must be handled as a technical subject but also as a political topic once water needs can lead to conflicts and ambitions by different factions evolving priority decisions [1]. Water resources quantitative assessment [2] [3] [4] has a special importance in the scope of the hydrological diversity approach [5]. In spite of being a rather new notion, geodiversity is defined [6] as the natural range (diversity) of geological (rocks, minerals, fossils), geomorphological (landforms, topography, physical processes), soil and hydrological features. It includes their assemblages, structures, systems and contributions to landscape. Water features are then elements of geodiversity being a very important agent in geological and biological processes and evolution. To be accepted as a useful tool, that diversity must be assessed according to objective methodologies in order to be used for nature conservation and land-use planning, as biodiversity currently is [7]. Common geological, geomorphological, soil or hydrographical maps are important in qualitative, but not in quantitative diversity assessment. In addition, as technical documents, they are difficult to read for non-specialists, thus limiting their use in routine planning. In that scope, the first results on the assessment of water resources diversity in the Ceará State (Brazil) are presented. This work followed a methodology based on hydro and climatological data, spatial information and GIS procedures analysis.

II. METHODS

Relevant outcomes [8] [9] [10] [11] on water resources quantification using GIS based procedures were considered in the development of the method for the assessment of the hydrological diversity in the Ceará State. Ceará is one of the 27 states of Brazil, located in the northeastern part of the country, on the Atlantic coast, covering an area of 148,016 km2. With about 8.5 million inhabitants it is the eighth-largest Brazilian State by population. Ceará lies partly upon the northeast slope of the Brazilian Highlands, and partly upon the sandy coastal plain. The rivers of the state are small and, with one or two exceptions, become completely dry in the dry season. The largest is the Jaguaribe River, which flows entirely across the state in a northeast direction. Several data was acquired and a database was created for eventual analysis and processing. The database includes: DEM (Digital Elevation Model) of Ceará State based on the SRTM (Shuttle Radar Topography Mission) 90 metres per pixel resolution and enhanced to 30 metres resolution [12]; rainfall and discharge data (34 years series) in selected locations [13]; spatial information in vector format [14]. Methodological procedures included: statistical analysis of a 30 years sequence rainfall and discharge data and its distribution all over the territory; DEM treatment for automatic fluvial channels, networks and watersheds generation; hierarchy order of fluvial channels according to Strahler model [15]. Microsoft Excel© software was used to perform statistical operations. ESRI ArcGIS© 10.1 version, ESRI Arc Hydro© extension and Quantum GIS© 2.6.1 version software were used in DEM production, water resources analysis and GIS procedures.

A. Fluvial network, channel orders and watershed delimitation

The DEM is a computational representation of the altitude distribution in Ceará State, using a pixel grid with 30 metres of

In: Geomorphometry for Geosciences, Jasiewicz J., Zwoliński Zb., Mitasova H., Hengl T. (eds), 2015. Adam Mickiewicz University in Poznań - Institute of Geoecology and Geoinformation, International Society for Geomorphometry, Poznań

resolution. From it a set of information can be analysed and different maps can be produced: hypsometry (Fig. 1); slopes; aspect; morphological surfaces; hydrography; runoff flow directions. Besides, it is an important tool in erosional patterns, roughness textures and geomorphological analysis, allowing tridimensional visualization of different features [16].

In order to establish the fluvial network definition, the channel order classification and the watersheds delimitation the following tasks were performed using the ESRI Arc Hydro© tool:

1. Assemblage of the mosaic from the original DEM files;

2. Conversions in datum projection (from WGS 84 to SIRGAS 2000 - 24S Zone);

3. Cropping of the DEM mosaic, accordingly to the limits of the Ceará State area.

4. Specific in-software procedures to fluvial network and basins delimitation → Fill Sinks → Flow Direction → Flow Accumulation → Stream Definition → Stream Segmentation → Catchment Grid Delineation → Catchment Polygon Processing → Drainage Line Processing → Adjoin Catchment Processing → Drainage Point Processing → Batch Point Generation → Watershed Delineation → Export shapefile

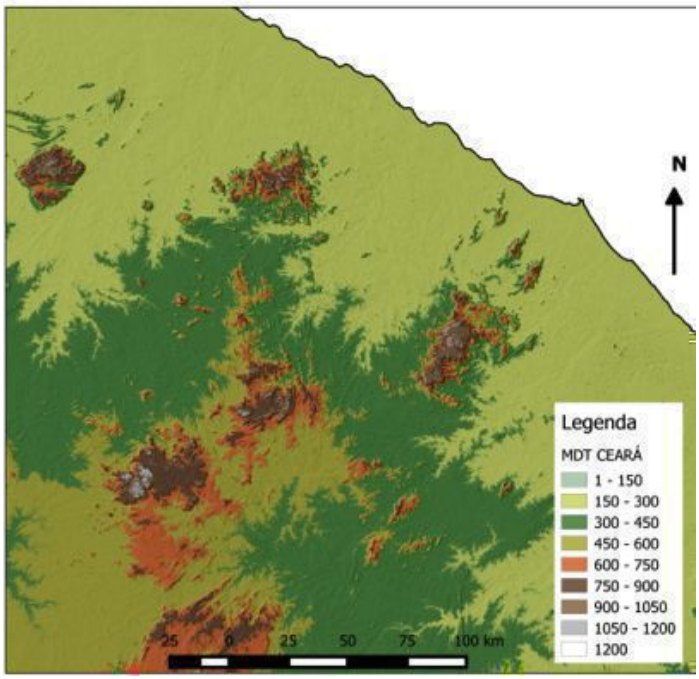


Figure 1. Digital Elevation Model (DEM) with 30 m resolution of the northeastern sector of Ceará State (Brazil).

B. Rainfall and discharge analysis

The climatological and hydrological features regarding the proposed method were handled by the following procedures:

1. Research and acquisition of official rainfall data from 1974 to 2014;

2. Average values for more than 700 precipitation stations, from automatic calculation using Microsoft Excel© software.

3. Exclusion of stations with absent or irregular values and inclusion of stations that have at least 85% of complete rainfall information for the 1974-2014 period;

4. Calculation of discharge historical average values for 69 stations, from the rainfall average values (34 years period and year 2014) and the discharge values of the year 2014;

5. Data exportation to ESRI ArcGIS© and Quantum GIS© software;

6. Interpolation of rainfall (Kriging method) and discharge (Inverse Distance Weighting) values.

III. RESULTS

The processing of values according to the described methodology provided maps with the distribution of historical rainfall (Fig. 2) and fluvial discharges (Fig. 3) in Ceará State.

Seven hierarchy orders (levels) were credited to rivers in result of the DEM analysis. Then, watersheds were classified according to the river hierarchy, and a polygon was produced for each river segment considered in the analysis [17]. Level 1 and level 2 watersheds were excluded to avoid a large number of polygons thus level 3 rivers express the 327 watersheds defined in Ceará State. These are included in 57 level 4, 13 level 5, 3 level 6 and 1 level 7 watersheds.

IV. DISCUSSION

The annual rainfall average values (Fig. 2) in Ceará State range from 284 e 1400 mm, constituting a large disparity (1116 mm) between some regions. The northeastern sector of the state has the highest rainfall values mostly due to the Atlantic influence and the variety of air fronts in different times of the year. The lowest values in the central-western sector (less than 300 mm per year) are related with the local inland atmospheric circulation [18]. These climatic features have an important role in a water resources overview. The river discharge values (Fig. 3) are even more wide-ranging, between 7 m3/s and 12069 m3/s because different types of river were included in the analysis and also regarding the station location, if more upwards or downwards the watershed.

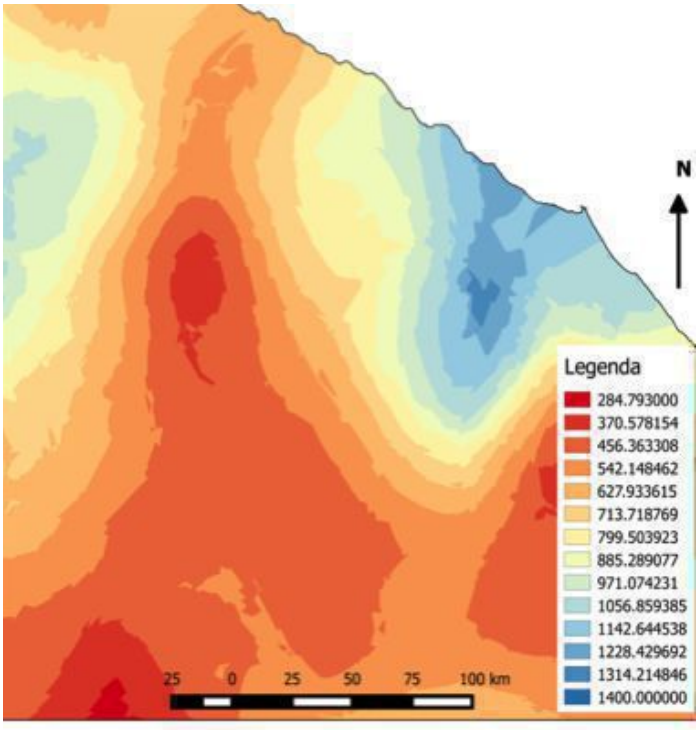


Figure 2. Average values (34 years series) of annual rainfall (in mm) in the northeastern sector of Ceará State (Brazil).

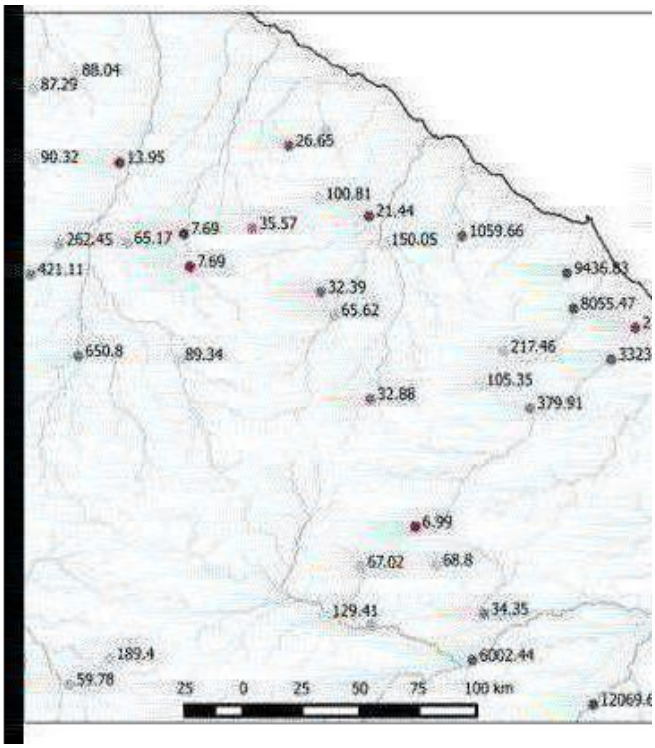


Figure 3. Average values (34 years series) of river discharge (in m3/s) in the northeastern sector of Ceará State (Brazil).

However, considering rivers and watersheds of the same level, the highest discharge values are present in the northeastern sector of the state, combining the influence of the highest rainfall and the specific fluvial dynamics in that region.

These are some preliminary results aiming to quantify the water resources and their distribution in a large region with important within climatic differences. They constitute a basis for the knowledge of regional issues concerning water needs, flood and droughts events and even engineering solutions for water resources management. Although at this point we look forward to discuss and define the best way to represent water resources diversity. The improvement of these preliminary results in a second stage of quantification is expected, using data interpolation techniques and eventually producing a hydrological diversity index and the map of the water resources diversity of the Ceará State.

ACKNOWLEDGMENT

The authors express their gratitude to the Brazilian research fostering institution 'Cordenação de Aperfeiçoamento de Pessoal de Nível Superior' (CAPES) for awarding the Ciência Sem Fronteiras (CSC) PhD scholarship that enabled this work and for the financial support given by the Fundação para a Ciência e a Tecnologia (FCT) to the Institute of Earth Sciences (Pole of the University of Minho), which partially supported this research.

REFERENCES

[1] Abers, R., 2010. "Água e política: atores, instituições e poder nos Organismos Colegiados de Bacia Hidrográfica no Brasil", Annablume, São Paulo, 248 p. (in Portuguese).

[2] Singh, V., and Fevert, D., (2000). "Mathematical models of large watershed hydrology", Water Resources Publications, 914 p.

[3] Mariño, M., and Simonovic, S., 2001. "Integrated Water Resources Management", International Association of Hydrological Sciences Publication nº 22, 74 p.

[4] Yan, D., Wang, H., Li, H., Wang, G., Qin, T., Wang, D., and Wang, L., 2012. "Quantitative analysis on the environmental impact of large-scale

water transfer project on water resource area in a changing environment"., Hydrology and Earth System Sciences, 16: 2685-2702.

[5] Simić, S., 2011. "Hydrological heritage within protection of geodiversity in Serbia - legislation history". Journal of the Geographical Institute Jovan Cvicic, 61(3): 17-32.

[6] Gray M., 2013. "Geodiversity: Valuing and Conserving Abiotic Nature", 2nd Ed., Wiley, 508 p.

[7] Pereira D.I., Pereira P., Brilha J., and Santos L., 2013. "Geodiversity Assessment of Paraná State (Brazil): An Innovative Approach". Environmental Management, 52(3): 541-552.

[8] Chiang, S., Tsay, T., Ni X., and Stephan J., 2002. "Hydrologic regionalization of watersheds. II: applications". Journal of Water Resources Planning and Management, 128(1): 12-20.

[9] Alcamo J., Döll, P., Henrichs, T., Kaspar, F, Lehner, B., Rösch, T, and Siebert, S., 2003. "Development and testing of the WaterGAP 2 global model of water use and availability". Hydrological Sciences Journal, 48(3): 317-337.

[10] Lorandi, R., and Cançado, C., 2002. "Parâmetros físicos para gerenciamento de Bacias Hidrográficas", In Schiavetti A., and Camargo A. (Eds.) "Conceitos de Bacias Hidrográficas: teorias e aplicações, Editus, p. 37-65 (in Portuguese).

[11] Werth, S., and Güntner A., 2010. "Calibration analysis for water storage variability of the global hydrological model WGHM". Hydrology and Earth System Sciences, 14: 59-78.

[12] Miranda, E. (Coord.), 2005. "Brasil em Relevo: monitoramento por Satélite", available in the EMBRAPA website, at http://www.relevobr.cnpm.embrapa.br (in Portuguese).

[13] COGERH, 2015. Precipitation and fluvial discharge data for the Ceará State, available in the Companhia de Gestão dos Recursos Hídricos website, at http://www.hidro.ce.gov.br (in Portuguese).

[14] IBGE, 2015. Digital cartography of the Ceará State, available in the Instituto Brasileiro de Geografia e Estatística website, at http://www.ibge.gov.br (in Portuguese).

[15] Strahler, A., 1957. "Quantitative analysis of watershed geomorphology". Transactions of the American Geophysical Union, 8(6): 913-920.

[16] Araujo, A., and Silva, A., 2011. "Modelagem de áreas de escoamento superficial a partir do Modelo Digital de Terreno". GEOUSP - Espaço e Tempo, 30: 194-204. (in Portuguese).

[17] Oliveira, S., 2008. "Metodologia para delimitação e análise multivariada de atributos morfométricos de bacia de drenagem usando modelo digital de elevação hidrologicamente corrigido". Master Thesis in Geography, University of Brasilia, 74 p. (in Portuguese).

[18] Ferreira, A., and Mello, N., 2005. "Principais sistemas atmosféricos atuantes sobre a região nordeste do Brasil e a influência dos oceanos Pacífico e Atlântico no clima da região". Revista Brasileira de Climatologia, 1(1): 15-28. (in Portuguese).

Assessing contextual information from SRTM data as a basis for classifying landform types. Case study: dune fields

Adriana Sărășan
Department of Geography
West University of Timișoara
Timișoara, Romania
adriana.sarasan@gmail.com

Lucian Drăguț
Department of Geography
West University of Timișoara
Timișoara, Romania
lucian.dragut@fulbrightmail.org

Abstract—**During the recent years landform classification and mapping has been one of the most active areas of geomorphometry. However, there is still a lack of studies approaching the problematic of classifying repeating patterns of landform types by analyzing digital elevation models (DEMs). Therefore, our interest in such methods stems from the need to relate landforms to context. This approach relies on the potential of landscape metrics to evaluate landforms patterns and account for spatial context in geomorphometric analysis, as basis for classifying landform types. The quantification of landscape metrics has been carried out on DEMs, previously discretized through a segmentation process based on the following morphometric variables: elevation, elevation skewness, profile curvature, dissection and surface relief ratio. Each of these variables were classified using an unsupervised algorithm for accomplishing a series of limits imposed by the concept of landscape metrics and further statistical analysis. In order to test the transferability degree of landscape metrics among different dune fields, a set of statistical analyses was carried out. The proposed methodology has been applied via freely available SRTM DSMs in different terms of roughness within the dune fields. The current approach provides a first prospect regarding the usefulness of landscape metrics as land-surface variables. We expect the additional information on pattern and context to be crucial in the ontology of landform types.**

In: Geomorphometry for Geosciences, Jasiewicz J., Zwoliński Zb., Mitasova H., Hengl T. (eds), 2015. Adam Mickiewicz University in Poznań - Institute of Geoecology and Geoinformation, International Society for Geomorphometry, Poznań

The potential accuracy of the survey of landform changes using archival orthophotos: case study of the Białka River valley

Maciej Hajdukiewicz
Department of Geomatics,
Kielce University of Technology
Kielce, Poland
e-mail: mhajdukiewicz@tu.kielce.pl

Abstract. **The orthophotos were prepared from archival aerial photos of the Białka valley taken in 1977, 1981 and 1994. As a part of this process, ground control points were measured with use of a digital orthophotomap with EPSG 2180 georeference system and digital terrain models (DTM), georeferenced in the same way. The accuracy of measurements was verified during aerotriangulation of the photos. To improve the methodology of archival photos orhthorectification, analysis of the accuracy of control points was made, indicating that it depends on the scale, the age and quality of the archival photos and the location of control points. It was found that the control points localized on such objects as pole bases, crossroads (meant as point of crossing of centerlines of roads), corners of buildings and crossings of the borderlines of parcels, provide sufficient accuracy of aerotriangulation and an exterior orientation, due to their unambiguous identification on the archival aerial photos and physical stability over the whole period during which the photogrammetrical flights had been undertaken.**

I. INTRODUCTION

The orthorectification of irregular blocks of aerial photographs was conducted for the study of river channel changes in the Polish Carpathians based on archival cartographic and photogrammetric materials. The selected aerial photos were grouped in time horizons (air raids) from the years 1977–1994, covering the area of the Białka valley from the village of Jurgów to the river mouth to the Dunajec.

It was assumed that only horizontal variability of the river channels would be analyzed. The vertical changes shall be a subject of separate study. Preliminary analysis of the acquired archival photogrammetric materials led to the conclusion that the minimum terrain size of the resolvable detail is about 0.5-1 m and so is the potential accuracy of the surveys to be made on these materials. It was considered as sufficient in geomorphological studies of river channels. Therefore, in the orthorectification process of these materials, two sources of data were provided for gaining control points: a contemporary digital orthophotomap and digital terrain model, both providing sufficient accuracy for the study. As follows from previous experience, accuracy of field survey of control points with a GPS receiver is an order of magnitude greater than the precision of measurement of point location on photogrammetric material [1]. Otherwise, this method causes problems with proper identification of the control point. Proper selection and measurement of ground control points was the crucial issue for the accuracy of the orthorectification. The discussion of this operation with regard to archival aerial photos processing is the purpose of this paper. This work also aims to demonstrate that contemporary digital orthophotomap and DTM are the measuring material that is sufficient to obtain control points for the purpose of photogrammetric studies used in geomorphological research.

II. MATERIAL AND METHODS

The following aerial photos were acquired for the study:

1977 year - 8 pictures at approx. scale 1:20,000,

1981 year - 21 images at approx. scale 1:6000,

1994 year - 6 images at approx. scale 1:30,000.

The material for the survey of control points consisted of: digital orthophotomap of 2009 (pixel size of 0.25 m), Polish state reference system “1992” (EPSG 2180) and digital terrain model (DTM) of 2009 in the form of TIN (triangular irregular network, with linear interpolation of the planes), obtained using

In: Geomorphometry for Geosciences, Jasiewicz J., Zwoliński Zb., Mitasova H., Hengl T. (eds), 2015. Adam Mickiewicz University in Poznań - Institute of Geoecology and Geoinformation, International Society for Geomorphometry, Poznań

stereophotogrammetrical method, georeferenced as described above.

Measurement of the control points comprised:

– identification of the terrain object with suitable properties on orthophotomap and archival aerial image,

– measurement of its horizontal position on orthophotomap (planar coordinates in „1992" reference system) and its altitude on DTM referenced vertically to the geoid GRS 1980,

– measurement of the control point position in the pixel coordinate system of background aerial photo frame.

The remaining part of orthophoto processing methodology is consistent with the methods adopted in Polish state surveying services [2].

Because of the variability of local accuracy of orthophotomap and DTM, it was assumed that the number of control points should be 2-3 times greater than it is necessary to align and orthorectify the block of archival aerial photographs. The control points were measured in the groups of 2-3 points in close proximity. This method helps to maintain proper block alignment accuracy and to eliminate incorrectly measured control points, if necessary. Thus, the local and the average error of control point location (both horizontal and vertical) would be maintained in the previously assumed limits.

The control points were localized on:

– corners of buildings

– intersections of roads, understood as an intersection of their axes

– balk tripoints

– basis of the low voltage net and telephone net poles.

The main condition for each control point was its visibility on the overlapping aerial photographs in the block; another one was their unchanged location in the years 1977–2009. Figure 1 presents an example of a control point located on the basis of a low voltage net pole. In this case, the main condition of accurate location of the point is sun light direction and the presence of the shadow visible on the image of 1981 (Fig. 1A), and the orthophotomap of 2009 (Fig. 1B). Irregular shape of the aerial photo blocks made it difficult to meet these conditions. Therefore, 4 to 5 iterations of the control points selection and the alignment of block images were carried out for each archival aerial photo raid. The results of the survey and alignment were considered acceptable due to the accuracy of the block alignment criterion. It was assumed that an RMS error should be less than the theoretical accuracy of the measurement point on the digital orthophotomap with a pixel size of 0.25 m. According to the accepted standards of measurement accuracy, in this case it is equal to the triple size of a pixel, i.e. 0.75 m [3]. The second criterion is that the measurement deviation should not exceed the measurement accuracy of the source material at individual points. Depending on the results of the alignment, the control points with the highest error were eliminated. Where no good results were obtained with this method, in the next stage new control points were selected, if the former ones appeared to be situated on the objects that might have changed their position.



Figure 1. Example of location of a control point on the low voltage pole basis; A – aerial photo of 1981, B – orthophotomap of 2009.

III. RESULTS AND CONCLUSIONS

The number of control points measured for each air raid was:
year 1977: 20 control points
year 1981: 18 control points
year 1994: 14 control points.
Subsequently, an aerotriangulation and the alignment of the aerial photo blocks were performed. The results of this operation for each of the air raids were as follows:
year 1977 – 1 point rejected, 19 used, the average RMS error: x

0.176 m, y 0.153 m, z 0.139 m;
year 1981 – 1 point rejected, 17 used, the average RMS error: x 0.071 m, y 0.062 m, z 0.048 m;
year 1994 – all the 14 points used, the average RMS error: x 0.009 m, y 0.011 m, z 0.007 m.
The value of residuals at individual control points ranges from 0.01 to 0.5 m (Fig. 2). Most of residuals for individual control points is less than 0.4 m; the largest values are for the 1977 air raid (marked as "77") and the smallest ones for the air raid from 1994 (marked as "94"). It implies that measurement errors were small enough to allow the performance of aerial triangulation of the photos with the previously assumed accuracy. The vertical residuals range from 0.01 to 0.28 m (Fig. 3), and as previously described, ,the largest values of horizontal residuals were found for the 1977 air raid, and the smallest for the 1994 air raid (described as "77", and "94" in Fig. 2), that determines the potential exactness of the stereo digitization accuracy. All these values are less than the previously accepted value of acceptable measurement error. The results of aerotriangulation and the alignment affected the exactness of orthorectification of the images. An average error of translation was less than 0.79 m. Most frequently, in the case of aerial photos of 1977 and 1981, the error was in the range of 0.2-0.3 m; the largest individual values of the error were found for the vertical coordinate in the photo from 1994 raid.

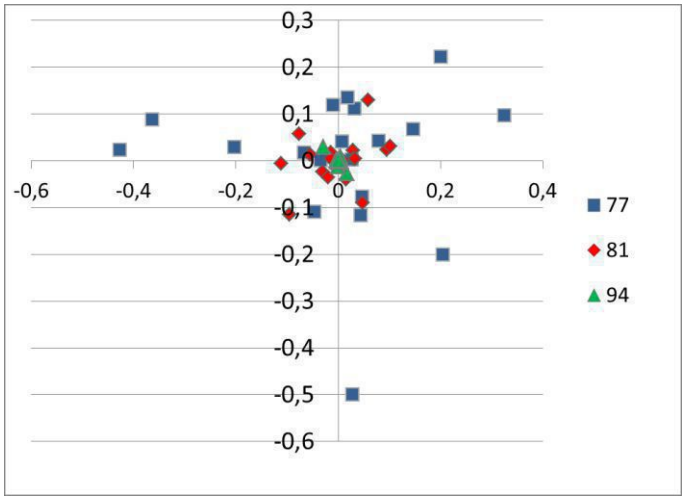


Figure 2. Horizontal dispersion of the residuals of the control points for each air raid. X and Y axis scaled in metres.

The errors were caused by radiometric non-uniformity of the material (photos taken at different parts of the day and at different light), that resulted in the improper identification of the tie points on individual photos. In this case, accurate measurement and alignment of control points allowed to identify and eliminate the tie points with the largest errors.
A strong relationship between the value of the observed error and the age of aerial photos was found. This can be explained by the photographic material distortion that could have occurred during its storage, before scanning, what affected the accuracy of the interior orientation and, consequently, the accuracy of aerotriangulation. Another important factor was the radiometric quality of the material: the best, but not uniform, for the pictures of 1994, significantly worse for those of 1977 and the worst for the images of 1981. In the case of images of 1994, it caused errors at the tie points, described above. In the remaining cases, it made the precise location of control points difficult, which led to a lower accuracy of aerotriangulation.

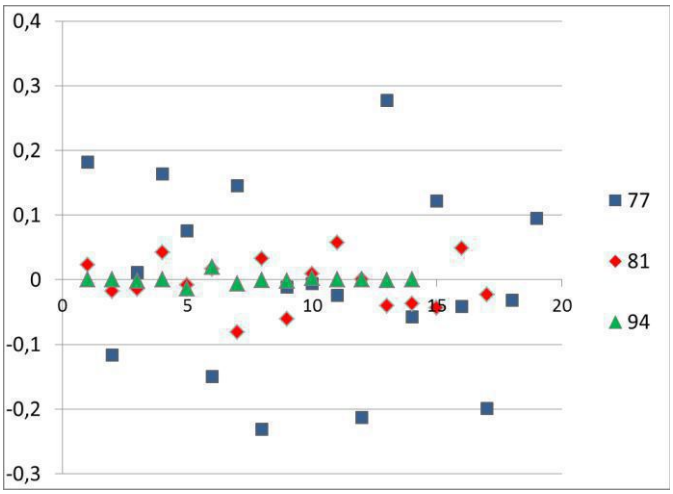


Figure 3. Vertical dispersion of the control points residuals; X axis presents number of the control point, Y axis scaled in metres.

Satisfactory results of aerotriangulation constitute the basic condition for exact measurements of the landform change on the orthophotomap, as well as in three-dimensional technique. They have been the result of careful selection and location of the control points; however, the rejection of some of them was necessary, in a situation where the deviation of measurements at a given point considerably exceeded the acceptable range. Apart from the aforementioned factors, other ones also had an impact on the quality of orthorectification: the changes of the shape of the objects, which were used to locate the control points, and the landform changes, mainly vertical, of the terrain where control points were located. The last mentioned issue, especially if meant to be studied with use of photogrammetrical methods (digitization on the stereopair of archival aerial photos), is so far

insufficiently recognized in Poland. The improvement of the methods of orthorectification of the archival aerial photos gives an opportunity to expand the research in this area.

ACKNOWLEDGMENT

This study was performed within the scope of the Research Project DEC-2013/09/B/ST10/00056 financed by the National Science Centre of Poland.

REFERENCES

[1] Boroń, A. and Borowiec, M., 2003, „Aerotriangulacja archiwalnego, nieregularnego bloku zdjęć zalesionych terenów górskich", Archiwum Fotogrametrii, Kartografii i Teledetekcji, 13 B, 315-324.

[2] Michałowska, K., Głowienka, E. and Mikrut, S., 2007. Opracowanie technologii przetwarzania archiwalnych materiałów fotogrametrycznych do badań zmienności krajobrazu na przykładzie Słowińskiego Parku Narodowego. Archiwum Fotogrametrii, Kartografii i Teledetekcji, 17B, 495-504.

[3] GUGiK, 1999. K-2.7-Zasady wykonywania prac fotolotniczych. Wytyczne techniczne, Warszawa.

Identification and morphometric properties of landslides in the Bystrzyckie Mountains (Sudetes, SW Poland) based on data derived from airborne LiDAR

Milena Różycka, Aleksandra Michniewicz, Piotr Migoń, Marek Kasprzak
Institute of Geography and Regional Development
University of Wrocław
Wrocław, Poland
milena.rozycka@uni.wroc.pl; aleksandra.michniewicz@uni.wroc.pl; piotr.migon@uni.wroc.pl; marek.kasprzak@uni.wroc.pl

Abstract—**Geomorphometric indices are used to characterize a group of recently recognized landslides in the Bystrzyckie Mts (SW Poland). LiDAR DEM was the primary data source. Geomorphometric approach helped to differentiate landslides in terms of form which likely reflects different mechanisms of movement. Topographic Wetness Index highlights drainage patterns within the landslides and emphasizes differences between slopes affected and not affected by landslides.**

I. Introduction

LiDAR-based Digital Elevation Models (DEMs) are powerful tools in landslide recognition, especially in vegetated areas with otherwise obscured local geomorphological features. They are also very useful in morphometric description of landslide terrains, which enables to express landform features quantitatively, helps landslide classification, and fosters comparative analysis. These high-resolution airborne spatial data have been recently made available in Poland, opening new perspectives for landform recognition and their quantitative characterization. In the Sudetes (SW Poland) screening of DEMs derived from LiDAR data has revealed, among others, an existence of a large number of relict landslides which so far have largely escaped attention during field mapping. In this contribution we apply selected geomorphometric indices for a group of newly recognized landslides in the block-faulted massif of the Bystrzyckie Mountains, Middle Sudetes.

II. Landslide occurrence and morphology

Three landslide affected terrains have been investigated in the Bystrzyckie Mountains (Fig. 1). Two of them (below Mt Jagodna and Mt Toczek) occur within the mountain fronts developed along fault zones that separate the western part of the Orlica – Śnieżnik Dome, which is built by crystalline rocks, from the Upper Nysa Kłodzka Graben filled with sedimentary rocks. The third landslide (at Mt Złota) is located within a complex fault-generated escarpment that bounds the Bystrzyckie Mountains

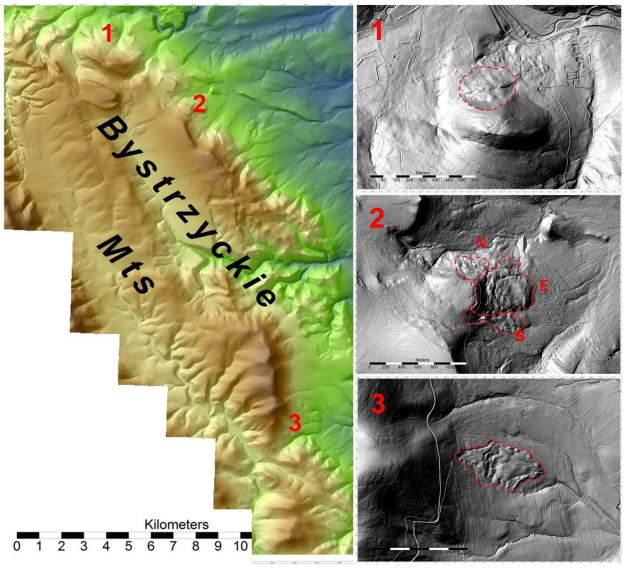


Figure 1. Location map of landslide terrains in the Bystrzyckie Mountains (1 – Złota, 2 – Toczek, 3 – Jagodna). Landslide extent indicated by dashed red lines.

In: Geomorphometry for Geosciences, Jasiewicz J., Zwoliński Zb., Mitasova H., Hengl T. (eds), 2015. Adam Mickiewicz University in Poznań - Institute of Geoecology and Geoinformation, International Society for Geomorphometry, Poznań

from the north. These landslides have been identified for the first time through detailed analysis of LiDAR-based digital elevation models and only one of them (Jagodna) has been briefly mentioned by Ranoszek [1], but whitout either boundary delimitation or more through analysis of landslide terrain.

The Jagodna landslide occurred within the lower section of the escarpment, genetically connected with the Kamieńczyk-Jagodna Fault and underlain by Cretaceous clastic deposits of Upper Nysa Kłodzka Graben in the zone of their flexural bending [1]. Kozdrój [2] mapped the position of the landslide on the Detailed Geologic Map of the Sudetes, sheet Poręba, indicating its partial fluvial dissection by streams fed from springs located in the fault zone. Landform inventory suggests that the slide was rather shallow and may have turned into mudflow in the distal part.

The second area with distinct geomorphic signatures of landslide activity is located on the northeastern edge of the Toczek plateau spur (753 m a.s.l.), whose eastern part is cut by the Długopole-Paszków Fault – a structure responsible for the origin of the Długopole Dolne-Polanica faulted escarpment. It likely consists of two separate landslides, with head scarps perpendicular to each other, that re-moulded morphology of the northern and eastern sides of the spur. In addition, surface morphology suggests the presence of a third landslide further to the south which travelled down a pre-existing valley. Upper Cretaceous jointed quartz sandstones are exposed in the main scarps of both landslides. Above the eastern head scarp a series of trenches occurs, indicating ongoing, probably deep-seated deformation of the rock mass. A LiDAR-based DEM reveals complex morphology of the slide area, with a range of second-order bulges, benches, linear depressions, and superimposed bodies in the toe area. Hence, the presence of a compound landslide may be inferred or alternatively, multiple phases of activity.

The third landslide occurs on the northern slopes of the Złota massif (635 m a.s.l.). Similarly to the previous case, jointed quartz sandstones, which build the upper part slope, have been moved downslope toward valley bottom of the Bystrzyca Dusznicka River. Landform pattern suggests rotational displacement of a single block.

III. Geomorphometry of landslide terrains

Morphometric characteristics of landslides have been measured directly from DEM or calculated from other parameters. They include: landslide area (A), maximum length (L), horizontal length (L_h), maximum width (W), L/W ratio, maximum height above sea level (H_{max}), minimum height above sea level (H_{min}), vertical range ($H = H_{max} - H_{min}$), slope (S), aspect (A), travel angle (α), main scarp height (h), main scarp slope (s), Topographic Wetness Index range ($TWI_{max} – TWI_{min}$) (Table I).

The Toczek landslide complex is characterized by the largest area among the landslides presented here. It reaches approximately 0.65 km^2 in total, but can be split into three separate landslides one next to another (“northern”, “eastern” and “southern”), referred to as Toczek N, Toczek E and Toczek S from now on. Toczek E has the largest extent, about 0.43 km^2, which is the value far exceeding the area of other landslides, not only from the other parts of the Toczek complex (Toczek N – 0.10 km^2) and (Toczek S – 0.12 km^2), but also from the other parts of the Bystrzyckie Mountains – Jagodna (0.28 km^2) and Złota (0.04 km^2).

The landslides vary in terms of the maximum length and variation in this parameter appears to reflect the type of surface displacement. The longest feature (Jagodna, 917 m) represents a shallow translational slide and is more than five times longer than the shortest one (Złota, 178 m) recognized as a rotational slide. The L/W ratio further differentiates the landslides into three categories, likely corresponding with the type of movement. Jagodna and Toczek S have this index above 1.5 and both show features compatible with slides turning into flows. Values close to 1 characterize compound landslides at Toczek (N and E), while the rotational Złota slide has the L/W ratio close to 0.5.

Vertical range, defined as the difference between the most and least elevated spot within the landslide, varies from 80 m (Złota) to 182 m (Toczek E) and influences the travel angle value (α). This parameter is based on the landslide vertical range (H) and horizontal length (L_h) ($\alpha=\arctan(H/L_h)$) and can be used as an indicator of landslide mobility and the volume of displaced material [3, 4]. Because decreasing value of the travel angle is connected with an increasing volume of mass movement, this parameter suggests that the largest volume of displaced material typifies the Jagodna landslide ($\alpha = 8.8°$), whereas the smallest volume would have been involved in the Złota rotational landslide ($\alpha = 26.7°$). Assuming the average thickness of the Jagodna landslide body for 5 m, as suggested by landslide body cross-sections, the total volume displaced would be c. 1.4×10^6 m^3 of material. The depositional part of the Złota landslide (3/4 of the total area) has an average thickness of 10 m, hence the total volume involved is c. 0.37×10^6 m^3.

The height of the head scarp of the landslides computed from DEMs ranges from 13 m (Jagodna) to 32 m (Toczek E), whereas their inclination are from 30° (Jagodna) to 39° (Złota). It was difficult to delineate the head scarp of the Toczek S landslide and the very indistinct slope steepening in the valley head suggests a shallow translational movement in the first stage of activity.

Landslides of this sort, with obscured source areas but evident depositional parts are not uncommon in the Sudetes [5,6]. The varied morphology of the head scarp of the Jagodna landslide contrasts with the other ones, which are characterized by scarps with rather low sinuosity.

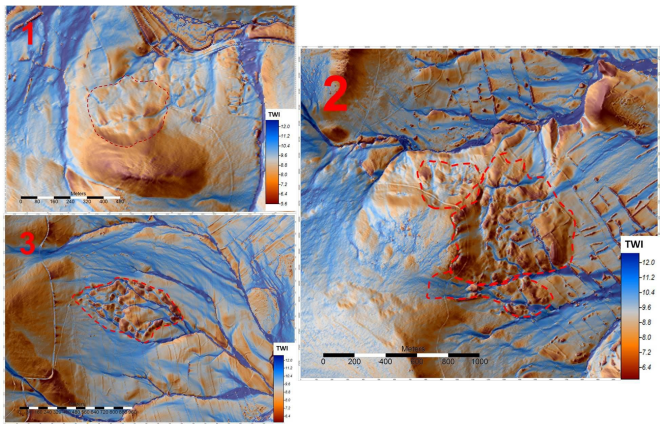


Figure 2. Map of Topographic Wetness Index of investigated landslide terrains derived using SAGA GIS software (1 – Złota, 2 – Toczek, 3 – Jagodna).

The presence of landslides is highlighted by the TWI (Topographic Wetness Index) (Fig. 2). Slopes affected by landslides are characterized by contrasting TWI values because of the varied morphology of the respective landslide bodies (low values assigned to the bulges and high to linear depressions). This is most evident in the case of Jagodna and Toczek E landslides. The differences between the maximum and minimum TWI values (dimensionless) assigned to grids within the perimeter of these landslides attain 20.0 and 19.3, respectively. TWI values on the adjacent parts of the slopes, whose morphology has not been affected by landsliding, are generally lower and in each case less diverse in space.

There are some similarities in theoretical water flow pattern between landslides of similar type. TWI images of simple (Złota) and compound (Toczek N and Toczek E) rotational landslides indicate linear outflow parallel to the main scarps. On the surface of the Toczek E landslide three zones of higher TWI values correspond to the linear depressions between rotated blocks, whilst there is only one such zone within the Złota landslide. In the other two landslides (Jagodna and Toczek S) preferential surface drainage is straight downslope, along the margins of the failed mass or within it.

IV. Final remarks

Landslide geomorphometry presented here helped to characterize surface morphology in more objectively way and proved a good tool to provisionally distinguish landslides of different types. However, this is a pilot study which will be extended in the future. Further research, apart from field work, will be aimed at more detailed quantitative description of particular landforms within the landslides and exploration of differences between slopes affected and not affected by large-scale mass movements. Comparative analysis with landslide populations from elsewhere in the Sudetes [5] will also be attempted.

TABLE I. Morphometric characteristics of landslides in the Bystrzyckie Mountains.

Morphometric characteristics	Landslide				
	Złota	***Toczek N***	***Toczek E***	***Toczek S***	***Jagodna***
area (A) [km^2]	0.04	0.10	0.43	0.12	0.28
max. length (L) [m]	178	334	752	758	917
horizontal length (L_h) [m]	159	313	730	744	906
max. width (W) [m]	308	418	755	266	473
L/W ratio	0.58	0.80	1.00	2.85	1.94
max. height a.s.l. (H_{max}) [m]	593	686	714	716	630
min. height a.s.l. (H_{min}) [m]	513	571	532	570	490
vertical range (H) [m]	80	115	182	146	140
slope (S) [°]	23.4	19.2	13.9	13.4	9.9
travel angle (α) [°]	26.7	20.2	14.0	11.1	8.8
main scarp height (h) [m]	28	32	23	*	13
main scarp slope (s) [°]	39	36	35	*	30
$TWI_{max} - TWI_{min}$	17.7	18.3	19.3	18.3	20.0

* head scarp difficult to delineate

References

[1] Ranoszek, W., 1998. "Morfologia progów tektonicznych obramowujących Rów Górnej Nysy", Acta Universitatis Wratislaviensis, 2061, Prace Instytutu Geograficznego, A9, 23-36.

[2] Kozdrój, W., 1990. Szczegółowa mapa geologiczna Sudetów 1:25 000, arkusz Poręba, Państwowy Instytut Geologiczny, Warszawa.

[3] Hutchinson, J. N., 1988. "General Report: Morphological and geotechnical parameters of landslides in relation to geology and hydrogeology" In

Proceedings of the Fifth International Symposium on Landslides, Edited by: Bonnard, C., Balkema, Rotterdam, 3-35.

[4] Dewitte, O., and A. Demoulin, 2005. "Morphometry and kinematics of landslides inferred from precise DTMs in West Belgium", Natural Hazards and Earth System Sciences, 5(2), 259-265.

[5] Migoń, P., K. Jancewicz, and M. Kasprzak, 2014. „Zasięg obszarów objętych osuwiskami w Górach Kamiennych (Sudety Środkowe) – porównanie map geologicznych i cyfrowego modelu wysokości z danych LiDAR", Przegląd Geologiczny, 62(9), 463-471.

[6] Migoń, P., A. Kacprzak, I. Malik, M. Kasprzak, P. Owczarek, M. Wistuba, and T. Pánek, 2014. „Geomorphological, pedological and dendrochronological signatures of a relict landslide terrain, Mt Garbatka (Kamienne Mts), SW Poland", Geomorphology, 219, 213-231.

Geomorphometric attributes of channel heads initiated by seepage erosion in a postglacial zone (NW Poland)

Małgorzata Mazurek
Institute of Geoecology and Geoinformation
Adam Mickiewicz University in Poznań
Poland
gmazurek@amu.edu.pl

Abstract—**Channel initiation, which is a key factor in the evolution of landforms, is caused by a combination of various hydrogeomorphic processes. This study supplies quantitative data about the size of channel heads driven mostly by groundwater seepage in lowland areas. The chief aims of the present paper is to examine the geometry and morphometry of channel heads in NW Poland and identify the nature of the erosional effect of groundwater outflows. Detailed topographic studies were conducted in selected 24 channel heads (in the form of headwater alcoves) judged to be representative in hydrogeomorphological terms in the southern part of the Parsęta catchment (NW Poland). Morphometric surveying of headwater zones made it possible to identify morphological effects of groundwater seepage erosion in a postglacial landscape.**

Headwater alcoves of various forms are often distinctive features of the postglacial relief of the Parsęta catchment. Those predominating in the study area are compact landforms, semi-circular and narrowing, or paraboloidal, elongated in outline, as evidenced by the low values of the indices of form Cf and circularity Ck as well as the elongation index Cw. A small proportion of headwater alcoves located in scarps are complex, composed of several alcoves combined by a common outflow. The elongation is primarily due to backward erosion along the long axis of an alcove, but in favourable morphological conditions it may have been predetermined by the shape of the initial forms. The scarps closing alcove heads can reach heights of more than ten metres. The transition of alcove slopes into a flat bottom takes place via a clearly marked segment of a concave slope. The diversity of channel head morphology is related to the areal extent of the contributing area, structural or lithological variability which locally increases hydraulic conductivity, and the character and discharge of groundwater outflows.

I. INTRODUCTION

The channel initiation mechanisms are closely connected with the water flowpath characteristics of the slope system. In the lowland area of central Europe with its high sediment infiltration capacity, groundwater seepage erosion can be the primary mechanism that controls channel initiation (e.g. [3], [11]) and the development of a valley head (e.g. [1]). Within zones of groundwater emergence, the combined action of groundwater, water flowing at the surface and mass movement leads to the development of channel heads in form of headwater alcoves. Lack of data on the geomorphometry of channel heads makes it impossible to identify the nature of the erosional effect of groundwater outflows and their contribution to the formation of river valleys. Still, groundwater outflows are not fully appreciated as a morphogenetic factor in temperate zones [9] due to climate fluctuations and changes in land cover that result in lowering of the groundwater table, which diminishes the significance of this erosional factor and weakens the coupling between the outflows and the erosional landforms associated with them.

The objective of the present paper is to examine the geometry and morphometry of channel heads in the southern part of the Parsęta drainage basin (NW Poland) (Fig. 1A). The determination of the place and formation of the beginning of a river channel initiated by groundwater outflows is of key importance for the modelling of the stream network development. Detailed topographic studies were conducted in selected 24 channel heads (Fig. 1B) judged to be representative in hydrogeomorphological terms.

In: Geomorphometry for Geosciences, Jasiewicz J., Zwoliński Zb., Mitasova H., Hengl T. (eds), 2015. Adam Mickiewicz University in Poznań - Institute of Geoecology and Geoinformation, International Society for Geomorphometry, Poznań

II. STUDY AREA

The study area comprises the southern part of the Parsęta catchment, which covers an area of 617.2 km^2 and is situated in the borderland between the South Baltic Lakeland and the South Baltic Coastal Lowland. In the Parsęta basin's geological structure, a fundamental role is played by the complex of 52- to 214-m-thick Pleistocene and Holocene deposits, which comprise five and locally six levels of tills, glaciofluvial sands and gravels, river sands, and ice-dam silts and sands [11]. Channel heads develop within a variety of landforms, e.g. on scarps of morainic uplands, slopes of subglacial tunnel valleys, kettle-holes and river terraces, and slopes of kame hummocks and dead-ice moraines. The diversity of hydrogeological conditions results in various types of outflows, which largely occur in the contact zones between glaciofluvial or fluvial sand-gravel deposits, glacial sands or erosion pavement, and their underlying semi-permeable tills or poorly permeable loamy sands. As to the location of the outflows in terms of relief morphology, they can be found along the entire length of alcove slopes or can be concentrated at the base of steep slopes.

III. METHODS

The small size of headwater alcoves found on the Polish Plain makes it impossible to derive their morphometric characteristics on the basis of topographic maps. Exact topographic measurements were taken using a combined method employing a GPS receiver Leica SR530 and a total station ELTA R55w. The ordinary kriging method was employed to perform interpolation in DEM grid of 0.5 m-resolution. The morphometric analysis was conducted for 24 channel heads (Fig. 1B) on the basis of a digital elevation model. The physical-geographic characteristics employed in the description of the geometry (e.g. shape index Cf, circularity index Ck, elongation index Cw, etc.), morphometry and relief of a headwater alcove are those used both in the morphometric analysis of river catchments ([2], [4], [7], [13]) and individual landforms, like gullies, landslides, glacial cirques, or atolls ([5], [6], [8]).

IV. RESULTS

The field investigations and Geographic Information Systems analysis carried out so far have supplied quantitative data about the size of headwater alcoves developing in lowland areas in loose postglacial deposits. They are compact landforms, poorly branched, semi-circular or elongated in outline. The headwater alcoves within which tachymetric measurements were taken have small bottom areas averaging 516 m^2 (70-4626 m^2). The maximum length of an alcove bottom range from 13.5 m to 112.3 m, with an average of 35 m. The maximum width of the alcove bottom perpendicular to the length varies between 4.6 m and 63.5 m, with an average of 18.3 m. The maximum length/maximum width ratios remain greater than 1 and average 2.3, which shows that at the sites under study alcove bottoms are generally elongated (the elongation index Cw=0.61 on average) and narrow. However, the elongation cannot be treated only as a result of the seepage erosion of their heads as the predominant process. In the three forms under study, the high L/W figures, reflect the elongation of older forms variously modified by seepage erosion. The lowest indices of form Cf and circularity Ck are displayed by channel heads developing within older, inherited landforms: gullies and denudation-erosional valleys.

The scarps closing alcove heads can reach heights of more than ten metres. The height of the slope Hs closing the channel head is defined as the difference in the altitude of the first break of slope and the flattening at its foot passing into the bottom. The height of the steps and headwalls closing Hs measures from 0.7 m to 10.0 m. The mean gradients of concave and concave-convex slopes assume from 12 to 38°, their range being smaller within alcove bottoms, from 3 to 16°. The transition of alcove slopes into a flat bottom takes place via a clearly marked segment of a concave slope (Fig. 1C). The formation of the footslope is an effect of the direct impact of headwater erosion on the alcove slopes. The transition of the slopes into a headwater zone bottom with a considerably smaller gradient is effected through a short length of a concave foot slope. The ratio of the gradient of the bottom Sb to that of the head wall Ss [8] reflects the nature of contact of the slope system with the channel system. The ratio varies from 0.03 to 0.42, which indicates that the beginning of a channel is marked with an abrupt change of slope, thus making it fairly easy to identify a bottom with a much gentler gradient.

Digital elevation models (DEMs) with a horizontal resolution of 0.5 m and the morphometric parameters of headwater alcoves they yielded, as well as an analysis of their topographic and hydrogeological location and the nature of groundwater outflows, provided a basis for distinguishing three morphological types of headwater alcoves in the southern part of the Parsęta catchment [11]:

1. The most numerous group embraces basin-like alcoves. This type (I) includes landforms with bottoms elliptic in plan, small and compact, displaying the widest differences in extreme heights.
2. The next type (II) of bowl-like headwater alcoves covers extensive alcoves or their complexes, with maximum length and width figures as well as broad bottoms with low slopes (Fig. 1C).
3. Type III includes spindle-like alcoves, small, elongated and narrow. Here belong largely alcoves located in older denudational depressions and erosional-denudational dissections and small valleys whose bottoms and slopes are

now being modified by headwater processes. They display wide differences in height and considerable slope gradients. The channel head is closed by a low step resulting from the dissection of the bottom of the initial forms due to erosion by groundwater outflows. The morphometry of the group of elongated and narrow alcoves in the southern part of the Parsęta catchment is similar to the landforms in the Łódź Hills (Central Poland), which were examined by [12]. Their common morphological features result, among other things, from the similarity in the geological structure (glacial sands and tills, fluvioglacial sands) and hence from the groundwater flow conditions and outflow type.

There are a few alcoves that do not fall into any of the three morphological types distinguished: poorly developed, in the initial stage of formation, of slight depth, and with no clearly marked bottom. This type is characteristic of young alcoves with low-discharge outflows in their area.

V. Conclusion

Channel heads determined by groundwater outflows that assume the form of an alcove or a set of alcoves develop within hollows of varying genesis or dissect slopes to form their own headwater depressions (i.e. valley heads). The variability of parameters describing channel heads reflects the original relief, which can be regarded as a factor partially accounting for the shape of the channel heads and a factor conducive to the location of groundwater outflows and seepage erosion. The lithology and stratigraphy of Pleistocene and Holocene deposits in the study area control the shape, orientation and size of the alcoves ([10] and [11]).

The formation of channel heads is an effect of co-operation and interaction of such influences as seepage erosion, slope processes, and fluvial accumulation and erosion. Depending on headward erosion, gravitational mass movements, and the possibility of deposits being removed by water, the alcoves grow in width and depth. Such a pattern of processes leads to the formation of steeply inclined alcove slopes with a distinct concave section at the foot that passes into a flat bottom. The rate of alcove development is fast if groundwater outflows are able to remove all the gathering colluvial material and other debris from the foot of the slopes. Values of the morphometric parameters and indicators show an increase in height differences and elongation of the alcoves, which may be associated with the rejuvenation of the relief of scarps and slopes in postglacial areas. The characteristics of channel heads as described in physical-geographic terms as well as deposits found in them (peats, calcareous sinter) can be helpful in, e.g., reconstructing of changes in the groundwater table, interpretating of stages in their development.

Acknowledgment

The presented study is part of a wider research completed in the Institute of Geoecology and Geoinformation. The author would like to thank all those who helped her during field survey, and the reviewers for valuable comments.

References

[1] Ahnert, F., 1998. “Introduction to geomorphology”, Arnold, London, 352 p.

[2] De Scally, F., Slaymaker, O., and I. Owens, 2001. “Morphometric controls and basin response in the Cascade Mountains”, Geografiska Annaler 83, A 3: 117-130.

[3] De Vries, J. J., 1976. “The groundwater outcrop-erosion model; evolution of the stream network in the Netherlands”, Journal of Hydrology 29: 43-50.

[4] Engstrom, W. N., 1989. “Morphometric analysis of mountain drainage basins in the Basin and Range Province, USA”, Zeitschrift fűr Geomorphologie 33, 4: 443-453.

[5] Federici, S. R., and M. Spagnolo, 2004: “Morphometric analysis on the size, shape and areal distribution of glacial cirques in the Maritime Alps (Western French-Italian Alps)”, Geografiska Annaler 86 A, 3: 235-248.

[6] Garcia-Ruiz, J., Gomez-Villar, A., Ortigosa, L., and C. Marti-Bono, 2000. “Morphometry of glacial cirques in the Central Spanish Pyrenees”, Geografiska Annaler 82 A, 4: 433-442.

[7] Gregory K.J., and D.E. Walling, 1973. “Drainage basin: Form and processes”, Edward Arnold, London, 458 p.

[8] Hattanji, T., and Y. Matsushi, 2006. “Effect of runoff processes on channel initiation: comparison of four forested mountains in Japan”, Transactions, Japanese Geomorphological Union 27: 319-336.

[9] Higgins, C. G., 1984. “Piping and sapping: Development of landforms by groundwater outflow”. In Groundwater as a geomorphic agent, Edited by: LaFluer, R. G., Allen & Unwin, Boston: 18-58.

[10] Mazurek, M. , 2006. “Morphometric differences in channel heads in a postglacial zone (Parseta catchment, West Pomerania)”, Questiones Geographicae 25A: 39-47.

[11] Mazurek, M., 2010. “Hydrogeomorfologia obszarów źródliskowych (dorzecze Parsęty, Polska NW)” (in Polish, with English summary), Seria Geografia 92, Wyd. Naukowe UAM, Poznań, 308 p.

[12] Moniewski, P., 2004. “Źródła okolic Łodzi” (in Polish, with English summary), Acta Geographica Lodziensia 87, 140 p.

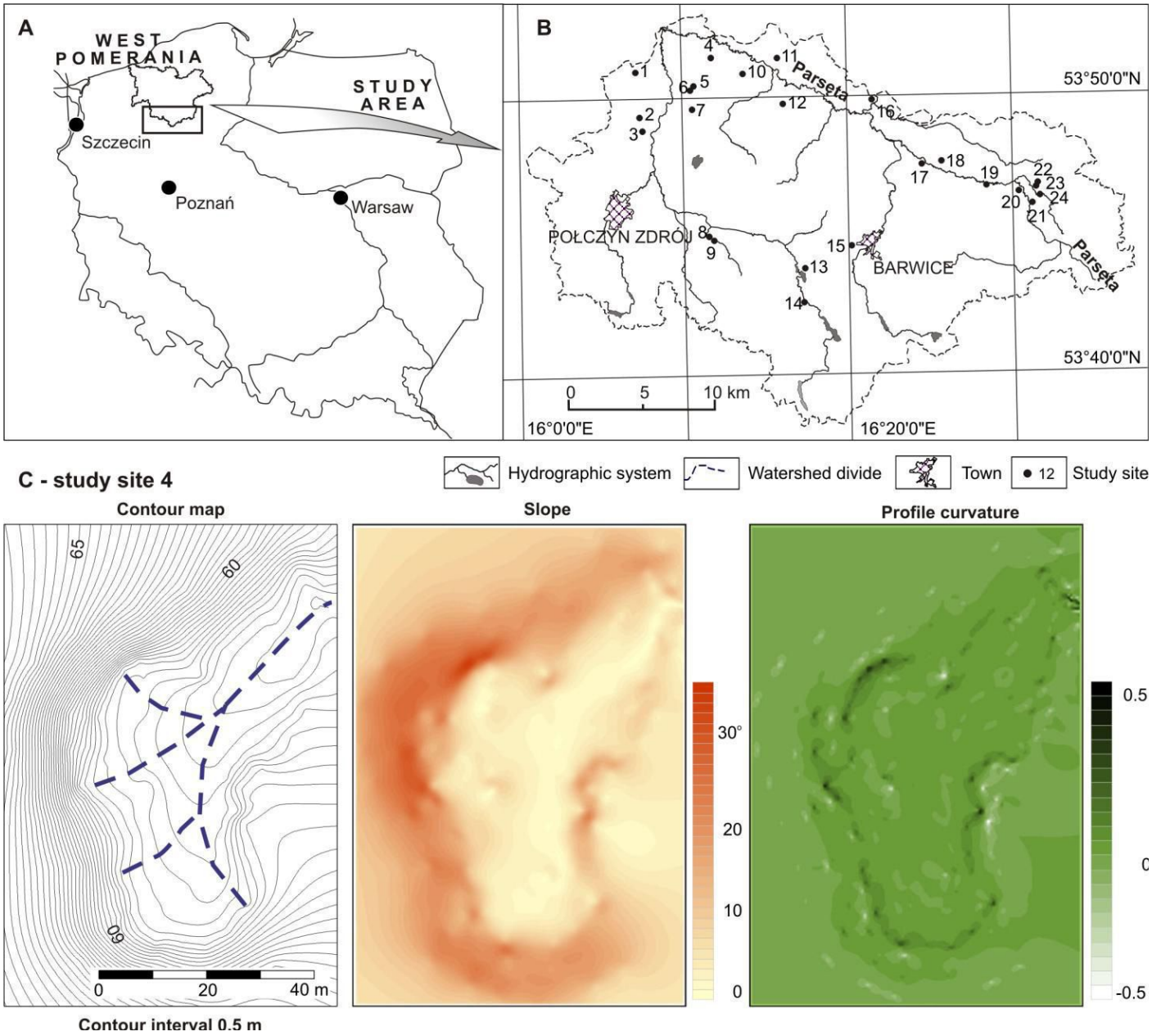


Figure 1. Location of: A. study area, B. study sites in the southern part of the Parsęta catchment; C. study site 4: contour map with hydrographic elements, slope and profile curvature

Understanding large wood deposition during floods: a modelling approach

Ruiz-Villanueva, V., Stoffel, M.

Institute of Geological Sciences
University of Bern
Bern, Switzerland
virginia.ruiz@dendrolab.ch

Hajdukiewicz H., Wyżga, B.

Institute of Nature Conservation
Polish Academy of Sciences
Kraków, Poland
hanahaj@gmail.com

Abstract— **The aim of this contribution is to improve the knowledge about factors controlling large wood deposition in the Czarny Dunajec River in Poland, combining direct field observations, a 2D numerical modelling approach and GIS. Numerical modelling is a powerful tool to analyse different aspects that govern wood deposition, because models can be used to run scenarios and can be analysed fully at any space and time. We used a numerical model to simulate different flood magnitude events and to analyse wood deposition in two different river reaches. Preliminary results gave information about sites of preferential wood deposition, wood retention capacity and relationships with the river morphology. We found contrasting patterns regarding wood retention capacity in the single-thread and the multi-thread channels. We observed that the deposition of wood is not static but dynamic and significantly depends on the hydrological regime. The importance of flow depth in particular is confirmed by the fact that the elevation of deposited logs is strongly linked to the water level. Therefore, flood magnitude is the main factor controlling wood deposition.**

I. INTRODUCTION

Analysis of wood deposition in rivers has shown that complex river morphology and flow patterns play a crucial role in determining potential sites of wood retention [1]. Besides other parameters influencing wood distribution along the channels such as recruitment processes, forest stand and age and forest and river management, geomorphology is a major control on the distribution of large wood in rivers [2]. Flood frequency and magnitude are also significant factors influencing the distribution of large wood in rivers [3].

Nowadays there are still few direct observations of wood transport and deposition [4]. It is even more difficult to obtain data after several floods of different magnitude, with very few cases of data after extreme flood events [5].

Where retained, wood creates and induces a variety of landforms enhancing the complexity of the physical habitat of fluvial systems [1]. Thus we still need to better understand the spatial patterns of large wood distribution and the controls on these patterns.

The aim of this contribution is to improve the knowledge about factors controlling large wood deposition in the Czarny Dunajec River in Poland, combining direct field observations, a 2D numerical modelling approach and GIS analysis. We analysed wood deposition in two different river reaches with contrasting geomorphic configuration.

II. MATERIAL AND METHODS

A. Description of the hydrodynamic modelling of large wood

Recently, a numerical model for simulating wood transport was proposed [6]. It simulates large wood transport together with the hydrodynamics by means of a Langrangian discretization. The method couples the flow variables calculated with the hydrodynamic module to update the position and velocity of tree logs at every time step. It considers incipient wood motion, performing a balance of forces (the gravitational force acting in a downstream direction; the friction force in the direction opposite to flow; and the drag force, acting in the flow direction) acting on each single piece of wood (assuming logs as cylinders). The hydrodynamics and wood transport are coupled; thus, the hydrodynamics influence the wood transport, but the presence of wood also influences the hydrodynamics. An additional term in the 2D Saint Venant equations is included in the flow model as an additional shear stress at every finite volume, resulting from the presence of logs.

In: Geomorphometry for Geosciences, Jasiewicz J., Zwoliński Zb., Mitasova H., Hengl T. (eds), 2015. Adam Mickiewicz University in Poznań - Institute of Geoecology and Geoinformation, International Society for Geomorphometry, Poznań

B. *Inlet flow and wood scenarios*

Data from the Koniówka water-gauge station was used to characterise the inlet flow. The data was used first for the calculation of flood discharges of given probability/recurrence interval (for running different inlet discharge scenarios) and next, the available rating curve was used to calibrate roughness (Manning's n). Roughness coefficients were obtained from the delineation, both in the channel and the flooding areas, of homogeneous land units in terms of their roughness (roughness homogeneous units; RHU) and using in situ measurements of sediment size in selected transects. All RHUs delimited in the field were digitized using a GIS, and afterwards a possible range of roughness values was assigned to them applying different empirical equations (Meyer-Peter and Muller, Bray and Strickler) in the transects. Different discharge ranges were run to calibrate the obtained Manning roughness values for high and low flows, and estimate the obtained error.

Assuming that wood recruitment is only occurring upstream from the studied reaches, a number of logs per minute was defined to enter the simulation. In any case, an exact number of logs is simply an approximation. To characterise each piece of wood entering the simulation, we established ranges of maximum and minimum lengths, diameters and wood density. Stochastic variations of these parameters together with log position and angle with respect to the flow were then used.

The scenarios were designed to be physically reliable and in agreement with the characteristics of the study river, the Czarny Dunajec.

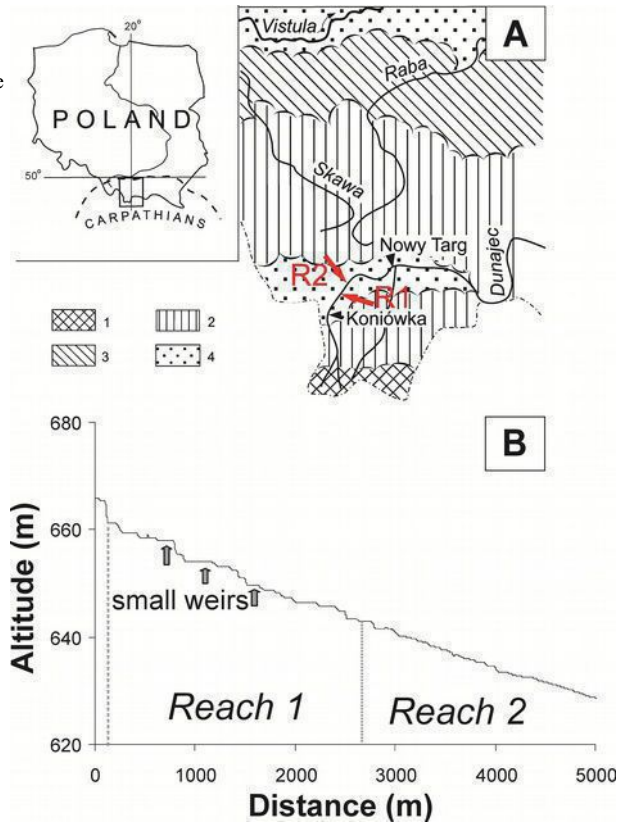
C. *GIS analysis of the model results*

For each model run, sites with wood deposition were projected on channel centerline, the boundary of low-flow channel and channel banks. The intersection of the projection line with the channel centerline indicated the position of each deposition site along the length of the investigated reaches. The altitude of deposition sites was read from digital elevation model (DEM) and compared with that of the intersection points of the projection lines with low-flow channel boundary, hence providing information about the relative elevation of each wood deposit above low-flow water surface in the reaches. The height of both channel banks in the channel cross-sections with wood deposits was determined and the lower one of two channel banks was considered in further analysis. Finally, the elevation of each deposition site in relation to the lower channel bank was established by comparing their altitudes read from the DEM.

III. STUDY SITE

The Czarny Dunajec River (Figure 1) drains the Inner Western Carpathians in southern Poland. It rises at about 1500 m above sea level (a.s.l.) in the high-mountain Tatra massif, with the highest peak in the catchment at 2176 m a.s.l. In the Tatra Mountains foreland, the river formed a non-cohesive alluvial plain consisting of resistant granitic and quartzitic particles transported from the Tatras and sandstone gravel delivered to the Czarny Dunajec in the upper part of the foreland reach. The studied reach falls from an altitude of 670 to 626 m and is 5 km long.

Figure (A)



Location of the study area in the Polish Carpathians and location of the Czarny Dunajec River and studied reaches (R1 and R2). Physiogeographic regions of southern Poland: 1 – high mountains; 2 – mountains of intermediate and low height; 3 – foothills; 4 – intramontane and submontane depressions; (B) Longitudinal profile of the Czarny Dunajec in the studied reaches.

Characteristic features of the hydrological regime of the river are low winter flows and floods occurring between May and August due to heavy rains, sometimes superimposed on snow-melt runoff. Mean annual discharge of the river amounts to 4.4 $m^3 s^{-1}$ at Koniówka, where the catchment area is 134 km^2 and

where the model was calibrated. This gauging station is situated a few kilometres upstream of the study reaches, but catchment area and river discharges increase little between the station and these reaches.

The riparian forest is composed of alder and willow species with predominating young, shrubby forms of *Alnus incana, Salix eleagnos, S. purpurea and S. fragilis,* less frequent stands of older *A. incana* trees and occasional *S. alba* trees.

An interesting feature of the selected part of the river course is the high variability of the river width and morphology. This enabled us to distinguish two different reaches representing single-thread (R1) and multi-thread (R2) channel morphologies. The single-thread reach is partially channelized with one or both channel banks lined with gabions or rip-rap, and a few drop structures reduce the slope locally. Both studied reaches may be considered large channels with respect to in-stream wood.

The high width variation in the study reaches must be reflected in differences in the availability of large wood retention sites. As already observed [5], the largest quantities of wood (up to 33 t ha^{-1} according to some field inventories after floods) were stored in wide, multi-thread sections where transporting ability of the river was low. In contrast, very low amounts of wood were retained in narrow single-thread sections of regulated or bedrock channels where unit stream power of flood flows was higher. These observations were made after a 7-year flood in 2001 (peak discharge of 94 m^3 s^{-1}) during an intensive post-event field campaign when wood storage was analysed.

IV. PRELIMINARY RESULTS AND DISCUSSION

Preliminary results gave information about sites of preferential wood deposition, wood retention capacity and relationships with the river morphology. We observed that wood retention capacity differs significantly between both reaches (p-value = 0.001). It is higher in the multi-thread channel than in the single-thread one for all the flood scenarios and log types considered. We also identified the preferential sites for deposition (Figure 2), and combining all the scenarios will allow to estimate wood deposition probability.

For the single reach 1, and for low magnitude (high frequency) floods, the preferential sites for wood deposition are the main channel, bars and the forested areas very close to the main channel. For reach 2 and frequent floods, bars, vegetated islands and forested islands are the preferential sites for wood deposition.

We hypothesized that one of the main controls on wood deposition is the relative elevation of the depositional sites. For each reach, this relative elevation of deposition sites (above low-flow water surface and above lower channel bank) was compared between particular discharges using Kruskal-Wallis Anova. Results confirmed that the deposition elevation changes significantly with changing flood magnitude. However, no statistically significant differences in the bank height at the river cross-sections with wood deposits were found in either of the reaches. It seems important because allows to consider differences in the relative elevation of deposition sites as resulting from differences in the hydraulic characteristics of different flows rather than from different bank heights.

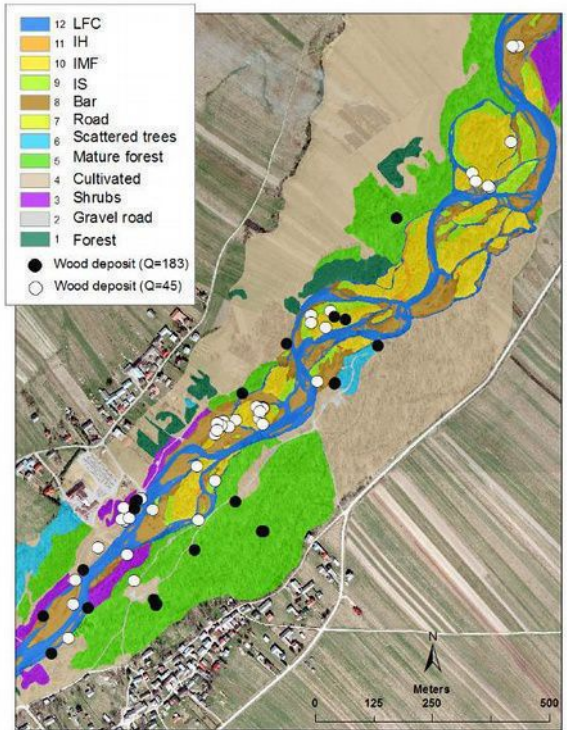


Figure 2. Example of the spatial distribution of wood deposits in the multi-thread reach for two flood scenarios considered.

The two reaches differ significantly in relative elevation of wood deposition above low-flow surface for all flood magnitudes. However, when the relative elevation of wood deposition above lower river bank is considered, significant differences were found only for the higher flood magnitudes (Figure 3).

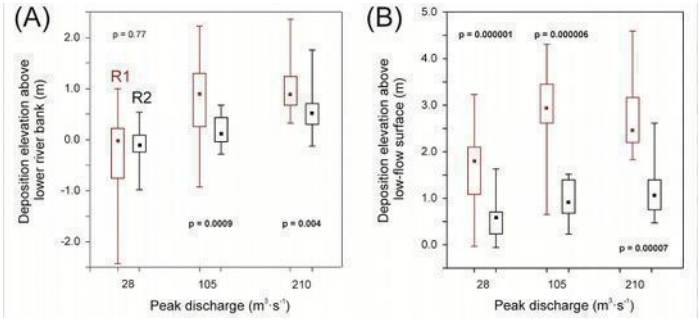


Figure 3. Comparison of the elevation of wood deposition in relation to the lower river bank (A) and the low-flow water surface (B) between reach 1 and reach 2. Statistical significance of the differences between the reaches at different peak discharges, determined by Mann-Whitney test, is indicated. p-values <0.05 are shown in bold.

Differences in the relative elevation of wood deposition between the two reaches apparently increase with increasing flood magnitude, but they become statistically significant once a certain flood magnitude is attained.

ACKNOWLEDGMENTS

This work was supported by the project FLORIST (Flood risk on the northern foothills of the Tatra Mountains; PSPB no. 153/2010).

REFERENCES

[1] Gurnell, A., 2012. “Fluvial Geomorphology: Wood and river landscapes”. Nature Geoscience, 5(2), 93–94. doi:10.1038/ngeo1382

[2] Wohl, E., Cadol, D., 2011. “Neighborhood matters: patterns and controls on wood distribution in old-growth forest streams of the Colorado Front Range”. Geomorphology 125, 132–146.

[3] Moulin, B., Schenk, E. R., Hupp, C. R., 2011. „Distribution and characterization of in-channel large wood in relation to geomorphic patterns on a low-gradient river”. Earth Surface Processes and Landforms, 36(9), 1137–1151. doi:10.1002/esp.2135

[4] MacVicar, B., Piégay, H., 2012. “Implementation and validation of video monitoring for wood budgeting in a wandering piedmont river, the Ain River (France)”. Earth Surface Processes and Landforms, 37(12), 1272–1289. doi:10.1002/esp.3240

[5] Wyżga, B., Zawiejska, J., 2010. “Large wood storage in channelized and unmanaged sections of the Czarny Dunajec River, Polish Carpathians: implications for the restoration of mountain rivers”. Folia Geographica, Series Geographica Physica 41, 5-34.

[6] Ruiz-Villanueva, V., Bladé-Castellet, E., Sánchez-Juny, M., Martí, B., Díez Herrero, A., Bodoque, J. M., 2014. “Two dimensional numerical modelling of wood transport”. Journal of Hydroinformatics. doi: 10.2166/hydro.2014.026.

Soil surface roughness quantification using DEM obtained from UAV photogrammetry

Cezary Kaźmierowski[1] Jakub Ceglarek[1],
Sławomir Królewicz [1], Jerzy Cierniewski [1]
[1] Department of Soil Science and Remote Sensing of Soils
Adam Mickiewicz Universityc
Poznań, Poland
cezark@amu.edu.pl

Jarosław Jasiewicz [2]
[2]Geoecology and Geoinformation Institute
Adam Mickiewicz University
Poznań, Poland
Michał Wyczałek[3]
[3]Institute of Civil Engineering, Division of Surveying
Poznan University of Technology
Poznań, Poland

Abstract— **The soil surface roughness is one of the most susceptible to variation in time and space characteristic, and depends on many variables like cultivation practices or soil aggregation. Various indices are used for its quantification, in microscale soil roughness is commonly expressed by HSD calculated from DEM of small sample area. The source of DEM can be close range photogramethry or laser scanning. However, for the scale of whole field that approach gives unclear separation, and new approach, based on geomorphons gives better results.**

I. INTRODUCTION

The soil surface roughness is one of the most susceptible to variation in time and space characteristic [1]..To estimate the soil surface roughness, a number of methods have been used: pin and profile meters [2], shadow analysis [3], photogrammetric processing of photographs [4], laser scanners [5]. The soil surface roughness depends on the farming practices [6], [7], and "intrinsic" soil aggregation resulting from rearrangement of particles, flocculation and cementation [8]. The shape of soil surface so far has been quantified using roughness indices, computed from their DEMs with defined horizontal and vertical spatial resolutions. The HSD expresses the height standard deviation of a soil surface area within its delineated basic DEM unit [9], whereas the T3D is the ratio of the real surface area within the DEM unit to the flat horizontal area of the unit [10]. Higher values of these indices express higher surface roughness. Those indices allowed to quantify the roughness of small sample area representing various cultivation practices. (11). Recently developed concept of geomorphons (12) used for landform classification and mapping. This technique could be applicable to quantify soil roughness. The objective of present studies is transition from quantifying surface roughness of sample area into quantifying surface roughness for whole field area.

II. METHODS

Analysis were performed for surface containing two bordering field, formed by two farming tools: northern part by seeder and southern by roller At that scale, variation of other soil variables is negligible. Selected field is located in Wielkopolska province in Poland.

Digital elevation model was prepared using photogrammetric processing of 127 aerial photographs taken with hexacopter from about 10m height above the ground level (Fig. 1). Photos were made with Sony alfa 6000 camera with 24Mb pixels matrix. The location of four ground photo mark points were measured with Topcon geodetic GPS with the assumed accuracy about 1mm (horizontal and vertical) in national coordinates system 2000 zone 6 (EPSG number: 2177). Photogrammetric processing was based on Agisoft Photoscan Proffesional 1.1.6 software.

Three classical parameters were calculated directly from DEM using GrassGIS: standard deviation of DEM, standard deviation of residual and standard deviation of prominence.

Digital elevation model obtained in the Photoscan was processed in *r.geomorphon* extension for Grass GIS software (13). Using this algorithm geomorphon forms were calculated for each pixel, and based on that calculation, following parameters were also calculated: intensity, exposition, range and texture. All models were then averaged for 1x1m spatial grid.

In: Geomorphometry for Geosciences, Jasiewicz J., Zwoliński Zb., Mitasova H., Hengl T. (eds), 2015. Adam Mickiewicz University in Poznań - Institute of Geoecology and Geoinformation, International Society for Geomorphometry, Poznań

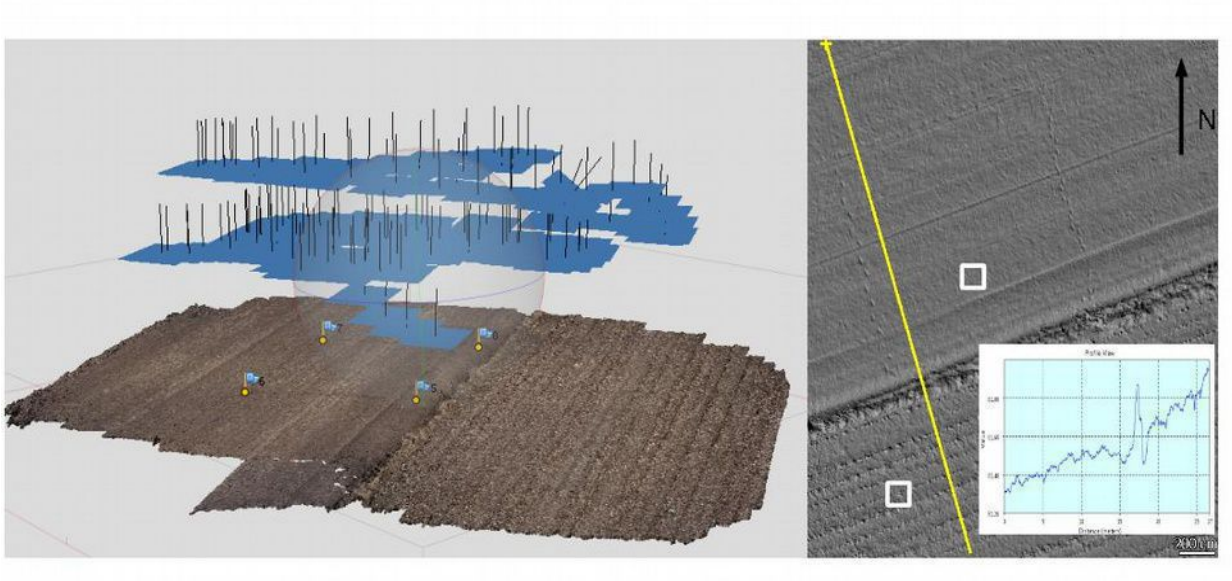


Figure 1. Aerial photos layout (blue rectangles) with generated point cloud (left) and shaded relief with transaction showing height above sea level(right) Examples of area for roughness indices calculation are highlighted in by rectangular.

III. Results

The computed mean pixel size of digital photos used in photogrammetric processing was about 0.25 cm. The computed point cloud consist of near 12 mln points, giving 19500 points per square meter. The cloud point data was processed for noise filtering. Then digital elevation model was computed using minimal curvature interpolation method with 1cm pixel spatial resolution.

So far, surface roughness was quantified based on the sample areas depicted as bounding boxes on Fig. 1. Based on those samples, HSD for northern part of field would have value of 14 mm and 33 mm for southern part and T3D values 1.02 and 1.07 respectively. For this work, HSD is calculated for whole field instead of just a sample. Parameterization of surface roughness was performed for height standard deviation of three measures of DEM and results averaged to 1x1m blocks are presented on figure 2. First model (Fig.2A) shows standard deviation of heights without detrending and while it does show differences between northern and southern part, it also contains a lot of noise. The thin border between two parts is wrongly classified as separate category. In this example, micro scale differences of roughness resulting from cultivation practices are not disconnected from field scale trend resulting from relief. Second model (Fig. 2B) shows standard deviation of prominence, which is a difference between averaged, smoothed surface and height of a pixel shows better results than previous model, but it still highlights border between northern and southern part as an independent structure, which is an error. Both of those methods point at necessity of detrending. The third model (Fig. 3C) is standard deviation of residuals, which is a way of detrending and is showing the best results among those three models. Compared to two previous models, border is relatively thinnest and separation between two areas is better. Nonetheless, it still isn't completely clear. However, generally we can observe that northern area is described by lower values of HSD compared to southern area. Obtained results suggest that precise quantification of HSD values for various farming practices calculated for small samples (11) is not clear when applied to the whole field scale.

Applying geomorphons methodology at 1cm horizontal resolution allows recognition of common classes of (micro)landform elements (Fig. 3A) in similar manner to classification of earth landforms. The northern part that is characterized by lower roughness shows dominance of gemomorphons associated with flat terrain, while southern part that has higher roughness contains more geomorphons associated with uneven terrain. The second model, showing geomorphons classified into exposition (Fig. 3B) which is difference of minimal point from the neighborhood and

central cell and is most similar to prominence used in classical measurements of soil roughness.

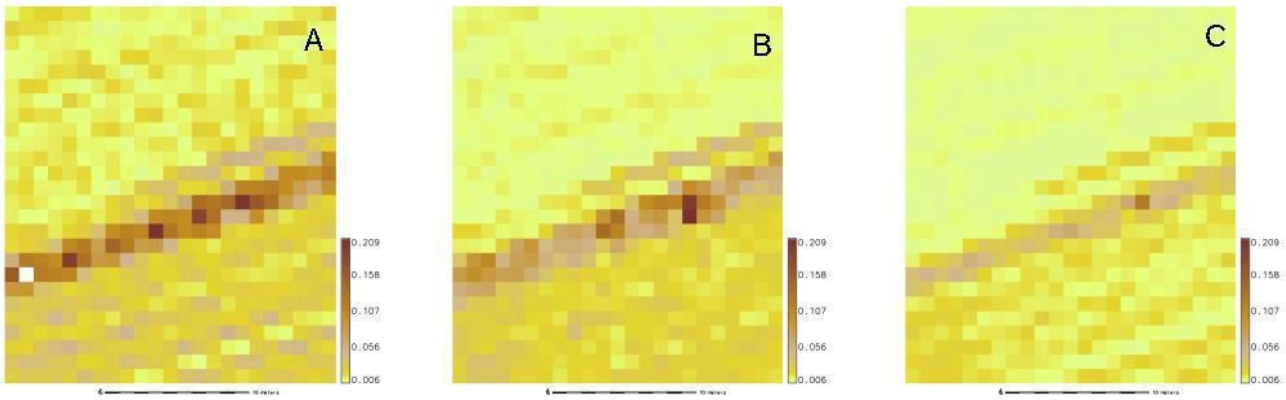


Figure 2. Three different roughness indicators: A standard deviation of DEM, B standard deviation of prominence and C standard deviation of residuals.

As can be observed, both of those indicators differentiate between northern and southern parts of the field, showing that the northern part is generally more flat, while southern is characterized by higher roughness. It's worth noting that exposition model shows even the footprints of a person left while setting local reference grid. Presented results show that this approach is sufficient for microstate modeling of surface state. Other indices (texture, intensity and range) were also calculated and they show similar ability to distinguish between northern and southern surfaces.

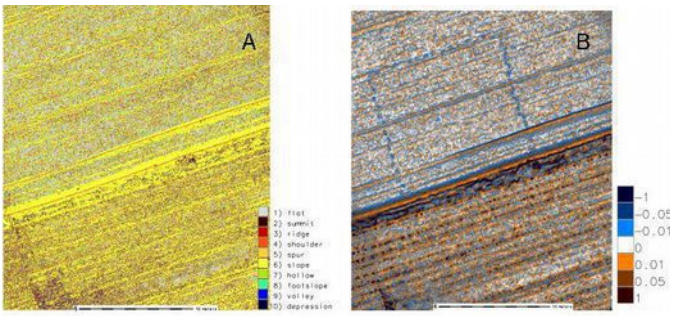


Figure 3. Models obtained using geomorphons methodology: landform classes (A) and exposition (B).

Two models (Fig. 4), obtained by averaging texture and exposition values for 1x1 m resolution grid show very clearly the distinction between smooth and rough surfaces. Texture shows percentage of geomorphons that are not flat or sloped (peak, pit, valley and ridge), whereby higher value of texture means more rough surface. Exposition shows difference between minimal point from the neighborhood and central cell and values close to zero reflect flat surface. Big advantage of both of those indicators is clear separation of flat and rough surface, while border between them is not highlighted as another feature itself.

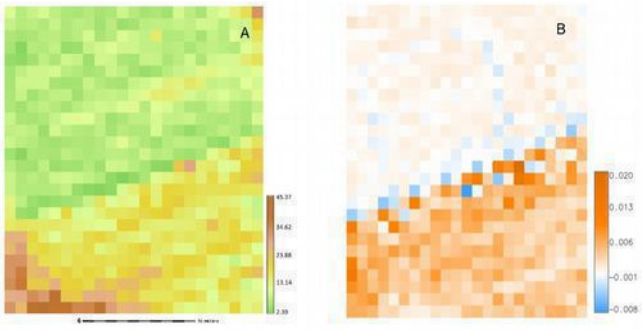


Figure 4. Models averaged for 1x1m spatial resolution showing texture (A) and exposition (B).

IV. Conclusions

Parametrization soil surface roughness at field scale is more difficult than similar task at scale of laboratory samples or for small samples of the field because for bigger scales calculations global trend can influence results. Using classical indicators like HSD, even after conducting detrending the clear separation is not achived. Adopting methodology used previously in

geomorphology, based on premise of local neighborhood seems to work well independently of scale of analyst, and without being affected by global trend. Approach based on geomorphons manages to quantify surface roughness even at field scale really well, and without falsely highlighting borders between classes as another object.

ACKNOWLEDGMENT

This work was supported in part by the Polish National Science Centre under grant 2014/13/B/ST10/02111.

REFERENCES

[1] C. L. Bielders, P. Baveye, L. P. Wilding, L. R. Drees, C. Valentin, "Tillage-induced spatial distribution of surface crusts on a sandy Paleustult from Togo Soil," Soil Sci. Soc. Am. J., vol. 60, no. 3, 843–855, 1996.

[2] M. J. M. Römkens, S. Singarayar, C. J. Gantzer, "An automated non contact surface profile meter," Soil Till. Res., vol. 6, pp. 193–202, 1986.

[3] R. García Moreno, A. Saa Requejo, A. M. Tarquis Alonso, S. Barrington, M. C. Díaz, "Shadow analysis: A method for measuring soil surface roughness," Geoderma, vol. 146, pp. 201–208, 2008.

[4] M. Zribi, V. Ciarletti, O. Taconet, J. Paillé, P. Boissard, "Characterization of the soil structure and microwave backscattering based on numerical three-dimensional surface representation: analysis with a fractional Brownian model," Remote Sens. Environ., vol. 72, pp. 159–169, 2000.

[5] F. Darboux, C.-h. Huang, "An instantaneous-profile laser scanner to measure soil surface microtopography," Soil Sci. Soc. Am. J., vol. 67, pp. 92–99, 2003.

[6] N. Baghdadi, O. Cerdan, M. Zribi, V. Auzet, F. Darboux, M. El Hajj, R. Bou Kheir, "Operational performance of current synthetic aperture radar sensors in mapping soil surface characteristics in agricultural environments - application to hydrological and erosion modeling," Hydrol. Process., vol. 22, pp. 9–20, 2008.

[7] J. Cierniewski, A. Karnieli, C. Kaźmierowski, S. Królewicz, J. Piekarczyk, K. Lewińska, A. Goldberg, R. Wesołowski, M. Orzechowski, "Effects of soil surface irregularities on the diurnal soil broadband blue-sky albedo variation," IEEE J. Sel. Top. App. Earth Observ. Remote Sens., vol. 99, 2014.

[8] S. W. Duiker, F. E. Rhoton, J. Torrent, N. E. Smeck, R. Lal, "Iron (hydr)oxide crystallinity effects on soil aggregation," Soil Sci. Soc. Am. J., vol. 67, pp. 606– 611, 2003.

[9] P. Marzahn, D. Rieke-Zapp, and R. Ludwig, "Assessment of soil surface roughness statistics for microwave remote sensing applications using a simple photogrammetric acquisition system," ISPRS J. Photogramm. Remote Sens., vol. 72, pp. 80–89, 2012.

[10] O. Taconet and V. Ciarletti, "Estimating soil roughness indices on a ridgeand- furrowsurface using stereo photogrammetry," Soil Tillage Res., vol. 93, pp. 64–76, 2007.

[11] Jasiewicz, J., Stepinski, T.F., Geomorphons — a pattern recognition approach to classification andmapping of landforms, Geomorphology (2012), http://dx.doi.org/10.1016/j.geomorph.2012.11.005

[12] Stepinski, T., Jasiewicz, J., 2011, Geomorphons - a new approach to classification of landform, in : Eds: Hengl, T., Evans, I.S., Wilson, J.P., and Gould, M., Proceedings of Geomorphometry 2011, Red lands, 109-112.

-

Assessment of an extreme flood event using rainfall-runoff simulation based on terrain analysis in a small Mediterranean catchment (Vernazza, Cinque Terre National Park)

Claudia Scopesi, Ivano Rellini, Marco Firpo
Department of Earth, Environment and Life Sciences
University of Genova
Genova, Italy
claudia.scopesi@unige.it

Michael Maerker
Department of Earth Sciences
University of Firenze
Firenze, Italy

Elmar Schmaltz
Faculty of Science, Institute of Geography
University of Tübingen
Tübingen, Germany

Silvia Olivari
Coordinamento Territoriale per l'Ambiente per il Parco
Nazionale delle Cinque Terre
Corpo Forestale dello Stato
Monterosso, Italy

Abstract—**The main aim of this study is the assessment of an extreme precipitation event causing a flash flood in the Vernazza catchment, Cinque Terre on the 25th of October 2011. We utilized a rainfall-runoff model taking into account five important factors: i) the morphology, ii) the geological settings, iii) the landcover/ landuse distribution, iv) the soil characteristics, and v) the precipitation input. The model calculates the water balance for the soil surface, which results in the partitioning of rainfall in surface runoff and infiltration. The latter was regionalized based on measured soil infiltration data using a constant head permeameter. The runoff algorithm was implemented in a GIS environment supposing that evapotranspiration can be neglected for this event. We show that morphometric parameters yield valuable and important input information for the models and can be utilized as first hazard screening approach. Moreover, the results obtained provide important information for the preparation of plans and strategies of risk management in the Cinque Terre National Park.**

I. INTRODUCTION

The Vernazza catchment (eastern Liguria, La Spezia province) is located along the Tyrrhenian side of the northern Apennines (Fig. 1). It shows typical geomorphological features and characteristics present in most of the Ligurian coastal catchments. It has a small catchment area of about 5.7 km², very steep slopes due to the proximity of the Apennine mountains and hence is characterized by short flow length and stream morphologies often controlled by tectonics. Finally the torrents show considerable erosive power and the capacity to transport sediments because of their steep profiles. The bedrock is mainly composed by a sandstone-claystone flysch (Macigno Fm., Tuscan Nappe), and a pelitic complex (Argille e Calcari di Canetolo Fm., Canetolo Unit). Particular land-use pattern characterize the study area. The slopes have been almost completely terraced for vineyards and olive groves during the past millennium. Following the abandonment of farmers in the last century, terraced slopes have been progressively abandoned and covered by a Mediterranean scrub and pine vegetation succession.

The climate is Mediterranean, characterized by hot and dry summers and mild winters. The mean annual precipitation at Levanto, located along the coast 10 km W of Vernazza, is 1048 mm, with maximum rainfall occurring in October with a mean value 156 mm.

In particular, on October, 25th 2011 a heavy rainfall affected the Cinque Terre area and especially the Vernazza catchment. A cumulative daily rainfall of 539 mm was recorded, with high intensities up to 153 mm/h and 328 mm/3h. [1]. This event triggered several slope movements and floods, causing 13 death casualties, severe structural and economic damages. In this study we develop a simple approach to simulate the extreme event of

In: Geomorphometry for Geosciences, Jasiewicz J., Zwoliński Zb., Mitasova H., Hengl T. (eds), 2015. Adam Mickiewicz University in Poznań - Institute of Geoecology and Geoinformation, International Society for Geomorphometry, Poznań

25th of October 2011 in order to assess the spatio temporal dynamics and pattern of the event. Therefore, we conducted a terrain analysis in order to derive detailed morphometric information that was subsequently utilized in the modeling procedure and also yield valuable information concerning a first flood hazard screening of the area.

II. MATERIALS AND METHODS

Our proposed model is a simply conceptual model, schematized in figure 2 and described below.

The catchments has been equipped with a weather station measuring precipitation, air temperature, radiation, wind speed and direction, and relative humidity. Moreover we installed a multi-parametric measuring device within the river to measure river runoff and sediment discharges in terms of suspended loads.

The precipitation input was regionalized for the catchment using a co-Kriging interpolation method where also the elevation was inserted; we used precipitation data recorded during the flood in all the weather station working in the area. (Fig. 3)

A geological map and a land use map has been derived from high-resolution color aerial photos, available maps (CARG - La Spezia - sc. 1:50000) and validated by a detailed field survey.

We generated a digital elevation model (DEM) with 5 m resolution. This DEM is based on an interpolation of contour lines of a 1:5.000 topographic map (Carta Tecnica Regionale Ligure, 2007) using a thin plate spline algorithm proposed by Hutchinson (1996) [2]. The DEM was preprocessed with low pass filtering to extract artefacts and errors like local noise and terraces [3] using ARCGIS 9.2 (© ESRI, 2004). Subsequently, the DEM was hydrologically corrected eliminating sinks using the algorithm proposed by Planchon and Darboux (2001) [4].

The DEM was the basis for a detailed terrain analysis performed in Saga GIS [5]; We used SAGA 2.0.3 software to derive the topographic indices at a 5 m resolution. The layers were post-processed and transformed into ascii raster data with the same spatial reference and resolution.

We derived various Topographic Indices such as:

the Topographic Wetness Index (TWI) [6] , calculated as:

$$TWI = \ln(As / \tan(Slope))$$

and the Stream Power Index (SPI) [6], calculated as:

$$SPI = \ln(As * Slope)$$

Where As is the specific catchment area estimated using one of the available flow accumulation algorithms

Moreover we derived the Transport Capacity Index (TCI), that is the calculation of slope length (LS) factor as used by the Universal Soil Loss Equation (USLE) [7], based on slope and specific catchment area (As, as substitute for slope length).

We calculated also the Flow direction and flow accumulation indices to quantify topographic control on hydrological processes. Flow accumulation is calculated as upslope contributing (catchment) area using the multiple flow direction approach of Freeman (1991) [8].

For the hydrologic characteristics of the soil, we made field measurements in the soil; we used a Compact Constant Head Permeameter (Amoozemeter) [9] to obtain the saturated hydraulic conductivity (Ksat) of the different type of soils and a Hood-Infiltrometer [10] to measure the surface infiltration. We obtained 27 measurements with the Amoozemeter at a depth of 25 cm from the soil surface and 6 measurements with the Hood. We regionalized the data for the entire catchment using Universal Kriging of Saga GIS.

Geological, Land cover, Elevation and TWI grid were insert during the interpolation analysis, supposing that soil hydrologic characteristics are mainly related to the catchments' parent material, land cover typology and the topographic settlement. The first result is the realization of the soil infiltrability map (Fig. 4).

Finally we calculated the potential Runoff, subtracting the soil infiltrability grid from the rainfall grid, supposing that evapotranspiration can be neglected during heavy rainfall events. Consequently, the water balance is reduced to a function of precipitation input and infiltration capacity of the surface.

To obtain the real volume of water that concentrate in the river we applied a weighted Flow Accumulation procedure using SAGA GIS, and we inserted the potential Runoff raster as input raster for applying a weight to each cell.

The river runoff was calculated in m^3/day. The result of Flow Accumulation (Fig. 5) is a raster of accumulated flow to each cell, as determined by accumulating the weight for all cells that flow into each downslope cell. The calculation was finally validated with measured runoff registered by the multi-parametric device at the outlet of the catchment.

III. RESULTS

The topographic indices such as catchment area and flow accumulation yield a first rough estimate of areas endangered by flood events. Moreover, indices like TWI, SPI and TCI provide information about areas at risk concerning landsliding, soil erosion and gullying. With the simple hydrological model we finally calculated potential runoff owing to an extreme

precipitation event, such as during last flood event happened in 5 Terre National Park on October, 25th 201.

The result is shown in figure 5.

Our rainfall-runoff model estimate a maximum discharge of 52 thousand m^3 / day, which is about 6000 liter per second, in the river network.

This rainfall-runoff model could be a very important tool in the preparation of plans and strategies of risk management in the Cinque Terre National Park, above all related to possible climatic changes scenarios.

A. *Figures and Tables*

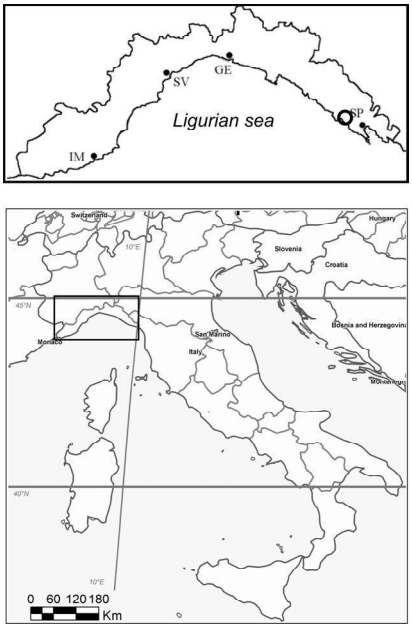


Figure 1. Study area

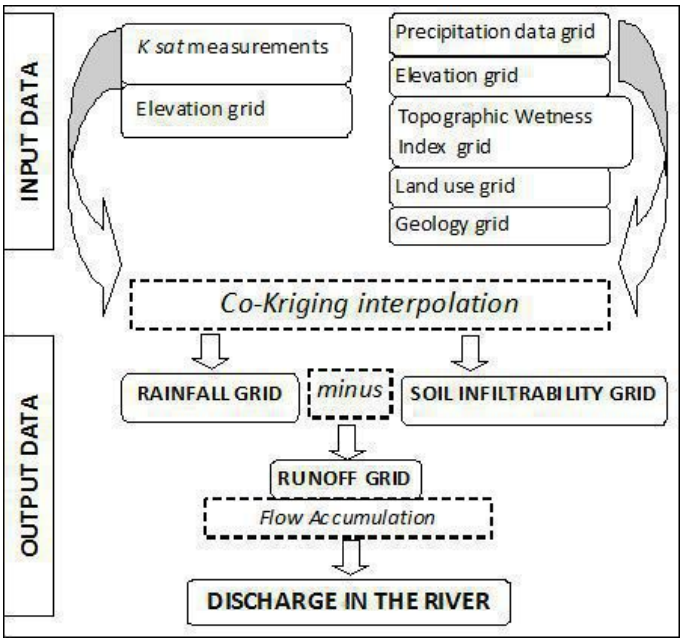


Figure 2. Conceptual map of proposed rainfall-runoff model

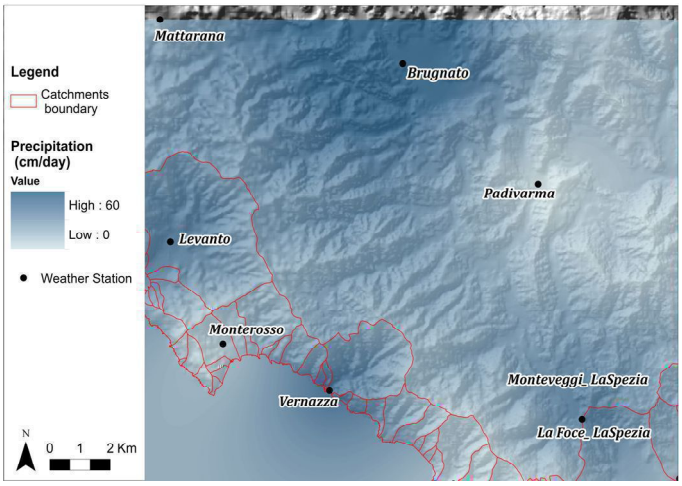


Figure 3. Regionalization of maximum precipitation event recorded during the flood of the 25th October 2011

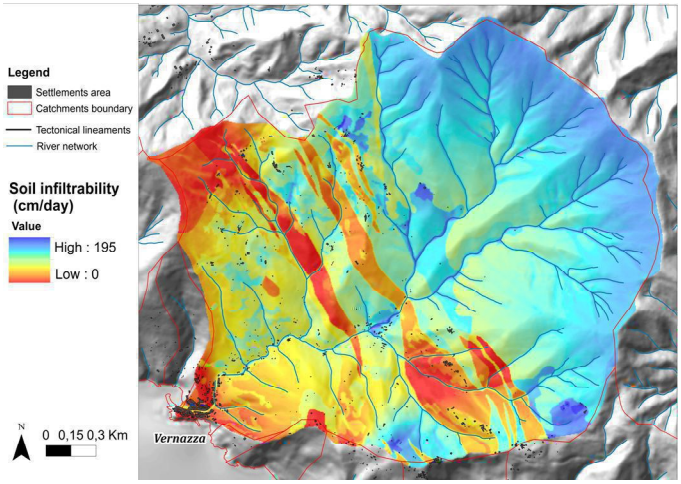


Figure 4. Soil infiltrability map

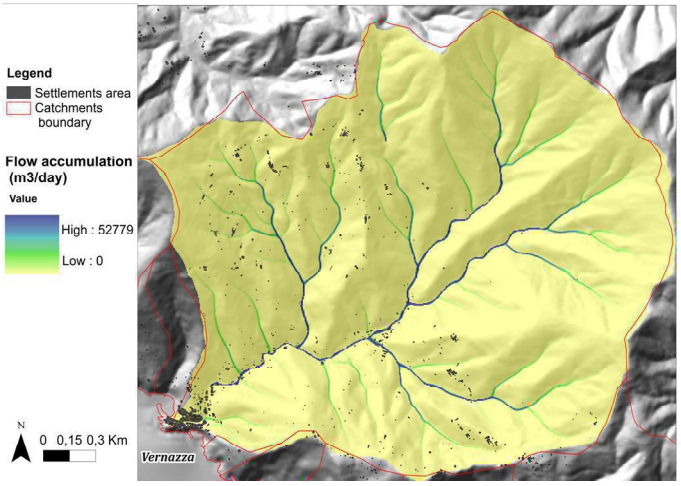


Figure 5. Flow Accumulation map resulting by the rainfall-runoff model

REFERENCES

[1] Cevasco, A., Brandolini, P., Scopesi, C. & Rellini I. , 2013. "Relationships between geo-hydrological processes induced by heavy rainfall and land-use: the case of 25 October 2011 in the Vernazza catchment (Cinque Terre, NW Italy)", Journal of Maps, 9, 289-298.

[2] Hutchinson, M. F. 1996. "A locally adaptive approach to the interpolation of digital elevation models". In Proceedings, Third International Conference/ Workshop on Integrating GIS and Environmental Modeling.

[3] Vorpahl, P. Elsenbeer, H. Märker, M. & Schröder, B. 2012. "How can statistical models help to determine driving factors of landslides?" Ecological Modelling, 239, 27-39.

[4] Planchon, O. & Darboux, F. 2001. "A fast, simple and versatile algorithm to fill the depressions of digital elevation models". Catena, 46, 159–176.

[5] Conrad, O. , 2007. " SAGA - Entwurf, Funktionsumfang und Anwendung eines Systems für Automatisierte Geowissenschaftliche Analysen". electronic doctoral dissertation, University of Göttingen.

[6] Beven, K.J. & Kirkby, M.J., 1979. "A physically-based variable contributing area model of basin hydrology". Hydrological Science Bulletin, 24, 43-69.

[7] Wischmeier, W.H., Smith, D.D. 1978. "'Predicting rainfall erosion losses – A guide to conservation planning" . Agriculture Handbook No. 537: US Department of Agriculture, Washington DC.

[8] Freeman, G.T. 1991. "Calculating catchment area with divergent flow based on a regular grid". Computers and Geosciences, 17, 413-22.

[9] Amoozegar, A. 1989. "A Compact Constant-Head Permeameter for Measuring Saturated Hydraulic Conductivity of the Vadose Zone". Soil Sci Soc Am J, 53(5), 1356-1361

[10] Schwärzel, K., Punzel J. 2007. "Hood Infiltrometer: A New Type of Tension Infiltrometer". Soil Sci Soc Am J 71(5): 1438-1447.

Spatial distribution of hypsometric curves within the Parsęta River drainage basin (Poland) as a geoindicator of geomorphological hazards

Zbigniew Zwoliński
Institute Geoecology and Geoinformation
Adam Mickiewicz University in Poznań
Dzięgielowa 27, 61-680 Poznań, Poland
zbzw@amu.edu.pl

Ewa Sznigir
Poznań, Poland

Abstract—**The article presents the changeability of hypsometric parameters calculated for hypsographic curves in 235 catchments of the Parsęta River drainage basin. Catchments with convex curves are more susceptible to the destructive effects of extreme denudational processes, whereas catchments with concave curves are better prepared for the affecting of a wide range of denudational processes of various magnitude.**

I. INTRODUCTION

Clarke and Orrell [1], as well as Baulig [2], reproached geomorphometry for the fact that the analysis results of a small study area cannot be translated into a bigger area, as the occurrence of landforms is irregular, non-continuous and unpredictable. Hettner [3] claimed that morphometric methods do not have any meaning in the explanation of origin. Dorywalski [4] thought that the transition from qualitative to quantitative studies shows the development of a science, allows to determine precise terms, and eliminates the researcher's subjectivism. Geomorphometry is a science of determining and analysing relief elements in quantitative terms (Hengl, Reuter 2008). Measurements are most frequently taken in topographic maps, digital elevation and terrain models, satellite images or air-photos, and not on the basis of field study. Measurements and statistical methods constitute the basis to create coefficients and indexes, making it possible to describe landform in a quantitative way, which is more precise and explicit that general verbal description. This direction was initiated by Humboldt [5] and Ritter [6], and developed by American geomorphologists in mid-20th century. Strahler [7] was one of them; he initiated the analysis of river drainage basins by hypsographic curves.

The study objective is to determine the morphological and evolutionary diversification of catchments in the Parsęta River drainage basin through their hypsographic curves in the context of secular and extreme processes. According to Strahler [7], the shape and course of the hypsographic curve should render the drainage basin's relief age diversification and evolution extent. The objectives of this study, which uses the concept of hypsographic curves, are the following: to obtain hypsographic curves of catchments of the Parsęta River drainage basin and to attempt to find a relationship between the shape of the hypsographic curves and the spatial position of the catchments, as well as to interpret the role of curves in the course of denudational processes.

Strahler [7] compared hypsographic curves with three river catchments which differed in the development of relief. He noticed that the shape of the curves depends on the relief development phase. The bigger sediment loss resulting from erosion in a given area, the older the relief. Therefore, a hypsographic curve with a convex shape corresponds to the early development phase, an S-shaped curve shows the mature phase, and a concave curve indicates the old-age phase.

II. STUDY AREA

Calculations of hypsometric curves was conducted for the Parsęta River drainage basin (Western Pomerania). The Parsęta River drainage basin includes the 131.6 km long Parsęta River

In: Geomorphometry for Geosciences, Jasiewicz J., Zwoliński Zb., Mitasova H., Hengl T. (eds), 2015. Adam Mickiewicz University in Poznań - Institute of Geoecology and Geoinformation, International Society for Geomorphometry, Poznań

valley, and its area is 3145 km^2 [9]. The relief of the Parsęta River drainage basin is of postglacial nature.

III. METHODS

A digital elevation model DTED2 with grid cells of 35 m × 35 m constitutes source data for the Parsęta River drainage basin. Hypsometric curves were described with the following parameters: hypsographic curve integral, hypsometric skewness, hypsometric kurtosis, probability density function skewness, probability density function kurtosis, catchment size, circularity. Catchment limits in *.SHP format come from the Computer Map of Polish Hydrographic Division [8]. The Parsęta River drainage basin was divided into 235 catchments.

IV. RESULTS

A. *Hypsographic curve integral*

Curve integral is the surface area determined by the hypsographic curve and the graph axes. The higher the value, the more convex the curve; the lower the value, the more concave the curve. However, the value of the curve integral does not explicitly determine its shape. Curve integral values fall in the range between 0.17 and 0.77, with the mean value equal to 0.43 (Fig. 1). The lowest values occur in the middle part of the drainage basin. These are catchments located very close to the Parsęta River or constituting the River's catchments of the first order. The highest values are characteristic for catchments located at the outskirts of the drainage basin, in the vicinity of a drainage divide of the first order. These areas have the biggest absolute altitude. Hypsographic curve integral serves well to distinguish between catchments, i.e. for young catchments the curves are concave, and for mature catchments they are convex (Fig. 2).

B. *Skewness*

Values of the hypsometric skewness parameter for the Parsęta River drainage basin catchments fall in the range between 0.037 and 1.24, with the mean value equal to 0.48 (Fig. 3). All hypsographic curves have positive skewness. It is difficult to confirm the correctness in the spatial distribution of hypsometric skewness. Catchments with the lowest skewness values border catchments with the highest value of this parameter. However, there are more catchments with the lowest value of the parameter in the north-west part of the drainage basin.

C. *Kurtosis*

For the Parsęta River drainage basin catchments the kurtosis values fall in the range between 1.33 and 4.41, with the mean value equal to 2.2 (Fig. 4). The highest kurtosis values occur in the north-east part of the drainage basin, next to the Radew River catchments, whereas the lowest values — in the north and central part of the drainage basin.

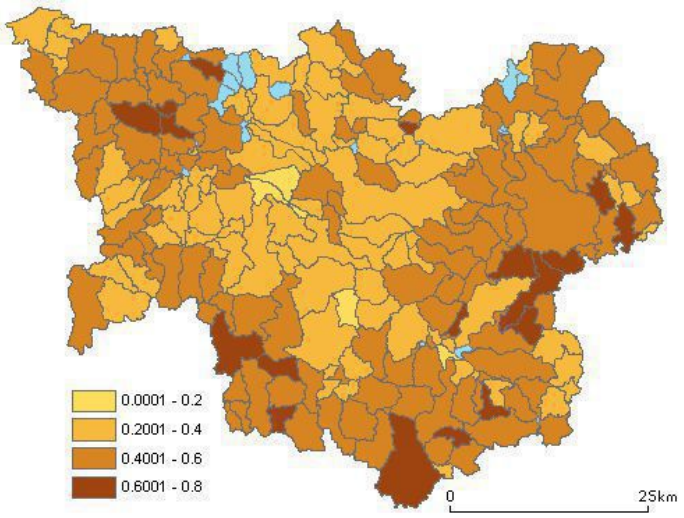


Figure 1. Map of the Parsęta River drainage basin showing spatial diversification of hypsographic curve integral. Blue colour means that no data are available

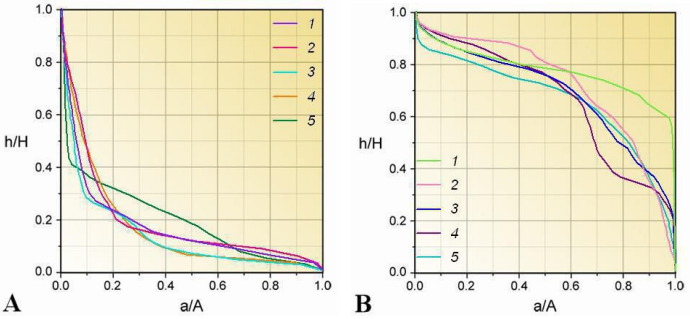


Figura 2. Hypsographic curves of the Parsęta River drainage basin catchments with the lowest (A) and the highest (B) value of hypsographic curve integral
A: 1- the Parsęta River from the Mogilica River to the Liśnica River (R), 2- the Parsęta River from the tributary from near Sadkowo to Dębnica (L), 3- the Liśnica River from the tributary below Żytelkowo to the mouth, 4- the Parsęta River from Gęsia to Perznica (R), 5- the Pokrzywnica River from the tributary from near Zwartowo to Młynówka (L)
B: 1- Tributary from Kłopotowo, 2- Tributary from near Zajączkowo, 3- Rosnowski Channel, 4- Tributary from Górowino, 5 – from Debrzyca to Łęczna (R)

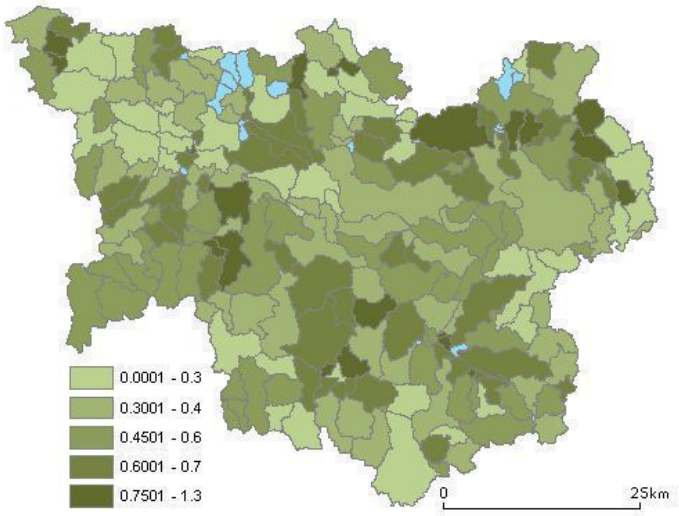


Figure 3. Map of the Parsęta River drainage basin showing spatial diversification of hypsometric skewness. Blue colour means that no data are available

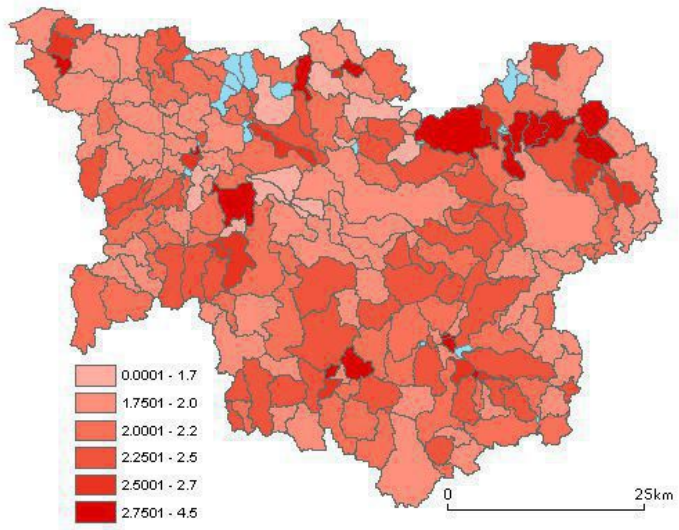


Figure 4. Map of the Parsęta River drainage basin showing spatial diversification of hypsometric kurtosis. Blue colour means that no data are available

D. Probability density function skewness

Probability density function skewness for the Parsęta River drainage basin catchments takes values in the range from -13.3 to 1.9 (Fig. 5). The highest values of probability density function skewness are visible in the central part of the drainage basin. The lowest values are characteristic for catchments in the south edge of the drainage basin, as well as its east and south-east part.

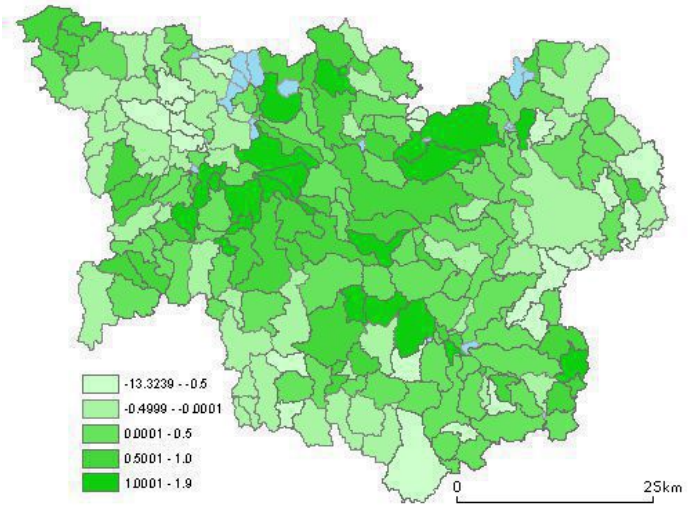


Figure 5. Map of the Parsęta River drainage basin showing spatial diversification of probability density function skewness. Blue colour means that no data are available

E. Probability density function kurtosis

The values of the probability density function kurtosis fall in the range between -119.9 and 4.62, with the mean value equal to 1.27 (Fig. 6). The definite majority of the Parsęta River drainage basin hypsographic curves have kurtosis values lower than 3, which means that their distribution is flatter than normal distribution. The lowest values of probability density function kurtosis can be found in the north-west part of the drainage basin; catchments with the highest values are evenly distributed on the whole drainage basin, no regularity can be found in their distribution.

F. Catchment size

The size of the Parsęta River drainage basin catchments is very diversified. The smallest catchment has only 0.17 km², whereas the biggest - over 89 km². The average size is 14 km². The smallest catchments are usually direct catchments of the Parsęta or the Radew Rivers, i.e. riverside catchments. The biggest catchments are located farther from the biggest rivers. They can be found in the central and west part of the region (Fig. 7).

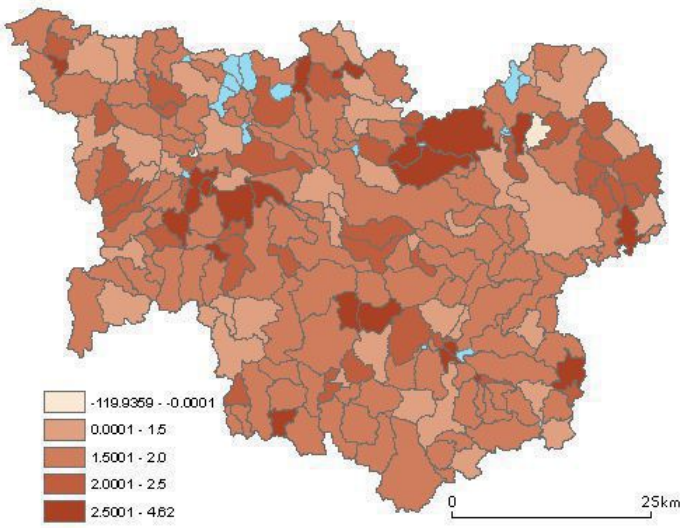


Figure 6. Map of the Parsęta River drainage basin showing spatial diversification of probability density function kurtosis. Blue colour means that no data are available

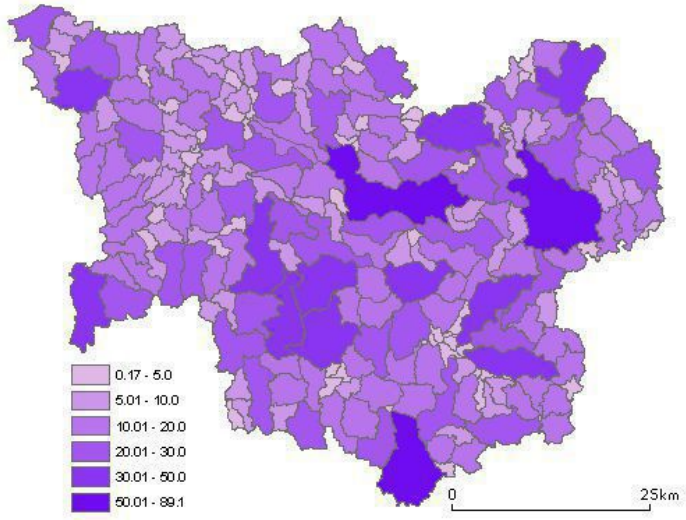


Figure 7. Map of the Parsęta River drainage basin showing spatial diversification of catchment size

G. Catchment circularity

The circularity of the Parsęta River drainage basin catchments falls between 0.22 and 0.81, with the mean value equal to 0.45 (Fig. 8). The biggest number of catchments with the smallest circularity are located in the central part of the drainage basin; they have the characteristic elongated shape. Most circular catchments are evenly distributed across the entire drainage basin.

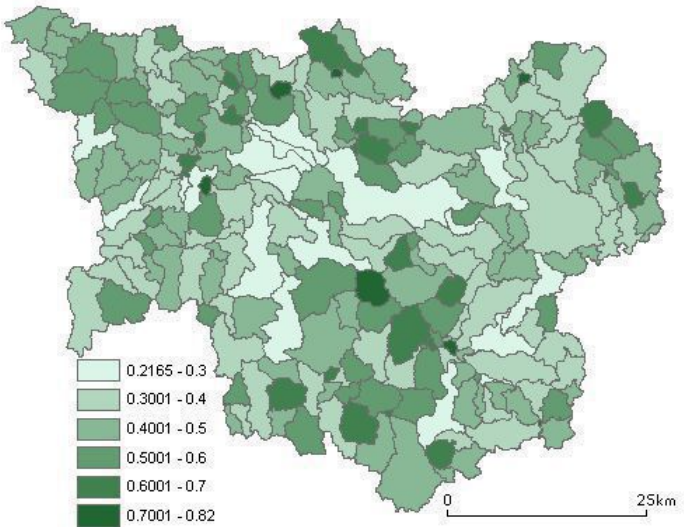


Figure 8. Map of the Parsęta River drainage basin showing spatial diversification of catchment circularity

V. CONCLUSIONS

The hypsographic curves of the Parsęta River drainage basin catchments are very diversified. They represent all landform development types distinguished by Strahler (1952). This proves high geodiversity of the study area. Parameters of the hypsographic curves distinguished by Strahler (1952) and Harlin (1978) are suitable for describing curve shape with numbers.

The Parsęta River drainage basin catchments can be divided into two groups. The first includes catchments located in the central part of the drainage basin. The shape of their hypsographic curves is concave, which is confirmed by the curve integral, as well as the low values of kurtosis and probability density function skewness. Whereas catchments located on the outskirts of the drainage basin have hypsographic curves with a more convex shape. Observing the denudational processes, both secular and extreme, which take place in the Parsęta River drainage basin, it is appropriate to conclude that catchments with convex curves are more susceptible to the destructive effects of extreme denudational processes, whereas catchments with concave curves are better prepared for the affecting of a wide range of denudational processes of various magnitude.

REFERENCES

[1] Clarke J.I., Orell K., 1958. An assessment of some morphometric methods. Department of Geography Durham Colleges in the University of Durham, Occasional Paper Series 2.

[2] Baulig H., 1959. Morphométrie. Annales de géophysique 68: 385-408.

[3] Hettner A., 1921. Die Oberflächenformen des Festlandes. D. G. Teubner, Leipzig and Berlin.

[4] Dorywalski M., 1953. Matematyczno-statystyczne metody w geomorfologii. Przegląd Geograficzny 25(1): 61-71.

[5] Humboldt von, A., 1825. Personal narrative of travels to the equinoctial regions of the New Continent during the years 1799-1804. London.

[6] Ritter, C., 1826. Über geographische Stellung und horizontale Ausbreitung der Erdteile. Berlin.

[7] Strahler A.N., 1952. Hypsometric (area-altitude) analysis of erosional topography. Geological Society of America Bulletin 63: 1117-1142.

[8] Krajowy Zarząd Gospodarki Wodnej, 2010. Komputerowa Mapa Podziału Hydrograficznego Polski (MPHP) 2010. Krajowy Zarząd Gospodarki Wodnej, Warszawa.

[9] Zwoliński Zb., 1989. Geomorficzne dostosowywanie się koryta Parsęty do aktualnego reżimu rzecznego. Dokumentacja Geograficzna 3/4: 1-144.

Relevance of moving window size in landform classification by TPI

Zbigniew Zwoliński
Institute Geoecology and Geoinformation
Adam Mickiewicz University in Poznań
Dzięgielowa 27, 61-680 Poznań, Poland
zbzw@amu.edu.pl

Estera Stefańska
Turek, Poland

Abstract—**The article presents the problem of the calculation window size relevance in the classification of landforms using the TPI for two diversified areas: lowland and alpine. It was found that the best results are obtained by magnifying the bigger window five times in relation to the smaller window.**

I. INTRODUCTION

Relief analysis is used in many studies of nature, as it is assumed that landform plays a leading role in the hierarchy of environmental components in any complex studies of landscape within the scope of physical geography or even human or economic geography. Relief classes can be distinguished on the basis of geomorphometric characteristics obtained from the digital elevation model. Most frequently, such maps are prepared for the purpose of geomorphological [1], [2], geological [3], or pedological studies [4], [5], [6]. It is appropriate to emphasise that the geomorphometric classification of relief constitutes the basis for typological classification. This study endeavoured to distinguish discrete relief classes of similar geomorphometric characteristics.

II. STUDY AREA

Relief classification was conducted for two areas: the lowland area of the Parsęta River drainage basin and the alpine area of the Polish Tatra Mountains. The Parsęta River drainage basin — belonging to the Baltic Sea Basin — includes the 131.57 km long Parsęta River valley and tributaries, and its surface area is 3145 km^2 [7]. The relief of the Parsęta River drainage basin is of postglacial nature. The Tatra Mountains are the highest massif in the Carpathian Mountains with distinct high-mountain relief [8]. The 53 km-long and 18.5 km-wide Tatra Massif takes up the surface area of 750 km^2, of which the Polish Tatra Mountains take up about 174 km^2. Despite their orographic tightness, The Polish Tatra Mountains divide into two mesoregions: the West Tatra Mountains and the High Tatra Mountains.

III. METHODS

Relief classification based on the topographic position index (TPI) proposed by Weiss [9] is quite commonly used. The author presents two methods allowing to distinguish a different number of classes. The first method results in the division into 6 relief classes: 1) valley bottom, 2) lower part of slope, 3) flat area, 4) middle part of slope, 5) upper part of slope, and 6) peak/culmination), whereas the second method allows to distinguish 10 classes: 1) deeply-incised valleys 2) shallow valleys/outflow network on slope 3) source areas/little valleys on hills 4) U-shape valleys 5) flat areas 6) long slopes 7) upper parts of slopes/mesas 8) little hummocks in valleys 9) hummocks on slopes/little hummocks on flatlands 10) mountain peaks/ridges.

Two DEMs were used. The first, which included the Parsęta River drainage area, is characterised with grid cells of 31 × 31 metres (DTED Level 2). The second model, which includes the Tatra Mountains area, is characterised with grid cells of 10 × 10 m. The topographic position index *(TPI)* is a quantitative relief index calculated from T. Dilts's scripts[1]. The selection of an appropriate calculation scale for the assumed goal is crucial in the calculation of the topographic position index. The scale means the size of the moving window used to calculate the index. The moving window defines the vicinity used to calculate the mean value to which values from individual cells are compared. The establishing of the calculation scale has

[1] www.arcscripts.esri.com

In: Geomorphometry for Geosciences, Jasiewicz J., Zwoliński Zb., Mitasova H., Hengl T. (eds), 2015. Adam Mickiewicz University in Poznań - Institute of Geoecology and Geoinformation, International Society for Geomorphometry, Poznań

fundamental influence on the TPI value for a given cell. Depending on the size of the vicinity, the topographic position index calculated for the same cell may be positive, close to zero, or negative. Generating the TPI from DEM in different scales allows to determine and analyse relief forms of various sizes. In relation to terrain morphology, TPI calculations in a small scale allow to determine local hummocks and depressions. Whereas calculation in a larger scale indicates main, large landforms. Appropriate combinations of TPI values calculated in a smaller and in a suitably larger scale allow to distinguish 10 relief classes.

IV. RESULTS

The relief classification in the Parsęta River drainage area was based on the TPI determined in a moving calculation window of 3 × 3 cells. The TPI value in this scale was compared successively with the TPI calculated in the windows of 7 × 7, 15 × 15, 31 × 31 and 63 × 63 cells. The calculations resulted in maps shown in Fig. 1 a-d. The TPI calculation window size was selected with the aim to have the first window as small as possible. For the TPI calculated in a larger scale, windows were selected in such a way that their size increased more or less in a geometric progression, while the odd-number length of window side was kept.

In the landform classification made for the Parsęta River drainage area on the basis of the TPI calculated in the windows of 3 × 3 and 7 × 7 cells, over 76% of the surface area belongs to class 5 (Fig. 1a) corresponding to flat areas (with average local height of 1.83 m, average slope of 1.3°, and mean values for planar and vertical curvature equal to zero). Almost 10% of the surface area belongs to class 4 — river valleys (with average local height of 4 m, average slope of 2.8°, planar curvature mean value of -0.05, and vertical curvature mean value of 0.09; thus the curvatures indicate a valley area with a profile characteristic for a concave slope) and almost 10% of surface area belong to class 7 – upper convex parts of slopes (with average local height of 4.3 m, average slope of 2.98°, planar curvature mean value of 0.07, and vertical curvature mean value of -0.08). The remaining 7 classes take up less than 4% of the surface area, of which class 6 takes up about 2%, and classes 1 and 10 — less than 1% each. With this calculation scale, class 8 was not distinguished, whereas classes: 2, 3, 9 take up trace surface area.

In the classification based on TPI calculated in the windows of: 3 × 3 and 15 × 15 cells, three classes: 5 (50%), 4 (24%) and 7 (24%), prevail in terms of the surface area taken (Fig. 1b). On the other hand, in the classification based on TPI calculated in the windows of 3 × 3 and 31 × 31 cells (Fig. 1c) class 4 (34.81%) takes up the biggest surface area, followed successively by class 7 (32.67%) and class 5 (30.24%). Classification results based on TPI calculated in the window of 3 × 3 and 63 × 63 cells show further increase in the surface area of classes 4 and 7 (Fig. 1d). In this classification, the percentages of these classes are 41% and 38%, and the percentage of class 5 is only 19%. Such a proportion of classes for the Parsęta River drainage area has to be considered incorrect.

Classifications were also made for the Parsęta River area with the initial window increased approximately two times. The initial small scale TPI was determined in a moving calculation window of 7 × 7 cells. In this classification, the TPI values in a larger scale were determined in the windows of 15 × 15, 35 × 35, 71 × 71 and 141 × 141 cells. Analogically, the larger scale TPI calculation windows were intended to increase, approximately, in a geometric progression in relation to the initial window. Results of this classification are presented in maps (Fig. 2).

For the TPI in the windows of 7 × 7 and 15 × 15 cells (Fig. 2a), the biggest surface area in this classification is taken up by: class 5 (with average local height of 1.62 m, average slope of 1.16°, and mean values of curvatures equal to zero) – 49%, 4 (with average local height of 2.43 m and average slope of 1.73°) – 15%, 7 (with average local height of 2.62 m and average slope of 1.86°) – 14%, and classes 1 and 10 (10% each). An increase in the percentage of class 1 (deeply-incised valleys) and class 10 (ridges) can be observed in comparison with the previous classifications (Fig. 1); previously, the classes took up less than 1% of the surface area. In the window pair of 7 × 7 and 35 × 35 cells (Fig. 2b), there are the following classes: 5 (26%), 4 (27%) and 7 (25%). In the next window pair of 7 × 7 and 71 × 71 cells (Fig. 2c), the biggest surface area is taken up by classes: 4 (33%), 7 (30%), 5 (15%) and classes 1 and 10 (almost 8% each). In the last window pair of 7 × 7 and 141 × 141 cells (Fig. 2d), the biggest surface area is taken by classes: 4 – 36%, 7 – 33%, 5 – 10%, and classes 1 and 10 – 7% each.

In the analysis of the topographic position index for the area of the Polish Tatra Mountains, efforts were made to select the size of the initial TPI calculation window in such a way, as to make possible the comparison of results obtained with the analysis for the Parsęta River drainage area. The comparability of results was achieved by calculating the TPI in windows covering similar surface area of terrain. Because the DEM for the Parsęta River drainage area is characterised by a grid cell of 31 × 31 m, and the DEM cell size for the Polish Tatra Mountains is 10 × 10 m, the decision was made to calculate the topographic

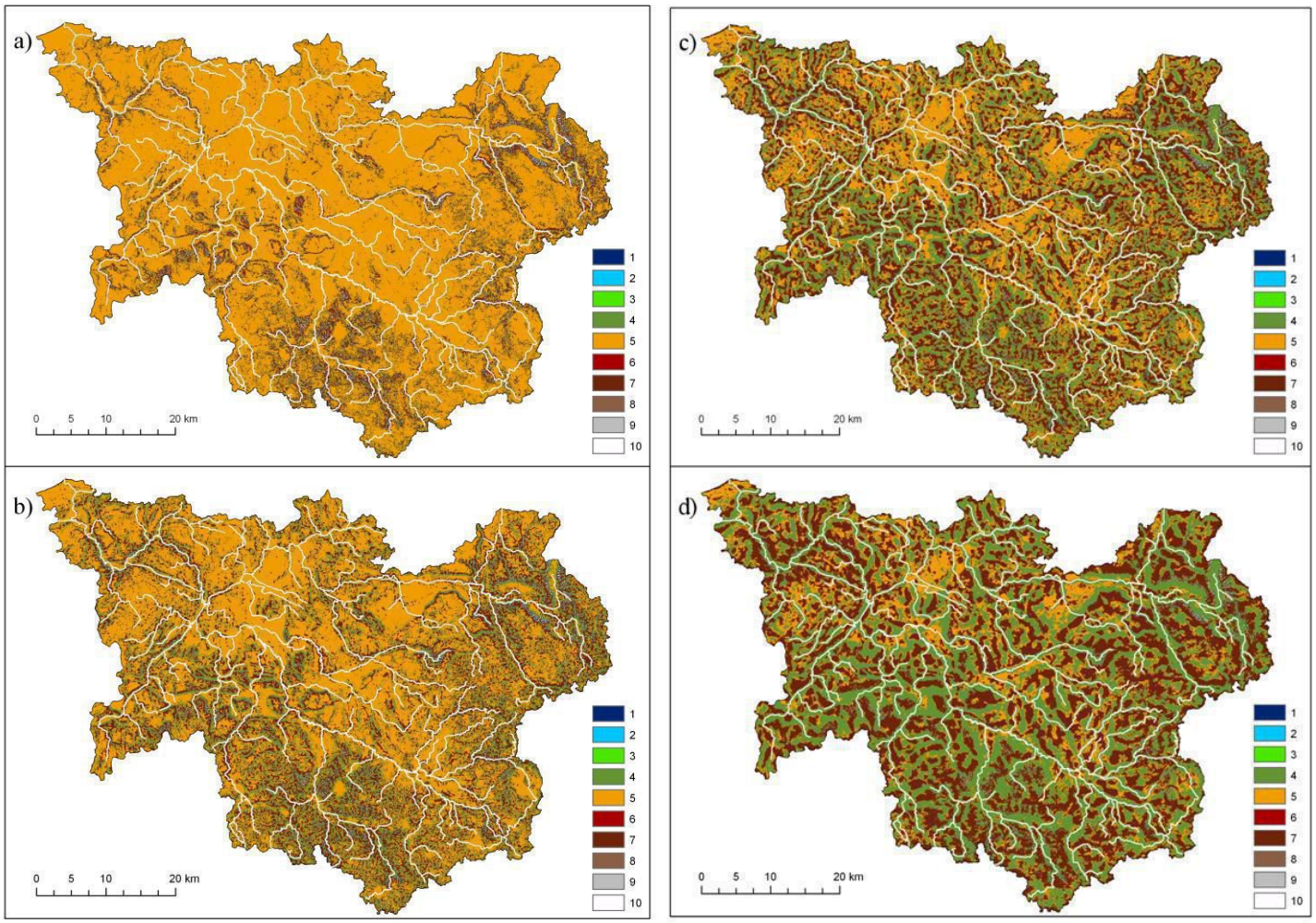


Figure 1. Landform classification for the Parsęta River drainage basin on the basis of TPI in different moving windows
a) 3 × 3 and 7 × 7 cells, b) 3 × 3 and 15 × 15 cells, c) 3 × 3 and 31 × 31 cells, d) 3 × 3 and 63 × 63 cells; 1-10 – explanation in section Methods

position indexes for this area in windows three times bigger than for the Parsęta River drainage area. Thus, the TPI analysis was made for the Tatra Mountains area in the windows of: 9 × 9, 21 × 21, 45 × 45, 93 × 93, and 189 × 189 cells. The second series of classifications was made based on the initial TPI calculated in windows which were three times bigger: 21 × 21, 45 × 45, 105 × 105, 213 × 213, and 423 × 423 cells. Results obtained according to this classification proved to be too general, therefore, their presentation was abandoned.

Landform classification made on the basis of the TPI calculated in the windows of: 9 × 9 and 21 × 21 cells (Fig. 3a) includes classes: 1 – deeply-incised valleys (19%: average local height of 12.5 m and slope of 24°, mean planar curvature of (-1.01) and mean vertical curvature of (1.07)), 4 – U-shaped valleys (17%: average local height of 7 m, average slope of 14°, mean values of planar and vertical curvature of: 0.11 and -0.06), 6 – long slopes (15%: average local height of 5.5 m, average slope of 12°, mean values of planar and vertical curvature: 0.01 and 0), 7 – upper parts of slopes (18%: average local height of 6 m, average slope of 13°), and 10 – mountain peaks/ridges (18%). As can be observed in Figure 3a, classes 1 and 10 prevail in the Tatra Mountains area with a contribution of classes 4 and 7. Class 5 – flat area – takes up the biggest surface area within the Podtatrzański Trench. In the area of Gubałowskie Foothills,

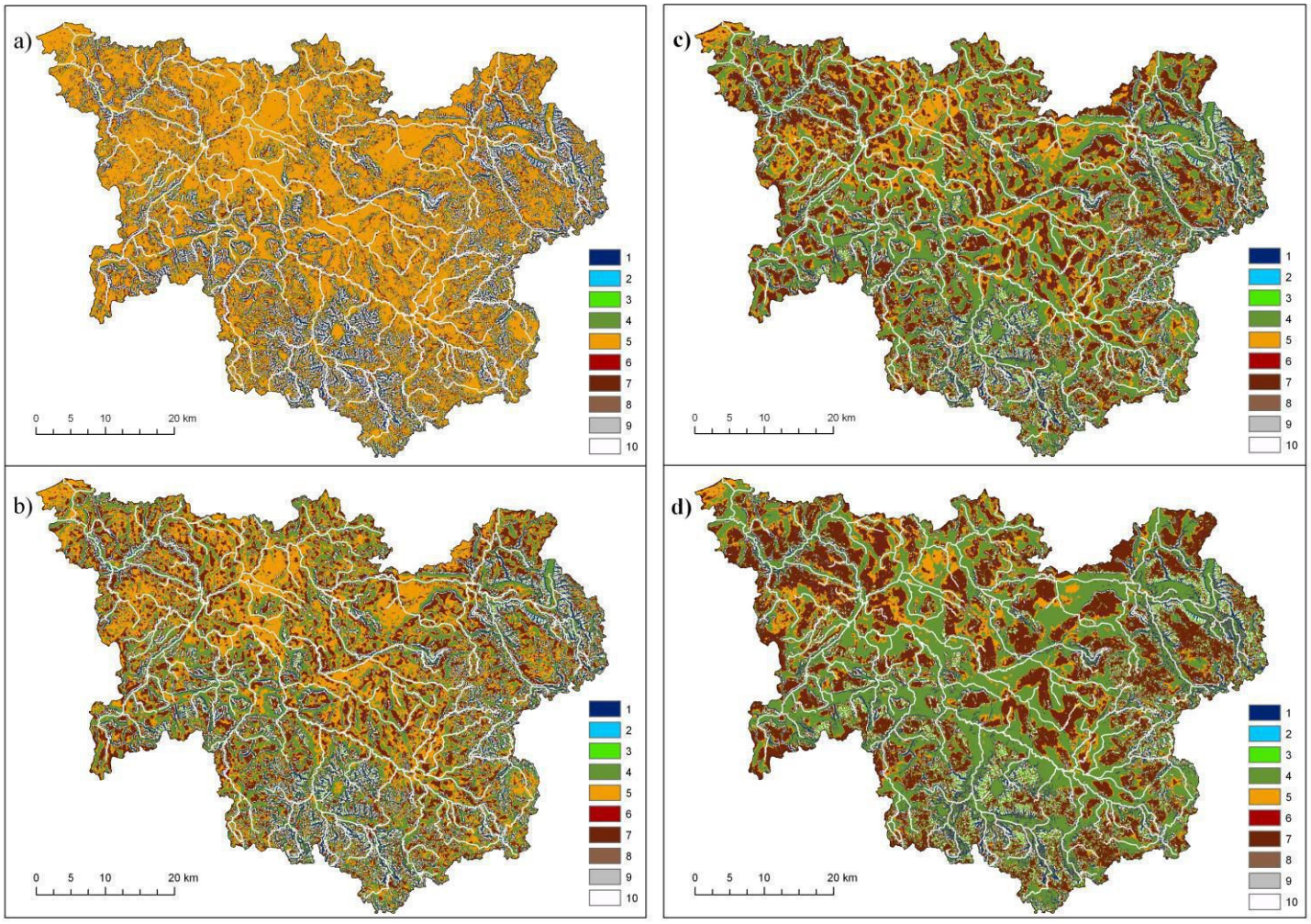


Figure 2. Landform classification for the Parsęta River drainage basin on the basis of TPI in different moving windows
a) 7 × 7 and 15 × 15 cells, b) 7 × 7 and 35 × 35 cells, c) 7 × 7 and 71 × 71 cells, d) 7 × 7 and 141 × 141 cells; 1-10 – explanation in section Methods

the dominant percentage of classes 6 – long slopes and 7 – upper parts of slopes with a contribution of class 4 – U-shaped valleys can be observed. In the Bukowińskie Foothills, when compared with the Gubałowskie Highland, an increase in the percentage of classes 1 and 10 can be noticed.

In the window pair of 9 × 9 and 45 × 45 cells (Fig. 3b), the percentage of classes 4 (25%) and 7 (25%) increased, and the percentage of class 6 (5%) decreased. In turn, change in the window pair to the size of 9 × 9 and 93 × 93 cells (Fig. 3c) caused a change in the surface area taken up by individual classes. In the last classification of landform for the windows of 9 × 9 and 189 × 189 cells (Fig. 3d), the biggest surface area is taken up by classes: 4 (31%), 7 (25%), 1 (15%), 10 (13%), 8 (8%), and 3 (7%).

V. CONCLUSIONS

The best results in the TPI calculations were obtained when a relatively small calculation window was determined. For the Parsęta River drainage basin, a window of 7 × 7 cells (217 × 217 m) proved the most suitable. Whereas for the Tatra Mountains area, a window of 9 × 9 cells (90 × 90 m) was the best. It can be judged that the more diverse the relief of the area under study, the smaller calculation window should be used. Unfortunately,

the window size must be determined using the trial-and-error method, but focus must be maintained on testing small windows.

The analysis of a classification of up to 10 relief forms allows to judge that for the Parsęta River drainage area the best results were obtained by calculating the topographic position indexes (used in the analysis) in the windows of 7 × 7 and 35 × 35 cells (Fig. 2b). In the case of the Tatra Mountains the best results were obtained for the windows of 9 × 9 and 45 × 45 cells (Fig. 3b). Thus, it can be judged that this method gives the best results with the second calculation window being approximately five times bigger than the first one. At the same time, the size of the first window should be adjusted to relief changeability in a given area and correspond approximately to the smallest landform to be distinguished.

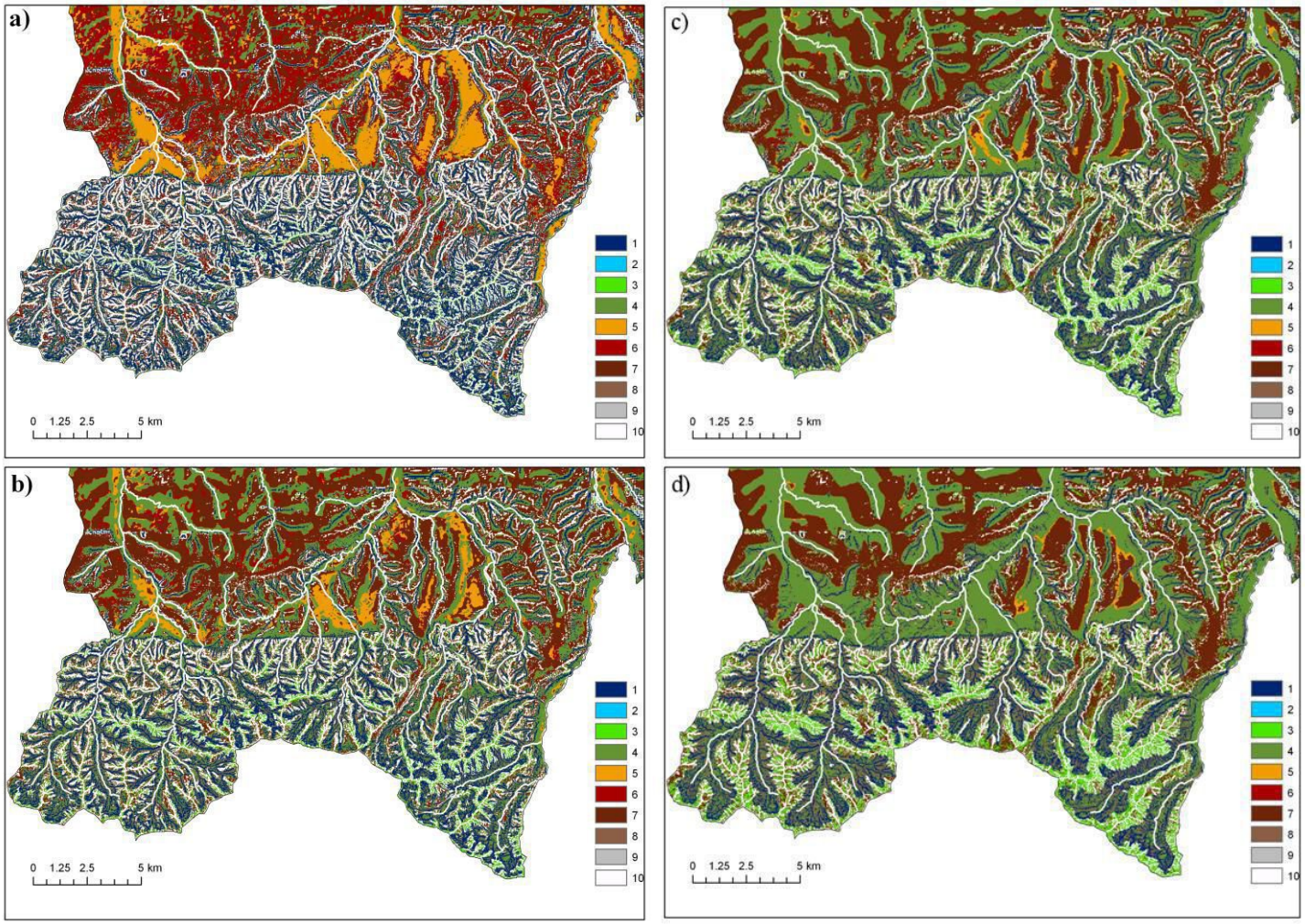


Figure 3. Landform classification for the Tatra Mountains on the basis of TPI in different moving windows
a) 9 × 9 and 21 × 21 cells, b) 9 × 9 and 45 × 45 cells, c) 9 × 9 and 93 × 93 cells, d) 9 × 9 and 189 × 189 cells; 1-10 – explanation in section Methods

REFERENCES

[1] Etzelmüller B., Romstad B., Fjellanger J., 2007. Automatic regional classification of topography in Norway. Norwegian Journal of Geology 87: 167-180.

[2] MacMillan R. A., Pettapiece W. W., Nolan S. C., Goddard T. W., 2000. A generic procedure for automatically segmenting landforms into landform elements using DEMs, heuristic rules and fuzzy logic. Fuzzy Sets and Systems 113: 81-109.

[3] Jordan G., Meijninger B.M.L., van Hinsbergen D.J.J., Meulenkamp J.E., van Dijk P.M., 2005. Extraction of morphotectonic features from DEMs: Development and applications for study areas in Hungary and NW Greece. International Journal of Applied Earth Observation and Geoinformation 7: 163–182.

[4] Saadat H., Bonnell R., Sharifi F., Mehuys G., Namdar M., Ale-Ebrahim S., 2008. Landform classification from a digital elevation model and satellite imagery. Geomorphology 100(3-4): 453-464

[5] Milevski I., 2007. Morphometric elements of terrain morphology in the Republic of Macedonia and their influence on soil erosion. International Conference: Erosion and Torrent Control as a Factor in Sustainable River Basin Management, Belgrade – Serbia, 25-28 IX 2007.

[6] Irvin B. J., Ventura S. J., Slater B. K., 1997. Fuzzy and isodata classification of landform elements from digital terrain data in Pleasant Valley, Wisconsin. Geoderma 77: 137-154.

[7] Zwoliński Zb., 1989. Geomorficzne dostosowywanie się koryta Parsęty do aktualnego reżimu rzecznego. Dokumentacja Geograficzna 3/4: 1-144.

[8] Klimaszewski M., 1988. Rzeźba Tatr Polskich. Państwowe Wydawnictwo Naukowe. Warszawa.

[9] Weiss A., 2001. Topographic Position and Landforms Analysis. Poster presentation, ESRI User Conference, San Diego.

International Society for Geomorphometry (ISG) is a non-commercial, nongovernmental association of researchers and experts, open for free exchange of knowledge and opinions about various aspects of DEM processing. The aims of the ISG are:

- To improve understanding of the properties of the land surface, as analysed quantitatively from Digital Elevation Models and from digital or paper maps;
- To advance the techniques used in land surface (terrain) analysis;
- To foster international collaboration in the quantitative analysis of the land surface;
- To run a web site (geomorphometry.org) to facilitate communication between scientists and students, advertise relevant conferences and make available public-domain data sets and scientific papers;
- To promote international conferences on geomorphometry and digital terrain analysis, initially every two years.

Traditionally Geomorphometry conference is linked to the workshops, which are designed for both young adepts of geomorphometry and those professionals who want to extend their expertise. For more info about ISG please refer to geomorphometry.org

Organisers:

Institute of Geoecology and Geoinformation
Adam Mickiewicz University in Poznań

International Society for Geomorphometry

Co-Organisers:

Association of Polish Geomorphologists

International Association of Geomorphologists' Working Group on Landform Assessment for Geodiversity

Partners:

Head Office of Geodesy and Cartography

Esri Polska

Bogucki Wydawnictwo Naukowe

ISBN 978-83-7986-059-3